UNIVERSITÀ DEGLI STUDI DI MILANO

DEPARTMENT OF PHYSICS

PHD SCHOOL IN PHYSICS, ASTROPHYSICS AND APPLIED PHYSICS
CYCLE XXXII

The role of (sub-)stellar companions on the dynamical evolution of protoplanetary discs

Disciplinary Scientific Sector FIS/05

Supervisor of the Thesis: Professor Giuseppe Lodato

Co-supervisor of the Thesis: Dr. Davide Fedele

Director of the School: Professor Matteo Paris

PhD Thesis of:
Maria Giulia Ubeira Gabellini

Anno Accademico 2019-2020

Commission of the final examination:

External Referee:
Professor Laura M. Perez, Dr. Antonio Garufi

External Member:
Professor Francois Menard, Professor Guillaume Laibe

Internal Member:
Professor Giuseppe Lodato

Final examination:

Date 16 September 2020

Universitá degli Studi di Milano, Dipartimento di Fisica, Milano, Italy

To Max and my mother
for their tireless presence

MIUR subjects:

FIS/05 - Astronomy and Astrophysics

PACS:

96.35.-j ; 97.82.-j

Contents

Preface

Moonlight (A. Martini, 1932, Antwerp)

"Pronaque cum spectent animalia cetera terram,
os homini sublime dedit caelumque videre
iussit et erectos ad sidera tollere vultus"

"While other animals look downwards at the ground,
he gave human beings an upturned aspect, commanding them
to look towards the skies, and, upright, raise their face to the stars"

(Metamorphoses, I, 84-86, Ovidio, 8 d.C.)

Protoplanetary discs and exoplanets in the high resolution era

General context and motivation

Since ancient times, human beings were fascinated by the origin of the Earth and the sky. Exploring and discovering the unknown is something intrinsic in our nature since prehistory. People started with exploring our planets and questioning about the significance of the sky full of stars. Since thousands of years before the ancient Greeks, there are many examples that can be found to prove that. The paintings in e.g., the Lascaux cave (35000 - 10000 years ago) show one of the first representation of constellations of stars that were visible at those times. The ancient Greeks developed astronomy as it is nowadays known and started to take observations of our planets and the solar system architecture. Aristotle (340 BC) gave solid evidences of the fact that the Earth is spherical and of the presence of five of the planets of our solar system. Later, Copernicus introduced the idea of a geometrical model of the solar system. The architecture of the solar system started to give the first constrains about the process of star and planet formation. Theories have been developed (starting from Swedenborg, Kant and Laplace) regarding the formation of stars from the collapse of a primordial nebula. This leads to the formation of a disc of gas and dust: the birthing place of planets. This theory was proved observationally thanks to spatially resolved discs observations of young stars in the Orion nebula cluster with HST in the '90 of the XX century.

The existence of worlds other than ours has always intrigued people in the past and speculations have been made since several centuries, starting with the attempts of Giordano Bruno (1548-1600) and Galileo (1564-1642), followed by Huygens (1698), who reported an extra-solar planet detection, and several others. Instruments, however, did not have the sensitivity to perform these detections and it was revealed that all the discoveries were false claims. This may give an idea on how the observational capabilities and techniques used to discover planets are challenging and have to be advanced. Until 1995, astronomers knew just the eight planets of our solar system. Drawing a global planet formation scenarios was not possible at that time and our system was though to be unique. A first discovery of two exoplanets orbiting around a pulsar was the one of PSR B1257+12 A and B (Wolszczan & Frail 1992; Wolszczan 1994). Nicely, few years later, an exoplanet orbiting a main sequence (MS) star (51 Peg) was detected through radial velocity technique by Mayor & Queloz (1995), opening the way to a completely novel field. Hundreds of exoplanets started to be discovered through the same technique in the following years. Since this discovery was of fundamental importance to start a completely new field in Astronomy, in 2019 Mayor & Queloz have been awarded by a Nobel price in Physics. After this period, another method became feasible thanks to the great developments in the field of high-contrast imaging (HCI, see Section 6): a direct detection of a planetary mass companion was made by Chauvin et al. (2005). At the same

time, other planets have been found through the transit method thanks to the space telescope Kepler (Borucki et al. 2004). This telescope has a high photometric sensitivity and provided so far the largest number (>2600) of confirmed exoplanets discoveries in a very specific region of the sky. A new generation space telescope is TESS, which at the same way exploits the transit method but it scans the entire sky targeting the brightest stars like ours. For this reason, this field has grown incredibly in the last few years, going in 30 years from no detection to a huge number of diverse exoplanets population in our Galaxy. The variety of exoplanets is extremely wide: just few of them have features similar to our Earth and many more are completely different.

Different planet formation theories have been developed in order to explain the diversity of planetary architectures, although each of them has uncertainties and shortcomings. It is believed that, even though the mass of protoplanetary discs is dominated by gas, the dust component of a disc plays a crucial role in providing the material, from which the solid cores required for the planet formation process are built. One of the most accredited model for giant planet formation is the "core accretion" scenario, where the first step toward planet formation is the growth of dust grains into larger and larger aggregates and eventually planetesimals (e.g., Testi et al. 2014). Another scenario proposed is the gravitational instability model which may happen at large separation and ends up in the formation of only giant planets.

We note that planets found around main sequence stars are easier to be detected since the host disc has been almost completely accreted. However, in order to shed light on planet formation, the statistics on the "mature" planets alone is not enough. We need to search for planets while they are embedded in their native disc. Observations taken around young pre-main sequence may be able to image planets while they form. The connection between planets and host discs can be key to figure out the physical mechanism responsible for the formation and evolution of both planet and discs. In most cases, however, observations typically reveal the influence of a companion on the disc morphology rather than the companion itself. Moreover, confirmed companions within an observed disc are rare. It is thus fundamental also to determine the disc structure to infer the putative companion properties. In particular, recent observations started to show also a variety of circumstellar discs structures, particularly at (sub-)millimeter wavelengths. Explaining the dynamics, radiative processes and chemical structure of these discs is not trivial due to their complexity. Multiwavelengths observations are fundamental to verify the proposed scenarios.

Observations in the (sub-)millimetre were performed for the first time thanks to instruments such as the Submillimeter Array (SMA), the Plateau de Bure Interferometer (PdBI) and the Combined Array for Research in Millimeter-wave Astronomy (CARMA). Using the Very Large Array (VLA), it became possible to observe also at cm wavelengths. Thanks to the second generation of (sub-)millimetre facilities such as the NOrthern Extended Millimeter Array (NOEMA) and the Acatama Large Millimeter Array (ALMA) it becomes feasible to spatially resolve the discs. Observations at such long wavelengths are made through the interferometry technique, which allows to produce high-resolution and high-sensitivity observations. The detection of discs in the near-infrared was opened by the Hubble Space Telescope (HST), the Subaru telescope (with the project SEEDS) and NaCo (NAos-COnica, Lenzen et al. 2003) at the Very Large Telescope (VLT). More recently, the disc and planet detection increases thanks to the capabilities offered by the new generation of purpose-built high-contrast instruments such a SPHERE (Spectro-Polarimetric High-contrast Exoplanet REsearch instrument, Beuzit et al. 2019) at the VLT or GPI Gemini Planet Imager, Macintosh et al. 2014). Moreover, in the next future, further development of this field will come through James Webb Space Telescope (JWST),

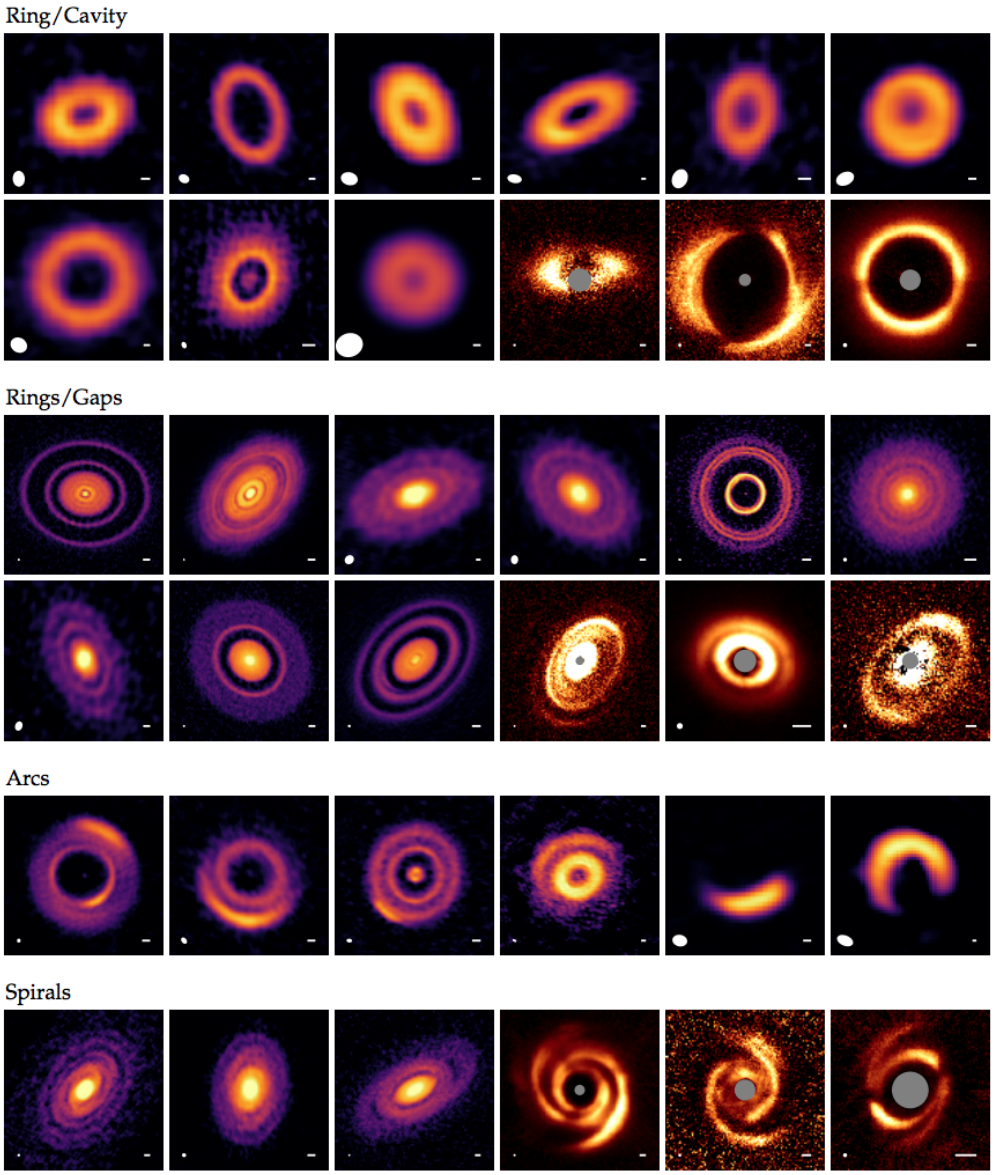

Figure 1: Gallery of images of different protoplanetary discs morphologies presented in Andrews (2020) for both ALMA (purple colors) and SPHERE (red colors). The images have different resolutions (white ellipses in the lower left) and different scaling (10 au scalebars in the lower right). On top of the SPHERE images it is shown the coronagraph in gray. The rows shows: images of Ring/Cavity (first and second rows), Rings/Gaps (third and fourth rows), Arcs (fifth row) and Spirals (sixth row). For names and reference of the images, we refer to Andrews (2020).

Extremely Large Telescope (ELT), Next Generation VLT (NG-VLT) and Square Kilometre Array (SKA), which will extend even more the observational constrain that we have now.

The new flow of data coming online in particular thanks to the e.g. ALMA and SPHERE instruments, probing gas and large/small grains distribution, started to give us constrain on the planet formation and evolution in a completely different perspective. While ALMA is more sensitive to large, millimeter-sized dust grains, observations with VLT/SPHERE are a very powerful tool to investigate the distribution of the small dust grains which are dynamical coupled to the gas. At the same time near-IR extreme adaptive optics systems (e.g. VLT/SPHERE) are able to easily detect faint (sub-)stellar companions orbiting around the pre-main sequence stars. Recent high-resolution, high sensitivity observations at near-IR and ∼mm wavelengths have revealed a plethora of substructure such as spirals (e.g., Muto et al. 2012; Pérez et al. 2016; Benisty et al. 2017; Rosotti et al. 2019a), gaps (e.g., ALMA Partnership et al. 2015; Andrews et al. 2016; Fedele et al. 2018; Pérez et al. 2019) and horseshoes (e.g., van der Marel et al. 2013; Marel et al. 2016; Cazzoletti et al. 2018) in protoplanetary discs. Some systems display many of these features together. Some examples are shown in Fig. 1 where both ALMA and SPHERE results are shown with a different color code. We refer to Andrews (2020) for names and references of all the targets shown.

The most extraordinary and, to date, unique example of a planet discovered and confirmed inside a gap is PDS 70 b (Keppler et al. 2018), detected with SPHERE. At the same time, high resolution ALMA observations similarly detected a wide transitional disc in the same system. Thus, the study of specific disc geometries (e.g., single or multiple gaps, cavities and spirals) is fundamental to link the perturbed dust and gas surface density with the presence of a companion and eventually detect it. The disc dynamics is dominated by the gas, but dust grains are crucial because they dominate the opacity budget and they mainly determine the thermal structure of the disc. Micron-sized dust grains follow the same distribution of the gas, while millimeter grains settle towards the midplane and tend to concentrate into the local pressure maxima of the gas. The origin of the sub-structures around pre main sequence stars has multiple, equally plausible explanations: disc instabilities (e.g. Regály et al. 2012; Kratter & Lodato 2016), planetary or sub-stellar companions orbiting around the central star (e.g. Ataiee et al. 2013; Ragusa et al. 2017; Dipierro et al. 2018b; Price et al. 2018a), dust growth near the snow lines (Ros & Johansen 2013; Okuzumi et al. 2016; Stammler et al. 2017), or variable illumination (Montesinos et al. 2016) due to disc self-shadowing. Some of them can be also explained through dead zones and vortices (Pinilla et al. 2016). Given the complexity of the systems considered, the synergy between theory and observations is essential. Hydrodynamical simulations including gas and dust in the presence of stellar/substellar companions are needed to constrain the properties of (unseen) companion(s). Moreover, simulations can guide observations by offering limits on the properties of the companion(s), so more targeted observations can be made to directly detect them.

Outline of the Thesis

As previously explained, in order to find clues to understand the origin of exoplanets and the Solar System, we need to observe planets while they form inside their natal protoplanetary discs. The discs that present a cavity (transitional discs) or a gap in the dust radial profile are for this reason particularly interesting. These features can, indeed, be due to the presence of a planet carving the gap/cavity. The main goal of this thesis is to combine multi wavelength observations both through ALMA and SPHERE to be able to discriminate between different formation processes in systems that show disc sub-structures. This thesis is divided in three parts:

- **Part I** provides an introduction to the research topics of this thesis. In particular, Chap. 1 describes the observational aspects of both protoplanetary discs and planets/binaries observations. We described the general framework behind the planet formation. Chapter 2 focus on the gas dynamics, dust dynamics and on the thermal structure of the disc. Chap. 3 describes the two most accredited scenarios of planet formation: core accretion and gravitational instability.

- **Part II** explores the observations of disc sub-structures with a particular focus on ALMA data in thermal continuum and, where present, in gas. Chapter 4 provides an overview of the disc geometries observed and on the most accredited formation scenarios. Some of these structures can be visible also in scattered light, thus we provided a comparison with it. Chap. 5 presents the work on a recently published paper: "A dust and gas cavity in the disc around CQ Tau revealed by ALMA" (Ubeira Gabellini et al. 2019). Discs such as CQ Tau with a clear depletion in ALMA gas and dust distributions are, indeed, of particular interest in the study of protoplanetary disc evolution and planet formation process because they tell us about gas and dust distributions independently. ALMA observations of the continuum emission and CO isotopologues were analyzed and compared with thermochemical models and hydro-dynamical simulations.

- **Part III** focus on the description of the analysis of the sample of Herbig stars imaged by SPHERE. We introduced the topic through an overview on the high contrast imaging techniques (Chap. 6). The following four Chapters describe the analysis done on a survey of 22 Herbig stars with SPHERE. In particular, Chap. 7 presents the whole survey of discs regarding a paper in preparation: "An unbiased SPHERE-IFS Survey of 22 Nearby Herbig Ae/Be Stars: Are All Group I Discs Transitional?". The aim of it is to test the model prediction of Maaskant et al. (2013, 2014) that the large near-infrared excess observed in the Spectral Energy Distributions (SEDs) of Group I Herbig Ae/Be stars can be explained by the presence of a large gap in their discs; while in Group II sources such large gaps should be not present.

  In one of the targets observed, we detected and confirmed ($\sim$ 3 yr later) the presence of a novel companion gravitationally bound to the young star MWC 297. This is discussed in Chap. 8 and presented in an ApJ Letter "Discovery of a low-mass companion embedded in the disc of the young massive star MWC 297" (Ubeira-Gabellini et al. 2020). This discovery was made in several bands and with different techniques, finding that the companion is at large separations ($\sim$245 au) and massive ($M_{comp} \sim 0.1$–$0.5\ M_{\odot}$).

  Chap. 9 describes in more detail each of the disc sub-structures showed in Chap. 7 and compares them with previous ALMA or PDI observations. We found that HD 100453, HD 100546, CQ Tau have a disc structure which resembles a spiral; HD 169142 and HD 141569 have a ring-like disc; finally, AK Sco and T Cha presents an highly inclined disc. We note that, in our sample, Group II sources present mainly thin rings with large cavities, while Group I discs have different shapes (e.g. spirals). Moreover, spirals detections are compatible with high values of scale height (see Appendix C).

  Finally, in Chap. 10, we describe the routine developed by us to improve the quality of the post-processing technique used to detect, on one side, the disc emission and, on the other, point-like sources. The difference with previous methods is that the pipeline does not just exploit the known radial variation of stellar artifacts with

wavelength, but also the information of the spectral slope of the star. This slope is, indeed, expected to be different between planets, discs and stars.

- In Chapter 11, I present my conclusions, explain future developments of this field and explain follow-ups projects to the work presented in this thesis.
- The appendix is divided into four parts: Appendix A describes in general the instruments SPHERE and ALMA; Appendix B shows the analysis on the significance of the data described in Chap. 9 and of different observing days; Appendix C presents a basic model performed with RADMC3D of the SED of the targets of Chapter 7 to give predictions on the disc emission coming from a flat or flared disc and to compare with the results of Chap. 7 and 9; Appendix D describes the literature of the targets studied in Part III.

Part I

Introduction

Concetto spaziale. Holes, oil e sand on canvas (L. Fontana, 1951, Milan)

Chapter 1

Observations of protoplanetary discs and companions

The study of extrasolar planetary systems together with their natal protoplanetary discs has become progressively more important in the last decades. It is by studying them that we can make statistical studies of the range of outcomes of the planet formation process. The reservoir of solid material that forms the building blocks of planets comes from the submicron-sized dust grains present in the original molecular cloud core.

In order to estimate the global initial conditions at the beginning of the planet formation process, we need to give constraints on the surface density distribution of dust and gas in protoplanetary discs. High angular resolution instruments start to provide us with spectacular images of discs and of the planets that they host, thus constraining the physical processes that determine their coupled evolution. Such observations often show structures that might be related to the presence of forming planets. Indeed, in the case of the presence of gaps or cavities, one of the possible scenarios for their formation is the clearing mechanism due to a young planet (e.g., Crida et al. 2006).

1.1 Star and disc formation

Stars form from the gravitational collapse of molecular clouds cores (Hoyle 1960). A molecular cloud perturbation can break the pressure equilibrium and start to gravitationally collapse. Fig. 1.1 shows some examples of protoplanetary discs formed within the Orion molecular cloud. In particular we show proplyds, which are externally ionized protoplanetary discs.

The typical size of molecular cloud cores can be estimated through the Jeans criterion: a first-order perturbation analysis of the response of the medium to small perturbations (Jeans 1902; Hartmann 2009). The typical length scale, Jeans length (λ_J), is defined as the maximum wavelength of small perturbations above which the medium is stable:

$$\lambda_{\rm J} = \frac{c_s\sqrt{\pi}}{\sqrt{G\rho_g}} \tag{1.1}$$

where G is the gravitational constant and ρ_g is the density, assuming that the medium is infinite, static and homogeneous. c_s is the sound speed, that, if the temperature is constant, can be defined as:

$$c_{\rm s}^2 \equiv \frac{\partial P}{\partial \rho} = \frac{k_{\rm B}T}{\mu m_{\rm H}} \tag{1.2}$$

where $k_{\rm B}$ is the Boltzmann constant, μ is the mean molecular weight and $m_{\rm H}$ is the mass of a Hydrogen atom. This criterion (Eq. 1.1), strongly dependent on temperature and density, sets the critical size above which initial inhomogeneities in the cloud become

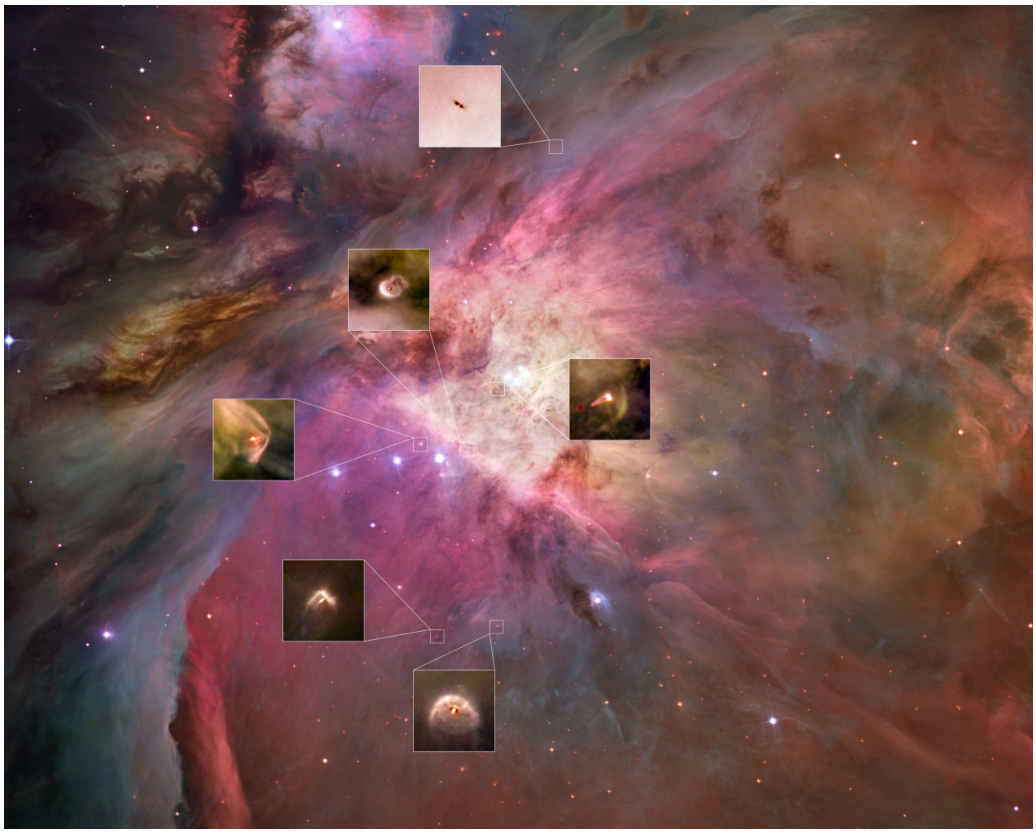

Figure 1.1: The gorgeous Orion Nebula is home to tens of what could be young planetary systems. The influence of the star produces different systems: proplyds (externally ionized protoplanetary discs) and dark silhouette against the background of the bright nebula. Brighter discs are produced by bright stars which heats up the gas in the nearby discs, whereas the ones father out do not receive as much energetic radiation from the star, so they can only be detected as a dark silhouette due to the presence of dust which absorbs background visible light. Thanks to that is is possible to to study the properties of the dust grains, forming planets. Credits: Nasa, Esa, M. Robberto.

gravitationally unstable and fragment to form protostars. A typical molecular cloud with density $\sim$ 100-1000 mol/cm^{-3} and T$\sim$10-15 K, has $\lambda_J \sim 0.4$pc. Density and temperature play an important role in setting the critical mass below which the molecular cloud collapse starts. The Jeans mass indeed is $M_{\rm J} = \rho_g c_{\rm s}^3$. This fragmentation can be enhanced by the presence of turbulence, called gravo-turbulent fragmentation formation mechanism (e.g. Hopkins 2013).

A way to distinguish between different stages of planet formation has been identified through the measure of disc accretion signatures in the optical or the distribution of warm circumstellar material in the infrared. In particular, distinct groups has been identified firstly by Lada & Wilking (1984) and formalized into 3 classes by Lada (1987) through an infrared classification (see Section 1.2). In the initial stages, a spherical infall of gas creates the central protostar (Class 0 of Fig. 1.2). The density has become sufficiently high for the gas to become opaque to infrared photons and the collapse is slowed down

to a quasi-static contraction.

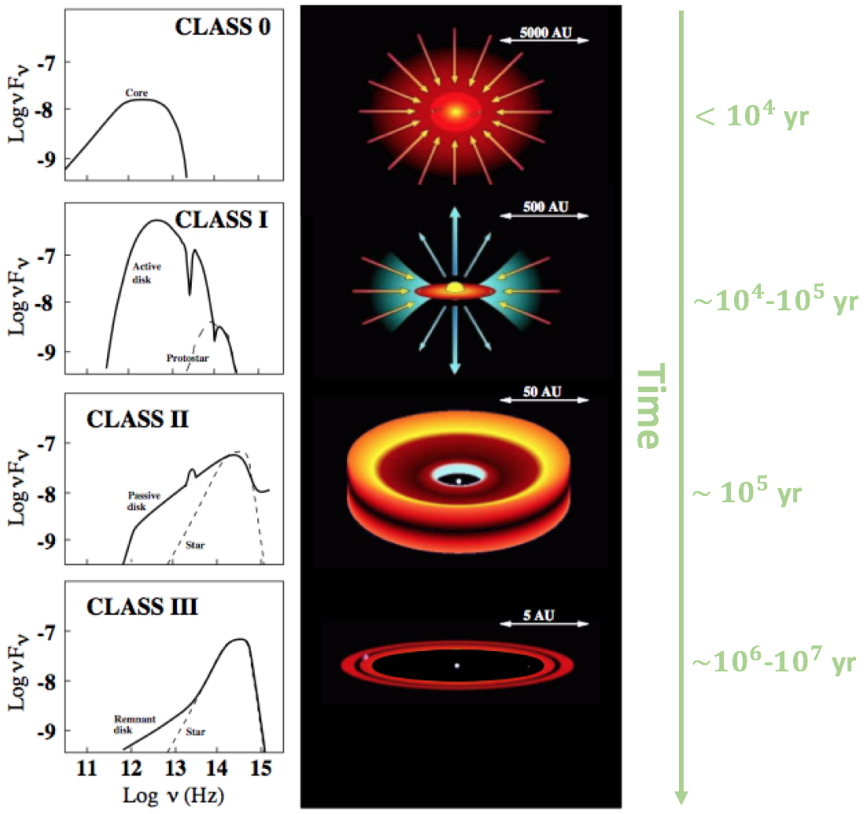

Figure 1.2: Diagram illustrating the different phases of the star and circumstellar disc formation process (left) with the expected SEDs (right). The shape of the SED corresponds to a classification of stellar objects shown (Class 0, I, II, III). Image adapted from Isella (2006).

In the absence of any rotation, the gas present in the cloud core would freely collapse into the central star and accrete onto it (Hartmann 2009). Molecular clouds, however, do rotate and angular momentum plays a key role in the formation and evolution of a disc. The collapse of a rotating gaseous cloud leads to the formation of a circumstellar disc with size of the order of hundreds of au in a typical time of $\sim 10^4$ yrs. The envelope accretes for approximately $\sim 10^5$ yrs onto the forming disc, whose features are dependent on the angular momentum content of the molecular cloud core inside which the star forms (Terebey et al. 1984; Shu et al. 1987). At the same time, outflows can remove angular momentum in this stage of evolution (e.g., Pudritz & Ray 2019). Importantly, once the disc is formed, it continues to accrete onto the central protostar while the angular momentum is redistributed thanks to the accretion process or removed from the system through jets and outflows. This is the 'main infall phase' and it is the transition between Class 0 and Class I object. It is worth remarking that at this evolutionary stage the circumstellar discs could be massive enough to be self-gravitating (see Chapter 3), thanks to the mass loading of the infalling material from the surrounding envelope. In these early stages we refer to it as 'protostellar disc'. The systems so formed can be identified as class I young stellar objects (YSOs) as shown in Fig. 1.2. Some of these class I objects,

FU Orionis stars (Reipurth 1990), have episodic accretion burst visible as short-lived luminosity brightening. During the accretion outbursts, the accretion rate may increases from 10^{-7} $M_\odot$/yr to 10^{-4} $M_\odot$/yr and the luminosity increases by a factor of 10 - 15 (Elbakyan et al. 2018). The outbursts may last for a period of several decades.

When the infall of material from the molecular cloud ceases ($\sim 10^5$ yr), the system is characterized by a circumstellar disc accreting onto the central Pre-Main Sequence (PMS) star. These discs are considered to be the birth place of planets and thus they are also called 'protoplanetary discs'. At this stage (0.5 - 1 Myr), most of the disc material has been accreted on the star. This stage corresponds to the Class II phase. Historically Class II PMS stars have been classified in two main groups: T-Tauri stars and Herbig Ae/Be stars. T-Tauri are solar analogs with strong magnetic fields, violent stellar activity, X-ray radiation and intense FUV (Bertout 1989). They might be considered as low-mass pre-main sequence stars (Walker 1956). Herbig stars are, instead, defined as the stars with spectral type A or B, with emission lines, infrared excess due to hot or/and cool circumstellar dust and with luminosity class from III to V (Waters & Waelkens 1998). Their magnetic fields are weaker and also their non-convective envelope imply a quieter stellar activity (Waters & Waelkens 1998).

Emission lines spanning from UV to IR wavelengths can be used as accretion diagnostics to estimate typical accretion rates of low-mass objects (see Section 1.3.5). H_α width at 10% of peak intensity is considered a tracer of accretion just for T Tauri (Mendigutía 2013). Another accretion diagnostic is to detect an excess emission in the Balmer continuum, where photospheric and chromospheric emission of the stars is very small. In particular most stars show clearly the Balmer Jump at the Balmer edge, which is defined as the ratio of observed emission (photospheric plus accretion) at $\lambda = 360$ nm divided by the one at $\lambda = 400$ nm. Even if less prominent excess, also the accretion continuum emission in the Paschen continuum (346 nm $< \lambda <$ 820 nm) may be used. Mass accretion rates typically range between 10^{-9} and 10^{-12} $M_\odot$/yr for T-Tauri stars and 10^{-6} and 10^{-9} $M_\odot$/yr for Herbig stars (Natta et al. 2006). Inside this class of protoplanetary discs an important place is taken by the 'Transitional discs'. They were first identified by the Infrared Astronomy Satellite (IRAS) as objects with a large depletion in opacity in the Near-Infrared (NIR) (Wolk & Walter 1996), interpreted as related to inner disc clearing mechanisms. In particular objects with no detectable near-infrared excess have been called "classical" transition discs (Muzerolle et al. 2010), interpreted as objects with sharp, but empty inner holes; whereas the ones with a small infrared excess, and thus a less deep gap, have been called "pre-transition" discs (Espaillat et al. 2007; Espaillat et al. 2010). It is not clear whether they are in a transition phase or not.

When most of the material coming from the disc has been accreted leaving a residual debris disc composed mostly of solids the object is in the Class III. In this stage, the disc component is called planetary "debris" disc because the small left-over mass is through to be second generation dust, formed after the collision of larger bodies.

1.2 Spectral Energy Distribution

The Spectral Energy Distribution (SED) indicates how the energy, produced both from the stellar blackbody and internal stress, is distributed over frequencies after being processed through the disc or envelope material. In this regards, it is important to define the "IR excess" as an excess of the stellar infrared emission with respect to the black-body spectrum expected when considering a stellar effective temperature. In the following, we will describe how the SED can be used both to distinguish between the different classes previously described or to derive disc structure properties for pre-main sequence stars.

1.2.1 Infrared classification of young stellar objects

The different stages of the star formation process can be observed through the analysis of the SED. This classification is based on the measure of the spectral index (s) of the emitted flux (F_λ) in the wavelength range of 2 μm$< \lambda <$ 100μm (Lada 1987; André 2002; Armitage 2010), defined as:

$$s = \frac{\partial log(F\lambda)}{\partial log\lambda} \tag{1.3}$$

Fig. 1.2 shows how different the SEDs are in the different stages of star formation. In red and yellow the different SED contribution are shown. For Class 0, the sources are young and the predominant emission comes from millimeter wavelengths. Optical emission lines are indeed obscured by the collapsing envelope and the IR emission is not present because the dust in the envelope is too cold (T $\sim$ 30 - 50K). Class I targets are visible in the near-infrared with a rising SED toward far-IR wavelengths, while the optical source is heavily embedded and, typically, not visible.

The "infrared-excess" emission is typically due to the reprocessing of stellar radiation by the circumstellar dust (Hartmann 2009). The dust present in the discs absorbs energy from the central star at short wavelengths, comparable to dust grain size, and then re-emits it at far-infrared wavelengths. The envelope at such wavelengths is sufficiently optically thin that the radiation can escape. For both these classes the spectral index increases with wavelength ($s >$0). When the emission produced from a dusty disc is optically thick in the infrared and optically thin at the millimeter wavelengths, we have instead a Class II object. Its spectral index is typically $-4/3 \lesssim s \lesssim 0$. In these systems their emission lines can trace accretion onto the central star and strong IR/sub-mm excess can be present. The star is usually visible at optical wavelengths and many show emission lines. Finally, the SEDs of Class III objects present very weak infrared excess, weak emission lines, they are optically visible and they are consistent with a reddened stellar photosphere. The spectral index is $\sim$ -3, typical of a single blackbody. These objects corresponds to optically thin accretion discs.

1.2.2 SED of a pre-main sequence star

If we consider the SED of a pre-main sequence star, it contains information both about the star properties (in the optical / near-IR) and the disc properties. Each part of the SED show a different contribution to the SED of a PMS star for what regards the temperature, the surface density structure and optical properties of dust (Fig. 1.3). The emission can be divided in five main contributions (Fig. 1.3):

- Ultraviolet and optical wavelengths are dominated by the PMS emission. The stellar properties can be derived though a fit of this contribution with a black body spectrum (see Chapter 8 and Appendix C).

- Thermal emission coming from the hottest dust next to the star dominates the near-infrared region. The dust sublimation temperature is typically in the range of $\sim$1000 - 2000 K. The disc is optically thick at these wavelengths, thus its emission is directly related to the temperature and the area of the emitting region. At these wavelengths, scattering plays an important role and can be used to infer structural properties of disc.

- The emission coming from silicates is typical in the mid-infrared part of the SED and can provide us important evidences about the optical and physical properties

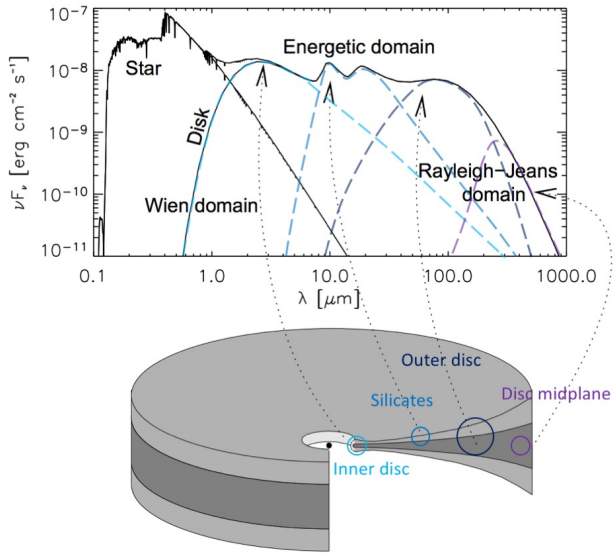

Figure 1.3: Scheme of a Spectral Energy Distribution showing the different contributions playing a role. In yellow it is shown the stellar emission, in red and blue the inner and outer disc contribution and finally, in purple, the thermal emission coming from the midplane. Image adapted from Dullemond et al. (2006).

of dust grains (composition, porosity, shape, size). The size and shape in particular can tell us at which step the grain growth is.

- The far-infrared part of the SED probes the thermal emission of dust grains at the disc surface at a few tens of au radial scale. The emission (typically optically thick) can be used to infer the temperature radial profile. This can tell us also important information about the disc structure such as the flaring angle (see Sec. 2.4 for the definition) and the scale height.

- The sub-mm wavelengths are, in general, optically thin and the emission is a probe of the dust temperature, density and opacity, related to the grain properties, particularly in the disc midplane.

The thermal emission traces colder (warmer) material at longer (shorter) wavelengths, if we assume the disc to be in thermodynamical equilibrium (Rybicki & Lightman 1979). Warm material is expected to be closer to the star and, thus, the SEDs offers a wavelength to radius map tracing different radial region of the disc at different wavelengths (Dullemond et al. 2007). The SED was extensively used to characterize the structure of circumstellar discs before the advent of high resolution imager and interferometer able to spatially resolve the disc. Disc models based just on the SED fitting are highly uncertain because the emission considered comes from the whole disc. On one side, multi-wavelength data help to break some degeneracies (e.g., between temperature, surface density, dust properties), on the other side many other parameters remain still degenerate. Now, this information can be combined with resolved disc structures to gain insight on the grain growth process and dust and gas dynamics to break some structural degeneracies.

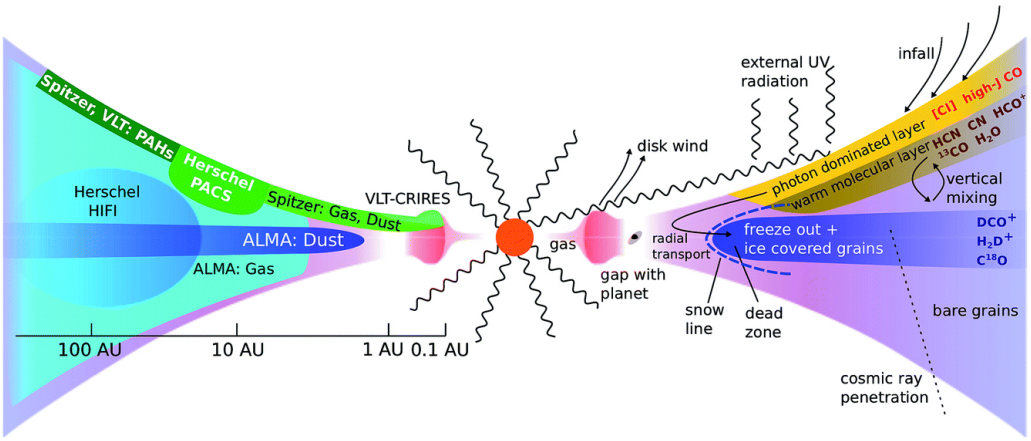

Figure 1.4: Diagram taken from van Dishoeck (2014), showing on the right the physical mechanism playing a role in a gaseous protoplanetary disc and on the left the different instruments able to probe the gas distribution in the different regions.

1.3 Protoplanetary disc properties

Protoplanetary discs are gas-, dust-rich discs, coming out from the star formation process. In the following we will describe their properties and spatial distribution.

1.3.1 Composition and chemistry

Protoplanetary discs are expected to be composed by gas ($\sim$ 99% in mass) and dust ($\sim$ 1%) (Goldsmith et al. 1997; Bergin & Williams 2018). The gas is primary composed by H_2 and then by He. Together with oxygen, carbon and nitrogen they form most of the ices (e.g. water ice, CH_4, NH_3, CO and its isotopologues). Different compounds have different condensation temperature (T_{cond}): the ones defined as volatiles have a T_{cond} between 10 and 200 K; iron, nickel metallic alloys and silicates have 200 $<T_{cond} <$ 1500K and are fundamental for rocky cores; and, finally, the refractory materials (e.g. calcium oxyde and aluminium) have $T_{cond} >$ 1500K. A synthetic scheme of the gas distribution is presented in Fig. 1.4. Snow lines are defined as the radius where a molecule modify its phase: from the gas phase to being frozen out (van Dishoeck 2014). The cartoon shows at which disc radii the snow lines are present in the disc. The presence of snow lines allows coating of grains with water ice and facilitate the coagulation of grains and eventually planet formation. Different species have different snow line positions in view of their binding energy leading to a selective freeze-out. Furthermore, at large radii the stellar UV/X-rays photo-dissociate and photo-ionize molecules close to the surface.

The dust plays an important role making the protoplanetary discs optically thick at most wavelengths. A schematic image of the dust grains distribution is presented in Fig. 1.5. The micron-size dust grains follow the gas distribution and trace the upper layers structure. Their effect is twofold: they mainly reprocess part of the incoming stellar light and partially scatter it. The effect is to shield the disc midplane from radiation and to heat the layers below the surface. The stellar emission is not able to reach the midplane which remains cold ($\sim$10 - 20 K). This allows gas volatiles to freeze-out onto the grains and to have interactions between grains and gas on the surface.

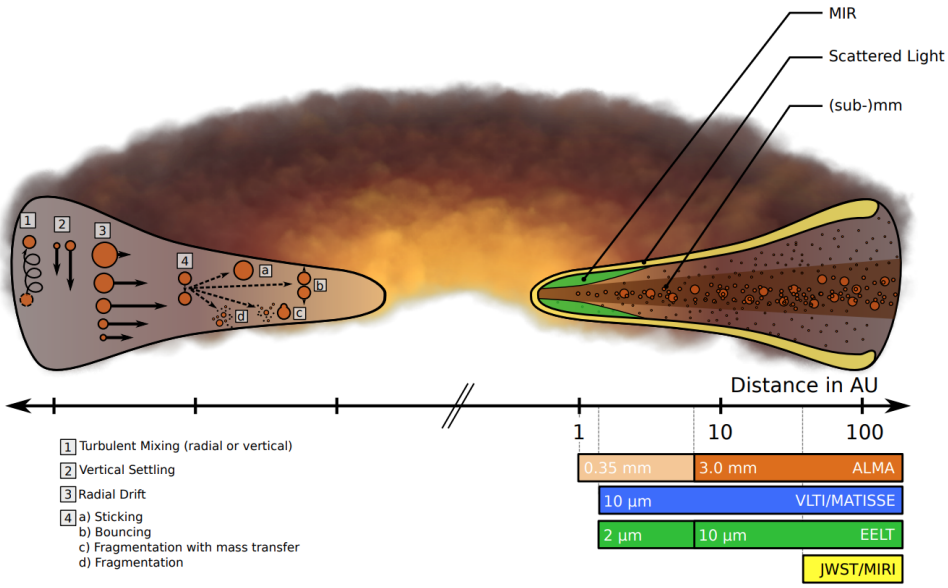

Figure 1.5: Diagram taken from Testi et al. (2014), showing the dust settling toward the midplane (right), the different processes involved (left). Observations probe the surface distribution with scattered light, the inner disc with MIR and the disc midplane at sub-mm wavelengths.

1.3.2 Radial profiles and disc extension

The disc radius was estimated for the first time using the silhouette images of discs obtained with HST in Orion (Fig. 1.1) finding a large dispersion in size. Other studies successively showed an even larger dispersion ranging from 10 to 1000 au (e.g. Hughes et al. 2008; Andrews et al. 2009; Isella et al. 2009; Andrews et al. 2010). Initially, it was not clear whether there was a correlation between the disc size from sub-mm observations and the stellar properties. The size of the disc through gas (CO line) observations appeared to be larger than in the sub-mm continuum observations (Andrews et al. 2012; Walsh et al. 2014; Canovas et al. 2016) by an average factor of two (Ansdell et al. 2018, see Fig. 1.6). Birnstiel & Andrews (2014a) gave two possible explanations to the different radial extent between gas and dust. The first one regards an optical depth effect (Dutrey et al. 1998; Guilloteau et al. 1999): while the ^{12}CO emission (tracing the gas) is optically thick, the continuum emission is optically thin; for this reason it is simpler to detect small amounts of material at large radii in the gas with respect to what happens for the dust. The second option is related to the presence of dust growth and inward drift (e.g., Dutrey et al. 1996; Birnstiel & Andrews 2014a; Weidenschilling 1977). A combination of both grain growth and optical depth effect is possibly the reason behind it (e.g., Ansdell et al. 2018, Trapman et al. 2020). Moreover, the continuum emission of the disc appears to be more extended for submillimetre dust grains with respect to larger grains which instead are distributed closer to the central star (see Pérez et al. 2012, 2015; Guidi et al. 2016). This confirms that dust processing and size-sorted radial migration may take place.

The gas density profile can be described in general by a power law plus exponential

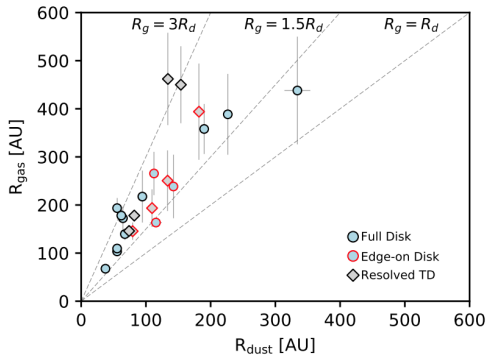

Figure 1.6: We show that the gas disc radii is a factor two larger than the dust radii (Fig. taken from Ansdell et al. 2018). The plot is done for a sub-sample of 22 discs in the Lupus star forming region observed with ALMA.

tail (e.g., Andrews et al. 2009; Pérez et al. 2012) and parameterized as following:

$$\Sigma_{\rm gas} = \Sigma_{\rm c} \left(\frac{R}{R_{\rm c}}\right)^{-\gamma} \exp\left[-\left(\frac{R}{R_{\rm c}}\right)^{2-\gamma}\right] \tag{1.4}$$

where $\Sigma_{\rm c}$ is set by the dust mass and it is relative to the value of the dust profile at the critical radius $R_{\rm c}$. The value of γ defines how steep the profile is. We underline how important it is to constrain the disc radii in both gas and dust first of all because the bulk of the disc mass is at large radii, secondly because if the disc evolves viscously the outer disc radius determines the evolution timescale, and finally because it gives us constrains on the importance of environmental effects such as stellar feedback.

It is important to diagnose whether discs undergo viscous spreading, driven by viscosity or angular momentum removal by winds. As underlined above, large dust drift inwards; however, the dusty disc size generally increases with time similarly to the one of gas. This is due to the fact that, even if most of the dust initially grows and drifts rapidly onto the star, the residual part follows the gas. The prediction of viscous models that dust flux radius increases with time, however, can be observed just with long ALMA integration times and when measuring a relatively high fraction of the disc flux ($\sim 95\%$) (Rosotti et al. 2019b). The value typically considered is, instead, 68 per cent of the disc flux that traces large grains and not the physical extent of the disc (e.g., Rosotti et al. 2019b). This happens because the dust grains in the outer disc are small and with low sub-mm opacity. Population surveys, however, do not have enough resolution to trace the mass radius or the sharp outer edge in the dust distribution. They just trace the outer limit of where the grains have significant sub-mm opacity, which is observed to be shrinking with time (Rosotti et al. 2019b).

1.3.3 Vertical profiles

The vertical height in protoplanetary discs cannot be ignored. In particular, there is a marked separation between radial and vertical motion of solids (Laibe 2014): dust settles vertically much faster than typical radial drift. Gas and dust are affected by settling in different ways. Dust grains settle depending on their size: large grains settle to the midplane, while small grains well coupled with the gas do it on a longer timescale (see

Section 2.1.2). The gaseous discs are typically flared, which means that their vertical scale height to radius (z/r) increases linearly with radius. For flat discs, instead, z/r is constant. The degree of flaring angle and its difference from a flat disc geometry can be studied through the SED in the near- and far-infrared regime. In such a way, it is possible to probe small grains distribution, well coupled to the gas in the inner and intermediate disc regions, tracing the full vertical extent of the gas disc. The flaring angle is, in general, highly degenerate with the value of the scale height of the disc $H(r)$. The vertical structure is produced by a equilibrium between the vertical component of stellar gravity and the disc thermal pressure. The first tends to make the disc thinner, the second thicker. The disc thickness can be estimated through measurements of the temperature in the disc. A typical disc has in general a disc aspect ratio of $H/R \sim 0.1$. Moreover, we note that in the innermost part of the disc, typically there is a puffed-up inner rim (see Fig. 1.4). This is produced by the high energy photons hitting the disc.

Thanks to the IRAS, it was found that there is more infrared emission than what expected for a flat disk geometry and thus that the discs may be flared Kenyon & Hartmann (1987). Direct evidences of the presence of flared discs was found by Hubble in the dark silhouettes of discs in the Taurus (Burrows et al. 1996) or Orion (Smith et al. 2005) regions.

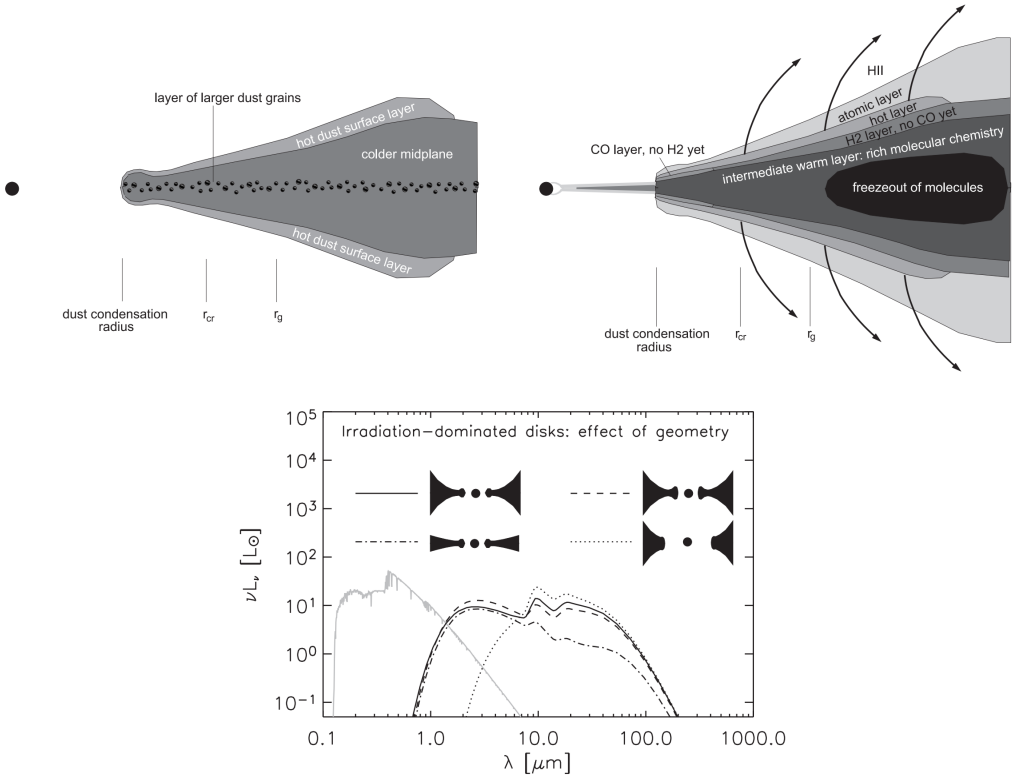

Figure 1.7: Figure adapted from Dullemond et al. (2006), showing the structure of a flaring protoplanetary disc, in dust (left) and gas (right). On the bottom, a scheme presenting how the Spectral Energy Distribution should change with different disc geometries, from flat to flared, with a cavity or a typical of puffed up inner rim.

1.3.4 Mass

One of the still open problems in understanding the disc and planet formation and evolution is the measurement of the total disc mass. The total disc mass is composed by gas (up to 99% initially sourced from the interstellar medium) and by dust for the remaining part (Bohlin et al. 1978). The two species undergo a different dynamical and chemical process during the disc lifetime. The main constituent of the gas is H_2 which is very difficult to measure due to its weak emission: it has only quadrupoles transitions in the infrared and most of the gas is not warm enough to excite those transitions. To measure the disc mass it is thus necessarily to find another constituent that can trace the disc spatial distribution and mass more concentrated in the midplane. As described in de Gregorio-Monsalvo et al. (2013), dust and gas do not spatially coexist in protoplanetary discs. The most extensively used method to infer the disc mass is to measure the mass of the dust component measured at (sub-)millimetre (continuum) wavelengths where emission is optically thin. Another possibility is to estimate the gas mass using molecular line observations of less abundant chemical species, such as HD or carbon monoxide (CO) and its isotopologues. The uncertainties arise from the chemical abundances with respect to H_2 and the dust-to-gas ratio assumed. Strong indeed are the indications of variation of the dust-to-gas ratio and in the efficiency of grain growth processes across the whole disc. Consequently this leads to a variation of the optical properties of dust grains which affects the mass derivation. Below we will describe briefly the two techniques mostly used to derive the disc mass.

Derivation of the total mass through the (sub-)millimeter emission flux

The mass of a circumstellar disc is typically derived from the measurement of the dust component of the disc through observations in the (sub-)millimeter. The emission is mostly optically thin at these wavelengths and the flux can be used as a tracer for the mass of the dust in the disc. Let us consider a vertically isothermal disc in thermal equilibrium. The distance from the observer is d and the angle i is the inclination with respect to the line of sight of the observer. The total flux at frequency ν is:

$$F_\nu = \frac{2\pi \cos\ i}{d^2} \int_{R_{\rm in}}^{R_{\rm out}} B_\nu(T(R)) \left[1 - \exp\left(\frac{-\tau_\nu}{\cos i}\right)\right] R\ {\rm dR} \tag{1.5}$$

where $R_{\rm in}$ and $R_{\rm out}$ are the inner and outer radius of the disc, B_ν and τ_ν are respectively the surface brightness and the optical depth at frequency ν. The optical depth τ_ν can be directly derived from the opacity κ_ν as

$$\tau_\nu = \Sigma_{\rm d} \kappa_\nu \tag{1.6}$$

Here we make the assumption that the dust opacity is invariant with the line of sight perpendicular to the plane of the disc and that the optical depth is dominated by the optically thin dust fraction. Since the dust is optically thin at millimeter wavelengths, we can approximate:

$$1 - \exp\left(\frac{-\tau_\nu}{\cos\ i}\right) \sim \frac{\kappa_\nu \Sigma_{\rm d}}{\cos\ i}. \tag{1.7}$$

From the dust surface density ($\Sigma_{\rm d}$), assuming a dust-to-gas ratio $\epsilon = 0.01$ (as for the interstellar medium, see Bohlin et al. 1978), we can derive the gas surface density $\Sigma_{\rm g}$=$\Sigma_{\rm d}/\epsilon$). We can make use of the Rayleigh-Jeans approximation for the Planck's law: $B_\nu = 2\nu^2 k_B T/c^2$, considering that we are in the long wavelengths regime. Let us assume that

the temperature and surface density profile can be parameterized as: $T(R) \sim T_0(R/R_0)^{-q}$ and $\Sigma_{\rm g}(R) \sim \Sigma_{\rm g,0}(R/R_0)^{-p}$, where $\Sigma_{\rm g,0}$ and T_0 are the values at some reference radius R_0. Using these assumption, we can integrate Eq. 1.5 and obtain F_ν:

$$F_\nu = \frac{2k_B\kappa_\nu\nu^2\epsilon}{d^2c^2} M_{\rm disc} T \left(\frac{R_{\rm out}}{R_0}\right)\left(\frac{2-p}{2-p-q}\right), \tag{1.8}$$

where the disc mass

$$M_{\rm disc} = \frac{2\pi\Sigma_{g,0}R_0^2}{2-p}\left(\frac{R_{\rm out}}{R_0}\right)^{2-p}. \tag{1.9}$$

The value κ_ν can be estimated through an opacity prescription for the dust (e.g. Beckwith et al. 1990):

$$\kappa_\nu = \kappa_0 \left(\frac{\nu}{10^{12}{\rm Hz}}\right)^\beta {\rm cm^2 g^{-1}} \tag{1.10}$$

where $\kappa_0 = 0.1$ and β is a power law index typically $\sim$1 for protoplanetary discs. Note that κ_0 and β depend on dust properties such as grain size, composition and porosity.

From equation 1.8 is thus possible to derive the disc mass from the observed flux in the (sub-)millimetre waveband. This estimate of the total disc mass suffers from large uncertainties that we summarize below:

- This derivation makes use of the assumption of optically thin emission in the Rayleigh-Jeans limit. This is known not to be valid in the inner part of the disc ($R < 10$ au), thus we probably miss a significant fraction of the total mass.

- Emission of bodies larger than $\sim$cm are not traced through millimeter observations, since their opacities are low in this wavelength regime. A significant mass can be hidden in grains of these sizes.

- The dust opacity depends on the gas-to-dust ratio considered. In the case of the opacity prescription in Eq. 1.10, it assumes a fiducial interstellar gas-to-dust ratio of 100. This, however, is not always constant through the disc and might evolve over time, since dust and gas components are characterized by different dynamics and evolutionary timescales.

- The dust opacity depends also on the grain sizes, which can be larger than the ones of the ISM. Grains are composed by larger grain size would correspond to a lower opacity and an increase of the inferred disc mass. Moreover, it is valid for grain sizes up to a maximum size $a_{\rm max} \sim 3$mm (e.g. Draine 2006). For many discs, however, the grain size are larger than this value with a consequent lower contribution of large grains in the mass derivation. The result is thus uncertain because strongly dependent on the amount of larger grains and the opacity to be considered.

- Another critical issue in the mass derivation above described is the assumption of no scattering opacity at long wavelengths. The work by Sierra & Lizano (2020) has discussed this issue, addressing the difference between the spectral indices and the SED as a function of albedo and optical depth. In particular, if scattering effects are considered, there is a decrease of the expected emission at optically thick millimeter wavelengths. This has the consequence to have disc masses of about one order of magnitude higher than the one derived though models with pure absorption (Zhu et al. 2019).

For this reason, the mass derived in this way is generally a lower limit of the total dust mass and can be better called (sub-)millimetre dust mass. We note that dust disc mass measurements on protoplanetary disc were recently performed through ALMA surveys of populations. These surveys show that young protoplanetary disc (e.g. Lupus, Ansdell et al. 2016; Chamaeleon I, Pascucci et al. 2016) present higher dust disc mass with respect to the mass of the intermediate-aged and evolved populations (e.g. σ Orionis cluster, Ansdell et al. 2017; Upper Sco association, Barenfeld et al. 2016), showing thus a trend with age (see Fig. 1.8). Moreover, Powell et al. (2019) measured dust masses from

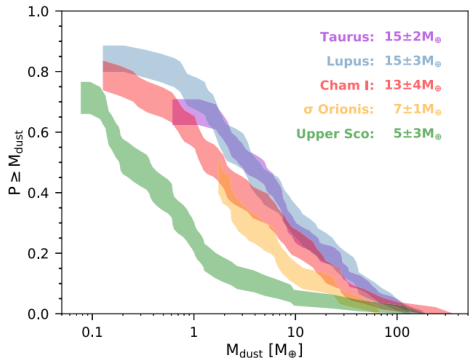

Figure 1.8: The cumulative distributions of gas mass in different star forming regions, showing how the disc mass decreases with age (Figure taken from Ansdell et al. 2017).

multi-wavelength observations. They derived a novel method to determine the location of dust lines by modeling the interferometric visibilities at multiple wavelengths. The method exploits the different disc radial extents at different wavelengths, considering the grain growth, radial drift and systems age to derive the disc surface density profile. The resulting disc mass is larger that the one estimated from integrated optically thin dust emission. It was also shown that dust is a more robust tracer of total disc mass than CO.

Disc mass from CO isotopologues emission

As mentioned above, considering that H_2 cannot be used in the study of the gas component, a possibility is to use HD, the closest chemical counterpart of H_2. Bergin et al. (2013) and McClure et al. (2016) detected HD emission in a few protoplanetary discs with the Hershel Space Observatory: TW Hydra, DM Tau and GM Aur. These studies suggest that the discs are more massive than what derived with other techniques. However, currently, there are no far-infrared telescopes able to observe HD low-J transition at 112 μm (J = 1 - 0) and 56 μm (J = 2 - 1) and it is not possible to further use this technique to measure the disc masses. The second most abundant molecule after H_2, CO, has observable rotational lines emission at millimeter (mm-)wavelengths routinely observed in discs with a high signal-to-noise ratio (e.g., Dent et al. 2005). Through molecular lines observations it is, then, possible to infer the gas mass independently from the dust content. CO lines have optically thick emission, so it is not possible to derive the mass directly from CO. The less abundant CO isotopologues (^{13}CO, C^{18}O, C^{17}O, ^{13}C^{18}O) have line emission optically thinner than that of ^{12}CO. In particular, C^{18}O, depending on the actual mass, may trace the gas content down to the midplane.

It is important to consider in this regards that the overall abundance of C and O seems to be under abundant in discs with respect to the ISM (e.g., Yu et al. 2017;

Molyarova et al. 2017) and this changes the ^{12}CO-to-H_2 conversion. This conversion seems to underestimate the mass reservoir with respect to measurements with e.g. HD. Moreover, isotope selective photodissociation processes may alter the conversion from e.g., C^{18}O to ^{12}CO and between all the other isotopologues (e.g., Pérez et al. 2015; Miotello et al. 2014, 2016). Two processes are responsible for the decrease of the isotopologue abundance: freeze-out in the midplane and ultraviolet photo-dissociation close to the surface (e.g., Visser et al. 2009; Williams & Best 2014; Miotello et al. 2014; Woitke et al. 2016). The first consists in the condensation from the gas phase with a consequent freezing onto dust grains. This phenomenon is expected to lock a significant fraction of CO on grains in the midplane (Tielens et al. 1991; Qi et al. 2013, 2015), particularly in the cold ($\sim$20 K) outer part of the disc. The exact value depends on the specific disc properties. Photodissociation, instead, is an isotope-selective process that regulates the abundance of gas phase CO in the emitting layer of discs. CO photodissociation is, indeed, controlled by line processes subject to self-shielding (van Dishoeck & Black 1988). For a CO column density threshold, the UV absorption lines can saturate (become optically thick) and the photodissociation rate decreases sharply with the effect of preserving molecules in the interior of the disc (Bruderer 2013). Considering that the abundances of isotopologues are different, less abundant isotopologues self-shield deeper into the disc (Miotello et al. 2014) and can remain photodissociated (Visser et al. 2009). This makes photodissociation an isotope-selective process that has to be taken into account in order to properly derive the total disc mass. Photo-dissociation and freeze-out processes are functions of space and time and thus high is the uncertainty in converting their flux to the one of H_2. Few studies start to show that using CO tracers the disc mass is underestimated (see e.g. Ansdell et al. 2016; Miotello et al. 2017; Ubeira Gabellini et al. 2019). Ansdell et al. (2016) found that the gas mass derived in most Lupus discs is lower than a Jupiter mass, which is lower than the disc masses inferred from HD detection (reported above) and a gas-to-dust ratio lower than in the ISM. This leads to two hypotheses, the first is that at the time of the observations the giant planet formation was already largely complete, the second is that there is some chemical reaction not still properly understood and considered, like a carbon depletion by up to two orders of magnitude. According to a work done by Manara et al. (2016) millimetre-sized dust mass may better traces the total disc mass with respect to CO line emission considering the many uncertainties in the gas mass derivation.

1.3.5 Mass accretion rate

One of the most important process is the accretion of mass from the disc to the star. The instrument VLT/X-Shooter is a high resolution spectrograph able to produce high quality spectra from which it is possible to derive host star properties such as the accretion rate onto the star. Accretion rates are generally measured from (a) the strength of the hydrogen recombination lines; (b) the veiling of photospheric lines due to accretion shocks. The first method is related to the fact that the stellar magnetic field truncates the innermost part of the disc and the gas falls almost freely onto the star along magnetic field lines. This allows to measure e.g., Hα emission, emitted during the 'magneto-spheric accretion' phase. The second method is related to an excess continuum in the UV which allows a measure of depletion in the absorption lines intensity.

It was found a correlation between the accretion properties (e.g. mass accretion rate) and the respective stellar mass for objects in regions with different ages (e.g., ρ-Ophiuncus, Manara et al. 2015; Lupus, Alcalá et al. 2014; σ-Ori, Rigliaco et al. 2012), in particular considering the diagrams L_{acc}-$L_\star$ and $\dot{M}_{acc}$-$M_\star$. Successively, Manara et al. (2017) derived the mass accretion rate in the Chamaeleon I star-forming region. They found a correlation

between accretion luminosity and stellar luminosity, with a steeper relation under a certain threshold, more compatible with a broken power-law fit. For lower mass stars, the steeper relation can be interpreted both as a faster evolution in the past or with different accretion regimes in different stellar mass ranges. Finally, the authors found two regions in this plane empty of objects. In particular, the one relative to low stellar masses, just above the observational limits imposed by chromospheric emission ($\sim$0.3 - 0.4$M_\odot$), are in the typical mass ranges where photoevaporation is known to be effective. Moreover, the mass accretion rate is found to be compatible with the value expected for photoevaporation, which suggests a rapid dissipation of the inner disc.

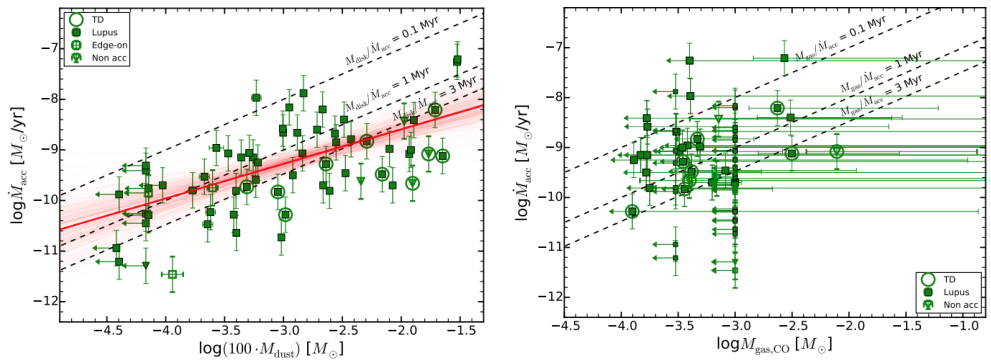

Figure 1.9: Images taken from Manara et al. (2016) showing the mass accretion rate versus the total disc mass derived through dust (millimeter observations) and gas (CO measurement) disc mass.

The combination of these evidences with ALMA observations in the millimeter allow Manara et al. (2016) to find a linear relation between the dust mass of protoplanetary disc and the mass accretion rate of young stars (Fig. 1.9). This relation has been postulated from viscous accretion theory, considering in particular the total disc mass. The authors showed that the total mass derived through millimeter measurements is more reliable than the mass derivation through CO, due to the large number of upper limits. The linear relation was found between the mass accretion rate and the disc dust mass, with a gas-to-dust ratio of a hundred (see Fig. 1.9). This shows an important evidence: that the mass accretion rates, which are properties of the inner part of the disc, are also related to the outer disc properties.

Theoretical works tried to explain such observations. Lodato et al. (2017) compared simple viscous diffusion models with recent surveys results for young protoplanetary discs. They found good agreements with Lupus star forming region data and a linear correlation between mass accretion rate and disc mass, if the viscous timescale is comparable to the disc age. At the same time, Mulders et al. (2017) investigates the relation between disc mass and mass accretion rate. They found no correlation between the M_{dust} and $M_\star$ and $\dot{M}_{acc}$ and $M_\star$ relations. For a constant viscosity the models can explain the observed parameters, but with a over-prediction on the correlation. They suggest this to be produced by the fact that the observed scatter in $\dot{M}_{acc}$ and $M_\star$ is not primordial and there are other physical processes playing a key role, like grain growth and radial drift. The other option is that the observed scatter is primordial, but discs have not evolved much and have a low viscosity or a large initial disc radius.

Finally, Manara et al. (2019) performed a general study on the current planet popu-

lation synthesis models with the aim to describe the formation of planets starting from the protoplanetary disc phase, which rely on the poorly constrained protoplanetary discs properties (e.g. disc masses and mass accretion rates). They found that disc models used in planet population synthesis substructures predict mass accretion rate similar to what is observationally found, but with a lower spread of values, due to the small spread of viscous timescales used. Two populations of sources show interesting features: models where giant planets have formed and where a cavity is present (transitional discs, see Section 1.4.2). They found that the first class have many weakly accreting discs, which is not in agreement with prescription for planet accretion, which predict higher accretion rates. For the discs with large cavities, the observed accretion rates are higher then the models prediction.

1.4 Recent observations: I Discs

As described in Section 1.1, different "classifications" given to circumstellar discs refer to different composition and evolutionary stages. In the following, we will describe the observations of protoplanetary discs, transitional disc and debris disc, mostly studied during this thesis.

1.4.1 Protoplanetary discs

Protoplanetary discs are though to be the birthing place of planets and for this reason it is key to understand their evolution. The high angular resolution and sensitivity of ALMA and SPHERE allow to reveal a variety on the protoplanetary disc structures that was before unknown. Their typology are various from horseshoes, gaps, cavities and spirals (ALMA Partnership et al. 2015; Andrews et al. 2016; Canovas et al. 2016; Pérez et al. 2016, review of Casassus 2016, Long et al. 2018b, DSHARP, Andrews et al. 2018a - Fig. 1.10). Several are also the interpretation that have been made on such structures (see Chapter 4). It is thus fundamental to perform multi-wavelength observations and to study different molecules to constrain the properties of each disc component. One of the most investigated source so far is HL Tau (ALMA Partnership et al. 2015) that shows a disc with a sequence of rings and gaps. HL Tau is a young source evolving from SED Class I to Class II which contains a massive compact disc as well as highly collimated outflow, perfect target to study planet formation at early times. One of the main explanation for the pattern of gaps and rings indeed is that they might be produced by embedded protoplanets (Dipierro et al. 2015b). Spirals structures has been detected copiously in the near-IR and in a few cases a spiral is also detected in (sub-)millimetre observations (Pérez et al. 2016; Christiaens et al. 2014; Rosotti et al. 2019a; Dong et al. 2018b). The two most widely accepted scenarios to produce them are: the presence of a planet orbiting around the central star (Muto et al. 2012; Dong et al. 2015b) or the development of gravitational instabilities (Cossins et al. 2010; Dong et al. 2015a). We refer to Chapter 4 for a description of the different shapes observed in protoplanetary discs and the explanation of the models to reproduce e.g. spiral- and gap-like features.

1.4.2 Transitional discs

The presence of a peculiar class of protoplanetary discs was identified for the first time by Strom et al. (1989b) as a weak or no near-IR excess, but a strong far-IR excess in the SED emission (Fig. 1.11). This signature was interpreted as caused by the presence of an inner hole. For this reason they were considered, at the beginning, in transition

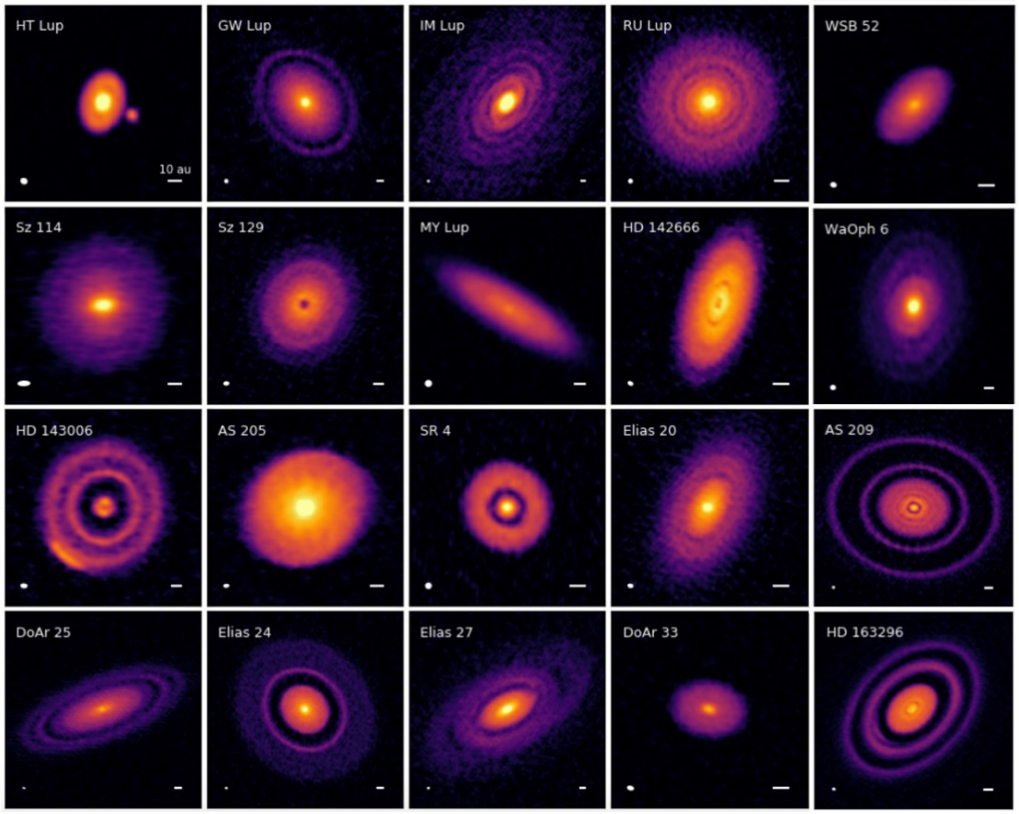

Figure 1.10: High resolution ALMA observations of the DSHARP sample (Andrews et al. 2018a) showing a variety of structures in protoplanetary discs.

between optically thick gas/dust-rich discs extending up to the stellar surface to object where the disc has been dispersed, hence the name 'transitional'. This inner hole can be most probably due to both disc dispersal (accretion and disc winds) or to the presence, for example, of an inner binary (Marsh & Mahoney 1992). Moreover, such discs start to show a wide range of (non-)axisymmetric structures detected in both near-infrared scattering and (sub-)millimetre dust thermal emission. For this reason transitional discs are excellent candidates to study and test the planet formation theories and to understand what drives disc dispersal. An interpretation of the different SED was made by Espaillat et al. (2014) shown in Fig. 1.11.

Moreover, observations show the presence of objects with strong near- and far IR excesses, but a mid-IR excess deficit. These targets have been identified by Espaillat et al. (2007) as pre-transitional discs, with an inner disc followed by an annular gap. This can be an initial stage of disc clearing towards a large inner cavity. The presence of a silicate feature at 10 μm is possibly due to very small (< 1 μm) optically thin dust present in the cavity. Considering that the small grains are dynamically coupled with the gas (see Chapter 2), this suggest that these systems have the dust cavity partially filled with gas. In some transitional discs the dust depletion inside the cavity does not correspond also to a gas depletion of the same amount. ^{13}CO and C^{18}O molecular lines have been found inside dust cavities (e.g. Pontoppidan et al. 2008; Bruderer 2013; van der Marel

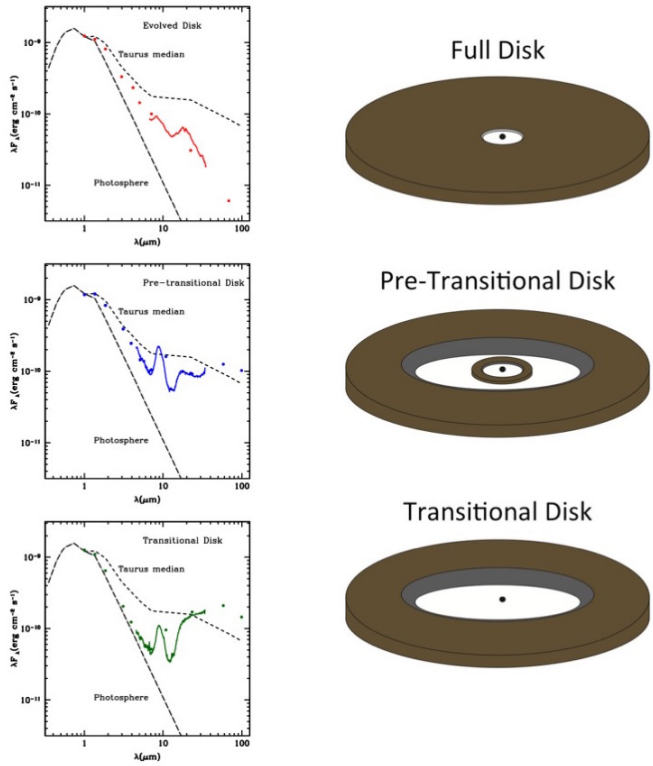

Figure 1.11: Observed SED (left) of a full evolved disc (top), pre-transitional (middle) and transitional (bottom) disc. All the color lines have to be compared with the dashed black line, a typical young full disc. If an optically thick inner disc is present (top, middle pannels) a near-IR contribution is visible in the SED. The pre-transitional disc seems to be the predecessors of transition discs with large cavities. The transitional disc (bottom) has a significant lack of IR excess. Moreover, the silicate feature at 10 μm (bottom pannel) is due to optically thin dust. Image adapted from Espaillat et al. (2014)

et al. 2016). The gas cavity extent is in general twice as small in radius than the dust cavity (Bruderer et al. 2014). Together with this, the accretion rates of such systems are comparable to T-Tauri disc accretion rates: 10^{-7} - 10^{-8} $M_{\odot}$/yr (e.g. Espaillat et al. 2007; Manara et al. 2014), meaning that a significant mass reservoir of gas in the inner disc is present. In some cases, see Fig. 1.11, the presence of a cavity is also associated with a stronger FIR excess compared to a typical SED. The stellar irradiation, indeed, normally is absorbed by the inner disc at NIR wavelengths. When a cavity is present, it is instead absorbed and re-irradiated by the outer disc.

With the advent of the old generation of sub-mm interferometers (e.g., SMA, PdBI), the hypothesis of the presence of dust hole or cavities in these discs has been confirmed (e.g., Brown et al. 2008; Andrews et al. 2009; Pérez et al. 2014). Near-IR instruments (e.g., Subaru/HiCiao, VLT/NACO), tracing polarized emission from the surface, were able to resolve large gaps (e.g., Quanz et al. 2011; Hashimoto et al. 2012; Avenhaus et al. 2014b). The lack of emission can be related to a lack of dust emitting temperatures from one to a few hundred K in the inner disc regions. We note that observations of transition

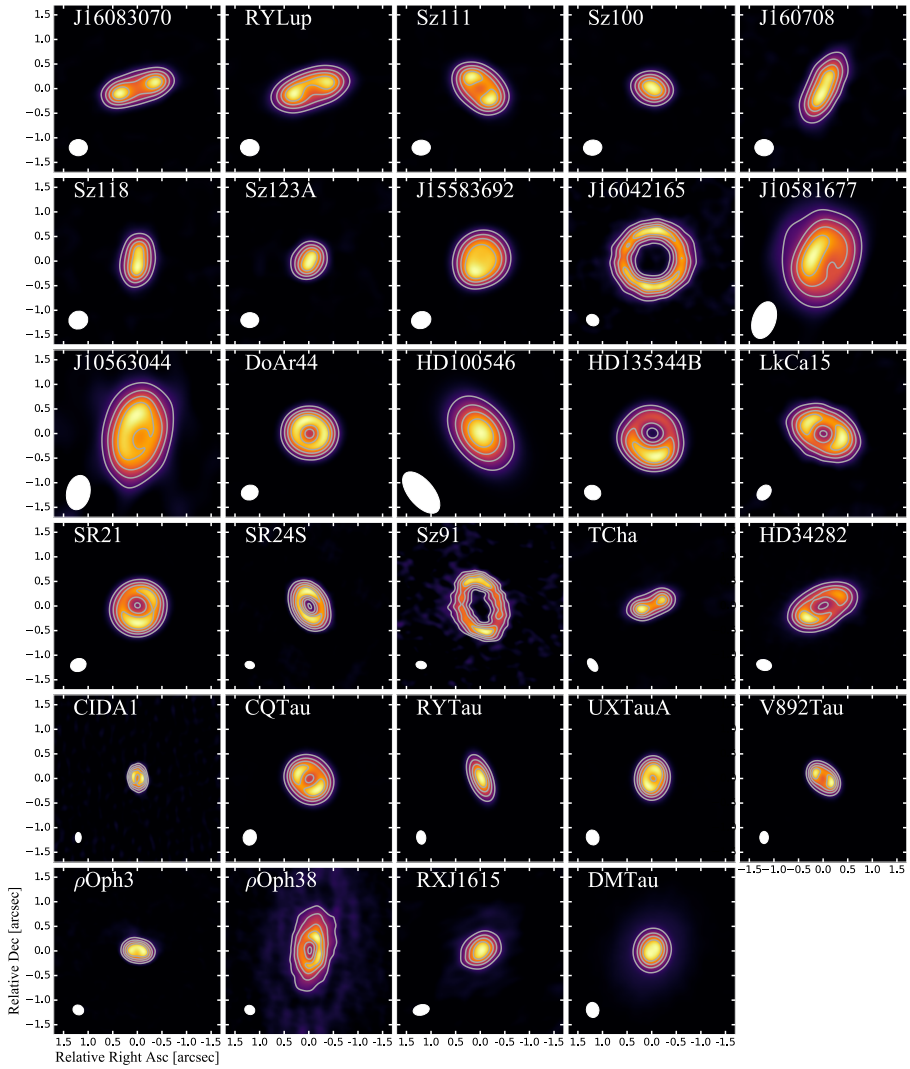

Figure 1.12: Gallery of transition discs imaged with ALMA in the dust continuum (Pinilla et al. 2018).

discs have been biased towards discs surrounding Herbig Ae/Be stars. Their discs are not always brighter than the ones of T Tauri in optical/IR, but Adaptive Optics requires a certain threshold in stellar brightness and, thus, the more luminous Herbig stars are easier to observe. At millimeter wavelengths, stellar propriety may be related to dust mass and, thus, to disc brightness even if this is not straightforward. We note that the bias is no longer true as to date we have many more observations on TTSs (e.g., Avenhaus et al. 2018; Garufi et al. 2020). Meeus et al. (2001) classified Herbig Ae/Be discs based on the slope of the far-IR continuum: Group I and II. In particular, the SED of Group I sources have a strong near- to far-IR excess, whereas the one of Group II sources have a much weaker far-IR excesses. For further details on this, we refer to Chapter 7. The first hypotesis was that Group I discs where flared and Group II flat, showing an evolution from

Group I to Group II, as a result of dust settling (e.g. Dullemond & Dominik 2004). In a later work by Maaskant et al. (2013) their different taxonomy is identified as two distinct evolutionary paths coming from a primordial ancestor. The question about their origin is still open and in Chapter 7 we will study this in detail. With the current generation of high-resolution imagers a sample of transitional discs has been detected with polarized scattering images at NIR. The images present a wide range of different structures such as gaps and spirals (e.g. Stolker et al. 2016; van Boekel et al. 2017, see Chapter 4). In any case, the origin of these large cavities is still a topic under debate. The most likely dominant processes involved in the origin of transitional discs are: dynamical clearing by stellar or planetary companion(s) (Lin & Papaloizou 1979), photoevaporation (e.g. Clarke et al. 2001; Alexander et al. 2014) and dead zones (i.e. regions of low ionization, MRI quiescent and low viscosity, e.g. Regály et al. 2012; Flock et al. 2015). I will describe these theories in details in Chapter 4. Moreover, for what regards a comprehensive description of the class of transitional discs both from an observational and theoretical point of view we refer to Espaillat et al. (2014) and Owen (2015).

1.4.3 Debris discs

Debris discs are found around stars with an age ranging from ten to hundreds of Myr. They are optically thin with low mm-sized dust masses ($< 0.1 M_{earth}$) and very little evidence for gas due to their evolved state (Wyatt 2018). The disc material is indeed dispersed through photoevaporation, stellar winds, accretion onto the star and/or formation of giant planets. In such discs dust grains are reprocessed through collisions between planetesimals. The composition of dust is, indeed, most likely not primordial. Smith & Terrile (1984) for the first time obtained a resolved image of a debris disc around β Pictoris. From that moment on, thanks to new instruments, debris discs have been imaged both in scattered light and in direct thermal emission, showing a wide variety of disc geometries: from rings to warps and brightness asymmetries (Boccaletti et al. 2015; Su et al. 2017; Hughes et al. 2018). We note that some of the disc structures observed are similar to the one of the younger transitional disc and they might originate at that stage. The only disc that was sometimes classified as debris disc and sometimes as transition disc is HD 141569 (e.g., Mawet et al. 2017a). Its dust mass content is indeed intermediate, but its far-IR excess is much closer to Class III sources. This disc is young compared to the other debris disc. The interest in these type of discs is mainly due to the study of planet-disc interactions to constrain better the feature of the putative planet perturber. These systems allow also to deepen the knowledge of, for example, planetesimal collisions and gravitational perturbations from stellar flybys (Hughes et al. 2018). Considering the main focus of this thesis is on younger sources, we defer the readers to a review of Hughes et al. (2018) and Wyatt (2018) for a comprehensive description of debris discs.

1.5 Recent observations: II Companions

Companions in the disc might be stellar, brown dwarf or planetary companions. In this section we will first describe each category of objects and secondly we will focus on the description of planetary companions and the detection techniques used to discover them.

1.5.1 Stellar binaries

The formation of binaries is an important element of the star formation process. Binaries can form also around less massive objects such as brown dwarfs. Stars and brown dwarfs,

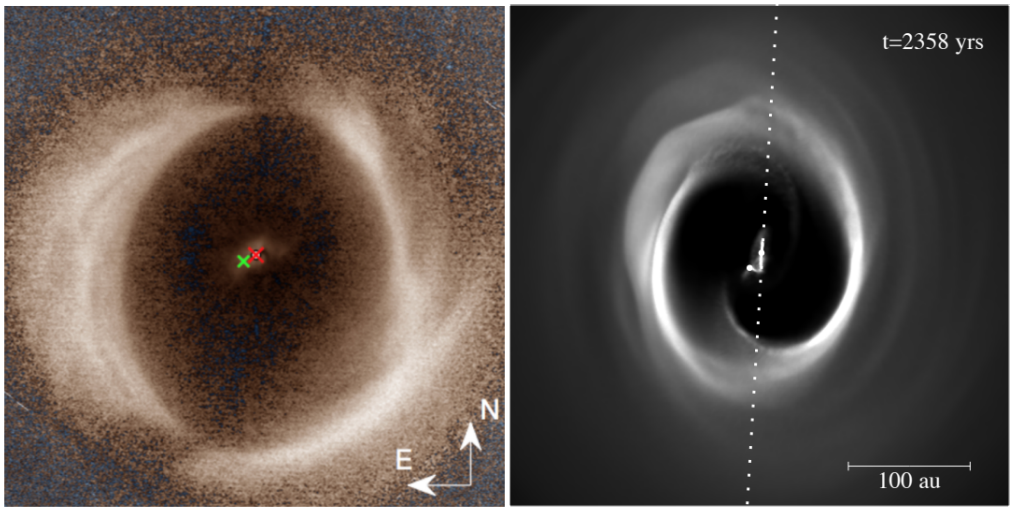

Figure 1.13: Protoplanetary disc structure produced by the close binary in HD 142527 (Price et al. 2018a) with a large cavity and shadows. It is possible to observe the scattered light observations (left) and the simulations performed with a close binary (right).

indeed, share similar multiplicity properties (e.g. frequency, separation, and mass ratio distributions), suggesting similar formation scenario for both. Interestingly, the presence of such binary systems, if still embedded in their protoplanetary disc, may produce peculiar features on the disc itself:

- the truncation of the circumbinary disc or of the disc itself. The tidal truncation in multiple systems was tested observationally by Manara et al. (2019) in the millimeter continuum, who found results in agreement with the theory under some conditions (e.g. large eccentricities or dust radii $\lesssim$ gas radii).
- the formation of a polar disc (e.g. Aly et al. 2015; Kennedy et al. 2019) or of an inner disc misalignment (Facchini et al. 2013).
- the presence of shadows (e.g. Facchini et al. 2018a; Benisty et al. 2017; Kraus et al. 2020).
- the formation of cavities whose size depends on the disc and binary properties (Hirsh et al. 2020).
- the formation of dust horseshoes in transitional discs (e.g. Ragusa et al. 2017; Price et al. 2018a).

Spectacular examples of protoplanetary disc structures produced by stellar binaries are e.g., HD 142527 (Price et al. 2018a, Fig. 1.13), GG Tau A (Cazzoletti et al. 2017; Aly et al. 2018; Brauer et al. 2019). Another example is the binary of KH15D (Lodato & Facchini 2013; Smallwood et al. 2019). Recent studies by Ruíz-Rodríguez et al. (2016) found that the spectral energy distribution of $\sim$ 40% of the transitional discs in their sample of T-Tauri stars can be explained by the presence of a binary system. An even larger fraction is known to be present for later type stars (Duchêne & Kraus 2013).

1.5.2 Definition of brown dwarf and planets

Brown dwarfs (BDs) are objects too light to become stars and to sustain hydrogen fusion reactions, but not as light as planets. At the same time, exoplanets are defined as planets orbiting stars other than our Sun and the more massive ones are called Giant Planets (GPs). The standard distinction between BDs and GPs is the one adopted by the International Astronomical Union (IAU): the boundary is set at the Deuterium burning (D-burning limit, $\sim$0.012 $M_{\odot}$). Chabrier et al. (2000) suggested that D-burning has no impact on star formation and a negligible impact on stellar/BD evolution. From this point of view, the brown dwarf and planet mass domains can overlap, i.e. there is no clear mass separation. Formation in the disc versus the field is instead the main difference: a planet forms in a disc, orbiting, at least initially a central star. Brown dwarfs instead form more similarly to star, possibly through gravitational collapse. Chabrier et al. (2014) propose the following classification scheme. They define "Brown Dwarfs" as (A) free floating objects below the hydrogen burning minimum mass no matter whether they are massive enough to ignite deuterium burning; and (B) objects that are companions to a parent star or another BD, but exhibit compositional and mechanical (mass-radius) properties consistent with the ones of a gaseous sphere of global chemical composition similar to the one of the parent star/BD. In contrast, "giant planets" are defined as companions of a significantly more massive central object. This is a necessarily condition, giving the fact that bulk properties strongly depart from the ones just mentioned. This definition allows for a mass overlap between the two populations, as supported by the observations. We must observe that Chabrier et al. (2014) seem to neglect the fact that D-burning can actually have a decisive influence on star formation. D-burning can play indeed a fundamental role in setting the typical stellar mass, which is nearly coincident with critical mass for H-burning (Krumholz 2011). However, the distinction between these type of objects is still object of debate and no clear answer has been found. Possibly in the next future, Gaia will help to disentangle these scenarios providing a large number of discoveries (Perryman et al. 2014).

At the same time, many properties are shared between giant planets and brown dwarfs. Two examples are interesting in this regard. The B9-type star κ And hosts a companion with a mass of $\sim$ 10 - 20 M_{Jup} (Carson et al. 2013), straddling the DB limit. However, due to the very massive primary, the mass ratio of the κ And system is only 0.5 - 1.0%, very similar to the HR 8799 and β Pic planets. Moreover, the companion resides at a comparable orbital separation, $\sim$ 40AU. This might imply a similar formation mechanism, which would support the fact that planet formation can produce companions that approach or exceed the DB limit, as has been suggested by theoretical models. One example of the opposite situation is 2M 1207 b (Chauvin et al. 2005), which is a $\sim 4M_{Jup}$ companion to a $20M_{Jup}$ brown dwarf (Mamajek 2005). In this case, the companion is firmly in the non-BD regime, but with a system mass ratio of 20%, the couple appears may be best described as an extension to low masses of the brown dwarf binary population, rather than a true planetary system (Lodato et al. 2005). The general conclusion from the direct imaging surveys performed so far is that very wide and massive objects in the giant planet mass domain are rare, with many of the surveys yielding null results. These results can be used to place formal constraints on the underlying planet and brown dwarf population. In particular, the GDPS survey (Lafrenière et al. 2007a) leads to the conclusion (at 95% confidence) that less than 28% of the stars host at least one 0.5-13 M_{Jup} planet in the semi-major axis range of 10-25 au, less than 13% host a corresponding planet at 25-50 au, and less than 9% at 50-250 au.

1.5.3 Brown Dwarfs

Brown Dwarfs (BDs) are substellar objects with mass M$\lesssim$0.075 $M_\odot$, low enough that H-burning reaction is not ignited in their cores, unlike main-sequence stars. There are several lines of evidence indicating that BDs have the same formation process as the stars (Luhman 2012). Like stars, categorized by spectral classes, BDs are classified as type M, L, T, and Y in order of decreasing surface temperature. At the same time, they share with stars properties such as multiplicity, mass accretion rates, the presence of circumstellar discs and spatial distributions at birth. Their Initial Mass Function (e.g. Chabrier et al. 2014, Robberto et al. 2020) appears to be a continuation of the low-mass star function with no break. Brown dwarf seems to collapse in an isolated environment, similarly to the gravitational collapse mechanism leading to protostars (e.g. André et al. 2012). At the low mass limit, one normally sets at $\sim 13 M_{Jup}$ the boundary between very low-mass BDs and gas giant planets (see Section 1.5.2).

An interesting feature that characterize the brown dwarf population is the "Brown Dwarf desert", which indicates the observed lack of companions in the mass range 10-100 M_{Jup} (i.e., 1-10% of the primary mass) in the separation range covered by radial velocity studies (up to a few au) around Sun-like stars (Chabrier et al. 2014). The frequency of companions increases if one moves to smaller or higher masses (Mayor et al. 2011), pointing to separate formation mechanisms for planetary and stellar/BD companions. More recent studies with radial velocity suggests that BD desert may not be as "dry" as thought at the beginning (e.g. Duchêne & Kraus 2013; Guillot et al. 2014; Troup et al. 2016).

1.5.4 Exoplanets

Planetary companion are, instead, expected to form not through top-down gravitational collapse of a larger core, but through gravitational instability or core accretion inside a circumstellar disc (see Chapter 3). In Fig. 1.14, we show the distribution of all the exoplanets found up to September 2019 with the use of different techniques. The population of exoplanets detected is different from the one detected in our solar system. Examples of them are giant planets at short to mid-separation (hot Jupiters), giant planets at large separations (cold gas giants), planets with masses between that of Earth and Neptune, at short orbital periods which can be rocky (super-Earths) or gaseous (mini-Neptunes) or a combination of both. There is an observational bias to detect low-mass planets (e.g., mass equal to the Earth) at large separation. This can be seen in Fig. 1.14 as a triangle in the detection below which no detection has been made.

In the following, we will distinguish between two type of exoplanets: the older ones detected around main-sequence (MS) stars and the younger ones around young pre-main sequence stars (PMS). The first class of objects are observed since more than two decades. They have large multiplicity and variety. The second class of exoplanets are typically embedded in their native disc, and for this reason are less easy to be found. Finding planets while they form is important in order to study the disc-planet interaction needed to reconstruct their formation and evolution. During this thesis we will focus on this second class of objects.

Exoplanets around main sequence stars

Exoplanets detected around Main-Sequence (MS) stars are older and easier to observe since the disc material has been mostly accreted onto the star. These system were observed using both indirect and direct techniques:

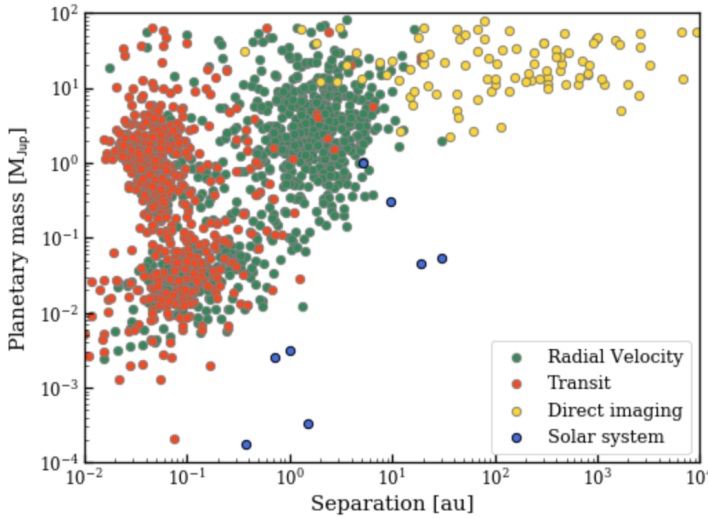

Figure 1.14: Exoplanets divided in colors for different detection techniques: direct imaging (yellow), transit (red) and radial velocity (green). In blue are the planets of our solar system (blue). The catalogue of exoplanets detection has been taken from exoplanets.eu and it is complete up to September 2019.

- Indirect techniques have been used to infer the presence of planets, such as **radial velocity**, **astrometry**, **transit** and **microlensing**. To a first approximation, planets are orbiting around their more massive host star. However, both star and planets motion is around the common center of mass. This produces perturbations in the radial velocity measurement and astrometric position of the star. The radial velocity and astrometry indirect methods use respectively these evidences. Moreover, when the orbit of the planet is such that the planet can alter the observed intensity of the stellar flux, the so called transit and microlensing techniques can be used.

- The technique used for direct detection is the **direct imaging** of exoplanets (see Section 1.5.5. This technique is not the easiest to perform due to the difficulty to disentangle the light of exoplanets from the bright emission of the star.

Each of these techniques have observational biases in the parameter space. For example, radial velocity and transit techniques usually detect massive planets that orbit closer to their host stars, while microlensing and astrometry are sensitive to wider orbits. For astrometry, the center-of-mass displacement amplitude indeed increases with orbital period. The parameter space observed from direct imaging is wide separations and massive objects. Typically observations taken with different techniques have to be combined in order to be able to derive planets properties. The first giant planet detected around a MS star is 51 Peg b (Mayor & Queloz 1995) through the radial velocity technique. This discovery started a completely new field and was awarded with a Nobel prize in the 2019.

The direct imaging detections of giant extrasolar planets started to grow thanks to the improved capabilities of the instruments. The detection number is still low, both for observative limitations and because the percentage of direct imaging of giant planets at large orbits is low with respect to the one at close separations (e.g. Lafrenière et al. 2007a). The contribution of the stellar emission is indeed less strong and the intrinsic

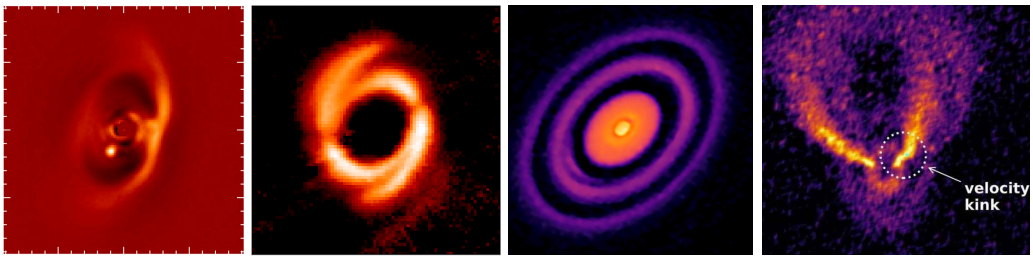

Figure 1.15: SPHERE observations of companion in PDS 70 B (left, Keppler et al. 2018) and a spiral structure induced by a companion in HD 100453 (center left, Benisty et al. 2017); high resolution ALMA observation of HD 163296 (center right, Andrews et al. 2018a) and kink detection of the planet around HD 97048 (right, Pinte et al. 2019).

emission of massive planets larger. We note that this method can be applied both for brown dwarf detection and for planets. Direct imaging observations have the advantage to detect the (projected) separation and position angle of the companion with respect to its host star at different epochs, allowing us to measure its trajectory. Moreover, if direct imaging is combined with spectral information it can, at the same time, allow the spectral characterization (e.g. effective temperature, extinction, surface gravity, spectral type). Through evolutionary models it is then possible to derive mass, radius and age. Examples of giant planets detected through direct imaging around MS stars are HR 8799 (Marois et al. 2010b) and β Pic (Lagrange et al. 2010). HR 8799 has four planets orbiting around, while β Pic has a single planet detected so far. They all have masses well into the planetary mass regime ($\sim$5 - 10 M_{Jup}, less than the D-burning limit), mass ratios to their primaries of less than 1%, and indications of sharing a common orbital geometry, both with each other (for the HR 8799 system) and with the debris discs that exist in both systems.

Exoplanets around pre-main sequence stars

Exoplanets detected around young pre-main sequence (PMS) stars are embedded and thus more difficult to be observed. At the same time, the young companion is still contracting and it is intrinsically brighter. The presence of the disc tends to obscure the emission of the star in the same way as planets do and methods based on the variation of the stellar luminosity cannot in general be used. Radial velocity is difficult to be performed on young stars due to the high chromospheric variability, which makes harder to detect the doppler shift. Astrometry may in principle be used, however the detections made with it are rare due to the extreme precision needed to measure the central star position. Currently, new-born planets can be inferred based on three different diagnostics:

- The first diagnostic is the direct detection of planets in the near-IR. To date this is the most appropriate technique to study exoplanets around young stars. For young objects, the complexity related to the subtraction of the stellar light is added to the need of disentangling the disc from planet emission. Two major problems in direct imaging are angular resolution and contrast. We refer to Section 1.5.5 for what regards the details on this technique. This direct method detects just massive planets at large separations. Moreover, the high performance of the last generation extreme-AO instruments combined with with low-spectral resolution integral field spectrographs (e.g., SPHERE) allow to spectrally characterize the exoplanets

(through HCI techniques). This is key to probe their atmosphere, the amount of extinction around them, to constrain if there is a long-lived circumplanetary disc and thus their mass. Direct imaging allow also to detect the exact orbit of the companion if it is followed up in time.

- An indirect method is by looking at the morphology of dust and gas emission where an embedded planet might induce the formation of characteristic rings and gaps (see center Fig. 1.15, e.g. DSHARP Andrews et al. 2018b, Fig. 1.10).
- Finally, a novel indirect method has been proposed, based on the detection the signature of the planet gravitational force on the velocity field of the gas surrounding it (e.g. Pinte et al. 2018b; Teague et al. 2018; Pérez et al. 2020).

The simultaneous detection of a planet using multiple diagnostics offers a great potential to reinforce the individual detections and allows for a more accurate determination of the properties of the planet and to calibrate the different techniques. The unique example of a protoplanet discovered combining direct detection and the presence of a dust gap is the one of PDS 70B (Keppler et al. 2018, 2019, left Fig. 1.15). A putative planet in HD 97048 has been instead detected through a kinematical signature within a gap (Pinte et al. 2019). Still missing is the combination of direct detection and kinematical evidence. In the following subsection, we will describe the three methods above quoted and we will provide some examples.

1.5.5 Detection of young exoplanets

I. Direct imaging

Direct imaging of exoplanets requires very high angular resolution and contrast (see below for details). Typically these observations are performed in the IR. While the SPHERE instrument has greatly enhanced our capabilities in detecting young planets, the number of objects detected in this way is still low. We are able to reach adequate contrast to detect planets in the infrared only for the most luminous planets. Moreover, although we are able to detect the planet, its mass is not easy to derive. The conversion from luminosity to mass depends indeed on uncertain planetary evolutionary tracks and, if the planet does not fully open a gap in the disc (Sanchis et al. 2020), on the extinction of the disc. Moreover, if the planet is still accreting embedded in its natal disc, the presence of the circumplanetary disc (CPD) emission have to be taken into account. Szulágyi et al. (2019) showed that the CPD is typically brighter than the embedded planet in near-IR and this add complexity in the derivation of the planetary mass which may be, for this reason, overestimated. In this section, we will describe in particular the detection of young and embedded exoplanets. This technique and its peculiarity is anyway applicable to all exoplanets detections.

Angular resolution. In order to be able to resolve the companion's orbits, instrumentation has been optimized to reach very high angular resolution. The angular separation (β) needed to resolve the companion is the one between the star, at a distance d from us, and the planet with semi-major axis a_p and eccentricity e_p is:

$$\beta = a_\mathrm{p}\frac{(1-e_\mathrm{p})}{d} \tag{1.11}$$

At a distance from the star of 100 pc, for example, the angular resolution required for a planet orbiting around the host star at a separation of 5 au is 50 mas. It is thus

understandable how difficult this measurement can be. Ground-based Adaptive Optics (AO) system and space telescopes are able to probe the larger angular scales ($\gtrsim$50 mas) at near-infrared (NIR) wavelengths, whereas interferometers can detect companions at higher angular resolution. Planet detection can be performed using the concept of nulling interferometry (e.g. Cockell et al. 2009), even if a sufficient number of baselines is needed or the sparse aperture masking (SAM, e.g. Ireland 2013), which uses the insertion of a mask filled with small holes in an intermediate pupil plane. The angular resolution needed has to be compared with the angular resolution θ of the telescope:

$$\theta \sim \sin\theta = 1.22\,\frac{\lambda}{\mathrm{D}} \tag{1.12}$$

where θ (in radians) is the angle at which the first minimum occurs in the Airy pattern, D is the telescope diameter and λ is the wavelength observed. If we consider λ=1 μm, a separation of 5 AU and a distance from the star of 100 pc, the diameter of the telescope needed in principle is $\sim$5 m. Observations can be made on earth and on space. On earth seeing, e.g., wave-front corrugations produced by atmospheric turbulence, can affect the angular resolution, whereas space telescopes are not. In order to correct for this, Adaptive Optics system have been developed. We note also that this type of observations typically exploit the use of a coronagraph, able to obscure part of the emission coming from the star for a separation correspondent to the Inner Working Angle (IWA). This improves the signal-to-noise of the planet, but it does not allow to observe any planet at separation smaller than the IWA. A description on AO and coronagraphy is made in Chapter 6.

Contrast. The other observational limit to overcome in direct imaging is the contrast between the host star and the companion. Importantly, the planet luminosity is composed by three contributions: the first is the reflected light from their parent star ($\mathrm{L_{p,r}}$), the second is its intrinsic luminosity due to internal heat ($\mathrm{L_{p,i}}$) and the third emission is from reprocessed stellar light ($\mathrm{L_{p,eq}}$), significant at very short separation. The first is dominant at UV wavelengths and the second and third at IR wavelengths. The brightness corresponding to stellar emission is:

$$L_{\mathrm{p,r}} = \frac{A_{\mathrm{Bond}} L_\star}{8}\left(\frac{R_\mathrm{p}}{a_\mathrm{p}}\right)^2 \phi(t) \tag{1.13}$$

where $\phi(t) = 1 - \sin(i_\mathrm{p})\sin(2t/P)$ is an orbital phase factor, R_p is the planet radius, a_p is the separation from the host star and A_{Bond} is the Bond albedo of the planet (ratio of the total reflected light to the total bolometric incident light). The reflected luminosity have to be mostly considered for very short separation giant planets. In the case of most of exoplanets detected with direct imaging this contribution is usually negligible.

The internal heat, instead, is typically produced by gravitational contraction which transforms potential energy into thermal energy. When planets form, their intrinsic luminosity is comparable to the one of brown dwarf, and it is visible for the same mechanism. Stevenson (1991) gave an expression based on polytropic equations of state to describe its intrinsic luminosity:

$$L_{\mathrm{p,i}} \sim t^{-5/4} M_\mathrm{p}^{5/2} \kappa^{0.3} \tag{1.14}$$

where t, M_p and κ are respectively the time spent on the object formation, its mass and the gas opacity. The youngest and more massive the companion is, the easiest is to detected it with direct imaging techniques (see Fig. 1.14). Self-luminous planets have the effective temperature much larger than their radiative equilibrium temperature and the

host star is less luminous if it is not already in its pre-main sequence phase. This gave a better planet/star contrast and allow easier detections. At the same time the complication in this is that if planets are young they can be embedded in their natal disc, and this can add difficulties in distinguish them from the disc contribution. Disentangle disc and planet emission is still challenging. Moreover, as described previously, the presence of the CPD add complexities in disentangling the planet contribution from the one of the circumplanetary disc. At near-IR wavelengths (J, H, K bands), indeed, a moderately accreting circumplanetary disc may be as bright as a late M-type brown dwarf or a 10 M_J planet with a "hot start" (Zhu 2015). Particularly, if the planets are massive enough to open deep gaps, their contrast is particularly poor in the near-IR (Szulágyi et al. 2018, 2019). The best contrast between the CPD and the circumstellar disc is indeed reached at sub-mm/radio wavelengths, or, for massive planets, in the 10-micron silicate feature vicinity (Szulágyi et al. 2018, 2019). Crucial is, thus, to observe planets not only in the near-IR, but also mid-IR bands (L', M, N bands; Zhu 2015).

For older (mature) planets, instead their intensity coincides with reprocessed incident stellar light and their effective temperature may coincide with the radiative equilibrium temperature (dependent mostly on radius and $T_\star$).

$$L_{\rm p,eq} = 4\pi\ R_{\rm p}^2\ \rho\ \sigma\ T_{\rm eq}^4 = 4\ \pi\ R_{\rm p}^2\ \rho\ \sigma \left(\frac{1 - A_{\rm Bond}}{4\ f}\right) \left(\frac{R_\star}{a_{\rm p}}\right)^2 T_\star^4 \tag{1.15}$$

The optimal contrast for young planets is typically reached in the L′ band, while for older planets longer wavelengths are a better choice. In any case the contrast in the optical is in general worse than in the thermal IR, considering that the stellar emission is brighter (for a mature Jupiter-like planet the contrast in the IR will be $\sim 10^{-8}$, see Skemer et al. 2015, Fig. 1.16).

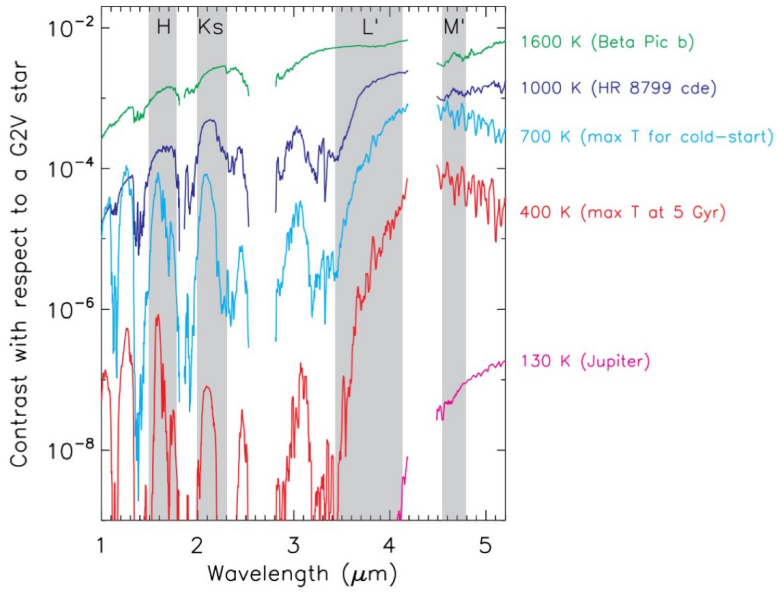

Figure 1.16: Contrast curve of planets with different effective temperature versus star as a function of wavelength in the near-IR. Adapted from (Skemer et al. 2015).

At the same time, longer wavelengths imply lower angular resolution (keeping fixed

the telescope diameter). A compromise between these angular resolution and contrast has to be reached. In the near-IR atmospheric thermal background emission and absorption from molecules in the atmosphere add difficulties in observations made with ground based telescopes. Post-processing techniques combined with the application of a coronagraph have been implemented to reach better contrast. A faint companion would otherwise lie in the photon noise, defined as the square root of the number of photons detected ($\sigma = \sqrt{N_{\rm ph}}$), of the diffraction pattern produced by the Airy ring, whose typical brightness is:

$$L_{\rm ring} = L_\star \left(\frac{\beta}{\theta}\right)^{-3} \tag{1.16}$$

Detections. We note that in order to perform high contrast imaging (HCI), it is not enough a high angular resolution and contrast. Self-luminous protoplanets are typically detected in thermal IR light. Due to their extremely faint scattered light, planets are indeed not suited to be detected by polarized light. Polarized light observations are mainly used to detect emission coming from the disc surface, considering that the differential technique that involves polarized light is more efficient at removing the stellar component of the observed flux and thus it reaches a better contrast. The light coming from planets is, instead, in general weakly polarized (e.g. by the planetary atmosphere) and the flux is so low to be currently undetectable (see Chap. 6). The images obtained in total intensity needs to be post-processed in order to go from calibrated to high contrast images (HCI). To do that, typically methods such as Angular and Spectral Differential Imaging (ADI and SDI respectively) are used. For details on the HCI and on the different techniques, we refer to Chapter 6. We note that post-processing techniques are quite aggressive routines and may create spurious detections. For sources where both a planet and a disc are present, it is not trivial to disentangle the different features. For this reason, it is important to confirm the point-like sources observed through observations at different epochs and Bands, and where possible perform a spectral characterization.

Several are the examples of claimed detections of protoplanets. Quanz et al. (2013a) claimed the discoveries of 'bright features' around the Herbig Ae star HD 100546 using NACO in L′ direct imaging. New companion candidates were detected around the same target at a separation of 10 and 50 au (Currie et al. 2015) in L′ (no detection in K band). However, later on it was shown that the candidates detected in HD 100546 could instead trace an extended disc feature (Mendigutía et al. 2017a; Rameau et al. 2017; Follette et al. 2017). At the same time, in the transitional disc around T Cha, Huélamo et al. (2011) claimed a protoplanetary detection. Olofsson et al. (2013) showed that the signal found around T Cha could be derived from the asymmetric disc emission. A tentative detection at 0.″15 around HD 169142 (Biller et al. 2014; Reggiani et al. 2014) was made within the bright ring seen in polarized light. This detection has been questioned later on due to the correspondence of the inner rim of the bright ring (Ligi et al. 2018; Pohl et al. 2017a). In the large cavity of LkCa 15 two companions were found at 14 au and 18 au (Kraus & Ireland 2012; Sallum et al. 2015) based both on SAM L′ and H_α detections. Later on, Thalmann et al. (2016) detected in polarimetry a bright inner edge of the disc in the same position where the companions were claimed. There was also a claimed detection in HD 131399 (Wagner et al. 2016) and in MWC 758 at 20 au (Reggiani et al. 2017).

The only detected and confirmed embedded planet within the gap of a transition disc is the one orbiting around PDS 70 (Keppler et al. 2018). It is a young planet of $\sim$ 5 - 10 $M_{\rm Jup}$ at a projected separation of 22 au. The cavity was also observed with ALMA in the dust continuum and ^{12}CO by Keppler et al. (2019). We note that almost all the

companions claimed so far, with the exception of PDS 70 B, were identified in L′ and then doubt arise about their real nature. It is important to confirm more planets inside the cavity of transition discs in order to constrain the dynamical clearing scenario (see Section 4.1.2), very promising in the theory of gap and cavities formation.

II. Gap or cavities in disc structures

A second diagnostic to search for embedded planets is by looking at the morphology of either or both the dust and the gas emission, mostly at mm wavelengths, where the companion may induce the formation of characteristic rings and gaps (see, e.g. the prototypical cases of HL Tau, Isella et al. 2016 and the recent compilation of gaps and rings in the DSHARP, Huang et al. 2018, Andrews et al. 2018b and in the Taurus surveys, Long et al. 2018b). This hypothesis has been tested extensively by comparing ALMA observations with the disc emission derived through detailed hydrodynamical and radiative transfer simulations (e.g. Dipierro et al. 2015b; Clarke et al. 2018). This method is simple and potentially powerful to infer the presence of planetary companion. However, it suffers from a number of uncertainties: first, planets are not the only possible explanation for the formation of rings (alternatives being condensation fronts at snowlines or dead zones in the disc, see Chapter 4); secondly, due to the required assumptions on the disc physics and dust properties, it is very uncertain to determine the planet properties (such as its mass) based on dust or gas morphologies (Zhang et al. 2018). Moreover, a natural question is why given the large number of discs that show structures at tens of au, the Jupiter-like planets observed so far in the same separation range have numbers so low. If gaps are the signature of planets, it is possible to deduce the planet mass from the gap morphology. This exercise was performed using surveys of observed discs (e.g. Taurus and DSHARP targets, Lodato et al. 2019; Bae et al. 2018; Zhang et al. 2018). In all of them, the planets occupy a distinct region in the parameter space with respect to the exoplanet population (Fig. 1.14), non accessible with the current techniques. Direct imaging technique success in detecting planets at large separations but with larger masses than the ones estimated though this technique. On the other hand, transit and radial velocity methods are not able to reach such large separations even if they reach similar mass values. The planetary mass derived through the gap width measurement (or comparing the disc morphology with simulations) is in agreement with the theoretical expectation of the minimum mass to carve a dust gap. For low viscosity (α <0.01), the gap width, defined as the distance between the location of the brightness minimum in the gap and the ring peak, scales with the planet Hill radius, with a proportionality constant (see Pinilla et al. 2012a; Rosotti et al. 2016; Fung & Chiang 2016; Facchini et al. 2018b). Interestingly Lodato et al. (2019), found that these putative young embedded planets, would end up being cold Jupiters after accreting and migrating. We need to keep in mind that a single planet can open multiple gaps (e.g., Fedele et al. 2018; Zhang et al. 2018; Dong et al. 2018a) and multiple planets can open a single gap (Zhu et al. 2011) depending on the disc properties (e.g.viscosity, pressure, Pinilla et al. 2012a; Fung et al. 2014), thus there is not always a one-to-one correspondence between gaps and planets.

III. Kinematic signatures of the planets

The third novel diagnostic for plant formation in discs is based on detecting the signature of the planet gravitational force on the velocity field of the gas surrounding it. In a typical case, with no perturbers, the disc orbits around the host star mostly at Keplerian velocity because the central star is much more massive than its protoplanetary disc. CO

emission line profiles observations confirmed this hypotesis (e.g. Sargent & Beckwith 1987; Guilloteau & Dutrey 1998). However, the presence of a planet can perturb this profile. Several ways to detect this signature have been proposed recently, either by looking at azimuthally averaged radial velocity profiles (Teague et al. 2018), or at the characteristic kink in selected velocity maps (Perez et al. 2015b; Pinte et al. 2018b, 2019, 2020), or, finally, through the presence of an asymmetry in the velocity fields (moment one map of line emission), once the Keplerian background has been subtracted (Pérez et al. 2020). In particular, the first recent indirect detection using two of these techniques was done on HD 163296 B by Pinte et al. (2018b), Teague et al. (2018).

The method used by Pinte et al. (2018b) is based on the fact that embedded planets launch spiral waves at Lindblad resonances inside and outside their own orbit (e.g. Ogilvie & Lubow 2002), with a consequent disturbance of the local Keplerian velocity pattern. Perez et al. (2015b) also predicted that the kinematics associated to the circumplanetary disc should be detectable through ALMA data observations. Typically, a keplerian disc shows a butterfly pattern in the velocity maps (de Gregorio-Monsalvo et al. 2013; Rosenfeld et al. 2013a). Looking at a single channel, the emission is shown as an isovelocity curve coming from the upper and lower surfaces. If a perturber is present, there will be a twisted emission and the wake of a spiral, due to the deviation from keplerian velocity produced by an embedded planet. Through a simple model with two infinitely thin emitting surfaces, it is possible to infer the position of the companion (projected distance and PA). However, in order to derive the planetary masses, observations have to be combined with simulations. The strong evidence to relate this perturbation to the presence of a planetary companion is that the emission is highly localized in both space and velocity, and the kink is detected over a small range of channels. With this first

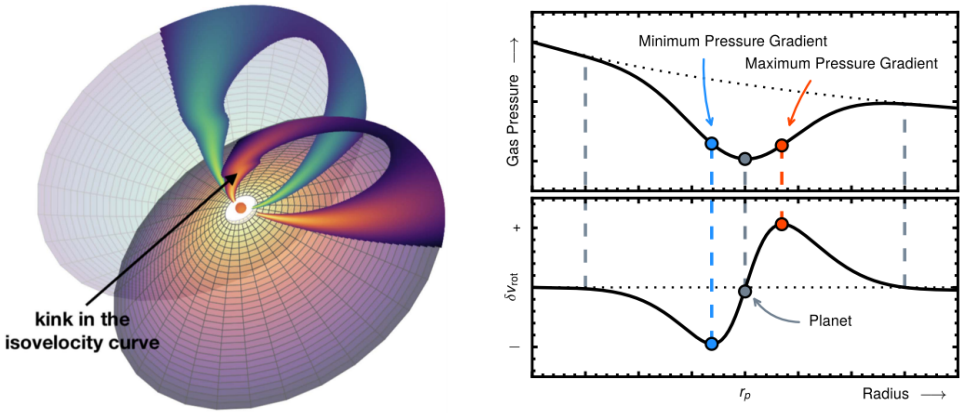

Figure 1.17: On the left, we show the geometry of a inclined flared disc coming from the upper and lower emitting layer. In the presence of a perturber, a 'kink' distortion of the velocity can be observed (Figure taken from Pinte et al. 2018b). On the right, we present how the pressure and the rotation velocity can be affected by the presence of a planet (Figure taken from Teague et al. 2018)

method a signature of a protoplanet with mass of 2 M_{Jup} at a separation of 260 au was detected by Pinte et al. 2018b (Fig. 1.17, left panel). The signature consisted in a 15% deviation from Keplerian rotation around the star in both Band 6 and 7 for two different ^{12}CO transitions.

Independently, another work by Teague et al. (2018) used a different technique to

detect planetary companions. This is based on a new way to measure the rotation curves of CO isotopologue emission to probe the local pressure gradient (see Fig. 1.17, right panel) and to distinguish deviation from the keplerian velocity with extreme precision. The gas rotation is dependent on the pressure of the total gas and it is not affected by uncertainties due to gas-to-dust ratios or local chemical abundances. The deviation can be produced either by disc structures or by a Jupiter-mass planets. The first step performed is to measure the emission height: it is important to deproject each pixels and measure any changes in the vertical direction of $\delta v_{\rm rot}$. The moment one map is fitted with a Keplerian rotation pattern assuming a value of the position angle as in Pinte et al. (2018a). The emission surface is then modelled as a Gaussian Process (GP) which assumes that the observations are described by a smoothly varying function (Teague et al. 2018), giving more flexibility to the process. The GP model found may show depressions in the emission surface which are typically in the same position of the gap locations. This can be a sign of a reduction in the local scale height or perturbation in the CO column density. Moreover, the velocity components (v_ϕ, $v_{\rm R}$, $v_{\rm z}$) can be derived in each annulus of the disc using the inferred emission surface and compared with the keplerian velocity. The planet would produce a change in the local pressure gradient with a consequent change in the rotation velocity (Kanagawa et al. 2015). In particular, it creates a minimum in the gas pressure and a maximum in the velocity pattern (see Fig. 1.17, right panel). This would generate "meridional flows" towards the center of the gap. An embedded planet, indeed, may open a gap in the gas and, at the midplane, may drive material away from itself for effect of the Lindblad torques. The gas pressure drops in that position as well as the local gas scale height. The presence of both regions of low pressure and high pressure generated a flow towards regions of low pressure i.e. the center of the gap. This flow is traced with optically thick ^{12}CO observations. Through this method, Teague et al. (2018) detected two companions in HD 163296 (at 83 au and 137 au). Both the companions are futher in with respect to the companion detected by Pinte et al. (2018b).

Similarly Pinte et al. (2019) perform a kinematic detection of a few Jupiter-mass planet orbiting around HD 97048 located at 130 au inside a gas and dust gap of the host disc. This is the first indirect detection of a companion inside a gap, which can explain both the dust/gas disc structure and the kinematic signature. This is an important discovery because it reveals that at least some gaps are the result of planet-disc interactions. Moreover, Pinte et al. (2020), detected other nine kinks that may be related to companions inside their gap or at the end of a spiral structure in DoAr 25, Elias 2-27, GW Lup, HD 143006, HD 163296, IM Lup, Sz 129 and WaOph 6, eight out of 18 circumstellar discs observed by DSHARP. For these observations, the localized deviations from Keplerian rotation were found over a small range in velocity and radial extent. Some of these images are, however, with low signal-to-noise and require confirmation.

We note that this method is more reliable than the one of deriving the mass of the companion through gap width. The width and depth of a gap in sub-millimetre thermal emission, indeed, depends both on the mass of the planet and on the Stokes number, which is derived from the local gas density and dust properties, typically not well constrained. The technique above described instead, is based on kinematics of gas and it is more reliable. The problem in doing this type of observations is the large amount of time that has to be requested to both spatially and spectrally resolve the distortion. Combing the information about gap and kinematics is something important in order to better constrain the gas density and dust properties.

Chapter 2

Gas and dust in protoplanetary discs

As explained in the previous Chapter, the interstellar medium material is composed by gas and dust. Gas is predominant and dust is just 1% of the total mass of the material. Gas is composed mainly by hydrogen, whereas dust is predominantly composed by silicates. In Section 2.1 we will describe the gas dynamics in a protostellar disc, whereas in Section 2.3 we will present the dust dynamics. In Section 2.4, we will describe the thermal structure of the disc. We refer to Pringle & King (2007), Clarke & Carswell (2014), Armitage (2010) for a detailed description of the topics of the current Chapter.

2.1 Gas Dynamics in Protoplanetary Discs

Once the disc has formed around the central protostar, as described in Chap. 1, the material orbits around the star in a gaseous and dusty disc. These systems are called "accretion discs". The type of central object around which the disc orbits strongly influences the nature of the physical processes taking place inside it.

2.1.1 Equation of motion

The gas can be described as a continuous fluid. As a consequence, the evolution of accretion discs is determined by the basic equations of viscous fluid dynamics, the continuity equation:

$$\frac{\partial \rho}{\partial t} + \nabla \cdot (\rho \boldsymbol{v}) = -\rho \boldsymbol{\nabla} \cdot \boldsymbol{v} \tag{2.1}$$

and the momentum equation, commonly referred to as Navier-Stokes equations:

$$\frac{\partial \boldsymbol{v}}{\partial t} + (\boldsymbol{v} \cdot \boldsymbol{\nabla})\boldsymbol{v} = -\frac{1}{\rho}(\boldsymbol{\nabla} p - \boldsymbol{\nabla} \cdot \boldsymbol{\sigma}) - \boldsymbol{\nabla}\Phi \tag{2.2}$$

where p stays for pressure, ρ is the mass density and Φ is the gravitational potential. Φ has both the contribution from the point-like objects (e.g. stars and planets) and the disc self-gravity. We will neglect for now this latter contribution and describe it in Section 2.2. We note that for the gas equation we do not set any index.

The stress tensor σ describes the effect of viscous forces in transporting angular momentum and dissipating energy across the disc. It provides a conversion of mechanical energy into heat which drives the accretion flow. The stress tensor is composed by the shear and bulk viscosity parameters. Classical shear viscosity depends on the fact that, in a disc, material at different radii moves with different angular velocity. This produces a viscous stress and an exchange of angular momentum between the material moving at different velocities. Thus, the stress is related to the local rate and strength of strain

between fluid elements ($R\Omega'$). The bulk viscosity is related to the compression of fluid and, if the gas is ideal, it can be neglected. In protostellar disc, the non-local mechanisms of angular momentum transport can also exist and in this case there is not any more a linear proportionality between stress and local gas properties strain.

It is possible to make some assumptions to simplify the equations described in the previous section and to analyze the accretion disc theory.

- First of all, we will use the thin-disc approximation, which means that the disc radial extent is larger than the disc thickness H (for protostellar discs $H/R \sim 0.1$). This approximation allows to simplify the calculations thanks to the integration of the equation of motion in the vertical direction. The quantities are thus evaluated per unit surface instead of per unit volume. We note, however, that protostellar disc not always are thin. This approximation thus has to be taken with caution.

- Secondly, it is important to adopt cylindrical polar coordinates (R, ϕ, z) with the protostar in the center and the disc in the $z = 0$ plane. The disc is, in first approximation, considered axisymmetric and the azimuthal gradients vanish. In such a way all the quantities can be considered independent from the azimuthal coordinate ϕ. The azimuthal velocity depends only on the radial coordinates $v_\phi = v_\phi(R)$. This approximation cannot be considered valid in the presence of non axisymmetric structures (e.g. spiral or horseshoes).

- The dynamical timescale is much shorter than the typical timescale over which the disc evolves, thus we can also consider that the radial velocity component is smaller than its azimuthal component (i.e. $v_R \ll v_\phi$), otherwise the disc would accrete onto the central star in less time than the one required for an orbit.

- We assume, in this Section, that self-gravity does not play a role. In general, indeed, the contribution from the point-like objects is way larger than the one coming from the disc self-gravity. Self-gravity can be neglected in particular if: $M_{\rm disc}/M_\star \ll H/R$. Standard, non self-gravitating disc models are based on the assumptions of centrifugal balance in the radial direction and hydrostatic balance in the vertical direction. The influence of self-gravity is described in Chap. 3 and 4.

- Viscosity is needed to produce the angular momentum transport required to allow the accretion of material onto the central star. Shear-forces are needed in this regards, whereas bulk viscosity can be neglected. Following this approximation we can re-write the viscous stress as:

$$\sigma_{\mathrm{R}\phi} = \eta R \frac{\partial \Omega}{\partial R}, \qquad \nabla \cdot \sigma|_\phi = \left(\frac{\partial}{\partial R} + \frac{2}{R} \right) \sigma_{\mathrm{R}\phi} \tag{2.3}$$

  where η is the shear viscosity coefficient. We note that angular momentum transport in discs seems to be driven by turbulence (see Section 2.1.5).

Given these assumptions, we can analyze in details the vertical, radial and azimuthal components of the continuity and Navier-Stokes equation. In particular, thanks to the approximation of thin disc, the disc behaves dynamically like a 2D system. This approximation is possible if we assume that the vertical motion of the gas and the vertical variation of v_R and v_ϕ are small. Moreover, if we assume that the viscous transport of angular momentum is slow, the orbital motion may be considered almost circular and

thus it is valid that: $v_z \ll v_R \ll c_\mathrm{s} \ll v_\phi$, where c_s is the sound speed. Integrating the Eq. 2.1 and 2.2 on the vertical direction we can rewrite:

$$\frac{\partial \Sigma}{\partial t} + \frac{1}{R}\frac{\partial}{\partial R}(R\Sigma v_R) = 0 \tag{2.4}$$

$$\Sigma\left[\frac{\partial v_R}{\partial t} - \frac{v_\phi^2}{R}\right] = -\frac{\partial P}{\partial R} - \Sigma\frac{\partial \Phi}{\partial R} \tag{2.5}$$

$$\Sigma\left[\frac{\partial v_\phi}{\partial t} + v_\phi\frac{\partial v_\phi}{\partial R} + \frac{v_R v_\phi}{R}\right] = \frac{1}{R^2}\frac{\partial}{\partial R}R^2 T_{R\phi} \tag{2.6}$$

where Σ, P and $T_{R\phi}$ are the vertically integrated versions of, respectively, ρ, p and σ_{ij}. We can define an average viscous parameter $\nu = \Sigma^{-1}\int_z \eta dz$, needed to describe how strong the viscous forces are in the disc. $T_{R\phi}$ is equivalent to:

$$T_{R\phi} = \nu\Sigma R\frac{\partial \Omega}{\partial R} \tag{2.7}$$

We note that in the case of accretion disc, the radial velocity is typically negative due to the material falling onto the host star.

2.1.2 Vertical, radial and azimuthal equilibrium

We consider now the vertical structure of the disc and the vertical hydrostatic equilibrium, in the thin disc approximation ($z \ll R$). Considering the approximations described in the previous section, the balance between the vertical pressure gradient and gravity forces is given by:

$$\frac{1}{\rho}\frac{\partial p}{\partial z} = -\frac{\partial \Phi}{\partial z} \tag{2.8}$$

The stress tensor does not have indeed a not-vanishing component in the vertical direction. Assuming that the pressure is barotropic ($p = p(\rho)$), the sound speed is defined as $c_\mathrm{s}^2 = \frac{dp}{d\rho}$ and that the disc is in hydrostatic balance, not self-gravitating, we can write the solution to the previous equation as a Gaussian profile:

$$\rho(z) = \rho_0 \ \exp\left[-\frac{z^2}{2H^2}\right] \tag{2.9}$$

where $H = c_\mathrm{s}/\Omega_\mathrm{k}$ is the typical vertical scale-length, $\Omega_\mathrm{k} = \sqrt{GM/R^3}$ is the keplerian angular velocity and ρ_0 is the density value at the midplane and thus it can be written in terms of the surface density as $\rho_0 = \Sigma/(\sqrt{2\pi}H)$. This shows how the temperature is linked to the disc thickness: the thermal pressure tends to expand the disc in the vertical direction against gravity. The disc aspect ratio can be thus defined as $H/R = c_\mathrm{s}/v_{\phi,\mathrm{k}}$, where $v_{\phi,\mathrm{k}} = \Omega_\mathrm{k}R$. If we require the gas to be thin, this is equivalent to requiring that the gas azimuthal motion is highly supersonic (i.e. $v_{\phi,\mathrm{k}} \gg c_\mathrm{s}$).

We now analyze the radial equilibrium and the centrifugal balance. We can assume stationarity and that the radial component of velocity is much smaller than the azimuthal one ($v_R \ll v_\phi$) as explained in the previous section and thus the radial component of Eq. 2.2 can be written as:

$$\frac{v_\phi^2}{R} \simeq \frac{1}{\rho}\frac{\partial p}{\partial R} + \frac{\partial \Phi}{\partial R} \tag{2.10}$$

Considering no self-gravity, the gravitational field depends just on the central object contribution and, in the limit of thin discs, it can be approximated as $\partial\Phi/\partial R \approx GM/R^2$. Moreover if we define as power laws the surface density ($\Sigma \propto \mathrm{R}^{-p}$) and the temperature ($T \propto \mathrm{R}^{-q}$), we can derive:

$$v_\phi = v_{\phi,\mathrm{k}}\left[1+\zeta\left(\frac{H}{R}\right)^2\right]^{1/2}, \qquad \zeta \equiv \frac{\partial \ln P}{\partial \ln R} = -\left(p+\frac{q}{2}+\frac{3}{2}\right) \tag{2.11}$$

Typically in discs, $p = 1$ and $q = 1/2$, thus $\zeta \simeq -11/4$. The conclusion is that pressure gradients, if negative, may alter the centrifugal balance with respect to the keplerian motion, and this is of the order of $(H/R)^2$. The material has stable circular orbits with sub-keplerian velocity. It does not need to orbit at keplerian velocity due to the additional support from the thermal pressure forces. The deviation appears to be small for the gas, but the fact that gas rotates at sub-keplerian motion plays an important role for dust as we will show in Section 2.3.4.

We finally discuss the azimuthal components of the Navier-Stokes equation which expresses angular momentum conservation. Combining Eq. 2.4 with Eq. 2.6, after some calculations it is possible to obtain the equation of angular momentum conservation for a viscous fluid disc:

$$\frac{\partial}{\partial t}(\Sigma R v_\phi) + \frac{1}{R}\frac{\partial}{\partial R}(R v_R \Sigma R v_\phi) = \frac{1}{R}(\nu \Sigma R^3 \Omega') \tag{2.12}$$

We note that the right-hand side of the equation is the only non-vanishing component of the stress tensor. This equation is fundamental in accretion disc theory also to understand that viscous forces are crucial for accretion. The left-hand side, is the Lagrangian derivative of the angular momentum per unit area $\Sigma R v_\phi$ of an annulus at a distance R from the host star: composed by the time derivative and by the radial advection of angular momentum. Finally, the right-hand side is the flux of angular momentum produced by the disc viscosity and it is related to the torque exerted by viscous force.

2.1.3 Steady state solution

In general protoplanetary discs are not in a steady state, but the study of the a stationary disc may help to understand better the disc evolution. If we consider the structure of a stationary disc, we neglect time derivatives in Eq. 2.4 and 2.12, we can immediately define two quantities:

$$\dot{M} = -2\pi R \Sigma v_R \tag{2.13}$$

$$\dot{J} = \dot{M} R^2 \Omega + 2\pi\nu\Sigma R^3 \Omega' \tag{2.14}$$

$\dot{M}$ is the constant rate of mass flux in a disc annulus and it is positive when the fluid is moving inwards (i.e. $v_R < 0$); $\dot{J}$ is the constant net angular momentum flux across an annulus of the disc. The first term of $\dot{J}$ is the angular momentum flux advected with the inward flow and the second one is the viscous torque, which is negative for a keplerian disc, meaning an outward transport of the angular momentum. Usually, such steady state solutions are obtained assuming that there is a region with "no torque" (Frank et al. 1985) where $\dot{J} = \dot{M} R_{\mathrm{in}}^2 \Omega(R_{\mathrm{in}})$. R_{in} is the location where $\Omega'(R_{\mathrm{in}}) = 0$ and the viscous torque vanishes. The region which connects the disc with the central object is called a boundary

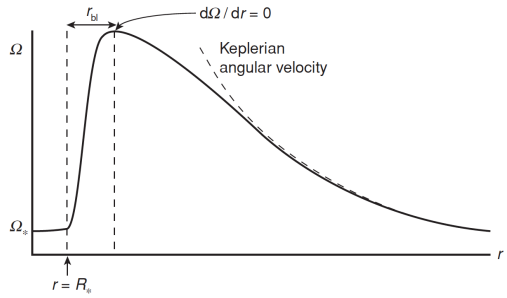

Figure 2.1: Illustration of the angular velocity profile which connects the outer disc to the slowly rotating star. The boundary layer is defined as $r_{\rm bl}$. In correspondence with the maximum of the curve ($R_{\rm in}$) $\Omega_{\rm k}'$ vanishes. Credits. Armitage (2010)

layer (shown in Fig. 2.1). In this region, there is an increase of the gas angular velocity with radius, contrary to what happens in the rest of the disc. After some calculations, we can write the profile $\nu\Sigma$ in the case of a keplerian disc as:

$$\nu\Sigma = \frac{\dot{M}}{3\pi}\left(1 - \sqrt{\frac{R_{\rm in}}{R}}\right) \tag{2.15}$$

In particular, $\dot{M} = 3\pi\nu\Sigma$ for $R_{\rm in} \gg R$. In a stationary disc, where we neglect time derivatives, we can combine the equations Eq. 2.4 and 2.12 and use the relation $v_\phi = R\Omega$. Thus it is possible to derive that:

$$v_R = \frac{1}{R\Sigma(R^2\Omega)'}\frac{\partial}{\partial R}\left(\nu\Sigma R^3\Omega'\right) \tag{2.16}$$

2.1.4 Time dependent solutions

The evolution of the surface density of an accretion disc can be derived inserting Eq. 2.16 in the Continuity Equation (Eq. 2.1):

$$\frac{\partial\Sigma}{\partial t} = -\frac{1}{R}\frac{\partial}{\partial R}\left[\frac{1}{(R^2\Omega)'}\frac{\partial}{\partial R}\left(\nu\Sigma R^3\frac{\partial\Omega}{\partial R}\right)\right] \tag{2.17}$$

This is closely related to the kinematic viscosity ν. We can see that in order to have disc evolution, we need to have $\nu \neq 0$. If we do not have viscosity to transport the angular momentum, each element would stay on its initial orbit. We note that if viscosity is constant, Eq. 2.17 can be considered as a diffusion equation evolving under viscosity. A simple dimensional analysis of its surface density structure shows that it evolves on a timescale of $t_{\rm visc} \equiv R^2/\nu$, called viscous time.

In order to solve Eq. 2.17, due to its complex dependence on viscosity, the general solution is obtained numerically. For a keplerian disc, if we assume that the viscosity is a simple function of radius (Pringle 1981; Hartmann 2009), the solution can be found also analytically. A first class of solutions has a constant viscosity and its initial condition goes under the name of "spreading ring" solution (Lynden-Bell & Pringle 1974a). The function is a diffusive evolution of the surface density distribution. As initial condition we assume the surface density to be characterized by an infinitesimal ring (δ function) of

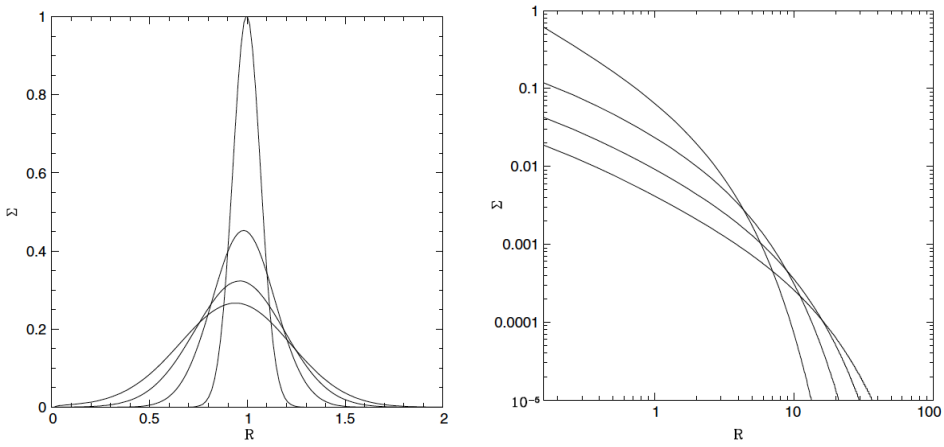

Figure 2.2: Surface density evolution of a Keplerian spreading ring - considering ν constant (left) and a radially truncated disc (right). The different lines represent different times increasing from top to bottom. Credits Lodato (2008).

mass M at radius R_0:

$$\Sigma(R, t = 0) = \frac{M}{2\pi R_0}\delta(R - R_0). \tag{2.18}$$

The surface density evolution solution is then:

$$\Sigma(x, t) = \frac{m}{2\pi R_0}\frac{x^{-1/4}}{\tau}e^{-(1+x^2)/\tau}I_{1/4}\left(\frac{2x}{\tau}\right), \tag{2.19}$$

where $x = R/R_0$, $\tau = 12\nu t/R_0^2$ and $I_{1/4}$ is the modified Bessel function of the first kind. We show the evolution of the solution over time (lines top to bottom) in the left panel of Fig. 2.2. Under the action of viscous forces, the ring spreads both inwards and outwards in order to conserve the total angular momentum. Viscosity thus acts to redistribute angular momentum between different annuli. The inner part of the disc loses angular momentum and accretes onto the central star, while the outer disc with an excess of angular momentum, moves outward. At late times, most of the mass is eventually accreted and just a negligibly small amount of mass is transported to infinitely large radii.

Another commonly used solution is the self-similar solution (Lynden-Bell & Pringle 1974a; Hartmann et al. 1998, see right Fig. 2.2), derived assuming that the viscosity scale as a power-law with the radius: $\nu \propto R^\gamma$, were γ is constant and there is a truncation radius. Its initial density profile may be considered as:

$$\Sigma(R, t = 0) = \frac{C}{3\pi\nu(R)}\exp\left[\left(\frac{R}{R_1}\right)^{2-\gamma}\right], \tag{2.20}$$

where C is a constant and R_1 is the value of an arbitrary truncation radius. It is thus possible to derive the self-similarity solution:

$$\Sigma(R, t) = \frac{C}{3\pi\nu(R)}T^{-(5/2-\gamma)/(2-\gamma)}\exp\left[\left(\frac{R}{R_1}\right)^{2-\gamma}\right] \tag{2.21}$$

where T is defined as:

$$T \equiv 1 + \frac{t}{t_\nu} \quad \text{with} \quad t_\nu \equiv \frac{1}{3(2-\gamma)^2} \frac{R_1^2}{\nu(R_1)} \tag{2.22}$$

As for the spreading ring, this solution shows how the disc spreads both inward, with an accretion onto the central protostar over time, and outward. The transition at which part of the material is moving inward and part outward is $\sim R_1(t/t_\nu)^{1/(2-\gamma)}$ and it increases with time. This phenomenon may be not easy to be observed (see Section 1.3.2, Rosotti et al. 2019b) for the sensitivity of the instrument. In both the solutions the evolution follows the viscous time described previously. The disc extent observed at a specific time in disc evolution may thus tell us something about the level of disc viscosity.

2.1.5 Turbulent angular momentum transport and viscosity

The evolution of angular momentum is key for the process of accretion in discs which depends on viscosity. It is thus extremely important to understand what is the physical process behind it, which is still the major unsolved problem in accretion disc theory. Standard kinetic viscosity produced by collisions between gas molecules is too low to account for the transport of angular momentum needed in accretion discs.

In order to see what can generate viscosity we need to perform an analysis of the evolution timescale related to this process. It can be shown that the ratio between the viscous time ($t_{\rm visc} \equiv R^2/\nu$) and the dynamical time ($t_{\rm dyn} = \Omega^{-1}$) can be connected to turbulence through the definition of the Reynolds number: $Re \equiv \Omega R^2/\nu$. It quantifies the intensity of viscous forces against the inertial forces. This number gives an information about the turbulence of the system: if Re is low, it means that viscous forces are dominant, whereas if Re is high, the fluid becomes turbulent (e.g. $Re > 10^5$). If we consider the standard kinetic viscosity for a typical disc, the timescale needed to accrete the disc would be extremely larger than the typical disc lifetime. Thus the collisional processes are insufficient to explain the viscosity process and viscosity must be much larger. The Reynolds number is found to be quite large in accretion discs and, thus, we can expect the development of turbulence. The transport mechanisms is more efficient in turbulent flows with respect to laminar ones considering the different way to exchange angular momentum. For turbulent phenomena, indeed, the angular momentum is transported through mixing of fluid elements (Turner et al. 2014). The viscosity derived in such a way would be several orders of magnitude larger than the one of collisions. The magnitude of turbulent transport is not well known in proto-planetary discs and it is not trivial to consider a model of turbulence to describe viscosity. For this reason, this 'anomalous' viscosity was parameterized by modellers in terms of an unknown dimensionless parameter (α), often described through the Shakura & Sunyaev (1973) prescription:

$$\nu = \alpha c_{\rm s} H. \tag{2.23}$$

The "turbulent" kinematical viscosity above described follows from the fact that the magnitude of viscosity is given by $\nu \sim \hat{v} l$, where $\hat{v}$ is the typical turbulent velocity and l is the typical size of the large eddies given by the disc thickness ($l \lesssim H$). If the turbulence would be highly supersonic, it will be easily dissipated through shocks, thus we can assume that $\hat{v} \lesssim c_{\rm s}$. Given this, it follows that $\alpha < 1$. α contains all the uncertainties about this phenomenon (Lodato 2007, 2008) and it is required $\alpha < 1$. The value $c_{\rm s}H$ represents the highest level of viscosity that can be sustained inside the disc. The value of α can vary depending on the source. In order to reproduce the expected disc lifetime in a disc, the

α value is typically considered $\sim 10^{-2}$ for protostellar discs. According to the turbulence theory, it is necessarily to have a mechanism able to constantly inject energy in the fluid at the largest scales in order to sustain the turbulent motion otherwise turbulence would decay with time for dissipative effects. Mechanisms such as magneto-rotational instability (MRI) or gravitational instability (GI) can be responsible for the angular momentum transport and may play an important role in sustaining the turbulence. This will provide a source of transport of angular momentum and energy inside the disc. GI is fully described in the following section, while we provide here a definition of MRI. MRI is an instability that arises from the action of the magnetic field in a disc and it may develop if there is a weak poloidal magnetic field and if the disc rotates differentially. It can lead to large scale mixing and turbulence very quickly.

Observational constraints to measure disc turbulence can be derived by looking at rotovibrational lines (Carr et al. 2004), low-resolution CO spectra at millimeter wavelengths (Dutrey et al. 1998), or, more recently, with the advent of ALMA, spatially resolved molecular spectroscopy (Simon et al. 2015). One of the main issue in the derivation of turbulence is the broadening degeneracy of turbulence with thermal emission and, secondly, with keplerian motion. Attempts with sub-mm observations were performed by e.g., Hughes et al. (2011) and Guilloteau et al. (2012) sensitive to the outer (>50 au) disc and in the inner region with infrared spectroscopy. The result starts to suggest a wide range of turbulent velocities between different protoplanetary disc systems. The variation in Keplerian velocity with scale height and pressure gradient contributions may complicate the measurement (Rosenfeld et al. 2013b). The power of spatially resolved molecular line emission observations opened the possibility to study the width and depth of the disc line profiles together with the spatial information needed to better constrain the vertical temperature structure. This allows to reveal a 3D picture of turbulence also in the in the outer disc. The great angular resolution and sensitivity of ALMA allowed more precise measurements at millimeter wavelengths. Simon et al. (2015), Flaherty et al. (2015), Teague et al. (2016), Flaherty et al. (2018) showed that the effect of turbulence and temperature may act in a different ways in spatially resolved images.

2.2 Self-gravity

Self-gravity is the mutual gravitational influence of the gas on itself, rather than the the gravity related to an external body. It can play an important role in regulating the evolution of protostellar and protoplanetary discs. In this regards, an important role is played by the disc mass. However, its derivation through observations is still challenging (see Sec. 1.3.4) and the methods used to derive it can lead to underestimates of the total disc mass. The possible increase of mass will enhance the probability to have self-gravity in the disc. We note that all type of accretion disc systems may be affected by self-gravity. The occurrence of self-gravity in discs is still low but there are indirect evidences of the fact that this process takes place in young discs (e.g. spirals, Chap. 4, luminosity argument, Sec. 3.2). We underline that, for self-gravitating discs, the evolution of accretion discs does not follow the assumptions of centrifugal balance in the radial direction and hydrostatic balance in the vertical direction. Below we underline the main differences with the discussion in Sec. 2.1.

- It is valid the thin-disc approximation and that accretion takes place on a long timescale (see Section 2.1).
- As described in Section 2.1, also for self-gravity, the evolution of accretion discs follows the continuity equation and Navier-Stokes equations. However the gravi-

tational potential of the Navier-Stokes equation has to take into account not just the contribution of the central point mass, but also that of the disc. In particular, $\nabla\Phi_{\rm sg}$ can be derived from the solution to Poisson's equation ($\nabla^2\Phi_{\rm sg} = 4\pi G\rho_{\rm g}\delta(z)$), where G is the universal constant of gravitation and $\delta(z)$ is the Dirac δ-function, if the thin-disc approximation is valid.

- **Vertical structure: hydrostatic equilibrium.** In the self-gravitating case, scale height has to be considered in a different way from previously described. The left hand size term of Eq. 2.8 is modified by:

$$\frac{c_{\rm s}^2}{\rho}\frac{\partial\rho}{\partial z} = -2\pi G\Sigma(z) \tag{2.24}$$

The solution of the hydrostatic balance can be computed analytically in the case of $c_{\rm s}$ constant i.e. self-gravitating isothermal slab. The density profile is not anymore gaussian (as in Eq. 2.8), but it is given by:

$$\rho(z) = \rho_0\ \frac{1}{cosh^2(z/H_{\rm sg})}, \tag{2.25}$$

where $H_{\rm sg} = c_{\rm s}^2/(\pi G\Sigma)$ is the thickness for a self-gravitating disc. It is important to note that when the contributions of the central star and of the disc are both important there is no analytical solution to the hydrostatic balance equation and an interpolation between the solution of the two approximations have to be used (Bertin & Lodato 1999).

In particular, for thin discs the vertical structure of the disc is affected by the disc self-gravity even when the disc mass is much smaller than the central object mass. This can be seen by comparing the thickness in both the not-self gravitating disc (H) and where self-gravity becomes important ($H_{\rm sg}$):

$$\frac{H_{\rm sg}}{H} = \frac{c_{\rm s}\Omega_{\rm k}}{\pi G\Sigma} = Q, \tag{2.26}$$

where the factor Q is the Toomre parameter (Toomre 1964, see Section 2.2.1). Self-gravity becomes important when Q$\sim$1 and thus the value of Q is used to address how much a disc is gravitationally unstable. This means that whenever self-gravity is important in the vertical direction, the disc is near the instability threshold for gravitational instability (GI). We note that it is possible to verify through simple calculus that Q$\sim$1 is equivalent to $\frac{M_\star}{M_{\rm disc}} = f\frac{H}{R}$. This allow us to derive a minimum mass required for the disc to be self-gravitating: if a disc is colder and thinner it is more probable it is self-gravitating.

- **Radial equilibrium: centrifugal balance.** The compact object in the center dominates in general the gravitational field for accretion discs, but sometimes the disc self-gravity has a considerable effect. This may happen when the disc and stellar mass are comparable. On the contrary, when the mass of accretion disc is much lower than the central object, the approximation described in Section 2.1 can be appropriate. The presence of self-gravity can modify Eq. 2.10 by:

$$\partial\Phi_{\rm disc}/\partial R \approx GM_{\rm disc}/R^2. \tag{2.27}$$

Consequently, self-gravity will modify also the solution v_ϕ (Eq. 2.11), such as it may be written more generally as:

$$v_\phi = v_{\phi,\mathrm{circ}} \left[1 + \beta \left(\frac{c_\mathrm{s}}{v_{\phi,\mathrm{circ}}} \right)^2 \right]^{1/2}, \tag{2.28}$$

where $v_{\phi,\mathrm{circ}}$ is the circular velocity in the absence of pressure such as $v^2_{\phi,\mathrm{circ}} = r(d\Phi/dR)$, and the gravitational potential depends on the regime considered. We note that the disc mass needs to be implausibly large for protostellar discs in order to dominate the rotation curve. However, if the disc is marginally gravitationally stable (Q$\sim$1) and $M_\mathrm{disc} = (H/R)M_\star$, self gravity can produce deviation from Keplerian motion of the order of H/R, stronger than the effect of pressure gradients to both gas and dust.

To conclude, for total disc masses small and such as $M_\mathrm{disc}/M_\star \sim H/R$, self-gravity affects the disc vertical structure. The rotation curve is, instead, only affected when the disc mass becomes comparable to $\mathrm{M}_\star$.

2.2.1 Gravitational instabilities development

One of the most important effects associated to self-gravity is the possibility to develop gravitational instabilities. In particular, the non-linear outcome of the instability can be violent and lead to disc fragmentation. On the other hand, the possibility of forming a long-lived spiral structure is related to the fact that the instabilities have a steady transport of angular momentum and self-regulate. For tightly wound perturbations ($m/(kr) \ll 1$), it is valid the Lin & Shu (1964) WKB dispersion relation, in the case of an infinitesimally thin disc:

$$(\omega - m\Omega(r))^2 = c_\mathrm{s}^2 k^2 - 2\pi G\Sigma|k| + \kappa^2 \tag{2.29}$$

where ω is the wave frequency, k is the radial wave number, m is the azimuthal wave number and κ is the epicyclic frequency (equivalent to Ω for a Keplerian disc) given by:

$$\kappa^2 = \frac{2\Omega}{R}\frac{d(\Omega R^2)}{dR}. \tag{2.30}$$

From this, we derive the stability criterion, which is:

$$Q = \frac{c_\mathrm{s}\kappa}{\pi G\Sigma} > 1 \tag{2.31}$$

The dispersion relation and stability criterion are valid in the case that the equilibrium structure of the disc is axisymmetric and that the disc is infinitesimally thin. Moreover, the relation shown for the vertical hydrostatic balance, shows that for $(c_\mathrm{s}\Omega)/(\pi G\Sigma) \sim 1$ the disc self-gravity contributes to the vertical hydrostatic balance equation as much as the central object. Finally, when $\omega^2 > 0$ a perturbation propagates in a wave-like way, if instead $\omega^2 < 0$ an exponentially growing instability arises. The first and the third terms of the dispersion relation are stabilizing factors, whereas the second one is a potentially destabilizing term. The first term, related to pressure stabilizes the disc at small wavelengths, whereas rotation (third term) is effective at stabilizing large scale disturbances. For gravitationally unstable discs ($Q < 1$), the most unstable wavelength is of the order of the disc thickness. We note that if the tightly wound approximation (Lau

& Bertin 1978) is not satisfied, we should introduce the dimensionless parameter J in addition to Q (see Lodato 2007). Gravitational Instability (GI) has the powerful ability to drive angular momentum transport and accretion of matter onto the central object (e.g under the form of a spiral structure in the disc). In order to maintain the turbulence for long enough, energy needs to be continuously injected at the largest scales. This is usually associated with the development of instabilities in the disc. In order to evaluate what is the stress induced by GI, we need to consider viscosity. Energy appears to be dissipated according to the expectations from a viscous model at least in the case of low mass discs. Low mass discs can support a relatively large spectrum of density waves, with different m and wave numbers of the order of $1/H$. In the presence of effective cooling, many of such waves can be easily excited. One possibility is that such waves interact with one another, undergo shocks and dissipation, and therefore do not propagate over large radial distances, especially if their typical wavelength is small. When Q is much different from unity, the disc is not non-self regulated and may be evolving in time (either in surface density or temperature), we need to use the relation by Lin & Pringle (1987, 1990), dependent from Q.

2.2.2 A self-regulation mechanism

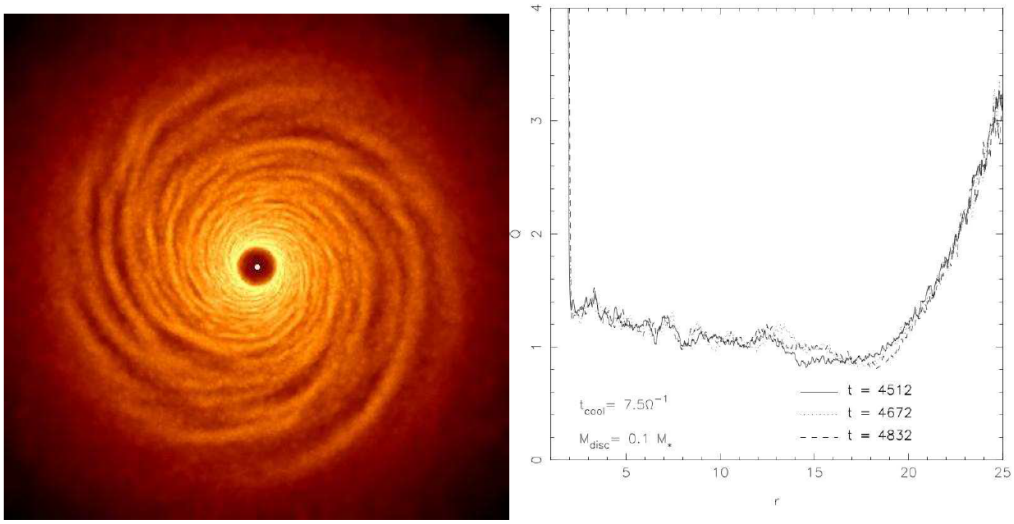

Figure 2.3: Numerical simulations by Lodato (2007) showing the development of a gravitational instability producing prominent spiral structures (left). On the right the radial profile of the azimuthal and vertical average of Q, which varies over the radius and in time (three curves). The values of M_{disc} was set to $0.1M_\star$ and t_{cool}=$7.5\Omega^{-1}$. Credits to Lodato (2007).

We now consider the non-linear regime of GI. A self-regulation mechanism is present where the Q parameters plays the role of an effective 'thermostat' for the disc temperature. The stability parameter Q is proportional to c_s, so colder discs are more unstable. If there are not other conditions, the disc cool down until it reaches marginal stability. At this point, the disc develops a gravitational instability in the form of a spiral structure (see left Fig. 2.3). The presence of shocks induced by the instability lead to an efficient energy dissipation and heat the disc. If sufficient heat is retained, the disc will heat back up,

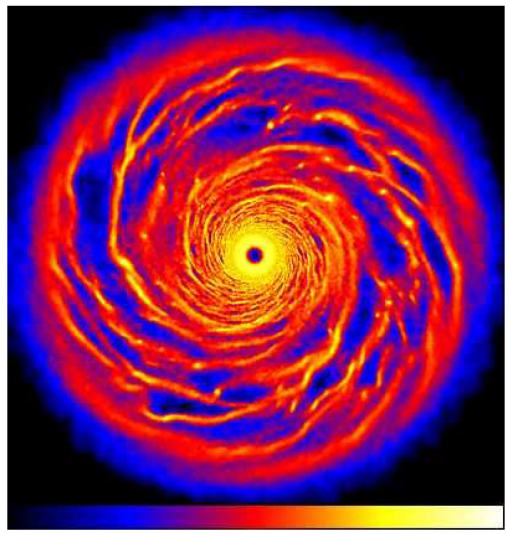

Figure 2.4: Numerical simulations showing an unstable self-gravitating disc which breaks up into numerous gravitationally bound clumps Lodato (2007). M_{disc} was set to $0.1M_\star$ and $t_{cool}=3\Omega^{-1}$. Credits to Lodato (2007).

quenching the instability and so on. This produces Q close to unity (see right Fig. 2.3). In order for this self-regulation process to work, the presence of a dissipative component is essential.

The instability provides heat on a timescale of the order of $t_{dyn} = \Omega^{-1}$; thus the thermostat have to be slower than this timescale. For this reason the cooling rate $\beta = \Omega t_{cool}$ (t_{cool} is the cooling timescale) parameter have to be larger than unity. The β is controlling the evolution and saturation of the instability and it is added to the Q and $M_{disc}/M_\star$ parameters. β also determines the efficiency with which the gravitational instability redistributes angular momentum and allows accretion. We call thermal saturation of GI when the cooling is relatively inefficient and the disc settles into a self-regulated state: spiral structure steadily transports angular momentum providing the heating required to balance cooling and keep the disc in thermal equilibrium. Interestingly if the disc mass is low, the transport induced by GI is local and analogous to viscosity. Finally, a relation between α and the cooling rate has been found by Pringle (1981). If the disc does not reach a quasi-steady self-regulated state, the disc will fragment into several bound objects. The non-linear stabilization of the perturbation only works if the heat generated by compression and shocks is not removed efficiently from the disc through cooling.

All these is valid as long as we assume that the only source of heating in the disc is that provided by the instability itself as it dissipates energy through shocks. However, protostellar discs are generally expected to be irradiated by either the central protostar, their natal envelope, or nearby stars. Irradiation has the effect of destabilizing the disc, because smaller amplitude perturbations can collapse.

2.2.3 Fragmentation

Fragmentation can occur if the saturation mechanisms fail to prevent runaway growth of perturbations and the unstable region of the disc will break up into bound objects

(Fig. 2.4). As the perturbations grow to non-linear amplitudes, their own self-gravity causes them to collapse and separate from the background disc. This will generate a reduction in local surface density and an increase in Q, shutting down the instability. This is extremely important in the case of protostellar discs because this can lead to the formation of bounded companions. Fragmentation can happen both as a consequence of the rapid cooling or of accretion. In particular, if we consider isolated discs, Q decreases due to a progressive drop in the temperature. The cooling time can be defined as:

$$t_{\rm cool} = \frac{U}{2\sigma T_{\rm disc}^4}, \tag{2.32}$$

where U is the thermal energy disc content per unit area. If the cooling is rapid GI cannot provide sufficient heating to counteract cooling, and the disc will fragment, most probably when:

$$t_{\rm cool}\Omega < \beta_{\rm crit} \sim 3 - 6. \tag{2.33}$$

In order to provide the required heating to reach equilibrium, self-gravity does not need to be very large in the case of relatively long cooling times; whereas for shorter cooling times, saturation amplitude of the spiral structure increases until it becomes too large to be sustained by the disc and ends up into fragmentation. There is a minimum value of $t_{\rm cool}\Omega$ needed to prevent fragmentation. Thus, fragmentation threshold can be considered in terms of how much angular momentum can be transported through self-gravity in a steady state. This is related to the inability of the disc to redistribute angular momentum on short timescales for a prolonged period of time. When the disc is, indeed, fed at a high accretion rate this can lead into fragmentation. The accretion of material, push the $Q > 1$ parameter to decline towards unity. In particular, if the infall of material (at some rate $\dot{M}_{\rm in}$) is smaller than the maximum possible rate that GI can provide, the disc mass will act as the regulator of transport (Zhu et al. 2012a); if the case is instead the opposite ($\dot{M}_{\rm in} > \dot{M}_{\rm max,GI}$), the disc will ultimately fragment (Kratter et al. 2008). Finally, there is a critical radius after which the disc can fragment identified by Matzner & Levin (2005) as 50 - 100 au and by Clarke (2009) after 70 au, while self-regulation is expected between 20 - 70 au.

2.3 Dust Dynamics in Protoplanetary Discs

As previously said, dust is just 1% of the total mass of the interstellar medium. Dust is composed of grains of different shape, dimension and porosity (see Testi et al. 2014 for a review). Dust particles can be considered as a pressureless and viscousless fluid. This is a valid approximation because the collision between dust grains has a really low probability to happen with respect to the collision with the gas particles in protoplanetary discs and there is no transfer of momentum associated with velocity differences between dust particles. The dust dynamics is regulated just by gravitational forces from the host star and areodynamical interaction with the gas. It has a different dynamics than the one of the gas and its dynamics has to be considered with different equations.

2.3.1 Dust-gas aerodynamical coupling

Dust and gas interact through the aerodynamical drag. The drag force tends to damp the difference in velocity between the solid and the surrounding fluid. It gives a measure of the intensity of aerodynamical coupling between the gas and the dust. This can happen

on a timescale which depends on the properties of both the solids and the gas present in the disc. The drag force is usually expressed as:

$$\boldsymbol{F}_{\rm D} \equiv -K\Delta\boldsymbol{v} \tag{2.34}$$

where $\Delta\boldsymbol{v}$ is the velocity difference between dust and gas and K depends on the regime on which particle are.

The drag force can be considered in two main regimes depending on the properties of dust particles a and of the environment: the Epstein (Epstein 1924) and Stokes regimes (Stepinski & Valageas 1996). The Epstein regime refers to grain sizes smaller than the mean free path: $a < 9/4\lambda_{\rm mfp}$. The drag force is thus computed by considering the transfer of angular momentum between collisions between individual gas molecules and the dust grain surface. The motion of dust is chaotic and collisions depend on the temperature of the gas. If particles are, instead, larger than the mean free path: $a > 9/4\lambda_{\rm mfp}$, they are in the Stokes regime. In this case, the gas particles behave like a fluid in which the dust is immersed and that transfer kinetic energy to the dust through viscous friction. The motion around the dust particle is dependent on the laminar or turbulent regime of the flow. The drag force depends on the Stokes regime on the Reynolds number: $Re_{\rm p} \equiv 2a \mid \Delta v \mid /\nu$, where a is the characteristic length-scale radius of the sphere inside the fluid, Δv is the characteristic relative velocity and ν is the kinematical viscosity. The different dependence on the Reynolds number gives rise to three different sub-regimes: Stokes I, Stokes II and Stokes III. It can be shown (e.g., Laibe et al. (2012)) that the typical value of the mean free path is $\lambda_{\rm mfp} \sim$10 m $\cdot$ (10^{-13} g cm$^{-3}/\rho_{\rm g}$). In most of the cases, thus, the drag force falls in the Epstein regime.

2.3.2 Stopping time

If we consider the gas velocity equal to zero, the stopping time $t_{\rm s}$ is the time needed for the drag force $F_{\rm D}$ to stop a dust particle that moves with velocity $v_{\rm p}$ inside the gas. The dust particle, indeed, does not follow the gas motion instantaneously, but requires a certain amount of time. Assuming that the drag force remains constant, the stopping time can be defined as:

$$t_{\rm s} = \frac{m_{\rm p} \mid \Delta v \mid}{\mid F_{\rm D} \mid} = \frac{m_{\rm p}}{K}, \tag{2.35}$$

where $m_{\rm p} = 4\pi\rho_{\rm p}a^3/3$ is the mass of the dust particle, $\rho_{\rm p}$ is the material density and a is the radius of the particle, if we consider a compact homogeneous uncharged sphere, moving at a relative velocity $\mid \Delta v \mid$.

If we consider linear drag regimes, such as the Epstein and Stokes regimes (e.g., Laibe et al. 2012), the drag force decreases during its action (see Eq. 2.34). The stopping time in the different regimes can thus be derived following Laibe et al. (2012) to be:

$$t_{\rm s} = \begin{cases} \frac{\rho_{\rm p} a}{\rho_{\rm g} c_{\rm s}} \sqrt{\frac{\pi\gamma}{8}}, & \text{Epstein regime,} \\ \frac{2\rho_{\rm p} a^2}{9\nu\rho_{\rm g}}, & \text{Stokes regime I,} \\ \frac{2^{0.6}\rho_{\rm p} a^{1.6}}{9\rho_{\rm g}^{1.4}|\Delta v|^{0.4}}, & \text{Stokes regime II,} \\ \frac{6\rho_{\rm p} a}{\rho_{\rm g}|\Delta v|}, & \text{Stokes regime III.} \end{cases} \tag{2.36}$$

In all the cases, the stopping time increases with the size of particles: $t_{\rm s} \propto a^r$, with $r \geq 1$. From this, it is possible to understand that larger particles are less coupled with the gas.

2.3.3 Stokes number

In order to quantify the intensity of the drag force compared to the dynamical forces in action, it is possible to define a dimensionless parameter, the Stokes number:

$$\mathrm{St} = \mathrm{t_s}\Omega_\mathrm{k} \tag{2.37}$$

where Ω_k is the Keplerian frequency. This number describes the aerodynamical properties of dust particles. If dust grains with different e.g. sizes have the same Stokes number, they behave aerodynamically in an identical way. The Stokes number relates the stopping time directly to the unperturbed orbital gas flow. When St$\ll$1, the dust is strongly coupled to the gas and dust particles follow exactly the same dynamics of the gas. This typically happens for small, μm-sized grains. In this regime the stopping time is, indeed, much smaller than the Keplerian timescale. For St$\gg$1, the coupling between gas and dust is weak and the two fluids evolve with no influence on each other. The intermediate regime St$\sim$1 is called marginally coupled regime and this is the regime where the coupling between gas and dust is expected to produce the most significant effects on the dynamics of both components.

2.3.4 Dust dynamics in laminar viscous flow

We here describe the dust dynamics in laminar viscous flow. However, not always the motion of the gas can be considered laminar: most of the times it is in a turbulent state with variation in time and space. Let us consider a mixture of dust and gas in a disc that is axisymmetric, thin, non-self-gravitating, viscous and vertically isothermal. The dust component is considered pressureless and inviscid. The dynamical evolution of dust density and velocity can be described by the following equations:

$$\frac{\partial \rho_\mathrm{d}}{\partial t} + (v_\mathrm{d} \cdot \nabla)\rho_\mathrm{d} = -\rho_\mathrm{d}\nabla v_\mathrm{d} \tag{2.38}$$

$$\rho_\mathrm{d}\left[\frac{\partial v_\mathrm{d}}{\partial t} + (v_\mathrm{d} \cdot \nabla)v_\mathrm{d}\right] = F_D - \rho_\mathrm{d}\nabla\Phi \tag{2.39}$$

where Φ is the gravitational potential. These equations are valid for the dust (Laibe & Price 2012) and have to be combined with the gas continuity equation and the equation of the gas momentum conservation (Eq. 2.1 and 2.2). These four equations (Eq. 2.1, 2.2, 2.38, 2.39) have to be solved simultaneously. We refer to Nakagawa et al. (1986) to find a steady state solution. The latter gas equation has to be modified by adding the inverse of the drag force to the right side of the equation. This goes under the name of back-reaction on the gas flow. The back-reaction is the dust feedback on the gas which may produce remarkable effects on the gas motion. In this, the dust-to-gas ratio plays a key role. Typically the dust-to-gas ratio is assumed to be 0.01 in protoplanetary discs, thus the disc mass contribution is dominated by the gas and the dust feedback is usually neglected. However, it is known that the dust-to-gas ratio is not constant throughout the disc and the dust feedback may affect the disc dynamics.

In protoplanetary discs, as explained in Chap. 2, gas dynamic is not easy to be studied, since the gas surface densities have to be derived from a combination of ^{12}CO, bright but optically thick, and other optically thin but faint tracers. On the contrary, instruments such as ALMA and SPHERE are able to observe with a great level of details the dust thermal emission of (sub)mm grains and the scattering of μm grains, respectively. Understanding the dust dynamics and how this relates to the gas is of fundamental

importance. This would help to better interpret the observations and get insights also on the gas dynamics, both regarding the formation of discs and their evolution.

There is a marked separation between the radial and vertical motion of dust. Typical radial motion follows the radial drift timescale, whereas vertical motion follows the vertical settling timescale. Below we give some details on what is the radial drift and dust settling.

Radial drift

Dust of mm and cm size typically settle into the midplane and can be subject to radial drift. Let us consider the motion of both gas and solids in the radial direction. The gas feels pressure and viscous forces that reduce its orbital velocities and thus it orbits at a sub-keplerian velocity. Eq. 2.11 can be written also as:

$$v_{\phi,\mathrm{g}} = v_{\phi,\mathrm{k}} \left(1-\eta\right)^{1/2}, \tag{2.40}$$

where:

$$\eta = \frac{d\log P}{d\log R}\left(\frac{c_\mathrm{s}}{v_\mathrm{k}}\right)^2. \tag{2.41}$$

When $P \propto R^{-n}$, it is possible to write $\eta = n(c_\mathrm{s}/v_\mathrm{k})^2 = n(H/R)^2$ and the pressure declines with radius as a power law with index $n > 0$. Solids act as a pressureless fluid and they feel only centrifugal forces and gravity: large grains (e.g., $a \gg$m) are completely decoupled from the gas and orbit at a keplerian velocity, whereas small particles (e.g., $a \ll$cm) can be considered to approximately orbit with the gas velocity. The intermediate-size objects ($\sim$ cm - m size) are less strongly coupled to the gas and thus they orbit at a keplerian velocity, which is faster than the gas velocity. They feel the sub-Keplerian gas motion as a continuous headwind in the azimuthal direction and a crosswind in the radial direction considering that the gas is moving inward. Thus these dust particles are decelerated, due to the lose angular momentum, migrate faster inwards. At the same time, gas feel a tailwind toward large radii for the conservation of angular momentum and drift toward the outer side of the disc.

In order to estimate their relative velocity, it is possible to approximate: $\Delta v_{\phi,\mathrm{g}} = v_{\phi,\mathrm{g}} - v_\mathrm{k} \approx \eta v_\mathrm{k}$. If we consider typical disc parameters: $n = 1$, $v_\mathrm{k} \sim 30$ km/s and $H/R \sim 0.05$, we found that $\Delta v_{\phi,\mathrm{g}} \sim 75$ m/s. The relative velocities between the two fluids generates drag as a function of particle size. Weidenschilling (1977) calculates the effect of the drag force on the dynamics of a generic particle, starting from the radial and azimuthal equation of motion:

$$\frac{dv_\mathrm{r}}{dt} = \frac{v_\phi^2}{r} - \Omega_\mathrm{k}^2 r - \frac{1}{t_\mathrm{s}}(v_\mathrm{r} - v_{\mathrm{r,gas}}) \tag{2.42}$$

$$\frac{d}{dt}(rv_\phi) = -\frac{r}{t_\mathrm{s}}(v_\phi - v_{\phi,\mathrm{gas}}), \tag{2.43}$$

where t_s is the stopping time as defined in Sec. 2.3.2. Considering that the azimuthal velocity can be approximated as the keplerian velocity, Eq. 2.43 can be converted in:

$$v_\phi - v_{\phi,\mathrm{gas}} = -\frac{t_\mathrm{s}}{2r} v_\mathrm{k} v_\mathrm{r}. \tag{2.44}$$

Then using Eq. 2.40 and Eq. 2.42, expanding $v_\phi^2 - v_\mathrm{r}^2$ and considering $v_{\mathrm{r,gas}} \ll v_\mathrm{r}$, we get:

$$\frac{dv_\mathrm{r}}{dt} = -\eta\frac{v_\mathrm{k}^2}{r} + 2v_\mathrm{k}(v_\phi - v_{\phi,\mathrm{gas}}) - \frac{1}{t_\mathrm{s}}(v_\mathrm{r}). \tag{2.45}$$

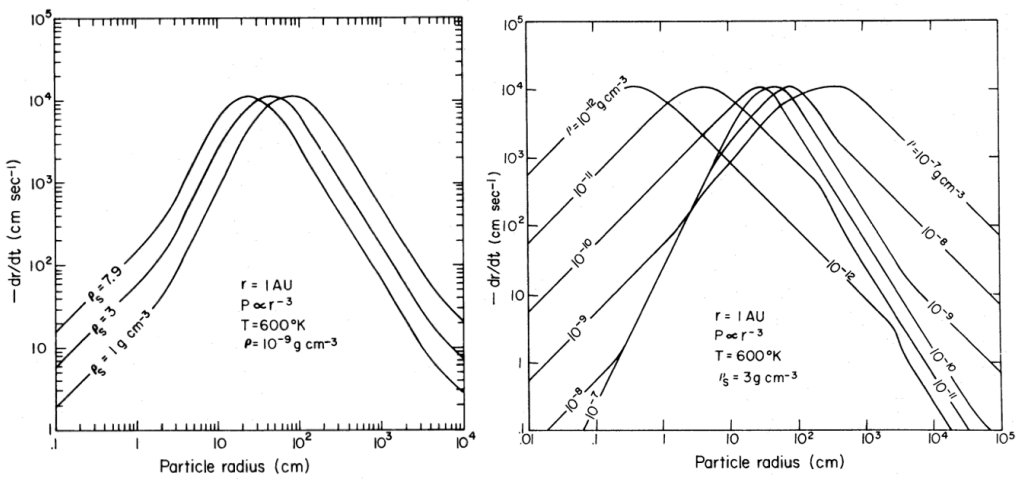

Figure 2.5: Radial velocity over particle size varying particle density (left) and gas density (right). Credits to Weidenschilling (1977).

If we consider the terminal velocity, we assume: $\frac{dv_\mathrm{r}}{dt} \sim 0$ and we obtain:

$$v_\mathrm{r} = -\frac{\eta v_\mathrm{k}}{\mathrm{St} + \mathrm{St}^{-1}}, \tag{2.46}$$

where the Stokes number (St) is defined as in Sec. 2.3.3 (see Fig. 2.5). This effect depends thus from the Stokes number of the particles. The peak of this function is for $\mathrm{St} = 1$, when the stopping time is equal to the inverse of the keplerian angular velocity. In this case we talk about marginal coupling and $v_\mathrm{r} = -v_\mathrm{k}\eta$. Far from this maximum, dust and gas are not coupled and dust does not migrate, whereas for $\mathrm{St} = 1$ particles can experience a strong inward migration. In the Epstein regime, this happens for grains of millimeter size, which is the size of grains typically observed by ALMA in the continuum. In Fig. 2.5, we show the radial velocity as a function of particle size (Weidenschilling 1977). This has an important effect on planet formation (see Sec. 3.1.2).

Vertical settling

We analyze here the motion of dust grains since the vertical distribution heavily affects the disc vertical appearance and thus the one of the SED. In particular, dust vertical settling produce size-sorted vertical distribution of dust grains at different radii. The settling can be described as an oscillator. In particular, the settle time can be generally described by the relation found by Youdin & Johansen (2007) and Laibe & Price (2014):

$$\Omega_\mathrm{k} t_\mathrm{settle} = \mathrm{St} + \frac{1}{\mathrm{St}}. \tag{2.47}$$

Small particles grains slowly settle toward the midplane in a long timescale; large grains, instead, behave like a vertical oscillation which damps in the settle time. In the intermediate regime which corresponds to $\mathrm{St} \sim 0.5$, the dust settling reaches the fastest rate of settling (Ω_k^{-1}) going quickly to the steady state. In any case, the settling time is a hundred times faster that the radial drift (described below), so the vertical and radial motion can be considered independent.

2.4 Thermal structure of the disc

There are two main sources of heating that can set the radial and vertical temperature profiles: viscous heating and passive heating from stellar irradiation (e.g. Dullemond et al. 2007). Active discs are the ones where the main source of heating comes directly from the physical processes acting inside the disc. Viscous heating is important in the denser inner parts of the disc. For passive discs, instead, the main source of heating comes from the central star. However, most of its energy is emitted at optical wavelengths at which dusty protostellar envelope are opaque. For a passive disc, a thin surface layer of the disc absorbs the stellar radiation and then re-radiates it in the infrared. This is described by the two-layer passive disc model (Chiang & Goldreich 1997), that is able to reproduce well the observed radial temperature profile of discs (e.g. Piétu et al. 2007), mainly for the outer disc. Not every disc can be explained just by models of re-irradiated discs. Some of them have a strong optical excess and ultraviolet continuum emission (Basri & Bertout 1989). This may be explained by the accretion of mass from a circumstellar disc and can be used to derive the accretion rate from the inner regions.

2.4.1 Source of heating

Disc heating is dependent by two primary components: accretion energy and host star irradiation. A third component relevant just in particular scenarios is external radiation. Thus it is valid the relation:

$$\sigma_{\rm SB} T_{\rm mid}^4 = 3/8 f(\bar{\kappa}) F_{\rm acc} + F_\star + F_{\rm ext}, \tag{2.48}$$

where $\sigma_{\rm SB}$ is the Stefan-Boltzmann constant and $T_{\rm mid}$ is the disc midplane temperature. $F_{\rm acc}$ is the energy flux associated with accretion which describes the release of gravitational energy as material moves through the disc and it is related to viscous dissipation. The function $f(\bar{\kappa})$ can be written as $f(\bar{\kappa}) = \bar{\kappa} + 1/\bar{\kappa}$, where $\bar{\kappa}$ is the Rosseland mean opacity. This reasonably captures how the accretion energy diffuses outward from the midplane in both the optically thick and thin regimes. The optical depth is a key factor to take into account since it can modify the propagation of heat from the midplane to the surface. $F_\star$ evaluates the irradiation from the host star, which may be composed by both the internal luminosity and the stellar accretion luminosity. For high mass stars H-burning dominates, while for low mass stars the stellar accretion luminosity dominates. Moreover, the impact of stellar irradiation on disc temperatures is highly dependent on the disc structure. Discs have indeed different geometries (e.g. flared or flat discs) and different materials which may vary the amount of irradiation scattered or reprocessed by the disc. The inner disc is more likely to be self-luminous and the outer disc can be irradiated more from the central star or external environment. $F_{\rm ext}$ is the energy flux associated with the external heating which can contribute to the disc temperature and can sets a lower threshold for the disc temperature.

2.4.2 Active discs

In this subsection, we derive the temperature profile of a disc whose heating is provided mainly by accretion. Let us define the inward flux of angular momentum in an annulus as $G(R) = 2\pi\nu\Sigma_{\rm g} R^3 \Omega'$. In the case of a Keplerian disc, $\Omega' = -3\Omega_{\rm k}/2R$ and $G(R)$ is negative, meaning that the angular momentum is transported outward far from the central object and thus most of its mass can accrete onto it, as described in the two time dependent solutions presented in Section 2.1.4. On the one hand, the viscous torques

redistribute angular momentum through the disc and allow accretion, on the other hand, a significant amount of gravitational potential energy is dissipated though viscous forces. We can define $D(R)$ as the energy dissipation per unit time and surface (Frank et al. 1985):

$$D(R) = -\frac{G\Omega'}{2\pi R} = \nu\Sigma_{\rm g}(R\Omega')^2 = \frac{9}{4}\nu\Sigma_{\rm g}\Omega^2. \tag{2.49}$$

The last equality is correct only in the case of a Keplerian disc. It is also possible to evaluate the the total power emitted by the disc in a steady state, assuming that the disc extends to infinity, and write the disc luminosity as:

$$L_{\rm disc} = \int_{R_{\rm in}}^{\infty} 2\pi R D(R) dR = \int_{R_{\rm in}}^{\infty} \frac{3}{2\pi}\frac{GM\dot{M}}{R^2}\left(1-\sqrt{\frac{R_{\rm in}}{R}}\right)dR = \frac{1}{2}\frac{GM\dot{M}}{R_{\rm in}}. \tag{2.50}$$

The luminosity is thus just half of the potential energy lost by the accreting matter, the other half is partially dissipated in the boundary layer where the gas accrete onto the central protostar.

If we assume that the disc is optically thick and in thermal equilibrium, the luminosity will be re-radiated like a black body: $D(R) = 2\sigma_{\rm SB}T_{\rm disc}^4$, where $\sigma_{\rm SB}$ is the Stefan-Boltzmann constant and $T_{\rm disc}$ is the surface temperature of the disc which can be derived exploiting Eq. 2.49 as:

$$T_{\rm disc}^4 = \frac{3}{8\pi\sigma_{\rm SB}}\frac{GM\dot{M}}{R^3}\left(1-\sqrt{\frac{R_{\rm in}}{R}}\right). \tag{2.51}$$

The temperature decreases with increasing radius, the disc is thus hotter in the inner parts. At large radii, it follows the relation: $T_{\rm disc} \propto R^{-3/4}$. This can help to understand how the central heating is produced by the dissipation of gravitational potential energy. We note that, although the viscosity is not explicitly present in this equation, it is implicitly present inside the $\dot{M}$ parameter. The mass accretion rate can be derived directly through observations of ultraviolet excess or H_α emission and thus the temperature is not affected by the uncertainty related to the origin of the disc angular momentum transport. For an actively accreting disc, the disc temperature at the midplane ($T_{\rm mid}$), where the disc is denser, can be derived from the temperature at the photosphere ($T_{\rm disc}$), thanks to the use of the mean optical depth (τ), derived from the Rosseland mean opacity ($\bar{\kappa}$):

$$T_{\rm mid}^4 \simeq \frac{3}{4}\,\tau\,T_{\rm disc}^4. \tag{2.52}$$

2.4.3 Passive discs

Typically protoplanetary discs are passive discs. The luminosity of passive discs is mainly produced by external processes, like the presence of the central star, and internal sources of heating are often small in comparison to it. The estimate of the temperature profile of a passive disc relies on simple analytical models (e.g. Chiang & Goldreich 1997) or on numerical radiative transfer simulations (see Section 2.4.4).

The light coming from the star is absorbed at the disc surface and heats the dust grains, which re-emit the energy deeper in the disc and eventually warm the midplane. In order to derive a correct temperature profile, it would be necessarily to know the shape of the disc surface (e.g. flared or flat geometry), because it plays an important role in the amount of light absorbed. It is also important to assume that the disc is in

Local Thermal Equilibrium (LTE). This is equivalent to assuming that the radiation is completely absorbed by the dust and re-emitted at longer wavelengths with the same rate and that the optical depth is the same for both absorption and emission. If we assume that the disc is flat and thin so that $H(R)$ is constant, the temperature profile is given by:

$$\left(\frac{T_{\rm disc}}{T_\star}\right)^4 = \frac{1}{\pi}\left[\sin^{-1}\left(\frac{R_\star}{R}\right) - \left(\frac{R_\star}{R}\right)\sqrt{1-\left(\frac{R_\star}{R}\right)^2}\right], \tag{2.53}$$

where $T_\star$ is the effective temperature of the star. At large radii thus, the temperature profile follows the same scaling with R as an active disc: $T_{\rm disc} \propto R^{-3/4}$. The total luminosity re-irradiated by the disc is $L_{\rm disc} = L_\star/4$.

The disc is however in general flared, which means that the disc surface intercepts a larger fraction of stellar light than in a flat disc. If the temperature increases, the disc will expand due to hydrostatic equilibrium and this would boost even more the flaring angle. Also in the case of a flared disc, we assume to be in LTE. This flattens the temperature profile and increases the total disc luminosity. If we assume that, for $R \gg R_\star$, the energy absorbed is balanced by the one re-emitted in the same region, it can be derived that:

$$\frac{T_{\rm disc}}{T_\star} = \alpha_{\rm irr}^{1/4}\left(\frac{R_\star}{R}\right)^{1/2}, \tag{2.54}$$

where $\alpha_{\rm irr}$[1] is the flaring angle of the disc, which depends on the radius, and $T_{\rm disc}$ is the surface temperature. Performing some assumptions on $\alpha_{\rm irr}$, it can be shown that the surface temperature of a flared disc is flatter than the one derived for a passive disc as expected, but also than an active disc. Viscous heating is thus thought to be more important for the inner disc, whereas irradiation dominates in the outer regions, in the case where the disc is opaque to the incoming stellar radiation.

The assumption that the disc is optically thick makes the derivation of the temperature profile for passive discs strongly simplified, because the absorption and emission properties in discs can be considered to be the same. However, in passive protoplanetary discs, for a fixed size of dust grains, the dust absorbs more efficiently the radiation with frequencies similar to the one of the peak of the stellar SED than the lower frequency ones of the dust thermal re-emission. The stellar radiation, thus, can penetrate a thin surface layer of the disc where $\tau_{\nu,\star} \sim 1$. The radiation is absorbed and re-emitted in the same layer which is optically thinner to the re-emitted frequency ($\tau_{\nu,\rm dust} \ll 1$). The absorption is thus more efficient than the emission. The inner layers do not receive the radiation coming from the star, but they receive the one re-emitted by the surface layer. The picture becomes thus more complicated. The efficiency between absorption and emission for dust grains have to be different. We refer to Chiang & Goldreich (1997) for a detailed analysis on that.

We note that the main difference between a flat and flared geometry can be due to the properties of dust. If the distribution of dust grains is well mixed to the gas ones, the disc will be flared and this can happen just if grains are small. They carry most of the opacity at optical and infrared wavelengths and are important to derive the disc temperature. In principle, thus, it would be needed to solve self-consistently the shape of the disc, to consider both thermal and hydrostatic equilibrium at every radius. A full treatment of

[1]The angle between the incoming light and the tangent to the disc surface for large radii if $H \lesssim R$ can be approximated by:

$$\sin\alpha_{\rm irr} \approx \alpha_{\rm irr} \approx \frac{dH_{\rm p}}{dR} - \frac{H_{\rm p}}{R}, \tag{2.55}$$

where $H_{\rm p}$ is the height of the disc photosphere ($H_{\rm p} \approx H$, Kenyon & Hartmann 1987).

this would need to be solved numerically, such as using Monte Carlo simulations (Pinte et al. 2006).

2.4.4 Radiative transfer

The complete formal radiative transfer equation can be written as:

$$\frac{dI_\nu}{d\tau_\nu} = -I_\nu + \frac{j_\nu}{\alpha_\nu} = -I_\nu + S_\nu, \tag{2.56}$$

where τ_ν is the optical depth defined as: $d\tau_\nu = \alpha_\nu ds$, s is the coordinate along a ray that denotes the distance traveled on that ray. I_ν is the surface emission brightness, S_ν is the source function which is defined as the ratio between the emissivity coefficient (j_ν) and the extinction coefficient (α_ν). If $\tau_\nu \gg 1$ the material considered is optically thick, while if $\tau_\nu \ll 1$ the material is optically thin. If we assume the source function (S_ν) to be constant, the solution to the Equation 2.56 can be written as:

$$I_\nu = I_\nu(0)e^{-\tau_\nu} + S_\nu(1 - e^{-\tau_\nu}) \tag{2.57}$$

If we assume that the initial surface emission brightness $I_\nu(0)$ is equal to zero:

$$I_\nu = \begin{cases} I_\nu \sim S_\nu, & \tau_\nu \gg 1, \\ I_\nu \sim \tau_\nu S_\nu, & \tau_\nu \ll 1. \end{cases} \tag{2.58}$$

Optically thick bodies thus emit more than optically thin materials. We note that in the LTE regime, the source function is equal to the thermal black body emission function (i.e. Planck function, $S_\nu = B_\nu$). In the case of an optically thick regime, this also means that $I_\nu = B_\nu$, while for the optically thin regime, the relation is complicated by the presence of τ_ν. We note that the optical depth is also defined as the opacity times the surface density: $\tau_\nu = \kappa_\nu \Sigma$.

Montecarlo radiative transfer

It is not possible to solve the radiative transfer equation in a multidimensional environment analytically. For this reason, radiative transfer codes are commonly used, such as Monte Carlo radiative transfer techniques (e.g. RADMC3D, Dullemond et al. 2012; MCFOST, Pinte et al. 2006, 2009). Through this technique the thermal structure and the observables can be computed simultaneously. The dust component dominates the opacities, thus the gas can be neglected when computing the continuum radiative transfer.

Monte Carlo radiative transfer relies on the stochastic nature of photon interactions. The radiation field is divided into many photon packages carrying an equal amount of energy and propagating through the grid cells of the density structure of the protoplanetary disc. The probability that a photon traverses an optical depth τ without interacting with the next cell is considered to be $p(\tau) \propto \exp(-\tau)$. The solution to the radiative transfer equation can be calculated by tracing rays along the line of sight if the source function (S_ν) of each grid cell is obtained with the Monte Carlo photons. The thermal structure is then simultaneously calculated given independently as input the opacities function. When a photon is absorbed, it will be re-emitted at a longer wavelength with an immediate temperature correction considering the opacity of its cell. The error on the thermal structure computation is given by the Poisson noise (derived from the square root of the number of photons). Increasing the number of photons thus the signal-to-noise

increases. When the regions have high optical depth, the computation time can largely increase for an increase of number of photon interaction inside a certain region. For this reason, a modified random walk approximation is introduced, which consists in using the diffusion equation of photons to derive the solution through a small number of computational steps. Monte Carlo radiative transfer can be used also for non axisymmetric discs, such as discs with gaps, inner disc warps, and spiral arms. In this thesis we will not describe the radiative transfer process more in details, considering this is not the main topic studied. However, we refer to Rybicki & Lightman (1979) for what regards the radiative processes in astrophysics.

2.4.5 Spectral Energy Distribution

If we consider that the disc material is in local thermodynamical equilibrium and optically thick ($I_\nu = B_\nu$, see Section 2.4.4), it is possible to derive the spectrum of the disc as a summation of weighted black bodies at a certain temperature, which corresponds to different radii. In order to give an estimate of it, we can integrate the black body brightness function across the disc, obtaining:

$$F_\nu \equiv \int_\Omega B_\nu(T) d\Omega = \int I_\nu \frac{cos\theta R dR d\phi}{D^2} = 2\pi \frac{2h\nu^3 cos\theta}{c^2 D^2} \int_{R_{\rm in}}^{R_{\rm out}} \frac{RdR}{\exp\left(\frac{h\nu}{k_{\rm B} T_{\rm disc}}\right) - 1}, \quad (2.59)$$

where $B_\nu(T)$ is the Plank function, D is the distance of the source and θ the disc inclination (a face-on disc has $\theta = 0$). $T_{\rm disc}$ is the disc temperature profile that can be parametrized as follows:

$$T_{\rm disc} = T_{\rm in} \left(\frac{R}{R_{\rm in}}\right)^{-q}. \quad (2.60)$$

The shape of the SED depends on the temperature profile as follows: for $h\nu \gg k_{\rm B} T_{\rm disc}$, so for small radii ($R \ll R_{\rm in}$), the disc is in the Wien regime, it has an exponential cutoff and it is related to the hottest annulus of the disc; for $h\nu \ll k_{\rm B} T_{\rm disc}$, which corresponds to large radii ($R \gg R_{\rm out}$), the disc is in the Rayleigh-Jeans regime and $F_\nu \propto \nu^2$. At intermediate frequencies, one can show that $F_\nu \propto \nu^{3-2/q}$. We note that if the disc is keplerian and stationary, in the case where the viscous accretion dominates, q will be equal to 3/4 and thus $F_\nu \propto \nu^{1/3}$. The spectral energy distribution (SED) is defined as the amount of energy carried at each wavelength and it is thus νF_ν.

Given the discussion of Sec. 2.4.4, if the disc is optically thick ($\tau_\nu \gg 1$), the emission spectrum can be considered like a black body; on the contrary, if the disc is optically thin ($\tau_\nu \ll 1$) the surface brightness becomes $I_{\rm obs} = \tau_\nu B_\nu(T)$. The disc geometry and the opacity, varying with frequencies, would play an important role and will lower the surface brightness below the black body spectrum curve. If a disc is optically thin, thus, it should be possible to derive disc properties such as dust mass (see Section 1.3.4) or the opacity dependence on frequency (see Section 2.4.6).

2.4.6 Dust properties (opacity, porosity, material, size)

Dust opacity together with dust radiative transfer are of fundamental importance to constrain from observations dust properties in protoplanetary discs. The dust opacity, indeed, determines the dust temperature and the optical depth as function of wavelengths. We note that small dust grains carry most of the disc opacity at optical or near-IR wavelengths and control the absorption of the stellar emission and the disc temperature.

At short wavelengths the dust opacity is so high that observations only trace a thin surface layer of the disc. Moreover, it is used to derive the maximum grain size and the total disc mass (see Section 1.3.4), needed to constrain the first stages of planet formation (Brauer et al. 2008). However, dust opacity is one of the greatest uncertainty in the study of protoplanetary discs. In general, to interpret observations a specific dust composition, structure and grain size over the whole disc is assumed. However, it is most probable that grains have different physical and chemical properties at different separation from the host star (see Pérez et al. 2015). Following Draine (2006), the grain size distribution is parametrized by a power-law as described in Mathis et al. (1977):

$$n(a) \propto a^{-q}, \tag{2.61}$$

where the particle size a is considered to have a minimum and maximum ($a_{\rm min} < a_{\rm max}$). Draine & Lee (1984) found that $a_{\rm min}$ can be considered as few $\mathring{A}$, typically $q = 3.5$ and $a_{\rm max} \sim \mu$m (in the ISM). In protoplanetary discs, indeed, the value of maximum particle size depends on the amount of grain growth. Grains of μm size typically grow via collisional agglomeration and gravitationally settle toward the disc midplane (see Section 3.1.1). Several are the evidences in this regards (e.g. Testi et al. 2014).

The dust opacity is influenced by the grain growth process, since it depends on grain sizes, grain shape, porosity and chemical compositions. Knowing how dust opacity varies in the protoplanetary disc is fundamental not only on the predicted continuum, but also for chemistry and emission lines. If particles are in the Rayleigh limit ($a \ll \lambda$), the dust opacity can be inferred to be a power-law:

$$\kappa_\lambda = \kappa_0 \left(\frac{\lambda}{\lambda_0} \right)^{-\beta}, \tag{2.62}$$

where κ_0 is a fiducial dust opacity valid at λ_0 and β is a good indicator of grain growth. It is possible to derive β in the Rayleigh-Jeans regime ($B_\nu \propto \nu^2$) considering it can easily be derived that $I_{\rm obs} \propto \nu^{\beta+2}$ (Testi et al. 2014). The value of β is strongly dependent on the size distribution of dust grains. It is indeed generally found to have a lower value in protoplanetary discs with respect to the one in ISM. This allows to better study the grain growth and evolution.

The composition of dust material is also a topic still under investigation. Typically it is considered a mixture between silicates, amorphous carbon and porosity. According to Min et al. (2011), following the solar system composition, the grain should be composed by 60% silicate, 15% amorphous carbon, and 25% porosity. In order to compute the opacity, it is possible to apply the Mie Theory if spherical particles are considered. However, the optical properties computed in the Mie Theory may dramatically deviate from realistically shaped particles, which typically are not homogeneous spheres. In order to overcome this issue, computationally demanding algorithms must be employed which, instead of a simple sphere, use a distribution of hollow spheres (DHS). This helps to avoid several artefacts of Mie theory (spherical resonances), better consider the real shape effects (Min et al. 2016) and study how optical properties vary with composition, size, shape and structure of grains (e.g., Min 2009).

2.4.7 Interaction between dust and radiation

A photon hitting a dust grain is either absorbed or deflected (scattered). In order to distinguish when the incoming photons are adsorbed or scattered we define the albedo

parameter (η_ν), which is the fraction of scattered light at a specific wavelength:

$$\kappa_\nu^{\rm scat} = \eta_\nu \kappa_\nu \quad , \quad \kappa_\nu^{\rm abs} = (1-\eta_\nu)\kappa_\nu, \tag{2.63}$$

and thus it is valid that $\kappa_\nu^{\rm scat} + \kappa_\nu^{\rm abs} = \kappa_\nu$. If for example, if a photon hits a transparent sphere with some refraction index and no light is absorbed, but it is redirected into another direction, this means that κ_ν is entirely a scattering opacity.

Photon scattering

Different are the forms of scattering e.g. reflection, refraction, diffraction and it can be forward or backward scattering depending on the scattering angle. It is thus important to take into account also this phenomenon. Important parameters to distinguish different scattering properties are: the observed incoming radiation wavelength λ, the grain size a and the complex refractive index (derived from the particle optical properties). In particular we can define three regimes:

- Rayleigh scattering ($\lambda \gg 2\pi a$). The particle is much smaller than the wavelength.
- Mie scattering ($\lambda \sim 2\pi a$). The particle size and wavelength are comparable.
- Geometric scattering ($\lambda \ll 2\pi a$). The particle is much greater than the wavelength, which means that the scattering can be calculated through e.g. ray tracing.

For a particle of size a at a specific λ, the distribution of scatter peaks at $\lambda \sim 2\pi a$, which means that optical/near-IR observations mainly trace μm-sized particles and millimeter observations trace mm-sized particles. Multi-wavelength images in the near-IR can help to test the models on dust settling, particularly if the disc is edge-on. Smaller grains are observed indeed higher up in the disc atmosphere and larger grains settled deeper (Dullemond & Dominik 2004; Pinte et al. 2007, 2008; Duchêne et al. 2010). At optical/near-IR wavelengths stellar light is mostly scattered by the disc, thermal emission indeed is limited to the few inner au. For grains size in the Rayleigh regime, the scattering can be neglected.

To understand how scattering behave, we have to define the scattering phase function, which is a probability function $p(\mu)$ that a scattered photon is deflected by an angle θ for which $\mu = \cos\theta$ at a given wavelength and it is strongly dependent on the grain size. In the Rayleigh scattering limit, $p(\mu)$ is close to isotropic (blue line of Fig. 2.6), which means that the scatter is uniform in all the directions. Particles larger than the wavelength have an anisotropic scattering emission (Min et al. 2016, red line of Fig. 2.6) and a phase function typically forward-peaked, which means that a very small fraction of photons is scattered at high angles. In order for these photons to be detected the discs should be highly inclined, but, however, this is not the case for the majority of the discs. Moreover, stellar photons scattered by large grains may go inside the disc, making it difficult to be traced (Mulders et al. 2013). We note that this is a great simplification.

Scattered light shed light also on the growth of dust grains. In particular it is possible to exploit three main diagnostics: the brightness asymmetries between the near and far side of the disc; the fraction of scattered light (albedo) at a specific wavelength and the disc colors. First of all, brightness asymmetries (e.g. Kudo et al. 2008) visible in observations of inclined discs may be useful to study grain size properties due to the phase function, since inclined discs allow to cover a larger interval of scattering angles. This may help to discriminate between different grains. The brighter front side indeed can often be considered as a sign for the presence of large grains whose scattering phase function is

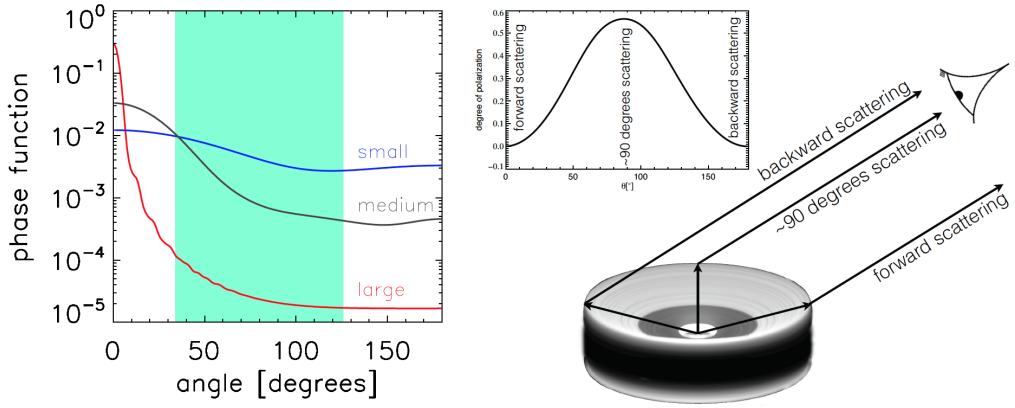

Figure 2.6: Scattering phase function (left) as a function of scattering angles for small (0.08μm), medium (0.25μm), and large (2.5μm) dust grains at 0.6μm wavelength (Mulders et al. 2013). Polarization phase curve as a function of scattering angles (right). The degree of polarization light coming from the disc is different depending on the location in the image (Min 2015).

dominated by forward scattering (Quanz et al. 2011). However, we note that appropriate studies on the phase function have still not been performed due to the complex disc geometries and polarization effects. Secondly, effective albedo was found to be lower than what expected, with the effect of a lower disc emission in scattered light. The reason behind it is that scattering emission by grains whose scattering phase function is forward peaked may be partially lost into the disc (Mulders et al. 2013). The ratio between the expected and effective albedo can thus shed light on the grain size distribution. Finally, disc colors are found to be different depending on the grain size: gray to slightly blue when the phase function is close to isotropic, reddish when the phase function is anisotropic (Debes et al. 2008, Rodigas et al. 2015a).

Another issue present in scattered light observations is to translate the observed scattered light observations into actual disc geometries (e.g., Stolker et al. 2016).

Polarization fraction

If we analyze the degree of polarization of the scattering emission, this can be an additional indicator of the particle size in the surface layer of discs. The intensity of polarization changes with wavelength, particle size, shape, and material of dust grains. The amount of polarization can be studied as a function of the scattering angle, called polarization phase curve (see Min 2015, Fig. 2.6). Particles much smaller than the wavelength of radiation reach 100% degree of polarization at a scattering angle of 90°. The peak function (at ~90°) suggests that the disc may be visible with a variation of polarized brightness. This will cause the backside and front side of the disc to be fainter in polarized intensity due to the intrinsically low degree of polarization of forward and backward scattering. Moreover, the degree of polarization is probably determined by the grain size (e.g., Min et al. 2016). On the contrary, larger grains do not polarize the incoming radiation from the star. Polarimetric Differential Imaging (PDI, see Section 6.4.2) techniques take advantage of the fact that the stellar light is often weakly polarized to observe micron-sized disc structures at high contrast ratios.

Self-scattering at long wavelengths

We note that when considering grains of mm-cm size, the scattering coefficient is much larger than the absorption coefficient at millimeter wavelengths. For this reason, a realistic radiative transfer solution in protoplanetary disc, should consider self-scattering effects (Sierra & Lizano 2020). Observations of the polarization pattern due to dust self scattering (e.g. Kataoka et al. 2016, Stephens et al. 2017, Bacciotti et al. 2018) and the anomalous low spectral indices (e.g. Dent et al. 2019, Liu 2019) suggest indeed that scattered light cannot be neglected when observing millimeter disc emission.

The computation of scattering effects on the radiative transfer equation was done firstly by Miyake & Nakagawa (1993), who found an analytic solution for the mean intensity of a plane-parallel slab including scattering. D'Alessio et al. (2001) used it to obtain the source function and integrate the radiative transfer equation in accretion discs models. Successively, Sierra & Lizano (2020) found that scattering causes a decrease in the emergent intensity with respect to the true absorption case if considering protoplanetary discs with large albedo. As a consequence, in the isothermal case, the inferred spectral indices at millimeter wavelengths can be modified and thus also the distribution of millimeter and centimeter dust grains (e.g. Beckwith & Sargent 1991). Moreover, scattering can modify also the shape of the SED when the albedo is large and the optical depth is higher than a specific threshold (Sierra & Lizano 2020). In particular, it was shown that if scattering effects are not taken into account, the emission at optically thin millimeter wavelengths can be misinterpreted and this may end up in an underestimate of the total disc dust mass (see Section 1.3.4).

Chapter 3

Planet formation theory

The process of planet formation is intimately linked to the process of star formation. Thanks to the improved observing capabilities and techniques, a growing number of low mass companions is found. This allows to test the models with unprecedented observational data statistics. The properties of exoplanetary systems are different from those of our Solar System, the only planetary system known until three decades ago (see Chapter 1). This is the case of e.g., "hot Jupiters", giant planets on close orbits such as the prototype 51 Peg B (Mayor & Queloz 1995). Other examples are the exoplanets on high eccentric orbits or at very large separations. Since the local disc mass at the location of hot Jupiters is low, we expect that they formed farther away in the disc and migrated inward afterwards.

How do planetary cores form inside protoplanetary discs is still an open problem. The main scenarios are core accretion (e.g., Pollack et al. 1996), gravitational instability (e.g., Boss 1997) and pebble accretion (e.g., Ormel & Klahr 2010; Lambrechts & Johansen 2012). According to the first model, planets form through a sequential aggregation of microscopic disc dust grains up to planetesimals (e.g., review of Testi et al. 2014) followed by planetesimals collision to form planetary cores and finally fast accretion of a gaseous envelope. Dust growth is efficient up to centimeter-sized pebbles, but for larger sizes, depending on the composition and structure of grains, there is also a not negligible possibility for pebbles to fragment and migrate in the disc. Moreover, the core accretion process is a relatively slow process, taking place over the course of several Myrs. An alternative scenario is related to the rapid growth of density perturbations induced by gravitational instabilities (GI). During the initial stages of disc evolution, density perturbations may produce bound clumps in the outer part of self-gravitating protoplanetary discs. It is, however, still controversial whether this model is able to produce Jupiter mass planets, or rather (sub-) stellar companions. For a review about self-gravity we refer to Lodato (2007) and Kratter & Lodato (2016).

3.1 Core accretion

The core accretion (CA) model was originally proposed to account for the formation of both terrestrial and gas giant planets in the Solar System. The model was developed by Safronov (1969, 1972) and Cameron (1973) respectively for what concerns the terrestrial planet and giant planet formation. A further development was performed by Mizuno (1980) and Pollack et al. (1996). The model is based on the sequential grow of solid component present in protostellar discs and it is a bottom-up process, contrary to the gravitational instability process that proceeds top-down. The growth process goes from μm size particles up to fully formed giant planets. Five main steps can be considered to

explain this scenario: physical collisions from μm up to cm-size, from cm-size up to km-size (planetesimals), from planetesimals to Earth-mass cores, the accretion of the gaseous envelope and, finally, the fast accretion of the envelope mass in the case of giant planet formations.

Interestingly, this model is thus able to produce almost all type of exoplanets detected through different techniques (see Chapter 1, Fig. 1.14). For terrestrial planets, the growth stops either after forming an Earth-mass core, if the core does not reach a sufficient size to start the envelope accretion, or after the gaseous envelope accretion, if there is not enough gas by the time it does reach a sufficient size. The process of giant planet formation is expected to take place beyond the snow lines of most abundant volatiles. In this region, indeed, there is a higher abundance of ices/solids, which can accelerate the core formation.

The limitation of this model is that the time-scale to create the solid core are long and the gas reservoir may have finished. Finally, the fast inward migration of the planetary core (Type I migration, see Section 4.1) before it reaches a sufficient mass to open a gap may or may not be consistent with recent observations of many companions in the inner regions (with indirect methods) and with just few at large separation through direct imaging (see Winn & Fabrycky 2015).

3.1.1 From interstellar dust to cm-size dust

The interstellar dust in the molecular cloud is made mainly by silicates and it has $\sim \mu$m size dimension. The first step is to grow interstellar dust through inelastic collisions from μm size grains up to cm-size. Following Armitage (2007), we define dust as small particles ranging from sub-micron to cm in scale, well coupled to the gas via drag forces. As described in Chapter 2, the dust particles present in the disc experience an aerodynamical drag force (which varies depending on the particle size) opposite to its relative motion with respect to the gas. First of all, collisions can happen during the settling phase. The normal vertical settling of μm size particles is counterbalanced by the presence of turbulence. Together with the settling, coagulation and grain growth through pairwise collisions can happen. Once particles increase their size settling is even faster toward the disc midplane. Collisions may occur due to the difference in settling velocity of particles, brownian motion, turbulence and differential radial velocities (Armitage 2007). Refined models are presented in Dullemond & Dominik (2005). Collisions depends upon individual properties of the grains: e.g. porosity, amount of silicates / carbonaceous material, grain shape. We refer to Testi et al. (2014) for what concerns experimental results regarding sticking features. In general, dust can grow up to mm / cm-size anywhere in the disc, though a balance between coagulation and fragmentation. Inside the snow lines, growth can happen beyond mm / cm sizes, but it is strongly limited by fragmentation. Outside the snow lines, grains grow to larger sizes because icy particles stick at higher velocities and it is less easy they will fragment.

3.1.2 Meter-size barrier problem and planetesimals formation

As described in Sec. 2.3.4, dust particles drift fast inward if St$\sim$ 1. The radial velocity ($v_{\rm r}$) function peaks at St= 1. Particles that are far from this maximum, instead, do not migrate. In particular if we consider a dust particle at $\sim$ 1 au of separation, the peak is obtained for particles of size of the order of 10 cm up to few m and the migration time scale is computed to be of the order of $\sim$ 50 yr. The meter- size grains, thus, accrete fast onto the star because the radial drift time scale is much smaller than the disc lifetime. This is one of the two aspects concurring to introduce the meter size problem or meter-

size barrier. The other one is the fragmentation and erosion of dust particles replacing the sticking or mass transfer that leads to the fragmentation and bouncing barriers. In this regards, Windmark et al. (2012a) performed models to study collisions, finding that bouncing collisions prevent the growth above millimeter-sizes (see Fig. 3.1). In this way

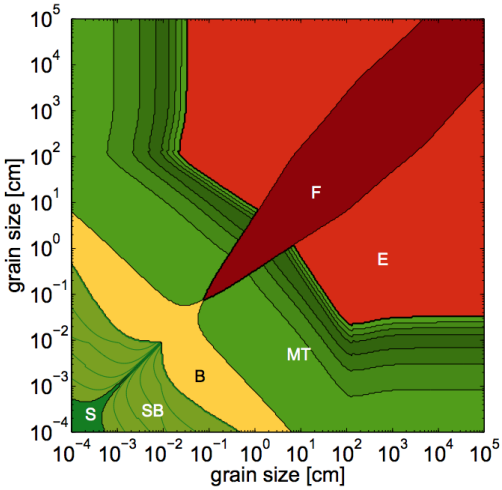

Figure 3.1: The collision outcome for particles with different sizes and relative velocity. Colors mark: Green growth-positive collisions; yellow growth-neutral; red marks growth-negative. Labels mark: 'S': sticking, 'SB': sticking to bouncing transition, 'B': bouncing, 'MT': net mass transfer, 'E': net erosion and 'F: fragmentation. Credits to Windmark et al. (2012a).

dust does not have a way to agglomerate to become km-size. To reach the planetesimals size, the dust has to overcome the meter size problem and increase up to km-size rapidly. This step is still unknown and cannot happen through collisions. Recently, Windmark et al. (2012a,b) show that a small number of cm-sized particles can be formed though vertical mixing or radial drift, acting as a catalyst for smaller particles. The bouncing barrier may be thus beneficial in the sense of preventing the growth of too many large particles that otherwise would fragment or fast radially drift.

All this happens if we consider the pressure as a monotonic function of the radius and no back reaction of the solids onto the gas. However, some appealing solution has been proposed. If something enables the formation of pressure maxima, such as a long-lasting spiral structure or a cleared gap, radial drift can be slowed or even locally reversed. In such a way, radial drift drives solids to concentrate into the pressure maxima (see Fig. 3.2). Several are the physical processes able to create pressure maxima, which can be persistent or local. The presence of a self-gravitating turbulence (see Section 3.2) may concentrate particles inside the spirals or in axysymmetric gas rings. Another option is that the edges of gaps carved by massive companions may form pressure maxima. This process will make the core accretion scenario faster. As we will explain below, the spiral can be created by GI in a self-regulated state. This enhanced density favours and speeds up collisional growth (Rice et al. 2004) in self-gravitating discs. Finally, the solid components can become gravitationally unstable (Rice et al. 2006b; Gibbons et al. 2014) possibly leading to the rapid formation of planetesimals. We note that such an early population of planetesimals can produce large rocky cores only if they have the possibility to staying long enough in the self-gravitating phase and if the collisions lead to growth instead of destruction (Walmswell et al. 2013).

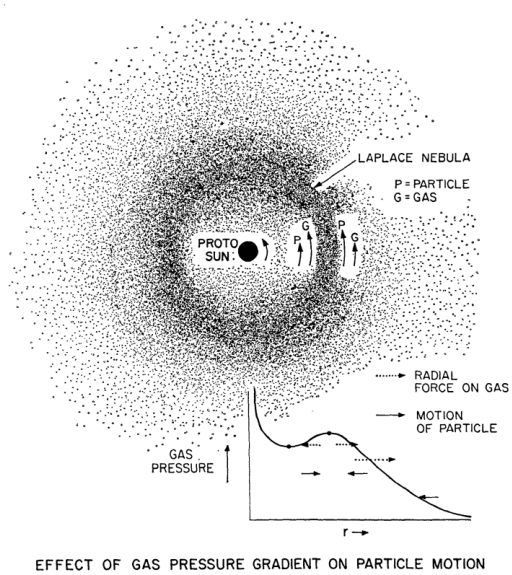

Figure 3.2: The effect of a pressure gradient with a local maximum allows particles to concentrate and to form faster larger grain size. This helps to overcome at the meter size problem. Credits to Whipple (1972).

Goldreich & Ward (1973) proposed a different scenario based on the idea that planetesimals may form thanks to vertical settling and radial drift with the formation of a dense dust sub-disc within which solids density exceeds local density. This can become gravitationally unstable, it can fragment, dissipate energy via collisions and eventually collapse into planetesimals. However, this model is quite difficult to work due to the difficulty to settle a layer of small grains up to densities high enough for gravitational instability to set in. A positive feature of this model would be the short time needed to form planetesimals.

Another hypothesis is the streaming instability (e.g., Youdin & Goodman 2005) followed by a gravitational collapse of pebble clouds (e.g. Simon et al. 2016). The streaming instability is the instability of aerodynamically coupled mixed of gas and dust particles in a keplerian disc. It is hard to settle a particle layer thin enough that the disc become gravitationally unstable. Anyhow, it is plausible that coagulation together with settling allow to locally have the density of gas and dust comparable. This condition would allow to form non-gravitational clumping of particles via streaming instability. These clumps can then collapse under self gravity to form planetesimals. In this regards, numerical simulations were done by e.g., Johansen et al. (2007). Simon et al. (2016) obtained that the population of planetesimals formed have most of the mass in large bodies.

Direct detection of planetesimals outside of our own solar system is not feasible, they are indeed too small to be directly observable as individual objects. These theories could be tested in e.g., the asteroids belt (Morbidelli et al. 2009). In the presence of turbulence, particle can cluster also thanks to the presence of local pressure maxima in zonal flows (e.g., Simon & Armitage 2014), at the edge of dead zones through the formation of vortices (Lyra et al. 2009) or photoevaporation which may form an inner hole in the disc and potentially trigger planetesimals formation (Alexander & Armitage 2007).

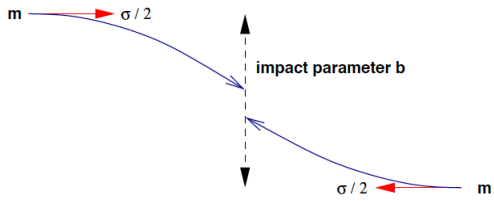

Figure 3.3: Effect of the gravitational focusing. Figure taken from Armitage (2007).

3.1.3 Beyond planetesimals

Once planetesimals have formed, their dynamics is influenced by the gas. The aerodynamical interactions may act to damp the eccentricity and inclination of planetesimals and, at the same time, turbulence generates surface density fluctuations and fluctuating gravitational forces that can excite eccentricity (Okuzumi & Ormel 2013). At this stage planetesimals grow through mutual collisions to form few earth cores. This can happen in two steps: the first is by runaway accretion followed by (slow) oligarchic growth (Kokubo & Ida 1998; Thommes et al. 2003); the second is through a boost of pebble accretion (e.g. Ormel et al. 2012). We note also that when the size of bodies become larger than 10^3 km, they have a gravitational coupling with the gas (see Section 4.1).

The km-size bodies can partially decouple from the gas and have a keplerian velocity, they keep growing through their mutual interaction. In particular, the gravitational interaction relevant to form planets are between planetesimals and, successively, between planetesimals and protoplanet. A massive planet, who gravitationally focuses other bodies toward itself, enhances the possibility of collisions. At the same time gravitational focusing can be in act also between two bodies alone. Let's consider two bodies of mass m that have an impact parameter b and a relative velocity σ.

$\mathrm{R_{min}}$ can be considered as the closest approach separation at which the planetesimal would have a velocity equal to $\mathrm{v_{max}}$. Considering the presence of gravitational focusing, we can use the conservation of energy and of angular momentum and write:

$$\frac{1}{4}m\sigma^2 = mv_{\mathrm{max}}^2 - \frac{Gm^2}{R_{\mathrm{min}}} \tag{3.1}$$

where $v_{\mathrm{max}} = b\sigma/(2R_{\mathrm{min}})$. The impact parameter b is defined as:

$$b^2 = R_{\mathrm{min}}^2\left(1 + \frac{4Gm}{R_{\mathrm{min}}\sigma^2}\right) \tag{3.2}$$

If we assume that $\mathrm{R_{min}} \lesssim \mathrm{R_s}$, where $\mathrm{R_s}$ is the body dimension, there will be a physical collision. The relative cross section for collisions results in:

$$\Gamma_{\mathrm{gf}} = \pi b_{\mathrm{s}} = \pi R_{\mathrm{s}}^2\left(1 + \frac{v_{\mathrm{esc}}^2}{\sigma^2}\right) \tag{3.3}$$

where $\mathrm{v_{esc}^2} = 4Gm/R_{\mathrm{s}}$, b_{s} is the impact parameter when $\mathrm{R_{min}} = \mathrm{R_s}$. For large values of v_{esc}/σ (known as Safronov number, Safronov 1972), planetesimals grow rapidly.

The collisions between two bodies can have different outcomes: most of their mass becomes part of the final body, the collision breaks the bodies into pieces which remains part of a single body and eventually form a rubble pile; or the fragments formed do not

remain bound and they disperse. The outcome can be due to different factors: the mass ratio and relative velocity between the bodies, the angle of impact, the rotation, shape and composition/porosity of the bodies involved.

Another aspect to be consider is whether encounters between bodies can be approximated as two-bodies encounter and below which conditions. It is indeed known that the presence of the host star can play a not negligible role and thus a three body encounter have to be considered. We consider the Hill radius as the radius at which the planet gravity dominates over the stellar gravity:

$$r_{\rm H} = \left(\frac{M_{\rm p}}{3M_\star}\right)^{1/3} a, \tag{3.4}$$

where a is the separation of the planet from the host star and $M_\star$, $M_{\rm p}$ are respectively the mass of the star and of the planet. The velocity at the Hill radius can be defined as:

$$v_{\rm H} \equiv \sqrt{\frac{GM_{\rm p}}{r_{\rm H}}}. \tag{3.5}$$

When $\sigma > v_{\rm H}$ the system is in a dispersion dominated regime and the planet gravity dominates, whereas for $\sigma < v_{\rm H}$, the shear dominated regime, a three-body regime has to be considered. Moreover, the bodies can either have a physical impact or be subjected to gravitational scattering. If we consider that a planetesimal encounters a planet, we need to compare the velocity difference between the two bodies (Δv) and the value of $\rm v_{esc}$. If $\rm v_{esc} \gg \Delta v$ scattering will indeed dominate over physical collisions. This is dependent on the separation of the planet from the host star: for close-in planets accretion dominates (see Kepler's super-earth planets), whereas for large separations scattering dominates. For this reason, it is difficult to form giant planets in situ. The terrestrial solar system planets are in an intermediate regime. The initial growth is slow if we do not consider the gravitational focus. Furthermore, rapid grow requires that σ remains low, planetesimals remain on almost circular orbits and the planet has planetesimals to collide with. There is indeed a finite supply and when it finishes, growth slows down. When this happens, the mass of the planet is called isolation mass. In particular, the planet can accrete planetesimal just if they are inside the 'feeding zone', whose size is set by the maximum distance where planet's gravity still perturbs planetesimal orbits as much as they may collide.

Finally, pebble accretion may play an important role in the last step in the formation of terrestrial planets. Small dust is indeed present in the disc for most of its lifetimes and remains coupled with the gas (Cleeves et al. 2016). In some systems grain growth can happen mainly through the accretion of small solids rather than through collisions with planetesimals (Ormel & Klahr 2010; Lambrechts & Johansen 2012). In order to distinguish between different pebble accretion mechanisms, we need to give a definition of the Bondi radius, which is the separation below which pebbles would experiment a strong deflection.

$$r_{\rm B} = \frac{GM_{\rm p}}{\Delta v^2} \tag{3.6}$$

We can define two regimes. The first is when $r_{\rm B} < r_{\rm H}$, the drift limited accretion. The velocity of pebbles that potentially will be accreted is set by radial drift. The second is when $r_{\rm B} > r_{\rm H}$, the Hill limited accretion. In this case, keplerian shear dominates the velocity. Particles suffer deflection due to the gravity of the planet just if other condition can be applied. For further details on this scenario we refer to Lambrechts & Johansen (2012).

The evolution of the size distribution of dust and planetary growth can happen in different ways (e.g. Lee 2000). The first is orderly growth, where the mass evolves linearly with time. The second is runaway growth, where the mass distribution follow a power-law distribution. A possibility is that at the beginning, planetesimals grow in the orderly regime: if $\sigma \gg v_{\rm esc}$ then $\dot{M}_{\rm p} \propto M^{2/3}$. When larger bodies are present gravitational focus become significant and runaway growth may occur: if $\sigma \ll v_{\rm esc}$ then $\dot{M}_{\rm p} \propto M^{4/3}$.

3.1.4 Gaseous envelope accretion

The first step of gas giant planet formation is similar to the one just described which is valid for the formation of terrestrial planets. Once the rocky core has formed, it starts to accrete a gaseous envelope, which leads to the formation of an atmosphere, initially in hydrostatic equilibrium. Moreover, the core continues to grow through the accretion of planetesimals / pebbles. This not only increase the core mass, but also release gravitational energy. The energy released at the core surface must be transported through the envelope, making the latter non-isothermal.

This process continues until the core reaches a critical mass (Mizuno 1980): the envelope cannot sustain the hydrostatic equilibrium any longer and a phase of rapid gas accretion may occur. In the initial model, this step, was predicted to be slow (Pollack et al. 1996), however, if planetary migration is considered, the growth rate can significantly accelerate (e.g. Bitsch & Johansen 2016). This stops when the planet is massive enough to open a gap or when the gas reservoir is no longer available because the disc is dispersed.

In order to keep the hydrostatic equilibrium, a balance between the object luminosity and the cooling rate have to be reached. Let's consider as total mass $M_{\rm t}$:

$$M_{\rm t} = M_{\rm core} + M_{\rm env} \tag{3.7}$$

where $M_{\rm core}$ and $M_{\rm env}$ are the mass of the rocky core (with a radius $\rm R_{core}$) and the envelope mass, extending from $\rm R_{core}$ to $\rm R_{out}$ (derived through thermal effects or tidal consideration). At the beginning, the luminosity, at first approximation, can be considered as dependent mainly on the core mass:

$$L = \frac{GM_{\rm core}\dot{M}_{\rm core}}{R_{\rm core}} \tag{3.8}$$

whereas the cooling is dependent on radiative processes. The hydrostatic equilibrium and radiative diffusion are regulated by the following equations:

$$\frac{dP}{dr} = -\frac{GM(r)}{r^2}\rho \tag{3.9}$$

$$F_{\rm rad} = \frac{L}{4\pi r^2} = -\frac{16}{3}\frac{\sigma_{\rm SB}T^3}{\kappa_{\rm R}\rho}\frac{dT}{dr} \tag{3.10}$$

where $\sigma_{\rm SB}$ is the Stefan - Boltzmann constant and $\kappa_{\rm R}$ is the Rosseland mean opacity. We assume that L and $\kappa_{\rm R}$ are constant, $M(r) \sim M_{\rm t}$, the temperature and pressure inside the planet are considered way larger than the ones of the outer boundary and the pressure follows the ideal gas equation of state (Armitage 2007). Using equations 3.1.4 and 3.10, we derive:

$$M_{\rm env} = \int_{R_{\rm core}}^{R_{\rm out}} 4\pi r^2 \rho(r) dr = \frac{256\pi^2\sigma}{3\kappa_{\rm R}L}\left(\frac{\mu m_{\rm p} G M_{\rm t}}{4k_{\rm B}}\right)^4 \ln\frac{R_{\rm out}}{R_{\rm core}} \tag{3.11}$$

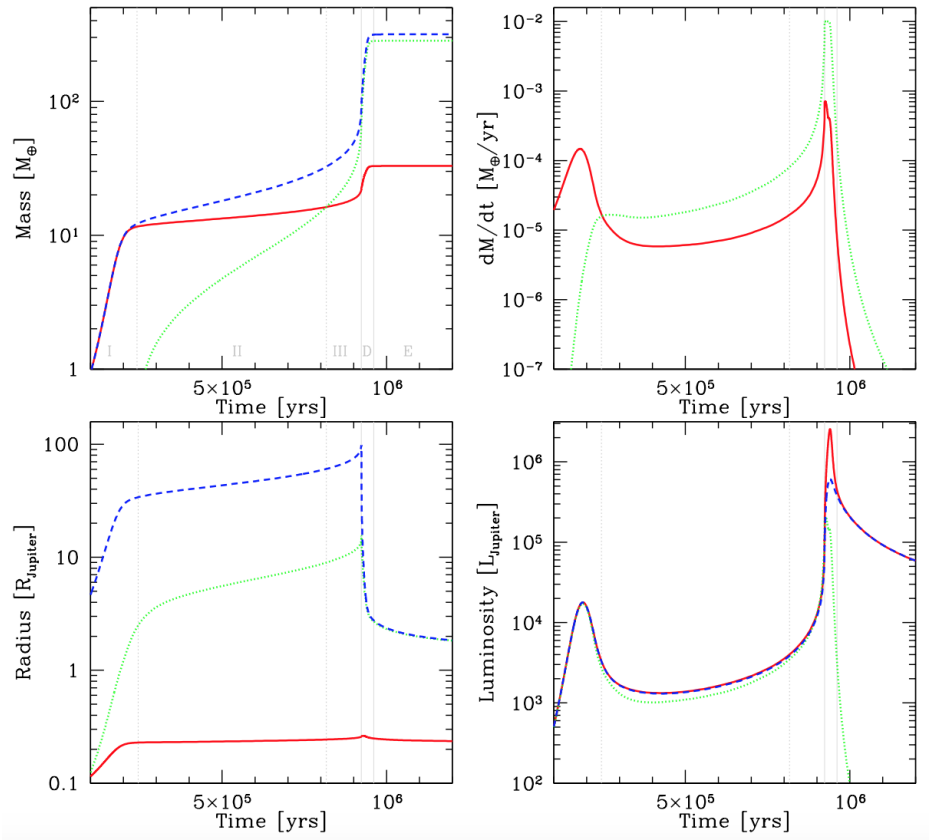

Figure 3.4: Simulation of the in situ formation of Jupiter at 5.2 au (Mordasini et al. 2012). Vertical lines show the major phases. Top left: the evolution of the core mass (red), the envelope mass (green) and the total mass (blue). Top right panel: accretion rate of solids (red) and gas (green). Bottom left: the evolution of the core radius R_{core} (red), the total radius (blue) and the capture radius for planetesimals (green); bottom right: total (red), internal (blue) and core (green) luminosity of the planet. Credits to Mordasini et al. (2012).

This equation shows that the envelope mass has a strong dependence on the total mass and a weaker dependence on the luminosity and thus on the mass of the core. The mass of the core can be written as:

$$M_{\rm core} = M_{\rm t} - \left(\frac{C}{\kappa_{\rm R}\dot{M}_{\rm core}}\right)\frac{M_{\rm t}^4}{M_{\rm core}^{2/3}} \tag{3.12}$$

Solving this equation, it is possible to find that there is an M_{crit} beyond which no solution is possible. If more gas is added to the M_{crit}, the contribution to self gravity is high enough that the envelope is compressed and not in hydrostatic equilibrium any more. The envelope will follow a fast contraction with more gas accretion. Ikoma et al. (2000) solved the equations through more detailed calculations, finding the critical mass to be:

$$\frac{M_{\rm crit}}{M_{\rm T}} \approx 12\left(\frac{\dot{M}_{\rm core}}{10^{-6}M_{\rm T}\ {\rm yr}^{-1}}\right)^{1/4}\left(\frac{\kappa_{\rm R}}{1\ {\rm cm^2 g^{-1}}}\right)^{1/4} \tag{3.13}$$

The dependence on the accretion rate of the core mass and on the opacity is low. Core accretion is a fast mechanism and faster the accretion is, larger the final mass will be. The main uncertainty in this scenario are: the opacity, the neglect of core migration and accretion through pebble (not considered in the initial model).

The mass of the envelope increases with the core mass faster than linearly, so once the critical mass is reached, the envelope starts to dominate the gravitational potential. Hydrostatic solutions cease to exist beyond a critical core mass which depends mainly on the accretion rate of solids and on the gas opacity. As a result, core starts accreting mass on its own thermal timescale until no more gas is available in the feeding zone of the planet, turning itself into a giant planet (Chabrier et al. 2014).

3.2 Gravitational Instability

Massive and/or cold gas discs may be self-gravitating. Discs may become gravitationally unstable if the Toomre parameter is $Q < 1$. The fact that self-gravity may be not negligible leads to two scenarios: the first is the stable angular momentum transport and the second is the non-linear phase of GI. The second scenario leads to fragmentation of the disc into bound objects in orbit around the primary star. For what regards the theory on self-gravity, we refer to Section 2.2.

3.2.1 Fragmentation and formation of a low-mass companion

A gravitational unstable disc may form bound objects in orbit around the primary star thanks to the disc fragmentation. The fragmentation may happen rapidly (few orbital timescales) when the cooling rate in the disc is sufficiently large ($\Omega t_{\rm cool} < 3 - 6$, see Section 2.2). The fragments will eventually evolve and accrete to form brown dwarf/low mass stellar mass (above the deuterium burning limit) more probably than planets and they should form at large separations. However, it is not unlikely that also Jupiter mass companions would form in such a way. Unstable discs are, indeed, massive and they can form large initial masses for fragments which will end up in gaseous companions. The discs potentially forming planetary mass companions are the one where there is no continuum infalling of material and where the companion will contract immediately after forming. The typical mass of a planet formed by gravitational instability can be derived from the most unstable wavelength ($\lambda = 2\pi H$ for a thin disc). The mass of the fragment will be:

$$M_{\rm f} \sim \Sigma\lambda^2 \sim \frac{4\pi}{Q}\left(\frac{H}{R}\right)^3 M_\star \tag{3.14}$$

Considering a typical case with the star host mass equal to $\rm M_\odot$, the disc aspect ratio equal to 0.1 and the disc marginally unstable ($Q \sim 1$), the $M_{\rm f} \sim 12 M_{\rm Jup}$. As described above, this model would only form the most massive observed planets. Considering that the fragment formed is massive, in order to end up like planets, they will require just a modest amount of gas. As described in Sec. 2.2, when Q is reduced such as non-axisymmetric instabilities set in, not always this means that fragmentation starts. The formation of spiral arms may indeed generate a stable self-gravitating state where heating balances the cooling. It is still open a debate which regards the question if the cooling time in protostellar discs can be short enough to induce fragmentation. In the opposite case, the disc will reach a balance between heating and cooling. We note that in real discs, the cooling time is set by both the opacity and by the mechanism of vertical energy transport. From analytical estimates, it was shown that, for standard opacities,

fragmentation happens only at very large distances from the central star, of the order of 50 - 100 au (Rafikov 2005; Clarke 2009). At such large separations, in the early stages the reservoir of mass is typically still present and thus the outcome is possibly very massive planets or brown dwarfs (Stamatellos & Whitworth 2009).

The fragment so formed will be gravitationally unbound, because the size implied by λ is larger than the Hill radius for the mass $M_{\rm f}$ (Kratter & Murray-Clay 2011). The problem arising immediately is if the fragment so formed can survive. In particular, the Hill radius R_H determines whether an object's self-gravity will dominate over tidal gravity. One must also consider that fragments may also be disrupted due to tidal interaction with other nearby fragments or spiral arms. On one hand, for typical discs, a large value of H/R cause the fragments to form relatively far apart with a low probability of them to collide. On the other hand, clumps can be disrupted by the spiral wave itself with a higher probability over many orbital timescales.

If the clump contracts under its own self-gravity, compressional heating causes the central temperatures and densities to rise. For temperatures higher than 1200 K, dust sublimation removes the dominant source of opacity and this accelerates the cooling (Bell & Lin 1994). Above 2000 K, rapid collapse arise driving toward planetary sizes thanks to molecular hydrogen dissociation. The evolution of clumps is different based on their initial mass. An important parameter is, thus, the presence or not of continued accretion from the background disc. The isolation mass sets an upper limit to the final mass and it is the mass that a secondary potential embedded in the disc can attain by accreting disc material within its own Hill sphere (Lissauer 1987). If the initial mass is large, it will carve a gap, reducing the accretion rate from the disc and eventually stall its own migration. In the opposite scenario: low mass fragments would remain semi-embedded and continue to accrete material. Moreover, given the interaction with the natal disc, they will possibly migrate inwards. For this reason, the fragments opening gaps have a completely different fate then the smaller ones. The massive companions able to open a gap follow the requirements of Lin & Papaloizou (1986) and Bryden et al. (1999):

$$\frac{M_{\rm clump}}{M_\star} = \left(\frac{H}{R}\right)^{5/2} \sqrt{\frac{3\pi\alpha}{f_{\rm g}}} \tag{3.15}$$

These companions are able to produce gravitational torques which repel material faster than viscosity can replenish it. If the mass of the companion is not so high, material still enter in the gap, going into circumplanetary discs and continue to fed the companion.

Fundamental to note that the maximum mass of a fragment created by GI, is below the gap opening mass, but likely able to grow what is needed to be able to carve a gap. In the meantime, fragments will start to migrate similarly to planets undergoing type I migration. We note that gravitational instability is a process characterized by a fast formation of the companion, typically gas giant planets with no sold core.

3.2.2 Evidences of self-gravity in young discs

There are just few indirect evidences to prove that self-gravity takes place in young discs. The first one is the presence of discs with spiral arm structure that can be both related to self-gravity or can be originated by the presence of a companion and neither of these theories can be ruled out (e.g., Pérez et al. 2016; Huang et al. 2018, 2020). Secondly, a mismatch of factors of 10-100 has been observed between the observed protostellar/PMS

luminosities and the expected accretion luminosities derived from basic energetic arguments for a typical disc (Hartmann & Kenyon 1996):

$$L_{\rm acc} \approx \frac{GM_\star \dot{M}}{R_{\rm in}} \approx 100 L_\odot \frac{M}{M_\odot} \frac{\dot{M}}{10^{-6} M_\odot/yr} \frac{R_{\rm in}}{4R_\odot} \tag{3.16}$$

where $\dot{M}$ is the infall rate, $R_{\rm in}$ is the inner disc radius estimated in an evolution of 1 Myr. In this regards, star forming core or turbulent filament eventually undergo a modified form of free fall collapse when self-gravity overcomes magnetic or turbulent pressures. For Class I, II objects in a simplified isothermal collapse, the rate of free fall collapse of material falling onto any disc like structure is given by Shu (1977) as $\sim 10^{-6}$M$_\odot$/yr, whereas the typical observed accretion rates from discs on to stars are 10^{-9}–10^{-7}M$_\odot$/yr.

This mismatch between infall and stellar accretion rates can be explained by the fact that discs at earlier times are more massive and can process more material at higher rate. Another possibility is that the disc-star accretion rates initially are not high with the consequent increase of the disc mass. Both scenarios are consistent with the hypothesis of self-gravity to happen. Another factor playing a key role is the interplay between gravitational instability driven accretion and magnetically dominated accretion driven by MRI turbulence (Armitage et al. 2001). Finally, Najita & Kenyon (2014a) have shown that typical protoplanetary discs do not have enough observed dust mass to account for the mass of planets (as derived from Kepler measurements). A possibility is that at early times disc mass was higher and grain growth started before what it is now believed.

3.2.3 The role of mass, accretion and stellar illumination for fragmentation

GI can occur during the early phases of low mass star formation, but not allow fragmentation to happen. Highly variable accretion or lower stellar illumination are needed to push these discs into the fragmenting regime. Moreover, more massive stars are thought to experience higher mass infall rates, which more easily exceed the maximum GI accretion rate. It is imperative to consider the impact of both stellar irradiation and infall in characterizing the behavior of these discs. The threshold for gravitational instability will have sometimes a temperature controlled primarily by stellar irradiation. At early times disc radii are controlled by feeding filament or infalling angular momentum from the envelope. As soon as the infall becomes less important, we can consider to be in the protoplanetary phase. The disc will lead to larger outer disc radii than that given by the circularization radius and with outer regions with very little mass, not any more significant for what concerns self-gravity. Accretion rate is primary due to the infall of material onto the disc. If this effect is present, the possibility to have fragmentation increases. This parameter is also important considering the disc temperature is dependent from it. Typically accretion rates are $\dot{M} = 10^{-8} - 10^{-3}$ M$_\odot$/yr in the case of discs with steady-state accretion. However, this is dependent on the specific surface density and temperature profile.

Protostellar discs are constantly fed material from the background core or filament and the state of the disc is controlled by competition between the infall rate and the disc-star accretion rate. The system is disc-dominated in the initial stage, while it is star-dominated in the evolved stage, after the main infall phase has finished. Self-gravity is thus expected to be more important for younger objects than for evolved ones. From a study of Andrews et al. (2013), indeed, it is possible to conclude that both angular momentum transport and planet formation caused by strong self-gravity are rare for systems evolved to Class II stage, based on the low disc masses and disc-star-mass ratio

derived. Younger Class 0 and I objects seems to be a factor of two more massive. On one side, the fact they the disc is still accreting from the envelope suggest that the mass of the disc is larger. On the other side, they are deeply embedded, the disc is typically not visible in the visible/IR, and this do not allow us to understand if this is an indication of self-gravity. On the contrary, for Class II objects the disc is detectable with a higher probability, but the main infall from the envelope has finished and the disc less massive. In young high mass stars some evidence of the presence of very massive discs started to be observed with hints some self-gravitating discs (Cesaroni et al. 2007).

In the case of solar mass-objects, self-gravity can happen in the early phases of star formation (e.g., Class I phase). The typical mass of protostellar discs range between 10^{-4} and few times 10^{-1} $M_\odot$ and the disc thickness is $H/R \sim 0.1$. T Tauri stars in the upper end of mass range are expected to be gravitationally unstable. T Tauri stars are expected to have already accreted much of their mass from the disc, so if self-gravity is still important at evolved stages, it must have dominated the dynamics even at younger stages (e.g., Class I). Moreover, typical values of accretion rate onto the star are quite low, ranging between $\dot{M} = 10^{-9} - 10^{-7}$ $\mathrm{M}_\odot$/yr. For this reason the disc luminosity is relatively small and the energy balance is mostly determined by the irradiation from the central star.

An interesting class of objects are the FU Orionis systems. They are protostellar systems undergoing large outbursts, during which their luminosity increases by as much as three orders of magnitude. The accretion rate in these discs can be quite high: $10^{-4}\mathrm{M}_\odot$/yr (Hartmann et al. 1993). Moreover, they are generally surrounded by dusty envelopes with their infall of material at a rate of $\sim 10^{-6}\mathrm{M}_\odot$/yr. These systems are relatively young (the mass have to be relatively large) and they show an excess in the mid infrared of the Spectral Energy Distribution, whereas for smaller wavelengths it is consistent with a standard steady state accretion disc. It is therefore plausible to associate the excess emission at mid-infrared wavelengths with the effect of self-gravity. A possibility is, indeed, that the development of a gravitational instability produces an increase of mass accretion rate and an emission stronger than what expected. However, ALMA images show to date no spirals, contrary to what is expected for self-gravitating discs.

Finally, we consider the case of massive stars, which behave in a completely different way. First of all, the typical contraction time is much shorter for high mass stars than for low mass stars: if $M_\star \geq 8M_\odot$, the star reaches the main sequence while still accreting matter from the surrounding protostellar core. For this reason, the protostar is expected to host a much higher disc mass and their properties should reflect more those of younger protostars (Class 0 or Class I). These systems observationally can be divided in: a) very extended (with sizes of $\sim 10^4$ au), very massive (with masses much larger than their central stars) and the luminosity of the central object is generally consistent with an O- type protostar ($M_\star > 20M_\odot$) or b) smaller sizes ($\sim 10^3$ au), smaller disc mass ($M_{\mathrm{disc}} < M_\odot$), and are generally associated with B-type stars ($8 < M_\star < 20M_\odot$). This second class can be considered as a proper disc. If we consider the outflow rate versus the accretion rate, it is clear that they cannot be balanced. The outflow rate is indeed of $10^{-4} - 10^{-3} M_\odot$/yr, whereas the maximum accretion rate is $2 \cdot 10^{-5} M_\odot$/yr, showing that it is not possible to steadily feed the outflow from the inner disc. Therefore, we expect the development of a series of recurrent global spiral structures which can temporarily transport angular momentum in a efficient way.

3.3 Conclusion

To summarize, core accretion model is strongly supported by the architecture of the planets in the Solar System. The time scale for core accretion is longer at large separations, as suggested by Jupiter who has more gas than the outer planet Saturn. Studies on the interior of the planets would be useful to test this scenario, which however, remains quite uncertain. In this scenario, if a greater surface density of planetesimals is present, the core accretion will be faster and reach the phase of runaway growth before the disc dispersal. The main steps for terrestrial or giant planet formation via core accretion are:

- Dust particles have pairwise collisions up to cm-size particles. It is still controversial how particles can form planetesimals due to the meter size barrier problem.
- Direct collisions, through gravitational focussing allow the growth beyond planetesimals. Pebble accretion may contribute to the accretion of planetary cores.
- Runaway growth follow the ordinary growth and stops when the bodies are massive enough to accrete nearby planetesimals. Oligarchic growth is the dominant process where largest bodies growth slowly than before untill they reach the isolation mass.
- Collision between planetary embryos may also happen. The time to built the terrestrial planets is $\sim$100 Myr.
- The formation of gaseous giant planets can be a consequence of the core accretion (Bodenheimer & Pollack 1986; Mizuno 1980). Giant planets from at the beginning a large core, as before described, and then accrete their envelopes.

The possibility of having disc instability, instead, is higher if the disc mass is high. Fragmentation is expected to occur for large radii even if at that distances the statistic of planet detection is low. The population of planets expected is of massive planets in wide orbits (Boley 2009) with different host metallicity distribution (Rice et al. 2003). The parameter Q (which measures how hot the disc is), the parameter $M_{\rm disc}/M_\star$ (which measures how massive the disc is) and the parameter $\Omega t_{\rm cool}$ (which measures how fast does the disc cool) are key parameters to understand the self gravity process. If Q is significantly larger than unity the disc is gravitationally stable, while if Q approaches unity it becomes unstable. If $\Omega t_{\rm cool} < 1$ the disc rapidly undergoes fragmentation and produces a number of gravitationally bound clumps, while for larger values of the cooling rate fragmentation is inhibited. For not massive discs ($M_{\rm disc}/M_\star < 0.25$), the disc is in a quasi-steady self-regulated state, the instability produces a tightly wound spiral structure and the transport of energy and angular momentum induced can be described with a simple viscosity parameter 'α'. For more massive discs, instead, the local approximation is not any more valid and global transport is expected to occur.

We note that in both planet formation theories the gravitational instabilities mechanisms may play an important role. In core accretion a still open problem, indeed, regards the formation of planetesimals. The possibility of develop gravitational instability in the disc and form long-lasting spiral structure, will allow the formation of local pressure maxima. This would allow the solids to migrate and concentrate in the maximum in a timescale much faster than the migration timescale.

Part II

Discs with cavities, gaps or spirals

Squares with concentric circles, oil on canvas (V. V. Kandinskij, 1913, Munich)

Chapter 4

Structures in protoplanetary discs

With the advent of high resolution imaging of protostellar discs, disc subtructures start to be unveiled in both sub-mm and near-IR wavelengths. This was possible thanks to the development of advanced imaging techniques: interferometry and high contrast imaging, described respectively in Appendix A and Chapter 6. Examples of new generation instruments exploiting the former technique is ALMA and the latter is SPHERE (described in Appendix A).

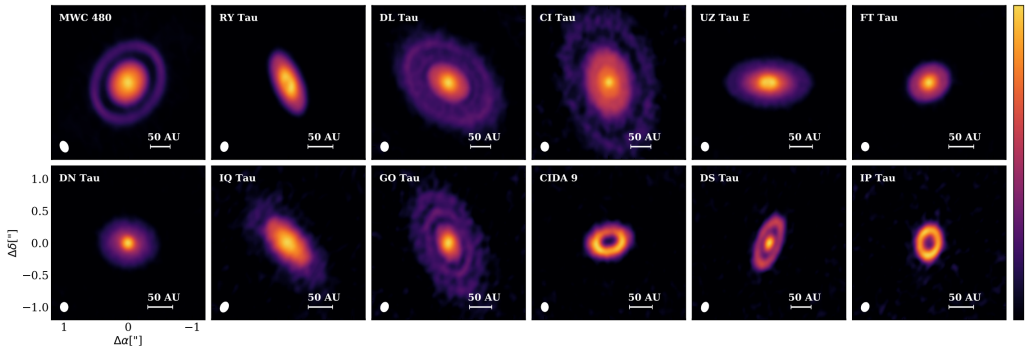

Figure 4.1: Gallery of images of the 1.3 mm continuum of protoplanetary discs imaged by Long et al. (2018a) for the Taurus region. The images are shown in order of decreasing mm flux from top to bottom.

Discs appear to have a huge variety of substructures (see Fig. 4.1). There are axisymmetric disc structures, such as cavities, gaps and rings; and asymmetric structures such as spirals, horseshoes and shadows. We note that cavities, which are empty holes in the density profiles, differ from gaps, defined as annuli with density reduction. Protoplanetary discs with cavities are in general referred to as transition discs. Moreover, these substructures can vary in the same source when observing at different wavelengths. It can happen, for example, to observe a cavity in the sub-millimeter and spiral arms in the near-IR. This is the case of CQ Tau, for which observations at different wavelengths where performed and presented during this thesis (respectively in Chap. 5 and 9). Several of these structures (e.g., gaps, cavities, spirals) suggest the presence of companions hiding inside them. As described in Section 1.5.5 it is challenging to detect young companions embedded in their natal disc through direct imaging. Finding observational signatures of the disc structure is thus important to indirectly infer their presence.

In this Chapter, we will review the observations of different disc substructures and their possible physical origin with a main focus on role that companion-disc interaction

may play for their formation. This mechanism is indeed at the basis of a formation theory of gaps (Section 4.1). We will describe under which conditions the presence of a companion can form cavities instead of gaps (Section 4.2) and other mechanisms to form them. To conclude, we will briefly describe also some asymmetric disc structures observed, such as spirals, which are relevant for the results in scattered light presented in Chap. 9.

4.1 Disc-companion interaction

Traditionally gaps/cavities in a disc are related to the presence of multiple or single embedded protoplanet(s) or sub-stellar companion(s) orbiting around the central protostar. The first investigations of this process were done by Lin & Papaloizou (1979); Goldreich & Tremaine (1980). The tidal interaction between the companion and the gas/dusty disc may form a gap around the companion orbit. Depending on the mass of the companion, the gap can be opened in dust and eventually in gas. In order to distinguish between different regimes, it is important to introduce the concept of torque experienced by the planet embedded in a disc and vice versa.

4.1.1 Torque at resonances

A powerful way to estimate the torque exerted onto the companion is to decompose it into a sum over partial torques in the resonant locations (Goldreich & Tremaine 1979). Resonances are locations where the companion strongly perturbs the motion of the orbiting gas. The angular momentum exchange occurs at resonant locations between the gas disc and the companion. We refer to Binney & Tremaine (1987) for the condition for resonances. A corotation resonance exists at radii where the gas angular frequency $\Omega = \Omega_{\rm p}$, where $\Omega_{\rm p}$ is the angular velocity of the companion measured on the inertial frame centered on the host star. We talk about Lindbland resonances when $m(\Omega - \Omega_{\rm p}) = \pm\kappa$, where m is an integer and κ is the epicyclic frequency defined as:

$$\kappa^2 \equiv \left(\frac{d^2\Phi}{dr^2} + 3\Omega^2 \right), \tag{4.1}$$

where Φ is the gravitational potential. In the case of a keplerian potential $\kappa = \Omega$. The Lindbland resonances are thus located at:

$$r_{\rm L} = \left(1 \pm \frac{1}{m} \right)^{2/3} r_{\rm p}, \tag{4.2}$$

where $r_{\rm p}$ is the companion orbital radius and m is the order of resonances. The resonances are locations where the planet can strongly perturb the motion of a particle and angular momentum exchange can occur between the planet and the gas disc. The interaction with the gas exterior to the companion orbit ($r_{\rm L} > r_{\rm p}$) increases the angular momentum of the gas and decreases the one of the companion, with a tendency for the companion to migrate inward. At the same time, the interaction with the gas interior to the planetary orbit ($r_{\rm L} < r_{\rm p}$) decreases the angular momentum of the gas and increases the one of the companion, with a planet outward migration. Due to the Newton's third law, the presence of a companion tends to repel gas from the companion orbit. This effect can be balanced depending on the presence of gas both in the interior and exterior of the co-orbital radius. The flux of angular momentum exchange at Lindbland resonances can be considered to be:

$$T_{\rm LR}(m) \propto \Sigma M_{\rm p}^2 f_{\rm c}(\xi), \tag{4.3}$$

where Σ is the surface density, M_p is the companion mass and $f_\mathrm{c}(\xi)$ is a correction factor which considers the fact that resonances very close to the companion contribute just slightly to the torque (torque cutoff function). ξ is defined as:

$$\xi \equiv m \left(\frac{c_\mathrm{s}}{r\Omega} \right)_\mathrm{p} \tag{4.4}$$

and it peaks at $\xi \simeq 1$ (Artymowicz 1993).

4.1.2 Dynamical clearing by planetary companions

For sufficiently large planets, the angular momentum flux of the planet dominates the viscous flux of the disc. The gas is thus repelled from high-m resonances and a gap can form in the surface density near the planetary orbit. We need to define the Hill radius as follows:

$$r_\mathrm{H} = \left(\frac{M_\mathrm{p}}{3M_\star} \right)^{1/3} r_\mathrm{p}, \tag{4.5}$$

where r_p, M_p and $M_\star$ are the companion separation and mass and the stellar mass. This relation requires that the mass ratio is $q \equiv M_\mathrm{p}/M_\star$. In particular, the presence of a planet may creates gaps in gas discs, if two conditions happen:

- **Thermal criterion.** The Hill radius of the planet is larger than the local disc scale height ($r_\mathrm{H} \geq h$) and the tidal torque exerted by the companion dominates on the viscous torque, that tends to close the gap (Lin & Papaloizou 1993). This condition is valid if the mass ratio between planet and star:

$$q \gtrsim 3 \left(\frac{h}{R} \right)_\mathrm{p}^3 \equiv \left(\frac{M_\mathrm{p}}{M_\star} \right)_\mathrm{th} \tag{4.6}$$

  For a typical disc, this means $q \sim 4 \cdot 10^{-4}$ implying a mass between the mass of Saturn and Jupiter. This condition is equivalent to the so-called thermal gap opening mass.

- **Viscous criterion.** Tidal torques are able to remove gas from the gap faster than it is filled back by viscosity (Goldreich & Tremaine 1980; Papaloizou & Lin 1984). If we follow Takeuchi et al. (1996), this condition means to have a mass ratio

$$q \gtrsim (c_\mathrm{s}/\Omega_\mathrm{p} r_\mathrm{p})^2 \alpha^{1/2}. \tag{4.7}$$

  For typical disc parameters ($h/R = 0.05$, $\alpha = 10^{-2}$), this means $q \gtrsim 10^{-4}$.

The companion will create a bump in the gas surface density distribution outside its orbit. The radius at which this happens correspond to the radial location where the viscous material inflow is approximately balanced by the expulsion of material due to the planet's tidal torque. As a consequence a pressure bump and a dust trap form in the outer disc. Dust grains of different sizes are also expected to have a different radial extent: they are trapped depending on their grain sizes and local gas properties. In the gas surface density bump, larger grains are, indeed, trapped more efficiently than small grains still coupled with the gas. The gas, and thus the small grains, extends closer to the planet orbit. This process is often called "dust filtration" (Rice et al. 2006a) and leads to dust and gas cavities that are different in size. Gaps cleared out by planets are, indeed,

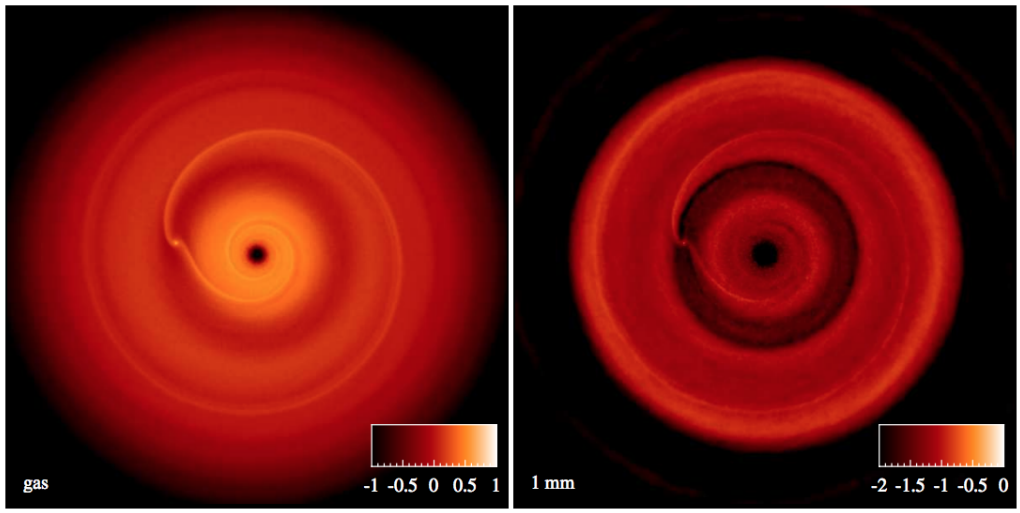

Figure 4.2: Simulations taken from Dipierro et al. (2018b), showing a low-mass planet carving a clear gap in dust (right) and a less prominent one in the gas (left).

expected to have smaller width in the near-IR images (which traces small dust) than in the sub-mm observations (which traces large dust).

We note that embedded planets are able to open dust gaps even though gas gaps are not carved. The gap formation in the gas indeed (with the conditions above cited) is not a necessarily condition for gap opening in the dust (Dipierro et al. 2016), particularly in the large grains not coupled with the gas. Considering that the dust is pressureless and inviscid, the gap opening is a competition between the tidal torque and the aerodynamic drag torque. Low mass planets are able to carve dust gaps, with no disturbance on the gas, thanks to tidal torques assisted by drag in the inner disc, but resisted by drag in the outer disc. This can happen if the Stokes number is $\mathrm{St} \gtrsim \mathrm{St}_{\mathrm{crit}} \sim 1$. If, instead, the mass of the planet is high enough, the planet will generate pressure maxima in the gas disc, as previously described. This mechanism will produce a partial or total gap in both gas and dust, with a deeper gap in the large grains. Discs indeed show gaps well defined in the millimeter emission and not in the gas distributions as shown in the hydrodynamical simulation in both gas (left) and dust (right) of Fig. 4.2. For what regards a detailed description of the criterion that define the minimum mass required to open a dusty gap, we refer to Dipierro et al. (2016).

4.1.3 Planet migration: type I and II

Gap formation is strongly related to planet migration due to the tidal torque exerted by the disc on the planet that leads to an exchange of angular momentum between the disc and planet. Gas-rich protoplanetary discs and planets interact while the nascent planet forms and this leads the planet to migrate inward depending on several parameters including, for example, the planet mass, the disc mass, the disc viscosity. In particular, in the protoplanetary discs, low mass planets are not able to carve a gap in the disc surface density profile and the outcome of the disc-planet interaction is the type I migration;

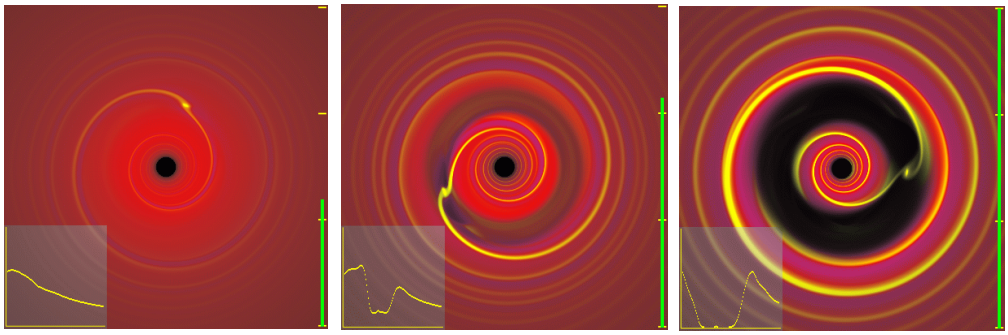

Figure 4.3: From left to right, we show the disc-planet interaction in the case of a small planetary mass (left), not able to open a gap in the gas (type I migration); a medium mass (center), able to open the gap in the gas but not completely; and a high planetary mass (right), which clears out completely the gap (type II migration). Figure adapted from Armitage & Rice (2005).

while high mass planets are able to open gaps and from that moment on they migrate slower (type II migration). In Fig. 4.3, we show simulations of three different planetary masses showing their implications for the gaseous disc (Armitage & Rice 2005).

If the mass of the planet is low ($M_{\rm p} \sim M_{\rm earth}$), the angular momentum flux due to the disc-planet interaction is negligible compared to the viscous transport of angular momentum. The surface density distribution is almost unperturbed and thus the gas is present at all the resonances locations. The planet, indeed, is not able to create a hole in the surface density distribution of the gas in the disc. The planet excites a spiral wave in the disc and, at the same time, the perturbation to the disc surface density produce a gravitational torque onto the planet. The net torque on the planet generates changes on the planet orbit, in the so-called **Type I migration** (see left Fig. 4.3). As shown in Section 4.1.1, the torque scales with the planet mass squared. At the same time, the time scale of migration is inversely proportional to the mass of the planet, and thus it is more rapid for the largest bodies in this regime. In general, Lindbland resonances exterior to the planet orbit are stronger than the interior ones, with a consequent inward migration. The total torque exerted on the planet includes not only the torque produced by the Lindbland resonances, but also the co-orbital torques. The gas that is co-orbital generates horseshoe orbits if seen in a frame corotating with the planet (see Fig. 4.4). The gas density varies and the torque produced may be even larger than the one produced by the Lindbland resonances because it is generated very close to the planet. Anyway both the torques are in general large and drive a rapid migration. Several studies were performed on the coorbital torques (e.g. Ward 1991; Paardekooper & Mellema 2006; Paardekooper & Papaloizou 2009; Paardekooper et al. 2011; Baruteau et al. 2014). Properties to be considered for Type I migration in addition to the planetary mass are: the profiles of surface density and temperature of the disc, the cooling time of gas particles and the efficiency of angular momentum transport in the horseshoe region.

If the mass of the planet grows, the tidal torque of the planet locally dominates over the viscous torque and the resonant interaction with the gas disc is stronger. The gas is repelled from the high-m resonances and the surface density drops in the vicinity of the planet's orbit, forming a gap and a lower disc surface density (see center/right Fig. 4.3, Section 4.1.2). At the beginning, the gas still present in the co-orbital region interacts with the planet. This stage is called **gap opening**, the condition for gap opening are described in Section 4.1.2.

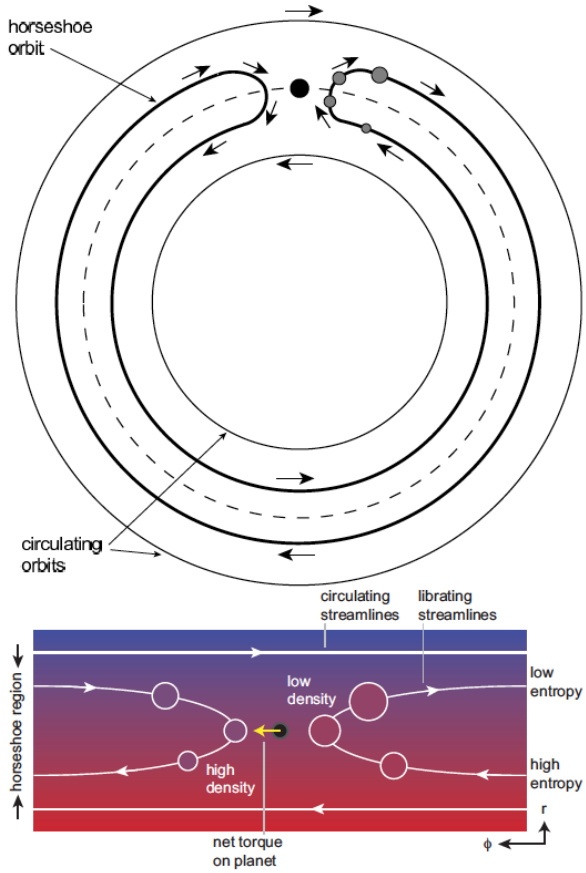

Figure 4.4: In this figure it is shown a low mass planet embedded in a gas disc. The upper figure shows a global view, whereas the lower image is a local view. It is shown the presence of a horseshoe in the reference frame of the planet, which generates a torque on the planet. Credits to Armitage (2007).

Once the planet is massive enough, an annular region with less material than the overall profile is formed. The orbital evolution becomes coupled to the gaseous disc viscous evolution. In particular, in the disc dominated migration (local disc mass exceeds the planet mass), the migration timescale tends to follow its viscous driven radial evolution. In planet-dominated regime, instead, in principle the planet would act as a slowly moving barrier, preventing the gas to flow inside. This will lead to an accumulation of gas at the gap edge, resulting in a slower migration rate. What happens in reality is that, once the gap has been opened, planets continue to accrete gas through tidal streams of material that bridge the gap (Lubow et al. 1999) in the form of a prominent spiral wave excited by the gas disc. The gas that is able to cross the gap edges is then captured inside the Hill sphere of the planet and accretes onto it. Typically, this effect decreases as the planet grows. This regime is called **Type II migration**: the orbital evolution of the planet is driven by the viscous evolution of the disc. Planet migrates at the same rate as the gas in the disc, keeping the same relative position inside the gap as they are coupled to the disc viscous evolution. Recently, numerical simulations by Scardoni et al. (2020) show the

presence of an initial phase of fast planet migration, which slows down over time reaching the theoretical prediction. We note that Type II migration rate can be altered even if e.g. two planets approach each other such as their gaps overlap or they are captured in resonance (e.g. Masset & Snellgrove 2001), as probably happened the case of Jupiter and Saturn ("Grand Tack" model, Walsh et al. 2011 and Morbidelli & Crida 2007) or for HD 169242 (Toci et al. 2020). Moreover, in this scenario the planet exerts a feedback on the disc under the form of strong spiral density wave.

4.1.4 Observations of large gaps and rings

Several discs show large annular gaps and rings. As described previously, their presence suggest a possible connection with ongoing planet formation, even if this is not the only mechanism able to generate them. Before the era of high resolution imagers, the presence of gaps was already claimed. With the advent of the new generation of (sub-)millimeter interferometer ALMA, a great number of discs were observed with both single or multiple rings and gaps. Examples of them are: TW Hya, HD 97048, HD 169142, AS 209, V1094 Sco, MWC 480 and DS Tau (see Andrews et al. 2016; van der Plas et al. 2017b; Fedele et al. 2017, 2018; van Terwisga et al. 2018; Liu et al. 2019; Veronesi et al. 2020). We note that the presence of a gap is not exclusive and can be present in a disc together with other disc structures such as a cavity closer in. Moreover, few other cases were detected with concentric rings and multiple annular gaps with no evidence of clearing in their SED (e.g. HL Tau, HD 163296 and Elias 2-24, ALMA Partnership et al. 2015; Isella et al. 2016; Cieza et al. 2017; Dipierro et al. 2018b). It is still no clear whether those systems are the primordial stage of a transitional discs or they will never evolve in TDs.

4.2 Theories of cavities formation

Many are nowadays the systems that show dust cavities. Different mechanisms have been proposed so far to be the responsible for such cavity structures observed in transition discs. A reliable mechanism should be able to explain the three main features in TDs: large cavities, deep dust cavity reduction with respect to the outer disc and high accretion rates on to the central star ($\gtrsim 10^{-8} M_\odot/yr$). The main processes invoked so far are:

- Dynamical clearing by (sub-)stellar or planetary companion (e.g. Papaloizou et al. 2007). This mechanism is the same as the one described in Section 4.1.
- Dispersal by (photoevaporative) winds (e.g. Clarke et al. 2001), which is known to be a dominant process to disperse the disc as soon as the accretion on the star subsides.
- Magnetohydrodynamical (MHD) winds and dead zones ((e.g. Flock et al. 2015; Pinilla et al. 2016), Section 4.2.3), which are believed to play a key role for both planetesimal formation and disc evolution. We note that vortices are thought to be generated at the outer edge of a dead zone.

These processes are not mutually exclusive and can probably operate at the same time (Williams & Cieza 2011; Rosotti et al. 2013, 2015; Jennings et al. 2018). Rosotti et al. (2013) found that giant planet formation could accelerate disc dispersal and an interplay with the X-ray photoevaporation may be at the basis of the origin of transitional discs with large mass accretion rates and large cavities (Rosotti et al. 2015). In particular, quantifying the amount of dust and gas content inside the cavity of transitional discs is of

fundamental importance in order to distinguish between different clearing mechanisms. Below we describe separately each scenario.

4.2.1 Dynamical clearing

As described in Section 4.1, full gaps (cavities) can be carved by single (or multple) planets or by a (sub-)stellar companion. Below we describe the results on both the clearing from planetary and from (sub-)stellar mass companions proposed as possible explanations of the observed cavities.

Planetary companions

A companion more massive than the one required to carve a gap (described in Sec. 4.1) exerts a stronger torque on the disc and it is able to open a larger gap until completely clear the cavity. In particular, the more massive the companion is, the higher is the efficiency of small dust cavity clearing, together with a larger cavity radius and a sharp cavity edge for large grains (e.g. Crida et al. 2006). We refer to the Chapter 5, for a detailed study on the cavity formation through dynamical clearing by a massive planet. In this mechanism, the viscous inflow of material is balanced by the expulsion of material exerted by the planet's tidal torque. It is possible to form a cavity with a different size in dust and gas thanks to the dust filtration phenomenon. On one side, large grains are trapped in the gas pressure maxima produced outside the planet orbit on a timescale dependent on their grain sizes and local gas properties. On the other side, gas and small grains can be carried across the disc gap (Rice et al. 2006a; Dipierro et al. 2016). The dust grains spatial difference explained by dust filtration Pinilla et al. 2012b is compatible with observations (e.g., Follette et al. 2013). A greater statistic of multi-wavelength observations is needed to better test this scenario and to show the radial variation for different grain sizes.

Another important property to consider is the accretion rate onto the star. The typical accretion rate measured inside Transition Disc is high (Owen 2014) and similar to the one of a typical T-Tauri discs. This suggests the presence of gas inside the dust hole and a companion not massive enough to deplete both gas and dust. This is however not in agreement with the observation of a NIR deficit in moderately accreting transition discs (Zhu et al. 2012b). Large dust grains are indeed trapped, but small grains coupled with the gas may replenish the cavity. Since small particles dominate the opacity at near-infrared wavelengths, we would expect to have a strong near-IR excess (similar to the one of primordial discs), not the deficit observed in the SED of such discs. There are several possible explanations for it. First of all, a possibility is the presence of multiple planets in the inner discs able to carve a full dusty cavity (e.g. Dong et al. 2015a; Zhu et al. 2011; Duffell & Dong 2015). In this scenario, however, dust cavities will be much shallower and wider than the ones carved by single planets and they are not able to reproduce the level of dust depletion in observations (Duffell & Dong 2015). The accretion rate will significantly drop with respect to the unperturbed state (Zhu et al. 2011), in contrast with observations. Planets are indeed expected to heavily accrete the surrounding gas (Lubow & D'Angelo 2006): the majority of accretion occurs onto the planet, and around a 10% of the accretion flow goes inside the planetary orbit and eventually reaches the star. On the other hand, very massive planets can explain large density depletion inside the cavity both in gas and dust, but fail in explaining the high accretion rate. A possibility to explain some of these features in the combination of several mechanisms at once (such as clearing by a companion and photoevaporation - see Section 4.2.2).

Finally, the presence of circumplanetary discs surrounding a companion is expected to

be observable, but they still remain not detected (Szulágyi et al. 2018), with the exception of the one of PDS 70 b (Isella et al. 2019).

Sub-stellar companions

If the companion-to-star mass ratio is large, typically $q \gtrsim 0.04$ (D'Orazio et al. 2016), a cavity is expected to be opened. A study on the cavities size in dependence on the disc and binary properties was performed by Hirsh et al. (2020). Accretion streams are present going from the cavity edge to circum-individual discs and providing in such a way a mechanisms to feed the star (Ragusa et al. 2016).

We note that, in nearby star-forming regions, the fraction of discs seen in a transitional phase is calculated to be $\lesssim 10 - 20\%$ (e.g. Williams & Cieza 2011). This fraction varies as a function of the mean age of each region and if pre-transitional disc are included (e.g. Muzerolle et al. 2009). The number of binary detection is still low and in many discs the presence of a (sub-)stellar companion has been excluded up to much smaller radii. This may suggest a limit on the maximum semi-major axis of the (sub-)stellar companion, which however will not allow the formations of such large cavities. If we consider that the companion is in an inclined or eccentric orbit, their projected separation will appear lower than its real semi-major axis. Another possibility is that such companions are still embedded in the disc and thus more difficult to be observed. Some examples of (sub-)stellar companions detected in transition disc cavities are CoKu/Tau4 (Ireland & Kraus 2008) with a binary separation of ∼8 au. HD 142527 has an M-dwarf companion (Lacour et al. 2016) at ∼30-50 au from the primary star and with an eccentric/inclined orbit (Price et al. 2018a). GG Tau is a known quadruple system with a almost equal mass binary and a detected circumbinary disc in the IR (Cazzoletti et al. 2017; Aly et al. 2018; Brauer et al. 2019).

Eccentricity in a gas-rich disc

Massive companions are often observed to be on eccentric orbits. Small eccentricities may be excited during migration, but this cannot explain alone the large values of eccentricities. We refer to Goldreich & Tremaine (1980) for considerations regarding it. Eccentricity growth depends on the possible balance between the relative strength of external Lindbland resonances, acting to excite eccentricity and non-coorbital corotation resonances, which act to damp eccentricity. For massive companion present in the gap the Lindblad resonances from the external part of the disc can excite the eccentricity of the object (Dunhill et al. 2013; Ragusa et al. 2018).

Moreover, the evolution of binary systems can proceed with a significantly different orbital inclination than the one of the disc. A relative misalignment of the orbital plane of the companion with respect to the circumbinary disc, can evolve up to a polar configuration (Aly et al. 2015; Owen & Lai 2017; Martin & Lubow 2017). This process can be also used to explain the presence of an inner disc misalignment with respect to the outer disc, if there is some mechanisms able to break the disc and separate it into two parts not communicating with each other. An eccentricity-inclination oscillation of the companion might be produced by the fact that the outer disc could act as a third body able to excite the Kozai-Lidov mechanism[1] (Kozai 1962; Lidov 1962; Bitsch et al. 2013). A general agreement regards the fact that sub-stellar and brown dwarf objects have a not-negligible

[1]The Kozai-Lidov mechanism is a secular interaction between a wide-binary companion and a planet. The orbit of the binary system may be perturbed under certain conditions, resulting in a long-period oscillation of both the eccentricity (e) and the inclination (i) conserving the value $\cos i\sqrt{1-e^2}$.

eccentricity growth if they are embedded in their natal gas disc (e.g., Dunhill et al. 2013), whereas for masses similar to the one of Jupiter this is not so clear: instabilities can boost non-zero eccentricities up to $e \sim h/R$ (D'Angelo et al. 2006; Duffell & Chiang 2015).

4.2.2 Photoevaporation

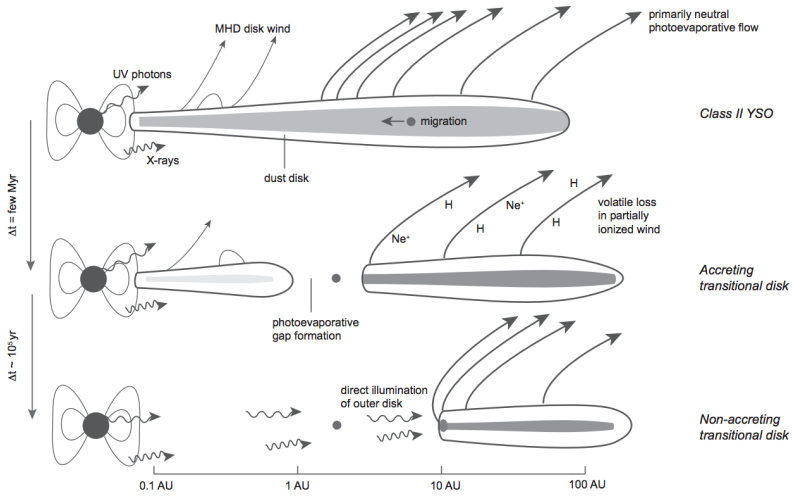

Figure 4.5: Figure taken from Alexander et al. (2014), showing the photoevaporation process in action.

As shown in Section 1.2, the Spectral Energy Distribution profiles of transitional discs show a lack of emission in the NIR, while an excess is present at the FIR. This gives strong indications of a removal of small dust grains from inside out in the hypothesis of the discs to be in a transition between optically thick gas/dust-rich discs to disc-less objects (Owen 2015). In this regards, photoevaporations is one of the main mechanism able to trigger disc dispersal from inside out and it can be considered as a threshold process. Particularly, this can explain large cavities, through a balance between the photoevaporation rate and the viscous accretion. The high-energy irradiation (UV and X-rays) coming from the central star interacts with the gas in the inner regions of the disc. The gas will be removed from the disc through a pressure supported wind, if the irradiation energy and flux are high enough to increase the thermal energy of the gas over the the binding energy to the tidal potential of the star. Considering that small grains are coupled with the gas, they will be also removed. In the first phase (∼Myr), viscous accretion is dominant in the disc evolution. After this period, photoevaporative wind mass loss rate and viscous accretion rate becomes comparable. The hot gas is photoionized and it is removed from an annular gap in the inner regions of the disc both in gas and small dust grains (Clarke et al. 2001). The radius at which this happens depends on the temperature and the star mass (Alexander et al. 2006), e.g. for solar-type protostars, this happens at ∼10 au. The innermost regions, then, continue to viscously accrete. This phase lasts ∼0.1 Myr. When the whole inner disc has accreted, the outer disc is directly exposed to the radiation from the star and the dissipation of the outer disc is thought to be fast (Alexander & Armitage 2007). Typically these systems can be observed with both low gas and low dust in the cavity, due to the high efficiency in removing gas in this phase with respect to e.g.

dynamically-carved cavities. The cavities predicted are small ($\lesssim 10$ au) and the accretion rates are low. Typically the accretion rate for photoevaporation models is $10^{-8}M_{\odot}/yr$ (Owen et al. 2011), low with respect to observations of TDs. Several are the driving mechanism of photoevaporation including FUV, EUV, X-ray. Important to note is that the exact value of mass-loss rate is still unknown.

4.2.3 Other scenarios proposed

Other scenarios proposed to explain the presence of cavities are: dead zones (Pinilla et al. 2016), dust grain growth (e.g.Dullemond & Dominik 2005) and the photophoresis (Krauss et al. 2007).

Dead zones are the regions of low ionization, where the magneto-rotational instability is suppressed (e.g. Flock et al. 2012). Low ionization is possibly present in locally very high density regions where not enough photons are able to penetrate. At the edge of dead zones a pressure bump can form, preventing dust grains to drift inwards. Moreover, the rate of gas flow decreases with the accumulation of gas in the outer edge. This does not allow migration and, consequently, a ring-like feature in both gas and dust components can form (Flock et al. 2015). The ring is in general located at a similar location (Pinilla et al. 2016) in both the gas and dust component. Together with the presence of dead zones, MHD winds can produce a difference in the inner radii position between the two component. MHD winds are produced by the magnetic field that is able to extract part of the ionized circumstellar material (not energetic enough to be alone removed) from the disc and thus to efficiently extract disc angular momentum. Dead zones can increase the turbulence present in the disc and generate asymmetric vortices at (sub)mm wavelengths (Ruge et al. 2016). An observational prediction to disentangle dead zones from the others formation mechanisms for observed large cavities is related to the gas distribution. The gas surface density is not expected to be greatly affected by the presence of dead zone, while both clearing by a massive companion and photoevaporation are expected to lower the gas surface density in the cavity (Fung et al. 2014; Pinilla et al. 2016). Moreover, typically, dead zones can explain ring-like structures, but not large cavities.

Grain growth was considered as another possible mechanism (e.g. Dullemond & Dominik 2005; Ciesla 2007; Birnstiel et al. 2012a). The process of grain growth may produce a decrease of the optical depth due to the fact that opacity of large grains is very low, leading to a less efficient emission (Draine 2006), this would mean that cavities do not necessarily indicate a low level of dust density. However, while the grain growth theory predicts that the SED of a typical transitional discs have a sharp transition between cavity and outer disc (e.g. Birnstiel et al. 2012a), the variation from cavity (optically thin) to outer disc (optically think) should be smooth not like observed in the (sub-)millimeter images. Moreover, this mechanism does not alter the gas profile significantly (Bruderer 2013) and to have difficulties in explaining the large observed cavities at (sub-)mm wavelengths (Birnstiel & Andrews 2014b).

Photophoresis is another mechanism able to stop the inward drift of large bodies from 1 mm to 1 m, exploiting the difference in temperature between the illuminated dust particles and shadowed gas. In particular, a particle illuminated will absorb partially the flux and will have a higher temperature. This will cause a slow movement from the hot to the cold part with a consequent torque and linear force produced. In particular, a thermal creep is induced by the momentum exchange between the illuminated solid and the gas.

4.2.4 Observations of Transitional Discs

Transitional discs (TDs) are a well studied class of circumstellar discs, considering their potential connection with planetary or (sub-)stellar companion formation. A large sample on transitional discs was put together by van der Marel et al. (2016). They have a distinct shape in the SED (see Chapter 2) and a variety of substructures.

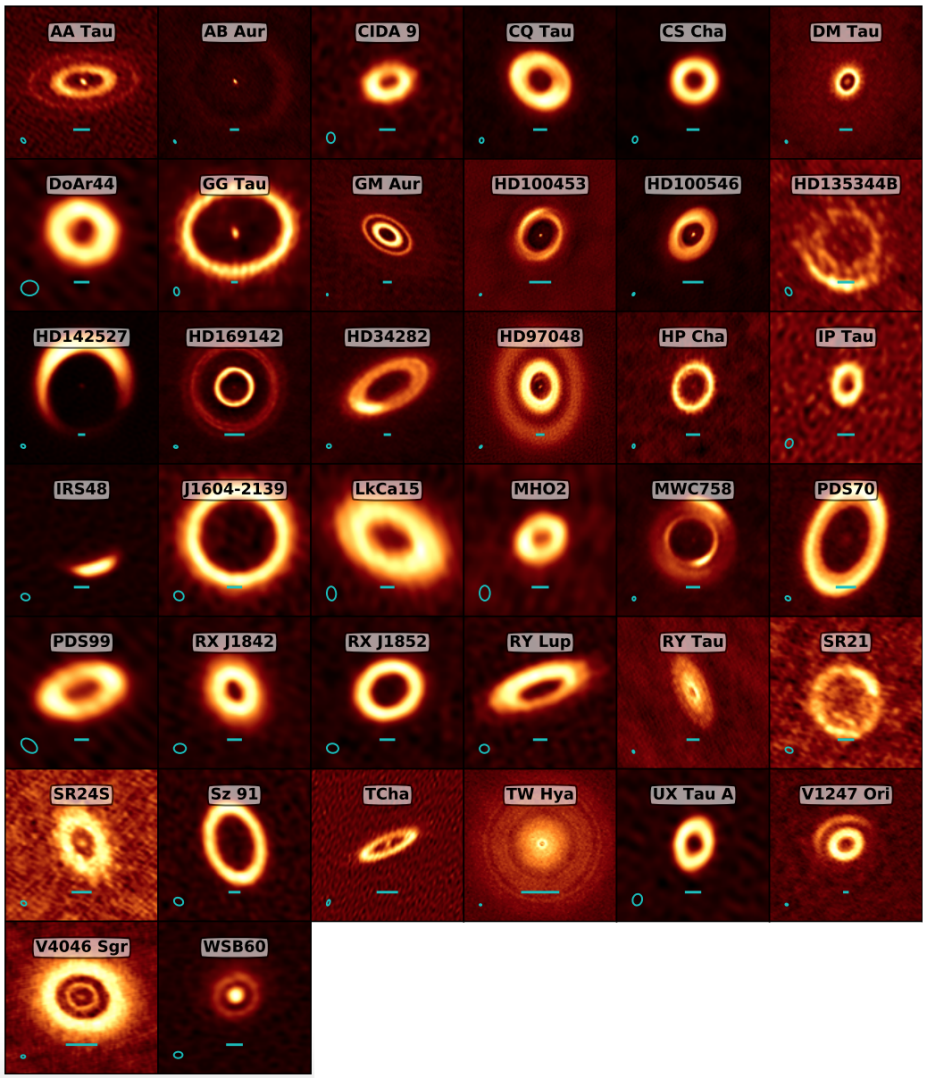

Figure 4.6: Gallery of 38 transition discs imaged with ALMA in the continuum. The scalebar shows the dimension of the image and it corresponds to 30 au and the beam size is shown on the left. Credits: Francis & van der Marel (2020).

Some of them have been observed with SMA (e.g., Brown et al. 2009, Andrews et al. 2011) for the first time in the sub-mm finding large cavity sizes ($\gtrsim$ 15 au). Later on, resolved ALMA observations of large cavities in the sub-mm were presented in Pérez et al. (2014), van der Plas et al. (2017b), Long et al. (2017), Pinilla et al. (2018), Long

et al. (2018b), Andrews et al. (2018b) The presence of a cavity in the (sub-)mm continuum does not imply that it is present also in the gas. It is not easy to spatially resolve the disc structure in the gas, but there are examples of cavities observed with ALMA in ^{13}CO and C^{18}O (see Section 1.3, e.g. HD 135344 B, DoAr 44 and IRS 48, van der Marel et al. 2016). Usually the gas cavities, if present, are smaller than mm continuum observations (e.g. RX J1604 and SZ 91, Zhang et al. 2014; Canovas et al. 2015). Moreover, gas cavities typically show smaller depletion than dust cavities (e.g. HD 142527 and SR 21, Casassus et al. 2013b; van der Marel et al. 2016). At the same time, it is not necessarily obvious that a cavity depleted in large grains (millimeter continuum wavelengths) is also depleted in small grains, coupled with the gas. Polarimetric images of cavities seen in near-IR are for example HD 100546, (Garufi et al. 2016); HD 100453, (Benisty et al. 2017); HD 135344B, (Stolker et al. 2016); HD 142527, (Avenhaus et al. 2017); RX J1615-3255, (de Boer et al. 2016); LkCa 15, (Thalmann et al. 2016); TW Hya, (van Boekel et al. 2017). As between gas and large grains, often the cavity sizes do not match (e.g. Garufi et al. 2013; Follette et al. 2013; Pinilla et al. 2015); sometimes, the cavity appears to be depleted in the same way in both large and small grains (e.g. see RXJ1604, Mayama et al. 2012; LkCa 15 Thalmann et al. 2014). Finally, Owen (2016) found that transition discs with larger holes (R_{cav} $\gtrsim$20 au up to $\sim$100 au) seems to have larger mm-flux (mm-bright), while mm-faint transition discs show relatively small gap sizes ($\lesssim$10 au). The high accretion rates ($\sim 10^{-8}$ M_{sun}/yr) of the mm-bright discs does not appear to be affected by the very large holes. The mm-faint discs show instead lower accretion rates ($\sim 10^{-10}$-10^{-9} M_{sun}/yr). This seems to be in principle counter-intuitive when interpreting transition discs in terms of photoevaporation models. Photoevaporation alone cannot be sufficient to explain mm-bright discs and are likely rare and long-lived objects. The typical presence of gas reservoir inside the cavity (van der Marel et al. 2018) suggests indeed an origin via sculpting by low-mass companion. On the contrary, small sizes of mm-faint transition discssuggest a scenario where photoevaporation plays a key role (see Section 4.2.2).

Constraining the formation scenario of cavities is tricky. Directly detecting close-in ($\lesssim$10 au) low-mass stellar companions is challenging for high contrast imaging both for the resolution and the contrast needed. Typically these type of observations are, indeed, done with the use of a coronagraph (see Section 6.2) which makes us blind in the inner regions of the discs.

4.3 Asymmetric disc structures

4.3.1 Spiral arms

Spiral arms seen in protoplanetary discs most probable trace density waves, in a similar way to the spiral arms present in galaxies. In the case the arms were, instead, material rotating at keplerian velocity there would be a large difference in the velocity rotation between the inner and outer part of the spiral and, consequently, the spiral would disappear after few orbital periods. In the case of density waves, the presence of shocks along the spiral may increase the temperature and puff up the disc vertical scale height. This larger vertical scale will be visible in scattered light observations: a small difference in pressure scale height can be enough to explain the observed contrast of spiral arms in near-IR (Juhász et al. 2015). Moreover, the value of pitch angle can be determined by the sound-speed distribution (dependent from the temperature) in the disc which sets also the pressure scale height.

Origins: embedded companion or gravitational instability

The most common explanations for this type of substructures are two: the first is the presence of a planetary/ (sub-)stellar companion orbiting around the central star in the outer part of the disc (e.g. Dong et al. 2015b); the second is the development of gravitational instabilities (e.g. Cossins et al. 2010; Dong et al. 2015a). The presence of dust traps, stellar flybys are also used to test the formation of spirals. Dust traps correspond to local maxima in the dust surface density distribution (see Section 4.3.3) and are believed to launch spiral density waves in the same way as embedded planets. The presence of a spiral and a dust trap seems to be indeed related, considering the large number of discs where spiral arms pass through the location of the claimed dust trap (e.g. HD 135344 B, MWC 758). Stellar flybys are extremely unlikely considering the typical distance between stars in the case of planet formation. For Class 0/I systems, Tobin et al. (2011, 2016) have shown that the infall of part of the envelope can follow spiral-like shapes which can connect different components. The great diversity of the spiral arms so far observed suggest that more than one mechanism can be at the origin of all observed spirals. In the following, we will briefly describe the formation via an embedded companion of gravitational instability, and describe some of the recent observations. We note that also combination of an embedded companion and gravitational instability may also explain such disc structures.

Spirals can form through an angular momentum exchange between the accretion disc and **embedded companions** with high companion-star mass ratio (Lin & Papaloizou 1979). At the same time, Goldreich & Tremaine (1979) showed that density waves forms under the presence of any planets embedded in the disc, considering they are a rotating external gravitational potential. The density waves forms mainly at the Lindblad and corotation resonances. Successively, Ogilvie & Lubow (2002) has analytically studied the spiral profile generated in such way: a single spiral arm corresponds to the position where constructive interferences between density waves launched from Lindblad resonances in the disc. When a shock forms the dissipation of angular momentum is not linear (Rafikov 2002). If the planet is massive enough the shock can form near the planet, with a consequent open pitch angle of the spiral due to a shock propagation faster than the local sound speed. This can explain the large pitch angles observed without invoking an unrealistic disc scale height (Benisty et al. 2015). Several are the diagnostic which can be used to verify the possibility of a companion launching a spiral: the contrast, the number of spiral launched and the separation between primary and secondary spiral arms (Dong & Fung 2017a; Bae & Zhu 2018; Fung & Dong 2015). A more massive companion can induce brighter spiral arms with respect to the average disc emission and, typically, launch two spirals. The planet rotate and the density waves forming the induced spiral will co-rotate with it. This is another important way to discriminate if this scenario is happening and how frequent it is.

Another option is the formation of spirals via **gravitational instability**. For a description of the mechanism behind it we refer to Chapter 3. If the disc is massive enough, the formation of spirals can happen as a consequence of its own gravity (e.g. Durisen et al. 2007). Under the assumption that structures induced by GI correspond to density waves as the one of embedded companions, more massive discs with respect to the primary ($q \gtrsim 0.25$) tend to enhance low-m modes (e.g. m=2, Dong et al. 2015a), have wide pitch angles and higher mass accretion rate. On the contrary, lower mass discs produce less defined structures. According to Tomida et al. (2017), GI-induced spirals do not correspond to material arms. This suggests that, particularly for Class 0/I discs the presence of continuus infalling material would keep the structure for a longer time than what expected

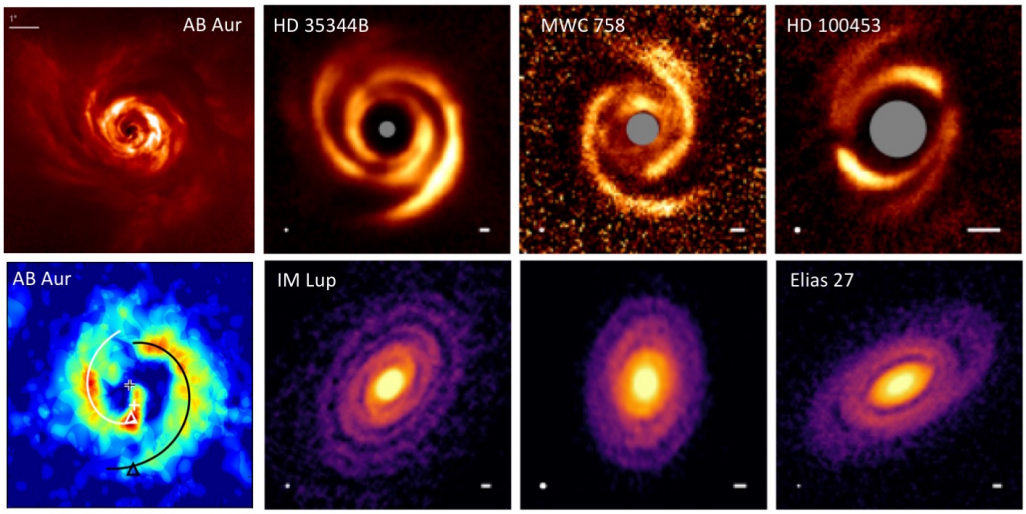

Figure 4.7: Examples of protoplanetary discs with spiral-like structure observed in scattered light (with SPHERE-PDI, top), in the CO emission lines (ALMA, bottom left: AB Aur) and in the millimeter continuum (ALMA, bottom right). In particular in HD 100453, it is possible to distinguish two-side shadows. Credits. Andrews (2020) and references therein with the exception of AB Aur: Boccaletti et al. (2020) (SPHERE) and Tang et al. (2017) (ALMA).

through GI. Spirals may be interpreted thus as density waves induced by the development of gravitational instabilities (Dipierro et al. 2015a). This lead to the formation of significant overdensities in spiral arms particularly for centimetre sized particles. Moreover, Dipierro et al. (2015a) found spatial spectral index variations across the disc, which reveals that the dust trapping produces a large grains migration. Another possibility is that gravitational instability together with embedded companions can produce spirals in the case of marginally stable discs (Pohl et al. 2015) in the outer disc. In this case, the contrast is expected to be quite large and with tightly wound arms.

Observations

In circum-stellar discs, the first detections of spiral arms was done through HST (e.g. Grady et al. 2001). Since then, a huge variety of spiral patterns has been observed both in transitional discs and in much younger sources (Class 0/I protostars). Spirals can present different features depending on the wavelength observed (between e.g. near-IR and continuum, Muto et al. 2012; Garufi et al. 2013; Christiaens et al. 2014; Benisty et al. 2015; Garufi et al. 2016; Stolker et al. 2016; Rosotti et al. 2019a). The spiral-like disc can be with a single arm or multiple arms. Some of the first detected spirals are AB Aur and HD 100546, detected by HST (e.g. Grady et al. 1999, 2001), tracing the surface of the disc through scattered light observations of small grains. Several other discs with spiral arms were detected afterwards through polarimetric images (e.g. with SPHERE). An example of this is the two-arms disc spiral found around HD 100453 (Benisty et al. 2017). Spirals present in the surface do not obviously correspond also to spirals in the large grains distributions. Some examples of spiral arm disc in scattered light are shown in Fig. 4.7. Detections of spiral arms in sub-mm continuum (e.g. with ALMA) are indeed rare. Elias 2-27 is an example where a spiral has been detected in the continuum (band

6, Pérez et al. 2016; Huang et al. 2018). This detection shows that these spirals are imprinted in the mid-plane.

Testing whether spiral-like structures are present also in the gas distribution is not easy. This is however important in order to verify if the gas show the same structure of scattered light observations and because it can help to better constrain the disc geometry. High resolution and high sensitivity observations are needed to spatially resolve the disc substructure, particularly in the gas tracers (e.g. CO isotopologues) fainter than the continuum. Typically the tracers used are ^{13}CO and C^{18}O, optically thin, whereas the ^{12}CO, typically optically thick, can be used to provide a brightness temperature profile. Spiral structures were observed in the line integrated (Tang et al. 2017, AB Aur) and peak intensity maps (Christiaens et al. 2014, HD 142527) of ^{12}CO (2-1 emission). The quantity commonly used to characterize the morphology of the spiral arms is called pitch angle, defined as the angle between the tangent to the spiral and the local azimuthal vector for each point of the spiral. In order to properly measure it, the disc has to be deprojected (using inclination and PA of semi-major axis) to see it as on a face-on view. Typically pitch angles span from 10° to 30°. The variation in the spiral contrast is other observable used in general. The contrast is measured as the ratio between the peak of emission in the arms and the background surface brightness. Contrast typically ranges between values of 1.5 and 3 (e.g., Pérez et al. 2016; Dong & Fung 2017b). Interestingly, both the pitch angle and the contrast can vary even inside the same spiral arm, giving us clues to understand the formation of this peculiar structure. Finally, it is important to consider the number of spiral arms observed, the separation between the different arms and their relative strength.

4.3.2 Shadows

Localized dark lanes are observed in protoplanetary discs as secular two-sided shadows, single-sided moving shadows or transient individual shadows. In particular, azimuthal surface brightness reductions in the scattering emission may be produced by the presence of a warped disc (or a misaligned inner disc) that cast shadows in the outer part of the disc. In the following, we will briefly describe the generation of a warp and observations of shadows.

Origin: warped disc

The dynamical interaction between the disc and a close binary (or a massive planet) on an inclined orbit may produce a disc misalignment (Mouillet et al. 1997; Arzamasskiy et al. 2018) and the development of warps. The tidal torques caused by the binary potential can also generate an inner truncation radius of the disc. If the mass ratio between the stars is low, the gravitational potential becomes more spherically symmetric and the disc is less affected by an external torque with the consequence of a smaller amplitude of the warp (Lodato & Price 2010; Facchini et al. 2013; Lodato & Facchini 2013). High viscosity, instead, allows the warp to propagate diffusively and it aligns with the binary plane at the inner edge. The twist depends on the value of viscosity. A misaligned disc can be produced also by a planet with mass larger than 0.01 $M_\odot$ (Owen & Lai 2017) with the development of a warp. If the planet is on an eccentric orbit and it is carving a gap in the circumbinary disc, then possibly the precession of the companion with respect to the inner disc enters in resonance. This leads to a significant inner disc misalignment. The same phenomenon can be produced by an inclined planet (Nealon et al. 2018). In

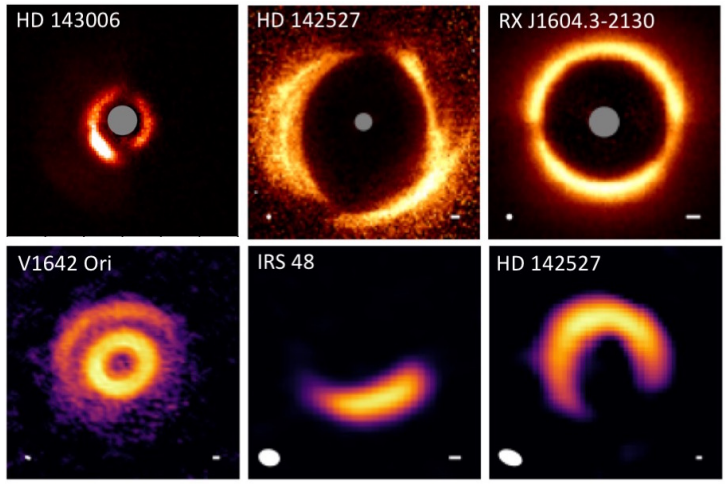

Figure 4.8: Examples of protoplanetary disc asymmetries and shadows (with SPHERE-PDI, top; ALMA, bottom). Credits. Andrews (2020) and references therein with the exception of HD 143006 (Benisty et al. 2018).

particular, the planet needs to be massive enough to separate inner and outer disc. The inclination of the planet is then able to drive a relative tilt and twist between the inner and outer disc. The discriminant feature to generate the warp remains in any case the planet mass. In general, warps originate in the inner part of the disc which is optically thick at NIR wavelengths. This can produce the formation of two-sided shadows similar to those observed (Whitney et al. 2013). The most accredited scenario for this type of structures remains the presence of a (massive) companion in the disc. We refer to Juhász & Facchini (2017); Facchini et al. (2017) for a extensive study on the observable features of warps in circumbinary discs.

Observations

We here report some examples of shadows detected in discs and their interpretation. One of the first shadows reported in literature are the ones of GG Tau A. Itoh et al. (2014) found a counter-clockwise rotation of the western shadow, suggesting it to be cast by circumstellar material possibly produced by an inclined disc around the binary components (Köhler 2011). Recently Keppler et al. (2020) confirmed the presence of shadows and the putative presence of an inclined circumstellar disc, but they found the shadows to be stable.

In J1604-2130 as well as in HD 169142, a dip in the annular emission has been observed to move fast between different epochs (Mayama et al. 2012; Canovas et al. 2017; Quanz et al. 2013b; Bertrang et al. 2018). For HD 169142, the fast rotation rate of these shadows suggests the presence of a object (maybe a circumplanetary disc) orbiting at a few au separation from the star. More recently Stolker et al. (2017) found transient shadows in the disc around HD 135344 B, varying within a day.

As previously explained, a common explanation for the presence of the two-sided shadows is a misaligned optically thick inner disc, and more generally a warped disc (see previous section). In particular, this scenario has been tested in several systems. HD 142527 presents dark dips at the edge of the cavity in the scattered light (Fukagawa et al.

2006; Avenhaus et al. 2014b). Predictions of a tilted inner disc with an inclination of 70° (Marino et al. 2015; Price et al. 2018a) is consistent with observations. An observational confirmation of this comes from ALMA observations of CO rotational lines, which show almost free-fall velocities in the vicinity of the warp (Casassus et al. 2015a). Observations of GW Ori provide direct evidence of misaligned disc (Kraus et al. 2020). DoAr 44 host a disc that has similarly a two-sided shadows with consequent hypothesis of a misaligned inner disc casting two-sided shadows (Casassus et al. 2018). Moreover, HD 100453 were detected with two-sided dips (Benisty et al. 2017) where NIR interferometry observations are in agreement with the misalignment required to cast the observed shadows (Min et al. 2017). For both DoAr 44 and HD 100453, the shadows do not appear completely symmetric with respect to the central star. The case of HD 135344 B and HD 100453 are shown in Fig. 4.7. To conclude, the presence of shadows has been found also in the disc around the T Tauri star HD 143006. In particular, polarized scattered light observations with VLT/SPHERE at near-infrared shows a large-scale asymmetry, a ring and two gaps (Benisty et al. 2018). Two narrow dark regions are present in the ring suggesting shadowing effects, possibly related to a misaligned inner disc. High resolution ALMA images at 1.25 mm continuum emission shows several concentric rings, gaps and a bright arc exterior to the rings, resembling a vortex (Pérez et al. 2018). ^{12}CO observations reveal an inner disc depleted of CO emission (Pérez et al. 2018). Both Benisty et al. (2018) and Pérez et al. (2018) suggest the presence of an inner warped disc with a large misalignment possibly produced by an inclined binary companion.

4.3.3 Asymmetric dust distributions

Together with gaps and cavities, also azimuthal asymmetries are often found in protoplanetary discs at millimeter continuum wavelengths, typically inside Transition Discs. In the following we will describe how azimuthal asymmetries can be related mainly to the presence of dust traps or to a massive companion in the cavity and some observational examples.

Origin: dust traps, vortex or companion

Dust traps are local maxima in the dust surface density distribution. The mass trapped is estimated, through measurements on cm-size grains, to reach several Earth masses. A strong prediction for dust trap is that large grains (cm-wavelengths) are more azimuthally concentrated in the center than grains at mm-wavelengths (van der Marel et al. 2015; Casassus et al. 2018). This is indeed due to the presence of grain growth in the region. This can be observed through observations done at different wavelengths through which it is possible to derive the spectral index of the dust opacity β. Dust trapping can be produced by the presence of vortices (Regály et al. 2012). Vortices are high-pressure regions that can trap dust azimuthally and form dust asymmetries in the mm-wavelength (e.g. Lyra et al. 2009; Lin 2012). These vortices can form through the breaking up of Rossby waves (RWI, Lovelace et al. 1999; Li et al. 2000, 2001) typically at the edge of a dead zone (Regály et al. 2012). Rossby waves can be launched by a pressure/surface density bump in the radial disc profile. If the modes are unstable, an instability (RWI) can start. We refer to the work done by Cazzoletti et al. (2018) on HD 135344 B for a study on the vortex induced dust trapping. For an azimuthal trap, indeed, variation on the grain size maximum location is expected on the azimuthal direction and the smaller grains should be inside the vortex.

On the other hand, the asymmetric emission, azimuthally concentrated dust traps

and the eccentricity development at the edge of the cavity can be also produced by a companions of different mass (mass ratio$>$ 0.05) with respect to the primary star (Ragusa et al. 2017). If the companion is not enough massive, there is no noticeable difference from a ring-shape mm-size dust distribution (Pinilla et al. 2012b); whereas more massive companions allow the presence of azimuthally concentrated dust traps. Giant planets are expected to open a gap (Dipierro et al. 2015a; Rosotti et al. 2016). The edges of these gaps can become unstable against Rossby wave instability and create a pressure maximum at the outer edge of the gap. This maximum allows pebbles from mm to meter sizes to concentrate in a local space, to interact and eventually merge, allowing the so called dust trapping.

Observations

Asymmetric dust distributions were observed in multiple disc surveys (e.g., Brown et al. 2009; Andrews et al. 2011; Isella et al. 2013) using SMA. With the advent of ALMA, the observations of these asymmetries were resolved (e.g. Oph IRS48, van der Marel et al. 2013; HD142527, Casassus et al. 2013a; SR 21, Pérez et al. 2014; AB Aur, Tang et al. 2017; HD135344 B, Cazzoletti et al. 2018; HD 143006, Pérez et al. 2018). These asymmetries have the shape of a crescent or horseshoe with a mild or high variation in flux, they can be single or double clumps. These structures sometimes corresponds to an enhanced structure in the near-IR, such as in the case of HD 135344 B. In order to study such substructures the azimuthal extent has to be studied. The dust asymmetries usually do not correspond to a gas surface density enhancement. This measurement is, however, quite difficult due to the complex chemistry of the less abundant CO ipotopologues, which trace the gas density (e.g. HD 142527, van der Plas et al. 2017a). Moreover, further studies have shown that the overdensity seen at mm-waves is less compact than at cm-wavelengths (Casassus et al. 2015b; van der Marel et al. 2015; Casassus et al. 2018), which is a strong prediction for dust trap (see paragraph above).

Various hypothetical explanations have been made about this type of structures so far. First of all, they were identified as vortices (see Section 4.3.3), a potential birthing place for planets (Regály et al. 2012). An alternative scenario is that horseshoes in transitional discs can also be produced by a massive companion orbiting around the host star (Ragusa et al. 2017). This is based on the eccentricity development at the edge of the cavity produced by the binary. Finally, they can also be produced by spiral density waves launched by the binary inside which enhanced mm-dust emission (Price et al. 2018a).

In the case of HD 142527, gas does not appear to have a sufficient density for gravitational instability to happen (Muto et al. 2015) in the asymmetry. For HD 135344B (Cazzoletti et al. 2018), instead, the authors found the disc to be compatible with a vortex trapping dust particles. In order to constrain this scenario they measured a strong decrease of the spectral index at the center of the vortex, consistent with the presence of large grains inside. Moreover, they detect an azimuthal shift of the peak of the vortex with wavelength and a decrease of the azimuthal width of the vortex for longer wavelengths. The same target was also studies as a test case in Veronesi et al. (2019), who propose the structure of HD 135344B to be ascribed to the presence of two massive planets.

Chapter 5

A dust and gas cavity in the disc around CQ Tau revealed by ALMA

Based on the paper by **M. G. Ubeira Gabellini**, A. Miotello, S. Facchini, E. Ragusa, G. Lodato , L. Testi, et al. : "A dust and gas cavity in the disc around CQ Tau revealed by ALMA" published in Monthly Notices, 486, 4638-4654, 2019. Royal Astronomical Society.

The combination of high resolution and sensitivity offered by ALMA is revolutionizing our understanding of protoplanetary discs, as their bulk gas and dust distributions can be studied independently. In this Chapter we present resolved ALMA observations of the continuum emission ($\lambda = 1.3$ mm) and CO isotopologues (^{12}CO, ^{13}CO, C^{18}O $J = 2 - 1$) integrated intensity from the disc around the nearby ($d = 162$ pc), intermediate mass ($M_\star = 1.67\,M_\odot$) pre-main-sequence star CQ Tau. The data show an inner depression in continuum, and in both ^{13}CO and C^{18}O emission. We employ a thermo-chemical model of the disc reproducing both continuum and gas radial intensity profiles, together with the disc SED. The models show that a gas inner cavity with size between 15 and 25 au is needed to reproduce the data with a density depletion factor between $\sim 10^{-1}$ and $\sim 10^{-3}$. The radial profile of the distinct cavity in the dust continuum is described by a Gaussian ring centered at $R_{\rm dust} = 53$ au and with a width of $\sigma = 13$ au. Three dimensional gas and dust numerical simulations of a disc with an embedded planet at a separation from the central star of ~ 20 au and with a mass of ~ 6–$9\,M_{\rm Jup}$ reproduce qualitatively the gas and dust profiles of the CQ Tau disc. However, a one planet model appears not to be able to reproduce the dust Gaussian density profile predicted using the thermo-chemical modeling.

5.1 Introduction

Protoplanetary discs are the natural outcome of the star formation process (Shu et al. 1987). Material infalling from the pre-stellar core is channeled into the central star and, due to angular momentum conservation, eventually forms a disc. Since the earlier stages of this process, planetary systems form from the material present in the circumstellar discs. The structure and evolution of protostellar discs are important keys in understanding the planet formation process. The main scenarios currently considered for planet formation are the core accretion model (e.g. Pollack et al. 1996) and disc instability (e.g. Boss 1997). According to the former scenario, planets form through the sequential aggregation of the solid component present in protoplanetary discs and eventually form planetesimals (e.g. review of Testi et al. 2014). The embryo accretes through a balance between collision of planetesimals and fragmentation until it has obtained most of its mass (Birnstiel et al. 2016). After this, a rapid gas accretion can occur which leads to

the giant planet formation. The alternative scenario is related to the development of gravitational instabilities (GI) during the initial stages of the disc evolution. In the outer part of self-gravitating discs, if the disc-star mass ratio is higher than the disc aspect ratio ($M_{\rm disc}/M_\star \gtrsim H/R$), the rapid growth of the density perturbations induced by GI may produce bound clumps, although the effectiveness of this model to produce Jupiter mass planets is controversial (e.g. review of Kratter & Lodato 2016). Independently of the exact planet formation process, it is clear that grain growth plays an important role in the evolution and dynamics of the disc.

Young massive planets are expected to imprint signatures on the dust and gas structure of their parent protoplanetary disc, such as cavities, gaps or asymmetries, which can be detectable in the scattered light and thermal emission of discs. Thanks to the new facilities, like the Atacama Large Millimeter/submillimeter Array (ALMA), SPHERE on the Very Large Telescope (VLT) and GPI at the Gemini Telescope, such signatures are now observed with relative ease (e.g. Garufi et al. 2013; van der Marel et al. 2013; Benisty et al. 2015, 2017, 2018; ALMA Partnership et al. 2015; Pérez et al. 2016; Andrews et al. 2016; Isella et al. 2016; Fedele et al. 2017, 2018; van der Plas et al. 2017b; Pohl et al. 2017a; Hendler et al. 2018; Dipierro et al. 2018b; Liu et al. 2018b; Long et al. 2018b; Clarke et al. 2018). Of particular interest are those discs whose emission shows a dip at NIR wavelengths in the Spectral Energy Distribution (SED), indicating a decrease in the NIR grain opacity. Although there is no agreed explanation of what causes the dip in the NIR, possibly this can be related to the presence of a depletion of small dust grain in the inner disc regions. The flux emission at longer wavelengths resembles the typical emission coming from a dust-rich object in the outer regions (Strom et al. 1989a; Calvet et al. 2005). These discs are referred to as transitional discs (TDs) (Espaillat et al. 2014). The term 'transitional' indicates that these objects may be in a transition phase from optically thick gas/dust-rich discs extending inward to the stellar surface to objects where the disc has been dispersed. Whether all discs go through such a phase is however still debated. These discs are anyway excellent candidates to test planet formation theories.

Quantifying the amount of dust and gas content inside the cavity of transitional discs is of fundamental importance in order to distinguish between different clearing mechanisms. The main processes invoked so far are: 1) Dispersal by (photoevaporative) winds (e.g. Clarke et al. 2001), 2) Dynamical clearing by a (sub-)stellar companion (e.g. Papaloizou et al. 2007), 3) MHD winds and dead zones (e.g. Flock et al. 2015; Pinilla et al. 2016). Grain growth was considered as another possible mechanism (e.g. Dullemond & Dominik 2005; Ciesla 2007; Birnstiel et al. 2012a). However, recently it was found not to alter the gas profile significantly (Bruderer 2013) and to have difficulties in explaining the large observed cavities at (sub-)mm wavelengths (Birnstiel & Andrews 2014b). Photoevaporation, dynamical clearing and dead zones are the most accredited scenarios. These processes are not mutually exclusive and can probably operate at the same time (Williams & Cieza 2011; Rosotti et al. 2013).

One of the main goals of current planet-formation studies is to find planets still embedded in protoplanetary discs, in order to catch the planet formation process as it happens. A potential detection of a planet in discs with cavities may put strong constrains on formation timescales and eventually explain characteristics of observed exoplanets (Simbulan et al. 2017). The statistics of planet candidate detection in cavities of discs is still low, but the capabilities of new instruments are beginning to provide us with some new companion candidates (e.g. Quanz et al. 2013a; Reggiani et al. 2018). Recently, Keppler et al. 2018 have detected and confirmed a point source within the gap of the transition disc around PDS 70. Considering the difficulties to obtain a secure direct detection, a complementary method consists of inferring the presence of protoplanets by looking at

structures in discs, and comparing them with planet-disc hydrodynamical simulations to derive constraints on planetary masses (Jin et al. 2016; Rosotti et al. 2016; Liu et al. 2018a; Dipierro et al. 2018a).

Before ALMA, the spatial distribution of gas and dust were considered to be similar, and the mm-continuum data was used to trace the gas content assuming a gas-to-dust ratio ~ 100 (similar to the interstellar ratio). Recent observations, on the contrary, reveal a discrepancy between the gas and dust disc sizes. The disc emission observed at short wavelengths (or in CO emission lines) is more extended than the disc emission observed at long wavelengths (Tazzari et al. e.g. 2016) and there is now evidence for the presence of gas inside the dust cavity (Andrews et al. 2012; van der Marel et al. 2013; Bruderer et al. 2014). Moreover, dust grains have probably grown into larger aggregates and their spectral index may even vary across the disc (Rodmann et al. 2006; Guilloteau et al. 2011; Pérez et al. 2012; Birnstiel et al. 2012b; Menu et al. 2014; Pérez et al. 2015; Tazzari et al. 2016; Liu et al. 2017). This leads to different distributions of micron- and millimeter-sized grains (Garufi et al. 2013; van der Marel et al. 2013; Pohl et al. 2017a; Feldt et al. 2017). In order to overcome the uncertainties in the estimate of such profiles, a direct measurement of molecular gas is necessarily to determine the spatial distribution of gas and how the gas-to-dust ratio varies in protoplanetary discs (Bergin et al. 2013; Miotello et al. 2014; Williams & Best 2014; Miotello et al. 2017; Zhang et al. 2017).

One of the methods currently used to probe the spatial distribution of gas is to detect the line emission of one of the most abundant molecular species, i.e. CO and its less abundant isotopologues. The dominant constituent of the gaseous disc, H_2, lacking a permanent electric dipole moment, is difficult to detect; whereas the second most abundant molecule, CO, can be a possible alternative to probe the gas content. ^{12}CO is the most abundant isotopologue, but its low-J rotational transitions become optically thick at low column density. For this reason it is a poor tracer of the gas content, however, its emission lines are a good probe to constrain the temperature at the disc surface. Less abundant isotopologues, such as ^{13}CO and, in particular, C^{18}O have less optically thick lines, which can be used to trace the gas down to the midplane (van Zadelhoff et al. 2001; Dartois et al. 2003). Importantly, optically thin tracers can give a more accurate measure of the gas column density.

The main processes regulating CO abundances, freeze-out and isotope-selective photodissociation, need to be taken into account when interpreting CO isotopologues lines (Miotello et al. 2014, 2016). Recent ALMA discs surveys (Ansdell et al. 2016; Pascucci et al. 2016; Miotello et al. 2017; Long et al. 2017) found very low CO-based gas masses, confirming the discrepancy between CO and HD mass estimates in brighter discs (e.g. Bergin et al. 2013; McClure et al. 2016). Different processes sequestering elemental carbon may be at play in protoplanetary discs, affecting the CO emission significantly (Bruderer et al. 2012; Bergin et al. 2013; Favre et al. 2013; Miotello et al. 2017; Yu et al. 2017; Molyarova et al. 2017, see Section 5.4.3).

CQ Tau is an ideal candidate to perform a comparative analysis between observations and simulations. While it is not a transitional disc by definition (since it has NIR+MIR/FIR ratio not too low), the CQ Tau disc is known to have a cavity at mm wavelengths in the dust continuum (Tripathi et al. 2017; Pinilla et al. 2018). In this chapter, we report ALMA observations of the system in both continuum and CO integrated intensity at unprecedented angular resolution and model the gas and dust emission to determine the disc density structure. This structure is then compared to global three dimensional hydrodynamical simulations of a disc hosting a planet. The chapter is organized as follows: in Section 5.2 we describe the properties of the target and the ALMA

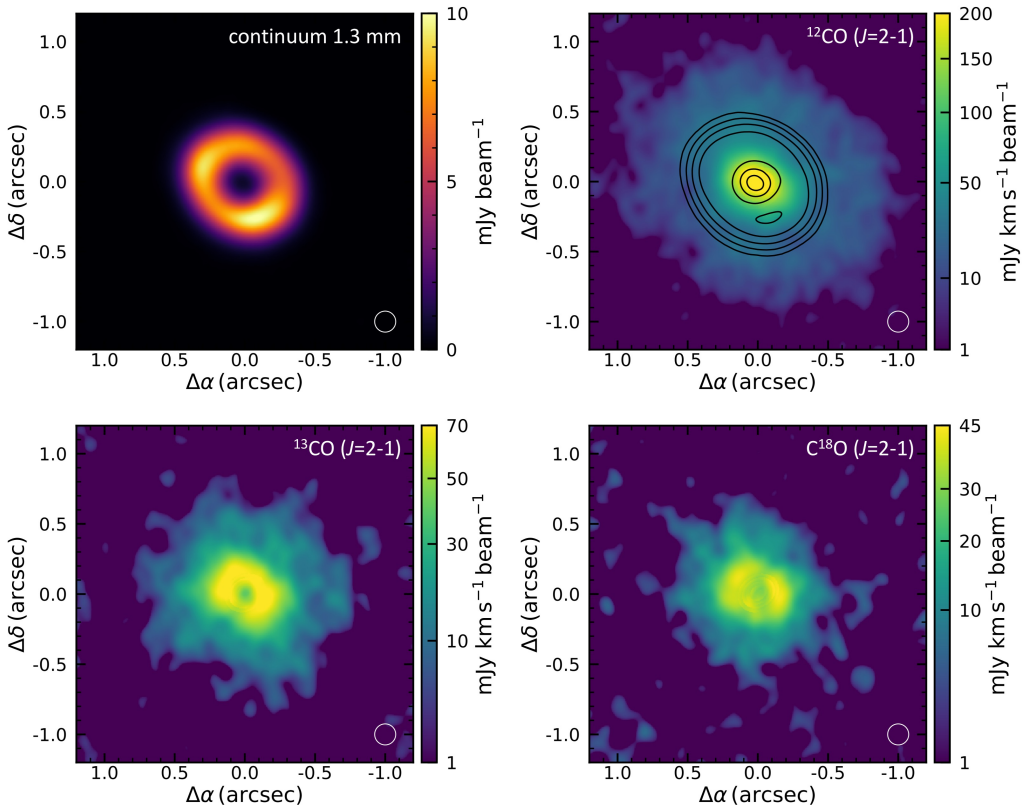

Figure 5.1: ALMA observation of the continuum at 1.3 mm on the upper left panel and zero-moment maps of ^{12}CO (upper right), ^{13}CO (lower left) and C^{18}O (lower right) J=2-1. On top on the ^{12}CO image we overplot the contours of the continuum respectively at 20, 40, 80, 160, 320 σ. The white circle in the lower right corner indicates the size of the beam: $0\farcs15$, corresponding to ~ 24 au.

observations. In Section 10.5.1 we present the method used for the modeling. In Section 5.4 we described the modeling results from the physical-chemical code DALI (Dust And LInes, Bruderer et al. 2012). In Section 5.5 we studied the possibility of the cavity to be cleared by an embedded planet through a set of hydrodynamical simulations which allowed us to derive the planet mass and location. Moreover, we discuss the results from the hydro simulations with the physical-chemical code DALI and compare them with other possible mechanism to open a cavity (Section 5.6). Finally we conclude our work with Section 5.7.

5.2 Observations

5.2.1 Target properties

CQ Tau is a variable star of the UX Ori class with a spectral type F2 (see Table 5.1). It is a young (∼10 Myr), nearby (162 pc, Gaia Collaboration et al. 2016), intermediate

Table 5.1: Stellar properties of CQ Tau.

[1]SpT	[5]L_* ($L_\odot$)	[5]M_* ($M_\odot$)	[5]age Myr	[2]$T_{\rm eff}$ (K)	[3]d (pc)	[4]σ_d (pc)	[6]$A_{\rm V}$ (mag)
F2	10	1.67	10	6900	162	2	1.9

References: 1. Herbig 1960; Natta et al. 2001 2. Testi et al. 2001 3. Gaia Collaboration et al. 2016 4. Bailer-Jones et al. 2018 5. The luminosity L=6.6 $L_\odot$ from Garcia Lopez et al. 2006 (d=130 pc) is re-scaled considering the new distance from GAIA; the value of mass and age considering the new luminosity where derived using the tracks of Siess et al. (2000). 6. The extinction was measured by fitting the SED shown in Fig. 5.4.

mass (1.67 $M_\odot$) star, surrounded by a massive circumstellar disc (Natta et al. 2000). The continuum emission at mm-wavelength was observed with different instruments: OVRO interferometer (Mannings & Sargent 1997); the Plateau de Bure interferometer at 2.9 and 1.2 mm (Natta et al. 2000); VLA at 7 mm and 3.6 cm (Testi et al. 2001). The analysis of the SED at mm-wavelengths allows us to infer that dust has grown up to grains larger than the typical ISM size (Testi et al. 2001, 2003; Chapillon et al. 2008). The disc was already observed with the the IRAM array by Chapillon et al. (2008) who detect a weak disc emission in ^{12}CO. Mendigutía et al. (2012) gave an upper limit for the accretion rate of CQ Tau equal to $\log(\dot{M}_{\rm acc}) < -8.3\ M_\odot\ {\rm yr}^{-1}$, whereas Donehew & Brittain (2011) measured $\log(\dot{M}_{\rm acc}) \sim -7\ M_\odot\ {\rm yr}^{-1}$. This suggests that the CQ Tau disc has a high accretion rate.

Banzatti et al. (2011) presented intermediate resolution observations taken with VLA (1.3 - 3.6 cm), PdBI (2.7 - 1.3 mm) and SMA (0.87 mm). They estimate the dust opacity index to be $\beta \sim 0.6 \pm 0.1$, assuming that the opacity follows a power-law function of the wavelength λ: $\kappa_\lambda \propto \lambda^{-\beta}$. Combining these new data with previous measurements, the authors were able to probe the significant grain growth occurring in the disc, with the largest grains growing up to ∼cm size. Trotta et al. (2013) found also an indication of grain growth variation with radius, where larger grains were found in the inner disc, compared to the outer disc. In a recent work by Tripathi et al. (2017), the authors detected a cavity in the continuum intensity profile of CQ Tau in SMA archival data. Pinilla et al. (2018) presented CQ Tau observations with ALMA finding the presence of a dust cavity in the continuum. The disc was also observed in scattered light (PDI) by Benisty et al. (2020, in prep.).

5.2.2 Data

Observational Strategy and Data Reduction

We present Band 6 ALMA data of CQ Tau (RA = $05^{\rm h}35^{\rm m}58.46712^{\rm s}$; dec = $+24°44'54.0864''$) from three separate programs executed during Cycles 2, 4, and 5 (2013.1.00498.S, PI: L. Pérez, 2016.A.00026.S, 2017.1.01404.S, PI: L. Testi). The ALMA correlator was configured to observe simultaneously CO(2–1), ^{13}CO(2–1), and C^{18}O(2–1), as well as the nearby continuum at 1.3 mm. The array configurations used for Cycles 2, 4 and 5 are respectively C34.6, C40.7 and C43.8.

Data calibration was performed by ALMA following the standard Quality Assessment procedures for each of the three programmes. After downloading the datasets, we reapplied the calibration tables and extracted the CQ Tau data from each of the four datasets (the Cycle 5 observations included two separate executions). We corrected the data for the known proper motion of the star and performed one combined iteration of phase only

self calibration. The combined datasets were then imaged to produce the continuum and integrated line intensity images used in this chapter. For the purpose of the analysis presented in this chapter, we imaged the data using a Briggs weighting with a robust parameter of +0.5 and a Gaussian restoring beam of 0.″15, corresponding to a spatial resolution of ∼24 au. This choice was made to maximize the sensitivity to the line emission and for the purpose of deriving average radial intensity profiles of the disc emission. A detailed analysis of the disc at full angular and spectral resolution will be presented in a forthcoming paper. The observation set used in this chapter is shown in Figure 5.1, the noise levels achieved are: 30 μJy beam^{-1} in the continuum, and 5 mJy beam^{-1} km s^{-1} in the line integrated intensity maps. We expect the intensity scale of these observations to be accurate within $\sim$ 10%, as described in the ALMA Technical Handbook[1].

The line emission from the disc shows a clear rotational pattern dominated by the Keplerian motion around the central star. To compute the integrated intensity maps analyzed in this chapter, we first compensate for the Keplerian velocity pattern, then we integrated the emission in each spatial pixel using an optimized range of velocities. The procedure we followed is very similar to the one presented in Yen et al. (2018) and Ansdell et al. (2018). The parameters used for the Keplerian motion subtraction compensation are: stellar mass $M_\star = 1.67$ $M_\odot$, distance from the Sun d=162 pc, position angle of the disc major axis pa=55 deg, and inclination i=35 deg, which optimize the subtraction of the Keplerian pattern for our dataset and are consistent with the values derived by Chapillon et al. (2008) (noting the different definition of the position angle, complementary to ours).

Observational results

The map of the continuum emission (upper left of Fig. 5.1) presents a compact disc with a clear cavity. The integrated intensity ^{12}CO map (upper right of Fig. 5.1) reveals the presence of gas inside the cavity seen in the continuum. The emission is centrally concentrated and the majority of the intensity comes from the inner part of the disc. Considering that we expect ^{12}CO emission to be optically thick, the increase in emission in the inner regions of the cavity is likely due to higher temperatures, and not directly related to the gas surface density (this will be better quantified with the models described in the following section). The ^{13}CO integrated intensity map (lower left panel of Fig. 5.1) shows a decrease of emission in the inner regions of the cavity. The C^{18}O integrated intensity map (lower right panel of Fig. 5.1) shows a cavity at the same location as in ^{13}CO. The continuum and CO isotopologues radial intensity profiles, shown in Figure 5.2, are obtained with a radial cut on the major axis. The difference between the profiles of the three CO isotopologues can most likely be explained by the different optical depths (e.g. Fedele et al. 2017). The error bars shown in Figures 5.2 are computed as the dispersion of the measured points inside the bin.

Focusing on the outer disc, the continuum extends radially up to $\sim$ 0.″5 in radius, while the ^{12}CO emission extends up to $\sim$ 1″. As it was already shown for other discs (Panić et al. 2009; Andrews et al. 2012; Rosenfeld et al. 2013c; Canovas et al. 2016; Ansdell et al. 2018), the gas disc extent on average seems to be a factor of two larger in radius with respect to the mm dust discs. The emission shows azimuthal asymmetries, both in the continuum and lines. For the purpose of this study, we limit our analysis to the general properties. A follow-up paper will be focused on them in details.

[1]https://almascience.eso.org/documents-and-tools/cycle5/alma-technical-handbook

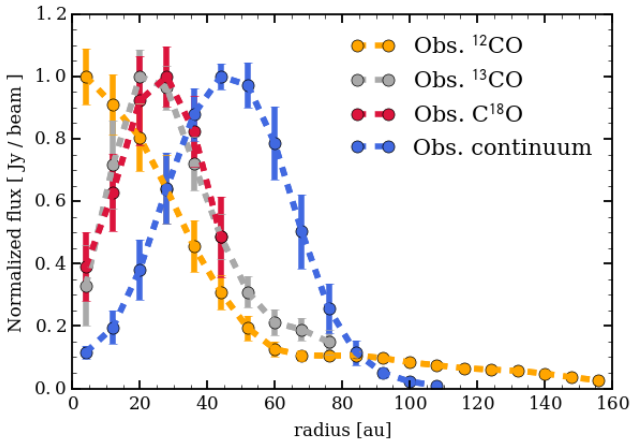

Figure 5.2: Observational profiles done with a radial cut on the major axis of the continuum (blue), ^{12}CO (orange), ^{13}CO (gray) and C^{18}O (red). Each profile is normalized to the peak value. The lines are derived from the moment zero maps.

5.3 Method

The aim of this work is to obtain a physical-chemical disc model that can simultaneously reproduce the dust and gas emission properties, with a particular focus on the disc cavity. In addition to the thermal continuum and CO isotopologues maps previously described, we additionally recover information from the SED, with data taken from previous studies, as described in Table 5.3.

5.3.1 Thermo-chemical modelling with DALI

In order to determine the gas and dust temperature and molecular abundances at each position in the disc, we use the physical-chemical code DALI (Dust And LInes, Bruderer et al. 2012; Bruderer 2013) that self-consistently computes the physical, thermal and chemical disc structure. Given a density structure and a stellar spectrum as inputs, the continuum radiative transfer is solved using a Monte Carlo method to calculate the dust temperature $T_{\rm dust}$ and local continuum radiation field from UV to mm wavelengths. The chemical composition of the gas is then obtained by a chemical network calculation of all the cells. The chemical abundances enter a non-LTE excitation calculation of the main atoms and molecules. The gas temperature $T_{\rm gas}$ is then obtained from a balance between heating and cooling processes. Since both the chemistry and the molecular excitation depend on $T_{\rm gas}$ and vice versa, the problem is solved iteratively. The code is 2D in R-z. Finally, spectral image cubes are created with a ray tracer fixing the inclination of the disc in the sky at 33°, assuming perfect azimuthal symmetry. Note that in the DALI modelling the hydrostatic equilibrium is not solved.

5.3.2 Gas and dust profiles

We adopt two different surface density radial distributions for the gas and for the mm-sized dust components (see Fig. 5.3) to reproduce the observations shown in Fig. 5.2. For the gas, the density structure follows the simple parametric prescription proposed by

Table 5.2: *Model parameters.* The fourth column reports the explored range of values for each parameter and the best representative values are presented in boldface.

	Species	Parameter	Range
Vertical structure		h_c [rad]	0.05; 0.07; 0.075; 0.1; **0.125**; 0.15; 0.2
		ψ	0; **0.05**; 0.1; 0.15; 0.2; 0.25; 0.3
Radial structure		R_0 [au]	20; 15; 25; 30; 35; 40; **56**; 60; 100; 200
		$R_{\rm sub}$ [au]	**0.2**
Self similar density profile (Eq. 5.1)	gas	$\Sigma_{0,\rm gas}$ [g cm^{-2}]	1; 2; **2.5**; 5; 7.5; 10; 12.5; 15; 20; 25; 30; 38; 50; 60
Self similar density profile (Eq. 5.1)	small dust	$\Sigma_{0,\rm small}$ [g cm^{-2}]	0.375; **0.0375**; 0.00375
	gas,small dust	$R_{\rm cav}$ [au]	5; 10; 15; **20**; 25
	gas,small dust	$\gamma_{\rm gas}$	0; **0.3**; 0.5; 0.7; 1.; 1.5
	gas,small dust	$\delta_{\rm gas}$	10^{-4}; 10^{-3}; $\mathbf{10^{-2}}$; $5{\cdot}10^{-2}$; 10^{-1}; 1; 10^{1}
Gaussian ring (Eq. 5.2)	large dust	$R_{\rm dust}$ [au]	52; **53**; 55; 60
	large dust	σ [au]	10; 11; 12; **13**; 14; 15; 20; 25
	large dust	$\Sigma_{0,\rm dust}$ [au]	**0.6**
Dust properties		Size small grains	**0.005μm - 1μm**
		Size large grains	**1μm - 1cm**
		$q_{\rm small}$	**3.5**
		$q_{\rm large}$	**3**
		χ	**0.2**

Andrews et al. (2011), which consists in a self-similar solution of viscous accretion disc models (Lynden-Bell & Pringle 1974b; Hartmann et al. 1998):

$$\Sigma(R) = \Sigma_0 \left(\frac{R}{R_0}\right)^{-\gamma} \exp\left[-\left(\frac{R}{R_0}\right)^{2-\gamma}\right] \tag{5.1}$$

where R_0 is the disc characteristic radius, Σ_0 the surface density normalization ($\Sigma(R_0) = \Sigma_0/e$) and γ is the power law index of the surface-density profile. The millimeter dust emission can in principle be modeled with the same prescription (Eq. 5.1, see Section 5.4.4 for further explanation), but CQ Tau shows a clear ring-like shaped continuum which can be more naturally described by a Gaussian ring. Furthermore, also Pinilla et al. (2018) have recently modeled CQ Tau lower angular resolution continuum observations with an asymmetric Gaussian profile. We therefore model the large grains density profile with a Gaussian radial profile:

$$\Sigma_{\rm dust}(R) = \Sigma_{0,\rm dust} \exp\left[\frac{-(R - R_{\rm dust})^2}{2\sigma^2}\right] \tag{5.2}$$

where $\Sigma_{0,\rm dust}$ is the maximum value of the density distribution, $R_{\rm dust}$ is the position of its center and σ is its width.

Two different dust populations are considered into DALI, not only large (1 μm - 1 cm) but also small (0.005 - 1 μm) grains. While the radial distribution of large grains is described by Eq. 5.2, small grains follow the gas distribution presented in Eq. 5.1, with a different surface density normalization (Σ_0), taken equal to $\Sigma_{0,\rm small}$. The size distribution of dust grains is: $n(a) \propto a^{-q}$, where q is the grain size distribution index, taken as $q = 3$ for large grains and as $q = 3.5$ for small grains, and the maximum size of grains considered is $a_{\rm max} = 1\,$cm. We choose a value of $q = 3$ for large grains after performing a test with a value of 3.5. In order to reproduce the SED profile at mm size grains, indeed, we needed to give more weight to the mm size grains (see Fig. 5.4).

Both continuum and line ALMA data show the presence of a cavity in the inner regions of the disc as shown in Fig. 5.1. The size of the cavity and the amount of depletion is not the same for the dust and gas components. We call $R_{\rm cav}$ the gas cavity radius, while the dust cavity radius is set by the location of the Gaussian ring peak, $R_{\rm dust}$. Within $R_{\rm cav}$, the gas (and the small dust) surface density is lowered by a factor of $\delta_{\rm gas}$, whereas the large dust depletion is described by the Gaussian profile of Eq. 5.2, given a width of σ (see Fig. 5.3).

For the stellar photosphere we considered a blackbody with $L_* = 10\,L_\odot$ and $T_* = 6900\,$K (Table 5.1). We do not consider accretion onto the star, since the accretion luminosity contributes to less than 10% to the total luminosity of the star (Meeus et al. 2012) and such amount is mainly just important for the inner disc heating. The inner radius for both gas and dust in our models is set to 0.2 au, following the definition of the dust sublimation radius: $R_{\rm sub} = 0.07(L_*/L_\odot)^{1/2}$ au (assuming a dust sublimation temperature of 1500 K; Dullemond & Dominik 2005).

The vertical density distribution is taken to be a Gaussian with a scale height $H = Rh$, with:

$$h = h_{\rm c}\left(\frac{R}{R_0}\right)^{\psi} \tag{5.3}$$

where $h_{\rm c}$ and ψ are free parameters. The infrared excess in the SED is directly related to the parameters chosen for the disc scale height. The two different dust populations are

assumed not to follow the same scale height distribution. The large grains, that account for the bulk of the dust mass in the disc, are settled in the midplane; on the other hand, the smaller grains are well coupled with the gas and follow the same vertical profile. The small population has a scale height of H, whereas large grains have a scale height of χH, reduced by a factor $\chi = 0.2$ (see Fig. 1 of Trapman et al. 2017). Finally, dust opacities considered follow Weingartner & Draine (2001) for a standard ISM dust composition. The optical constants used to compute the dust opacities are as in Weingartner & Draine (2001) and Draine (2003) respectively for silicates and graphite and the mass extinction coefficients were calculated using Mie theory with the miex code (Wolf & Voshchinnikov 2004).

5.3.3 Determining the best representative model

We start our investigation by exploring the parameters listed in Table 5.2, taken from the values reported in literature (e.g. Testi et al. 2003; Chapillon et al. 2008; Banzatti et al. 2011; Trotta et al. 2013). We do not carry out any χ^2 minimization analysis as the complexity of the DALI disc models does not allow us to cover a wide set of parameter values. Nevertheless, we explore the parameter space starting from a sparse grid of models, which is then refined around the values obtained for the best representative models. The sub-mm continuum emission helps us to fix the parameters related to the radial distribution of large grains in the disc, the size of the dust cavity and the total dust mass. The temperature can vary, changing the vertical structure of the disc and the position or scale height of the cavity wall, which determines the amount of direct irradiation by the star that the disc can receive. Finally, the mid-IR part of the SED and the CO line radial profiles are sensitive to both density structure and temperature of the disc. In Table 5.2 the range of values used for each parameter are listed, where the best representative value is shown in bold face.

SED and radial profile of the continuum emission

Our first step is to look for a model that reproduces the SED profile between 0.36 μm and 3.55 cm. The optical part of the SED (from 0.36 to 3.4 μm) is affected by extinction and it is corrected considering the extinction law of Cardelli et al. (1989), with $R_{\rm v} = 3.1$. In order to match the stellar spectrum, an extinction of $A_{\rm v} = 1.9$ mag is required, consistent with previous works (e.g. Garcia Lopez et al. 2006). In our models the vertical structure ($h_{\rm c}$, ψ) is the main factor which can introduce a shadowing and lower the amount of exposed disc surface accessible to stellar light (Woitke et al. 2016). These are key parameters for the final temperature of the disc and to reproduce the observed NIR and FIR excess.

In order to describe the mm part of the SED, we vary $R_{\rm dust}$, σ and $\Sigma_{0,\rm dust}$, until we match simultaneously the radial profile of the ALMA continuum observations and the longer wavelengths points in the SED.

CO emission radial profiles

The following step is to reproduce the gas profiles of the three CO isotopologues. The CO isotopologues radial profiles are more radially extended than the continuum emission (as it is possible to see from the normalized profiles in Fig. 5.2). As many previous studies suggest, a single surface density profile for both gas and dust is not able to reproduce the continuum emission and the CO integrated intensity maps simultaneously, indicating that optical depth effects are not sufficient to explain the different radial extent (e.g. Facchini et al. 2017) as it is shown in the DALI modelling described in Section 5.4.

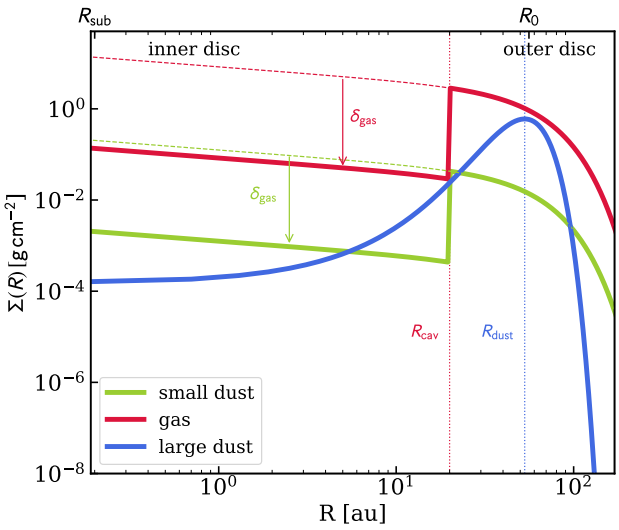

Figure 5.3: Surface density profiles of the best representative model for the three components considered: gas (red line), small grains (green line), and large grains (blue line). The dashed lines show the profiles of the surface density of the disc if the cavity was not present.

5.4 Results

5.4.1 SED representative model

In order to reproduce the SED profile (Fig. 5.4), we follow the approach described in Section 5.3.3. The two main observational constraints to set the best representative model for the SED are the Near-InfraRed (NIR) and Far-InfraRed (FIR) excesses which give information about the vertical structure of the disc, and on the illuminated area of the inner and upper disc layer respectively. We vary the values of h_c and ψ, which describe how much the disc is vertically extended and flared. In particular, the parameter which mostly affects the SED is h_c (Woitke et al. 2016). Our best representative values for these parameters are $h_c = 0.125$ and $\psi = 0.05$. The range of values under which our models match the observed SED are $0.1 < h_c < 0.15$ and $0.05 < \psi < 0.1$. We note that a variation in the stellar luminosity value can affect the choice of such parameters. Longer wavelengths are affected mainly by the total amount of mass present in the disc. Once the correct amount of total mass is found, we fix this value and vary the other parameters in order to find a good agreement with the ALMA continuum profile. As it is possible to see in Fig. 5.4, the observations are well described by our best representative model. Note that model and data diverge at the wavelength of 3.57 cm. This may be explained by free-free emission, which we do not model, and affects the integrated flux at cm wavelengths. We note also that the SED shows a near-infrared excess together with a resolved cavity in both dust and gas seen in the ALMA data. The small grains are the main responsible for the emission at such wavelengths and a small amount in the cavity is enough to reproduce the NIR emission.

Table 5.3: Values of the flux observation at different wavelengths. 1. Creech-Eakman et al. (2002), Mannings & Sargent (1997); 2. Banzatti et al. (2011), Testi et al. (2003); 3. Thi et al. (2001); 4. Oja (1987); 5. Cutri et al. (2003); 6. Mendigutía et al. (2012)

Wavelength [μm]	Flux [Jy]	Reference
0.36	0.055	4
0.43	0.201	4
0.55	0.378	4
0.7	0.169	5
0.9	1.23	6
1.235	1.08	5
1.66	1.54	5
2.16	2.28	5
3.4	2.6	3
6.9	2.1	3
9.6	7.1	3
12	4.4	1
17	13.1	3
25	14.7	1
28.2	21.6	3
60	16.58	1
100	12.52	1
870	0.421	2
1.3E+3	0.103	2
2.7E+3	22E-3	2
3.4E+3	13.1E-3	2
6.9E+3	2E-3	2
13.4E+3	2.8E-4	2
35.7E+3	7.9E-5	2

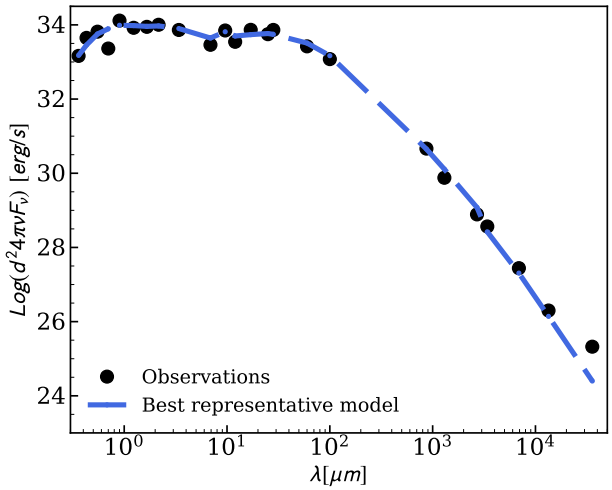

Figure 5.4: Spectral Energy Distribution (SED) profile. The black dots are the observations as described in Table 5.3. The blue dashed line is our best representative model (see Table 5.2).

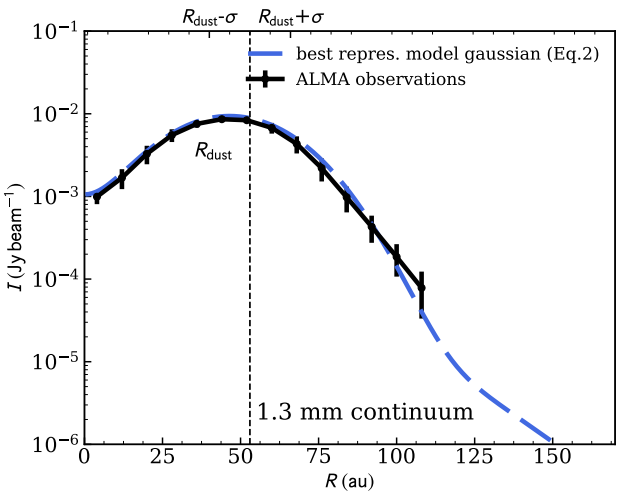

Figure 5.5: Dust continuum taken at 1.3 mm with ALMA. The radial cut on the major axis of observation (black line) is shown along with our best representative model (blue line): Gaussian profile.

5.4.2 Radial profiles

In order to compare our models with our ALMA observations, we convolve the model results with a Gaussian beam of of 0.″15, which simulates the resolution of the observations, both for the continuum and the CO isotopologues. We perform a radial cut along the major axis of the continuum and moment zero maps, which has a better resolution compared to an azimuthally averaged profile, in order to compare with our 2D models.

A Gaussian ring for large grains

Inspired by the work of Pinilla et al. (2018), we have employed a Gaussian functional profile, as previously discussed (see Eq. 5.2). As best representative parameters we find a center peak position of $R_{\rm dust} = 53\,$au and a Gaussian width of $\sigma = 13\,$au. Our results are consistent with Pinilla et al. (2018) work where the best model had a Gaussian peak radius of $\sim 46\,$au and respectively an inner and outer width of $\sim 11\,$au and $\sim 17\,$au. The peak of the Gaussian is $\Sigma_{0,\rm dust} = 0.6\,{\rm g\,cm^{-2}}$. The simulated continuum emission profile is plotted in Fig. 5.5 (blue line) along with the data points (black line). The data are always matched by our model within the error bars, and from now on we will refer to this as the best representative model for the large dust component.

Gas radial profile

We use the CO isotopologues observations as a proxy for the gas distribution. In Figs. 5.6 we plot the ^{12}CO, ^{13}CO and C^{18}O observed radial profiles, along with a selection of our DALI models. In the disc inner regions, where CO lines are more optically thick, the gas temperature plays a big role and strongly depends on the small grains distribution. We implement a relatively high surface density normalization of small grains $\Sigma_{0,\rm small} = 0.0375$

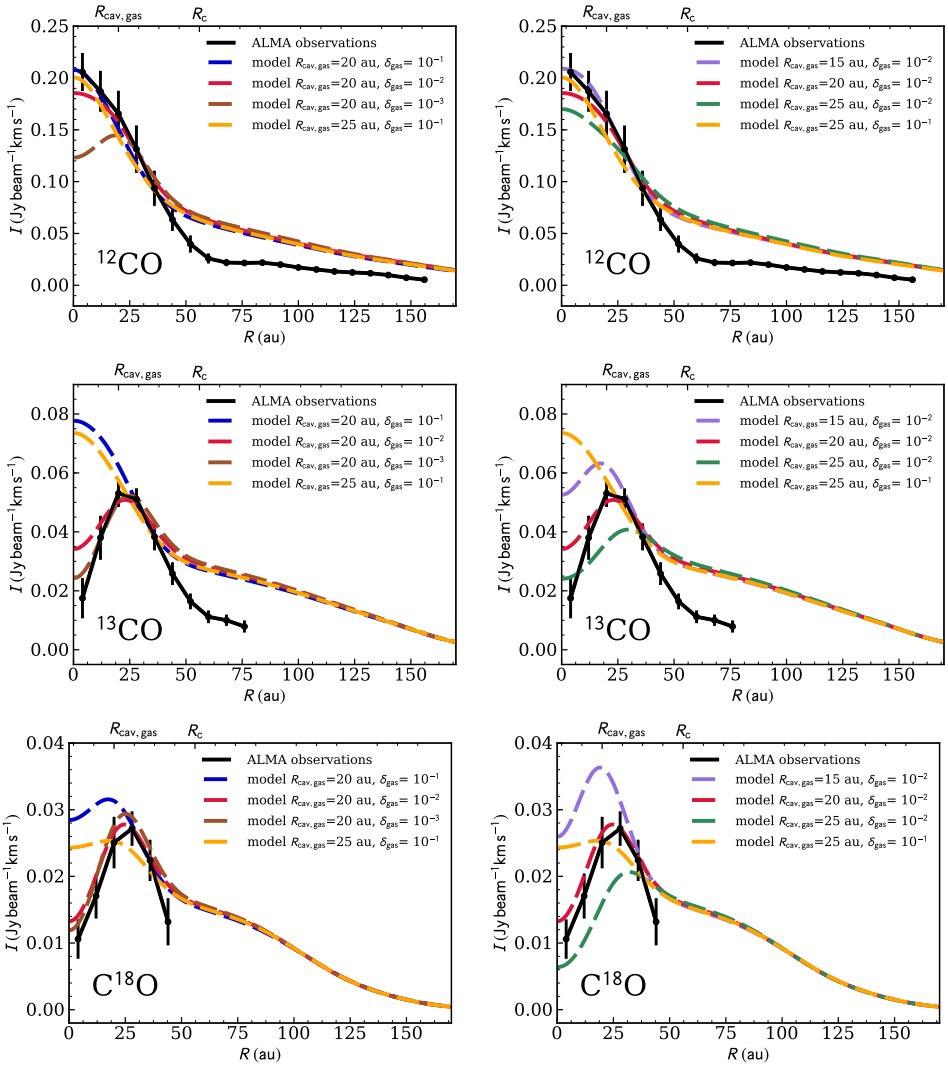

Figure 5.6: ALMA observations radial cut on the major axis (black line) for gas in the three different isotopologues of CO (top: ^{12}CO, middle: ^{13}CO, bottom: C^{18}O). Along with our best representative model (red line), on the right we show additional models varying R_{cav}, while on the left we vary δ_{gas}. Moreover, we present an additional model (orange), that still describes well the ^{12}CO profile and it is useful for the model results (see below).

g cm^{-2}. Setting a higher column density of small grains, while keeping fixed the amount of gas, shifts the dust τ=1 layer upwards and, consequently, a more significant amount of UV photons is absorbed there. The location of the CO isotopologues τ=1 layer does not change significantly but the gas temperature at the emitting layer is reduced as the UV flux is reduced. Moreover, a smaller amount of UV flux can produce a decrease of the dust temperature and consequently, due to thermal balance, can contribute to a lower gas temperature. Accordingly, simulated integrated intensities are lower. A smaller $\Sigma_{0,\mathrm{small}}$ would lead to higher integrated intensities than what shown in Fig. 5.6, with a worst match with the observational data. All CO isotopologues model results shown in Fig. 5.6 are obtained assuming a gas profile (Eq. 5.1) described by the following parameters: $\gamma_{\mathrm{gas}} = 0.3$, $\Sigma_{0,\mathrm{gas}} = 2.5$ g cm^{-2} and a cutoff radius of $R_0 = 56$ au. The models always over-predict the emission in the outer disc (^{13}CO in particular). Our focus is however on the cavity, as we are interested in constraining which may be the clearing mechanism. Future studies will attempt to give a better description of the CQ Tau outer disc.

We explored different values for the size and depletion of the cavity (respectively R_{cav} and δ_{gas}) to estimate the best representative model and to gain insights about their degeneracies (Fig. 5.6). Observations agreed with a gas depletion factor of $10^{-3} < \delta_{\mathrm{gas}} < 10^{-1}$. The top left panel of Fig. 5.6 shows that the ^{12}CO profile cannot be described by a model with a depletion factor of 10^{-3}, otherwise the ^{12}CO emission would also show a depression at small radii. Furthermore, ^{13}CO and C^{18}O profiles suggest that the depletion factor has to be smaller than $\delta_{\mathrm{gas}} \lesssim 10^{-1}$ (models shown in blue and yellow do not match the data). Finally, the cavity size is constrained to be larger than 15 au and smaller than 25 au. Our best representative model is shown with a red line in Fig. 5.6 and assumes $R_{\mathrm{cav}} = 20$ au and $\delta_{\mathrm{gas}} = 10^{-2}$. The gas has a smaller cavity radius ($R_{\mathrm{cav}} = 20$ au) than the large dust grains ($R_{\mathrm{dust}} = 53$ au). The depletion in gas within the cavity is found to be similar to the one of the large grains (see Fig. 5.3).

5.4.3 Dust-to-gas ratio

Fig. 5.7 shows the cumulative function of mass as a function of the radial distance from the star of both the gas (red) and the dust (blue, small and large grains together) for our representative model. The dust-to-gas ratio is not uniform across the disc, and is close to 0.1. We compute the total mass for the three different components of our best representative model: $M_{\mathrm{gas}} = 3,2 \cdot 10^{-3} M_{\odot}$; $M_{\mathrm{small\,dust}} = 4.9 \cdot 10^{-5} M_{\odot}$; $M_{\mathrm{large\,dust}} = 2.3 \cdot 10^{-4} M_{\odot}$. The global dust-to-gas ratio for this model of CQ Tau is ~ 0.09. This value is higher than the typical ISM values of ~ 0.01, but it is consistent with recent findings from ALMA surveys of protoplanetary discs in different star-forming regions (Ansdell et al. 2016, 2017; Pascucci et al. 2016; Miotello et al. 2017; Long et al. 2017). The CO isotopologues emission lines are found to be generally faint compared with the disc continuum emission, resulting in low CO-based gas masses and high CO-based dust-to-gas mass ratios. This may be interpreted as rapid disc physical evolution via loss of gas, or alternatively, as chemical evolution due to carbon depletion processes. The latter may occur if carbon is sequestered from CO and it is either locked into large icy bodies in the midplane, or converted into more complex and less volatile molecules (Aikawa et al. 1996; Bergin et al. 2014; Du et al. 2015; Eistrup et al. 2016; Kama et al. 2016; Yu et al. 2016). Current CO and continuum ALMA observations alone cannot distinguish between the two scenarios, but high dust-to-gas mass ratios hint at disc evolution, either physical or chemical. Independent gas mass measurements of discs have been obtained thanks to the detection on hydrogen deuteride (HD) with the PACS instrument on the Herschel Space Telescope in few discs (Bergin et al. 2013; McClure et al. 2016). When compared

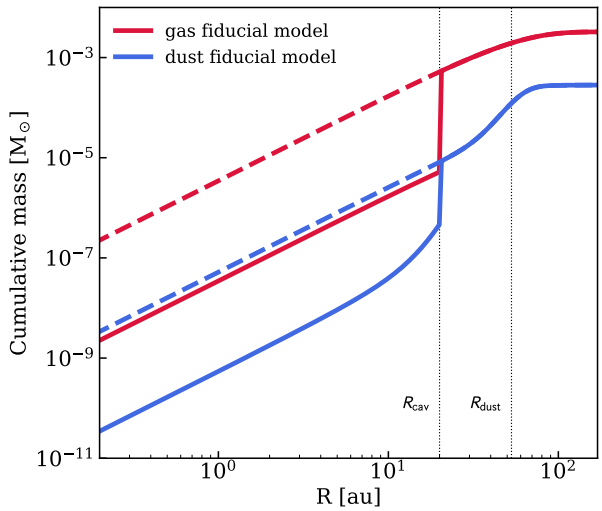

Figure 5.7: Radial profile of the cumulative function of mass of our best representative model (as shown in Fig. 5.3). The red line shows the gas behavior, while the blue line shows the dust component considering both the small and large grains; the dashed line shows the cumulative mass function without considering the presence of a cavity for both gas (red) and dust (blue). The global dust-to-gas ratio is ~ 0.09.

with CO isotopologues observations, such data shows that volatile carbon needs to be depleted by different factors depending on the source (Favre et al. 2013; McClure et al. 2016). Unfortunately, no facility is available today to reproduce this type of observations. Alternatives to constrain the level of volatile carbon and oxygen depletion in discs come from the observations of atomic recombination lines, such as [CI] (Kama et al. 2016) or from the detection of hydrocarbon lines (Bergin et al. 2016; Cleeves et al. 2018).

5.4.4 A further test for large dust grains: self similar density profile

In order to model the large dust grains density profile we also attempted to use a self-similar density profile as done for the gas (see Eq. 5.1). In this case, we used the same cutoff radius as for the gas (R_0=56 au), but with a different $\gamma_{\rm dust}$ and surface density normalization of large dust grains $\Sigma_{0,\rm dust}$, allowed to vary independently. The best parameters for large dust grains are found to simultaneously reproduce both the observations of the ALMA continuum radial profile and the SED. The power law index of the surface density distribution is $\gamma_{\rm dust} = -0.7$ and the surface density normalization is $\Sigma_{0,\rm dust} = 0.85$ g cm^{-2}.

To model the inner region of the disc, we consider that the size of the cavity and the amount of depletion can be different between the dust and gas. We choose as dust cavity radius $R_{\rm cav,dust}$ and as dust cavity depletion $\delta_{\rm dust}$ that are allowed to be different from the gas ones. The dust cavity has a radius of 28 au with a depletion of a factor $\delta_{\rm dust} = 10^{-2}$. The proximity of the cavity edge with the cutoff radius implies that the dust is concentrated in a narrow ring.

The self-similar density profile reproduces the observed SED (it overlaps the Gaussian ring SED, blue curve in Fig. 5.4). The resulting continuum emission profile is plotted in gray in Fig. 5.8 along with the data points (black line). From this plot it is possible to

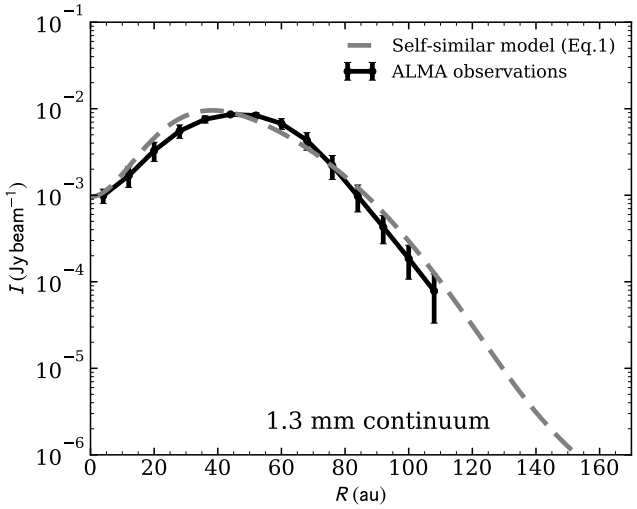

Figure 5.8: Dust continuum taken at 1.3 mm with ALMA. The radial cut on the major axis of observation (black line) is shown along with our best model obtained assuming a self-similar density profile of large dust grains which still can nicely describe our data (see Section 5.4.4). The dust cavity radius is at 28 au and the depletion factor is of $\delta_{\rm dustcav} = 10^{-2}$.

see that the self-similar density profile still describes well the large grains behavior.

5.5 Is the cavity induced by an embedded planet?

The cavity visible in the CQ Tau disc can be explained by several mechanisms: dispersal by (photoevaporative) winds, dynamical clearing by a (sub-)stellar companion, MHD winds and dead zones. In this Section, we focus on the study of the dynamical clearing induced by a companion using both analytical considerations (Section 5.5.1) and hydro-dynamical simulations (Section 5.5.2). We note that the profiles used for the fitting procedure with DALI are based on simplified physical models which qualitatively represent the characteristic features of the real profile. As a consequence, performing hydrodynamical simulations becomes of paramount importance in order to verify that the DALI models can be qualitatively reproduced in hydrodynamical models. This mechanism, indeed, leads to a hole/cavity empty of large grains which are filtered out, while the gas and small dust grains can still continue to be accreted by the central star (Rice et al. 2006a; Zhu et al. 2012b).

5.5.1 Analytical considerations

We explore the possibility that a massive planet located in the cavity region at a separation $R_{\rm p} \approx 15 - 25$ au is responsible for the gas and dust density structure we observe.

In order to open a gap in the gaseous disc, the planet mass $M_{\rm p}$ has to satisfy the

following criterion (Crida et al. 2006)

$$\frac{3}{4}h_{\rm p}\left(\frac{M_{\rm p}}{3M_\star}\right)^{-1/3}+\frac{50\nu_{\rm p}}{\Omega_{\rm p}R_p^2}\left(\frac{M_{\rm p}}{M_\star}\right)^{-1}\lesssim 1. \tag{5.4}$$

where ν is the viscosity parameter, $h_{\rm p}$ is the disc aspect-ratio at $R = R_{\rm p}$ (from here below, the subscript "p" indicates that the quantity is computed at the planet location) and $\Omega_{\rm p} \approx \sqrt{GM_\star/R_{\rm p}^3}$ is the standard Keplerian orbital frequency of the planet, where G is the gravitational constant. Using the disc parameters obtained from the DALI models in the sections above and using a Shakura & Sunyaev (1973) prescription for the viscosity at the planet location $\nu_{\rm p} = \alpha_{\rm SS}h_{\rm p}^2\Omega_{\rm p}R_{\rm p}^2$, assuming a fiducial value of $\alpha_{\rm SS} = 0.005$ (we motivate this choice in the next section), we obtain

$$M_{\rm p}\gtrsim 0.002\text{–}0.006M_\star \approx 3\text{–}9\ M_{\rm J}, \tag{5.5}$$

where we have assumed $R_{\rm p} = 20\,$au, as suggested by the location of the cavity edge in the gas, and explored a range of values of the disc thickness $h_{\rm p}$ consistent with $h_{\rm c} = 0.07$–0.12 ($h_{\rm p} = h_{\rm p}(R_{\rm p}/R_0)^\psi$), which is poorly constrained by observations and constitute the source of uncertainty in Eq. (5.5). We notice that the minimum mass expected to open a gap is affected by our fiducial choice of $\alpha_{\rm SS}$. In particular, lower values of $\alpha_{\rm SS}$ would require lower planet masses ($M_{\rm p} \approx 0.3\,M_{\rm J}$ with $\alpha = 10^{-4}$ and $h_{\rm p} = 0.07$) in order to satisfy the criterion.

Assuming $M_{\rm p} = 3$–$9\,M_{\rm J}$, an estimate of the gap width Δ produced by such a planet can be obtained using Lin & Papaloizou (1979)

$$\Delta \approx \left[\left(\frac{M_{\rm p}}{M_\star}\right)^2\frac{\Omega_{\rm p}R_{\rm p}^2}{\nu_{\rm p}}\right]^{1/3}R_{\rm p} \approx 20\ \text{au}. \tag{5.6}$$

The gas depletion factor provided by such a planet is given by (Kanagawa et al. 2018)

$$\frac{\Sigma_{\rm min}}{\Sigma_0} = \frac{1}{1+0.04K} \approx 0.05\text{-}0.08 \tag{5.7}$$

where

$$K = q^2h_{\rm p}^{-5}\alpha_{\rm SS}^{-1}. \tag{5.8}$$

We note that the condition to open a gap in the gas is a sufficient condition to open a gap also in the dust (Dipierro & Laibe 2017).

The presence of the planet can reduce the mass flux across the planet orbit, depending on the disc thickness and planet-to-star mass ratio (Farris et al. 2014; Young & Clarke 2015; Ragusa et al. 2016). If the planet migration rate is slower than the viscous spreading of the disc, such a "dam" effect induces a reduction of the disc density downstream of the planet orbit, producing as a consequence an extended cavity rather than a thin gap structure. Gap opening planets undergo the so-called Type II migration, which occurs on a timescale (Syer & Clarke 1995; Ivanov et al. 1999)

$$t_{\,\rm typeII} \approx \frac{M_{\rm p}+M_{\rm d}^{\rm local}}{M_{\rm d}^{\rm local}}\,t_\nu \approx 2\text{–}3.3\,t_\nu \approx 4\text{–}6\times 10^3 t_{\rm orb}, \tag{5.9}$$

where $t_{\rm orb} = 2\pi\Omega_{\rm p}^{-1}$ is the planet orbital period. In Eq. 5.9 we assumed $M_{\rm p} = 3$–$9\,M_{\rm J}$ and $R_{\rm p} = 20\,$au and $M_{\rm d}^{\rm local} = 4\pi\Sigma_{\rm p}R_{\rm p}^2 \approx 4\,M_{\rm J}$, that is approximately the amount of

gas contained within the planet orbit, as estimated again based on the DALI modeling above. We thus expect that in the current situation a planet of $M_{\rm p} \gtrsim 3M_{\rm J}$ should be able to produce a gap in the inner disc. Furthermore, the migration timescale being larger than the viscous time could in principle favour the depletion of the inner disc producing a cavity.

5.5.2 Numerical Simulations

We perform a set of 3D numerical simulations of a planet and a gas + dust accretion disc using the code PHANTOM (Price et al. 2018b) in order to find the mass of the planet producing the density structure expected from the DALI modeling of the observations.

We use a locally isothermal equation of state: the gas temperature is a radial power-law that produces a disc thickness $H = h_{\rm c}(R/R_0)^{\psi}R$ (where $\psi = 0.05$, bold parameter in Table 5.2). The planet and the star are modeled by two sink particles (Bate et al. 1995). The planet is initially on a circular orbit and is allowed to accrete and migrate. The sink particles exert the standard gravitational force on gas and dust particles. The motion of the sinks is computed step by step from the force they exert on each other and from the back-reaction of the disc. Particles are considered accreted when their distance from the sink is below the sink radius (see next section), and they are gravitationally bound to it.

The profile of "large" dust grains in the DALI modeling describes the properties of a vast population of different grain sizes ($1\mu{\rm m} \lesssim a_{\rm large} \lesssim 1{\rm cm}$). In our simulations however, we do not follow a dust population with a grain size distribution, but we only model individual sizes.

To describe the dynamics of dust grains we adopt the one fluid algorithm developed in Laibe & Price (2014), Price & Laibe (2015) and Ballabio et al. (2018) for large grains (for which we considered two different sizes: $a_{\rm large} = 0.1{\rm mm}$ and $a_{\rm large} = 0.5{\rm mm}$). All grain sizes we used are characterized by a Stokes Number ${\rm St} < 1$ throughout the entire disc, so that the dust dynamics is correctly described by the one fluid SPH algorithm (Ballabio et al. 2018).

We performed some simulations using also an additional family of dust grains of size $a_{\rm small} = 1\,\mu m$, with the aim to investigate the dynamics of small dust particles that are part of the modeling with DALI. We notice that, as expected and previously discussed in Sec. 5.4.2, very small dust grains ($a_{\rm small} = 1\,\mu{\rm m}$) reproduce closely the dynamics of the gas, being tightly coupled to it. As a consequence, we choose not to investigate the dynamics of $a_{\rm small} = 1\,\mu{\rm m}$ grains since the information about their distribution can be inferred by merely rescaling the gas profile with the appropriate dust-to-gas ratio.

Angular momentum transfer, allowing gas accretion, is provided by SPH artificial viscosity. We choose the artificial viscosity parameter $\alpha_{\rm AV} = 0.2$ in order to have an equivalent Shakura & Sunyaev (1973) turbulent parameter $\alpha_{\rm SS} \approx 0.005 - 0.01$ throughout the entire disc. Our choice of $\alpha_{\rm SS}$ is dictated by the minimum viscosity required in an SPH numerical simulation in order to properly provide shock resolution.

Each simulation is evolved for $t = 60\,t_{\rm orb}$, which corresponds to ~ 4500 years. We run all our simulations with $N_{\rm part} = 7.5 \times 10^5$ particles. We also run two simulations using a larger number of SPH particles ($N_{\rm part} = 1.5$–2.2×10^6) in order to check the reliability of our results at lower resolution.

Initial conditions

The initial conditions of our simulations consist of a planet with mass ranging $M_{\rm p} =$ 3–$9M_{\rm J}$ at a separation from the central star of $R_{\rm p} = 20\,{\rm au}$. The choice of the planet mass

Ref.	0.1 mm	0.5 mm	M_p	R_p	h_c	N_part
1	x		$3\,M_\mathrm{J}$	20 au	0.07	7.5×10^5
2	x		$6\,M_\mathrm{J}$	20 au	0.10	7.5×10^5
3	x		$9\,M_\mathrm{J}$	20 au	0.12	7.5×10^5
4		x	$3\,M_\mathrm{J}$	20 au	0.07	7.5×10^5
5		x	$6\,M_\mathrm{J}$	20 au	0.10	7.5×10^5
6		x	$9\,M_\mathrm{J}$	20 au	0.12	7.5×10^5
7	x		$9\,M_\mathrm{J}$	20 au	0.12	1.5×10^6
8	x		$9\,M_\mathrm{J}$	20 au	0.12	2.2×10^6

Table 5.4: Summary of the numerical simulations. Ref. is the reference number of the simulation, 0.1 mm and 0.5 mm refer to the large dust grain size we used, M_p is the planet mass, R_p its separation from the central star, h_c is the disc aspect-ratio at $R_0 = 56$ au and finally N_part is the total number of particles. Simulations 7 and 8 are convergence tests that we performed with a larger number of particles.

and its separation from the star has been made starting from the considerations in Eq. (5.5).

We run simulations using three different couples $(M_\mathrm{p}, h_\mathrm{c})$ for which the gap opening criterion in Eq. (5.5) is satisfied. We note that the disc aspect-ratio h is poorly constrained from observations considering that it is strongly affected by the estimate of the luminosity of the star (as previously discussed).

The planet is initially completely embedded in the disc, that is assumed to have an unperturbed density profile (no cavity is present at the beginning of the simulation neither in the gas nor in the dust density profiles). The gas initial surface density profile uses the parameters obtained from the power-law DALI density model (bold parameters in Tab. 5.2, i.e. dashed red curve in Fig. 5.3, respectively) without depletion. The large dust grains initial density profile uses for simplicity the self-similar DALI model introduced in Sec. 5.4.4, but using a tapering radius larger than R_0 ($R_\mathrm{taper} = 70$ au): the steep profile at large radii observed in the large dust grain surface density profile from the DALI modeling is the natural outcome of large dust grains radial drift; as the simulation starts, the large grains drift inward and the dust density profile steepens. This demonstrates that the narrow dust ring observed with ALMA is most likely due to radial drift of large dust grains.

It should be noted that thicker discs are more efficient in transporting the angular momentum throughout the disc. As a consequence, as can be seen in Eq. (5.4), for a fixed mass of the planet, the gap opening in the gas becomes progressively less efficient as the disc aspect-ratio grows. This, in fact, introduces a degeneracy for the couples of parameters (M_p, h), that is confirmed by the results of our numerical simulations.

In Table 5.4 we report a summary of the simulations that better reproduce the profiles from the DALI modeling. We note that our high resolution runs (simulations 7 and 8 in Table 5.4) show overall good agreement with lower resolution runs except in the very inner region of the disc (see the end of Sec. 5.5.2).

Results

In all numerical simulations reported in Table 5.4 the planet rapidly ($t \approx 15\,t_\mathrm{orb}$) carves a gap in the initially unperturbed disc (both in the gas and in the dust), as expected from the gap opening criterion presented in Eq. (5.5).

Fig. 5.9 shows the results of our numerical simulations, from left to right with $M_\mathrm{p} =$

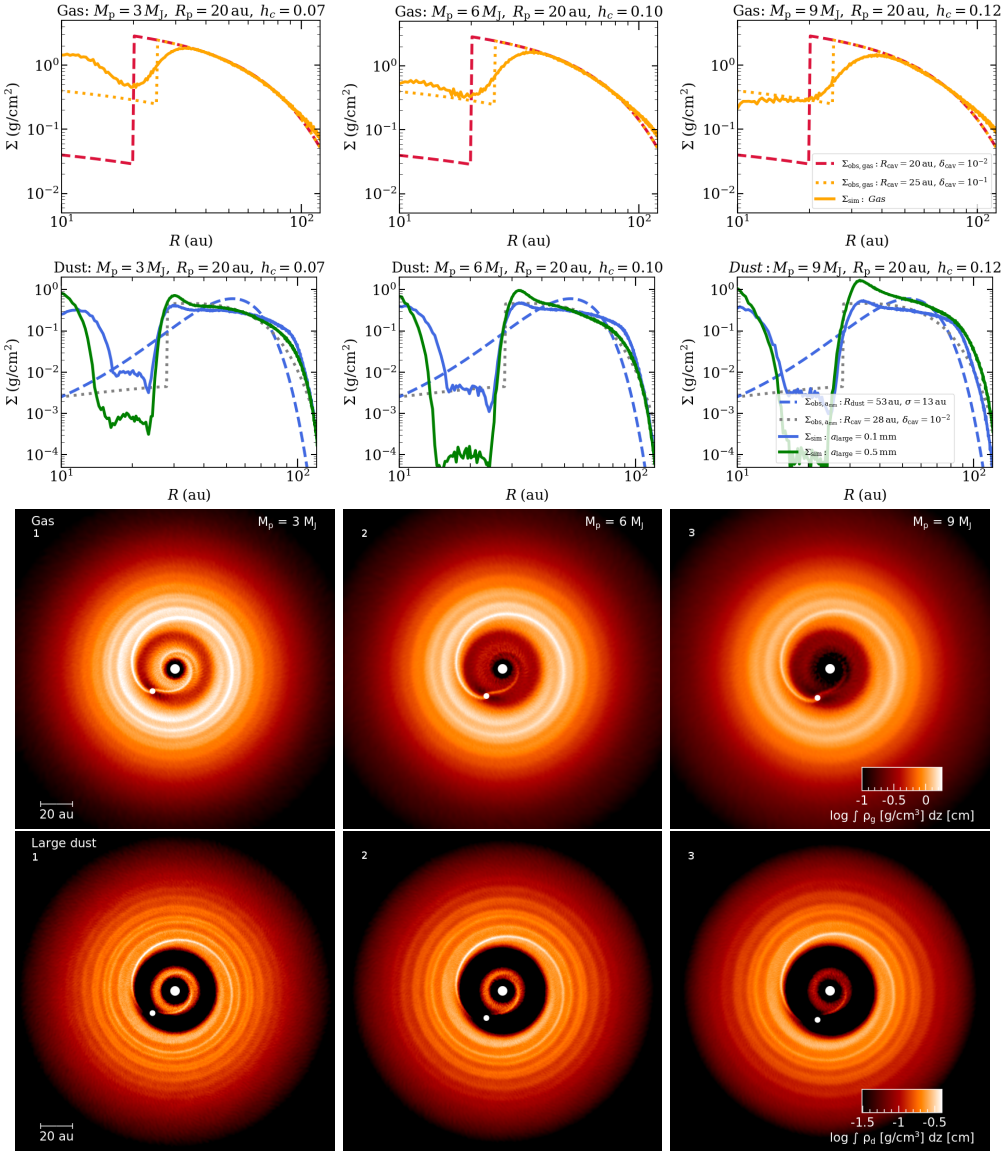

Figure 5.9: Profiles (top row) and colour plots (central and bottom row) of the surface density of both gas and dust. Different columns show the results of simulations for different planet masses M_p and aspect ratios h_c. The first row and second row show the azimuthally averaged surface density of gas and dust, respectively. In particular from our simulations of gas (orange solid curve), large dust grains $a_{large} = 0.1$ mm (blue solid curve, from left to right simulation 1, 2, 3, respectively) and $a_{large} = 0.5$ mm (green solid curve, from left to right simulations 4, 5, 6, respectively) after $t \approx 60\,t_{orb}$ of evolution, to be compared to the surface density profiles obtained from the DALI modeling for the gas (red dashed and orange dotted curves, producing the CO isotopologues emission in Fig. 5.6 with the same colours) and for the large dust grains (blue dashed and grey dotted curves producing the continuum emission profiles in Fig. 5.5 with the same colours). Dashed curves represent the best denisty models from DALI, while dotted ones are those DALI models that best fit the simulations. The third row shows the surface density colour-plot of the gas (from simulations 1, 2, 3, as indicated in the left top corner of the images). The fourth row shows the surface density colour-plot of the large dust grains $a_{large} = 0.1$ mm (from simulations 1, 2, 3, as indicated in the left top corner of the images). The colour-scale is logarithmic; the large white dot represents the central star and the small one shows the planet position.

3, 6 and 9 M_J, respectively, for the various species. The first and second row shows the azimuthally averaged density profiles for gas (orange solid lines), for 0.5 mm-sized dust (green solid lines), and for 0.1 mm-sized dust (blue solid lines). For a direct comparison, the same plots also show the surface density profiles obtained from the DALI modeling. The red dashed line is the reference model for the gas (boldface parameters in Table 2), which has a gas depletion factor of $\delta_{\rm gas} = 10^{-2}$, while the orange dotted line is the same model but with a smaller gas depletion in the cavity, $\delta_{\rm gas} = 10^{-1}$, and larger cavity size, $R_{\rm cav} = 25$ au. These gas profiles produce the red and orange emission profiles in Fig. 5.6, respectively. The blue dashed line shows the reference Gaussian ring density profile for the "large dust grains" obtained from DALI, which produces the blue curve in the continuum emission profile in Fig. 5.5; the grey dotted curve is the best-matching power-law density profile for the large dust grains obtained with DALI and discussed in Sec. 4.4, the dust continuum emission associated to it is the grey curve in Fig. 5.8. The third and fourth rows of Fig. 5.9 show the surface density colour-plots of the corresponding simulations in the upper panels (Ref: 1, 2, and 3 in Table 5.4).

In Tab. 5.4 we report also two convergence test runs using a larger number of particles and the same parameter choice as our fiducial model ($N_{\rm part} = 1.5 \times 10^6$ and $N_{\rm part} = 2.2 \times 10^6$ simulations 7 and 8, respectively). These high resolution runs are in good agreement with the lower resolution one throughout the entire disc both for gas and dust, apart from the inner disc region where at low resolution the lower density produces an increase of SPH artificial viscosity, and thus a spurious fast evacuation of the innermost part of the cavity.

We finally note that the mass of the planet does not change significantly during our simulations. In particular, in all cases, we observe a growth of the planet mass at the end of the simulation of a fraction of M_J. The correspondent growth rate at the end of the simulation is of $\dot{M}_{\rm p} \sim 5 \times 10^{-5}\,{\rm M_J\,yr^{-1}}$, consistent with the expected theoretical prediction for the planet accretion rate (see Eq. 15 of D'Angelo & Lubow 2008).

Radiative transfer modelling

We have processed our hydrodinamical model results using a radiative transfer tool (RADMC3D, Dullemond et al. 2012) for the dust component, in order to test if our SPH model is qualitatively consistent with the observations. The images obtained were, then, convolved with a gaussian beam of 0.″15 as done in DALI and compared with the observational data. In particular, we found the best agreement with the data in the model with the planet at $\rm R_p = 20$ au, $\rm M_{comp} = 6\ M_{Jup}$ and the size of large grains of 0.1 mm (see Fig. 5.10). We show the observations at 1.3 mm (black line) along with the synthetic dust flux profiles convolved based on radiative transfer calculation. The plots show the model presented in the Section 5.5.2 in green considering also the inner disc component; the model in yellow, instead, does not take into account the presence of inner disc and uses a cavity lowered of the same factor from the planetary radius up to the sublimation radius. Our simulation (both the yellow and green lines) well describe the outer disc, which reaches a semi-stable state in few dynamical timescales. Whereas, the inner disc is not well reproduced by the hydrodynamical simulations. Its flux is, indeed, higher than the one of observations, leading to a disc where the carved cavity is not well seen (see Fig. 5.10). We expect, however, the inner disc within the planetary orbit to drain with time on a longer timescale than the outer disc and this might affect the dust profile in the inner regions. With a lower inner disc emission, we would be able to reproduce qualitatively the depth and separation of the planet (yellow line in Fig. 5.10), main goal of hydro modelling we provided. A more detailed analysis on the inner disc will be addressed in

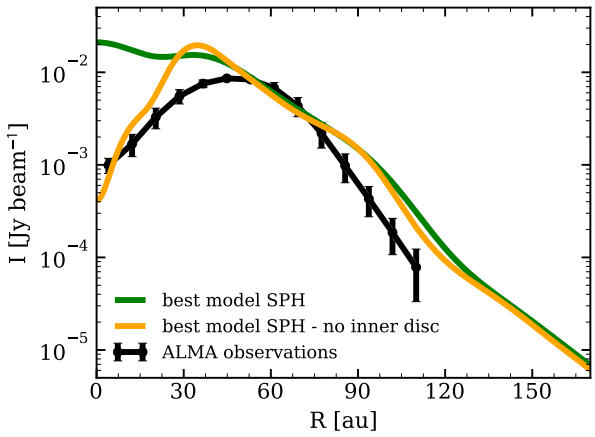

Figure 5.10: Radial profiles of the dust component of the hydrodinamical simulations after radiative transfer modelling. The black dots are our data in the continuum (1.3 mm); the green and yellow lines are respectively the model with and without the presence of the inner disc. The best model here listed is using $R_p = 20$ au, $M_{comp} = 6$ M_{Jup}. The size of large grains is taken as 0.1 mm.

future works.

5.6 Discussion

We here investigate if a planet could be responsible for the formation of a cavity in the gas and dust profile similar to the one found through the chemical-physical code DALI. We note the following:

1. A planet mass of the order of $3M_J$ does not reproduce the strong gas depletion in the inner disc inferred from the thermo-chemical modeling with DALI. On the other hand, a larger planet mass ($M_] \approx 6 - 9M_J$) does a much better job, although the $6M_J$ case requires a slightly thinner disc ($h = 0.1$) than that obtained from the DALI modeling.

2. Overall, we find both our gas and dust density profiles qualitatively reproduce the ones inferred from thermo-chemical modeling of the observed fluxes. However, we note two issues. Firstly, concerning the gas, the best representative DALI models predict a gas depletion factor of the order of 10^{-2}, which is not achieved in our simulations, that only show a gas depletion of 10^{-1} (see red and orange curves in CO isotopologues DALI model Fig. 5.6 and simulations Fig. 5.9). Such a high gas depletion is essentially required by the observed gap in ^{13}CO. A higher gas depletion might be achieved using smaller values of α_{SS} and h_c, or much larger values of the planet mass. The latter possibility is unlikely at this planetary location, since it would imply that the planet mass falls within the brown dwarf mass regime. Direct imaging observations, indeed, ruled out the presence of a companion with mass higher than 10 M_{Jup} beyond 20 au (Benisty et al. 2020, in prep.).

3. Concerning the dust, our hydrodynamical model involving one planet reproduces well the ring feature at ≈ 50 au, but not the inner region of the cavity, where an

inner dust disc close to the star still remains. While a semi-stationary state have been reached outside the planet orbit (i.e. we do not expect the gap edge location, depletion at the planet location and outer density profile to change significantly at longer timescales), we note that the dust in the inner disc decouples from the gas and is not effectively accreted onto the central star along with the gas. This implies that further depletion of the dust in the inner cavity might occur at later times.

4. Good agreement between the outcome of our simulations and the DALI gas density profile can be obtained with the model having $\delta_{\rm gas} = 10^{-1}$, $R_{\rm cav} = 25$; in particular, we note that the location of the cavity edge for the gas in this model ("orange" CO isotopologues DALI model in Fig. 5.6) is perfectly consistent with the density structure provided by a planet placed at $R_{\rm p} = 20\,$au in our simulations. This DALI model, despite not being the best representative for the gas, reproduces fairly well the fluxes for ^{12}CO and C^{18}O, but it fails in reproducing the ^{13}CO.

5. The dust profiles from the numerical simulations appear to best reproduce the DALI self-similar model (Section 5.4.4) with $\delta_{\rm dust} = 10^{-2}$ and $R_{\rm cav} = 28$ au (grey model in Fig. 5.8 and 5.9). The hydrodynamic density profiles, in particular those with $a_{\rm large} = 0.1$ mm, reproduce the location of the cavity edge and depth of the large dust grains density distribution of this model (see blue solid curves compared to grey dotted ones in Fig. 5.9). This does not occur for larger grains ($a_{\rm large} = 0.5\,$mm) that instead produce a deeper gap with respect to that in the modeling, as shown in the second row of Fig. 5.9.

6. Our hydrodynamical simulations are not able to reproduce the Gaussian density profile of the large dust grains that provides the best match with the continuum flux (blue curves in Fig. 5.5 and 5.9). We note that, in general, any planet model would predict a sharp disc truncation beyond the planet location instead of a shallow Gaussian depletion. As we show in Section 5.5.2, a sharp density feature is smoothed when synthetic dust flux profile have been created and then convolved. The results found can qualitatively describe the observations as well as the gaussian profile if the inner disc present in the simulations is neglected.

7. We find that the best match between our hydrodynamical simulations and DALI density profiles is provided by grains with $a_{\rm large} = 0.1$ mm with respect to those with $a_{\rm large} = 0.5$ mm; this suggests that the dynamics of the entire large dust grain population can be best described by the smaller (≈ 0.1 mm) sizes, rather than the larger ones (≈ 0.5 mm).

   A more accurate treatment would require a multi-grain approach (Hutchison et al. 2018; Dipierro et al. 2018a), in order to account for the different dynamics of different grain sizes characterized by different Stokes numbers.

5.6.1 Comparison with other possible scenarios

We here briefly discuss our results to explain the cavity together with other possible mechanisms:

Clearing mechanism. We find that a planet $M_{\rm p} = 9\,M_{\rm J}$ located at $R_{\rm p} = 20\,$au from the central star qualitatively (but not perfectly) reproduces the DALI modeling of gas and the large dust density distribution. The best match is obtained with 0.1 mm grains, implying that large dust grains behave qualitatively as fluid composed by grains with

that size. In particular, good agreement is obtained at large radii, where the simulations clearly show that the planet might produce a ring-like feature in the dust distribution. However, we were not able to reproduce the dust depletion, expected from the DALI modeling, in the inner cavity using a one planet model, and at the end of our simulations we are still left with an inner disc of dust around the star.

Photoevaporation. Models of photoevaporation predict small cavities ($\lesssim$ 10 au) and low accretion rates. The debate about what is the driving mechanism of photoevaporation between FUV, EUV, X-ray and what are the exact values of mass-loss rate is still open. In order for the photoevaporation to start the accretion rate have to drop below the photoevaporation rate. As soon as it starts, a cavity free from gas and dust is generated, with the very large grains rapidly migrating inward (Alexander & Armitage 2007). CQ Tau was considered by Donehew & Brittain (2011) and Mendigutía et al. (2012) to have a high accretion rate ($\dot{M}_{\rm acc} \lesssim 10^{-7}\ M_{\odot}\ {\rm yr}^{-1}$), which can be considered high for disc dispersal to be the main mechanism acting in the formation of the CQ Tau cavity (Owen 2016). A combination between the clearing mechanism and photoevaporation can, instead, be considered as a possible option (e.g. Williams & Cieza 2011; Rosotti et al. 2013, 2015) to be further investigated.

Dead zones. The suppression of magnetorotational instability inside the disc can create regions of low disc ionization, the so called "dead zones" (e.g. Flock et al. 2012). In these regions the rate of gas flow decreases with an accumulation of gas in the outer edge. At the same time the pressure maxima is able to trap large particles with a consequent ring-like feature in both gas and dust components (Flock et al. 2015). The ring is in general located at about the same radius (Pinilla et al. 2016) in both the components. However, when dead zones and MHD wind are present at the same time a difference in the inner radii position can be observed. The presence of dead zones can increase the turbulence present in the disc and generate asymmetric vortices in the disc (Ruge et al. 2016) at (sub)mm wavelengths. Such structures can be also created by disc-planet interaction if the α viscosity is low. We cannot exclude this mechanism by our observations. Higher resolution data are needed to better constrain the profile of the ring-like disc, mainly its symmetry and variability (Pinilla et al. 2016). However, dead zones can explain ring-like structures, but not cavities such as the one clearly present in the CQ Tau system.

A combination between the mechanism described above can be also a possible solution which, however, we will not address in this chapter.

5.7 Conclusions

Discs where it is possible to clearly distinguish a cavity are of particular interest in the study of protoplanetary disc evolution and of the planet formation process. In particular, we have studied the disc around the CQ Tau pre-main-sequence star. We have made use of spatially resolved ALMA observations of the dust continuum and of three CO isotopologues, ^{12}CO, ^{13}CO and C^{18}O, together with the observed SED of CQ Tau. We employed the chemical-physical code DALI to model the CQ Tau disc and to derive the surface density profile of the dust (small and large grains separately) and of the gas. Finally, we ran 3D SPH simulations to test whether an embedded planet could be able to create the observed disc structure. The main results from our analysis are summarized here:

- In the CQ Tau disc the gas radial extent is a factor of two broader than that one of the large dust grains;

- CQ Tau shows a clear cavity in both gas and dust, that can be described by different functional forms. Assuming that the mm-sized grains are distributed in a Gaussian ring, the Gaussian peak position is located at a distance of 53 au from the central star and the Gaussian width is $\sigma = 13\,\mathrm{au}$. The cavity is present also in the gas component. The cavity radius and level of depletion are degenerate, but they can be constrained with reasonable uncertainties: the radius is smaller than 25 au and larger than 15 au and the depletion has to be between 10^{-1} and 10^{-3} with respect to the profile of a full self-similar disc.

- The computed dust-to-gas ratio is not radially constant throughout the disc. Moreover, the global dust-to-gas ratio is found to be ~ 0.09, higher than the typical values assumed (~ 0.01) and most likely because of carbon depletion.

- We performed a set of SPH simulations in order to investigate whether the presence of a massive planet might be responsible for the radial structure of the CQ Tau disc. We find that a massive planet with a mass of at least $M_\mathrm{p} = 6 - 9\,M_\mathrm{J}$ located at $R_\mathrm{p} = 20\,\mathrm{au}$ from the central star can reproduce well the ring feature at ≈ 50 au but not the dust distribution in the inner cavity region of the best representative density model predicted using DALI. Also, our simulations do not reproduce the strong gas depletion within the cavity that appears from the best fit DALI modeling, although we caution the reader of possible degeneracies in both the thermo-chemical modeling (see above) and in the hydrodynamical modeling (for which a lower viscosity in the disc might reconcile the results).

Part III

SPHERE observations

Spiral staircase inside one of the towers (A. Gaudí, 1925-1978, Sagrada Familia, Barcelona)

Chapter 6

High-contrast imaging techniques

Detecting exoplanets and disc structures through direct imaging is challenging because of the high resolution and contrast needed. This can be achieved through High Contrast Imaging (HCI) techniques by suppressing the light of the central star and by removing the static aberrations (speckles). A planetary companion emission can be several magnitudes fainter than the star. Moreover, speckles add noise to the image. Currently, high contrast imaging can only be achieved from the ground with an adaptive optics system and typically making use of a coronograph and advanced post-processing algorithms. In this chapter, we will give a brief overview about high-contrast imaging techniques, their strength and weaknesses. Finally, we will explain how to derive the significance of point-like or disc detections and the contrast curves for the observations.

6.1 Adaptive optics

In order to image circumstellar material (e.g. protoplanetary discs, planets) orbiting around the targeted stars, telescopes/instruments able to perform high angular resolution observations are needed. Large telescopes are needed because the angular resolution is inversely proportional to the diameter of the telescope. Moreover, a large diameter will allow to collect more light and reach higher sensitivity. At the same time, atmospheric turbulence distorts the incoming wave front, leading to a substantial worse angular resolution. Adaptive Optics (AO) is able to deal with turbulence in real time, allowing to fully exploit the capabilities of large telescopes. An alternative to avoid the use of AO is to use space telescopes, such as HST or JWST in the next future, which do not deal with atmosphere. Nevertheless, building large space telescopes is not trivial and thus they have smaller diameters compared to the ground based ones. In Figure 6.1 we show a scheme of a simplified version of the different components of an AO system. The atmospheric turbulence, which can vary with time, distorts the incoming wave fronts at different atmospheric layers. To correct for this, an adaptive optics telescope has a secondary mirror and a beam splitter (BS) which splits the light in two: the transmitted part of the light goes to the science camera and the reflected part feeds the wavefront sensor (WFS), which measures the amplitude of the wavefront distortions (see Fig. 6.1). These information are processed by a Real-Time Computer which provides the required corrections to the actuators of the deformable mirror (both of primary and secondary) in order to flatten the wavefront.

6.1.1 Performance of AO systems

The performance of an Adaptive Optics system depends on several factors. A parameter used to quantify the overall performance of an AO system is the Strehl ratio (hereafter

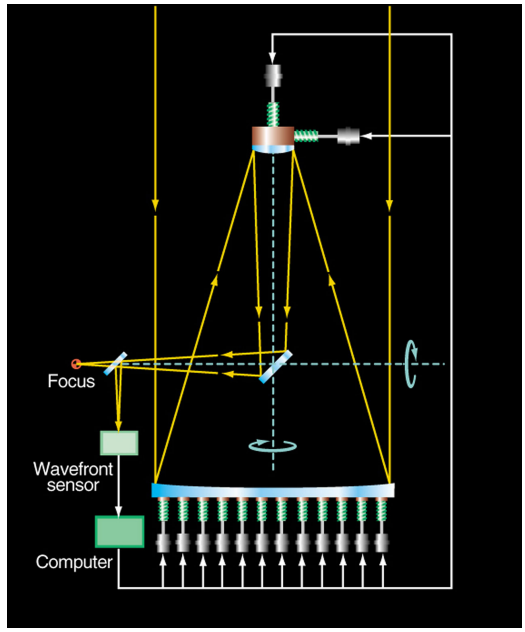

Figure 6.1: The VLT Active Optics System provides complete control of the VLT optics and optimizes its performance in all telescope positions. A stellar image is registered by the "wavefront sensor" and analysed to move the mirror supports accordingly to the corresponding correction signals generated. Credit: ESO.

Sr), defined as the peak intensity of a measured Point Spread Function (PSF) to the peak intensity of a perfect diffraction-limited PSF for the same optical system:

$$\mathrm{Sr} = \frac{\mathrm{I(x=0)}}{\mathrm{P(x=0)}} \tag{6.1}$$

where x stands for the position vector, I(x = 0) for the maximum intensity of the measured PSF and P(x = 0) for the maximum of the diffraction-limited PSF. Often the Strehl ratio is broken down into the Strehl ratio of each individual optical component in the AO system. The Strehl ratio is related to the wave-front errors via the Maréchal approximation (Sr = $\exp[-\sigma_\phi^2]$ $\exp[-\sigma_\chi^2]$), where σ_ϕ^2 is the wave-front phase variance and σ_χ^2 is the variance of the log-normal amplitude at the pupil plane (Marechal et al. 1994). The Maréchal approximation shows that the total Strehl ratio is the product of the Strehl ratios of the individual components as long as the phase errors of each component are uncorrelated. An effect of this is the presence in the images of a diffuse halo which is related to the performance of the adaptive optics of the instrument and do not allow high contrasts in the proximity of the star. To get a better signal-to-noise, it is necessarily to remove the halo produced by the star.

6.1.2 Speckles

Uncorrected quasi-static aberrations (speckles) are present in the vicinity of the star, which significantly degrades the achieved contrast in the image. Speckles are interference images of (atmospheric and/or instrumental) wavefront corrugations left uncorrected by

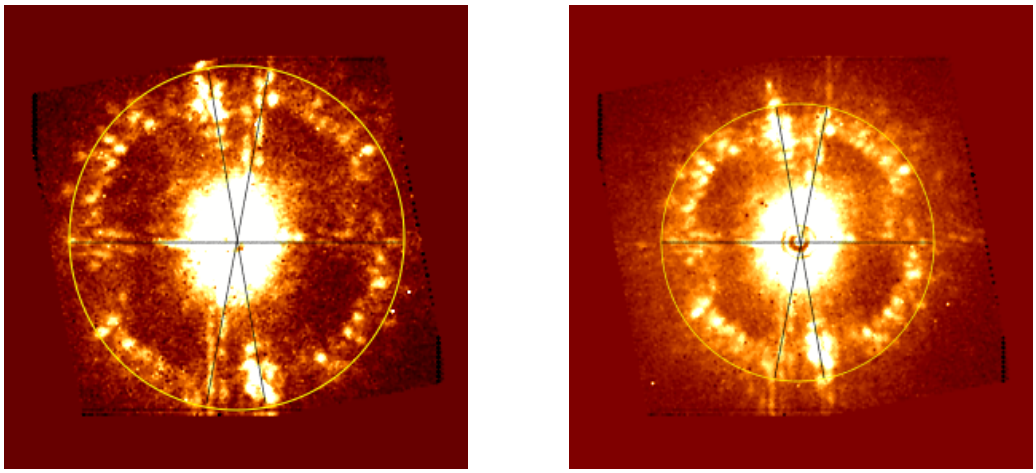

Figure 6.2: An example of speckle noise in one of the images of the sample of Herbig star studied by us (HD 190073, observations taken on the 2015-06-19). We show how the bright Airy ring is varying with λ (yellow circle) and the spikes produced by the VLT system (black). The image was taken with SPHERE-IFS. The image on the left show the IFS cube at 1.3μm, whereas on the right it is shown the same image at 1.0μm. We note that the speckle position varies with wavelength as expected.

the AO system with a typical size of a resolution element ($\sim \lambda$/D). An example is presented in Figure 6.2. Their position is a function of wavelength and they change in time as optics and atmosphere change. Speckles are visible as bright spots, similar to a real companion feature. Their brightness depends on the brightness of the star, the fraction (1 - Sr) of residual light in the halo and the angular separation to the star. The short-lived ($\sim$1-10 ms) atmospheric speckles are significantly reduced by AO, whereas that is not the case for the quasi-static speckles. They are primarily due to the secondary mirror's mechanical support called spiders. Considering their slow variation over time ($\sim$ min-hr), they are more difficult to identify and to correct for (Hinkley et al. 2007). These are named quasi-static aberration because their time variation depends on fluctuations of temperature or pressure, mechanical flexures, differential refraction effects depending on altitude, moving optics, guiding errors, or other phenomena (see e.g. Marois et al. 2005; Marois et al. 2006). Quasi-static speckles become dominant over signals that average out forming a central bright quasi-static pattern. In such a way the sensitivity to detect faint companions or disc structures cannot increase with integration time and the real features are hard to distinguish from the speckles (e.g. Marois et al. 2005). The strongest speckles signal are located at the Airy rings position and are called pinned speckles (Soummer et al. 2007). This signal results from an amplification of the stellar PSF variance levels. The total variance can be partitioned into two main contributions: one that can be suppressed directly by a coronagraph and one that cannot. The remaining component is removed by an appropriate observing strategy and post-processing analysis.

6.1.3 Adaptive Optics instrumentation

First generation AO instruments such as NACO at the VLT ($\sim$ 185 actuators) reach Sr$\sim$40% in H-band, Sr$\sim$60% in K_s-band and Sr$\sim$80% in L$'$-band for observations with average seeing and coherence time. By comparison, second generation AO instruments

such as SPHERE at the VLT which owns 41 x 41 actuators routinely reach Sr ∼85% in H band (e.g., Beuzit et al. 2008). The instrument SPHERE has an AO system called SAXO, a common infrastructure (CPI) and it consists of three sub-instruments: IFS, IRDIS, ZIMPOL (fully described in Appendix A). The high performance of the AO system corrects for turbulence and static optical aberrations and the possibility of applying a coronagraph. This makes SPHERE a powerful instrument to provide high contrast imaging, with excellent stellar PSF stability and suppression. The Adaptive Optics corrects the incoming wavefront up to a radius equal to 20 λ/D in the image plane (20 correspond to half the number of deformable mirror actuators across the pupil), which allow the coronagraph to efficiently remove the diffraction pattern down to a much fainter residual halo. For radii $>$ 20 λ/D, the AO system is not able to suppress any more the stellar halo, even if still corrects the PSF of off-axis sources. For the instrument SPHERE, beyond $\sim$ 1 arcsec, the AO correction is no longer relevant (the contrast depends on other parameters) and its performance behaves similarly to previous instruments (e.g., NACO). For more details on the SPHERE instrument, we refer to Appendix A. Differential imaging techniques are used to remove the residual stellar halo and/or speckles. These techniques are combined with the powerful ability of SPHERE to simultaneously observe images at different wavelengths or polarization states. The PSF stability, indeed, becomes critical with observations taken at different times.

6.2 Coronagraphy

The edges of the pupil are responsible for diffraction pattern and they correspond to a transition from the pupil interior and exterior. A lens images the light and this is typically where the detector would record the image. The image plane and the pupil plane are Fourier transforms of each other and this transition results in strong oscillations (diffraction rings) to the point-spread function (PSF). Both the stellar photon noise and the level of these diffraction wings makes difficult to distinguish the detection of faint structures or planets from the stellar signals. In order to suppress the coherent light coming from on-axis unresolved source a coronagraph is used and it is placed in the focal plane. This spot absorbs most of the light from the center of the field of view, so reduce both the photon noise and the central part of the Airy pattern coming from the star. When the pupil is reimaged by another lens any remaining light from the central star is mainly concentrated around the edges of the telescope pupil, forming rings around the edge of the aperture image and the secondary mirror image. Sometimes, an extra step can be present: the Lyot stop placed in order to block out the remaining rings of light from the central star.
The advantage of using a coronagraph is also that longer integration times are allowed before saturating the camera. A great variety of coronagraphs exists mounted on different telescopes. We refer to Mawet et al. (2012) for a review of small angle coronagraphs. In this thesis, however, we will focus in detail just on the coronagraphs used for the observations of the sample of Herbig stars described in the Chapter 7, 8, and 9.

6.2.1 SPHERE Apodized Lyot Coronagraph

During this thesis, we have made use of the instrument SPHERE. SPHERE is equipped with different types of coronagraph which have different working angles or spectral range. All the coronagraphs consist in a focal plane mask, followed by a pupil stop and sometimes preceded by an entrance pupil apodizer. Both Optical and near-Infrared coronagraphs are present. For our observations, we used the apodized Lyot coronagraph (ALC, Fig 6.3).

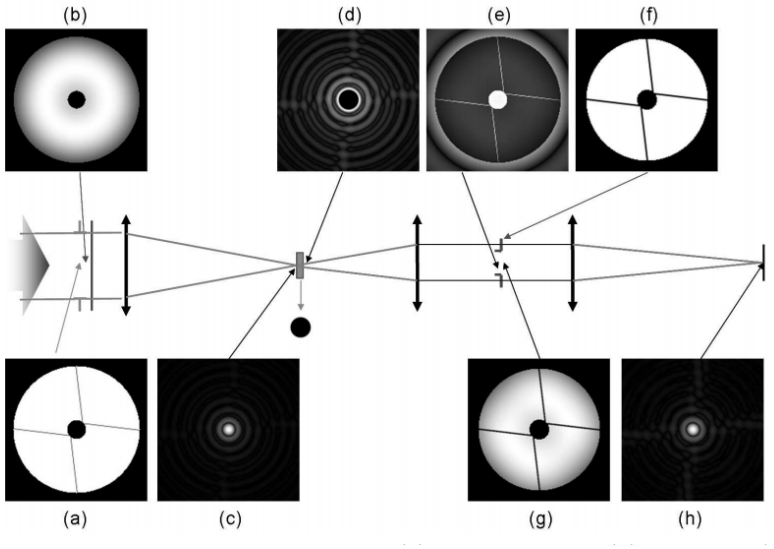

Figure 6.3: SPHERE Apodized Lyot Coronagraph: (a) Entrance pupil, (b) Apodizer, (c) Point spread function (PSF) at the focus of the telescope, (d) PSF when the Lyot occulting coronagraphic mask is settled, (e) Pupil image before the Lyot stop introduction, (f) Lyot stop, (g) Pupil image with the Lyot stop, (h) Final coronagraphic PSF. Credits Guerri et al. (2009).

A given apodizer and focal mask combination is optimal only at a particular wavelength. The optimal transmission profile of the apodizer depends on the size (in λ/D) of the focal mask. The combination of apodizer and focal mask used in our obervations were respectively APO1 and ALC2 with a diameter of 185 mas. The measured inner working angle (IWA) is defined as the separation that yields a transmission of 50% and it is 95 mas for the IFS YJ. The 90% of the flux is recovered at a separation of 130 mas from the center. However, below 200 mas, the transmission profile of the coronagraph can affect still the observation. The ALC Lyot stop has good transmission (92%) with a large outer radius (96% of VLT pupil). This was used in both the configurations IRDIFS-EXT and IRDIFS.

6.2.2 Neutral densities, centering through the waffle spots and reference stars

The neutral density (ND) is a filter that prevents most photons from reaching the detector. It can be used in order not to saturate the detector. Its transmission is a function of wavelength. The ND filters are common between IRDIS and IFS and identical to those in the CPI. In particular they have three degrees of attenuation: ND1, ND2, ND3. They are inclined with respect to the optical axis to avoid ghosts, and this causes a small shift of the optical path.

When a coronagraph is used, it is not possible to directly measure the star position. For IRDIS and IFS, the position of the star behind the coronagraph can be measured through the application of a waffle pattern to the deformable mirror. This consists of creating four replicas of the PSF, the so called "satellite spots", at a specific location (separation $\sim$14 λ/D) away from the coronagraphic mask. The orientation of such patter by default was chosen to be with position angle of the spots of 45°, 135°, 225° and 315°. By intersecting the line joining opposite spots, it is possible to find the star center with

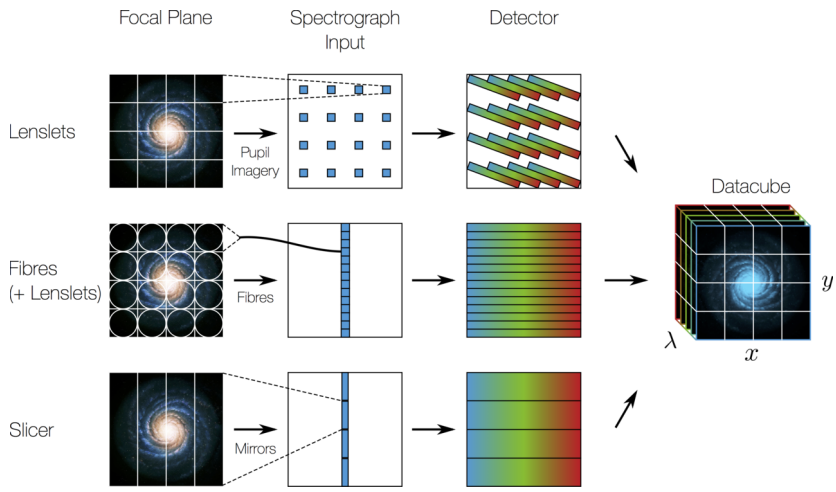

Figure 6.4: Integral field spectroscopy (IFS): three methods of championing through IFU: microlens array, a fibre array (with or without matrices) e image slicers.

a small error (∼2.5 mas).

Finally, observations are in general followed by a short (15 min.) observation of a PSF reference star. Reference star are isolated sources with typically no emission coming from the disc or from a companion that can be used to create a reference frame. In this way these images can be useful to test the post-processing methods used.

6.3 Integral Field Spectroscopy

In this Section, we will describe the concept of integral field spectroscopy (IFS), which we mostly used during this manuscript. These data cubes are powerful because they allowed us to obtain high-contrast imaging together with being able to characterize faint companions. An IFS is a device able to obtain spatially resolved spectroscopic information. Moreover, its importance is related to the fact that all the frames are taken simultaneously. In such a way the IFS is not dependent on meteorogical variation, but its field of view is smaller than for other type of instruments. The 3D information is captured by a 2D detector as the field of view is divided in different segments (spaxels). These segments are decomposed in wavelength using a diffraction grating, a prism or a combination of both (grism). Different concepts of how to split the field in separate sections for an IFS have been implemented in several instruments. Examples of them are: based either on a microlens array/ lenslet array, a fibre array (with or without lenslet) or image slicers (see e.g., Westmoquette et al. 2009, Fig. 6.4). Instruments such as SINFONI and ERIS on the VLT use the image slicers. Instruments such as NIRSpec on board of the JWST uses the same design (Posselt et al. 2004). This concept is mainly used for extended sources or crowded fields. The modern ways to better spectral characterize faint companions are: a) very low spectral resolution but high-contrast IFS (e.g., SPHERE/IFS, GPI Beuzit et al. 2008; Macintosh et al. 2014); b) long-slit spectrographs with low spectral resolution and intermediate raw contrast (e.g. SPHERE/LSS, Vigan et al. 2008; Hinkley et al. 2015); c) moderate-spectral resolution IFS (e.g., VLT/SINFONI, Eisenhauer et al. 2003). Finally, instruments such as NACO use a grism (prism+diffraction grating). For details about the specific IFS we used during this thesis: a lenslet-based integral field unit of the

SPHERE-IFS instrument, we refer to Appendix A. In general the lenslet array integral field unit is based on the use of a matrix of microlens. Each point of the astronomical image is imaged in order to have an magnification through the use of the micronlens. The signal coming out from each lens is diffracted and stored. These systems are able to analyze just a short range of wavelength in order not to overlap with other part of the image. The advantage is that the filling factor is high.

6.4 Observing strategy

In this section, we will briefly describe the observing strategies used in high contrast imaging and the most common post-processing techniques used, particularly focusing on the ones used in the context of this manuscript.

6.4.1 Pupil versus Field Tracking mode

In order to match the target's altitude and azimuth angle, both the pupil and the field rotate. In particular, the field rotation is the combination of the parallactic angle and altitude of the object, whereas the pupil rotation is directly related to the altitude of the object being tracked. The orientation of the observed field of view (FOV) changes as the celestial sphere rotates during the observation. Modern facilities are equipped by a derotator to compensate for the rotation of the field during the night. This allows two main different observing modes: field and pupil-tracking. The first one keeps fixed the field, whereas the the second one tracks the pupil (see left images in Fig. 6.5). Importantly, the SPHERE derotator allows stabilization both for field and pupil-tracking mode. When the derotator is allowed to move, the center of rotation is the central star. In the field-stabilized mode, for the whole observation, light from a specific location in the field of view always falls in the same location of the detector. The PSF variability is minimized for pupil-stabilized observations, considering most of the optical elements do not move. The relative rotation of the field with respect to the pupil is given by -p, where p is the parallactic angle. Advantages of the pupil-stabilized mode is that speckles (due to the telescope and to the instrument) do not move with respect to each other and provides the highest PSF stability. The possibility of having a speckle halo more stable, is typically preferred to have an optimal removal of this bright halo. Moreover, this allows the use of a differential imaging technique, called angular differential imaging (ADI). On the other hand, field-stabilized mode reduces concern due to flat-fielding with a more stable photometric time series and allow to readily stack the images to increase the SNR. Overall, a good compromise between rotation rate and the smearing of off-axis PSF have to be made.

6.4.2 Differential Imaging

The goal of differential imaging is to improve the image quality of the dataset going from AO corrected images to high-contrast images where the residual speckle noise is greatly reduced or suppressed. A wide diversity of differential imaging techniques have been proposed and used to build optimal reference/model images for subtraction of quasi-static speckles. The best PSF models have to be maximally correlated to the target image to allow the most effective subtraction of the stellar halo. Moreover, they need to present some diversity in order to have less self-subtraction of putative faint signal coming from companion or circumstellar disc. We will briefly summarize the different technique used in the field of high contrast imaging (non-exhaustive list) and then describe more

in detail the ones used during this thesis, namely Angular Differential Imaging (ADI), Spectral Differential Imaging (SDI) and Polarimetric Differential Imaging (PDI). Other techniques used are: reference star differential imaging (RDI), binary differential imaging (BDI), dual-band imaging (DBI). For more details and different techniques used in high contrast imaging, we refer to Mawet et al. (2012). RDI is based on the concept that the reference PSF is created through the observations of another star, reference star (RS). The reference stars are chosen to be similar in flux, spectrum and sky position and their flux is scaled before subtraction to the target star. This method has, for example, the weakness that it is not always easy to find reference stars close enough from the source targeted. BDI has an alternative differential imaging strategy (Rodigas et al. 2015b). This is similar to RDI with the peculiarity that the reference star is the binary companion. This is able to reach a high cross-correlation between the PSF of both the companion, however, for an optimal contrast the binary components should be well separated and share similar brightness. DBI was historically the first proposed method of differential imaging (e.g., Smith 1987; Racine et al. 1999). The beam splitter allows to take two simultaneous images in two adjacent filters. High contrast imaging of exoplanets are typically carried out with one filter centered on an expected absorption line in the spectrum of the exoplanet (e.g., CH_4 at 1.6 μm, Rosenthal et al. 1996) and one in the adjacent continuum. The images can be subtracted to each other giving a signal in the location of the companion. The same images can be used firstly applying ADI and then combining this information with the one just described. This method is also used to detect H_α, a tracer of accretion (Cugno et al. 2019). We note that different differential imaging techniques are suited for different target and scopes. For example, PDI is better suited than ADI to study discs and SDI is better than ADI for atomic jets. Below I will describe more in detail the ADI, SDI and PDI techniques. The first two were used to analyze the data presented during this thesis and the third is often use as a comparison.

Angular Differential Imaging

In pupil-stabilized mode, most speckles caused by instrumental artifacts are locked up in the pupil plane, whereas everything that is real such as a disc or companion will rotate as the field rotates. This is due to the differential rotation between FOV and pupil. The ADI technique (Fig. 6.5) exploits the fact that speckles are fixed and frames differentiated by angular diversity. The parallactic angle keeps tracks of the variation in rotation. The PSF stability is important for ADI. The best PSF stability is obtained when observing in pupil-stabilized mode. The PSF reference frame is built from the observed (non-derotated) datacube and then subtracted from each individual frames. The frames are then derotated and stacked to compose a master frame. There are many ways to built the reference frame: this is typically done through a median combination of the whole datacube (classical-ADI or median-ADI). Enough field rotation is needed to be sure to not self-subtracting the putative planet or disc emission (Marois et al. 2006). This technique was largely used to detect directly imaged exoplanets/substellar companions. An example of a spectacular direct detection made through ADI are the four giant planets around HR 8799 (Marois et al. 2008). The self-subtraction will affect the detection of point-like source: to determine the real flux of the object discovered, a study on the flux loss have to be made. In particular, it is common to use specific tools such as the negative fake companion technique (NEGFC) (e.g., Marois et al. 2010a; Lagrange et al. 2010). We note that, instead of using the median to create the PSF reference, more advanced techniques have been proposed such as the Principal Component Analysis (PCA) (see Section 6.5.2). By construction, ADI is however not best suited to study extended objects, particularly

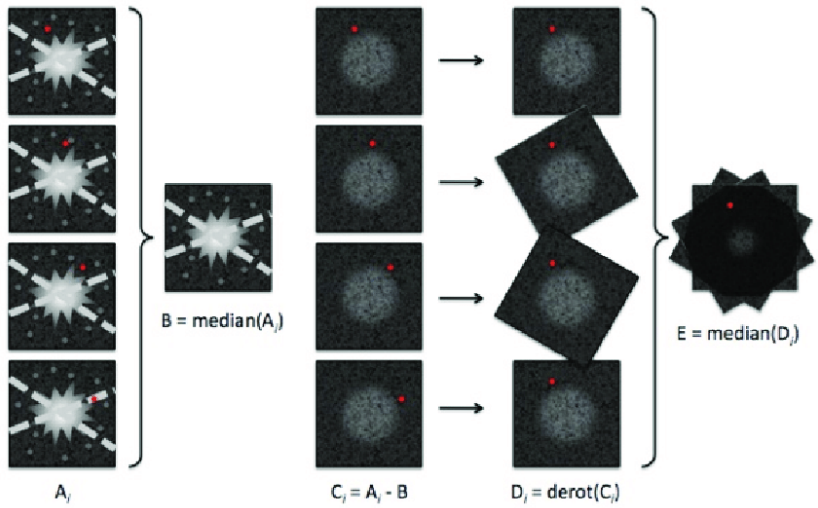

Figure 6.5: Principle of classical ADI (credit: C. Thalmann). On the left, it is shown a set of sequential images: the red point show the position of a companion that rotate, whereas speckles and stellar halo stays in the same position.

if their emission is axisymmetric. Caution must be taken when building the reference frames because they can include a significant amount of real emission from the disc. This will affect not just the total flux emission, but also the final disc shape (Milli et al. 2012), which can present extra artificial features.

Together with this another way to perform ADI is to firstly divide the field in concentric annuli and afterwards applying PCA separately to each of these annuli. Important is to choose annuli dimension as large as possible not to create artifact. This can be done through the choice of a parallactic angle threshold to build the model where the putative planet has rotated enough and thus the self-subtraction is minimized. The value to be used is the maximum value allowed to have still enough library to create the model.

Spectral Differential Imaging

The speckles come originally from the core of the PSF and from the Airy rings (mainly from the first ring) and they are strongly dependent on wavelength. The spatial position of real objects, such as discs and point sources, does not move with wavelength, whereas the position of speckles varies with wavelength according to the relation:

$$q = R\sin(\theta_{\mathrm{R}}) \approx 1.22\,\lambda R/D = 1.22\,\lambda N \tag{6.2}$$

where q is the radius of the first dark ring, θ_{R} is the angle of observation, (i.e. the angle between the axis of the circular aperture and the line between aperture center and observation point), R is the distance from the aperture, D is the aperture diameter (8.2 m, for VLT), N is the focal number of the lens. The intensity of the speckles decreases with increasing the wavelength. This is a fundamental piece of information that can be used to remove the artifacts from our images. This concept is used by Dual-band Imaging (DBI, see above) and Sparks & Ford (2002) firstly applied this method to Integral Field Spectrograph (IFS). Compared to DBI, IFS collects simultaneously multiple images at different wavelength improving the spectral deconvolution (Thatte et al. 2007). Moreover,

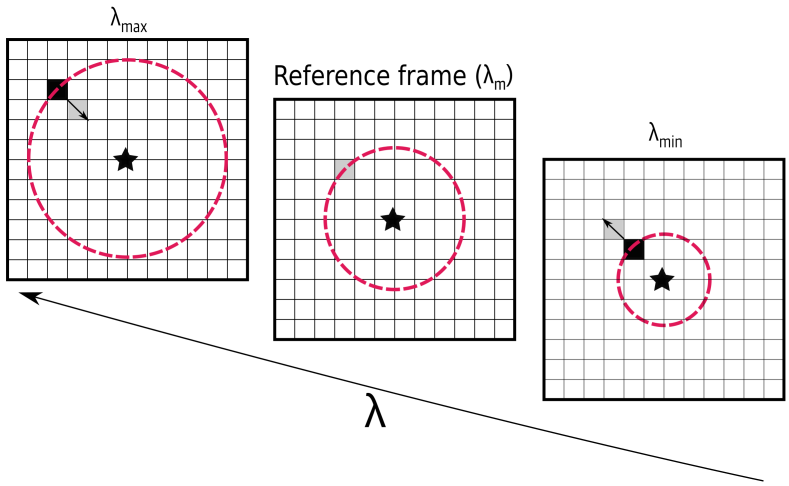

Figure 6.6: Workflow of SDI. The image shows how the speckles are moving with the wavelength ($\sim \lambda/D$, at larger wavelength, speckles are more distant from their star, see red ring). SDI consists in scaling the frames in order to have the speckles position at the location they would have in the reference frame (gray pixel) as in the central image (in this case shown as the reference frame).

the host star have different spectral features compared to the planet and in general also to the surrounding disc. Spectral differential imaging (SDI) consists in taking simultaneous images at two or more wavelengths to have a variation in the brightness of the planet (in and out of a molecular band). The cube of multi-wavelength images is rescaled to a common size where the speckles stays in the same position. A workflow of this process is shown in Fig. 6.6, where the red circle represents the speckles radial position changing with the wavelength, the black square represent the initial pixel shifted in the new position (grey square). Typically, the reference channel is chosen to be the last wavelength of the datacube, for an upscaling of all other spectral channels. Considering that the images are taken simultaneously, the PSF is very well cross-correlated and can be used to create a PSF model. It is, then, subtracted from each re-scaled image. After this, each spectral frame is scaled back to its original size and the spectral cube can be median-collapsed (or using more sophisticated algorithms) to increase the signal-to-noise of the detection. The advantage of using this technique is that the correlation between the frames is higher with respect to ADI, considering these images are taken simultaneously and tracks the same instantaneous speckle pattern. A combination of ADI and SDI can be used for IFS data with extreme-AO correction (e.g., Macintosh et al. 2015; Zurlo et al. 2016).

Polarimetric Differential Imaging

Polarimetric Differential Imaging (Mauron & Dole 1998; Kuhn et al. 2001) is based on the concept that stars are often weakly polarized, while light scattered by the dust particles in the circumstellar environments can be highly polarized. The polarization fraction onto planets has not been well constrained yet. The observing technique used is to combine simultaneous observations taken with different (orthogonal) polarization states. In such a way the stellar light is canceled and it remains mostly unchanged the disc scattered light. Typically PDI observations are described using the Stokes formalism (e.g. Tinbergen

2005) with four Stokes vectors: intensity (I), two components of linear polarization (Q, U), and circular polarization (V), negligible in protoplanetary discs. We note that PDI is not tracing all the scattered light coming from the disc, but just a fraction which depends on the amount of polarization of scattered photons. Typically this fraction is 10% of the total scattered light, which means that the other 90% of photons are thrown away and this increases the noise of the image. The only solution to get cleaner images is just to integrate longer. Moreover, the exact shape of the polarization degree is not known and the interpretation of PDI images suffers from this source of error. To date PDI is the best technique to unveil disc structures thanks to the higher contrast achieved.

Several are the instruments able to perform such observations: Subaru/HiCiao, VLT/NACO, and the new-generation instruments VLT/SPHERE and GPI, which unveiled a great number of protoplanetary discs structures.

6.5 Data reduction

The data reduction consists in general of two steps: a first one involves a basic calibration, which corrects for the systematics involved in the acquisition of astronomical images (described below); a second one involves the most advanced processing methods to get high contrast images (described in the previous section).

6.5.1 Basic Calibration

The main steps usually done in the basic calibration is to perform dark and instrument background subtraction, flat-field division in sequence. Bias level and dark current have to be corrected in any image. The first is obtained with zero exposure time, thus only containing noise due to the electronics; the second is the relatively small current due to charge accumulation within the detector during a given integration time. The dark frames, integrated for the same amount of time as the science images, help to remove these effects. The background thermal emission from both the atmosphere and the telescope/instrument itself is particularly important for observations in thermal IR and have to be subtracted. This measurement is done through empty sky regions observations. Pixel-to-pixel variations are not common, with the exception of cosmic rays, but large variation can be more significant. The flat field images, which consist in images of a uniform source of light, allow to correct for sensitivity variations. Detectors present dead, stuck, and hot pixels. It can be applied the bad pixels and cosmic rays correction, derived through a study of each pixel efficiency. Bad pixels are replaced by the median of the values of neighboring pixels, cosmic rays and hot pixels are filtered out through a sigma-filtering. In the ESO Pipeline described below, this was not set as default. On data that presents spectra acquisition, it is also derived the distortion coming from regions of the spectra and derived wavelength calibration coefficients.

We used the standard procedure (ESO pipeline[1]) in order to reduce SPHERE-IFS data. The pipeline creates a master dark, a master flat, which are subtracted from the raw images. It then generates a distortion map in order to correct for instrumental distortion, combines the images, re-arranges data to create the IFS cube (39 frames), and finally applies a wavelength calibration and distortion correction to the data. We did several tests to improve the images. First of all we modified several values inside "sph_ifs_science_dr"

[1]http://www.eso.org/sci/software/pipelines/sphere/ - version 0.24.0 and version 0.36.0 for the most recent data (taken after 2018)

without getting improvements: "ifs_science_dr_clean_mean_reject_high"=1, 20,10, 5; "ifs_science_dr_clean_mean_reject_low"= 1, 20,10, 5; "ifs_science_dr.badpixco.threshold"=50, 100; "ifs_science_dr.badpixco.fac"=5; "ifs_science_dr.badpixco.boarder"=100, 150; "ifs_science_dr.badpixco.sigma"=5. The only one that was modified is the parameter related to bad pixels corrections: "ifs_science_dr.badpixco.apply" was set to TRUE. We applied the bad pixel correction, not used in the default pipeline. We mainly focused on the IFS data. Examples of the direct data products produced by the SPHERE pipeline are shown in Fig. 6.2. The output of the ESO pipeline is a set of different images taken for the same day. Together with the IFS observations of our target, we obtained star center and flux images. We measured the position of the four echoes present in the star center images and derive the position of the star behind the coronagraph. Moreover, we derived the stellar spectrum from the flux image, where the star has an offset from the coronagraph.

6.5.2 Post-processing analysis: PSF subtraction

After the calibration, post-processing is needed to obtain final high contrast images. The most important task is the reconstruction of an PSF model to be subtracted from each frame. The final image is built combining all the PSF subtracted frames. There are different ways to build the PSF model.

- A simple way to do it imply using a median of the observed datacube. In the case of e.g., ADI this is called classical-ADI (Marois et al. 2006). The rotation of the field will allow to disentangle the signal coming from the speckles and the one coming from discs or planets and to respect the required diversity of the PSF model.
- The PSF model can also be constructed dividing the field in annuli to build a specific PSF model for each annulus of each frame: taking the median of the annulus in the limited amount of frames with a sufficient parallactic angle difference. This is called smart-ADI. This strategy is able to reach a compromise between cross-correlation and the minimization of self-subtraction.
- Other examples of refined algorithms to create a PSF model are: the Locally Optimized Combination of Images (LOCI) and Principal component analysis (PCA, described below). The first one was introduced by Lafrenière et al. 2007b and it is based on the idea of building the reference image from a linear combination of other images of the datacube, done locally. This method was improved with the name of damped LOCI (TLOCI, Pueyo et al. 2012; Marois et al. 2014). TLOCI is better able to recover flux loss because it adds the condition of maximizing the companion flux.

Principal component analysis

PCA was invented in 1901 by Karl Pearson to reduce the number of variables required to model a specific dataset. It is a statistical procedure that uses an orthogonal transformation to convert the observed datacube, made by possibly correlated variables, into a set of linearly uncorrelated variables (so-called principal components, PCs). They are ordered by decreasing variance and the first principal component has the maximum variability present in the data. The subsequent component have to be orthogonal to the other components. The resulting vectors are, then, a linear combination of the variables and an uncorrelated orthogonal basis set. The data is then projected onto those PCs new vectors.

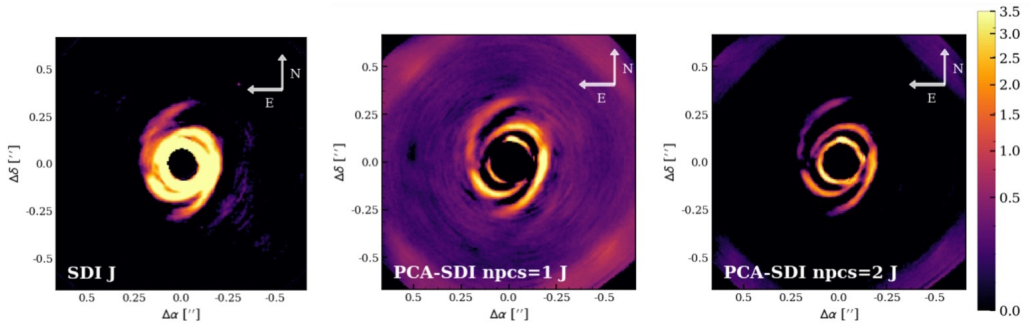

Figure 6.7: On the right a simple SDI method (see Chapter 10 were is called SRDI-PA); on the center and on the left the PCA-SDI method respectively for npcs = 1 and npcs = 2.

This idea was used for the first time in high contrast imaging by Soummer et al. (2012) and Amara & Quanz (2012) to built the reference PSF model. The PSF model is then subtracted to each projected frame on that orthogonal basis. In the Vortex Imaging Package Gomez Gonzalez et al. (2017a), the ortogonal base is built using the singular value decomposition (SVD, see e.g., Amara & Quanz 2012). We will focus on this technique considering we used VIP to post-process our data. The PCA combined with SVD method do the following steps:

- A flux normalization of the initial datacube (X) is performed. It is applied a mean centering: the temporal mean is subtracted to each frame so that the new average of the datacube is zero.
- The 3D cube, with zero average, is transformed into a 2D matrix S: each frame (dimension m) is represented by a 1D vector of the number of pixels in a frame (length n).
- PCA is then performed using the SVD of the covariance matrix (C=X^TX/(n-1)). SVD can be calculated using different libraries including the fast randomized SVD (Halko et al. 2009). We want to find new coordinate system of the eigenvectors for C (m x m). It is a symmetric matrix and so it can be diagonalized: C =VWV^T, where V is a set of orthonormal eigenvectors (called principal axes) and W is a diagonal matrix (m x m) of m eigenvalues.
- A singular value decomposition (SVD) of X is performed: X = USV^T, where U (m x m dimension) and V^T (n x n dimension) are unitary matrices and S is a rectangular diagonal matrix of singular values s_i (dimension m x n): eigenvalues in a decreasing order with only positive (or zero) elements found through:

$$C = X^T X/(n-1) = VSU^T USV^T/(n-1) = V\frac{S^2}{n-1}V^T \tag{6.3}$$

  This means that V is the principal axis and that the singular values ($s_i \sim \frac{S^2}{n-1}$) are related to the eigenvalues of covariance matrix.
- Considering we want to pursue a dimensionality reduction, we can project the data points onto the first k principal axes obtaining the principal components: X_i = X V_i= US. Thus, the initial datacube can be transformed in a set of ortogonal eigenvectors and eigenvalue through the covariance matrix.

- The PSF references $\mathrm{R}(\vec{x})$ are then built for each image $\mathrm{I}(\vec{x})$ as:

$$R(\vec{x}) = \sum_{\mathrm{i}=1}^{n_{\mathrm{pc}}} s_{\mathrm{i}} X_{\mathrm{i}}^{n_{\mathrm{pc}}}(\vec{x}) \tag{6.4}$$

  where s_{i} are the eigenvalues found from the projection of the image on the orthonormal basis of X_{i} truncated to its n_{pc} first elements.

- The reference images are subtracted to each frame, creating residual images that are then derotated and stacked.

This approach is similar to TLOCI regarding the PSF-suppression, but the self-subtraction is lower and the algorithm is faster (with the exception of the case: smart-ADI). The number of principal components used is the only free parameter in this method. In order to maximize the reduction of the signal-to-noise of the data, it is possible to verify which principal component maximize the contrast in the final image. This is done through the injection of fake companions in the raw image. The best principal component can vary in different frames and at different separations from the host star. This is done to maximize the signal coming from a point-like source; whereas in general for disc emission (more extended sources), the best choice is to stop at the first or the second principal components. During this thesis PCA was used predominantly. In particular, it was combined with classical-ADI, smart-ADI, SDI and a combination between ADI and SDI (Chap. 8, 7 and 9).

During this manuscript we have mostly used the Vortex Imaging Package (VIP) for what concerns the post-processing of SPHERE-IFS data that includes the PCA routine for the PCS model. VIP[2] is an open source package with a large set of routines written in Python (Gomez Gonzalez et al. 2017a, 2018).

6.6 Performance

6.6.1 Signal-to-noise

In the following Section, we will discuss how to determine the significance of a specific signal observed in the dataset after post-processing the image using PCA. In the calibrated images speckle noise follows a positively skewed modified Ricci distribution (Soummer et al. 2007). Using differential imaging algorithms, we subtract the correlated component of the stellar noise. A residual noise (σ) is still present and this will determine our ability to detect a companion. Thanks to the central-limit theorem (Marois et al. 2008), this effect is enhanced also by the combination of different post-processed frames. The detection significance can thus, in first approximation, be estimated using a gaussian statistics. This approximation do not stand in the vicinity of the central star (inside few FWHM), because the noise is highly variable both temporally and spectrally and for this reason a coronagraph is often used. The residual noise has a radial dependence and σ is higher in the proximity of the star. For this reason, the best way to estimate the noise is to use concentric annuli over the image. In the case of a specific signal in a small region of the image, the Signal to Noise Ratio (SNR) is measured as:

$$\mathrm{SNR} = \frac{x - \overline{x}}{\sigma} \tag{6.5}$$

[2]Available at https://github.com/vortex-exoplanet/VIP

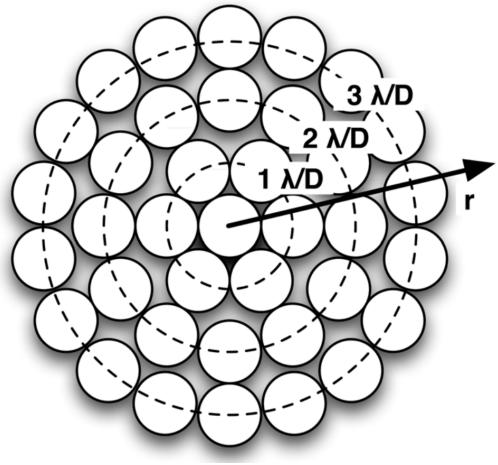

Figure 6.8: SNR derivation. Resolution elements for a given radius. The number of apertures is $\sim 2\pi R$ (here ranging from 1 to 3 λ/D). Credits. Mawet et al. (2014).

where x is the flux measured on a 1-FWHM aperture centered on the signal, $\overline{x}$ is the average taken on independent apertures at the same radius of the signal and the residual noise (σ) is measured as the standard deviation measured on the same independent apertures (Rameau et al. 2013). In such a way, however, the SNR will be nor properly constrained for small radii, giving the small amount of apertures available. In this situation, the Student t-test (Mawet et al. 2014) is more appropriate to estimate the SNR. This uses a t-distribution probability:

$$p_{\mathrm{t}}(x,\nu) = \frac{x-\overline{x}}{\sigma_{1,2}\sqrt{1/n_1+1/n_2}} \tag{6.6}$$

where $n_1 = 1$ is the number of resolution elements to test x and n_2 is the number of the remaining resolution elements ($n_2 = n-1$) over which the average intensity $\overline{x}$ is computed. The resolution elements are part of an annulus of λ/D width at a separation of R. In the case of $n_1 = 1$, $\sigma_{1,2}$ corresponds to σ_2 which is the standard deviation computed over the remaining resolution elements. The difference with the previous equation (Eq. 6.5) is that $\overline{x}$ and σ are measured in the n_2 other independent resolution elements located at the same radial separation. The significance of the detection is then computed through the measure of the false positive fraction (FPF) associated to that t-distribution:

$$FPF = \int_{\tau}^{\infty} p_{\mathrm{t}}(x,\nu)dx \tag{6.7}$$

where τ is the threshold decided. The FPF is then, in general, converted back to the standard gaussian confidence level. A 5-σ gaussian confidence level corresponds, indeed, at a FPF$\sim 3\cdot 10^{-7}$.

The signal-to-noise can be also evaluated through a signal-to-noise map, which uses a parallel implementation of the S/N map generation function here described. The best way of doing it is to use also the t-Student statistics (Mawet et al. 2014). The routine applies the S/N function at each pixel. These maps are commonly used to study point-like sources since they assume the presence of at most one point like source for each separation from the star. During this thesis we have in particular used the routine as implemented in VIP.

6.6.2 Contrast curves

Contrast curves are commonly used to assess the sensitivity of faint signals and also to constrain the level of non detection in our images. The contrast curves are defined as the ratio between the residual noise, corrected by the flux loss, and the stellar flux at each radius. These curves are produced for each radii to estimate the contrast above which the companion, if present, would be detected. The simple way of doing it is to measure the noise in concentric annuli of the final image and divide it by the stellar flux. However, this alone does not consider the amount of flux lost in the post-processing. To take that into account, it is necessarily to compute the throughput for that specific target, day and post-processing technique. This is estimated through the injection of fake companions of a known flux at different radii of the raw cube. It represents the fraction of flux recovered after using the post-processing method. The routine are in general quite aggressive and they subtract not only the stellar halo, but also a significant amount of flux coming from the faint signal (point-like source or disc), particularly in the vicinity of the star. The noise can then be corrected using the throughput information for a specific detection threshold decided (e.g., 3-σ or 5-σ). The recovered flux from the throughput and the noise can be derived using either the gaussian or the t-student statistics as described in Section 6.6.1. The contrast curve can also be converted into the delta magnitude between image and star and/ or to companion mass sensitivity. The latter needs some assumptions on the evolutionary models chosen to derive different masses and ages. Models commonly used are COND (Baraffe et al. 2003) and BT-SETTL (Allard et al. 2012) called hot-start models. The masses inferred through these models seem to be quite optimistic for sources at very young ages and they may underestimate the object mass. Cold or warm-start models, however, were considered too pessimistic in deriving the mass of directly imaged giant planets such as β Pic b and HR 8799 (Bonnefoy et al. 2013; Marleau & Cumming 2014). During this thesis, we collaborate to extend the contrast curve routine implemented and working for ADI 3D cubes, also to 4D IFS cubes in order to use post-processing techniques such as PCA-SDI and PCA-ASDI.

6.6.3 Standardized trajectory intensity mean (STIM) map

In a given observation, the standard way to assess the sensitivity of faint physical signals in the vicinity of a star is, as previously described, through contrast curves and signal-to-noise maps. However, this is not the best way to proceed in the case of extended disc emission, giving the fact that, in the disc, more than one point at the same separation from the star may be due to a real signal. The disc emission, then, affects the flux measurements in the independent apertures and artificially increase the noise level for each radius. That is the case of several sources described in Chapter 7 and 8. The methods $\mathrm{SNR}_{\mathrm{t,opp}}$ and the Standardized Trajectory Intensity Mean (STIM) map (Pairet et al. 2019; Christiaens et al. 2019a) use a similar idea of the classical SNR_t, but they are adapted to study extended disc structures. The noise is not estimated using independent apertures. The apertures are considered to be the same, but with opposite derotation paralactic angle of the residual frames (in the case of ADI). In this way, the images preserve the time dependence of residual speckle, but also they do not add authentic circumstellar signal in the noise/mean estimate (e.g., Marois et al. 2008). A limitation of this routine is that the number of independent apertures for small radii is not large enough. In order to overcome this problem, the STIM map is exploited. This uses the trajectory of speckles in the derotated cube of residual images to raise up the variation of pixel intensities. The residuals images, obtained after the use of the post-processing methods, have to be aligned North up and East left. The measure of the mean $\mu(x_{i,j})$ and standard deviation

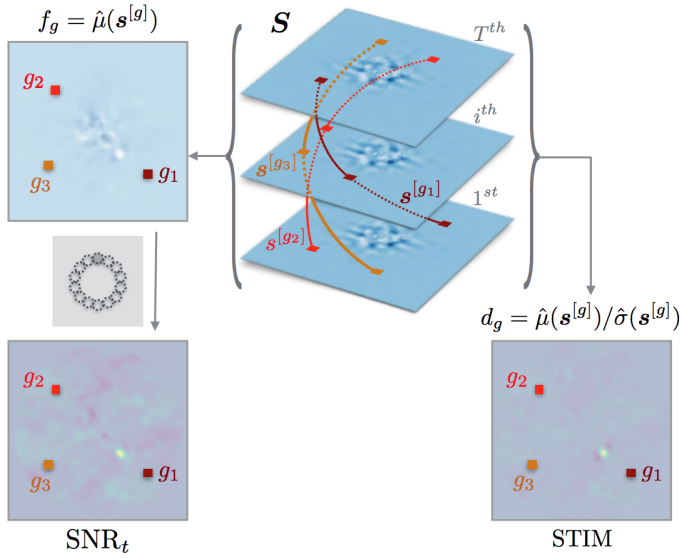

Figure 6.9: STIM map derivation versus SNR using the t-student test (SNR_t). Three different trajectories are shown. The SNR_t is built from the post-processed frame using resolution elements located at the same separation; the STIM map is directly constructed from the residual cube S. Credits. Pairet et al. (2019).

$\sigma(x_{i,j})$ is done on the trajectory $x_{i,j}$. From this, the 2D map (d in Fig. 6.9) is defined as $\mu(x_{i,j})/\sigma(x_{i,j})$ where a higher signal identify the authentic circumstellar signals (disc or planet) thanks to a relatively higher and more constant intensity of pixels. On the contrary, pixels without circumstellar signal have a relatively higher standard deviation because of the speckles variation on the trajectory in the derotated cube. The original definition of STIM map was done for ADI, Christiaens et al. (2019a) explained however that for SDI data the concept can be also applied using radial instead of azimuthal trajectories. In the case of the combination between ADI and SDI the STIM map will result in a cleaner final image. The residual cube to be used is 3D cube of residual images obtained. In order to understand what are the significant features, it is important also to compute the inverse STIM map obtained through the use of opposite parallactic angles. In such a way it will be possible to better identify the amount of residual speckle noise (as a threshold) present in the typical derotated STIM map. The signal above this threshold is, indeed, very unlikely to be produced by the residual speckle.

6.6.4 Companions characterization

Where a companion candidate is found, SPHERE-IFS data constrains potentially enough information to perform a spectral characterization of the data. Through VIP, we can use PCA in a single annulus centered on the radial location of the companion candidate in order to detect the significance of the detection. It is also possible to study the evolution of its signal varying the $\mathrm{n_{pc}}$ values. When the number of principal components is maximized to get the better signal-to-noise, it is possible to estimate a first guess of the parameters separation, position angle and flux at each wavelength. This process can be done through

a simplex sampler, implemented in VIP. Moreover, using the technique of the negative fake companion (NEGFC, e.g., Lagrange et al. 2010; Wertz et al. 2017), it is possible to retrieve the astrometry and photometry, together with theirs errors, of the companion candidate tested. NEGFC uses the injection of negative PSF templates in the calibrated cube (before post-processing) at a location of the companion candidate (given as first estimate). Through the techniques used to post-process the data, it is done a minimization of a certain figure of merit in the post-processed image. This figure of merit can be chosen to reduce either the standard deviation or the residual absolute flux measured in an aperture centered on the companion in the final image. This is an iterative process which stops when the figure of merit is minimized. This search can be done through a a Monte-Carlo Markov Chain (MCMC) sampler, as implemented in VIP.

Chapter 7

An heterogeneous SPHERE-IFS Survey of Nearby Herbig Ae/Be Stars: Are All Group I Discs Transitional?

Based on the paper by **M. G. Ubeira Gabellini**, D. Fedele, M. van den Ancker, G. Lodato, C. F. Manara, V. Christiaens, D. J. Price: "An heterogeneous SPHERE-IFS Survey of Nearby Herbig Ae/Be Stars: Are All Group I Discs Transitional?"[1] in preparation.

The process of discs clearing surrounding pre-main sequence stars is still an open question regarding the origin of planetary systems. In particular, it is still debated what is the main driver of the planet formation process and disc dissipation and how gas and dust interact in the circumstellar material. In the case of intermediate pre-main sequence stars, it is under investigation whether there is a temporal evolution between Group I and Group II sources (Maaskant et al. 2013, 2014; Meeus et al. 2001).

In this chapter, we report SPHERE-IFS observations of the disc around 17 Ae/Be Herbig stars and five F and G type stars (AK Sco, S CrA, T Cha, HD 142527 and CQ Tau). For the post processing of the SPHERE data, we applied the state-of-the-art technique for noise subtraction (PCA-SDI) through the Vortex Image Pipeline (VIP, Gomez Gonzalez et al. 2018) for removal of speckles and adapt it to post-process IFS-SPHERE data. The evidences on the spectral and angular variation of speckles compared to the different behavior of the disc and companion were used to remove the speckles from the IFS cube and to probe the disc structure of our sample of stars. This powerful technique allowed us to detect disc structures in six out of 22 sources. If we consider both AK Sco and HD 141569 as a Group II following the definition of Meeus et al. (2001), the fraction with detected discs with respect to the total sources is 0.6 ± 0.3 for Group I sources, whereas for Group II it is 0.2 ± 0.1. This result favors the scenario of Group I being all transitional and Group II not detectable, as predicted. This result is reinforced if we do not consider HD 141569 and we classify AK Sco as a Group I following Garufi et al. (2017): the fraction is respectively 0.7 ± 0.3 for Group I sources, and zero for Group II. The disc shapes detected are various, going from ring structures to spiral arms. Among the disc structures, we detect also companions.

The structure of the chapter is organized as follows: Section 7.1 we gave a general overview of the topic, in Section 8.3 and 7.3 we describe briefly the observational and target properties. Section 7.4 and 7.5 describe the method used focusing on the disc emission. The method characterization is presented in Section 7.6. The observational results are showed in Section 7.7. Finally, we conclude in Section 8.6.

[1] Based on observations performed with ESO Telescopes at the Paranal Observatory the with SPHERE under the observing programs 095.C-0787(A), 095.C-1001(A), 095.C-0389(A), 095.C-0298(H), 095.C-0298(A), 095.C-0298(B), 095.C-0298(C), 097.C-0865(B), 099.C-0212(C) and 298.C-5014.

7.1 Motivation and context

In the context of planet formation, the process of clearing of discs surrounding pre-main sequence stars is one of the most important, yet poorly understood, processes relating to the origin of planetary systems. Recent high-resolution, high contrast observations at near-infrared and sub-millimetre wavelengths have revealed a plethora of substructure such as spirals (e.g., Muto et al. 2012; Pérez et al. 2016; Benisty et al. 2015, 2017), gaps (e.g., ALMA Partnership et al. 2015; Andrews et al. 2016; Fedele et al. 2017, 2018; Dipierro et al. 2018b; Andrews et al. 2018a), cavities (e.g., van der Plas et al. 2017b; Andrews et al. 2018a; Ubeira Gabellini et al. 2019), shadows (e.g., Itoh et al. 2014; Stolker et al. 2017; Benisty et al. 2018) and horseshoes (e.g., Casassus et al. 2013b; van der Marel et al. 2013) in protoplanetary discs. The origin of these substructures is highly debated, with proponents arguing for 1) Disc instabilities (e.g. Kratter & Lodato 2016); 2) The presence of a companion orbiting around the central star (e.g. Papaloizou et al. 2007; Dong et al. 2015b; Ragusa et al. 2018; Dipierro et al. 2018b); 3) Dispersal by photoevaporative winds (e.g. Clarke et al. 2001); 4) Grain growth (e.g. Dullemond & Dominik 2005; Ciesla 2007; Birnstiel et al. 2012a) and 5) Variable illumination (Montesinos et al. 2016) due to the disc self-shadowing.

The dust present in the protoplanetary discs is heated by the central star and possibly by the viscous heating of accreting material and emits above photospheric levels at infrared to mm wavelengths. Circumstellar gas instead shows up in free-free emission at radio wavelengths and through absorption and emission in spectral lines and molecular bands. The near-infrared scattered light emission traces the distribution of micron-sized dust particles (which are dynamically well-coupled to the gas) in the upper surface disc layers; whereas (sub-)millimetre continuum emission is sensitive to the distribution of large grains near the midplane.

Questions still open regard what is the geometry of the circumstellar material and how gas and dust disc evolve in the distribution and in the composition during the planet formation process. The Herbig Ae/Be (HAeBes) stars are the most suitable targets to study the disc geometry through spatially resolved observations thanks to the large contrast in brightness between the disc/companion and the central star and their disc structure has been investigated in different ways. Indirect methods that uses the IR spectrum to obtain information on the disc structure do not provide unique solutions. The most direct method is with spatially resolved observations, which have started to become feasible since the nineteens with HST. These type of observations are extremely challenging in the optical and near-IR because of the large contrast in brightness between the disc and the central star (e.g. HD 142527: Avenhaus et al. 2014b; HD 135344B: Stolker et al. 2016; HD 169142: Ligi et al. 2018; HD 100453: Benisty et al. 2017).

Meeus et al. (2001) divided the HAeBe sample into two groups, based on the slope of the far-IR continuum: 'Group I' sources have a Spectral Energy distribution (SED) with a strong near- to far-IR excess, whereas 'Group II' sources have a much weaker far-IR excesses and a similarly strong near-IR excess as the Group I's. Traditionally, the Spectral Energy Distributions (SEDs) of Group I sources are explained by the presence of a strongly flared disc which intercepts and reprocesses a large fraction of the stellar radiation field, whereas the discs of the Group II sources is hypothesized to be mostly in the shadow cast by the inner rim of the disc, which is puffed up by the stellar radiation (Natta et al. 2001; Dullemond et al. 2001). A more recent work done by Maaskant et al. (2013, 2014), based on marginally resolved Q-band emission and the presence of ionized PAHs, has shown that the large near-infrared excess observed in the SED of group I Herbig Ae/Be stars can also be explained by inferring the presence of a large gap in their

disc. On the contrary, the SED of Group II sources is more continuous and would not have such a large gaps. In the proposed scenario, most of the continuum emission would originate in the rims of the puffed-up inner disc that shadows large parts of the outer disc. Strong support for this theory was found in the work done by van der Plas et al. (2015), who studied ro-vibrational CO emission in a sample of 13 HAeBes. Almost all HAeBes showed thermally excited CO, whereas vibrationally excited CO and a mismatch between the rotational and vibrational temperature was only found in Group I sources, which is consistent with the presence of moderately sized disc gaps. Such systems are in the process of converting their disc from a continuous structure to a disc with (multiple) gaps or even a cavity, possibly interspaced with planets. A particularly interesting class of discs is made by the so called 'Transitional Discs' (TDs) (Espaillat et al. 2014), which are expected to be in transition phase from an optically thick disc full of gas and dust extending almost up to the stellar radii to object where the disc is fully dispersed. Such discs are considered excellent candidates to test planet formation theories. For this reason finding clear relations between disc classes and TDs would be extremely interesting.

Garufi et al. (2017, 2018), exploiting high contrast imaging, provided for the first time a disc taxonomy study using high-resolution images of Herbig Ae/Be stars to derive some general properties comparing different disc structures. In order to do this, they used observations taken in Polarimetric Differential Imaging. They compared Group II and I disc structures finding a clear difference between the two types mainly due to the absence or presence of large disc cavities. In particular, the authors found that Group I discs are systematically brighter than Group II sources because of their cavity. In such a way they agreed than generally Group II discs are not evolved versions of the Group I ones. Moreover, Garufi et al. (2017) found that all Group II share a common feature: the absence of any large (>5 au) disc cavity, which acts to leave the outer disc un-illuminated. Group II discs can be low-mass or high-mass discs. The former are most likely small discs ($R_{out} \lesssim 20$ au), while the latter are large discs. Small low-mass discs cannot open large cavities and thus discs are not observable from direct imaging nor from the SED. High-mass Group II discs are fairly rare. An example of them is HD 163296, which is a self-shadowed disc and it has all the potentialities to develop a disc cavity during its evolution and thus to become Group I discs (Garufi et al. 2017).

As shown, Garufi et al. (2017, 2018) provided a first direct observational confirmation of the Maaskant et al. hypothesis. A strong prediction of the Maaskant et al. scenario is indeed that the outer edge of the dust gap should be visible in scattered light for the Group I sources, but not for the Group II's. The typical location of the outer edge of the dust gap is several tens of au (van der Plas et al. 2015). The study of Garufi et al. (2017) was performed through PDI, which allows to better subtract the stellar contribution, but it deals just with a small fraction of the scattered light (see Chap. 2.4.7). It is still so far lacking a confirmation done through observations in total intensity scattered light (e.g., with SPHERE-IFS). The comparison of IFS and PDI images would also allow to shed light on how the polarization fraction may depend on e.g., the disc geometry. If the Maaskant et al. scenario is correct, we expect to be able to spatially resolve rim-like structures in a significant number of the surveyed Group I sources, whereas all Group II's should be unresolved. The goal of this work is to provide a systematic, heterogeneous, survey of extended emission from HAeBe discs on sub-arcsecond angular scales with the high-contrast imaging facility SPHERE. This will allow us to test the Maaskant et al. hypothesis that all Group I HAeBes are transitional.

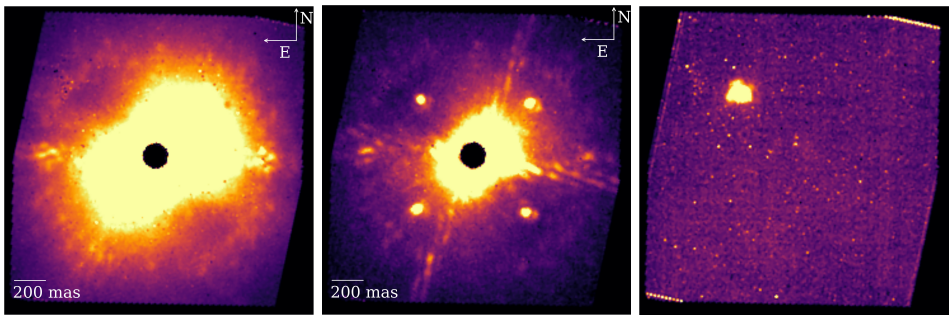

Figure 7.1: Stacked SPHERE IFS images of HD 139614 at $\lambda = 1.246$ μm obtained on 2015-04-21, showing the object behind the coronagraph (left), Star Center image (center), and the flux calibration image (right). The total field-of-view is $1\farcs8$ x $1\farcs8$ in all images. We used a color scale with the color bar going from a minimum value zero to the maximum value of the map divided by ten. This is done to show the peculiarity of each image.

7.2 Observations

Data on 22 HAeBe, F and G stars were obtained between May 2015 and August 2017 with SPHERE, the Extreme Adaptive Optics System and Coronographic Facility at the VLT. We refer to Chap. 6 and Appendix A for an overview on the technique and on the instrument. The observations have been executed either in the IRDIFS-EXT mode i.e. simultaneous Integral Field Spectroscopy (IFS), and dual-band imaging in the K-band, or IRDIFS mode, producing simultaneous IFS spectroscopy and imaging in the H-band. The IFS data are cubes of 39 monochromatic images in the near-IR wavelengths. The spectral resolution is R$\sim$50 for the IRDIFS mode (Y-J, $0.95< \lambda <1.35$ μm) or R$\sim$30 for the IRDIFS-EXT mode (Y-H, $0.95< \lambda <1.65$ μm). The Field of view of the SPHERE IFS is $1.73''$ x $1.73''$ and for the simultaneous imaging with IRDIS it is $11''$ x $11''$. The N-ALC-YJH-S coronagraph (inner working angle IWA$\sim$0.15$''$) was used for all targets with the exception of HD 142527 and HD 97048, which were observed without a coronagraphic mask.

We carried out a relatively deep (30 min.) exposure on the outer (150–1000 mas) disc. For each science targets, we obtained SPHERE "Flux and Star Center" calibration images. For the flux images, a set of images was taken by offsetting the central star from the coronagraphic spot (shallow 5 min. exposure) to measure the unsaturated peak flux of the star. This allows the measurement of the photometry at each wavelength and the contrast calibration. Moreover, in order to measure accurately the exact position of the star another set of calibration images was used: the Star Center images (e.g., Fig. 7.1, middle panel). They are produced by the adaptive optics system, which creates a waffle pattern on the deformable mirror to produce four replicas of the PSF hidden behind the coronagraphic spot at specific locations away from the coronagraphic mask. Localizing the four peaks is used to accurately measure the position of the star behind the coronagraph, which is placed at the center of the four echoes. Observations were in general followed by a short (15 min.) observation of a PSF reference star, which may help for instrumental artifacts called speckles (see Chap. 6). Almost all the targets of our sample described in Table 7.2 are observed with a help of a coronagraph. We decided to complete our sample with two sources (HD 97048 and HD 142527) where the coronograph was not applied for comparison.

Table 7.1: Target observational properties.

ID	day of obs.	sources	R.A. (2000.0)	Dec.	obs ID	obs. mode	Int. time[s]	Tracking
1	2015-07-18	HD 104237	12 00 05.12	-78 11 34.7	095.C-0787	IRDIFS-EXT	1568	FIELD
2	2015-08-26	HD 132947	15 04 56.06	-63 07 52.7	095.C-0787	IRDIFS-EXT	576	FIELD
3	2015-04-21	HD 139614	15 40 46.39	-42 29 53.6	095.C-0787	IRDIFS-EXT	2560	FIELD
4	2015-07-30	HD 142666	15 56 40.02	-22 01 40.0	095.C-0787	IRDIFS-EXT	2720	FIELD
5	2015-08-26	HR 5999	16 08 34.28	-39 06 18.2	095.C-0787	IRDIFS-EXT	1792	FIELD
5	2015-08-17	HR 5999	16 08 34.28	-39 06 18.2	095.C-0787	IRDIFS-EXT	2016	FIELD
6	2017-08-18	HD 145718	16 13 11.59	-22 29 06.2	099.C-0212	IRDIFS-EXT	1536	PUPIL
6	2017-08-20	HD 145718	16 13 11.59	-22 29 06.2	099.C-0212	IRDIFS-EXT	1536	PUPIL
7	2015-06-24	HD 150193	16 40 17.92	-23 53 45.2	095.C-0787	IRDIFS-EXT	2560	FIELD
8	2015-07-30	AK Sco	16 54 44.85	-36 53 18.5	095.C-0787	IRDIFS-EXT	2560	FIELD
9	2015-08-28	KK Oph	17 10 08.11	-27 15 19.0	095.C-0787	IRDIFS-EXT	2112	FIELD
10	2015-04-29	MWC 297	18 27 39.53	-03 49 52.1	095.C-0787	IRDIFS-EXT	1664	FIELD
10	2018-07-28	MWC 297	18 27 39.53	-03 49 52.1	0101.C-0350	IRDIFS-EXT	5760	PUPIL
11	2015-06-10	R CrA	19 01 53.66	-36 57 07.9	095.C-0787	IRDIFS-EXT	1792	FIELD
12	2015-06-12	S CrA	19 01 08.61	-36 57 19.7	095.C-0787	IRDIFS-EXT	2560	FIELD
12	2015-06-22	S CrA	19 01 08.61	-36 57 19.7	095.C-0787	IRDIFS-EXT	2720	FIELD
12	2015-06-25	S CrA	19 01 08.61	-36 57 19.7	095.C-0787	IRDIFS-EXT	2560	FIELD
13	2015-06-22	HD 179218	19 11 11.25	+15 47 15.6	095.C-0787	IRDIFS-EXT	2560	FIELD
14	2015-06-19	HD 190073	20 03 02.51	+05 44 16.7	095.C-0787	IRDIFS-EXT	2560	FIELD
14	2015-06-20	HD 190073	20 03 02.51	+05 44 16.7	095.C-0787	IRDIFS-EXT	2560	FIELD
15	2016-05-08	HD 97048	11 08 03.30	-77 39 17.4	097.C-1001	IRDIFS-EXT	760	PUPIL
15	2016-06-04	HD 97048	11 08 03.30	-77 39 17.4	097.C-1001	IRDIFS-EXT	760	PUPIL
16	2015-04-10	HD 100453	11 33 05.60	-54 19 28.5	095.C-0389	IRDIFS-EXT	1600	PUPIL
16	2016-01-16	HD 100453	11 33 05.60	-54 19 28.5	095.C-0389	IRDIFS-EXT	1280	PUPIL
16	2016-01-21	HD 100453	11 33 05.60	-54 19 28.5	095.C-0389	IRDIFS	1600	PUPIL
16	2016-01-23	HD 100453	11 33 05.60	-54 19 28.5	095.C-0389	IRDIFS-EXT	1280	PUPIL
17	2015-02-07	HD 100546	11 33 25.43	-70 11 41.3	095.C-0298	IRDIFS-EXT	1472	PUPIL
17	2015-05-04	HD 100546	11 33 25.43	-70 11 41.3	095.C-0298	IRDIFS-EXT	4096	PUPIL
17	2015-05-29	HD 100546	11 33 25.43	-70 11 41.3	095.C-0298	IRDIFS	3840	PUPIL
17	2015-05-30	HD 100546	11 33 25.43	-70 11 41.3	095.C-0298	IRDIFS	2304	PUPIL
17	2016-05-31	HD 100546	11 33 25.43	-70 11 41.3	097.C-0865	IRDIFS-EXT	4400	PUPIL
18	2015-05-30	T Cha	11 57 13.53	-79 21 31.5	095.C-0298	IRDIFS	3840	PUPIL
18	2015-05-31	T Cha	11 57 13.53	-79 21 31.5	095.C-0298	IRDIFS	2304	PUPIL
19	2015-05-16	HD 141569	15 49 57.76	-03 55 16.2	095.C-0298	IRDIFS	4096	PUPIL
20	2015-05-06	HD 142527	15 56 41.89	-42 19 23.3	095.C-0298	IRDIFS-EXT	2304	PUPIL
20	2015-05-14	HD 142527	15 56 41.89	-42 19 23.3	095.C-0298	IRDIFS-EXT	2304	PUPIL
21	2015-06-07	HD 169142	18 24 29.78	-29 46 49.4	095.C-0298	IRDIFS	6144	PUPIL
21	2015-06-28	HD 169142	18 24 29.78	-29 46 49.4	095.C-0298	IRDIFS-EXT	5120	PUPIL
21	2015-07-04	HD 169142	18 24 29.78	-29 46 49.4	095.C-0298	IRDIFS-EXT	512	PUPIL
21	2015-07-05	HD 169142	18 24 29.78	-29 46 49.4	095.C-0298	IRDIFS-EXT	3200	PUPIL
22	2016-12-21	CQ Tau	05 35 58.46	+24 44 54.09	298.C-5014	IRDIFS-EXT	7680	PUPIL

Notes. In this table we present the the day of observation, the name of the target, the astronomical coordinates, the proposal observing number, the observing mode, the total integration time and the telescope tracking mode. The top part of the Table refers to new data specifically obtained for this work (095.C-0787, 099.C-0212, PI: van den Ancker), while the bottom half includes archival data (097.C-1001, PI: Matter; 095.C-0389, PI: Apai; 095.C-0298, PI: Beuzit; 298.C-5014, PI: Testi).

7.3 Target properties

Targets were taken from the catalogues of Thé et al. (1994) and Vieira et al. (2003), and further selected to be (i) relatively nearby (d = 100–400 pc, as determined from either literature or associations with nearby star forming regions), so as to optimize our chances of spatially resolving the disc, (ii) sufficiently bright to get good AO correction with SPHERE (i.e. R < 11 mag), and (iii) observable from Paranal. The sample consists of 22 sources, of which 14 were taken within the ESO observing program 095.C-0787 (PI: M. van den Ancker) completed with seven of the targets included in the SPHERE Guaranteed Time Observation Programme target list with the addition of the CQ Tau target. SPHERE-IFS data on those stars were already present in the ESO archive (note that, for most of these targets, previous detections of spatially extended emission exist in the literature, so we can use these data to complete our sample statistics). For the others, new data were obtained and the present chapter contains the first analysis of these data. Together, our sample comprehends the most complete set of nearby known HAeBes and it is representative for the class of isolated HAeBes.

Table 7.1 summarizes the observations, including a distinction between the new data presented here and archival data. Table 7.2 contains the basic stellar and disc properties of the sample. The effective temperature was derived from the spectrum, and the age, luminosity and mass were taken from Vioque et al. (2018a) if possible. When the targets were not present in the sample of Vioque et al. (2018a), we derived the bolometric luminosity integrating under the SED, corrected for extinction. Finally, we derived mass and age from luminosity and effective temperature, using PARSEC isochrones (Bressan et al. 2012; Marigo et al. 2017) from 0.01 to 20 Myr and solar metallicity (Z=0.0152), as done in Vioque et al. (2018a). We chose the best match through a minimization of χ^2. We computed a weighted average of mass and age between the closest two isochrone points (Table 7.2). To estimate the error, we computed the discrepancy with the derivation of Vioque et al. (2018a) and with different models (e.g., Siess et al. 2000), resulting in an average discrepancy in mass of 0.3 $M_\odot$ and in age of 2 Myr. We warn the reader that systems with estimated ages below 20 Myr can have non negligible age spreads due to quite large observational uncertainties (e.g., Soderblom 2015). Regarding the classification of Group I versus Group II we followed the definition of Meeus et al. (2001) (see Tabel 7.2). We note, however, that HD 141569 was considered by van der Plas et al. (2015) to be neither a Group I or Group II, because it is a hybrid disc between Class II and debris disc phase. Also AK Sco is a peculiar target: following the definition of Meeus et al. (2001) it is a Group II (it has low far-IR excess), while considering the m_{30}-m_{13} criterion (see Garufi et al. 2017), it is a Group I.

In this way our sample consists of one of the largest and heterogeneous set of nearby (within $\sim$ 400 pc) known Herbig representative for the class of isolated Herbig, observed by SPHERE-IFS and analyzed in a consistent way. We refer to Appendix D where previous discoveries on each targets are fully described. The science observations were, most of the time, followed by a short observation of a PSF reference stars, i.e. stars with no circumstellar disc, to use as a check to test the post-processing method we used. Our reference star sample consists of 12 stars (see Table 7.3). They were chosen to be with spectral type and magnitude similar to the one of the stars used for our science case. Note that although our observations are relatively shallow, HAeBe discs are bright (H = 3.5-8.6 mag in our sample), so the main challenge in these observations is to correct for instrumental artifacts such as speckles.

Table 7.2: Target properties. We list in columns the name of the target, the region where they are, the distance with ref., the typology of the disc from the SED, the age of the target, the spectral type with ref., the effective temperature, the extinction, the bolometric luminosity, the mass and radius (derived from the other values reported) of the star, the IR over stellar luminosity and the disc detections. * Although a parallax is given for R CrA in the Gaia 2nd data release, the resulting distance of 95 pc would imply a distance much closer than the one of all other stars in the same star forming region, which is implausible. We therefore adopt the new distance determination by Mesa et al. (2019) for R CrA, whose value is close to the one found in a recent work by Dzib et al. (2018).

ID	Target name	Region	d[pc]	Ref.	Group	age [Myr]	Sp.T.	Ref.	Teff[K]	Av[mag]	log(Lbol)	M[$M_\odot$]	R[$R_\odot$]	L_{IR}/L_*	disc detections
1	HD 104237	Cha III	108	DR2	II	5 [A]	A4IVe+sh	V98	8410	0.29	1.33[A]	1.85[A]	2.4	0.28	no detections
2	HD 132947		382	DR2	II	4 [A]	B9V	L06	10500	0.34	1.61[A]	2.22[A]	1.9	0.07	no detections
3	HD 139614	Sco OB2-3	135	DR2	I	14 [A]	A7Ve	D97	7850	0.12	0.77[A]	1.48[A]	1.3	0.40	no detections
4	HD 142666	Sco OB2-2	149	DR2	II	9 [A]	A8Ve	D97	7580	0.96	0.94[A]	1.49[A]	2.0	0.31	no detections
5	HR 5999	Lupus 3	161	DR2	II	3 [A]	A5-7III/IVe+sh	T89	7930	0.49	1.72[A]	2.43[A]	3.8	0.41	no detections
6	HD 145718	Sco OB2-2	152	DR2	II	10	A5Ve	C10	9200	2.01	0.93	1.80	2.5	0.04	no detection
7	HD 150193	rho Oph	151	DR2	II	5 [A]	B9.5Ve	L06	10000	1.19	1.37[A]	1.89[A]	1.8	0.30	no detections
8	AK Sco	Sco OB2-1	141	DR2	II	8 [A]	F5+F5IVe	A89	6450	0.62	0.62[A]	1.40[A]	2.2	0.21	**inclined disc**
9	KK Oph	Sco OB2-2	221	DR2	II	18 [A]	A6Ve	H05	8500	2.32	0.71[A]	1.51[A]	1.3	1.50	no detections
10	MWC 297	(L515)	375	DR2	I	<1 [C,A]	B1.5Ve	D97b	23700	7.72	4.59[A]	16.9 [A]	9.17	0.07	no disc det.
11	R CrA		153*	M18	II	9	A1e-F7evar	V98	8200	3.30	0.99	1.89	2.2	–	no disc det.
12	S CrA	NGC 6729	130	DR2	II	9	G5Ve	C10	5770	1.32	0.38	1.45	1.0	–	no detections
13	HD 179218	L693	266	DR2	I	2 [A]	A0IVe	M01	9810	0.37	2.05[A]	2.98[A]	3.7	0.39	no detections
14	HD 190073		890	DR2	II	<1 [F]	A2IVpe	M01	8990	0.16	2.75[F]	5.60[F]	9.8[F]	0.31	no detections
15	HD 97048	Ced 111	185	DR2	I	4 [A]	B9.5Ve+sh	W87	10000	1.21	1.54[A]	2.25[A]	2.0	0.37	no detections
16	HD 100453	Sco OB2-4	104	DR2	I	7 [A]	A9Ve	G06	7390	0.05	0.79[A]	1.25[A]	1.5	0.68	**spiral disc**
17	HD 100546	Sco OB2-4	110	DR2	I	5 [A]	B9Vne	L06	10500	0.22	1.37[A]	2.05[A]	1.8	0.63	**asymmetric disc**
18	T Cha	DC300.2-16.9	110	DR2	I	9	G8e	S09	5570	1.30	0.35	1.41	2.0	0.30	**inclined disc**
19	HD 141569	(L169)	111	DR2	II	9 [A]	A0Ve	D97	9520	0.31	1.22[A]	1.86[A]	1.7	0.02	**ring detection**
20	HD 142527	Sco OB2-3	157	DR2	I	7 [A]	F7IIIe	V98	6260	1.23	0.96[A]	1.61[A]	4.2	0.38	no detection
21	HD 169142	Sco OB2-1	114	DR2	I	9 [A]	A5Ve	D97	8200	0.93	1.31[A]	2.00[A]	1.8	0.25	**ring detection**
22	CQ Tau		163	DR2	I[G]	9 [A]	F2	H60	6750[A]	0.87[A]	1.47[A]	1.7[A]	1.8	-	**asymmetric disc**

References: A89 = Andersen et al. (1989), C10 = Carmona et al. (2010), D97 = Dunkin et al. (1997), D97b = Drew et al. (1997), DR2 = Gaia Collaboration et al. (2018), G06 = Guimarães et al. (2006), H05 = Hernández et al. (2005), L06 = Levenhagen & Leister (2006), M01 = Mora et al. (2001), S09 = Schisano et al. (2009), T89 = Tjin A Djie et al. (1989), V98 = van den Ancker et al. (1998), W87 = Whittet et al. (1987), M18 = Mesa et al. 2019, H60 = Herbig (1960); A=Vioque et al. 2018a, C=Acke & van den Ancker 2006, F=Setterholm et al. 2018, G=Mendigutía et al. 2012.

7.4 Data Calibration

For all the targets described we have used the ESO pipeline[2] to reduce the IFS data. The data reduction was applied to a different set of images: the image with or without coronagraph applied, the Star Center image and the Flux calibration image. In particular, we used the Star Center image in order to accurately measure the position of the star behind the coronagraph and for the post-processing. We, instead, used the flux calibration image in order to estimate the stellar photometry at each wavelength. The pipeline creates a master dark, a master flat, which are subtracted from the raw images. It then generates a distortion map in order to correct for instrumental distortion, combines the images, re-arranges data to create the image cube of 39 wavelengths, and finally applies a wavelength-calibration and distortion correction to the data. Examples of the direct data products produced by the SPHERE pipeline are shown in Fig. 7.1.

7.4.1 Bad pixels corrections

In addition to these standard data-reduction steps, we applied a bad pixel correction, which is not used in the default pipeline. The output of the ESO pipeline is a set of different images for the same day with a specific orientation. This was in any case leaving with several bad pixels. In order to remove also them, we applied a bad pixel correction, using a function implemented in the Vortex Imaging Pipeline[3] (VIP, Gomez Gonzalez et al. 2017b). This is an iterative process that corrects clumps of bad pixels through sigma filtering (replacing by the median of neighbouring pixel values).

7.4.2 Coronagraphic or not coronagraphic PSF centering

In the case where the coronagraph was applied, we measured the position of the star from the center images in each frame using the four replicas present in such images, using VIP. To increase the signal-to-noise of the star replicas used for the centering, we used a high-pass filter which subtracts the image itself with a median low-pass filtered version of the image. We fitted the four replicas with a 2D Moffat function (in VIP) to derive the centroid of the star in each frame. We set the threshold to 5, 3 and 2 σ and took a median of the three central positions (the values found were really close). An example of the shift in x and y is shown in Fig. 7.2. This was done both for the couple of center images taken at the beginning (considered as their average) and for one at the end of the set of science images. In Fig. 7.3, we show one of the waffles images with on top the position found by the algorithm using the different threshold. In the case presented the center is found in all of them, showing how precise can be this measurement. We applied a mask in the inner part of the image to obscure the contribution coming from the center, which was confusing the method and giving less accurate results. We then interpolated the values of the derived center (taken at the beginning and end of the observations) considering the observation time of the science images. Finally, the error was considered to be the discrepancy in the value between two sequential sets of center images. The errors decrease with increasing wavelength.

In the case where no coronagraph was applied, the position of the star on the detector is moving over time and the frames are not perfectly centrated throughout the observations. To determine the exact location of the centroid for non-saturated non-

[2]http://www.eso.org/sci/software/pipelines/sphere/; v0.24.0; v0.36.0, for the recent data.
[3]https://github.com/vortex-exoplanet/VIP.

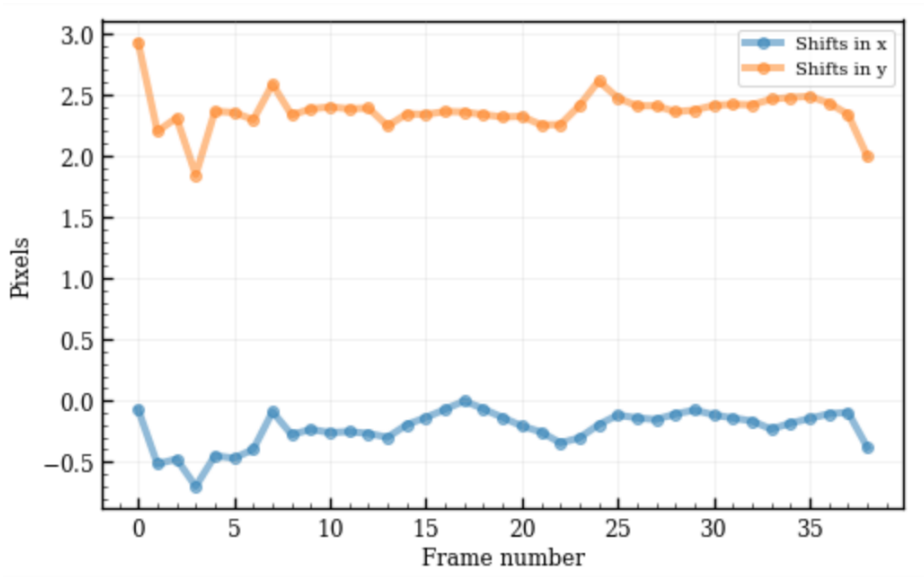

Figure 7.2: An example of the result on a fit of the four replicas with a 2D Moffat function (in VIP). The shift of the centroid of the star was derived in each frame. Here it is presented the case where the threshold was set to 2 σ.

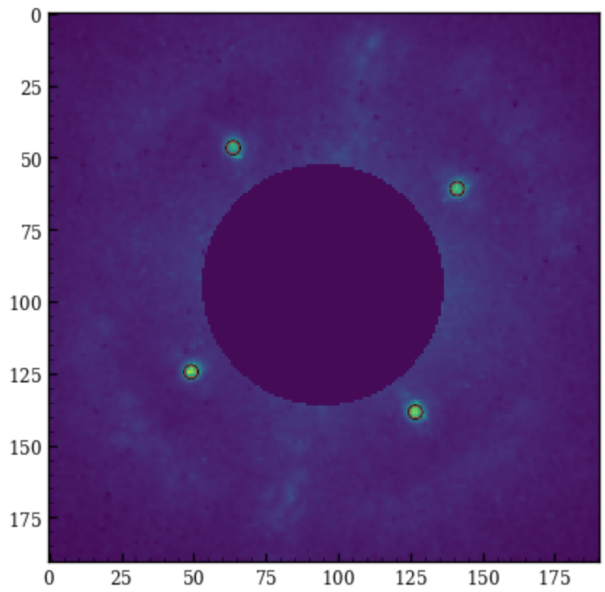

Figure 7.3: An example of a waffles image (at a specific wavelength) with on top (circle) the result on a fit of the four replicas with a 2D Moffat function (in VIP).

coronagraphic frames, we used a Gaussian fit on each cube. This fit was done using VIP for HD 142527 and HD 97048.

7.4.3 Post-processing with VIP

The ESO pipeline calibrated images have to be converted in order to be used by VIP. We thus implemented a pipeline (described in the Section above) which creates a format able to be used by VIP. This step is done in a completely automatized way. We inspected all the data here presented in all the steps. It was, indeed, important to use a semi-automatic routine and then do a visual inspection of intermediate products at several key steps of the process. Due to the differences in specific characteristics of the observation or of the source, we modified the pipeline to best post-process each of these data. The output from the ESO pipeline is composed by a set of images divided in DIT and NDIT. The information regarding the neutral density and rotation of the image is inside the header and it has to be applied before being used by VIP. In the following we will give a summary of the main steps needed for the post-process application, provided in the same order as they are performed in the pipeline implemented.

Rotation of the images

The first step is computing the value of the rotation of each cube taken simultaneously. The ESO pipeline gives as input the images not rotated and it does not provide a file of rotation angles. We astrometrically correct each image as described in the SPHERE Users Manual[4] (Section 8, Version P103) and in Maire et al. (2016). This is done in a different way for Field and Pupil tracking mode. For the Field tracking mode, the position angle (PA) corresponds to:

$$PA = TN + IFS_{\text{offset}} \tag{7.1}$$

where the IFS offset is fixed and equal to -100.48 deg and TN stays for True North, which can be found as: TN = ϵ-1.75, where ϵ is:

$$\epsilon = \arctan\left[\tan(ALT_{\text{START}} - PARANG_{\text{START}} - 2 * DROT2_{\text{BEGIN}} * \pi/180)\right] * 180/\pi \tag{7.2}$$

where ALT_{START} and $PARANG_{\text{START}}$ are the telescope altitude and parallactic angles at the beginning of the observations provided by the telescope control software and $DROT2_{\text{BEGIN}}$ is the position angle of the SPHERE derotator at the beginning of the observations calculated by the SPHERE lighting control unit (LCU).

In the case of Pupil tracking mode, instead,

$$PA = PARANGLE + TN + PUPIL_{\text{offset}} + IFS_{\text{offset}} \tag{7.3}$$

The True North was computed as for the field tracking mode, the value of ϵ is however different:

$$\epsilon = \arctan\left[\tan(ALT_{\text{START}} - 2 * DROT2_{\text{BEGIN}} * \pi/180)\right] * 180/\pi \tag{7.4}$$

The pupil offset is a constant value: +135.99 deg. ALT_{START} and $DROT2_{\text{BEGIN}}$ are the same as described above. For simplicity, during this survey we consider as paralactic angle (PARANGLE) the average between the values written in the header the paralactic angle at the star and the end of each DIT sequence. The possibility of doing an interpolation of paralactic angles through the sequence was also implemented. We have checked that this do not make a huge difference in the final results of this study, but makes the VIP

[4] https://www.eso.org/sci/facilities/paranal/instruments/sphere/doc/VLT-MAN-SPH-14690-0430_P103_phase2.pdf

routine extremely longer and with heavy outputs. Important to note that for both Field and Pupil tracking mode, the value of ϵ is equal to zero for data taken after the 13rd of July 2016. The rotation to be applied is -PA.

Neutral density correction

The next step is the correction for neutral density. From the keyword in the header: 'HIERARCH ESO INS4 FILT2 ID', we could access to the neutral density value used for the observations. In general, the neutral density was used in the "FLUX" image or in the observations taken without coronagraph in order to avoid saturation. We note that the value to correct the image is a function of the wavelength associated to a keyword inside the header. The neutral density used can be 'OPEN', meaning no neutral density was applied, ND1, ND2 and ND3.5 in a crescent order. In Fig. 7.4 it is shown the case of neutral density equal to ND2. We then, interpolated the given curve for the specific neutral density used with the IFS wavelengths and use these values to correct the image for.

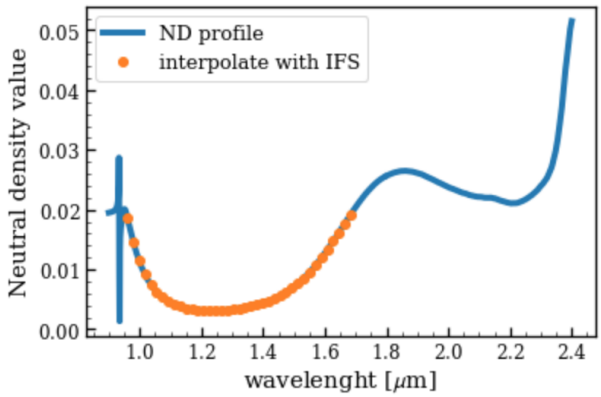

Figure 7.4: Neutral density profile for SPHERE-IFS. The blue line is the tabulated curve for a neutral density of ND2. The orange dots are the interpolated points for the wavelengths correspondent to IFS.

Imaging co-adding

The final step is the combination of the images with same position angle and the correction for the exposure time used. The ESO pipeline produce as many 3D cubes as the number of DIT times NDIT. We reduce the number of images by averaging the 3D cubes within the same DIT and with the same PA computed as described before. At the same time, we divided each 3D cube, by the exposure time of each set. In such a way the new cube is in ADU/s (Analog-Digital Units per second) units. The exposure time is just the value of DIT, because the images of different NDIT where not co-added. We note that without doing this step PCA is extremely CPU-intensive on cubes made of several thousand frames, and the results do not change much with this approximation. We then combine the calibrated cubes to have all of them in the same 4D cube, adding the temporal information.

7.5 Post-processing: PCA-SDI

The calibrated cube as described in the previous section, is still affected by quasi-static speckles produced by the star (Marois et al. 2006). Our data contains the following information: speckles change radial position with wavelength, while real features remain fixed (spectral information). This is key to the Spectral Differential Imaging (SDI) algorithm (e.g., Sparks & Ford 2002, see Section 6.4.2). Thanks to the use of IFS cubes, we can have the spectral information. The wavelengths are, indeed, taken simultaneously over an integration set. We used the principal component analysis (PCA, Sec. 6.5.2)-based algorithms in VIP to model and subtract the stellar PSF and associated speckles. PCA can be used coupled to other routines (see Chapter 9). For this study, we applied PCA with SDI, using the spectral information alone. For the purpose of this study we need to distinguish just if a disc is or not present: PCA-SDI is the most suitable because it do not subtract symmetric disc features. The ADI-based techniques, indeed, can distort the disc structures or delete the contribution coming from symmetric features. We refer to Chapter 9 for what concern the comparison on the disc structure observed using different techniques.

PCA-SDI has several advantages compared to traditional speckle noise reduction procedures such as angular differential imaging (ADI): (i) IFS data at different wavelengths are taken simultaneously, so our method is not sensitive to variations of the PSF over time; (ii) no field rotation is needed for speckle subtraction, so any star can be observed even if close to the zenith and (iii) there is no self-subtraction of extended emission (e.g., radially symmetric features as a ring in the protoplanetary disc). Clear disadvantages are that this does not subtract well the diffraction spikes due to reflections from the support structure of the secondary mirror of the VLT (for which ADI works well) and our field of view is small in comparison to the ADI technique (which can use regular imaging instead of an Integral Field Spectrograph). We note that our targets have been taken both in field and pupil tracking mode. For this reason, the only use of the ADI technique would be impossible considering it is feasible only when pupil tracking mode is applied.

A parameter relevant for PCA-SDI is to provide the scale list e.g. the values of wavelength of the IFS cube, divided by the maximum wavelength. The number of principal components (npcs) used to do PCA-SDI was set to one. We have also tested other values (see Chapter 9), but given the fact that best solutions have been found with different npcs for each source, we conservately choose the first value. We masked the central pixel with a circle of radius 80 mas in the images where the coronagraph was applied.

For each source, we used the same algorithm to have an homogeneous study over the whole sample. The cube of dimension 291 x 291 pixels, was cropped in size as 251 x 251. PCA-SDI, present a bright emission in the corners, so cropping the image helps to have a much cleaner images and better distinguish the presence of a disc emission in the inner disc part.

7.6 Method characterization

7.6.1 Reference Stars

We used the reference stars observed for our sample to better characterize our method. This is a sample of 12 stars and in three of them we found a putative binary companion (HIP 93580, HIP 96199, HIP 84147). We used the same method applied to the science targets (PCA-SDI). We note that the total exposure time for each of these targets is low ($\sim$ 64 s), much shorter than the total exposure time used for our science targets

Table 7.3: Reference stars properties. We note that we found point-like sources close to four of the reference stars in our sample. We do not include them in the ones used to test our methods.

Ref. Star	HIP 81903	HIP 93580	HIP 96199	HIP 101800	HIP 94651	HIP 99742
main star	HD 139614	MWC 297	R CrA	HD 190073	S CrA	HD 179218
V [mag]	6.199	5.815	6.94	5.418	6.97	4.946
SpT	A4V	A4IV/V	A0IV/V	A1IV	A3V	
note	double obs.	binary	binary	–	double obs.	–
Ref. Star	HIP 84147	HIP 76170	HIP 86098	HIP 81903	HIP 87794	HIP 77785
main star	HD 150193	HD 130437	AK Sco	HR 5999	V921 Sco	HD 132947
V [mag]	6.499	6.70	6.463	6.199	6.77	6.533
SpT	A0V	A2V	A4V	A9/F0IV	A5IV	
note	binary	–	–	double obs.	–	–

(see Table 7.1). We measured the peak flux of the contrast curve in the image with all the wavelengths combined (HJY) for the targets with no binary and where an evident maximum is present. Those reference stars, indeed, are expected not to have a disc. For this reason, the drop inside a certain radius in the contrast curve cannot be due to physical effects. We here report the average between the values of radius for which a drop in the flux was found: 107 mas for the HJY combined image. We see also in the reference stars images the presence of a bright ring at the edge of the coronagraph mostly symmetric, remnant of stellar light. The final radius where the PSF residual is found on average corresponds to 129 mas. We note also that the corner of the post-processed images is quite bright using PCA-SDI, mainly for images observed in FIELD tracking mode, as in the case of the reference stars. We note that the artifacts evident in the reference stars images are also present in our science targets. However, in this case the effect is amplified by the fact that the exposure time was shorter. The presence of the bright circle near the coronagraphic spot is due to the fact that the coronagraph is not able to completely remove the stellar PSF. Such axisymmetric feature cannot be removed by a purely radial stretching of the images as done in our method. In Table 7.3 we list all the reference stars used to characterize our method. The reference stars have a similar spectral type of our targets. In the table we listed the V magnitude and the spectral type. Moreover, we note where we found a putative binary companion around one of the reference stars or where there were more than one observations for source. In the case of HIP 93580, in order to produce the contrast curves, we had to estimate the companion flux through a simplex algorithm at all the wavelengths. In that was it was possible to remove the signal of the companion from the original data cube and process the contrast curve with no point-like source signal. The binary is indeed, really bright and it was creating a bump in the contrast curve signal. This is the same procedure done for the science targets.

7.6.2 Contrast curves, SNR and STIM map

For all our targets we used the contrast curves to estimate the sensitivity achieved in the final images (see Section 6.6.2). In all the contrast curves, we estimated a 1-σ noise and divide it for the throughput measured at each radius (see Fig. 7.6). In all the images, it is possible to see that they reach a better contrast for radii larger than 0.2 arcsec and smaller than 0.7 arcsec. We found the best contrast for the targets: HD 100453, HD 100546, HD 141569, HD 169142 and HD 190073, with delta magnitude reaching 14 magnitude. The worst contrast is, instead, achieved by HD 142527, HD 97048, S Cra,

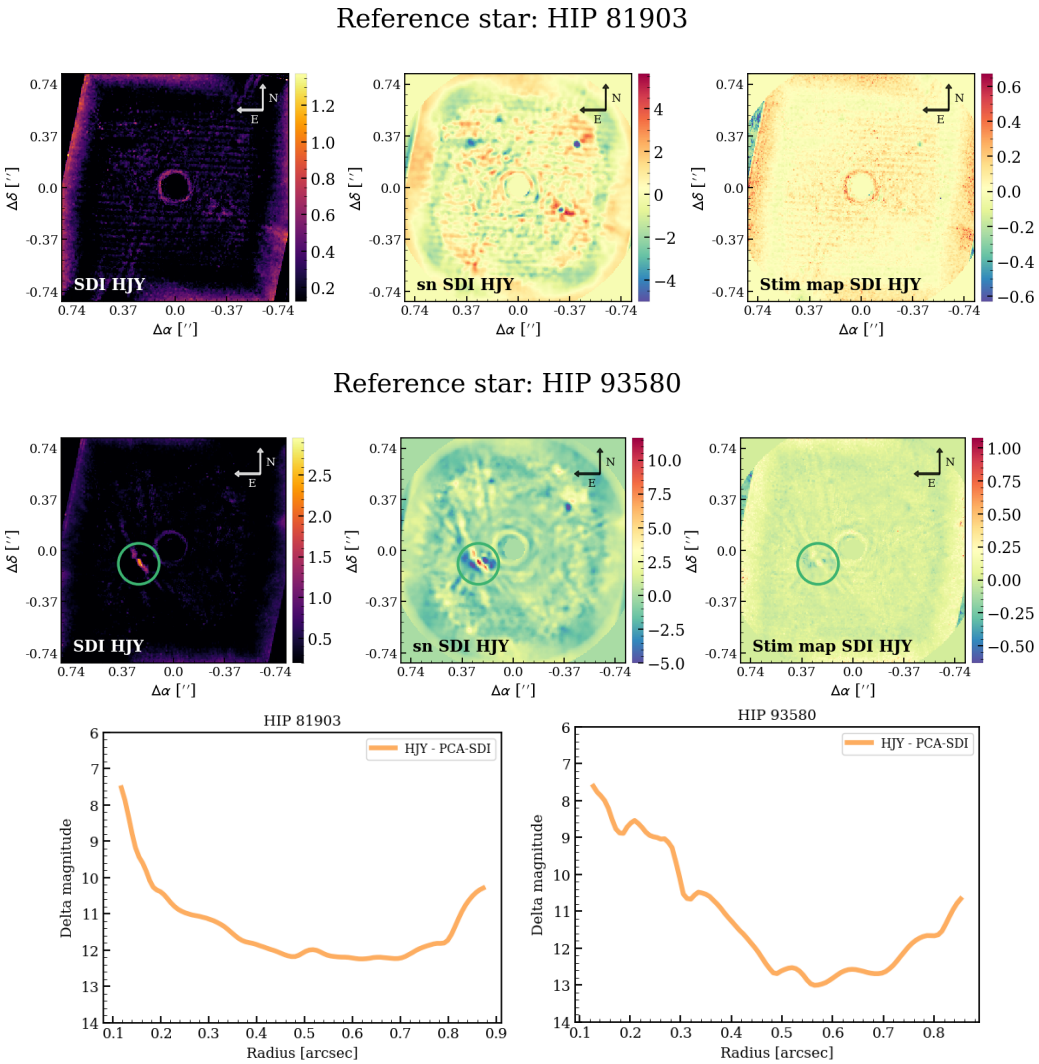

Figure 7.5: Final images for the reference star HIP 81903 (top) and HIP 93580 (central panel) after using the PCA-SDI method (left), the signal-to-noise of the image (center) and the STIM map (right). The reference star HIP 81903 shows an example of source with no disc and no companion. The reference star HIP 93580 shows the case of a companion candidate detection (green circle). The colorbar of the image on the left is in ADU/s, as minimum we used the measured standard deviation in an annulus far from the corner and from the inner part. We show the contrast curves for PCA-SDI for the two targets (bottom row).

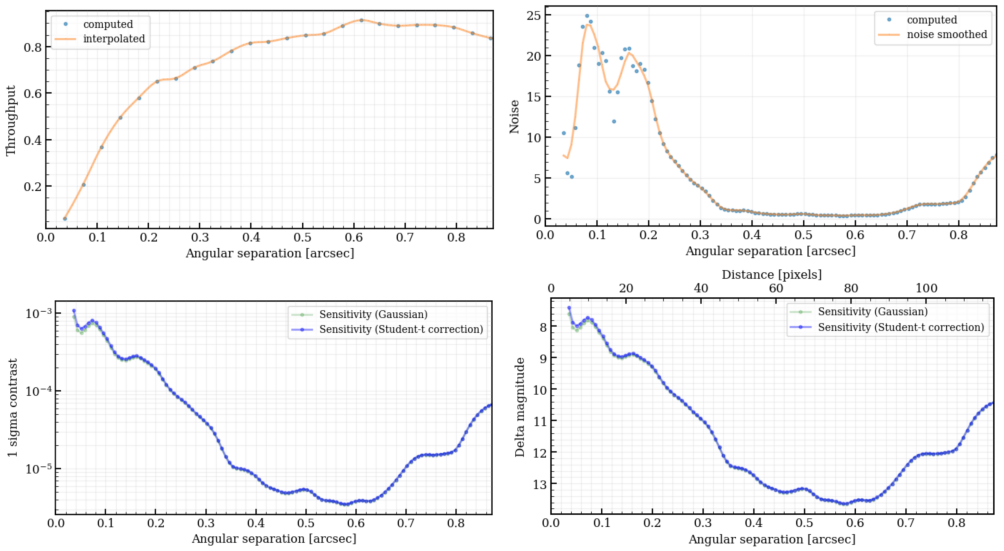

Figure 7.6: Throughput (upper left), noise (upper right), contrast (bottom left) and contrast in magnitude (bottom right) for the HD 100453 target of the observing day 2015-05-04 using the PCA-SDI method for the HJY wavelengths combined.

KK Oph and HD 145718, with a contrast worse than 10 magnitudes. The reasons of a so low contrast are different: for HD 97048, it may be related to the low exposure time and the absence of a coronagraph; for S Cra and KK Oph it may be related to the low stellar V magnitude and to technical problems. Finally for HD 142527 and HD 145718 it can respectively be due to the absence of a coronagraph and problems in the observations, the remnant of stellar emission is indeed quite high.

Moreover, we compared the results found with their signal-to-noise map (see Section 6.6.1) and with the STIM map (see Section 6.6.3). We underline that typically, for point-like source the common method used is the SNR map and for the extended disc emission it is used the STIM map. In the results so found using only the PCA-SDI method, the STIM map seems to be not completely optimized as in the works done by Pairet et al. (2019) and Christiaens et al. (2019a) who respectively used PCA-ADI and PCA-ASDI/PCA-ASDI. The reason stays in the fact that the STIM map is not implemented in VIP in order to deal with PCA-SDI alone. This is something it will be important to work on and to implement inside VIP. This result is thus preliminary. Particularly we verified that the post-processed image is not really affected by considering the images taken within the same DIT to have the same PA. Contrary to this, the STIM map is not perfectly working in such a way. We plan to redo the images shown using the full sample of images over time, remove bad frames and produce better STIM maps. This however, is computationally really expensive and it was not done for this study.

7.7 Observational results: Group I and Group II

7.7.1 Discussion of individual targets: Group I sources

The images of several Group I targets are completely different from the signal of the reference star sources. We have observed clear disc structures in five discs out of eight:

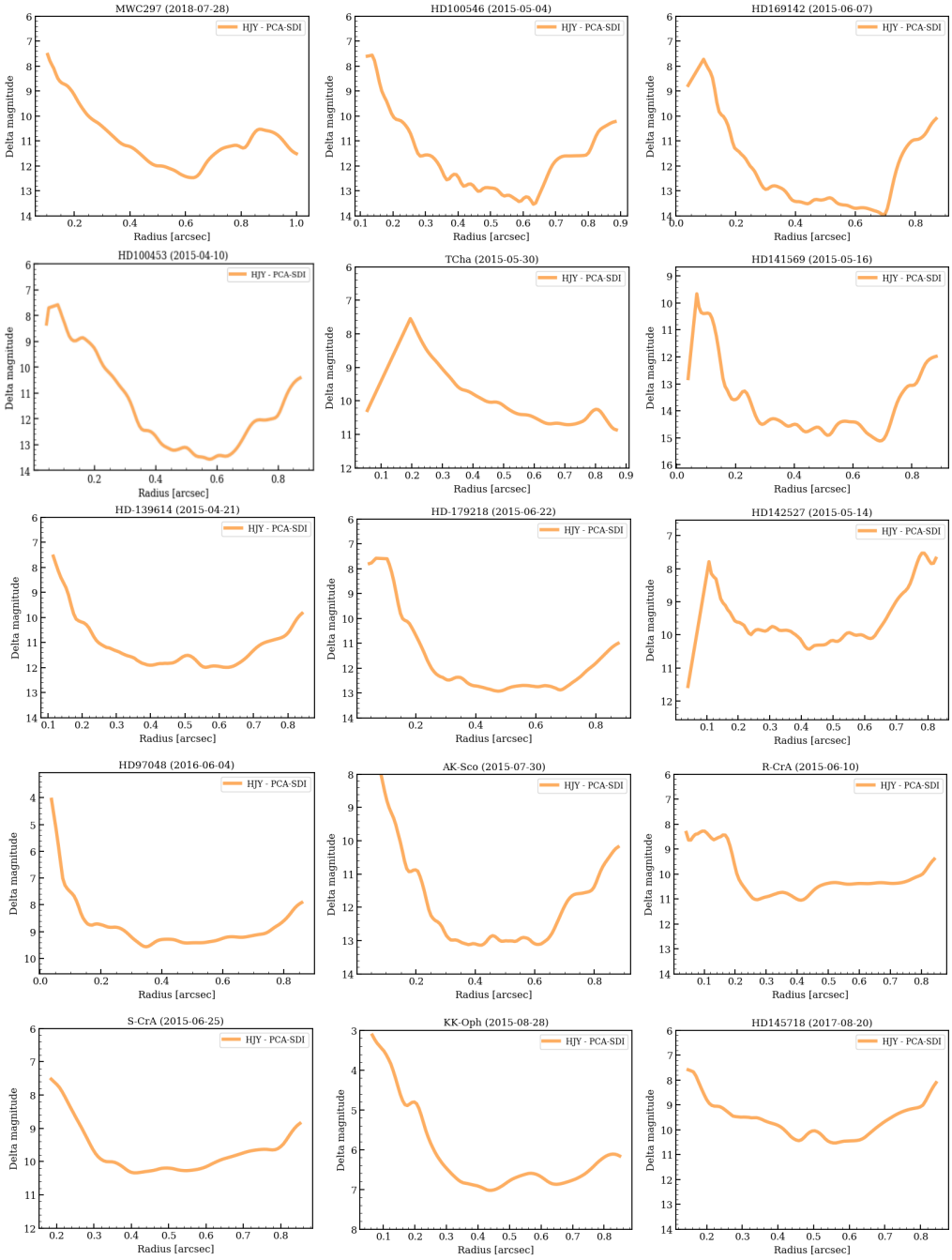

Figure 7.7: Contrast curves using PCA-SDI for the sample of 22 Herbig stars and F, G stars.

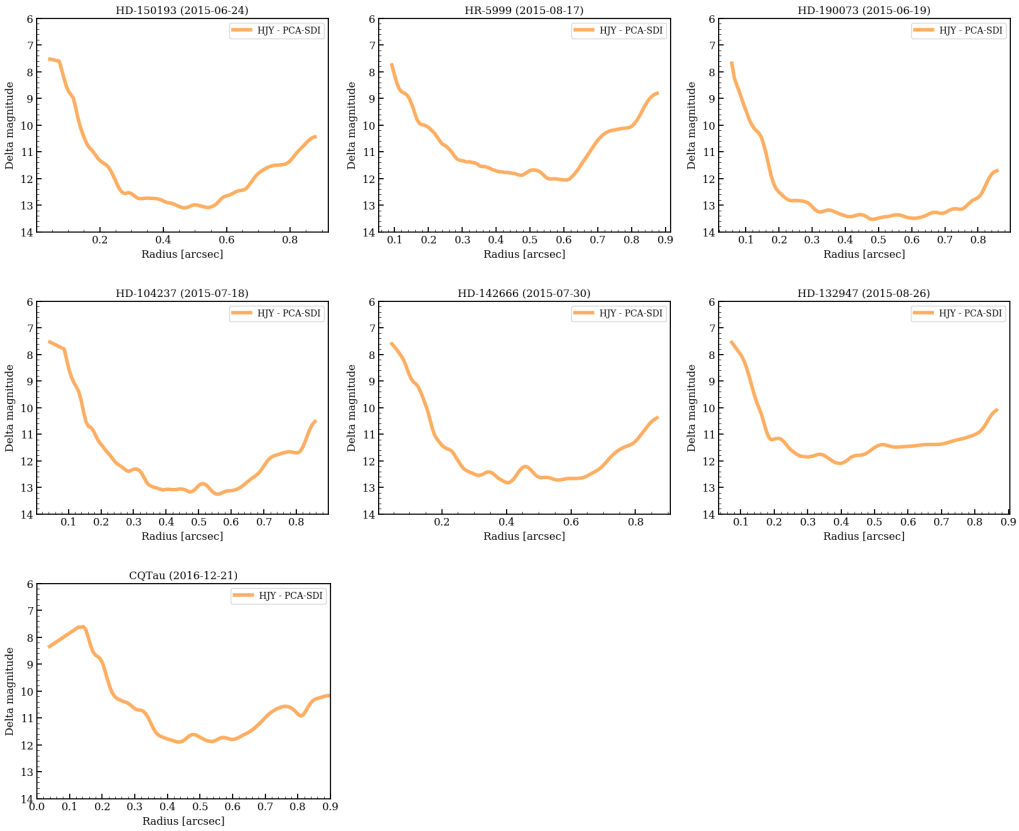

Figure 7.8: Continuation of Fig. 7.7.

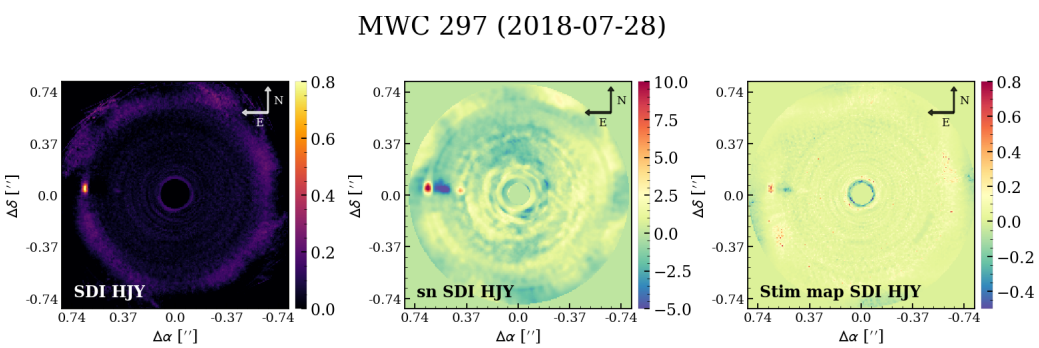

Figure 7.9: MWC 297 (day: 2018-07-28) using the PCA-SDI method with HJY combined - no disc detection has been found. A companion detection is clearly visible both in the SDI image (left, in ADU/s), SNR map (center) and STIM map (right). The central spot is the coronagraphic mask adopted in these observations.

HD 100546, HD 100453, HD 169142, CQ Tau and T Cha. This values do not take into account the two sources with no coronagraph applied. We can confirm also the presence of the companion detection made by Ubeira-Gabellini et al. (2020) although this is not the topic discussed in this Chapter.

MWC 297

We show here the observations taken on the 28th of August 2018 (see Fig. 7.9), which have a higher resolution of the ones of the 29th of April 2015. In both the images it is possible to clearly distinguish the presence of MWC 297 B (Ubeira-Gabellini et al. 2020), an early M-dwarf companion, at a distance of ∼245 au. The signal-to-noise of the companion detection is higher in the SNR map than in the STIM map. We believe that this is due to a high noise present in the single cubes before co-adding them. Some frames indeed, have a larger contribution of speckle noise. In order to have the STIM map cleaner a procedure to follow will be to reject the bad frames (with less total flux) and use just the ones with better signal-to-noise. The disc is not visible in these data, but this do not means it do not exists. As it is possible to see from the contrast curve for MWC 297, the contrast for this image is one / two order of magnitude higher than for HD 100453. This means that due to the presence of an host bright star, the stellar noise is higher and, thus, a disc structure is more difficult to be detected. The contrast profile is also less steep than the contrast of HD 100453. For a more complete description about the bright low-mass companion detected we refer to Chapter 8 and to Ubeira-Gabellini et al. (2020).

HD 100546

We present the observations of HD 100546 taken on four different days. In Fig. 7.10 we show the data observed on the 2015-05-04. The HD 100546 target presents a clear asymmetry in the disc. It is elongated and shows a brighter extended emission in the N-W. All the emission is principally on the upper side, but some fainter extension is present also in the lower part. The average disc extension is ∼ 700 mas. The presence of a cavity slightly larger than the coronographic spot is not clearly defined due to the noise still present near the coronagraph. The disc seems to be consistent with being inclined. The

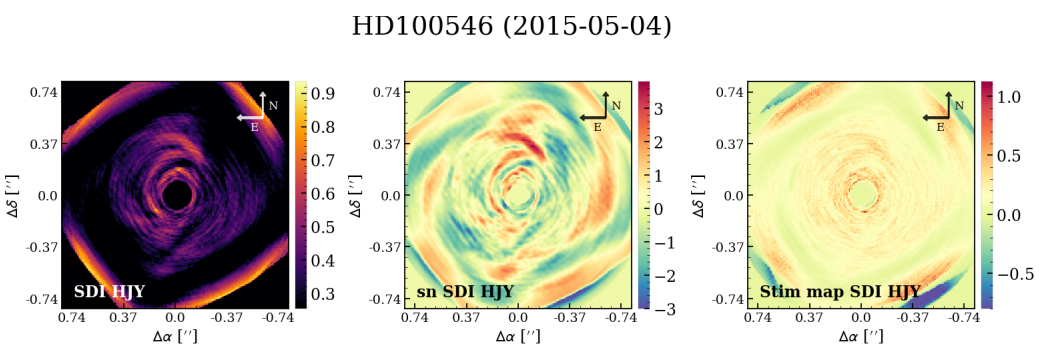

Figure 7.10: HD 100546 images of 2015-05-04 using the PCA-SDI method. An asymmetric disc is visible with multiple spiral arms. The bright spirals are visible also in the SNR and STIM maps. The color bar of the image on the left is in ADU/s.

disc asymmetry and the presence of prominent spiral arms are similar to the detection of Garufi et al. (2016) and Follette et al. (2017). Similarly as in Garufi et al. (2016), the disc extends mainly on one side.

HD 169142

In Fig. 7.11 we show the final image obtained after using PCA-SDI on the HD 169142 traget observed in YJ wavelength on the 2015-06-07. In this image it is possible to distinguish a bright ring at 200 mas next to the coronagraph. The inner most ring, is most probable fake and due to stellar emission not properly subtracted at ∼0.1 arcsec. In our total intensity scattered light images, it is possible to distinguish for the first time through SPHERE-IFS also second ring at the position of ∼500-700 mas. Its emission is slightly higher than 1σ noise and it was visible only in this observing day. The disc cavity is partially visible, although the presence of residuals makes this assumption debatable. In the images of Pohl et al. (2017a) and Ligi et al. (2018) taken with SPHERE-IFS it was debated whether the ring at 100 mas is real or due to artifacts. Polarimetric observations of Quanz et al. (2013b) with SPHERE-ZIMPOL, not sensitive most of the stellar emission, claimed the presence of a cavity, later confirmed by e.g., Bertrang et al. (2018).

Furthermore, the ring position at 180-200 mas is compatible with the detection of a bright ring done by Ligi et al. (2018) in total intensity. The second ring (∼500-700 mas) is at the same position of the one detected in PDI by Pohl et al. (2017a), Bertrang et al. (2018), but it was not detected by Ligi et al. (2018).

HD 100453

In Fig. 7.12, we show the high contrast image obtained after using PCA-SDI for HD 100543 on the 2015-04-10. The image presents a two spiral arms disc. The central dark spot is produced by the coronagraph and the ring present at ∼ 150 mas is probably produced a remnant of the stellar light left uncorrected. In PCA-SDI it is indeed not exploited the image rotation over time as done in PCA-ADI. First of all, we note that the spiral arms have a different intensity: the lower part is brighter than the upper part. Moreover, the emission of the upper spiral increases its intensity with increasing the separation. This could be due to the flaring angle of the disc: the outer emission is coming from an upper layer and may intercept more stellar light. Secondly, the two

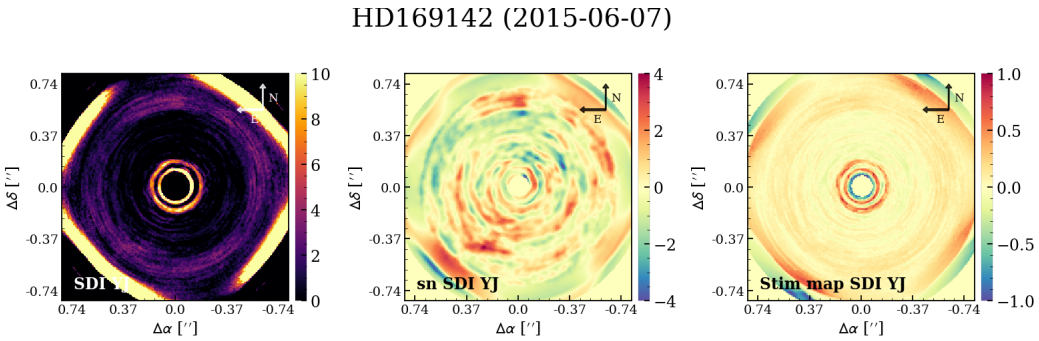

Figure 7.11: HD 169142 images of 2015-06-07 using the PCA-SDI method, which reveals a disc with two rings at ∼0.2″ and 0.5″. The innermost ring is probably due to a remnant of the stellar emission. The rings are visible in the SDI image (left, in ADU/s) and STIM map (right), even if the second one is faint. The SNR map (center) do not shown neither of the rings. The flux of the SDI image is multiplied by the r^2 to be able to show at the same time both the inner and the outer ring.

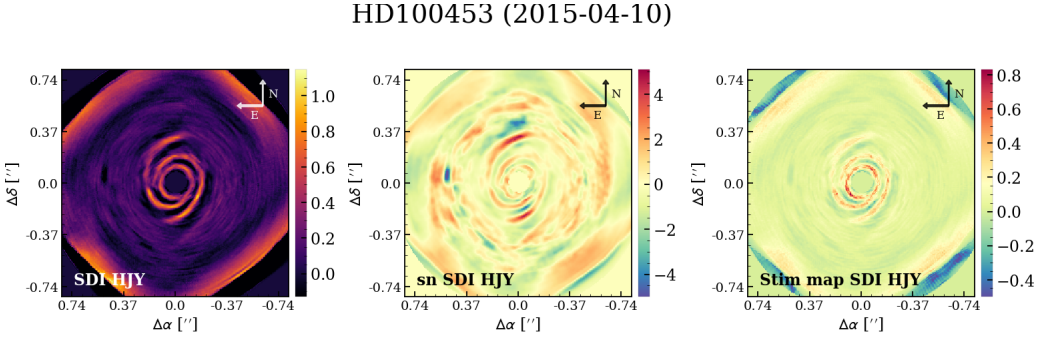

Figure 7.12: HD 100453 final image taken during the observing day: 2015-04-10 using the post-processing method PCA-SDI (left, in ADU/s). On the center it is shown the signal-to-noise map and on the right the STIM map, more suitable for disc characterization. We detect two spiral arms. The central dark spot is the coronagraphic mask adopted in these observations, whereas the bright ring at 100-200 mas is probably a remnant of the stellar light (see description of the reference stars Section 7.6).

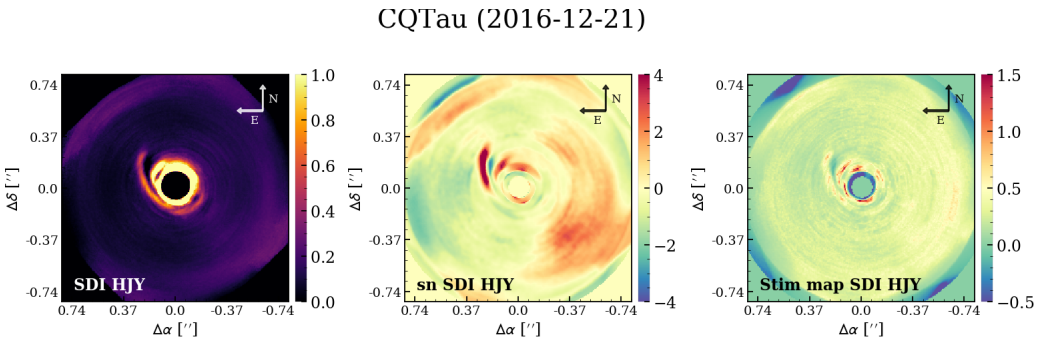

Figure 7.13: CQ Tau (day: 2016-12-21). The presence of a double spiral arms on the North-East side of the image is clearly visible. The bright emission at 0.1 arcsec is probably remnant of the stellar light. The color bar of the image on the left is in ADU/s.

spiral arms seems not to be connected, but they continue inside the disc as predicted if the spiral would be just produced by the M-dwarf (Wagner et al. 2015). Finally, it is possible to distinguish just one shadow pointing toward East and not the one toward West. This effect is not real, but it is produced by this technique we used (see Chapter 9). We note that the method used (PCA-SDI) allowed us to better constrain the disc shape in comparison to the ADI technique used by (Wagner et al. 2015). The STIM map (Fig. 7.12, right) shows the spiral arm to be not related to the speckle signal. The signal-to-noise map is noisier than the STIM map. It is indeed not suited to study bright disc emission. The fact that the spiral arms looks brighter in the tail of the SNR map is not real, but produced by the fact that the noise is lower for larger radii. This feature is indeed not visible in the STIM map. In agreement with the post-processed image, the STIM map contribution coming from the bottom spiral arm (the one next to the M-dwarf) is brighter than the top spiral arm. Both the presence of of the two spiral arms and the difference in brightness between the two arms are compatible with observations in polarized light by Benisty et al. (2017). The variation in the brightness of the top spiral arm was not evident.

CQ Tau

In Figure 7.13 we show the results obtained with PCA-SDI for CQ Tau on the observing day 2016-12-21. The image shows an asymmetric disc structure. A bright spiral, extending for 0.56 arcsec, is pointing toward North-East and it is going all the way down to the center of the image and then again upward in the South-West side. In the center of this structure there is a decreasing in the emission. At the opposite side of the South-West side described, it is possible to see a similar feature. In the inner part, the brightness is possibly coming from a PSF residual as detected in the reference stars. The SNR map shows two spirals with a good signal-to-noise. It is also present a third spiral arm in the Northern side,which corresponds to the separation of the fake ring, but it asymmetry may reveal a real structure. The STIM map is quite noisy. Also here it can be applied the same topic discussed for MWC 297 and the other targets previously described.

The emission coming from the long spiral pointing toward North-East is in agreement with the results of Uyama et al. (2020), who shows data in L′-band with Keck/NIRC2 and in H-band Subaru/AO188+HiCIAO. In their data, it is also visible a spiral inside that spiral spiral which is brighter than the outer spiral., as for us. Their data show just

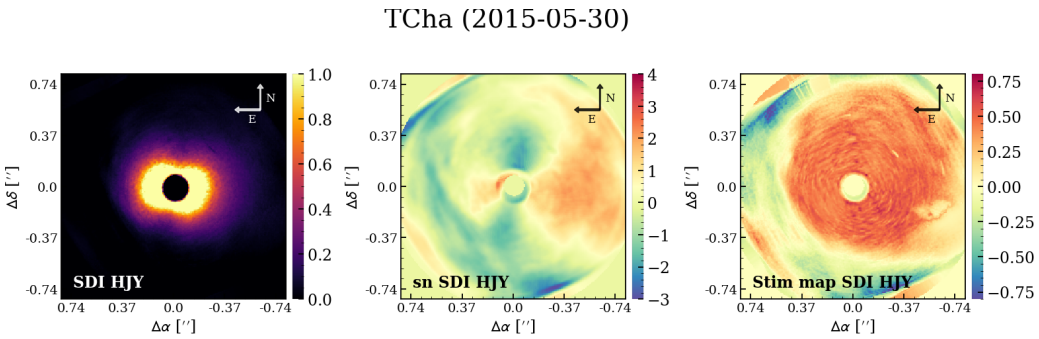

Figure 7.14: T Cha (day: 2015-05-30). Post-processed images with PCA-SDI (left, in ADU/s), SNR map (center) and STIM map (right).

the tail of the two spirals visible in our data. In our data, indeed, the outer spiral arm seems to continue longer than what seen in Uyama et al. (2020).

T Cha

T Cha was observed just in Y and J Band, using the IRDIFS mode. We show in Fig. 7.14 we show the observations taken on the 2015-05-31. Through those images it is possible to see an elongated emission. The images are, however, very noisy as the contrast curve shows. The flux and center images, indeed, are quite disturbed and with a low signal. It was not trivial indeed to obtain both the stellar spectrum and the center value of the image. Unfortunately the observations taken on the 2015-05-31 are even noisier and both the flux image and the center image were not possible to be used. We note that here we show just the results obtained with PCA-SDI. To give more strength at this detection, we analyzed it also with different techniques and different npcs. They show an edge on disc, although the signal is still quite low (see Chapter 9). To be consistent with the other observations presented in this Chapter, we will limit to comment the PCA-SDI method using the npcs equal to one.

Discussion on some sources with no detection

HD 139614 and HD 179218

HD 139614 was observed on the 2015-04-21 and the image was post-processed through PCA-SDI. Our data do not show any disc emission neither in the PCA-SDI image or in the STIM map (see the first row of Fig. 7.15). The only thing visible is the bright ring in the position of the PSF residual seen also in the reference stars post-processed images. We cannot confirm any disc structure neither the ring-like structure or the shadow observed through PDI observations with SPHERE (Muro-Arena et al. 2019) and GPI (Laws et al. 2019), even if the field of view is the same. We cannot, however, exclude the presence of a disc not visible due to the remnant of the stellar emission. The contrast curve is reaching just 12 magnitude, whereas almost all the detection of discs have a contrast curve going up to 14 magnitude. An observation with an exposure time higher such as the one of HD 100546 (2015-05-04) or of HD 169142 (2015-06-07) in PUPIL tracking mode might be able to detect such a disc structure. However, a further analysis on the comparison

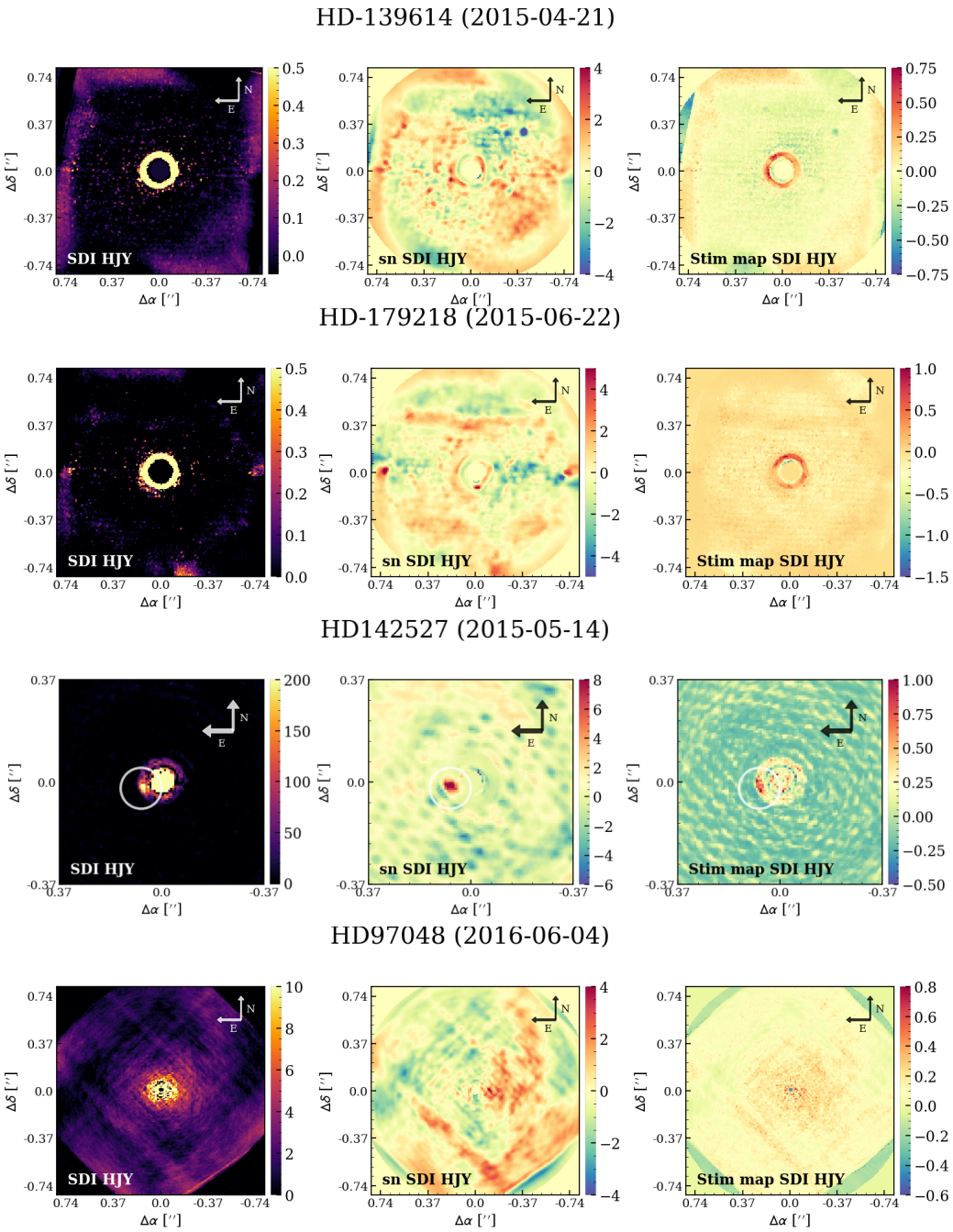

Figure 7.15: HD 139614 - obs. day 2015-04-21 (top row); HD 179218 - obs. day 2015-06-22 (second row); HD 142527 (third row) - obs. day 2015-05-14 and HD 97048 (bottom row) - obs. day 2016-06-04. This two last targets were observed with no coronagraph applied and the images are noisier. On the left we show the image after the post-processing through PCA-SDI (in ADU/s), the center the SNR map and on the right the STIM map. No disc detection is present. HD 142527 B is clearly visible in both post-processed image (left), SNR map (center) and STIM map (right).

between total intensity and polarized observations have to be made.

HD 179218 was classified according to Meeus et al. (2001) as a Group Isource with a flared disc structure. It was observed on the 2015-04-21 in FIELD tracking mode. In our data, however, it presents a behavior similar to HD 139614 (see the second row of Fig. 7.15). There is some emission larger than the bright fake ring, but the signal is too noisy to say if it is a spatially extended emission from a disc or not. The ring-like at ∼0.1 arcsec resembles the fake one of reference stars. We cannot confirm or refuse the claim of Wheelwright et al. (2010) of a detection of a companion around HD 179218 at a separation of ∼ 2.5 arcsec because it is outside the field-of-view of our IFS data.

HD 142527 and HD 97048

HD 142527 and HD 97048 were observed without coronagraph (see third and fourth rows respectively of Fig. 7.15). As we expected, in those targets our method works poorly. The contrast curves show, indeed, low values of contrast with no coronagraph and the images, indeed, are still dominated by the star. This happens because the star is really bright and the signal coming from the disc is low. For HD 142527, we can confirm the point-like source within 2σ of the position found by Claudi et al. (2019) with the same data: sep∼59.1±4.9 and PA∼107.8±0.8 deg (Δ Ra = -63.42, Δ Dec = -23.46). We note that this Chapter do not address the companion detection and for any description of the detection we refer to Claudi et al. (2019) and Christiaens et al. (2014).

7.7.2 Discussion on individual targets: Group II sources

We detected also disc structures in our sample of Group II targets. We observed a clear disc structure in the disc around AK Sco and HD 141569 and a companion to R CrA. As previously described we note that both AK Sco and HD 141569 are peculiar. AK Sco has a low far-IR excess, suggesting to be a Group II according to the definition of Meeus et al. (2001). However, according to a different criterion (m_{30}-m_{13}, Garufi et al. 2017) the target is similar to Group I sources. HD 141569, instead, has a disc mass in between the gas-rich phase and the debris disc stage. For this reason, this target cannot be properly identified neither as a Group I or II. Thus if we do consider AK Sco as a Group I and we do not take into account HD 141569, the disc detection for Group II discs would be zero.

AK-Sco

In our IFS images (observing day: 2015-07-30) it is possible to distinguish two bright features resembling part of an inclined disc (Fig. 7.16). We measured the disc emission on the direction of the two asymmetric features for an extension of ∼400 mas. The bright circle near the coronagraphic spot of our image can be still a left over stellar contribution. Moreover, the bright spot in the North-East side is not real and it is a ghost created by the bright flux images taken before. We cannot distinguish any difference in the emission of the two sides of the inclined disc. The result is in agreement with the images of AK Sco taken with IRDIS and IFS by Janson et al. (2016).

HD 141569

HD 141569 was observed on the 2015-05-16. We show our results in Fig. 7.17. The image was post-processed with PCA-SDI. We detected a ring-like emission with a large cavity. The emission has an asymmetric brightness and the ring seems to be continuous. The disc pointing toward North is barely visible, whereas the one pointing toward South is

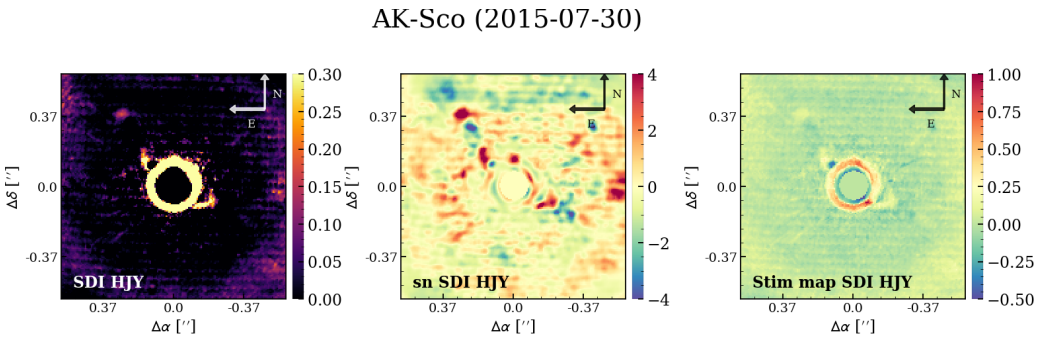

Figure 7.16: AK Sco (observing day: 2015-07-30). A disc is detected using PCA-SDI, showing an inclined disc in the post-processed image (left, in ADU/s), SNR map (center) and STIM map (right). A point-like source on the upper left panel seems to be a companion candidate, but it is due to a ghost created by the previous detection of the flux image, which falls exactly in that position. The bright ring at 0.1 arcsec is possibly an artifact.

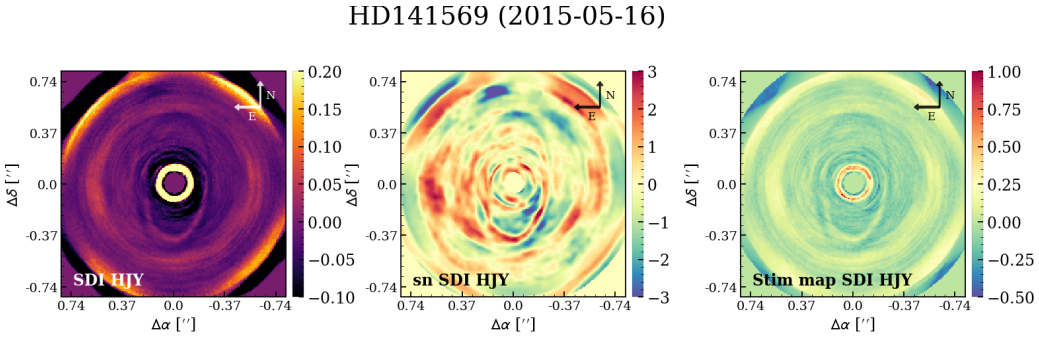

Figure 7.17: HD 141569 (day: 2015-05-16). A ring is present in the post-processed image with PCA-SDI (left, in ADU/s), SNR map (center) and STIM map (right). The Southern part of the disc is more visible. The Northern part is barely visible. No broken ring is seen.

brighter, as shown also by the SNR and STIM maps. The emission seems to come just from one ring. A second circle at 0.5 arcsec is visible, but possibly still part of speckle emission. Our results are in agreement with the detection of a ring-like emission with sharp edges inside 1″ as saw by Perrot et al. (2016) who performed a study using IRDIS and IFS on SPHERE. They used ADI to post-process their images and they found a broken ring. We cannot confirm it to be broken. (Mawet et al. 2017b) suggested indeed that it should be attributed at the routine used.

R CrA

In our image shown in Fig. 7.18, we show a bright companion very close to the central star ∼0.16 arcsec (25 au), as found by Mesa et al. 2019. The companion is visible also in all the combined frames for Y, J, H bands alone. In order to create these images we used the PCA-SDI method. The signal-to-noise map shows that R CrA B has a high signal-to-noise. In the SNR map it is possible to distinguish also an asymmetric emission with a prominent arm pointing toward the North-East as suggested by Mesa et al. 2019 and fully described by Rigliaco et al. (2019). The signal of both the companion and the

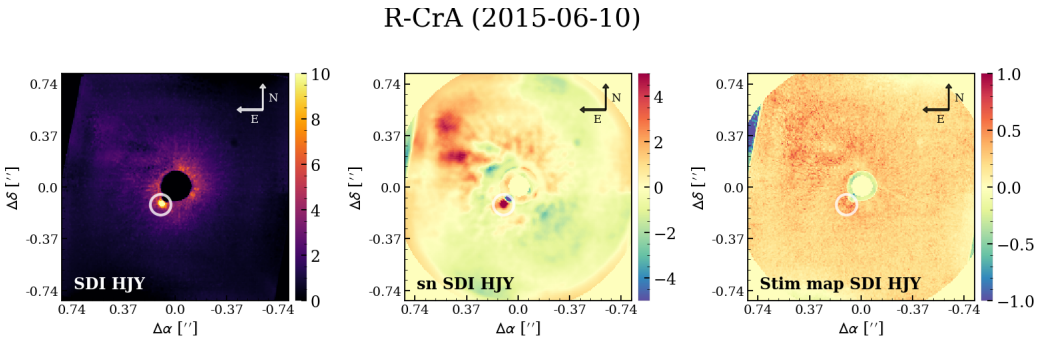

Figure 7.18: R CrA on the observing day 2015-06-10. The bright companion R Cra b is visible in both PCA-SDI image and SNR map. In the SNR map is present also an asymmetric emission on the North-East side. The STIM map do not show any of these features. The color bar of the image on the left is in ADU/s.

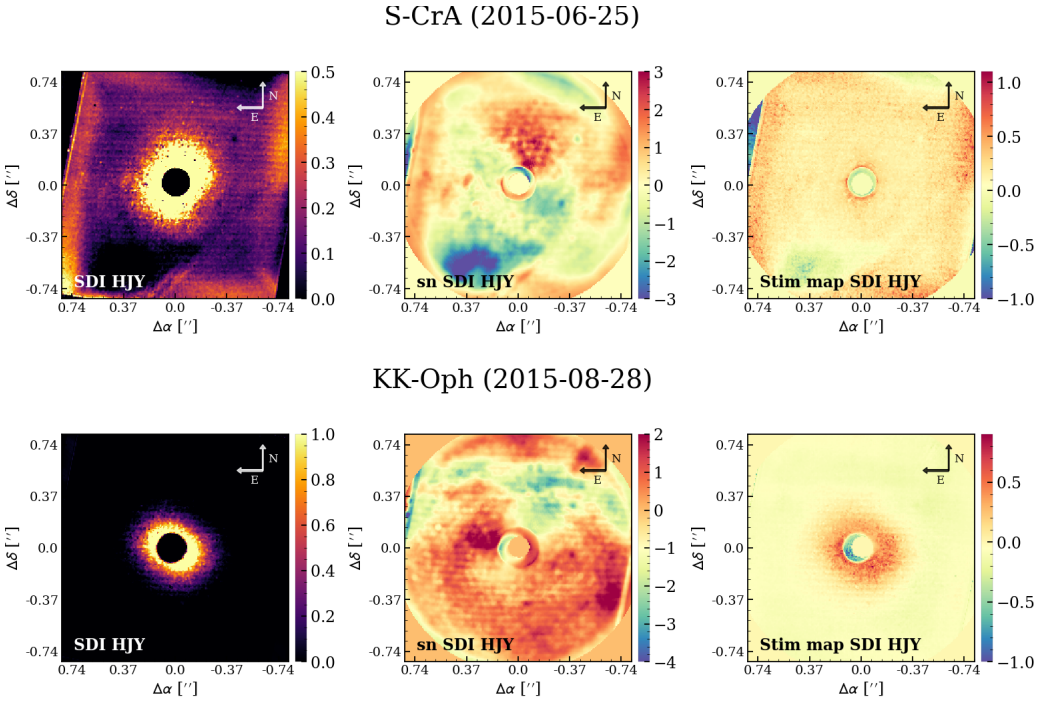

Figure 7.19: S CrA on the observing day 2015-06-25; KK Oph on the observing day 2015-08-28. Both the observations reached a low sensitivity, thus the emission visible in these targets can be still a remnant of the stellar light. The color bar of the left images are in ADU/s.

arm is not however visible in the STIM map. The same argument proposed for MWC 297 can be applied here.

Discussion on the sources with no detection

S CrA and KK Oph

For the S Cra target, in all the three different days of observations, both the center and flux images are quite noisy and faint, suggesting that probably those observations were disturbed by atmospheric condition. In the post-processed image with PCA-SDI (Fig. 7.19) a circular emission is visible. It is however difficult to say from these data if it is real or due to stellar emission which was not completely subtracted. The contrast curve shows, indeed, a low signal-to-noise ratio. For this reason, we consider this not to be a disc detection.

The post-processed images of KK Oph has a low contrast ratio. The reason of this is that the star center images were not properly observed and without them our method works not properly. The image seems to present an elongated emission (Fig. 7.19), but considering the noisy data reduction, this target needs further investigations. Moreover, also the flux images are extremely noisy, so the measure of both the stellar flux and the FWHM of the source is very uncertain.

HD 145718, HD 150193, HR 5999, HD 190073, HD 104237, HD 142666, HD 132947

All these targets are Group II sources and their images have a behavior similar to the one of the reference stars: just a bright ring next to the coronagraph is present and it is extended up to a separation of ∼100-200 mas. We note that as in the case of AK Sco, also for HD 142666, the bright point-like source visible in the image is not real but due to a ghost created by the bright emission of the flux image. HD 145718 is the only target among the other ones in this section to be taken in PUPIL tracking mode, the others are observed in FIELD tracking mode. The exposure time of HD 150193, HR 5999, HD 190073 and HD 142666 is of ∼2500 s; while for HD 145718 and HD 104237 is ∼1568 s; finally, for HD 132947 the exposure time is low (576 s).

7.7.3 The ratio between Group I and Group II

The ratio between the number of disc detection and the total number of sources for Group I and Group II respectively is: 0.6 ± 0.2 and 0.2 ± 0.1, if we consider the definition of Meeus et al. (2001). This result shows that the values found are different even if their error bars slightly overlaps and thus we can confirm the scenario proposed by Maaskant et al. (2013, 2014). The disc detection are: AK Sco and HD 141569 (for Group II) out of a total of nine and HD 100453, HD 100546, HD 169142, CQ Tau and T Cha (for Group I) out of a total of eight. The errors are computed as the ratio between the square root of the number of detection and the total number of sources for each Group. We excluded KK Oph, S Cra, for atmospheric conditions and the HD 97048 and HD 142527 targets because they were observed without the coronagraph. In all these targets, indeed, the contrast curves show worse contrasts than for the other targets reported.

This result is even reinforced if we consider another criterion for the classification (the m_{30}-m_{13} criterion, Garufi et al. 2017): AK Sco will be a Group I. Moreover, if we do not

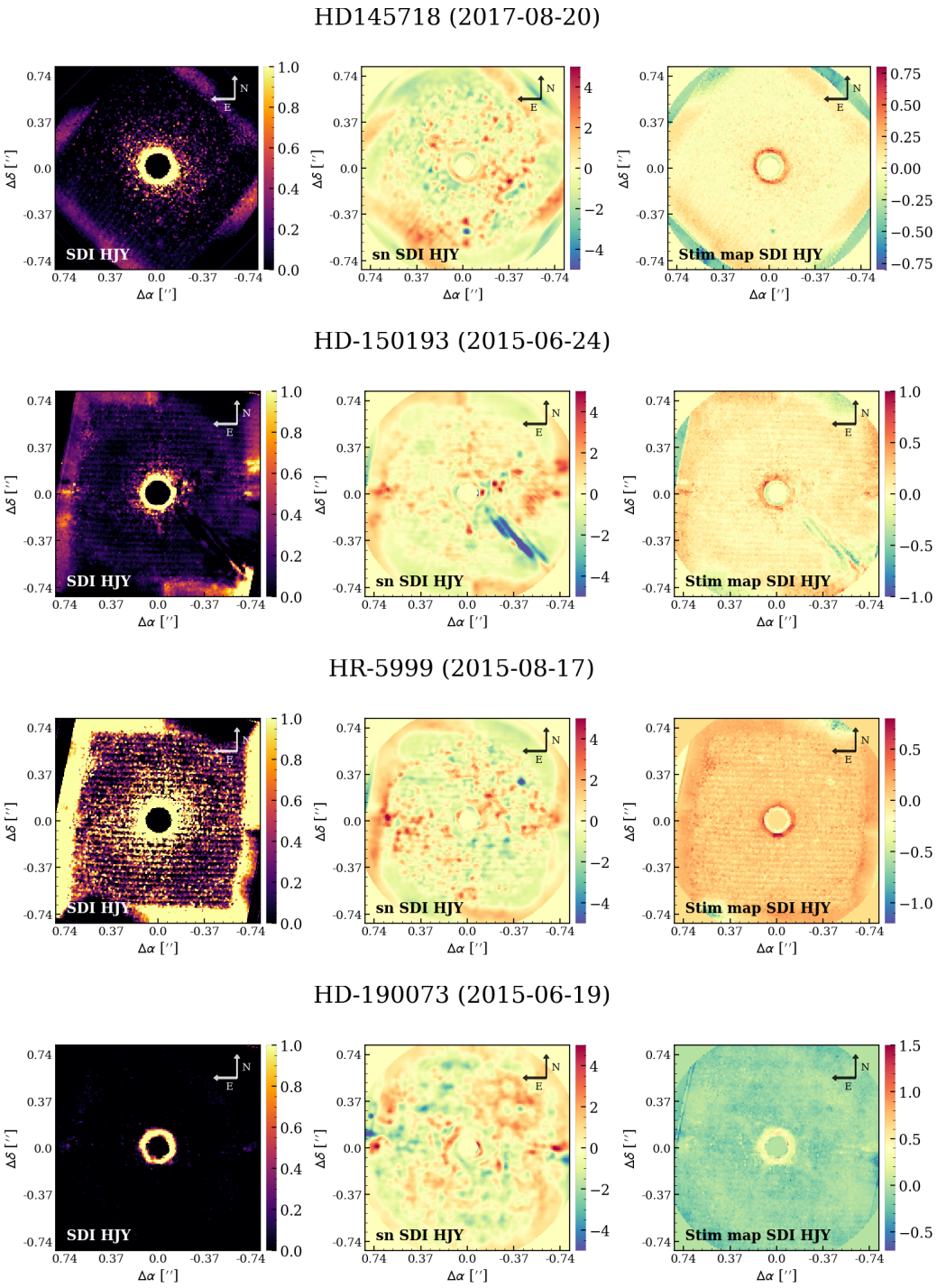

Figure 7.20: HD 145718 on the observing day 2017-08-20; HD 150193 on the observing day 2015-06-24; HR 5999 on the observing day 2015-08-17; HD 190073 on the observing day 2015-06-19. All these targets were considered with no disc detection. The inner ring similar to the reference stars behavior, probably not real. The color bar of the post-processed images (left) are in ADU/s.

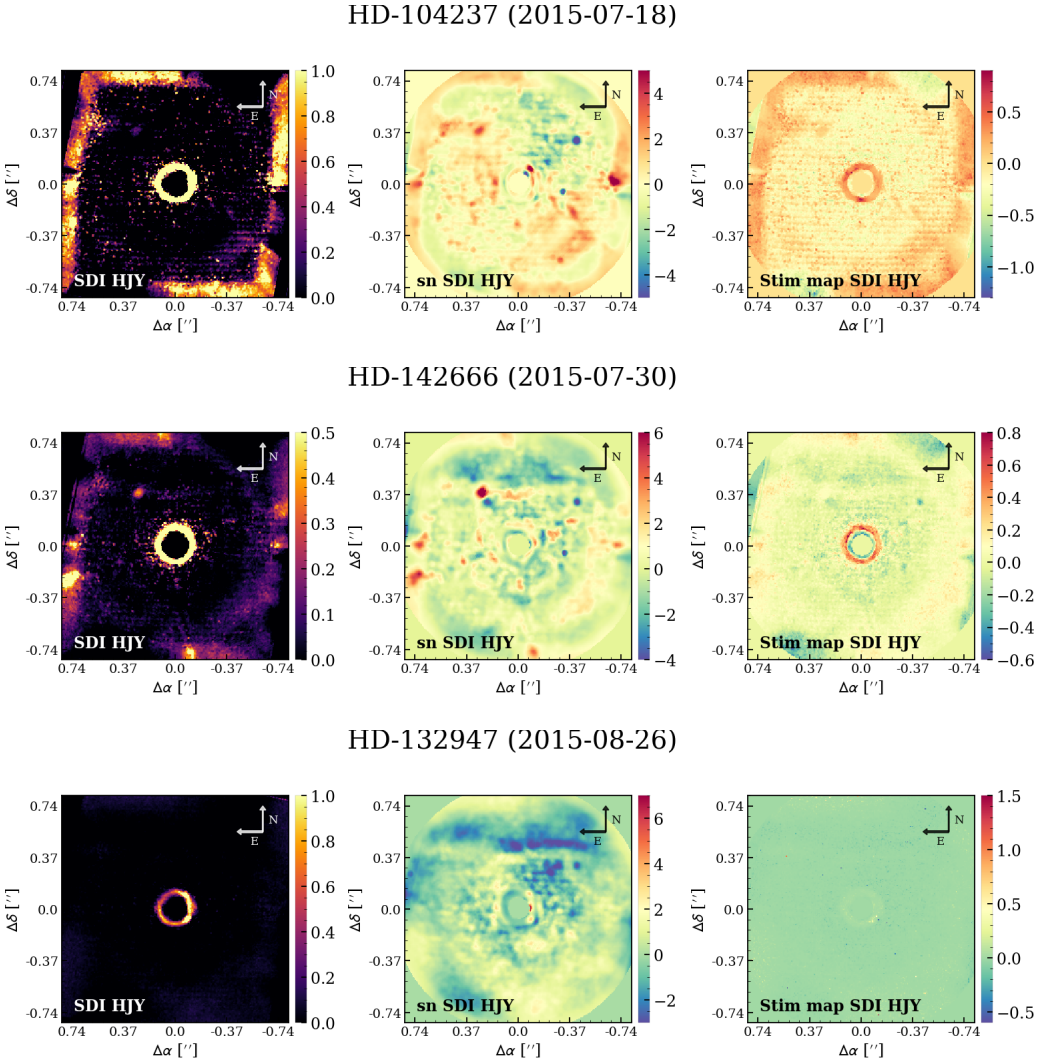

Figure 7.21: HD 104237 on the observing day 2015-07-18; HD 142666 on the observing day 2015-07-30; HD 132947 on the observing day 2015-08-26. No disc emission is recovered. The ring-like features are similar to the ones of the reference stars images; the point-like source visible in HD 142666 is a ghost created by the bright flux image taken before. The color bar of the post-processed images (left) are in ADU/s.

to take into account HD 141569 because it is in a transition phase to a debris disc, the ratio will be become: 0.7 ± 0.3, for the Group I, and 0.0 ± 0.0, for the Group II. Both AK Sco and HD 141569 are transitional discs: the former is quite old and it has dissipated all its mass and the latter is going toward the final dissipation stage. In particular, they are either with almost edge on discs or evolved (suggested by the large cavity).

The disc structures observed are various going from spiral arms to gaps and some of them present large cavities observed almost edge on. Group I targets share a common factor: the presence of large cavities and their geometries is complex: spirals, gaps, rings, edge-on discs. This suggests that the Group I targets detected are possibly dynamically perturbed and there is a still ongoing interaction with another companion. We analyze the different topology of disc structures in Chap. 9. Most of the targets with detected discs were observed in PUPIL tracking mode and with high integration times. Possibly more discs would be detected if the integration was longer and the contrast curves reached higher values (see models in Appendix C). In order to confirm the results here obtained the sample of targets will have to be enlarged. Moreover, it will have to be tested how much the observing strategy affected this result.

7.8 Summary and Conclusions

In this work we presented the analysis done on a survey of 22 Herbig stars and F, G stars using the post-processing technique PCA-SDI, in order to try to discriminate between different formation processes of Group I and Group II discs.

- This allowed us to detect seven discs, five for the Group I targets (HD 100453, HD 100546, HD 169142, CQ Tau and T Cha) and two for the Group II (AK Sco and HD 141569), according to the definition of Meeus et al. (2001). HD 100453, HD 100546, CQ Tau have a disc structure which resembles a spiral; HD 169142 and HD 141569 have a ring-like disc; finally, AK Sco and T Cha presents a highly inclined disc.

- The ratio between the disc detection and the total number of targets for Group I is 0.6 ± 0.3 and for Group II is 0.2 ± 0.1. The numbers are different, but their error bars overlap, and the number of disc detection in the Group II sources is small. Moreover, all the Group II sources detected are peculiar. AK Sco is a close binary with an inclined transition disc, which has a low far-IR excess (as Group II) and a high m_{30}-m_{13} (as Group I). Possibly this can be explained by the disc being old and having dissipated most of its mass (Garufi et al. 2017). HD 141569 is in a transition phase between a Class II and a debris disc phase. If we consider AK Sco as a Group I and we do not take into account HD 141569 (not fully a Class II) the result obtained previously will be reinforced. The ratio will be: 0.7 ± 0.3, for the Group I, and 0.0 ± 0.0, for the Group II. This suggests that sources that goes under the denomination of Group II are typically not detected, whereas it is plausible a relation between the Group I sources and a scattered light detection of the outer edge of the dust gap. The reason is however not simple as suggested by Maaskant et al. (2013, 2014): the Group I sources detected are transitional discs, but with a great variety of disc structures, not just simple cavities. Moreover, the so low number of Group II sources detected suggests that the Group II discs are typically either really small or large but self-shadowed (Garufi et al. 2017; Banzatti et al. 2018). Both are not detected: the former because the disc is inside the SPHERE IWA and the latter because the emission expected decrease rapidly with radius and

thus it is below the contrast curve. For a more detailed discussion regarding this, we refer to Chap. 9.

- A future work on this will be to adapt the STIM map derivation implemented in VIP to be properly work with the PCA-SDI method and to provide better suited STIM maps for the 22 sources here reported. Moreover, the derivation of the post-processed images will have to be done on the full cube, through the use of an interpolation of the position angle value present in the header to provide a more exact centering and a more efficient cleaning. Together with this the bad frames removal should be added.

- A future prospective on this is to compare the disc emission detected during this survey with the already known disc structures detected in Polarized Differential Imaging. An important still open question is indeed related to the derivation of the polarization fraction for the light scattered off in such discs. Having a large sample of discs would allow to statistically compare the values obtained with the predictions for different grain sizes, shapes and compositions. Moreover, it will be important to determine whether some disc regions have different values because of either different illumination, geometry, or dust properties. In such a way, we would be able to give prediction of the reason of no detection in IFS images when the discs are observed in PDI. This will allow to better constrain the observing techniques best suited for these type of observations.

- For a more detailed study on the target where a disc or companion discovery was performed we refer to Chapter 8 and 9. Moreover, in Chapter 10 we describe the development of a novel routine to post process the data, which combine the SDI technique with the spectral information. We refer also to Appendix C where we performed an SED fitting and a prediction of the consequent signal-to-noise expected in the near-IR at each radii and to Appendix D where a full description of the targets is done.

Chapter 8

Discovery of a low-mass companion embedded in the disc of the young massive star MWC 297

Based on the paper by **M. G. Ubeira Gabellini**, V. Christiaens, G. Lodato, M. van den Ancker, D. Fedele , C. F. Manara, D. J. Price: "Discovery of a low-mass companion embedded in the disk of the young massive star MWC 297 with VLT/SPHERE", published in Astrophysical Journal Letter, 890, 1, L8, Feb. 2020.

In this Chapter we report the discovery of a low-mass companion in the disc around the young Herbig Be star MWC 297 using high-contrast observations with the Very Large Telescope (VLT)/Spectro-Polarimetric High-contrast Exoplanet REsearch (SPHERE) instrument. We performed multi-epoch high-contrast imaging in the near infrared (NIR) with VLT/SPHERE-IFS. The companion is found at projected separation of 244.7±13.2 au and a position angle of 176.4±0.1 deg. From the spectrum, we estimate a mass of 0.1–0.5 $M_\odot$, the range conveying uncertainties in the extinction of the companion and in evolutionary models at young ages. The orbit coincides with a gap in the dust disc inferred from the SED. The young age ($\lesssim$ 1 Myr) and mass ratio with the central star ($\sim$ 0.01) makes possibly the companion comparable to PDS 70 b, suggesting a relation between formation scenarios and disc dynamics. The physical and orbital properties of MWC 297 B suggest formation via gravitational instability.

The Chapter is organized as follows: we present the properties of the target in Section 8.2, we describe the observations and the data reduction in Section 8.3 and we present the analysis, discussion and conclusions in Section 8.4, 8.5 and 8.6, respectively. The main results are summarized in Table 8.2.

8.1 Introduction

The formation of binary and its relation with the planet formation are still processes under investigation. Three are the mechanisms traditionally considered to form binary: capture, fission and disc or core fragmentation. In the first scenario, statistically unlikely, the two bodies forms separately and then become bound (Tohline 2002). In the second one, a fast rotating protostar which is contracting can split into two bodies, unlikely for large separations. Finally, binaries can form via disc fragmentation (Bonnell 1994) during the initial stages of disc evolution. Density perturbations may produce bound clumps in the outer part of self-gravitating protoplanetary discs. The disc mass needs to be sufficiently high, but some evidence of self-gravitating discs starts to be found around young high mass stars (Cesaroni et al. 2007). Core fragmentation (Bonnell et al. 1991), instead, involves perturbations during the phase of cloud collapse, then amplified by gravity. These binary star formation theories are best tested with direct imaging of young objects. But the number of low-mass companions around pre-main-sequence stars detected by direct imaging

remains low (e.g. Bowler 2016). The situation is improving thanks to purpose-built high-contrast instruments such as SPHERE (Spectro-Polarimetric High-contrast Exoplanet REsearch instrument, Beuzit et al. 2019) at the Very Large Telescope (VLT) and GPI (Gemini Planet Imager, Macintosh et al. 2014). Using these new instruments, Keppler et al. (2018) detected and confirmed a companion within the gap of the transition disc around PDS 70.

8.2 Target properties

The MWC 297 system (RA(J2000) = 18 27 39.527, Dec(J2000) = -03 49 52.05) is a young pre-main-sequence (< 1Myr) Herbig star of spectral type of B1.5, with a mass of $\sim$17 $M_\odot$ (e.g., Vioque et al. 2018b). It is located in the L515 region at a distance of $\sim$ 375 pc (Vioque et al. 2018b, Gaia DR2) and it was classified as a Class II, Group I source (Meeus et al. 2001) from the analysis of its spectral energy distribution (SED) (Mannings 1994). Manoj et al. (2007) studied the CO emission of MWC 297 through interferometric data. From the mm-spectral slope of the SED they argued that either the structure is very compact, or there is grain growth in the circumstellar environment. Malbet et al. (2007) found that the disc has a low inclination from simultaneous fitting of SED and visibilities, and together with the work by Monnier et al. (2006), shows that the radiation from the hot circumstellar material comes from the inner most part of the disc. Later, Acke et al. (2008) confirmed that the system is organized in a circumstellar disc and Weigelt et al. (2011) found the disc to be extremely compact through a study of the continuum visibilities. The disc has a low inclination $\sim$5° (Alonso-Albi et al. 2009) and present radiation from the hot circumstellar material coming from the inner most part of the disc. Vink et al. (2005) discovered an object further out than the one found by us. They suggested the presence of other companions further in will be relevant for the unexpected x-ray flaring for such an early-type object. Finally, Alonso-Albi et al. (2009) observed with VLA the disc at millimeter wavelengths. They modelled its SED using a two-component disc, where the inner disc was extending from $\sim$ 7.5 to 43.5 au and the outer part was from $\sim$ 300 to 450 au and a gap in between. The possible explanations for such gap are the presence of a companion and effects related to grain growth in the outer disc. However, the authors ruled out the hypothesis of a companion due to the apparent non-detection of any point-like source at the suggested distance ($\sim$ 270 au, all the values are rescaled to match current Gaia distance).

8.3 Observations and data reduction

8.3.1 Derivation of stellar properties

Table 8.1 summarizes the stellar and disc properties. The effective temperature and insterstellar extinction were derived following van den Ancker et al. (1998). In particular, the value of extinction (A_V=7.72 mag) was derived using an average of the color excess for $0.1 < \lambda < 0.9$ and used as in Cardelli et al. (1989) for dereddening with R_v=3.1. We derived the effective temperature ($T_{eff} \sim$ 23700 K) using a fit of the A_V corrected photometry using the Kurucz (1991) models (for $0.3 < \lambda < 1.2$). Luminosity, mass and age were adopted from Vioque et al. (2018b). We estimated the stellar radius based on L_{bol} and T_{eff}.

Table 8.1: Physical properties of MWC 297

Param.	Units	Value	References
d	pc	375±20	Gaia Collaboration et al. (2018)
Age	Myr	< 1	Acke & van den Ancker (2006)
			Vioque et al. (2018b)
Sp.T.		B1.5Ve	Drew et al. (1997)
Group		I	Meeus et al. (2001)
$T_{\rm eff}$	K	23700	this work
$A_{\rm v}$	mag	7.72	this work
$\log(L_{\rm bol})$	$L_\odot$	4.59	Vioque et al. (2018b)
M_*	$M_\odot$	16.9	Vioque et al. (2018b)
R_*	$R_\odot$	9.17	this work

Notes. d: Gaia distance; Sp.T.: spectral type; Group: Disc classification according to Meeus et al. (2001); $T_{\rm eff}$: effective temperature, A_V: extinction, $L_{\rm bol}$: bolometric luminosity; M_*: stellar mass; and R_*: stellar radius.

8.3.2 Observations

We observed MWC 297 on the 29th of April 2015 and on the 28th of June 2018 with SPHERE, the Extreme Adaptive Optics System and Coronographic Facility at the VLT. The observations were obtained under the ESO observing programs 095.C-0787 (PI: M. van den Ancker) and 0101.C-0350 (PI: M. G. Ubeira Gabellini) respectively (Table 7.1). Both observations were executed in the IRDIFS-EXT mode i.e. simultaneous Integral Field Spectroscopy (IFS), and dual-band imaging in the K-band, producing simultaneous IFS spectroscopy and imaging in the H-band. The first set of observation (2015-04-29) were taken with FIELD tracking mode, while for the second set (2018-07-28) we used the PUPIL tracking mode. The IFS data are cubes of 39 monochromatic images in the near-IR wavelengths. The spectral resolution is R∼30 for the IRDIFS-EXT mode (Y-H, $0.95< \lambda <1.65$ μm). The Field of view of the SPHERE IFS is $1.73''$ x $1.73''$ and for the simultaneous imaging with IRDIS it is $11''$ x $11''$. The N-ALC-YJH-S coronagraph (inner working angle $\sim 0.15''$) was used. The functionality of this coronagraph was described in Chapter 6.

We obtained SPHERE "Flux and Star Center" calibration images. The unsaturated peak flux of the star ("Flux" image), needed for the contrast calibration, is measured at each wavelength by offsetting the central star from the coronagraphic spot (shallow 5 min. exposure). Thanks to the Star Center images (see Section 6.2.2), for each frame we measure the position of the star behind the coronagraph placed at the center of the four replicas produced by the adaptive optics system and located at specific locations away from the coronagraphic mask.

8.3.3 Data reduction

We used the standard procedure (ESO pipeline[1]) in order to reduce the IFS data. In addition to these standard data-reduction steps, we applied a bad pixel correction, which is not used in the default pipeline, using a function implemented in the Vortex Imaging Pipeline[2] (VIP, Gomez Gonzalez et al. 2017b). This is based on an iterative process

[1] http://www.eso.org/sci/software/pipelines/sphere/; v0.24.0, for the first dataset; v0.36.0, for the recent data.

[2] Available at: https://github.com/vortex-exoplanet/VIP.

able to correct clumps of bad pixels through a sigma filtering (replaced by the median of neighbouring pixel values). The output of the ESO pipeline is a set of different images for the same day with a specific orientation.

For the centering, we used a high-pass filter on our center images which performed subtraction the image itself with a median low-pass filtered version of the image. This helped to increase the signal-to-noise of the star replicas. We have fitted the four replicas with a 2D Moffat function implemented in VIP to derive the centroid of the star in each frame. We have set the threshold to 5, 3 and 2 σ and taken a median of the three central positions (the values found were really close). This was done both for the couple of center images taken at the beginning (considered as their average) and for one at the end of the set of science images. We have, then, interpolated the values of the derived center considering the observation time of the science images. Finally, in order to derive the error on this measurement, we computed the discrepancy between the derived center of the first couple of center images at each wavelength separately and propagate them to derive all the errors. The errors decrease with increasing wavelength. This was done for both x and y position (in average σ_x=0.04 pixel and σ_y=0.08 pixel).

8.3.4 Post-processing using VIP

Calibrated frames are still affected by quasi-static speckles produced by the star (Marois et al. 2006). Two are the evidences present in our data that we used to post-process them: the speckles change position radially with increasing wavelength, while the real features stay in the same position (spectral information). This is at the foundation of the Spectral Differential Imaging (SDI) algorithm (Sparks & Ford 2002). Also, fixing the pupil of an altitude-azimuth telescope during an observing sequence, most quasi-static speckles remain fixed in the image, while real features rotate (angular information). Angular Differential Imaging (ADI) algorithm (e.g., Marois et al. 2006, Section 10.5.2) are based on this idea. The IFS cubes contain the spectral information, while angular information is available when the rotator is moved to maintained fixed the pupil (second epoch only).

As explained in the previous chapter, we used the principal component analysis (PCA) based algorithms as implemented in VIP to model and subtract the stellar PSF and associated speckles. For both sets of observations we applied PCA-SDI (Pueyo et al. 2012), using the spectral information alone, and PCA-ASDI, using both spectral and angular diversity (Pueyo et al. 2012) performed in a single step. This means that the multi-spectral frames are rescaled to align the speckles at the position of largest wavelength and processed with a single PCA low-rank approximation, e.g. the PCA library was produced using both the angular and spectral information. We tested the algorithm in two separate steps (Christiaens et al. 2019b), but obtained noisy final images. For the second set of observations we also used an other algorithm: PCA-ADI, using only the angular information, performed either in full frames (Soummer et al. 2012; Absil et al. 2013) or in concentric 2-FWHM wide annuli on individual spectral channels (see Section 6.4.2), defined as PCA-ANNULI.

8.4 Characterization of the companion

8.4.1 First epoch observations (April 2015)

We detected a bright companion in the outer disc of MWC 297 on 29th April 2015 located ∼246.4 au (657 mas) from the central star. The detection was obtained using the PCA-ASDI (Fig. 8.1, top left) and PCA-SDI techniques, with 4σ and 5σ significance. The

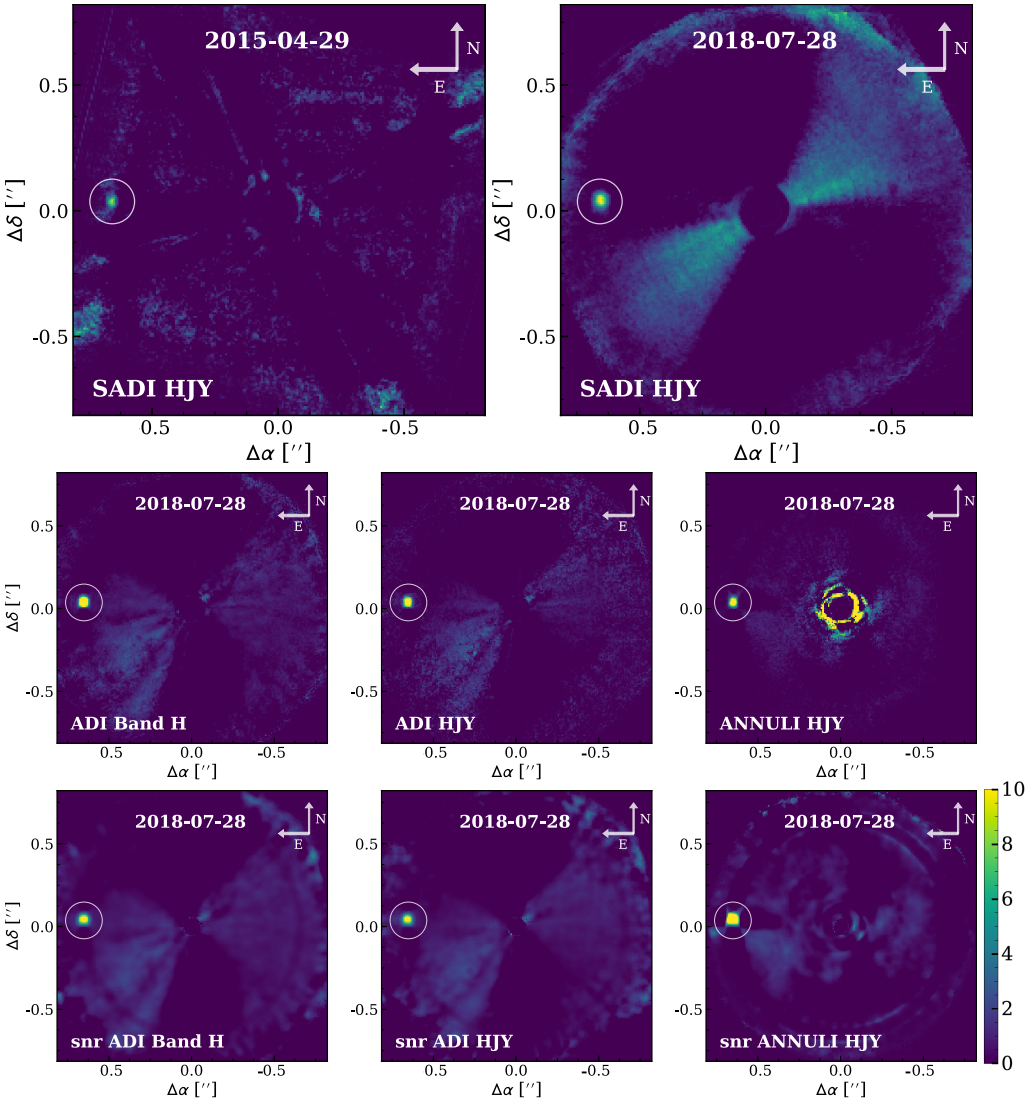

Figure 8.1: Top: Data reduced through PCA-ASDI for the observations of MWC 297 taken in 2015 (left) and 2018 (right) using all the wavelengths combined. Center: Data taken on 2018-07-28 using other two different techniques: ADI performed in full frame with just Band H frames (left), with all the frames combined (center right) and done in annuli (right). The combination of the frames in a final image was done using the median. Bottom: Signal-to-noise of the images of the central pannel. In all of the images shown, irrespective of the technique used, the signal of the companion is clearly distinguishable from the rest of the image (white circle). We note that we have produced also the Y and J Bands images using ADI where the companion was present but with decreasing flux and we have used also the SDI method with similar results.

companion was detected in the averaged H-band image (signal-to-noise$\gtrsim$4), but not in Y and J.

8.4.2 Second epoch observations (July 2018)

We performed follow-up observations with longer integration time on 28th July 2018. We re-detected the companion in H and J-bands with four different post-processing methods and a significance always higher than 4σ. The significance was estimated through the SNR routine of VIP. This calculates the S/N (signal to noise ratio) of a test resolution element in a residual frame. The implementation follows Mawet et al. (2014), using a T-student test.

We detected it also in the Y-band just with PCA-ADI. Figure 8.1 shows that the point-like source is detected regardless of the post-processing method (ASDI, ADI, ANNULI and SDI — not shown here) and of wavelength (Y, J and H, bands all show the companion). The post-processed image for the band H is presented in center left Fig. 8.1 using PCA-ADI. We note that the companion is visible also in the Y and J bands separately. We derived the flux of the companion in all the 39 different frames. In order to maximize the signal to noise of our companion in the final images, we perform a study on the best principal components (npcs) to be used for each frame. For each frame we independently tested the number of principal components which maximize the signal-to-noise. The SNR was computed in an annulus with same separation and FWHM of the detected source. In Fig. 8.2, we show the best npcs obtained for each frame.

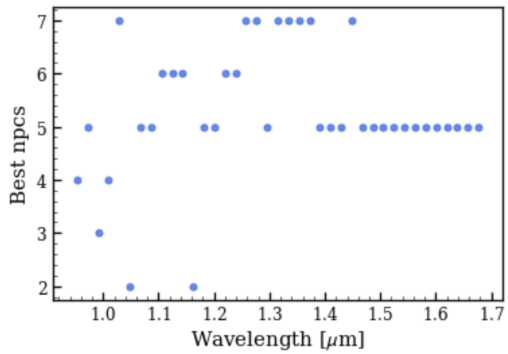

Figure 8.2: Best value of principal components obtained independently for each frame for the observations of MWC 297 on the 28th July 2018. The best number of principal components is chosen as the one which maximizes the signal-to-noise of the companion. We found that it is better to use for the MCMC routine in particular, each frame independently.

8.4.3 Spectro-astrometry

We carried out a Bayesian analysis based on Markov Chain Monte Carlo (MCMC) method coupled to the negative fake companion technique implemented in VIP to derive the position and the flux of the companion at each wavelength (e.g. the MCMC analyis on a specific frame is shown in Fig. 8.5, see Wertz et al. 2017). First we derived an initial guess for position and flux estimation using the Nelder-Mead simplex-based optimization (Nelder & Mead 1965) as implemented in VIP. We have then used these results as input for the MCMC simulation. This uses a negative fake companion technique (NEGFC, Marois et al. 2010a) to derive the results. The companion is injected in the original data cube as a negative PSF in order to delete completely the signal of the real companion. The process stops upon convergence to minimal absolute residuals in an aperture centered

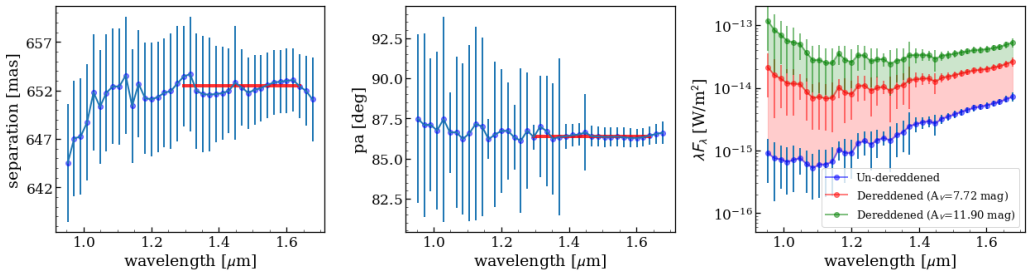

Figure 8.3: Fit done through the MCMC method on the observations of MWC 297 taken on the 2018-07-28. On the left the separation, in the middle the position angle and on the right the IFS spectrum of the companion in physical units. The red lines in the left and middle panels are the weighted average of separation and pa respectively. The spectrum of the companion (right panel) is provided undereddened (*blue points*), dereddened with the stellar value of A_V=7.72 mag (*red points*), and with A_V=11.90 mag, value obtained from the best-fit BT-SETTL models with extinction as free parameter (*green points*). The final astrometry of the companion were inferred in 1.29 μm $\lesssim \lambda \lesssim$ 1.64 μm spectral channels for the 2018 epoch, where the SNR of the companion is the highest.

on the location of the companion. Finally, this routine gives us the separation, position angle and the flux of the target with their errors, that are listed in Table 7.1.

Astrometry

Thanks to the MCMC method, for the second epoch, we derived the position of the companion (x_p and y_p) with their errors for each wavelength and we took the weighted average of them (red line in Fig. 8.3). For the first epoch, it was not possible to use the MCMC method, thus we performed a 2d gaussian fit to derive the position of the companion and we took the weighted average of the result of the method SDI and ASDI. We considered a pixel scale of 7.46 ± 0.02 mas/pixel (Maire et al. 2016), which is affecting the separation uncertainty. The separation uncertainty was computed as a sum in quadrature of the errors on the center, on the position of the companion and on the pixel scale for each frame (left Fig. 8.3 and Table 8.2). We note that we have taken into account the target distance error for the separation and its error in au shown in Table 8.2.

The position angle (PA) is affected by the error on the north angle determination considered to be -102.18±0.13 deg (Maire et al. 2016), used to derive the astrometry of the source. We propagate the errors on the measurement on the position and on the true north to get the final error shown in the middle panel of Fig. 8.3 and in Table 8.2.

As we show in Fig. 8.4, we suggest a companion comoving with the host star and its trajectory to be compatible with Keplerian motion. If the companion was a background star, it would move on a trajectory as shown by the black line: its proper motion after 3.25 yr exceeds the centroid discrepancy of the two observation sets (orange and blue), albeit within 2σ uncertainty. Assuming face-on circular orbit (the disc inclination is $\sim 5°$, Alonso-Albi et al. 2009), the keplerian motion would account for a shift in position angle of 1.26°, inside the error bar of the first detection.

Our 2-epochs astrometry does not rule out completely the possibility of a background object. Therefore, we use the TRILEGAL model of the galaxy to estimate the probability of the point source being a background star (Girardi et al. 2005). TRILEGAL yields a total number of 6553 stars with an H-band apparent magnitude brighter or equal to that

of the companion candidate ($H \leq 13.84$ mag; Sec. 8.4.3) within a $30' \times 30'$ patch of sky centered on the star, hence a density of 0.002 arcsec^{-2}. The probability of the point source to be a background object is thus $1 - \mathcal{P}(n = 0|\lambda = 0.002, B = 2) \approx 0.4\%$, where $\mathcal{P}(\lambda, B)$ is the spatial homogeneous Poisson point process probability with rate λ and area B. Given the separation of $\sim 0.7''$, we conservatively consider a $2'' \times 2''$ box centered on the star for the area.

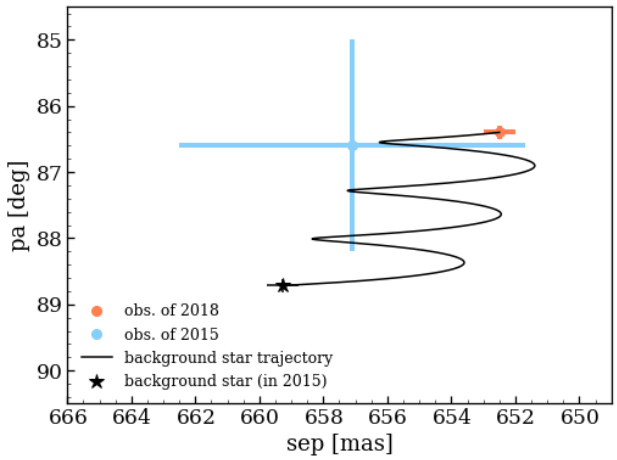

Figure 8.4: We show the measurement on the companion of MWC 297 for the data taken on the 2015 (light blue point) and on the 2018 (orange point) as tabulated in Table 8.2. Black line shows the trajectory for a background star going back to the 2015 epoch. If we consider the companion to be bound its keplerian motion in 3.25 yr would move the position of the companion of 1.26 deg (the disc inclination is small), inside the error bar of the first detection.

Spectro-photometry

The longer integration time of the 2018 data allowed us to detect the companion candidate at a significant level in all Y, J and H bands (the one of H band is shown in center left Fig. 8.1) and derive the spectrum of the companion (Fig. 8.3). For each frame, we measured the flux of the stellar emission using the "Flux image" and the flux of the companion estimated through the MCMC method described in Section 8.4.3. This method accounts also for the possible flux loss due to the aggressive routine used. The stellar flux error was considered as the discrepancy between the two sets of the "Flux" image measurements. Moreover, we converted the spectrum of the companion to physical units. To produce the final calibrated spectrum (Figure 8.3), we multiplied the measured spectrum of the companion by the ratio between the stellar flux in physical units, obtained though a polynomial fit of the stellar SED in the IFS wavelength range, and in ADUs in each spectral channel. For completeness, we also measured the total emission of the companion over the star in bands Y, J and H with errors (Table 8.2) and derived the apparent magnitude of the companion in those bands (17.30 mag, 16.21 mag and 13.86 mag, respectively).

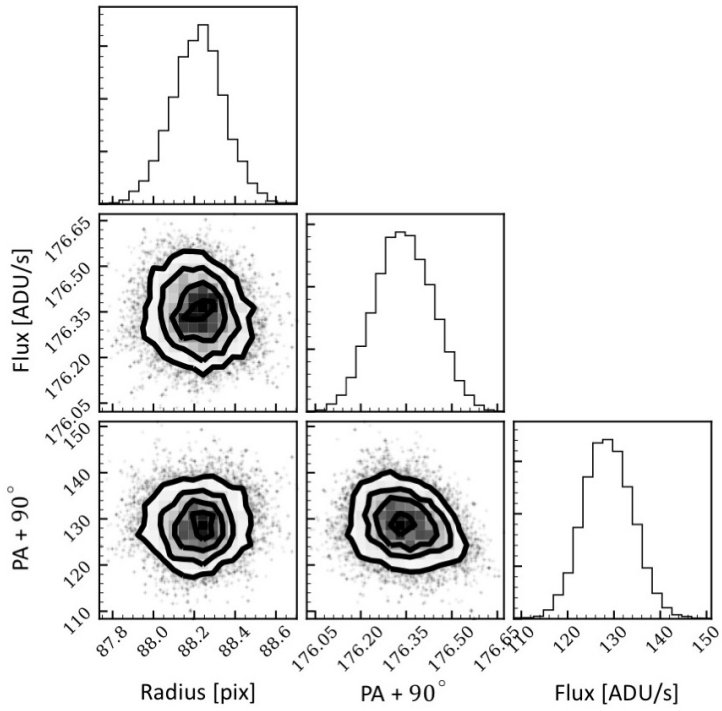

Figure 8.5: Derivation of the position (separation and position angle) and flux of the companion of MWC 297 through an MCMC method for a specific wavelength (λ=1.60μm). The separation (r) is shown in pixels (88 pix $\sim$ 651 mas), whereas the position angle (θ-90°) is in degrees.

8.4.4 Spectral analysis

The undereddened spectrum of the companion (*blue points* in the right panel of Figure 8.3) shows an extremely red slope, suggesting significant extinction. Fitting the central star SED suggests the latter has an extinction $A_V \sim 7.72$ mag. Nonetheless, the extinction affecting the companion is not necessarily the same as that of the star, as each component might be embedded and surrounded by their own dusty disc, in addition to any possible envelope still surrounding the system at that young age (e.g. Bowler et al. 2014; Mesa et al. 2019).

Therefore, we first followed a similar strategy as in Christiaens et al. (2018), and considered extinction as a free parameter in fits to a grid of BT-SETTL models (Allard et al. 2012). Our grid of BT-SETTL models contains 4 free parameters: effective temperature, $T_{\rm eff} \in [1200K, 5500K]$ in 100K steps; surface gravity, $\log(g) \in [2.5, 5.0]$ in 0.5dex steps; radius, $R_B \in [0.1\ {\rm R}_\odot, 3.5{\rm R}_\odot]$ in 0.01 $\rm R_\odot$ steps; and extinction, $A_V \in [0, 21]$ mag in 0.1 mag steps. We then considered the same grid but we fixed the extinction to A_V=7.72 mag (right Figure 8.3, *red* points), same as for the central star.

Next, we considered two libraries of template spectra. We first included all 76 pre-main sequence stars spectra compiled in Alcalá et al. (2014) and Manara et al. (2013, 2017), which are members of the TW Hya, σ Ori, Lupus I, III and IV star forming regions, spanning G5 to M8.5 spectral types. We also considered template spectra from the SpeX library (Burgasser 2014). We included all young dwarfs, identified based on their gravity class (limited to γ and δ, see Cruz et al. 2009) or their membership in young ($<$ 10 Myr

old) clusters. A total of 156 objects spanning M0 to L6 spectral types were considered for the fit. For either libraries, we considered two free parameters to account for different extinction and distance between observed and template spectra.

For all spectral fits, we convolved the models and templates with the IFS spectral response before binning them to the same wavelength sampling. We then minimized a goodness-of-fit indicator χ^2 that accounts for the spectral covariance of the IFS instrument (Greco & Brandt 2016; Delorme et al. 2017b).

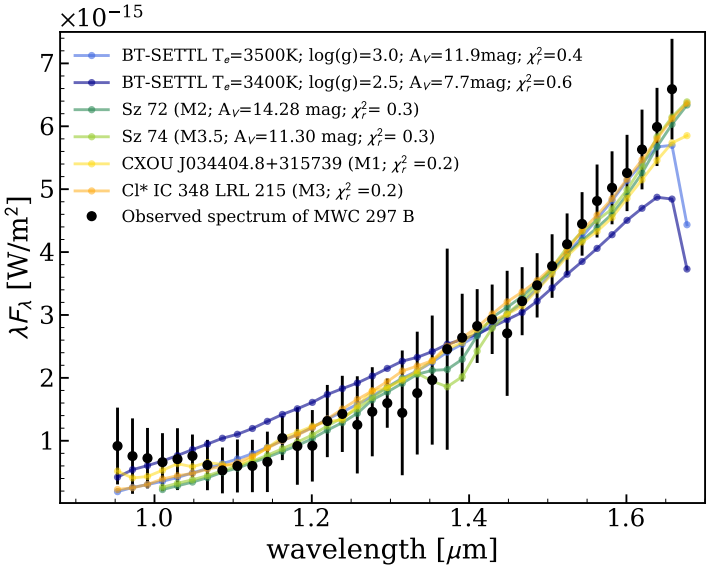

Figure 8.6: Best-fit BT-SETTL models with extinction as free parameter (light blue) and with A_V inferred from the central star (dark blue). Green and yellow curves show the best-fit YSOs and SpeX template spectra.

Figure 8.6 shows the best-fit BT-SETTL and YSOs template spectra (*blue* and *green* color) with the undereddened spectrum of the companion candidate (*black points*). With extinction as a free parameter, the best-fit BT-SETTL model has $T_{\rm eff} = 3500$ K, $\log(g) = 3.0$, $R_B = 1.13 R_\odot$ and $A_V = 11.9$ mag (*solid line*; $\chi^2_r \sim 0.4$), consistent with a young (very-low gravity), gravitationally contracting and embedded stellar mass companion surrounded by a lot of dust. By contrast, lower values of extinction (e.g. A_V =7.72 mag, *dotted line*), gave significantly worse fits.

The best-fit template spectra correspond to early M-type (M1 to M3.5) YSOs from (i) the 1–3 Myr-old Lupus I cloud (Sz 72 and Sz 74; Alcalá et al. 2014); and (ii) the ∼2 Myr-old cluster IC 348 (CXOU J034404.8+315739 and Cl* IC 348 LRL 215; Luhman et al. 2003). Interestingly, both the SpeX targets are located in the youngest part of the IC 348 cluster, where class 0/I objects have been identified (Luhman et al. 2003, 2016). In particular, they could also be class 0/I objects given their significantly lower differential extinction compared to the best-fit extinctions associated with the Lupus I and BT-SETTL spectra, suggesting $A_V \gtrsim 10$ mag for the companion.

Table 8.2: Observation log and MWC 297 B properties.

Obs. date†	Exp.	seeing	Δ PA	sep	sep	PA	ΔY	ΔJ	ΔH	M_B
	[s]		[deg]	[mas]	[au]	[deg]	[mag]	[mag]	[mag]	[$M_\odot$]
2015-04-29	1664	0.68	1.1	657.1±5.4	246.4±15.2	176.6±1.6	–	–	10.19±0.53	0.1–0.2
2018-07-28	5760	0.91	54.3	652.5±0.5	244.7±13.2	176.4±0.1	10.11±0.8	10.08±0.17	9.58±0.03	0.1–0.5

Notes. †Programs 095.C-0787 (PI: van den Ancker) and 0101.C-0350 (PI: Ubeira Gabellini), respectively. Table lists observation date, total integration time, mean seeing, total field rotation, separation (mas and au), position angle, delta magnitude (Y, J, H) and estimated companion mass. The telescope tracking mode is field-tracking and pupil-tracking respectively.

8.4.5 Mass estimate

Considering an extinction of $A_V = 11.9 \pm 1.0$ mag (Sec. 8.4.4), our de-reddened J- and H-band absolute magnitudes are 5.3±0.3 mag and 4.2±0.1 mag (using Cardelli et al. 1989), respectively. We compared the absolute magnitudes and colors with BCAH98, AMES-Cond and BT-SETTL (Chabrier et al. 2000; Baraffe et al. 1998; Allard et al. 2003) models that suggests a mass of ∼0.10–0.25 $M_\odot$. Comparing the T_{eff} and age with stellar isochrones (Baraffe et al. 2015) suggest a mass of 0.25–0.5 $M_\odot$ (Table 8.2). Considering that this estimate assumes an age of 1 Myr — the youngest available, but an upper limit for MWC 297 (Vioque et al. 2018b suggest ≈0.02–0.03 Myr) — the companion mass may be lower. This is consistent with the best fit YSOs and SpeX template spectra with mass ∼ 0.45-0.50 $M_\odot$, targets older (1–3 Myr) than MWC 297. For the 2015 epoch, we estimated the mass using only the dereddened absolute H-band magnitude, due to the lack of obvious detection in other bands.

8.5 Discussion

The 0.8% probability of being a background star (Sec. 8.4.3) suggests that the detected point source is a bound companion to MWC 297. Our spectral analysis (Sec. 8.4.4) further argues in favor of a young and embedded early M-dwarf. BT-SETTL models are uncertain at low gravity (e.g. Bonnefoy et al. 2014), and the template library lacks spectra younger than 1 Myr old, both suggesting an even less massive object. Moreover, the spectral fit is not able to reproduce exactly the observed spectrum (Fig. 8.6). Using dust extinction curves different from those assumed for the ISM may also improve the fit (e.g. Marocco et al. 2014). Furthermore, the very red slope possibly is partially due to excess dust thermal emission from a circum-secondary disc (e.g. Christiaens et al. 2019a) - with less extinction needed. Follow-up observations at longer wavelengths are required to better refine the characteristics of the companion and test the presence of a hot circum-secondary disc component.

Our detected low-mass companion might be carving the gap in dust thermal emission suggested by Alonso-Albi et al. (2009), based on the SED and 1.3 mm and 2.6 mm IRAM Plateau de Bure (PdBI) interferometer data. The resolution of the PdBI data ($1.''1 \times 0.''4$ for 1.3 mm and $1.''4 \times 0.''9$ for 2.6 mm), however, was too coarse to resolve the $0.''65$ separation between the central star and the source. Atacama Large Millimeter/submillimeter Array (ALMA) submillimeter continuum observations would allow to test whether the companion lies within a large annular gap.

In Fig. 8.7, we show our companion detection (blue) together with archival data taken from the exoplanets.eu database. The mass of our companion is set to $0.25\ ^{+0.25}_{-0.15}\ M_\odot$.

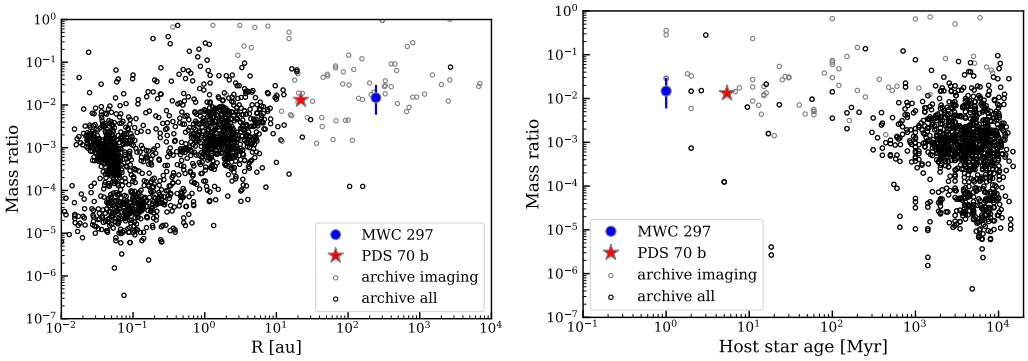

Figure 8.7: Ratio between the companion and the stellar host mass (y-axis) vs the separation from the central star (x-axis, top) or the age of the stellar host (x-axis, bottom). The empty circles represent the known exoplanets: in gray, direct imaging; in black all the other methods. The blue circle is our detection of our companion MWC 297 B; with a red star is shown PDS 70 b (Keppler et al. 2018). We note that, although our companion mass is large ($\sim$0.25$M_{\odot}$), its mass ratio is similar to the one of PDS 70 b.

With a red star we show the position of the recently discovered PDS 70 b protoplanet (Keppler et al. 2018). Our target is low-mass compared to the host star and at large separations from its central star, similar to other direct imaging detections. Moreover, Fig. 8.7 shows that our source present a mass ratio of $\sim 10^{-2}$, similar to the value found for PDS 70 b. Interestingly, the companion around MWC 297 is one of the few discovered around young host stars (bottom Fig. 8.7). We note also that many of the archival companions with ages below 10 Myr are sources still to be confirmed. The companion is young and of low-mass and it is placed in the same parameter space accessible by direct imaging techniques.

Given its interesting mass ratio and age, it will be fundamental to understand its evolution and interaction with the disc in order to understand the behavior of low mass ratio, which mainly affects the disc dynamics. Detecting already formed companions in these young discs is of paramount importance also to test whether binary formation happens on short timescales, as it is suggested by independent works (e.g., Greaves & Rice 2010; Williams 2012; Najita & Kenyon 2014b; Manara et al. 2018).

We note that the best-fit extinction is very high, but it is not the first time to detect an embedded young low-mass companion with large extinction (e.g. FW Tau C: Bowler et al. 2014; R CrA B: Mesa et al. 2019; TWA 30 B: Looper et al. 2010) Possibly it can have an edge-on disc (like TWA 30 B and FW Tau C - Looper et al. 2010; Wu et al. 2017). Follow-up with ALMA and at longer IR wavelengths (to probe any thermal excess emission) is required to confirm whether that is the case for MWC 297 B. High-contrast imaging at longer wavelengths can probe the earliest stages of binary formation: embedded and extinct target which is intrinsically colder and fainter than the typical ones found.

8.6 Summary and conclusions

In this work we have presented the detection of MWC 297 B, a low-mass companion detected in the H band on 2015-04-29 and confirmed in Y, J and H bands on 2018-07-28. Our astrometry favours the object to be gravitationally bound and spectral characterization strengthens the hypothesis of a very young (<1 Myr) low-mass companion. Its

separation is 244.7±13.2 au, its position angle is 176.4±0.1 deg for the 2018-07-28 epoch, its mass is $M_{comp} \sim 0.25^{+0.25}_{-0.15}$ $M_\odot$ with a high extinction of A_V=11.9 mag. This target is particularly interesting owing to its extremely young age, high extinction. The mass ratio is comparable to that of PDS 70 b, but in the stellar mass regime, suggesting a similar formation process for low mass companions around high and low mass stars. The presence of the discovered companion could be related to the gap in dust thermal emission suggested in Alonso-Albi et al. (2009).

8.7 Follow-up: theoretical explanation

The synergy between observations of disc structures at different wavelengths and the physical processes driving their formation and evolution has allowed to better constrain how, when, and where stars, brown dwarfs and planets form. However, this is not the case for high-mass stars. Even though their existence dominates the physics and chemistry of galaxies, their formation remains poorly understood. According to the stellar IMF, they form rarely. Moreover, for protostars of $M_\star < 20M_\odot$, massive discs should be present (Cesaroni et al. 2006), but short lived ($\sim 10^5$ yr). Two main classes of high mass star formation theory are currently discussed: monolythic collapse and competitive accretion (Tan et al. 2014). These theories have to be further investigated for example by determining whether the behaviour of the disc around high and low mass stars is similar (e.g. MWC 758, Dong et al. 2018b). Despite recent observational progresses, the exact nature of protostellar discs surrounding high mass stars remains unclear. Are they simply low-mass analogues, with a plethora of substructure to be found at multiple wavelengths, as in MWC 758 (Dong et al. 2018b)? Or are they entirely different, with no disc substructure? What does this imply for companion objects?

There is an intriguing comparison between the massive star MWC 297, which hosts a low-mass companion within its disc, and the low mass star PDS 70, which hosts a directly detected planet within its disc. In this massive environment, it is important to understand how a low-mass companion has been formed. In particular, we want to test if the gap suggested by Alonso-Albi et al. (2009) can be explained by the new companion detection revealed by SPHERE at a separation of $\sim$ 245 au.

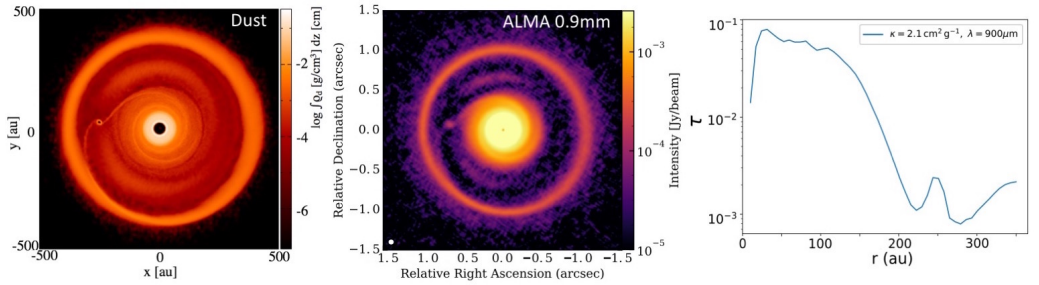

Figure 8.8: Left: Dust surface density of our SPH model of a disc made by a mixture of gas and mm dust with an embedded companion. Center: ALMA synthetic image at 0.9 mm. The stellar mass is set at $17M_\odot$, the beam size is 0.0248" and the water vapor to 1.262 mm. Right: Optical depth profile. We used MCFOST to compute the radiative transfer. Finally, we used the ALMA simulator to produce a synthetic image at 0.9 mm (center panel). The initial mass of the companion was set to 50 M_{Jup}.

It is well-understood that massive planets open gaps (e.g. Dipierro et al. 2016), so it is

likely that such a massive companion is responsible for the gap in dust thermal emission as proposed by Alonso-Albi et al. (2009). Moreover, such a massive companion is expected to host a circum-secondary disc ($R_{Hill} \sim 41$ au, $0.15''$ Szulágyi & Mordasini 2016, for the definition see Eq. 3.5), considering the companion mass and separation previously derived.

To test this scenario, we combined hydrodynamics and radiative transfer simulations performed a Smoothed Particle Hydrodynamic simulation with PHANTOM (Price et al. 2018b) of a disc with an embedded companion. The total disc mass was derived from a dust mass of $\sim$0.0023 $M_\odot$ (rescaled from Alonso-Albi et al. 2009). We modeled the gas and the mm-dust components using the one fluid method (Price & Laibe 2015; Ballabio et al. 2018) with 10^6 particles (Fig. 8.8, left panel). The simulations reported here focus on the interaction between the disc and the companion, already formed and embedded. Starting from this, we perfomed radiative transfer calculations with MCFOST (Pinte et al. 2006, 2009). We note that these simulations have been performed starting from a companion mass of $\sim 0.05 M_\odot$, lower than the one actually found. The result is thus just preliminary and was performed as a test. The next step will be to perform the same simulations using the actual companion mass and compare it to the results obtained here. This can provide a double-check for the companion mass estimate.

8.7.1 An ALMA follow-up proposal

We post-processed the result through the Common Astronomy Software Application (CASA) ALMA simulator to produce the synthetic image at 0.9 mm (Fig. 8.8, middle panel) by concatenating two measurement sets (antenna configurations C43.8 and C43.5 in band 7, 0.9mm) to have high resolution (~ 0.0248 arcsec) and at the same time do not lose flux. The high resolution is needed to detect at the same time the gap in the dust continuum emission (gap width estimated >100 au) and a possible spiral originates for the interaction with the companion (as seen in the simulation). Even just after a short evolutionary time (40 orbits), we observe the formation of a gap, which we expect to deepen as the simulation is evolved for longer timescales. In addition, we are also able to unveil the presence of a tight spiral and a circum-secondary disc. Evolving the simulation for longer timescales we do expect an even deeper gap. From our models we have derived the surface density profile and the optical depth as function of radius (assuming $\kappa \sim 2.1$ cm^2/g at 0.9 mm). The optical depth is lower than $\sim$0.1 in the whole disc (see left panel of Fig. 8.8), meaning that the disc is optically thin and we are sensitive to surface density variation. Considering that the total brightness of our simulated image is consistent with previous measurements of MWC 297 at 0.9 mm (Mannings 1994), we estimate the sensitivity from our CASA synthetic image. With the chosen setup, we are able to reach a S/N of ~ 16 (ring), ~ 120 (spiral) and ~ 7 (circum-secondary). Finally, if a circum-secondary disc around the companion orbiting in the gap exists, it will be resolved using a beam size of ~ 9 au, expected to be smaller than the diameter of the circum-secondary disc $\sim 0.3''$ (Szulágyi & Mordasini 2016). We are also currently testing the early phase evolution of this system to see that if the seed of the discovered companion could have been created by disc fragmentation due to gravitational instability or to other formation scenarios.

Chapter 9

Substructures in our Herbig stars sample

We performed a more complete analysis on the targets of the survey described in Chapter 7, where a clear disc detection was found (HD 100453, HD 100546, HD 169142, CQ Tau, T Cha, HD 141569 and AK Sco). For what concerns the companion detections in MWC 297, R Cra and HD 142527 we refer to Ubeira-Gabellini et al. (2020), Mesa et al. (2019) and Claudi et al. (2019) respectively. In particular, we used different techniques and performed an analysis over different Bands: Y, J and H. Moreover, we compared our results with millimeter emission and infrared polarized scattered light, if present. For what concerns the target properties, details on the observations and basic data calibration, we refer to the Chapter 7. In particular, we describe the detection of two symmetric spiral arms and shadows in HD 100453. Through total intensity scattered light observations, we detect wider spirals with respect to the one observed through PDI, following a similar structure of the ^{12}CO image observed with ALMA. Also in HD 100546 and CQ Tau, we detect multiple spirals that are less symmetric than the ones of HD 100453. Two face-on rings are visible in HD 169142. T Cha and AK Sco show an inclined disc with a cavity and, finally, HD 141569 presents multiple rings with a large cavity. Moreover, we found point-like sources in HD 169142 and CQ Tau using different methods and bands. For the former, we analyzed data of two epochs; for the latter, we performed a basic spectrum derivation. The following Chapter is organized as following: in Section 9.1 we describe the methodology used to post-process this sub-sample of data in comparison to what described in Chap. 7 and 8; in Section 9.2 we describe for each target: the studies previously reported, the main results obtained through SPHERE-IFS data, a comparison of the results with literature and an interpretation of the data; in Section 9.3 we provide a comparison of the different techniques used taking as example some of the targets here described; finally, we give a general conclusion in Section 9.4. We note that we show in Appendix B some complementary results to the ones described in this Chapter, particularly for what regards different observing days and significance of the results: contrast curves, STIM maps and SNR maps for different methods.

9.1 Methodology

With respect to Chapter 7, we performed a further analysis of the disc structures through the VIP code. In this case, we derived high contrast images from calibrated frames (still affected by quasi-static speckles), using both the spectral and angular information. The spectral information is related to the fact that speckles change radial position with wavelength, while real features remain fixed. We have already shown the post-processed images in Chapter 7. The angular information can be derived when the pupil of an altitude-azimuth telescope is fixed during an observing sequence. In this way, most quasi-static speckles remain fixed in the image, while real features rotate. In this Chapter, we

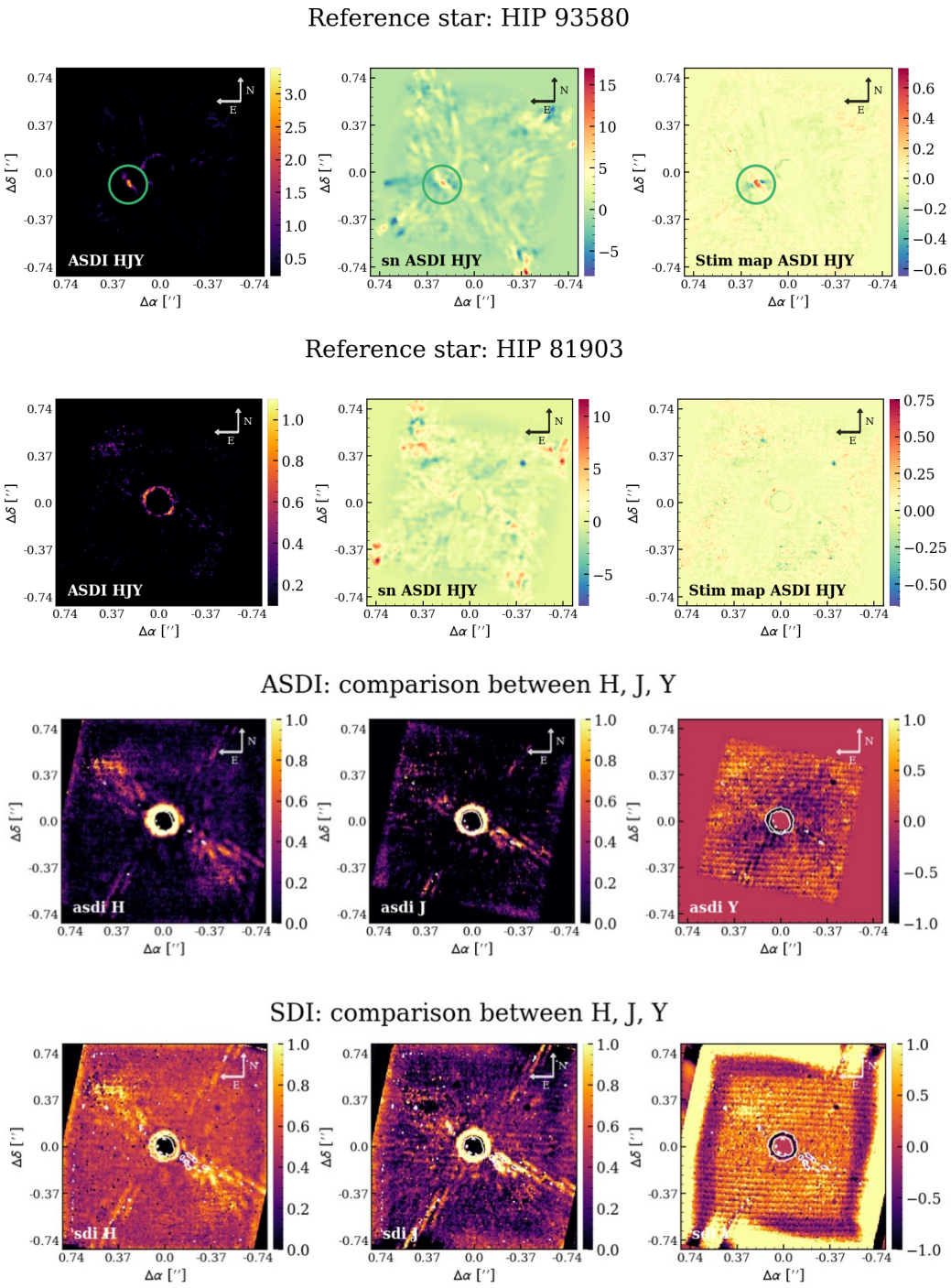

Figure 9.1: Final images for the reference star HIP 93580 (first row) and HIP 81903 (second, third and fourth row). The first two rows show the post-processed image after using the PCA-ASDI method (left), the signal-to-noise of the image (center) and the STIM map (right). A green circle shows the binary found around HIP 93580. The third row and the fourth row show the methods PCA-ASDI and PCA-SDI respectively for H (left), J (center) and Y (right) Bands.

used the same procedure adopted in Chapter 8: we used principal component analysis (PCA, Sec. 6.5.2)-based algorithms in VIP to model and subtract the stellar PSF and associated speckles. In particular, we used the PCA-ASDI method, using both spectral and angular diversity and PCA-ADI (performed in either full frame and annular version - PCA-ANNULI). We compared these results with the ones previously described. For the PCA-ADI technicalities we refer to Section 6.4.2. We note that the PCA-ANNULI used in this thesis always exploits both angular and spectral diversity done as in PCA-ASDI, but dividing the field of view in concentric annuli. Moreover, we tested also different values of principal components when needed.

9.1.1 Reference stars

For the reference stars behavior exploiting the PCA-SDI technique, we refer to Chapter 7. In this section we characterize the method used (PCA-ASDI, top rows of Fig. 9.1) with the behavior of reference stars. The rotational variation in FIELD tracking mode is in principle zero and thus it would not allow to perform PCA-ASDI, but in the reality there is always a variation of $\sim 1°$. If we consider it, without being able to fully exploit the angular information, the image post-processed with PCA-ASDI looks similar to the one obtained with PCA-SDI, but cleaner. It is important to underline the fact that the bright ring at the edge of the coronagraph, remnant of the stellar emission, is still present. While in PCA-SDI it is quite symmetric, using PCA-ASDI the ring is brighter on one side and fainter on the other one. The radial extent of the PSF residual is the same as for PCA-SDI. We analyzed also the difference of post-processed images derived either using just the single bands (Y, J, H) and with all of them combined (see bottom rows of Fig. 9.1). We measured on average a radial extent (R) of the bright ring of R$\sim$ 125 mas, for the H band; R$\sim$ 118 mas, for the J band; R$\sim$ 125 mas, for the Y band. We note that the ring in the Y band is visibly over-subtracted and thus it has negative flux values. Using both PCA-SDI and PCA-ASDI, the images look cleaner if Y J H Bands are combined. The remnant of stellar emission in H band is not subtracted enough, whereas the Y band is over-subtracted. The J band is the cleanest. If we consider the PCA-SDI image in regions far from the disc emission in the center and the corners, its average flux is not zero as expected, but it is equivalent to the standard deviation. PCA-ADI and PCA-ANNULI techniques were not tested for the reference stars, because the targets were observed in FIELD tracking mode. However, for the science targets where PUPIL tracking mode was used, we describe also the results obtained with those techniques. The analysis reported here shows how important is to combine different methods to study the disc structures. Each of them can better show a specific feature and all of them together can help to reconstruct the total disc emission in scattered light.

9.2 A variety of disc detections

In the current section, we give a brief description to each target considered, we present the main results obtained together with their comparison with previous observations in PDI, millimeter continuum, and, where possible, line emission. We analyzed the data through different techniques and using different bands. For clarity, in this section, we provide just the most meaningful results obtained.

9.2.1 Spirals and shadows in HD 100453

The target

HD 100453 is a ∼7 Myr Herbig star located in the Sco OB2-4 region. It is classified as a Class II, Group I source. For the properties of the HD 100453 target we refer to Table 8.1 and 7.1. In this target Benisty et al. (2017), detected the presence of a ∼0″.18 (∼ 18.5 au) cavity, two symmetric spiral arms and shadows in polarized scattered light with SPHERE/VLT. Collins et al. (2009) found HD 100453B to be physically bound to HD 100453A with a separation of 1″.025 and PA of 126°, a spectral type of M4.0V–M4.5V, and a mass of 0.21-0.30 $M_{\odot}$. Moreover, they detect another point-like source (called Star C) at PA=30° and separation ∼0″.8. HD 100453A has a proper motion opposite to the one of star C, indicating that this is, most probably, a background star. Wagner et al. (2018) confirmed HD 100453B to be comoving with the host star and constrained orbital parameters of the binary using different epochs observations. Hydrodynamical simulations tested the scenario of HD 100453B being the reason for the spiral structure detected by Benisty et al. (2017). Considering that the shadows are located at the root of the spirals, Montesinos et al. (2016) suggested that the shadows of HD 100453 are triggering the spirals. In the hypotesis made by Wagner et al. (2018) and Dong et al. (2016), the companion does not account for the shadows. In this scenario, they should be produced by the presence of a warped inner disc, as presented in Min et al. (2017) where the modeling of NIR interferometric data was performed. The large gap and possible warp could suggest the presence of another companion carving the detected cavity. Recently, ALMA Band 6 observations (van der Plas et al. 2019) reported an extended disc in CO emission around the primary star extending from ∼ 68 mas to 1″.10, almost coincident with the location of the secondary. The millimetre emission was found at a radius coincident with the northern spiral arm found in scattered light. Both of these features seems to be in contradiction with the standard picture of disc truncation (Artymowicz & Lubow 1994). The conclusion of this work was that the orbit of the companion should be significantly misaligned with the circumprimary disc and that possibly the companion is not responsible for launching the spirals, supporting the shadow origin of Montesinos et al. (2016). Rosotti et al. (2019a) propose an alternative scenario based on new band 7 ALMA observations at high-resolution. Their data present a clear sub-mm and gas CO counterparts to the scattered light observations, confirming that the spirals are actual structures on the disc surface density. The scattered light traces the spiral surface structure, whereas the continuum probes the disc midplane. There is thus a displacement in the spiral pitch angle depending on the tracer, as proposed by Juhász & Rosotti (2018). Finally, given the fact that the gas spiral points toward the companion, they confirm the scenario proposed by Dong et al. (2016). Given all these evidences, this system is a perfect laboratory to test different models of spiral formations with observations.

SPHERE-IFS results

We show here the disc detection of HD 100453 for four epochs observed between April 2015 and January 2016. In particular, we focus on the detection of the 4th of May 2015. In Fig. 9.2 (top left), we show the result obtained through the PCA-SDI method, using a number of principal components equal to two and combining all the frames (YJH). A disc with multiple spiral arms is clearly visible in the post-processed image. In particular, it shows two main spiral arms (S1 and S2) and two minor (S3 and S4), which appears to be the continuation respectively of S1 and S2. The names of the spiral arm detected are

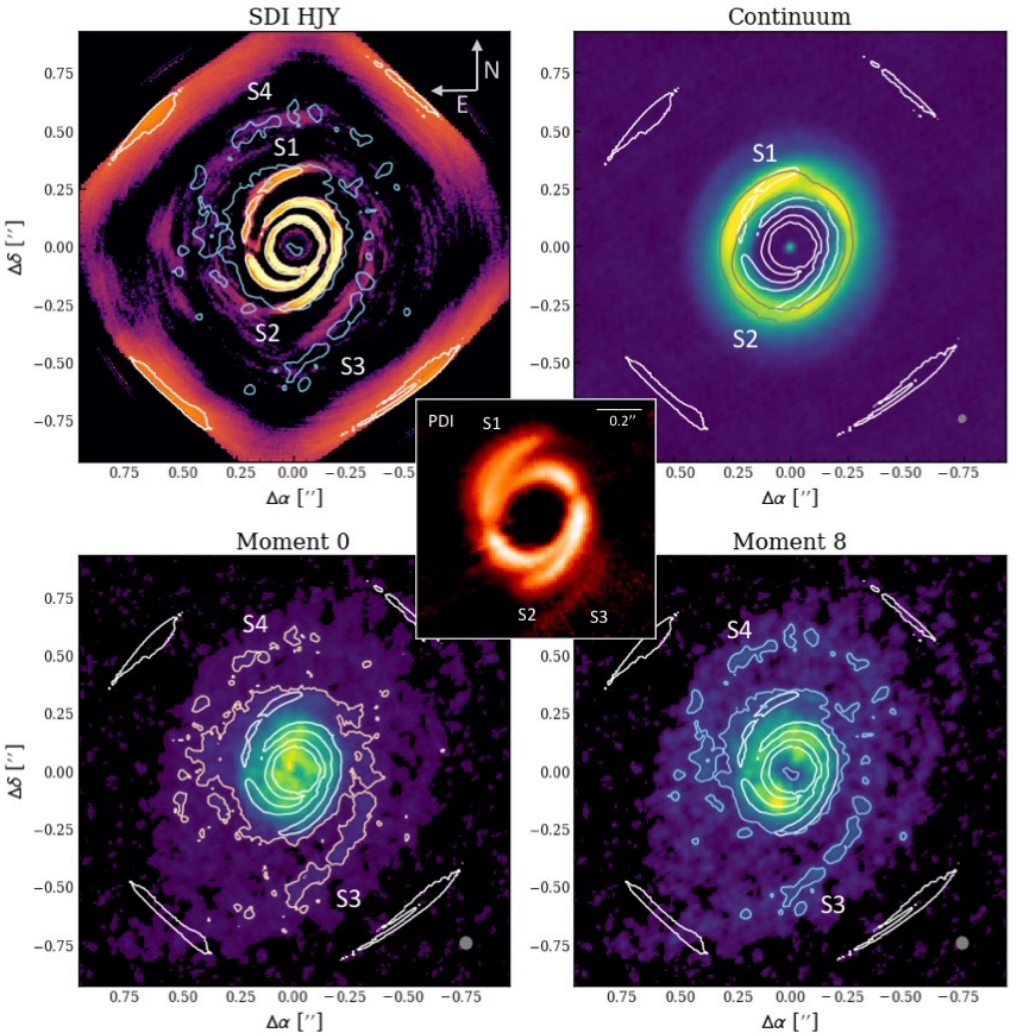

Figure 9.2: SPHERE image of HD 100453 (2015-04-10) post-processed with PCA-SDI (top left), using as number of principal component two; the images of the continuum (top right) and CO (moment 0 and 8, bottom) are given by the courtesy of Rosotti (described in Rosotti et al. 2019a); the J-band Q_ϕ (PDI) image scaled by R^2, with R being the distance from the star (Fig. 2 of Benisty et al. 2017, center). On top of each image, we show in white the contour of the SPHERE image. The contour of the continuum (gray), of the Moment zero (i.e. integrated intensity, pink), of the Moment eight (i.e. peak intensity, blue) are superimposed to the images itself as a comparison with our data. For ALMA continuum and CO, the beam size is respectively of 0.″036 x 0.″031 (pa=-38.36°) and 0.″054 x 0.″052 (pa=83°).

taken by the one of Rosotti et al. (2019a). We note that this image shows clearly that the spiral disc continues inside the millimeter cavity and it is not connected with the other spiral, as suggested by Montesinos et al. (2016). It is possible to distinguish the presence of the two shadows in a position correspondent to the scattered light images presented in Benisty et al. (2017). They can be thus associated to a real feature in scattered light, confirming what seen in polarized light. Moreover, we note that in this image the shadow inside S2 is less deep than the one in the S1 spiral arm. The shadows were not visible using npcs=1. A better contrast is achieved in this regards by the PCA-ASDI method (see Fig. 9.3). This was already visible in the images showed by Benisty et al. (2017), exploiting the ADI technique, where the data from Wagner et al. (2015) were used.

Moreover, the S2 spiral arm (Fig. 9.2) is brighter than the opposite spiral arm (S1), as seen better through the PCA-ASDI and PCA-ANNULI methods (see Section 9.3). Moreover, while S2 has a homogeneous luminosity, S1 starts with the same brightness, but it decreases its emission after the shadow and then it tends to slightly increase toward the end. This can be due to a different scattering coming from the two arms: forward scattering for S2 and backward scattering for S1. Moreover, the spiral pointing toward the North (S1) is not well defined, with some distortion in the emission. The brighter emission at the upper tail of S1 gives strength to the SED measurement that suggests a possible flaring effect. Finally, we note that the presence of central bright emission next to the coronagraphic spot can be due to the stellar contribution considering its similarity with the PSF residual in the reference stars images presented. We masked the region where the coronagraph was present (r$<$ 75mas). The emission coming from the inner region between 75 mas and the PSF residual can either be due to a real cavity or to the effect of the coronagraph. The coronagraph action is not sharp: it obscures completely the emission up to 75 mas and partially up to 185 mas of diameter.

Finally, a relevant and novel discovery we made through the method for PCA-SDI is that, using npcs=2, the two-arms of the spiral appear to continue up to $0''.5$, longer than previously detected. Different techniques (e.g., Fig. 9.3) show just the S1 and S2 spiral with a disc size of 250 - 300 mas. In Fig. 9.2, we superimpose the contour curves of the CO (Rosotti et al. 2019b) on top of the PCA-SDI image. The position of the spirals are almost coincident. Making the assumption that the scattered light traces the same spiral described by Rosotti et al. (2019a) in the CO, in Fig. 9.2, we note that the bright emission at the bottom of the image (present in both PCA-SDI and PCA-ANNULI) is not coincident with the gas emission, but it is shifted inside. Moreover, using the PCA-SDI technique the emission coming from the S1 arm appears to continue with the S3 arm. The S2 arm instead appears to continue in the S4 arm without showing any shift in the outer part. If we compare our images with the one of PDI by Benisty et al. (2017), we can see that S1, S2 and two shadows are present as well, but the S3 spiral is just partially detected and S4 was not visible. For this reason S3 was considered to be the back side of the disc.

Comparing the images taken during different observing days (Fig. 9.3), the two shadows described above for the 10th of May 2015 are visible also during the 21st and 23rd of January 2016. During the 16th of January 2016, using the PCA-ASDI method (bottom left corner of the image), we detected the M-dwarf already discovered by Chen et al. (2006) and confirmed by Collins et al. (2009) and Wagner et al. (2015). The disc detection is instead noisier than in the other epochs. We note that the observations taken on the 21st of January 2016 are in IRDIFS mode and so H band is not present, but the image presents features similar to the other ones.

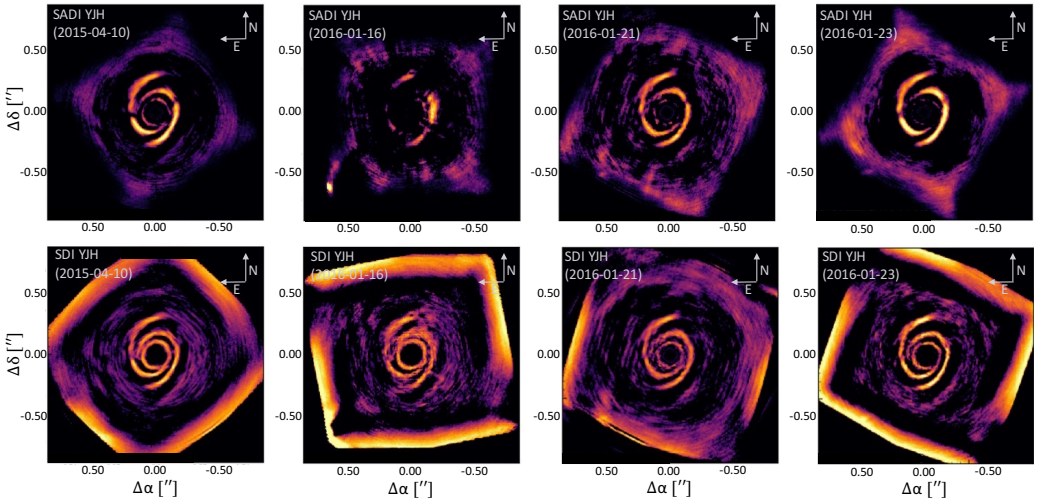

Figure 9.3: Observations of HD 100453 taken during different observing days, exploiting npcs = 1 and the methods PCA-ASDI (top) and PCA-SDI (bottom). During the 16th of January 2016, the disc detection is noisier than in the other days, but we detect through the PCA-ASDI method the M-dwarf already detected by Collins et al. (2009). The source is indeed on the bottom left corner of the image.

Discussion

These observations confirm the structure observed in polarized light. Similarly to the images taken with PDI by Benisty et al. (2017), the observations present two spiral arms (S1 and S2) and two shadows. We can thus confirm that the presence of shadows in total intensity, already seen in polarized light through observations of different days. The shadows are mainly visible using the PCA-ASDI technique. For the first time, we identified S3 and S4 as the prolongation respectively of S1 and S2.

The comparison between observing days at different wavelength may help to better understand the disc structure. In particular, different wavelengths trace the emission coming from different vertical layers. The continuum emission comes from the midplane layer; whereas the gas, in particular the optically thick ^{12}CO isotopologue, is emitted from the disc upper layers. At the same time, scattered light in the near-infrared is produced by micrometer grains and it originates in layers up in the disc vertical distribution. We note that the CO emitting layer is not expected to be emitted exactly at the same layer as the one of the H_2, most abundant gas tracer. If the scattered light emission traces the same emission of the gas, it is expected that scattered light emission comes from a vertical layer higher than the CO emitting layer. Considering that the disc is inclined of $\sim 34°$, the different position of the emission could be produced by a projection of different layers. We have evidences about the continuum, the gas and the scattered light. Giving these three components, an important follow up will be to measure the difference in the spiral position and derive the temperature profile of the disc. This will indeed shed light onto the spiral formation mechanism. The possibility inferred by Benisty et al. (2017) that the bright emission outside the principal double spiral arm is the back side of the disc is still a possible option.

Further modeling have to be done to test if the spiral detected in scattered light traces the same emission of the CO or if it is instead the back side of the disc. A simple way to test

this would be to inject a spiral with two different z/R and see what will be the projected spiral arm assuming a specific disc geometry (through the SED fitting). Moreover, doing this will allow us also to test if some of the structures observed may be produced by the routine used.

9.2.2 Multiple spirals in HD 100546

The target

HD 100546 is an 5 Myr old Herbig star located in the Sco OB2-4 region. It is classified as a Class II, Group I source. For the properties of the HD 100546 source, we refer to Table 8.1 and 7.1.

A planet candidate was recovered (HD 100546 B) around HD 100546 by Quanz et al. (2013a, 2015). The companion candidate was detected in L′ and M′ and its motion was consistent with comoving with the star. It was detected at a separation of ∼0.″457 and PA equal to ∼8.4° in L′. Using a completely different technique (spectroastrometry), Brittain et al. (2014) detected another companion candidate at ∼13 au. In particular, the astrometry of the OH spectral line profiles and their lack of time variability are consistent with the gas emission coming from an eccentric orbit seen almost stationary in the inertial frame. The same source was identified later as HD 100546 C by Currie et al. (2015), who detected it in H band with a PA of ∼ 148 - 154°. It is not clear whether it is a companion or a locally bright region of the inner disc.

An extended disc emission around HD 100546 was resolved by Walsh et al. (2014) using ALMA data in CO emission (radius ∼ 3.″8, equivalent to 390 au) and the continuum (radius ∼ 2.″2, equivalent to 230 au). An outer ring is visible in the continuum at 1.″8 with a width of 0.″7. Moreover, an inner disc cavity was resolved in polarized light, in the bands H, K_s and L′ using the NACO, GPI and SPHERE-IFS (Avenhaus et al. 2014a; Currie et al. 2015). Garufi et al. (2016) obtained polarized light images in the visible (SPHERE-ZIMPOL) and in H and K band total intensity using IRDIS-DBI and IFS. A complex morphology with arm-like structures and a cavity was detected. The cavity of 0.″11 of radius (in the visible) is elongated and it is compatible with an inclined disc (i ∼ 40 - 50 °) and a circular cavity. An extended emission in K band is found in the expected location of the outer planet candidate (b) and there is no gap associated to it. Moreover, the CO emission seen by Brittain et al. (2014) is located within the circumstellar disc. Follette et al. (2017) presented the results from optical and near-infrared high contrast images taken with the Gemini Planet Imager (GPI) and the Magellan Adaptive Optics system (MagAO). The observations were taken in polarized intensity and total intensity. They found an inner disc cavity at 0.″13 and a variety of spiral structures and they modeled the disc as a moderately inclined two-armed spiral disc. A disc asymmetry was found in new polarimetric images taken with SPHERE-ZIMPOL (Mendigutía et al. 2017b). The outer disc in their observations extends from 0.″12 to 0.″41, with an inclination of 44°. They report a detection of a 0.″18 bar-like structure which is crossing the gap. Walsh et al. (2017) presented detection of ^{12}CO with ALMA. The emission can be explained with an inner misaligned disc. Booth et al. (2018) studied the SO emission, a shock tracer, of HD 100546 finding asymmetric disc emission, suggesting a scenario where the possible inner disc warp is heated by the central star in the north-east side of the disc or it is tracing an accretion shock from a circumplanetary disc. Sissa et al. (2018) analyzed a dataset of data taken from SPHERE-IFS, SPHERE-IRDIS (with/without coronagraphs) and SPHERE-PDI. The disc extends up to 1″.8 using flux-conservative algorithms. The brighter part of the disc is of about ∼ 0.″3. They demonstrate that the brightest wings close to the star are a unique structure. They also found some bright emission in the

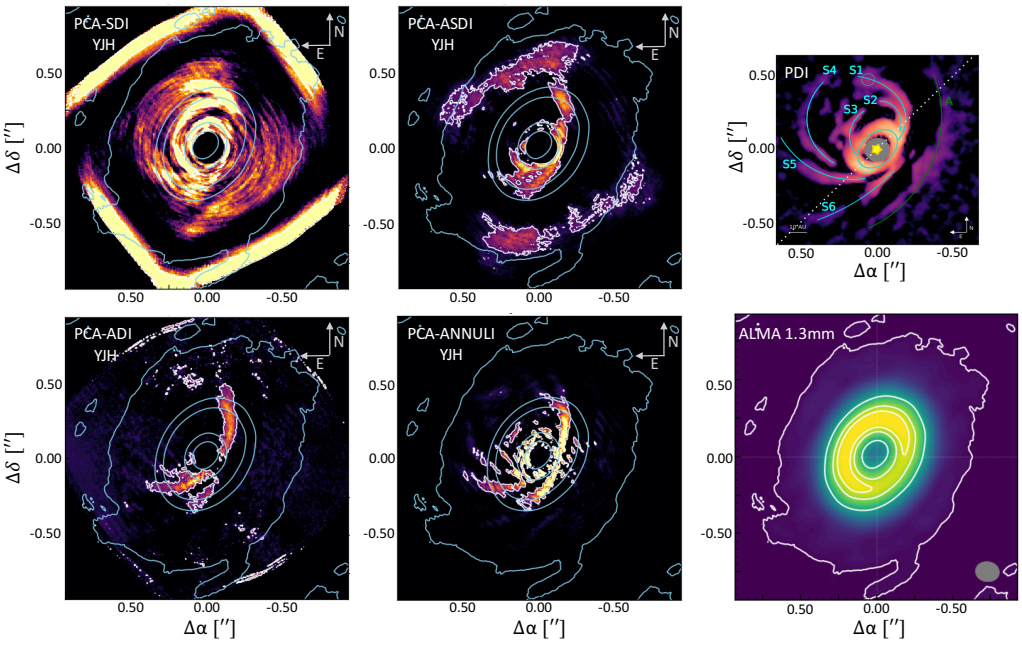

Figure 9.4: Emission of the scattered light observations of HD 100546 (2015-05-04) using PCA-SDI (top left), PCA-ASDI (top right), PCA-ADI (bottom left), PCA-ANNULI (bottom right) and npcs=1. On top with blue contours we show the continuum at 1.3 mm thanks to the courtesy of Dr. D. Fedele, the image is shown in the bottom right. The beam size of the ALMA continuum is of 0.″16 x 0.″13 (pa=7.15°). In the top right panel, we show Fig. 6 of Follette et al. (2017) taken in polarized light with GPI as a comparison of the spiral features visible: S1, S2, S3, S5, S6 are present also in our data, where S2 is the prolongation of S3. S4 and A are instead not visible. Our data do not show a connection between S1/ S2. A green circle shows the position of the companion identified by Quanz et al. (2013a).

position of HD 100546 B. Pineda et al. (2019) observed the disc at 870 μm and in the CO (3-2). They found an asymmetric ring between 0.″18 - 0.″36 with an optically thin continuum emission. They report a lack of continuum emission at the claimed companion position. They detect also spiral features in the CO integrated intensity map in the same position detected by scattered light polarized observations, suggesting a real spiral feature in the disc surface. Finally, Pérez et al. (2020) got recently high resolution ALMA observations at 1.3 mm, revealing a wide gap in the dusty disc. The disc is not symmetric and it presents fine radial and azimuthal substructures. The kinematics (using the ^{12}CO channel maps) is distorted particularly where the ring is brighter. Less distortion is found for the ^{13}CO and C^{18}O species, suggesting it to be due to vertical flows in the disc surface.

SPHERE-IFS results

We present here just the highest quality coronagraphic observations which are the ones of the 4th of May 2015. We will describe briefly the observations of the 31st of May 2016 (more details on Appendix B). A disc is clearly visible in the images post-produced through all the different techniques used, as shown in Fig. 9.4. The average disc extension is of $\sim$ 800 mas. The image shows different features through different methods. In Fig

9.4 (top right) we show the PDI observations (Fig. 6 in Follette et al. 2017), from which we take the names of the quoted features. In the PCA-SDI image we are able to recover the S1 spiral as in Follette et al. (2017) and the S2, S3 spirals appear to be connected. S5 and S6 are visible, also if better resolved in the PCA-ADI and PCA-ANNULI images. S6 and A are not detected in none of the technique used. In particular, all the techniques partially exploiting ADI, do not show the spiral arm in the East side of the image (S2, S3), strongly evident through the only use of PCA-SDI.

The presence of a cavity from our available data can be debated: the flux increases up to 0″.1. At radius equal to 0″.1 - 0″.15 a ring like emission is present possibly due to an undersubtraction of stellar light, visible in the bottom right side of the inner disc. The cavity is thus hard to be distinguished particularly using PCA-ASDI and PCA-SDI. The emission visible at 0″.2 toward North (in PCA-SDI, S7) appears to be larger than the typical PSF residuals and it is asymmetric. Moreover, the Norther spiral arm (S1) appears not to be an extension of S5/S6, in both the PCA-ASDI and PCA-SDI images. It is also not clear whether the S1 spiral arm is connected with S2 or not. For PCA-ANNULI and PCA-ADI the emission from a ring like structure basically disappear in the inner disc. The S2 spiral arm is not visible (separation of 0″.3) and S1 (separation of 0″.5) is less extended than what seen in the PCA-SDI image. This can be due to an effect of the ADI technique.

In green we show the position of the point-like source detected by Quanz et al. (2015), which appears to be on top of S1 in the PCA-SDI image. Sissa et al. (2018) recently claimed a detection of the same point-like source detected by Quanz et al. (2015). We cannot confirm however the presence of the companion in YJH band as shown by Sissa et al. (2018), where we detect the S1 spiral.

The S1 arm was detected already by Garufi et al. (2016), who saw a less extended spiral arm, and by Follette et al. (2017) (GPI), where the point-like source is on top of the S1 spiral. This non-detection does not exclude the possibility of the companion being present: the detection of Quanz et al. (2015) was made in the L′ and M′ bands, where scattered light (and local extinction) is almost negligible, and it should trace thermal emission; while near-IR scattered light observations are more affected by the disc extinction.

Finally, we compared our post-processed images with the continuum images thanks to the courtesy of Dr. D. Fedele using ALMA archival data. In Fig. 9.4, we show with blue contours the continuum at 1.3 mm. The inner cavity is smaller than the bright feature at 0″.2 (S7), suggesting it is real and at the edge of the cavity. The spiral structures in scattered light extends more than the brighter continuum emission and toward the East side, whereas the continuum shows a brightness asymmetry in the same location of the S2+S3 spiral detected by us. The fainter outer disc emission of the continuum extends up to 0″.8, whereas the one in scattered light is less extended.

Discussion

We follow the explanation made by Follette et al. (2017), who propose that the multiple spirals are generated by a 3 M_{Jup} planet at a separation of $\sim$ 0″.9 ($\sim$ 100 au). They made a hydrodynamics simulation which was post-processed through a Monte Carlo radiative transfer code and through the same routine they used for the science data in order to produce H band total intensity images at various inclinations. The simulation was not done to explain this disc in particular, but given the extension of the continuum emission, this starts to be an option. The best inclination found to describe the observations is $\sim$ 45°, similar to the one found by Garufi et al. (2016). The inner cavity could be instead produced by a second planet, invisible to our data, because it is inside the coronagrapic

mask. This is consistent with the gas to be highly perturbed at radii <60 mas within the dust gap (Pérez et al. 2020). The large scale kinematic effect may be explained by an accreting giant on an inclined orbit within the gap. From SPHERE SAM observations, Pérez et al. (2020) suggests that the putative inner companion should not be a stellar companion, but it should have a mass lower than 71 M_{Jup}.

9.2.3 The double ring structure of HD 169142

The target

HD 169142 is a 9 Myr old Herbig star located in the Sco OB2-1 region. It is classified as a Class II, Group I source. For the properties of the HD 169142 target we refer to Table 8.1 and 7.1. The observations by Panić et al. (2008) of the CO (J = 2-1) emission line and in the 1.3 mm dust continuum revealed the presence of a disc with an inclination of 13° and a position angle of 5°. The total mass of the gas was measured to be $\sim$ 0.6 - 3.0 $\cdot$ 10^{-2} $M_{\odot}$. Quanz et al. (2013b) presented PDI images of HD 169142, which reveals that the inner part of the disc ($< 0''.17$) has a depletion in dust, an annular gap between $0''.27$ and $0''.48$ and a discontinuity in the radial surface brightness profile at $0''.83$. An inner cavity is found in ZIMPOL-SPHERE images followed by a bright ring at a separation of $0''.18$ (21 au), an elliptic gap from $0''.25$ to $0''.47$ (29 - 55 au) and a second outer ring extending up to $\sim 1''$ (Pohl et al. 2017a; Bertrang et al. 2018)

Fedele et al. (2017) observed the target with ALMA in the gas (CO isotopologues J=2-1) and dust (1.3 mm) surface density structure. No dust emission was detected inside the cavity, which is of $\sim 0''.17$ (20 au), or in the dust gap which extends from $0''.28$ to $0''.48$ ($\sim$ 35-56 au). Moreover, the surface density of the inner cavity is reduced by a factor of 30 - 40. A similar structure in the dust was also previously discovered and modeled by Osorio et al. (2014) in the dust component at 7 mm with VLA. They detected gas inside both the dust cavity and the dust gap and they discovered that the gas component of the disc is much larger than the dust emission, extending up to $\sim 1''.5$ (180 au) in radius. Similarly to Fedele et al. (2017), Macías et al. (2019) found two dust rings, the first at $\sim 0''.17$ - $0''.28$ and the second at $\sim 0''.48$ - $0''.64$ with observations at 0.89 mm, 1.3 mm, and 3 mm with ALMA. This second ring was observed at high resolution by Pérez et al. (2019), who found that the ring is composed by three thin sub-rings. In agreement with previous polarimetric studies, Fedele et al. (2017) found that the size and position of the inner ring is consistent with dust trapping by a massive planet. Successively Macías et al. (2019) and Pérez et al. (2019) suggested that the presence of two giant planets at a location of respectively $R < 0''.17$ au and $0''.28 < R < 0.''48$ au could explain the double-ring disc detected. Moreover, Pérez et al. (2019) have been modeled the outer ring composed by multiple rings through a single migrating low mass planet. Finally, Toci et al. (2020), modeled the two-rings dusty disc together with the gas cavity considering the presence of two giant planets, finding that this structure can be a long lived feature, which give us constrains on the ratio between the masses and the position of the planets. Massive companion candidates were claimed to be detected in this system through direct imaging in the near-infrared (Reggiani et al. 2014; Ligi et al. 2018; Gratton et al. 2019) even if these detections have been found controversial.

SPHERE-IFS results

The HD 169142 target was observed for four nights (Table 8.1). We here present the results of the two epochs (2015-06-07 and 2015-06-28) with longer exposure time. In Appendix B we show more post-processed images regarding the second epoch and zoom-in views

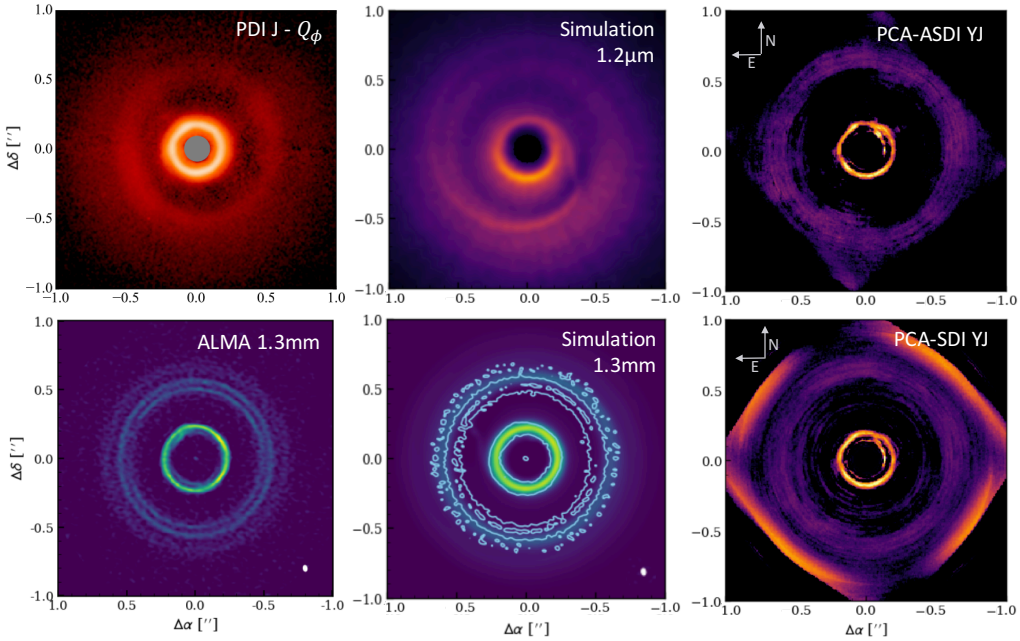

Figure 9.5: Observations of HD 169142 with PCA-ASDI (top right), PCA-ADI (bottom right) taken on the 2015-06-07, PDI J-band Q_Φ (Pohl et al. 2017a) (top left) and ALMA continuum at 1.3 mm (given by the courtesy of Dr. S. Perez, described in Pérez et al. 2019, bottom left). We note that here we used always npcs equal to one. In the center we show the simulations of Toci et al. (2020) at 1.3 mm (bottom) and at 1.2μm (top). We superimpose the contour curves of the observation of the ALMA continuum to the simulation at 1.3 mm for comparison.

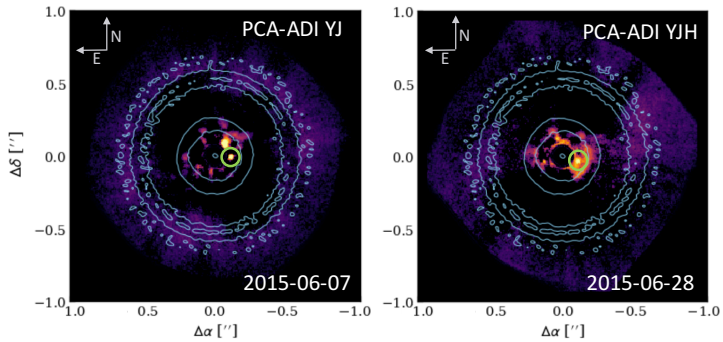

Figure 9.6: HD 169142 post-processed with PCA-ADI observed respectively on the 2015-06-07 (right) and on the 2015-06-28 (left), showing point-like detections. We note that here we used always npcs equal to one. We superimpose the contour curves of the continuum at 1.3 mm for comparison (see Fig. 9.5), which shows that the point-like sources are inside the millimeter continuum inner ring.

of the center of images varying bands and techniques (see Figs. B.2 and B.3). For the detection day 2015-07-05 we got similar post-processed images to the ones presented for 2015-06-28. During the observing day 2015-06-07, it is possible to distinguish three rings

in the PCA-ASDI and PCA-SDI images. It was visible a ring at $\sim$0$''$.1, a PSF residual left partially uncorrected by the techniques used (similarly to the previous targets described), here obscured for clarity of the image. The rings at 0$''$.2 and at 0$''$.5 - 0$''$.7 are real and almost coincident with the positions detected by Pohl et al. (2017a) through PDI observations. In the second epoch observations (see Appendix B) just the first ring at $\sim$0$''$.2 is confirmed and not the one at $\sim$0$''$.6.

In Fig. 9.5, we show a comparison between our scattered light disc emission using PCA-SDI (bottom right), PCA-ASDI (top right), the ALMA continuum observation of Pérez et al. (2019) at 1.3 mm (bottom left) and PDI observations in J-band Q_Φ (Pohl et al. 2017a, top left). The ALMA observation has a resolution similar to the one of our scattered light observations. It is possible to see that the rings detected by us correspond to the same spatial location of the ones in the continuum. The inner ring is less extended and peaks at the edge of the ring seen in the ALMA continuum (Pérez et al. 2019). The location of the outer ring is comparable to the one of Pérez et al. (2019), also if the peak is slightly more external. Moreover, we compared observations with the simulation of Toci et al. (2020), thanks to the courtesy of Dr. C. Toci, where two planets carve the dust and gas density profile. The hydrodynamical simulation was post-processed through MCFOST at 1.3 mm (bottom center) and at 1.2μm (top center). The first one has superimposed the contour of the ALMA observation at 0.07 Jy/beam for comparison. The inner ring is in agreement with the observation, while the outer ring is slightly more outside. The comparison with infrared scattered light observations (both PDI and total intensity) show a general agreement: the two rings, the gap and the inner cavity are present. The brightness asymmetry present in the simulation and not in the observations may be due to an inclination effect.

The images produced through PCA-ADI (Fig. 9.6), instead, present two-point like sources (observing days: 2015-06-07), in the same position of the PSF residual ring. Just one of point-like sources detected during the 2015-07-05 is visible in the second epoch, suggesting that the other one is an artifact of the post-processing technique. For a more detailed view on this, we refer to Fig. B.3 in the Appendix where a zoom-in view of images varying number of principal components is presented. We note that the observations taken on the 2015-06-28 have a lower exposure time with respect to 2015-06-07 and it is more affected by the presence of the stellar emission. The brighter companion, visible just in one epoch (on the top) is at a separation of $\sim$0$''$.106 and a pa$\sim$321°. The point-like source found in two epochs (bottom, green circle), instead, is at a separation of 0$''$.107 (12.5 au) and a position angle of $\sim$277°. The signal of the point-like source is pretty low and it is not possible to measure the emission in the single frames in order to perform a spectral characterization. Further observations with higher exposure times, are thus needed to confirm if these point-like sources are co-moving with the host star. The inner planet is modeled to be at 17 au in Toci et al. (2020) and it is slowly migrating inward. In any case, neither of these point-like sources can be related to the bright asymmetric feature at 0$''$.15 - 0$''$.2 seen in the data of Pérez et al. (2019) and described by Toci et al. (2020) (see Fig. 9.5), which is at about 35 deg. At the separation of the so found putative companion (bottom one), it should move of $\sim$ 36° in 2.4 yr (delay time between our SPHERE observations and ALMA data by Pérez et al. 2019) if their orbit is co-planar and not eccentric. In this case, they will be not compatible with such a feature. A further study on this is anyway needed.

Furthermore, we show the average radial profiles for HD 169142 (observing day: 2015-06-07) in Fig. 9.7 obtained for the PCA-ASDI method. We performed the same test also using PCA-SDI obtaining the similar results; this is not the case of PCA-ADI and PCA-ANNULI that delete most of the signal coming from the rings. The image has been

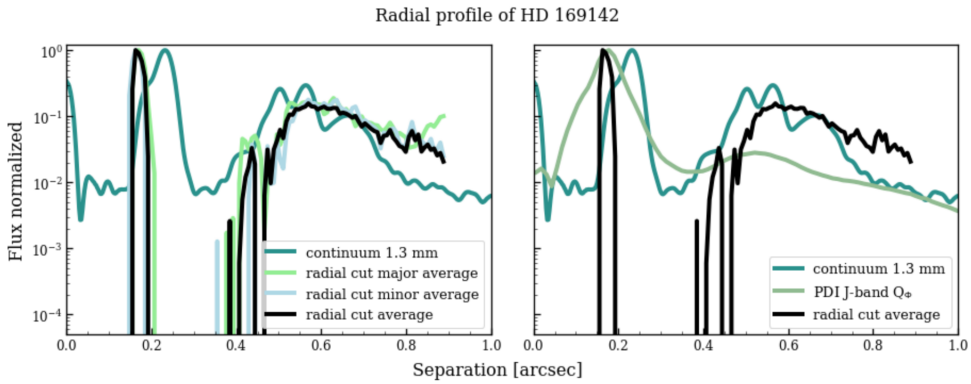

Figure 9.7: Radial profile of the HD 169142 image (2015-06-07) post-processed through PCA-ASDI method. On the left, we show the radial cut on the minor and major axis after rotating the image (light green and blue lines). Their average is the black line that is compared with ALMA continuum (Pérez et al. 2019) (dark green line) and PDI observations (Pohl et al. 2017a) (light green line). We note that all the profiles have been normalized to the maximum.

rotated using an inclination of 10°. We took a radial cut on the minor and major axis (blue and green lines, left panel) and performed an average (black line). Our results were then compared with ALMA continuum observation of Pérez et al. (2019) (dark green line, right panel) and PDI observations of Pohl et al. (2017a) (light green line, right panel). We note that all the profiles have been normalized to the maximum. The radial profiles show a shift of both PDI and total intensity images of the inner ring with respect to the millimeter data. The outer ring is puzzling because all the images show an extended emission from 0″.4 to 0″.8, but the peak of the continuum appears to be inside the one of the total intensity scattered light. PDI observations have a lower contrast of the rings with respect to the total intensity profile, but the peak appear to be more coincident with the one of the continuum.

Discussion

The disc detected is similar to what Pohl et al. (2017a) found in polarized scattered light. Two rings are present: the inner one is at 0″.2 approximately and the outer ring extends from 0″.5 up to 0″.7. In Pohl et al. (2017a), the outer disc extend up to about 1″. In our observations this is something difficult to test: in the PCA-SDI images the corners are noisy and thus the disc emission may be below the noise and in the other techniques the final field of view is too small. Polarimetric differential images indeed are more efficient at separating the stellar and scattered light from the disc thus as to highlight fainter signal from the circumstellar environment. At the same way, the image here observed can be useful to compare the emission found by polarized light and the one coming from total intensity at each point. This will be an important follow-up to test if the polarization fraction assumed until now is realistic for a face-on disc. The observations by Pohl et al. (2017a) are, indeed, spatially co-located with the CO emission found by Fedele et al. (2017). Moreover, the rings are compatible with the high resolution observation of the continuum by Pérez et al. (2019), which has an angular resolution similar to our data. The scenario proposed by Toci et al. (2020) is plausible: two planets are able to carve the inner cavity and the outer gap, keeping the inner ring long lived. The results of the

simulation ofToci et al. (2020) were already compared with ALMA continuum and CO data finding a good match. Thanks to the courtesy of Dr. C. Toci, we have also compared the scattered light emission of the model at 1.2μm, finding an overall agreement. A more exect test varying the grain size properties have still to be performed. Finally, we cannot confirm most of the point-like sources previously detected (Reggiani et al. 2014; Ligi et al. 2018; Gratton et al. 2019), which fall in the position of the inner ring detected. We found two bright spots at a separation of $\sim 0''.1$ in the observation taken on the 2015-06-07: the brighter one (on the top) is present just in this observing day, while the second (on the bottom) is visible in both epochs within a couple of pixels of error. The position of this second source is similar to the one found by Gratton et al. (2019) defined as 'blob A'. The separation of both point-like sources is similar to the one predicted by Toci et al. (2020) and in agreement with ALMA observations, but the PA is different and it seems not to be compatible with our detections if we assume a circular co-planar orbit. However, a more detailed study on this target have to be done to test whether this point-like source is real or not through astrometry and spectral characterization as performed in Chap. 8.

9.2.4 Multiple spirals in CQ Tau

For what concerns the target properties of CQ Tau we refer to Chapter 5, Table 8.1 and 7.1. To the description of the studies previously reported, we want to add the very recent work done by Uyama et al. (2020), who observed CQ Tau in the near-infrared, particularly in L$'$-band with Keck/NIRC2 and in H-band polarimetric observations with Subaru/AO188+HiCIAO. They detected new spiral arms, which corresponds to the ones afterwards called as S1 (in both data) and S2 (just through H-band polarimetric observations), and they did not detect any point-like sources. Moreover, they performed a characterization of the detected spiral.

SPHERE-IFS results

In this Section, we show the results obtained for the CQ Tau target on the observing day 2016-12-21. This observation has the highest total exposure time (7680 s) of our sample of targets, it was observed with the IRDIFS-EXT mode and in PUPIL tracking mode. A disc with multiple spiral arms is clearly visible thanks to all the methods used. Particularly the spiral arms with higher signal-to-noise are the same ones of the two detected in Uyama et al. (2020). The disc structure here visible is, however, more complex (see Fig. 9.8). For what concerns the names given to each spiral arm detected we refer to Fig. 9.8. There we show the images post-processed using different number of principal components (npcs) and methods. In particular, we present the results obtained through PCA-SDI using npcs = 2, 3, 4. The main spiral detected in Uyama et al. (2020) (from hereafter S1) is visibly more extended in our images using both PCA-ASDI and PCA-SDI. The result obtained with PCA-ADI is more similar to the one of Uyama et al. (2020). Finally, the PCA-ANNULI image shows more defined disc structures than PCA-ADI.

In all of the images shown, it is possible to distinguish the S1 and S2 spiral arms. In the top left Figure (npcs = 2, PCA-SDI), we show also the presence of the S3 spiral, which appears to be the continuation of S1 (using npcs = 1, 3, top center). The emission is lower in the center, where S1 seems to connect with S3 also if it is not clear weather or not they are really connected (see top center, zoom-in). Using npcs = 3, the S2 spiral appears to continue with the S4 spiral, even if the signal of this last one is quite low. Particularly using PCA-ASDI and PCA-ANNULI it is possible to distinguish also other features, called S5 and S6. Moreover, these images, together with the ones of PCA-

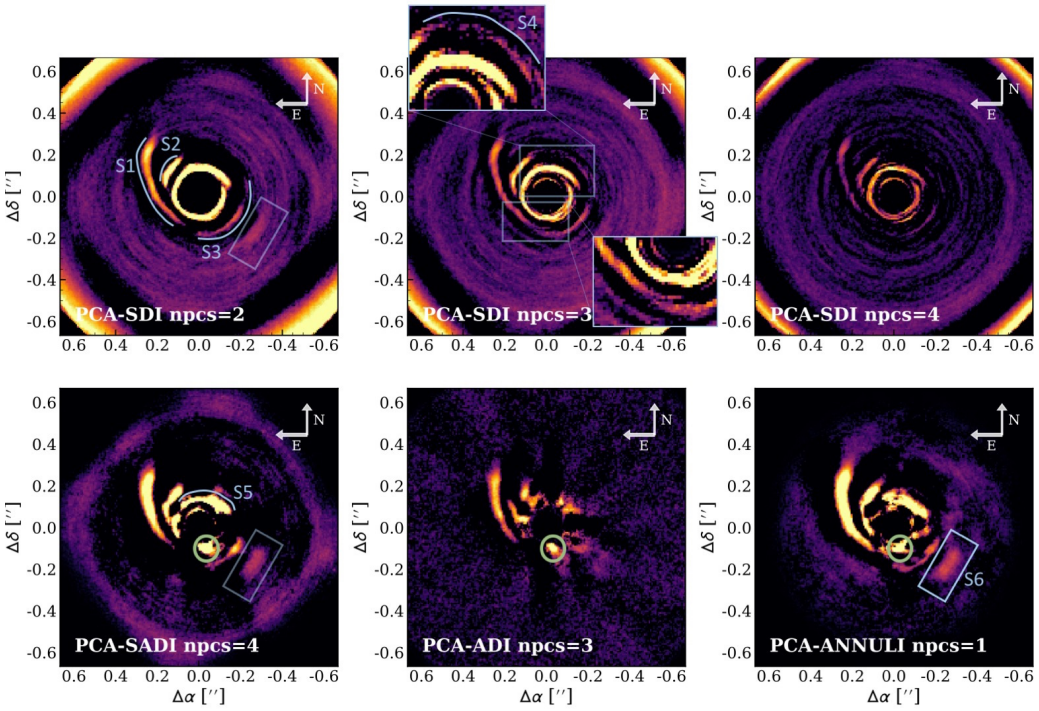

Figure 9.8: We present the SPHERE images of CQ Tau (2016-12-20) post-processed with PCA-SDI using npcs = 2 (top left), 3 (top center), 4 (top left); PCA-ASDI using npcs = 4 (bottom left); PCA-ADI using npcs = 3 (bottom center); and PCA-ANNULI using npcs = 1. In the images on the bottom it is visible a point-like source (green circle). We show the presence of the spiral arms S1, S2, S3, S4, S5, S6. A diagonal rectangular box shows the S6 spiral. Several of these features are present in more than one image.

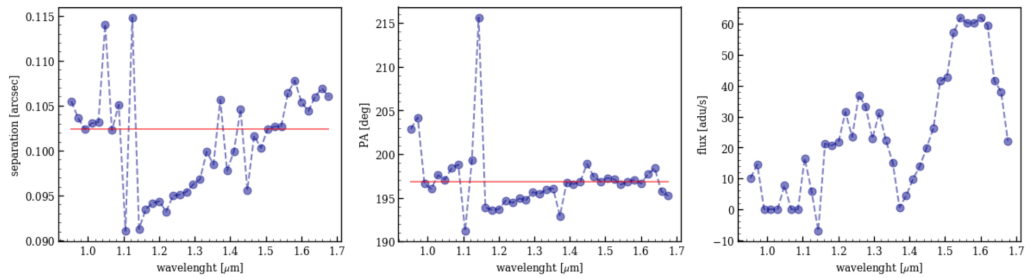

Figure 9.9: Derivation of separation, position angle and flux of the point-like source present in CQ Tau using Simple Simplex Nelder-Mead minimization. We derived on average a separation of $0''.102$ and a position angle of $196.8°$.

ADI, reveal the presence of emission coming from the point-like source at a separation of $\sim 0''.102$ and a position angle of $\sim 196.8°$.

Furthermore, we analyzed the detection of the point-like source. The point-like source is visible through different techniques: PCA-ADI, PCA-ANNULI, PCA-ASDI and using different npcs. Using PCA-SDI the point-like source is never visible. It is indeed in the inner part of the disc, where the bright PSF residual is more evident and obscures any other signal. A description of the signal-to-noise obtained varying techniques and number of principal components is shown in Appendix B to provide more evidences for this detection. We note that the point-like source is visible also in the combined images of Y, J and H bands, particularly when using PCA-ADI. Moreover, we ran a first estimate of the separation, position angle and flux through a Simplex Nelder-Mead minimization algorithm (Nelder & Mead 1965, Fig. 9.9). We derived on average a separation of $0''.102$ and a position angle of 196.8°, through the computation of the median of the spectral channels where $1.29\ \mu\text{m} \lesssim \lambda \lesssim 1.64\ \mu\text{m}$. In Fig. 9.9, we show that the point-like source is visible in almost all single frames. To complete this analysis, however, we will need to carry out a Bayesian analysis based on Markov Chain Monte Carlo method coupled to the negative fake companion technique. This will allow us to give also an error bar to each of the points measured. We will have then to convert the companion spectrum to physical units and perform a spectral characterization to derive its mass, as done for MWC 297 (see Chapter 8). This target seems to be surrounded by dust and thus the value of flux measured can be a combination of flux coming from the putative companion and from the circum-planetary disc.

Finally, in Fig. 9.10, we show the comparison between our results and the ALMA observations of the continuum at 1.3 mm (in the center, Ubeira Gabellini et al. 2019). The contour curves are taken at 20, 40, 80, 160, 320 σ, where σ = 2.45E-05 Jy/beam. The comparison highlight several interesting features. First of all, the spiral arms called S2, S3, S5 are at the edge of the continuum cavity. The S1 spiral starts at a separation immediately larger than the cavity depletion and continue up to the top crescent visible in the ALMA data. The less bright spiral arm called S6 is instead matching the bottom crescent observed in ALMA. The point-like feature is exactly inside the dust cavity.

Discussion

We detect multiple spiral arms in the total intensity scattered light data of CQ Tau. We find spiral-like features that we called S1, S2, S3, S4, S5, S6 and a point-like source. We thus can confirm the S1 and S2 spirals detected by Uyama et al. (2020). The spirals continue also inside the continuum cavity and S2, S3, S5 are found to be at the edge of the two crescent well visible in ALMA continuum data. The presence of a companion candidate at $0''.102$, which corresponds to $\sim$17 au, is really intriguing. The position of the planetary companion we estimated in Chapter 5 was indeed of 20 au (Ubeira Gabellini et al. 2019). Moreover, the spiral S1 seems to be broken in the point of conjunction with S3. These features are predicted in the scenario of a massive planet carving a cavity. The bright spiral arm S1, however, has a pitch angle large if compared with the simulations done by Ubeira Gabellini et al. (2019) and with a brighter emission. A possibility is that the companion is not co-planar, as previously suggested by us, and maybe eccentric. This may also explain the fact that our model do not perfectly match the CO depletion, which instead is supposed to be possibly more depleted if the orbit is not co-planar. In any case, further modeling have to be done to test this scenario. Moreover, the emission coming from the point-like source may also be due to disc emission, which is strong at these wavelengths. Further observations on this target at different wavelengths and through

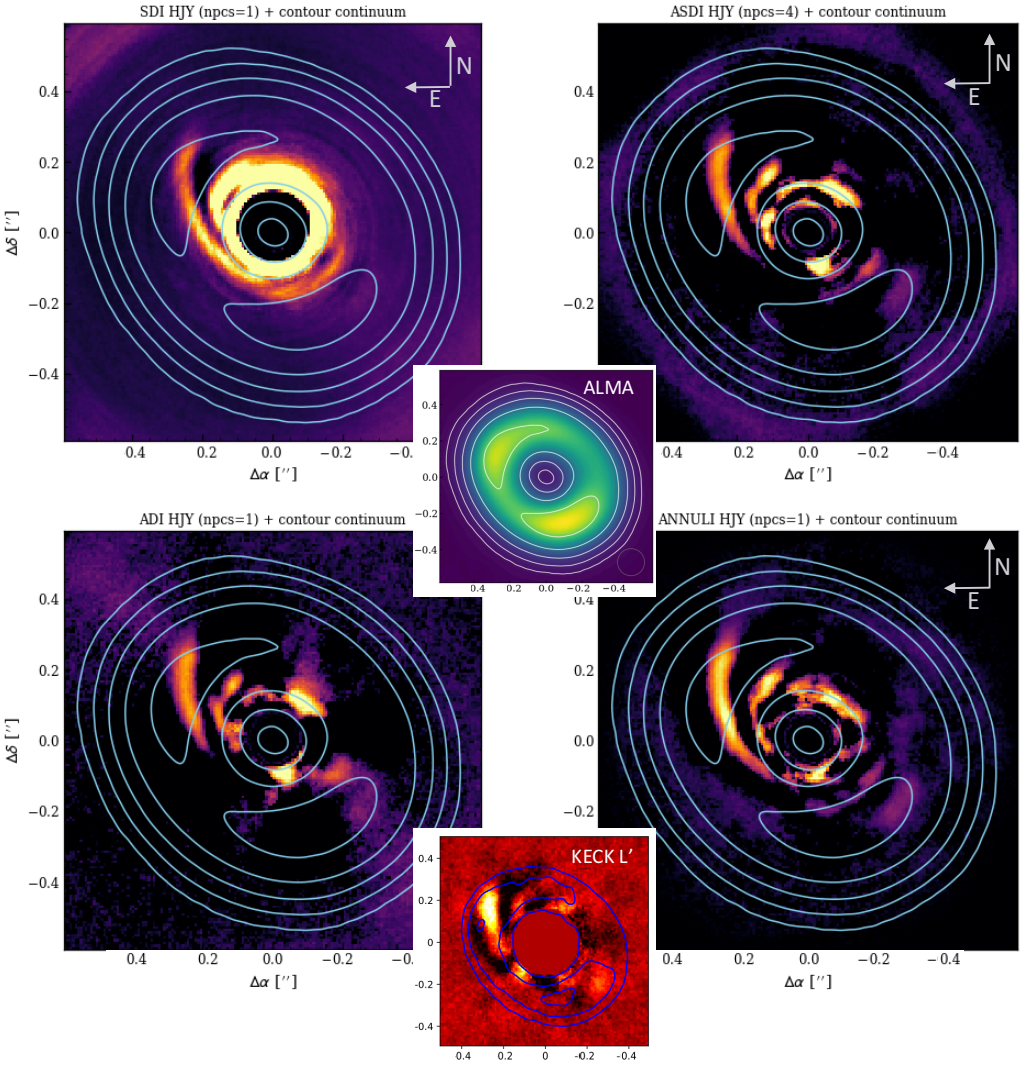

Figure 9.10: Comparison between the ALMA continuum observations at 1.3 mm (center) and the data here presented with the ALMA continuum contour superimposed (at 20, 40, 80, 160, 320 σ, where σ = 2.45E-05 Jy/beam). On the bottom, we show the L′ data as in Fig. 1 of Uyama et al. (2020). The image post-processed through PCA-SDI is shown using npcs=1, to better show the disc extension in the near-IR. The PCA-ADI and PCA-ANNULI images exploits npcs=1 to have a higher signal-to-noise of the point-like source. The PCA-ASDI image is presented using npcs=4, to show enhance the presence of the companion.

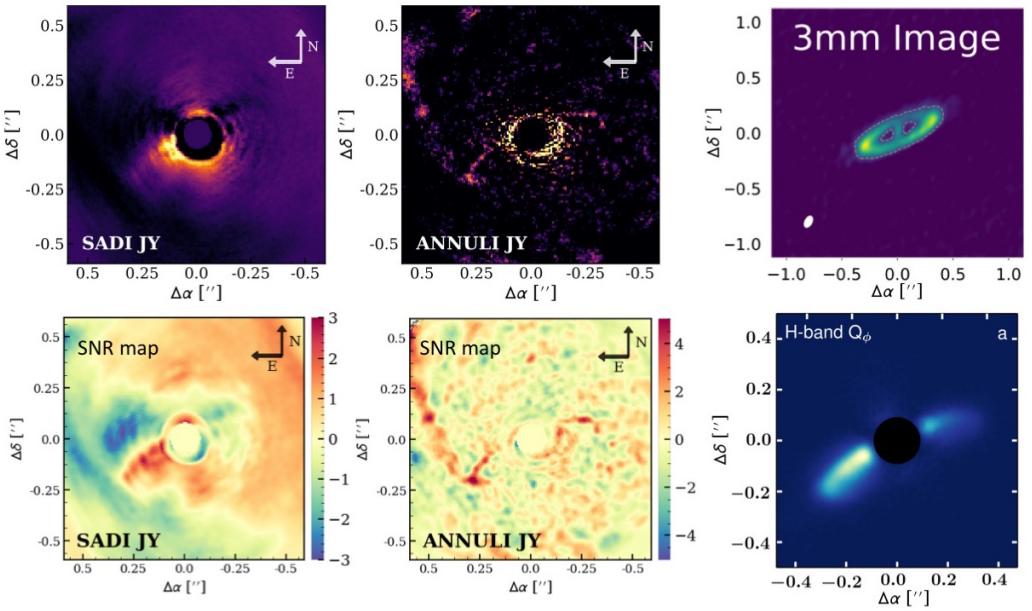

Figure 9.11: Post-processed images of T Cha obtained on the 2015-05-30 through the techniques: PCA-ASDI (left) and PCA-ANNULI (center) using npcs=2. On the top the post-processed images, on the bottom the signal-to-noise map. The disc is almost edge-on with an asymmetry in brightness (left), not visible using the aggressive method PCA-ANNULI. On the right, we show for comparison the ALMA continuum emission at 3 mm (Hendler et al. 2018, top) and the PDI observations in L′-band Q_Φ (Pohl et al. 2017b, bottom). We note that the images have different field of view.

kinematics are needed to better constrain the properties of the detected point-like source.

9.2.5 The large cavity of the disc in T Cha

The target

T Cha is an 9 Myr star located in the DC300.2-16.9 cloud at a distance of $\sim$ 110 pc (Gaia Collaboration et al. 2018). For the properties of the T Cha source we refer to Table 8.1 and 7.1. Olofsson et al. (2013) presented a study of the T Cha disc using an MCFOST model. Huélamo et al. (2015) measured the gas extent of the disc in the CO (3-2) emission of $\sim 2''.13$ (230 au) and in the ^{13}CO (3-2) emission of a smaller radius. The line intensity is similar at both sides, consistently with an uniform distribution of the gas. The 850 μm detection reveals the presence of a dusty inner disc. It shows two emission bumps (separated by $\sim 0''.37$), which suggests the presence of a dust inner gap and an outer radius of $\sim 0''.74$ (80 au). Finally, the authors derived an high inclination of $\sim 67°$ and a position angle of PA $\sim 113°$. Pohl et al. (2017b) performed polarimetric imaging with IRDIS together with IFS and ZIMPOL with the SPHERE instrument. The disc found has a brightness asymmetry, which can be explained by a small eccentricity of the disc with respect to the star maybe due to the presence of a companion. The disc has two coplanar inner and outer discs, separated by a gap of a $0''.28$ in size. The authors confirm that the main source of emission is coming from the inner disc. Considering the match with both the total intensity observations and the polarimetric images they consider a

dominant size of 10 μm. Hendler et al. (2018) through ALMA observations at 3 mm, found a highly inclined transition disc with a clear detection of an inner disc, a dust gap and an outer ring. The gap is of $\sim$ 0$''$.17 - 0$''$.26 (18 - 28 au). Comparing the ALMA images with the SPHERE detection the authors found that the mm-size grains are more extended than the scattered light images. The origin of the gap can be attributed to an embedded planet of $\sim$ 1.2 M_{Jup} (single planet scenario).

SPHERE-IFS results

The flux and center images are really noisy during the observing day 2015-05-31 and no clear spot is detectable. For this reason in this section, we show just the post-processed images for the day 2015-05-30 with a higher signal-to-noise. The detection of the inclined disc of T Cha is not trivial due to the low signal-to-noise. We performed the analysis using different number of principal components, in particular using npcs = 1, 2, 3 and the results are quite similar, using also higher values the noise was too high. In Fig. 9.11, we show the results obtained for npcs=2 (top), together with the signal-to-noise maps (bottom), which gives a stronger support to the features previously described. We detect an edge-on disc (inclined) with a disc size of $\sim$0$''$.6. In the image obtained through PCA-ASDI, the emission is mainly present in the left side of the image. The emission on the right side is visible, although the signal has the same brightness of the noise. The best disc shape is seen in the PCA-ANNULI image, even if it does not show the different disc brightness as in the other methods. The circular bright emission at 0$''$.1 is due to a ring remnant of stellar emission. In PCA-ANNULI we created the library needed to post-process the data through a wide range of separation and rotation going from 0.1 to 2. The reason behind this, is that using just the frames with larger e.g. separations, the ring in the center was brighter and the disc emission was less visible. As comparison we show on the right of Fig. 9.11 the ALMA continuum emission at 3 mm (Hendler et al. 2018, top) and the PDI observations in L$'$-band Q_Φ (Pohl et al. 2017b, bottom). We note that the field of view of these images is different from the ones of total intensity. In the PDI observations it is visible as well an edge-on disc with a difference in brightness. In the ALMA image, it is possible to see the back side of the disc, barely visible in our data and not visible in PDI.

Discussion

We detect through total intensity near-IR observations an inclined disc with a thin ring and a large cavity. An asymmetric brightness is visible using all the techniques with the exception of PCA-ANNULI. In particular, the brightness toward East is higher than the one toward West, explaining why the emission of the West side is not clearly recovered by all the techniques used. Using PCA-ANNULI, it is possible to clearly detect both sides of the disc. It is also visible the beginning of the backside of the disc, not visible with the other techniques. The cavity visible in the PCA-ANNULI image is of $\sim$0.$''$25 ($\sim$27 au), in agreement with the results of Pohl et al. (2017b). In Pohl et al. (2017b), it was used just one technique to analyze SPHERE-IFS data and it was not possible to see the difference in brightness between the two sides of the disc, visible just in PDI observations. Moreover, in both PDI and total intensity data the emission coming from the backside of the disc was not visible, partially detected in these images. The position of the ring emission in the near infrared is confirmed to be inside the peak emission of ALMA continuum data as found by Hendler et al. (2018). As suggested from this latter work, a planet can be responsible for the cavity observed.

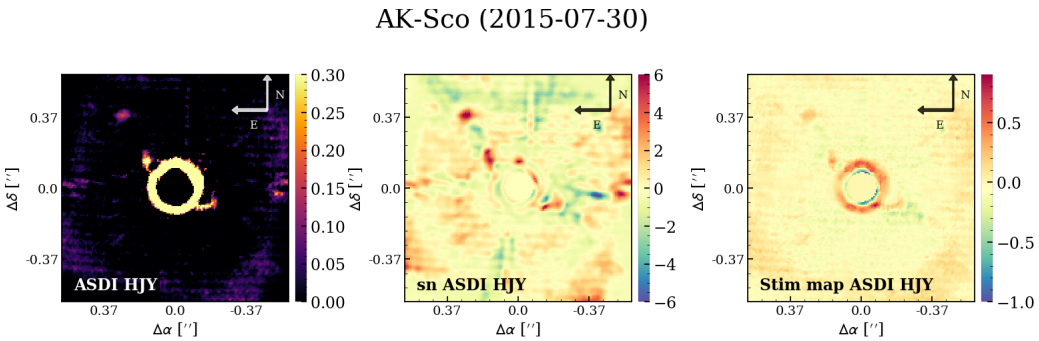

Figure 9.12: Post-processed images with PCA-ASDI for AK Sco taken on the 2015-07-30. On the left, we show the final image, on the center the signal-to-noise map and on the right the STIM map. The bright ring at 0″.1 is not real, but a remnant of the stellar emission. An inclined disc is visible in all the three images shown.

9.2.6 The inclined disc around AK Sco

The target

AK Sco is a young binary composed by two nearly equal stars of Spectral type of F5 and F5IVe (Castelli et al. 2020), with a primary mass of 1.40 $M_{\odot}$ (Vioque et al. 2018a). At the periastron they are separated by $\sim$ 11 stellar radii (Gómez de Castro 2009). The system is located in the Sco OB2-1 region and it is a Class II, Group II source, following the classification of Meeus et al. (2001). For the properties of AK Sco we refer to Table 8.1 and 7.1. Alencar et al. (2003) studied the accretion onto the AK Sco system and detected a massive dusty disc around the binary. Its inner disc was resolved with near-interferometric data by Anthonioz et al. (2015). Czekala et al. (2015) imaged its dust and gas components through ALMA and detected a compact disc around the binary. Janson et al. (2016) observed AK Sco with IRDIS and IFS, being able to distinguish two bright features resembling part of an inclined disc. Gómez de Castro et al. (2016) perfomed a study on the hydrogen Lyα line emission. They observed AK Sco during the periastron passage with HST, detecting a drop of the H_2 flux, possibly produced by the occultation of the stellar Lyα photons. Järvinen et al. (2018) reported a detection of weak mean longitudinal magnetic fields with HARPSpol and a variations in the Na I doublet lines and photospheric lines, suggesting accretion.

SPHERE-IFS results

The images here presented (Fig. 9.12) are similar to the ones obtained in the Chapter 7, because the observations were taken in FIELD and not in PUPIL tracking mode as the ones previously described. The rotational variation is in principle zero, and thus it allowed just the post-process with PCA-SDI. In the reality, however, there is always a variation of $\sim 1^{\circ}$ and if we consider it (as described in Sec. 9.1.1), it is possible also to post-process data with PCA-ASDI, also if not fully exploiting its potentiality. The image looks similar to the one obtained with PCA-SDI, but cleaner. We show in Fig. 9.12 the results obtained with PCA-ASDI (left), together with the signal-to-noise (center) and STIM (right) maps. An edge-on disc is visible with a large cavity. The disc size is of R$\sim$0″.25.

Discussion

Our observations confirm the detection of an inclined disc of 0″.25 of size as found by Janson et al. (2016). The inclined disc can be produced by a close binary of equal stars (Castelli et al. 2020). Interestingly, this observation is done through the FIELD tracking mode, showing the possibility of having a disc detection also through the use of this technique also if, in this case, not all the methods can be used. This is indeed, the only disc detection of the targets observed in FIELD tracking mode.

9.2.7 Multiple rings in HD 141569

The target

HD 141569 is 9 Myr Herbig star located at a distance of $\sim$ 111 pc (Gaia Collaboration et al. 2018). This disc is in a transition phase between the protoplanetary (Class II phase) and a debris disc stage. For the properties of HD 141569, we refer to Table 8.1 and 7.1. Perrot et al. (2016) performed a study using IRDIS and IFS on SPHERE. They claimed the detection of several structures inside 1″, in particular a bright ring with sharp edges. Mawet et al. (2017b) performed observations of the inner disc in the L′-band using Keck/NIRC2. The images show an inner system extending up to $\sim$ 0″.60 (70 au). In their best fit model, they found a maximum and minimum grain size respectively of $\sim$ 10 mm and $\sim$ 0.1 μm, which suggests that collision are present and the disc is very active. Moreover, they supposed that the fact that the disc is broken (described in Perrot et al. 2016) is an artifact of the ADI technique. White et al. (2016) observed a dusty disc at 870 μm with an extension of 0″.48 (56 au) with ALMA. They measured also the emission coming from the CO isotopologues. The emission of the ^{12}CO (3-2) is resolved from 0″.26 to 1″.81 (30 - 210 au). White & Boley (2018) suggested a disc with two component. Their data shows evidences of mm structure, with an inner disc between 0″.14 and 1″.39 (16 - 45 au) and an outer disc within 0″.82 and 2″.59 (95 - 300 au). Finally, Miley et al. (2018) observed the disc in 1.3 mm continuum, ^{13}CO (2-1) and a non-detection of C^{18}O. In the continuum emission, they detected a faint mm ring like structure at $\sim$ 1″.08 (220 au).

SPHERE-IFS results

We present in Fig. 9.13 the images obtained through the three techniques used: PCA-ASDI (left), PCA-SDI (center) and PCA-ANNULI (right). The PCA-ADI method gave a similar result as PCA-ASDI. In all of them, it is possible to distinguish a bright half-ring in the bottom side of the image. Thanks to PCA-ANNULI also the fainter part of the disc toward North is visible. In the same image two rings are visible. The ring appears to be not broken even if in PCA-ANNULI two shadows are present. It is hard to say if they are created by the method used because the other methods do not show the upper part of the disc neither. In Fig. 9.13 the STIM (bottom panel) maps show the same disc shape. Interestingly the bright bottom side of the ring appears to continue in the upper ring with a lower brightness. A bright stream of material going toward the center (on the right side of the image) is visible in the PCA-ANNULI image both through the STIM and the SNR maps (Appendix B). The disc size is larger than 1″.

Discussion

We found a disc structure similar to the one found by Perrot et al. (2016). The disc appears however, not broken and the rings are two, as seen in the PCA-ANNULI images.

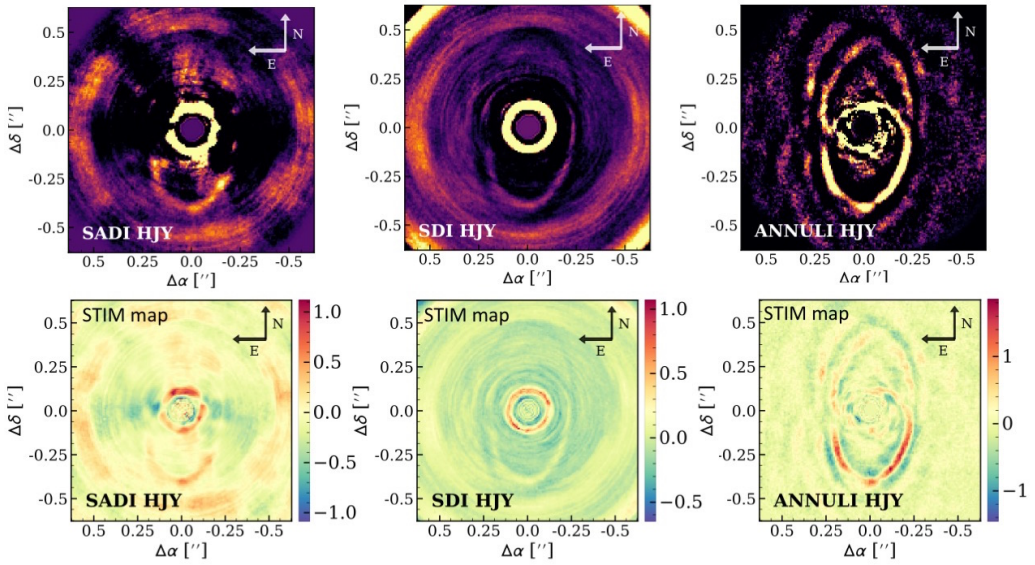

Figure 9.13: We present here the images obtained for HD 141569 on the 2015-05-16. The images are obtained through PCA-ASDI (left), PCA-SDI (center) and PCA-ANNULI (right). On the top post-processed images and on the bottom STIM maps. All the images show the presence of an extended disc structure with multiple rings and a large cavity.

The disc has a large cavity pretty clean of material. The disc is, indeed, in transition from a Class II to a debris disc. A stream of material going from the ring inward is also present. The inner cavity is of $\sim 0''.3$ - $0''.4$.

9.3 Comparison between the different techniques used

In this Section, we analyzed the post-processed images with the aim of comparing different methods used during the target analysis previously reported. In particular, we compared the results obtained combining all the frames (YJH or JH), the ones with single bands (H, J or Y) and different techniques (PCA-SDI, PCA-ASDI, PCA-ADI, PCA-ANNULI). Moreover, we analyzed the results using different values of number of principal components with the aim of maximizing the SNR and STIM maps. Finally, we described the improvement of the results we got in the inner disc using a keyword of VIP for the scaling that was not the default.

9.3.1 Different methods and wavelengths

In order to compare the results obtained combining all the frames (YJH or JH), the images at single bands (Y, J, H) and different techniques, we used as examples the HD 100453 (Fig. 9.14) and HD 100546 (Fig. 9.15) targets. In the figures shown, we superimposed the J-band contour for each method and fix the same color code for all the images in order to help the comparison. All the images shown were processed using as number of principal components one. For both the targets, we can observe that for the PCA-ASDI and PCA-SDI techniques the image in Y band seems to be over-subtracted, the one in H-band is under-subtracted and the J Band image is the one with the disc shape better

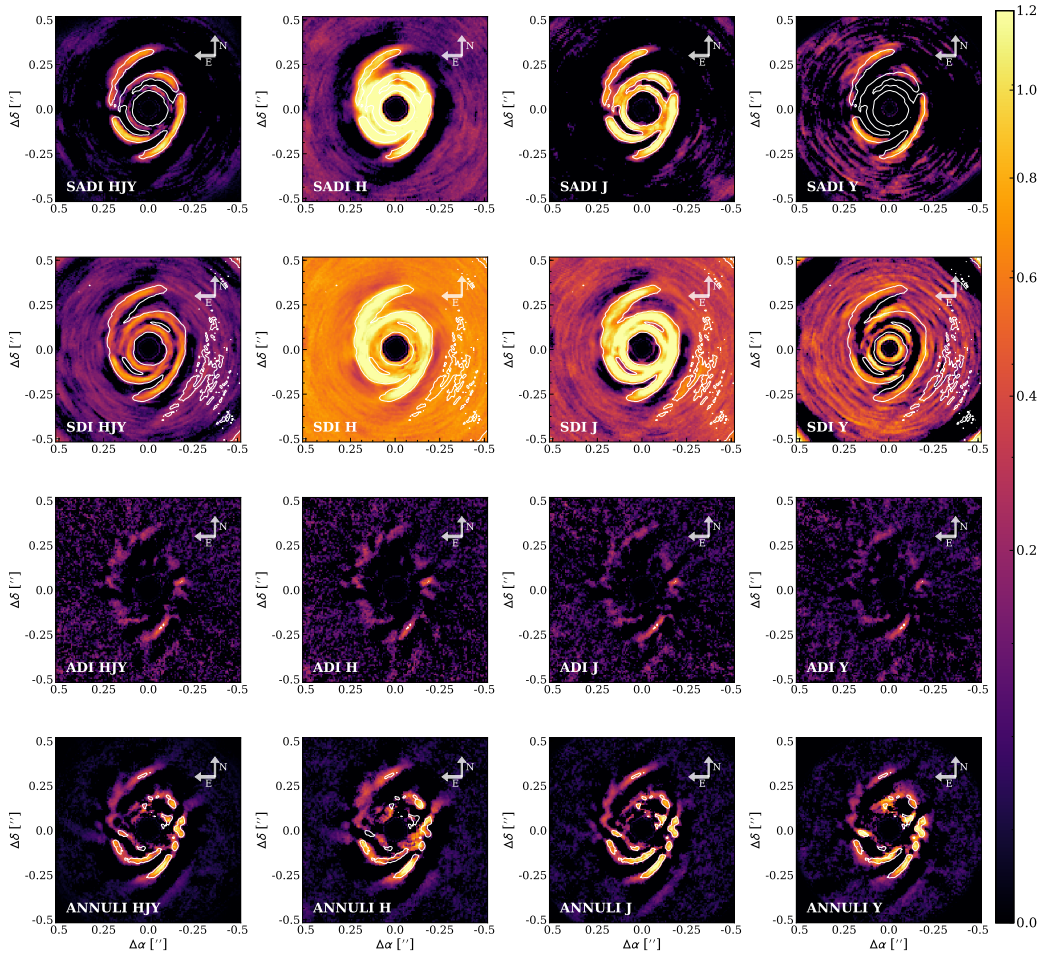

Figure 9.14: We show the results on HD 100453 with YJH combined (left), H band (center left), J (center right), Y (right). We present the results of PCA-ASDI (first row), PCA-SDI (second row), PCA-ADI (third row), PCA-ANNULI (last row).

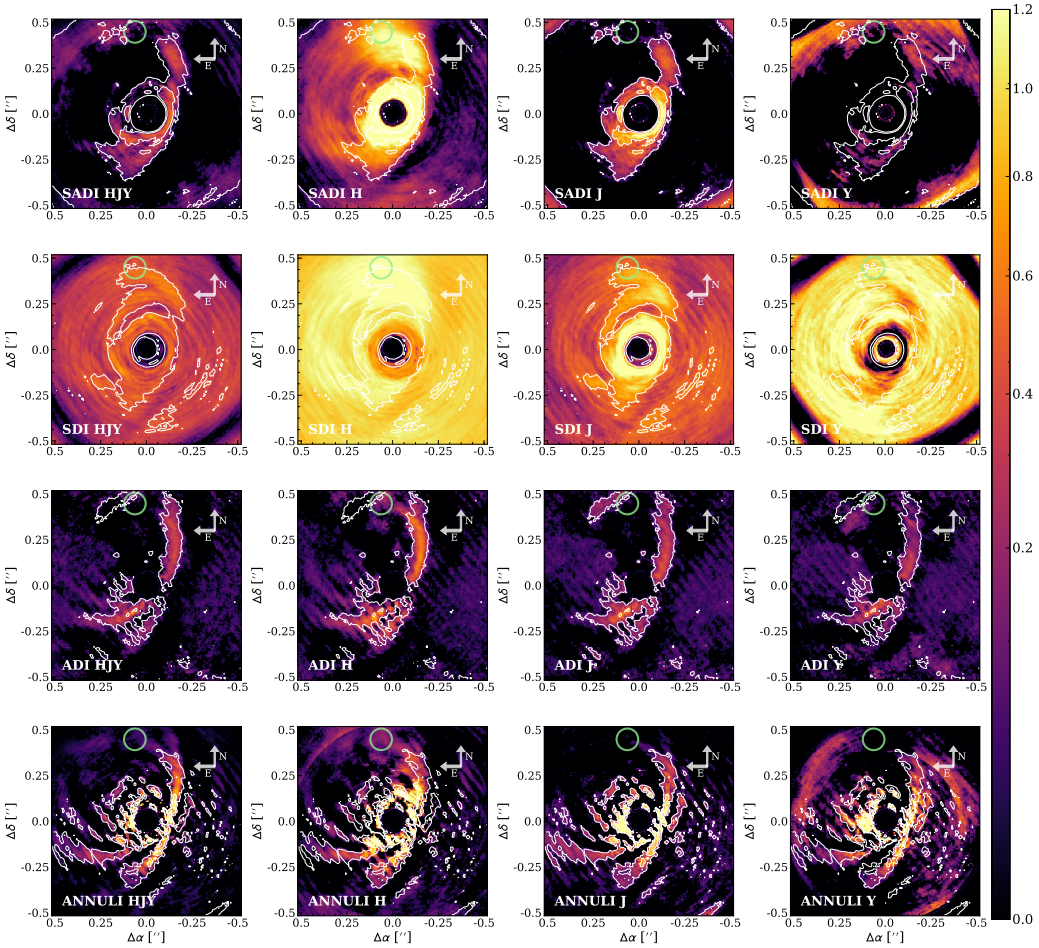

Figure 9.15: Results on HD 100546 with YJH combined (left), H band (center left), J (center right), Y (right). We present the results of PCA-ASDI (first row), PCA-SDI (second row), PCA-ADI (third row), ANNULI (last row). The green dot corresponds to the source seen by Quanz et al. (2015), Sissa et al. (2018). In these images, particularly in band H, the source appears to be instead part of the disc which in ADI it shifted upward compared to the spiral arm in SDI.

defined. This difference is not evident using the PCA-ADI and PCA-ANNULI methods. At the same way, the HJY image have a lower flux compared to the J-band image and a disc shape slightly different. Considering that most of the disc emission is recovered thanks to PCA-SDI method, the flux of the single bands images cannot be considered as correct in absolute values. A careful analysis of how the method works has to be done, possibly performing a forward modeling to test if these features are real and what is due to the technique used. The under and over-subtraction of the images may indeed modify artificially the results. Moreover, we note that PCA-ANNULI works better than the simple PCA-ADI. It is indeed able to recover the spiral arms in both HD 100453 and HD 100546 with a better signal-to-noise and with a more extended disc.

In particular, in HD 100453 (Fig. 9.14) we clearly detect a spiral disc structure with two arms in all the images shown. The signal coming from Y band in PCA-ASDI and

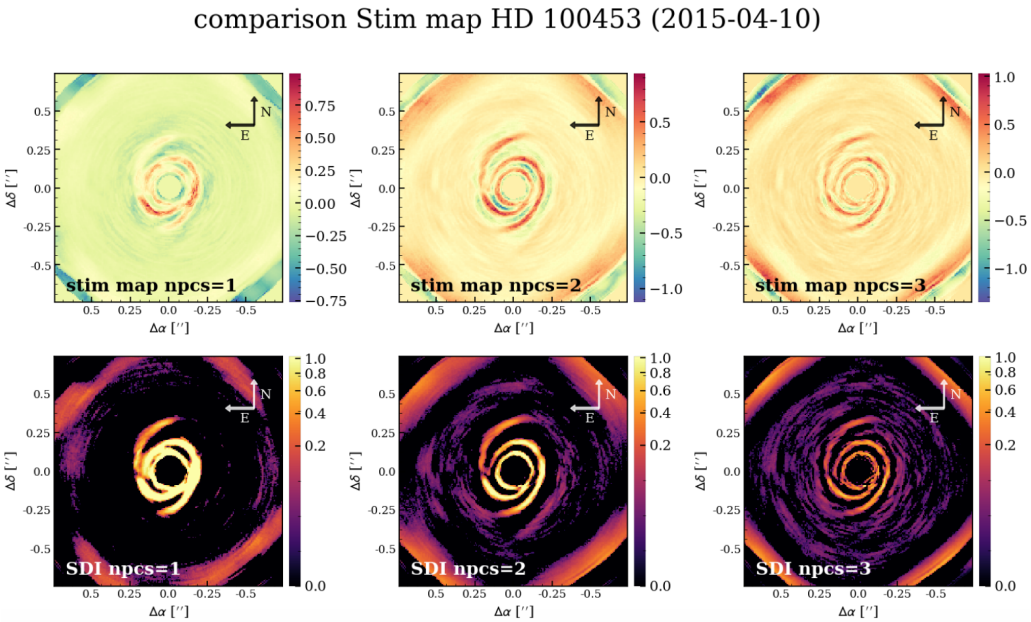

Figure 9.16: STIM map (top) and post-processed image (bottom) with PCA-SDI using as number of principal components one (left), two (center), three (right). The signal-to-noise is maximized in the central image, as it is possible to see from the relative STIM maps (top).

PCA-SDI seems to be shifted outward with respect to J and H band. However, this is not visible for the PCA-ADI and PCA-ANNULI methods and it is possibly produced by the post-processing method used. In Y band the over-subtraction is indeed quite strong. We note that PCA-ANNULI and PCA-SDI, in particular, allow to enhance the feature of a third arm pointing (S3) towards the M-Dwarf companion up to a separation of 0″.3-0″.5, the same one seen by Benisty et al. (2017). Moreover, the fact that the spiral arm pointing toward South-east (S2, see Fig. 9.2) is brighter than the opposite spiral arm (S1) is visible through almost all the methods and in particular thanks to PCA-ASDI and PCA-ANNULI. In the HD 100546 target (Fig. 9.15), at the same way, we saw features slightly different in each image. For example, the S1 spiral previously described is definitely visible in all the methods in H band, up to the green circle (position of the companion detected by Quanz et al. 2013a) and in the images of PCA-SDI. Moreover the S1 spiral, which was not so clearly connected to S2 in the YJH images shown before, appears to be visibly connected in the PCA-SDI (J-band) image.

Moreover, as a test we check weather observations taken in YJ are or not worse than the ones in YJH. We choose as a test case the HD 169142 target: the observations taken on the 2015-06-07 have indeed a coverage in just the YJ wavelength. The results are similar to the one obtained in the other day (with coverage YJH): the contrast curves reach slightly better values with YJ. Moreover, with this observation we were able to detect also the second ring located at a separation of 0″.5 - 0″.7.

9.3.2 Different number of principal components

We performed a test varying the number of principal components (npcs) used to post-process our images in order to maximize the STIM map signal. We choose as a test

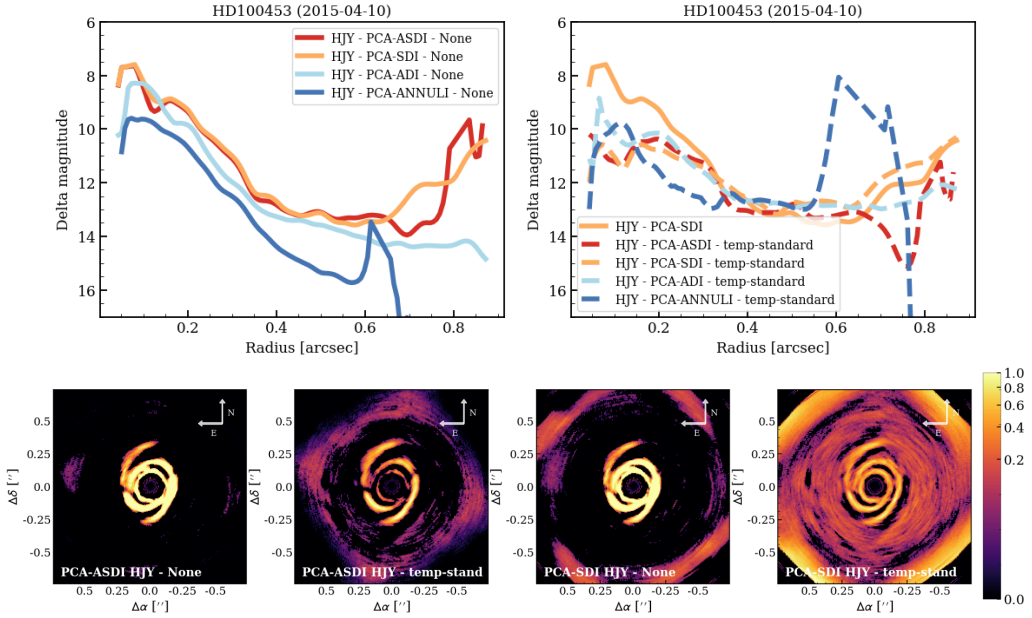

Figure 9.17: Contrast curves for the four methods used in the case of YJH combined for the observing day 2015-04-10. On the left we show the contrast curves where the scaling is equal to None (straight lines) and on the right the scaling is set to temp-standard (dashed lines). The color code for the different methods is kept the same. For comparison we kept the PCA-SDI curve using no scaling in the image on the right. The bottom row shows the different post processed images using PCA-ASDI and PCA-SDI using the two different scaling.

case the HD 100453 target observed on the 10th of April 2015. The signal is maximized for npcs equal to two. Using this method for PCA-SDI the noise of the image becomes lower and the spiral arms appear to continue longer than previously detected (Fig. 9.16). Interestingly, if we use npcs = 2 also both shadows detected in Benisty et al. (2017) are visible. This test was really important to unveil previously undetected features. The same practice can be applied to CQ Tau. Using PCA-SDI and npcs equal to one, the disc was detected but not with all the disc features were unveiled, still under the not fully subtracted stellar emission. Using values of npcs equal to two or three some of these features instead appears (see Figs. 9.10, 9.8). Finally, we have performed the same analysis also on HD 169142 and HD 100546, finding that for them the best npcs is one: with higher values of npcs more disc features were deleted. This can be explained by the fact that these discs are either very symmetric or fainter. We note that the PCA-SDI and PCA-ASDI methods particularly benefit of changing npcs. For PCA-ADI and PCA-ANNULI, instead, the best npcs is typically one.

9.3.3 The keyword 'Scaling'

We test a keyword present in the VIP routine called 'scaling'. It can be set as 'None' (the input matrix is left untouched, top left Fig. 9.17) or to 'temp-standard' (top right panel of Fig. 9.17). If the parameter 'temp-standard' is adopted, then the input matrix has a temporal mean centering and the pixel values are scaled to unit variance. This parameter is supposed to work better for methods such as PCA-ASDI. We compare the

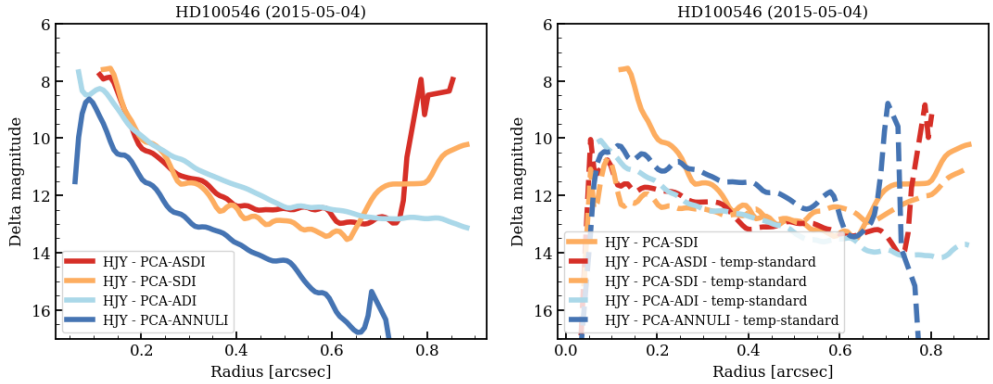

Figure 9.18: Contrast curves for the four methods used in the case of YJH combined for the observing day 2015-05-04. On the left we show the contrast curves where the scaling is equal to None (straight lines) and on the right the scaling is set to temp-standard (dashed lines). The color code for the different methods is kept the same. For comparison we kept the PCA-SDI curve using no scaling in the image on the right.

contrast curves and the images itself for the different techniques used in the case of Y J H combined. If the scaling is kept as default (top left Fig. 9.17), PCA-ASDI and PCA-SDI have a similar behavior, with a better contrast for PCA-ASDI for larger radii, which are visibly noisier in PCA-SDI. PCA-ANNULI and PCA-ADI have a better signal-to-noise, but they are not suited to study disc structures. With the 'temp-standard' parameter, the images looks cleaner in the inner part of the disc with a signal reaching a better contrast for R$\sim$0$''$.1 - 0$''$.3, in particular for PCA-ASDI and for PCA-SDI (bottom Fig. 9.17). In the outer disc the two scaling parameters work in a similar way if we consider PCA-SDI; temp-standard works better for PCA-ASDI and it works definitely worst for PCA-ANNULI and PCA-ADI. In the top right Fig. 9.17, we kept for comparison the PCA-SDI result using both no scaling (orange line) and scaling equal to 'temp-standard' (dashed orange line).

We performed a similar test on the HD 100546 target in the observing day 2015-05-04. In Fig. 9.18 we show the contrast curves for both the scaling parameters. We can confirm the trend seen for HD 100453: in the inner disc (R$\lesssim$0$''$.15) scaling equal to 'temp-standard' works better than no scaling, while in the outer disc it depends on the routine used. The use of scaling equal to 'temp-standard' is similar of the case where no scaling is applied if using PCA-ASDI and PCA-SDI methods, for PCA-ADI the results are comparable, while with PCA-ANNULI the results are definitely worse. To check weather this is or not a general behavior, these test should be done also on systems with not so bright disc structures.

9.4 General conclusion

9.4.1 Post-processing methods used

In the following we provide a brief summary of our findings regarding the different techniques used. Each of them allows us to see different disc components. For this reason, it is important to combine different methods to understand the overall disc structure. We summarize below our main findings:

- Typically it was difficult to distinguish small asymmetries such as shadows using PCA-SDI and npcs=1. An example of this is the case of HD 100453, the same features are instead visible using PCA-ASDI. Adding indeed PCA-ADI to PCA-SDI helps to increase the signal-to-noise. We note, however, that this may create not real asymmetric structures in the STIM map (see Appendix B, Fig. B.12), not visible with PCA-SDI (e.g., HD 169142). A combination of images with different methods is needed to discriminate between real or fake features.

- When the disc is really bright it is better to use a number of principal component higher than one. In such a way, it is possible to see e.g., shadows and outer disc features (e.g. HD 100453) or unveil the presence of fainter spirals (e.g. CQ Tau). It is key to use the npcs that maximize the disc emission in the STIM map (e.g. HD 100453, see Section 9.3). For HD 100453 this happen with npcs=2 and for CQ Tau with npcs=2, 3.

- Moreover, methods such as PCA-ADI and PCA-ANNULI delete all the symmetric disc features (e.g., HD 169142) and thus are not appropriate particularly with face-on ring structures. The PSF residual is instead better subtracted in images where PCA-ADI is applied, than in the PCA-SDI images alone.

- We note that even if some disc features (e.g., T Cha) are better resolved using methods such as PCA-ANNULI, it is not possible to see the brightness asymmetry present in the disc, which is instead visible using methods such as PCA-ASDI or PCA-SDI.

- Using for the VIP 'scaling' parameter the 'temp-standard' keyword instead of the default value, the emission coming from the PSF residuals is lowered for all the methods tested as shown by the contrast curves (Fig. 9.17, 9.18). For larger radii the methods achieve similar results for PCA-SDI, slightly better results for PCA-ASDI and worst results for PCA-ADI and PCA-ANNULI.

- Finally, we found that the best way to see disc structures is using the J band alone. The signal is indeed brighter and more defined than using the other Bands (H or Y). This is probably related to the fact that images in band H and Y are typically under and over subtracted. This can be partially improved by developing a code which subtracts the speckle signal and together it maximizes the disc emission. J band images are also brighter than the combined Y J H Bands, but some features (e.g. PSF residuals) are better subtracted in the Y J H Bands combined image.

To conclude, we note that each different technique allows to highlight a different disc feature, but none of them is in absolute the best. PCA-ADI and PCA-ANNULI help to unveil asymmetric and thin features (e.g., spirals and point-like sources), while PCA-SDI is able to better resolve symmetric features. PCA-ASDI combines strengths and weaknesses of the other techniques. Different npcs have to be tested in order to maximize the signal-to-noise and the signal in the STIM map. A more systematic analysis on how these techniques change with stellar and disc brightness, sky rotation and geometry is anyway still needed, possibly exploiting a larger sample and with similar exposure time and tracking modes.

Finally, we note that it would be important to improve the noise in the inner region of the disc, particularly where the PSF residual is still present. This region indeed typically corresponds to the inner cavity (e.g., HD 100453, CQ Tau, HD 169142, HD 100546) and its presence prevents putative planets to be detected in that location. Although ADI

techniques and 'scaling' equal to 'temp-standard' are able to partially delete it, the post-processed images remain noisy and with several point-like features. It is thus not possible to distinguish if they are real or artifacts. A way to disentangle stellar light from planet contribution may be to add to this analysis the spectral slope of each pixel in the image (see Chapter 10).

9.4.2 Seven disc detection

In this Chapter, we present seven discs detections. We note that three of them have a disc with spiral sub-structures, but not all the spirals look the same. In particular, HD 100453 has two symmetric spiral arms, two shadows and pitch angles similar for both the arms. We know, indeed, that the disc structure of this target is produced by the massive outer M-dwarf HD 100453B. Also CQ Tau and HD 100546 present disc structures with spiral arms, but they are different from the ones of HD 100453: they are multiple and with hints of them converging to an inner point. The three of them share the presence of an inner cavity of comparable size in large grains and spiral arms in scattered light. In HD 100453 the continuum itself shows two symmetric spiral arms, whereas this is not the case for CQ Tau (two symmetric clumps) and HD 100546 (one side asymmetry). We note that while HD 100546 was observed at a similar resolution of HD 100453, CQ Tau was not. A possibility is that they are produced by the same phenomenon (e.g., an outer companion) and the different disc shapes are due to different disc viewing angles (Dong et al. 2016; Dong & Fung 2017a). In all of them, however, this will not explain the inner cavity in the continuum emission. This is possibly produced by a second inner companion for CQ Tau and HD 100546, while the presence of tight spiral features in thermal emission in HD 100453 may suggest a different scenario.

All the other discs observed show ring structures (HD 169142, HD 141569, T Cha and AK Sco). In particular, HD 169142 has a face-on disc with two rings, possibly created by two planets. T Cha and AK Sco show an almost edge-on disc appearing as a single thin ring. HD 141569 has multiple rings and a large inner cavity, whose shape can be related to the inclination of the disc with respect to the line of sight or to the position angle. This disc is clearly different from the other ones: its large cavity together with its SED (see Appendix C) confirm it to be in an evolved stage going from Class II to debris disc. T Cha and HD 169142 are both Group I, but they look different: T Cha present a gap of 10 au in size and just a thin ring. Moreover, the far-IR emission (see SED in Fig. C.2) of T Cha is between the one of HD 169142 and AK Sco. We note that for all the targets and in particular for the ones where a depletion in scattered light emission is visible, we cannot say from these data whether it is a gap or a cavity due to the coronagraph. Both T Cha and AK Sco present similar disc features, similar to an almost edge-on disc, thus it is difficult to disentangle between a gap or effects due to projection.

For what regards the sample analyzed by us, we note that Group II discs are mainly not detected, while Group I discs show multiple disc structures. This is compatible with the fact that the far-IR emission is lower for Group II discs than for Group I. Group II discs are expected as described by Garufi et al. (2017) to have either small or self-shadowed disc and thus they are not visible. Moreover, small discs are expected not to evolve in Group I discs, while large discs may eventually be the precursor of Group I discs. This is what we mostly see. Following van Boekel et al. (2003) and Acke & van den Ancker (2004), we present a diagram with the IRAS $m_{12} - m_{60}$ color versus $L_{\rm NIR}/L_{\rm IR}$ (Fig. 9.19). We note that also a diagram showing F(30μm)/F(13.5μm) has been used successfully by many authors (e.g. Garufi et al. 2017), but we do not have the photometry at these wavelengths for all the targets. $L_{\rm NIR}$ is the integrated luminosity in the near-IR

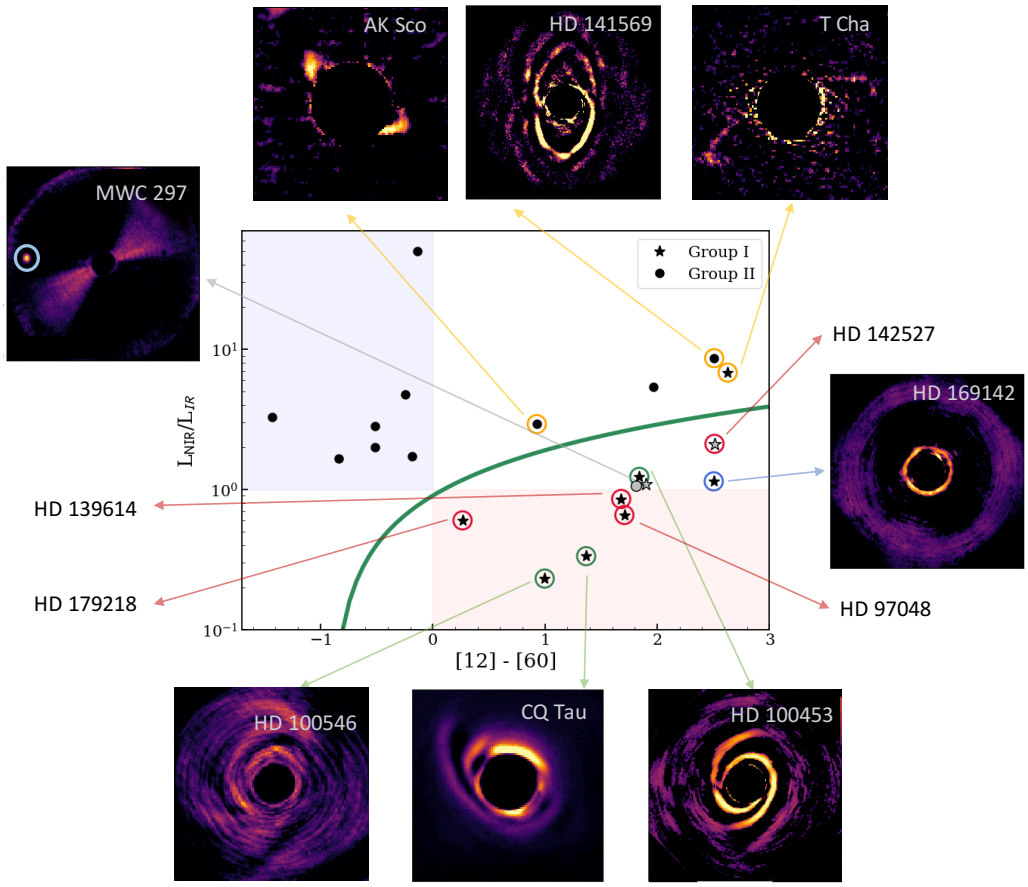

Figure 9.19: We show a diagram of the IRAS m_{12} - m_{60} color versus $L_{\rm NIR}/L_{\rm IR}$ following van Boekel et al. (2003). Group II are predominantly above the green line, while Group II sources are below. Rings or large cavities are above the line (yellow points), while spirals (green) and multiple rings (blue) are below. In red we show the non detection that we suppose are possible to be detected with better signal-to-noise data. With gray dot/stars, we show the sources where we detect a companion in scattered light.

computed from J, H, K, L and M band photometry; $L_{\rm IR}$ is the integrated luminosity derived from IRAS 12, 25 and 60 μm photometry. The photometric values used were collected from literature and they are quoted in Appendix (Table B.1) with the exception of CQ Tau and S Cra. For the former we used $L_{\rm NIR}/L_{\rm IR} = 0.12/0.36$ taken from Natta et al. (2001) and for the latter we do not have IRAS photometry and thus we could not place it into the graph. This plot was used to empirically distinguish between Group I (shown with stars) and Group II (shown with points) sources: as line to separate them, Acke & van den Ancker (2004) used $L_{\rm NIR}/L_{\rm IR} \lesssim m_{12} - m_{60} + 0.9$ (green line in Fig. 9.19). Below this line there are the Group I, while above Group II typically are present. In Fig. 9.19, we show the sources of our survey described during this thesis. We can see that most of the sources are divided as expected. The only Group I source that is above the line is T Cha, while R Cra is the only source defined as Group II that is below the curve.

In Fig. 9.19, we show with a blue box all the sources for which the SED decreases always from near-IR to far-IR. This means that $L_{\rm NIR}/L_{\rm IR} \gtrsim 1$ and m_{12} - $m_{60} < 0$. Those follow exactly the definition of Group II sources and are: HD104237, HD142666, HR 5999, HD 145718, HD 150193, KK Oph, HD 190073. The sources that are above the green line, but to the right of the blue box, are all detected with the exception of HD 132947, which however is way more distant than the other targets ($d \sim$ 380pc). These discs were classified according to Meeus et al. (2001) as Group II, with the exception of T Cha. On one hand, T Cha shares all the properties with the sources in the same parameter space: its disc is spatially resolved in scattered light with a thin ring disc and its SED is similar to the one of AK Sco. On the other hand, AK Sco may be considered as Group I according to another classification criterion (see Garufi et al. 2017). This can thus be considered as a gray area inside where we need a larger statistic to classify all these sources with a unique criterion. All of them, however, show a large cavity (HD 141569) or a thin ring (AK Sco and T Cha) and do not show any spiral structure (yellow circles), whereas we detect three spiral structure in Group I sources. Moreover, we can say also that HD 163296 (Muro-Arena et al. 2018), which is a Group II, is placed next to AK Sco: their SED are similar and in scattered light they show a single thin ring. A possible interpretation is that in the blue box all the disc should be small or self-shadowed, while the ones above the green line and with $m_{60} > m_{12}$ can be spatially resolved in near-IR as thin rings. How strong the far-IR emission is compared to the near-IR emission one may be depend on the amount of disc material in the inner disc.

Below the green line, almost all the sources are Group I, with the exception of R Cra (Acke & van den Ancker 2004). Its bright near-IR emission may be due to the close bright companion detected in scattered light by Mesa et al. (2019). We note also that all the sources with a companion detection are in this parameter space (MWC 297, R Cra, HD 142527) and they are presented with gray stars/dot, considering no disc detection was made, but we detected a companion. All the other sources are shown in black. For what regards the disc shape we underline that below the green line no single thin ring is detected, but just spirals (green circles) and multiple rings (blue circle), all Group I sources. The four sources presented with a red circle are the ones for which we do not have any detection, but that may be detected in principle if the observations would have a higher signal-to-noise (see Appendix C and subsection below). Let us consider the ring-like discs: HD 169142 (top-right of the graph below the green line) shows cleared and large gaps in both gas and dust and it has a large value of m_{12} - m_{60}, suggesting less material in the inner region. On the contrary, HD 139614 and HD 97048 have gaps that are less deep and evolved and more material present in the inner region. No ring detection is present for $L_{\rm NIR}/L_{\rm IR} < 0.65$. Moreover, let us consider the spirals: we note that CQ Tau

and HD 100546 show a similar structure with open and multiple arms and they are in the same area of the parameter space; HD 100453 has well defined symmetric spirals with a smaller pitch angle; and HD 142527 shows tight spirals in scattered light (Price et al. 2018a). In the outer disc, this may suggest that spirals more tight are thinner, while spirals with open arms are thicker. This hypothesis will have to be verified with models that include cavities and spirals and with an exact study of the pitch angle observed. To enlarge our sample, we note that also HD 135344 B (Stolker et al. 2016, 2017) and AB Aur (Boccaletti et al. 2020), defined as Group I, exhibit spirals in scattered light and they would fall below the green curve as all the other spirals.

9.4.3 Models results

We modeled the SED profiles of 21 of the sources presented in Chap. 7 through simple disc models (flat or flared) thanks to the use of radiative transfer calculations with RADMC3D (fully described in Appendix C). The models were chosen in order to vary less parameters as possible in the whole sample of discs. The only target not modeled in such a way is the disc around CQ Tau because its SED was modeled in details in Chap. 5 through the chemical physical code DALI. The parameters of the best model found are shown in Table C.1 (basic model). We note that the results found through these simple models are preliminary and they will have to be verified through more detailed SED models considering the presence of cavities, observed for most of the detected discs. We note that it was not possible to fit through a simple disc geometry T Cha and HD 141569 and thus we added respectively a gap and a cavity (Table C.2, Appendix C) to fit the SED profile mainly in the near-IR. We tested also the presence of a cavity for T Cha and a gap for HD 141569, but they were not compatible with the observations.

We underline here the main conclusions found through the modelling. First of all, with the best fit of the SED profile, we computed the contrast curves expected and compared them with the ones obtained for each source (for the epoch with better contrast). We found that almost all the sources where we detect a disc (HD 100453, HD 100546, HD 169142, T Cha, HD 141569) show model curves comparable with the observed ones. In AK Sco, the model is just slightly below the observed contrast curve. We note that its SED was fitted through a flat disc geometry (see Fig. C.2). The resolved image, however, show a thin ring, suggesting the presence of a gap: there is indeed a near-IR excess and just a small far-IR one. We note that we have not tested this scenario in the SED model fitting, but possibly this would allow the contrast curve of the model to become higher.

Moreover, we show that sources like HD 97048, HD 179218, HD 139614, which do not show any disc detection, are compatible with the models and suggest that with a higher signal-to-noise also those discs should be visible. For this reason, they were shown in Fig. 9.19 as red circles. Moreover, HD 142527 is known to have a cavity almost larger than our field of view. With a larger field and a proper model that takes into account the large cavity this may be visible too. All the other sources instead show model contrast well below the observations.

Interestingly, we can see that rings appear to have a different behaviour than spirals in terms of scale height: discs with spirals have high scale height, while rings structures appears to have lower scale height values (with the exception of AK Sco). It is indeed expected that spirals are more open when h/R is larger. Spirals (of every origins) are indeed density waves with a pitch angle related to h/R: if the scale height is large they appear as open spirals, while if it is small they are tight and may look like a ring. This correlation between spirals and scale height will have to be further investigated through the use of a larger sample of discs detected and considering models with cavities. In

the SED fitting, the presence of an inner radius larger than the sublimation radius is degenerate with the flaring angle. This would mean that the model can be different from the one here reported.

Moreover, the fact that Group I discs have different structures and three out of five of discs detected have spiral arms (not present for Group II discs) may suggest that Group I discs have dynamical perturbations still in act, able to vertically perturb the disc and not allowing the disc to settle toward flat geometries.

Chapter 10

A novel method for speckle noise suppression from SPHERE-IFS data: Spectral-Radial Differential Imaging (SRDI)

The idea behind the implementation of this routine is to improve the SDI technique. We used information both on the (known) spectral shape of the speckles and on the positional variation with wavelength (e.g. all pixels with a spectral slope significantly different from the spectral slope seen in speckles must have some contribution which is due to real emission). SDI, indeed, uses just the information on the positional variation of speckles with wavelength. We implemented it without including the PCA technique and without using VIP, as a test. This will be extra step important to be done in order to complete this analysis and provide an open source routine. Giving the fact that this was implemented from scratch, we describe every step done.

We created a map that contains the total contribution due to speckle noise per pixel. The speckles come originally from the core of the PSF and from the Airy rings (mainly from the first ring) and they are strongly dependent on wavelength. They follow the same spectral energy distribution of the star and they move with the wavelength. The basic idea is to take the IFS cube for each different DIT and re-scale all the different frames taken simultaneously, in such a way that the positions of the speckles are at the same coordinates (chosen as the coordinate of the medium wavelength λ_m) for all the frames. We analyzed the sources described in Chapter 7, without the inclusion of CQ Tau.

This Chapter is organized as follows: in Sec. 10.1, 10.2, 10.3 and 10.4 we describe the implementation of the method done as a test. The characterization of the method is presented in Sec. 10.5. Finally, in Sec. 10.6, we show a comparison between some of the results obtained. We note that this work is preliminary, but at the same time, it shows the future strength of this novel implementation.

10.1 Background estimate: constant and 2D background

The first step was to estimate the background level. This was done in two different ways: considering a constant background and a 2D background (see central Fig. 10.1). The background was then subtracted from the original image. The main goal of the 2D background estimate was to obtain an image where just speckles, point-like sources and asymmetries were present; whereas the constant background subtraction saves all spatially extended emission (from e.g. the disc) together with the asymmetries.

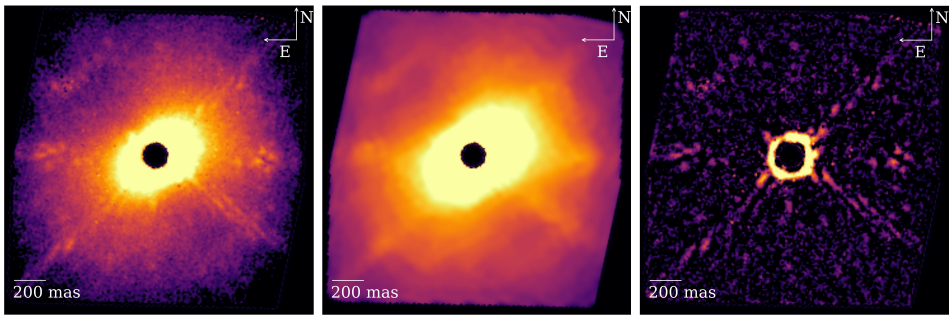

Figure 10.1: Background removal: the image after the constant background subtraction (left), the 2D background map (center) and the image after the 2D background subtraction (right). All the images are presented for the wavelength: λ =1.246 μm and for an individual exposure time (DIT) taken the same day as an example. We used a color scale going from a minimum value set to zero to the maximum value of the map divided by five. The colors are remapped onto a square root relation.

Constant background subtraction

The background subtraction was done taking the AO-corrected image at each wavelength (see left Fig. 7.1) and using the flux at all the pixels sufficiently far away from the central star (r >850 mas). We computed the median of the described region, constant value measured for each frame, that was subtracted from the original image. An example of the constant subtracted image is shown in the left panel of Fig. 10.1.

2D background subtraction

We estimated the value of the bidimensional background for each frame. We measured the local background level in boxes of 5 pixels size as the median value of the flux. The final value was calculated through an iterative process (of 20 interactions) discarding pixels values above or below a specified sigma level from the median (in our case $\sigma = 2$). This procedure creates a low-resolution background image which is then median filtered using a smaller box of 3 pixels size in order to suppress local under- or over-estimations. This method provides with a good estimate of the background level and avoids all the large difference in flux inside the images, considering just the smooth variations in the background. An example of HD 139614 after the bidimensional background subtraction is shown in the right panel of Fig. 10.1. We note that the extended emission is not present any more, but the artifacts (speckles) are still present in the image as point-like sources distributed in a ring-like configuration.

10.2 Simple Average sub-method: SRDI-SA, analogous to SDI

10.2.1 A map of speckles

As shown in the previous Chapters, after applying the ESO pipeline to the adaptive optics images coming from the SPHERE instrument, the images are still dominated by quasi-static aberrations. Knowing the central position of the targets thanks to the star center images, we created a new map where all the speckles are found at the same spatial position. In order to do so, we estimated the flux of the new re-scaled map, going from

the position of the new map ($x_{\rm fin}$, $y_{\rm fin}$) to the original map positions (x, y). The reference frame of the IFS images was chosen to be the intermediate wavelength (e.g., for the IRDIFS-EXT mode the central wavelength is $\lambda_{\rm m} = 1.3029$ μm). The polar coordinates that each pixel will have in the new map, $\alpha_{\rm fin}$ and $r_{\rm m}$ are defined as:

$$\tan(\alpha_{\rm fin}) = (y_{\rm fin} - y_{\rm c})/(x_{\rm fin} - x_{\rm c}), \tag{10.1}$$

where $y_{\rm fin}$ and $x_{\rm fin}$ are the new coordinates and $y_{\rm c}$ and $x_{\rm c}$ are the coordinate of the central position of the star,

$$r_{\rm m} = \sqrt{(x_{\rm fin} - x_{\rm c})^2 + (y_{\rm fin} - y_{\rm c})^2}. \tag{10.2}$$

The initial (unscaled) value of the radius of that pixel is:

$$r = \lambda/\lambda_{\rm m} \cdot r_{\rm m}. \tag{10.3}$$

With this, we computed the initial position of each pixels in the new map, respectively for x and y:

$$x = x_{\rm c} \pm \frac{r}{\sqrt{1 + \tan(\alpha_{\rm fin})^2}}, \quad y = (x - x_{\rm c})\tan(\alpha_{\rm fin}) + y_{\rm c} \tag{10.4}$$

where the two solutions for x correspond respectively to values lower or higher than $x_{\rm c}$. We then took the value of flux from the original image and we placed it in the correspondent pixel of the new map. We set to zero the flux of all the pixels at the border of the new image. Once we had the speckles at the same radial position for all the wavelengths, we averaged all the images. This was done using a weight for each frame, which indicates their different contribution. The weight was considered as the total flux of the image at each wavelength after applying the background subtraction.

10.2.2 Removal of speckles and results

After deriving the averaged weighted map, we performed the opposite procedure in order to re-map the speckle map to the original position of each frame. A flux normalization was applied to each new frame in order to have the speckles flux comparable with the original image. We multiplied each frame to the integrated flux of the original frame divided by the total flux of the map (already subtracted for the background), both computed in the annulus where most of contribution from speckles comes from. We, then, subtracted this map from the original background subtracted image. This procedure was done with the constant background image subtracted. We call this method: *sub-method Simple Average*, SRDI-SA. The results for HD 139614 are shown as example in the top row of Fig. 10.4. This procedure will result in a sub-optimal elimination of speckle noise, but has the advantage that there will not be any self-subtraction of spatially extended structures such as circumstellar discs. This procedure is similar to the basic SDI technique (described in Section 6.4.2), without considering PCA. It is thus less efficient than PCA-SDI as implemented in VIP. We underline again that this work was done as a test, to see how much the implementation of the spectral analysis inside SDI was improving the basic routine. As previously described, the next step will be to implement this inside PCA-SDI in VIP.

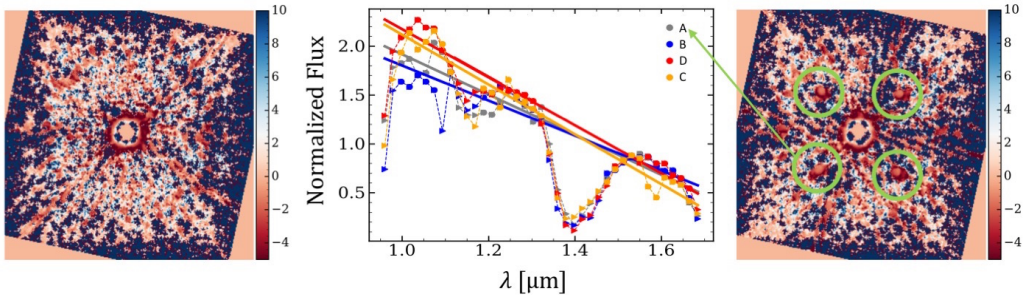

Figure 10.2: SPHERE IFS images of HD 139614 obtained on 2015-04-21, showing the slope image of our science case (left), the slope map of the replicas map (right) and a plot of the normalized flux versus the wavelength (center). The right panel shows the four replicas (green circle) with approximately the same slope value (in this specific case ∼-2). The four replicas are identified in the central panel with A, B, C, D clock-wise and a green arrow shows the replica A. Everything that has the same colour as the waffle pattern color can be likely dominated by speckle noise (light red).

10.3 Point-like Source sub-method: SRDI-PS

10.3.1 Speckles flag map

To be able to correct for the exact contribution of speckle noise at each frame, we implemented an extra step to the first simple average method (Section 10.2). This method is more powerful in detecting companion candidates, therefore we call it *Point-like Source* (SRDI-PS) sub-method. We used the 2D background subtracted images as input for all the procedure described in Section 10.2. We also used the information on the (known) spectral shape of the speckles in addition to the positional variation with the wavelength. In such a way, we can have more information on the amount of speckle contribution for each pixel.

The spectral profile of the speckles has the same wavelength-dependence as the central star, whereas the slope of a companion candidate or of the disc may follow a different profile. For this reason, we re-map each background subtracted frame in order to have the speckles at the same coordinate positions (the one of the central wavelength e.g., $\lambda_{\rm m} = 1.3029$ μm) as done previously. For each pixel in the remapped cube, it can be shown a spectral profile, from which it is possible to compute a spectral slope (see Fig. 10.2). The spectral profile was fitted without taking into account the frames where telluric absorption is present (1.11–1.19 μm, 1.3–1.45 μm), the first two frames and the last one (quite noisy due to the lower efficiency of the grism at these wavelengths). We normalize the spectral flux for each pixel to the averaged value of the central frames (1.19 μm $\lesssim \lambda \lesssim$ 1.3 μm). This was performed in order to have a spectral slope independent from the total flux. We, then, fitted our data with a straight line.

Each star has a different spectrum. Hence, the spectral slope of the speckles (which are dominated by uncorrected light from the central star) will also be different from star to star. We show the example of HD 139614 in Fig. 10.2, where a plot of the derived peak flux of the four replicas (identified in the plot with A, B, C, D clock-wise) is presented for each frame (center image). We fitted the points as described before and we derived their slope ($a_{\rm speckles}$), intercept and residuals. In particular, we averaged the slope values found and we define the speckle slope reference value (called $\overline{a}_{\rm speckles}$) for a specific target and

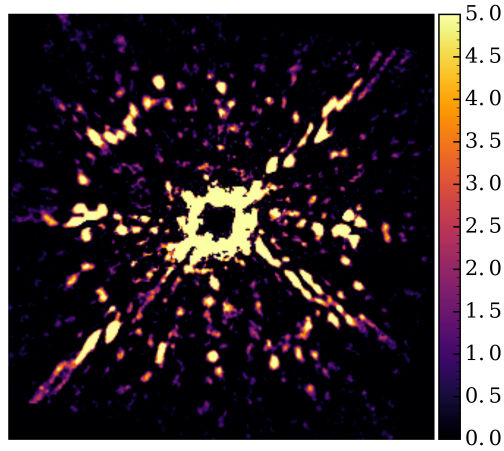

Figure 10.3: Speckle noise map for HD 139614 obtained on 2015-04-21 at $\lambda = \lambda_m$. This map is used for Method SRDI-PS (see Section 10.3).

day. This procedure was repeated for all the pixels and we thus create a map of slopes for the all center image (right Fig. 10.2).

We then derived the slope (a), intercept and residuals of each pixel for the target images. This provides us with a map of the spectral slopes as shown in the left panel of Fig. 10.2, similar to the map on the right, but without the four replicas. We compared this map with the $\overline{a}_{\rm speckles}$ value measured and used it to check which pixels are more affected by the speckles (in this case with light red colors). We note that the speckle map is in the position of the $\lambda_{\rm m}$ frame.

10.3.2 Flag map

Once we had the value of the pixel slopes a, we used an empirical relation (Eq. 10.5) to create a map of values able to discriminate between the speckle noise. We tested several functions that own two features: the function should be between zero and one and should be smooth. We found the best results using a sinusoidal functional form. We note that this formula is empirical and thus a more exact relation has to be still computed. This gives an estimate of the fraction of each re-mapped pixel's flux for which the spectral slope is consistent with speckle noise (values ~ 1):

$$f = \cos\left|\left(\frac{a - \overline{a}_{\rm speckles}}{a_{\rm max}}\right)^{1/2} \cdot \frac{\pi}{2}\right|, \tag{10.5}$$

where $a_{\rm max}$ is the maximum value of the slope map. We set the constrain that all the pixels have $|a| \leq$10. This was done to maximize the difference between the pixels dominated or not by speckle noise. We, then, set to one f if the argument of the cosine was greater than one in absolute values (pixels with a slope very different from the one of the speckles, i.e. dark blue points in right and left Fig. 10.2).

10.3.3 Removal of speckles and results

Once we constructed the flag map (Section 10.3.2), we multiplied it by the average map calculated as Section 10.2, using as input image the 2D background subtraction obtaining the image shown in Fig. 10.3. In this way, we created a map that considers the amount of speckles contribution and their position in a more exact way. With this map, we did the opposite procedure in order to re-map the averaged weighted map to the original position of pixels (x, y) for all the frames. We considered as weight the integrated flux of the map divided by the total flux of the 2D background subtracted image. At each frame, we subtracted the map created in such a way from the image where the bidimensional background subtraction was applied (results shown in the bottom row of Fig. 10.4).

The SRDI-PS method will offer an optimal removal of speckle noise. However, it may also over-subtract real spatially extended features in the images, and for this it is mostly suited for the detection of faint compact (point-like) sources.

10.3.4 Combining the images from the same day

The sub-methods described above were run independently on the set of images of the same epoch and source for each DIT.Once we got the final results for all the sub-methods, target and day, we corrected each image astrometrically, by the exposure time and neutral density as described in Section 7.4.3 and co-added them into a single data cube. In such a way we obtained a final image for each source which is the combination of all the observations of the day in the ADU/s (Analog-Digital Units per second) units. Finally, we created a set of three images from the IFS data cubes by doing an average over the wavelengths with no atmospheric absorption for the bands: H (1.45–1.66 μm, where possible), J (1.19–1.3μm) and Y (0.99–1.11 μm). An example of the post-processed images is shown in Fig. 10.4 (top row: SRDI-SA; bottom row: SRDI-PS) with the results of the two different sub-methods (rows) and the three bands (columns). It is important to stress that our method works the best if SPHERE data are provided in the IRDIFS-EXT mode (observation in all the three bands: Y, J, H) because the frames used to produce a speckle map are brighter.

10.4 SRDI-LD and SRDI-UD sub-methods

In order to probe the disc structure, we implemented another sub-method similar to the SRDI-PS sub-method. The only difference is in the use of the constant background subtraction instead of the bidimensional background. All the other steps were done is the same way. We call this method **Lower limit Disc sub-method** or **SRDI-LD**.

Moreover, we used also a **combination of both the point-like source and the lower disc sub-methods** to create an **Upper limit Disc sub-method** called **SRDI-UD**. At the same way of SRDI-LD, the goal of SRDI-UD is to probe the disc structure, but giving an upper limit disc value. In particular, this sub-method is clearly able to remove all the artifact that are not a continuum emission, but it leaves the image with a general emission coming from the star. In order to implement this sub-method, we used the flag averaged speckle map as implemented for the SRDI-PS sub-method. The speckles map was then re-scaled to the original position of each frame and subtracted to the original image where the constant subtraction was applied, as done for the sub-method SRDI-LD.

The reason of the SRDI-LD sub-method to be called “lower limit disc method” is due to the fact that there may be some over-subtraction of the real disc emission (mainly in the Y-Band) with resulting negative values. Whereas the SRDI-UD sub-method is

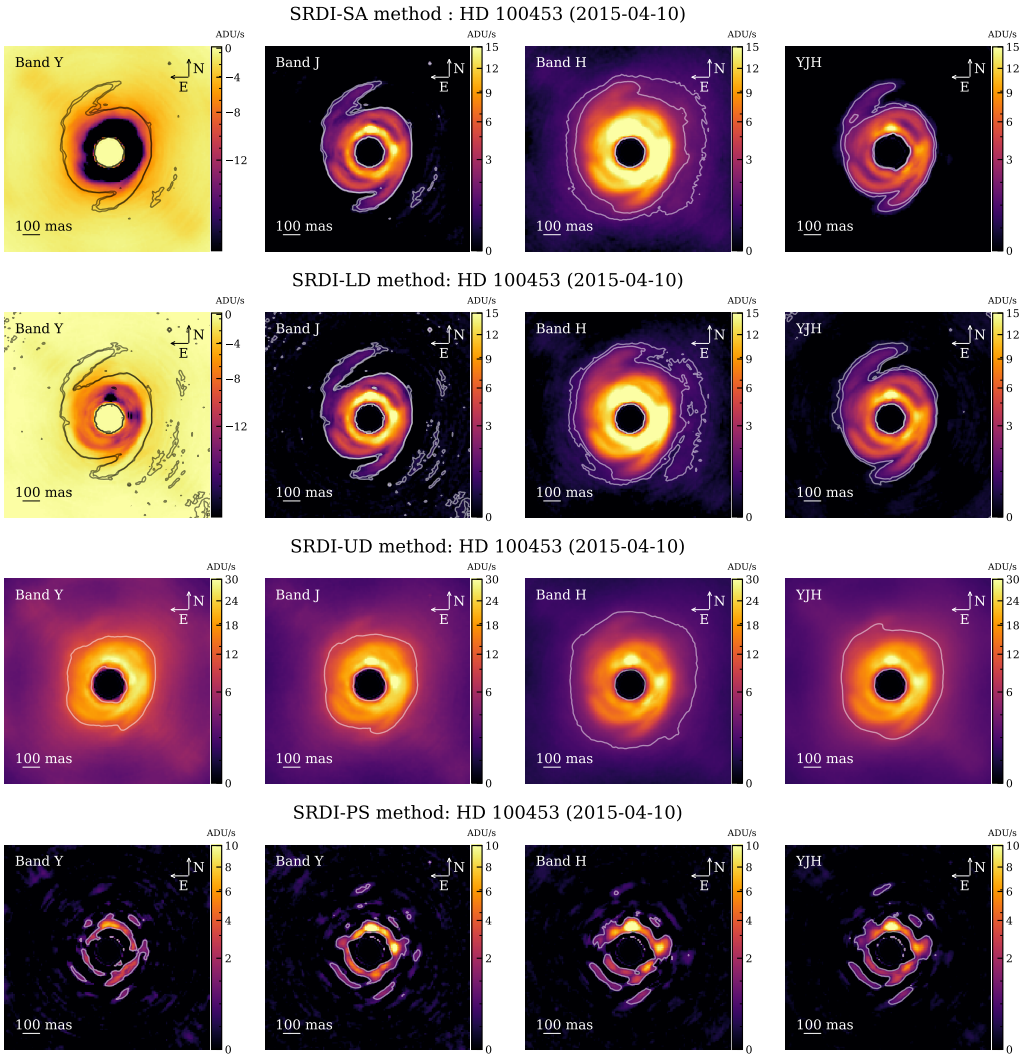

Figure 10.4: SPHERE IFS images of HD 100453 obtained on 2015-04-10. Results on the SRDI-SA (top); SRDI-LD (top center); SRDI-UD (bottom center) and SRDI-PS (bottom). Respectively: band Y (left), band J (center left), band H (center right) and YJH combined (right).The contour curves of SRDI-SA and SRDI-LD represent 15 and $30\sigma_{\mathrm{H}}$ (H Band), 5 and $15\sigma_{\mathrm{YJH}}$ (YJH combined), 5 and $2\sigma_{\mathrm{J}}$ (both J and Y Band), Y Band image is indeed negative. In the SRDI-UD and SRDI-PS, all the images show 15σ of the image itself. The FOV shown is of $\sim$1 arcsec.

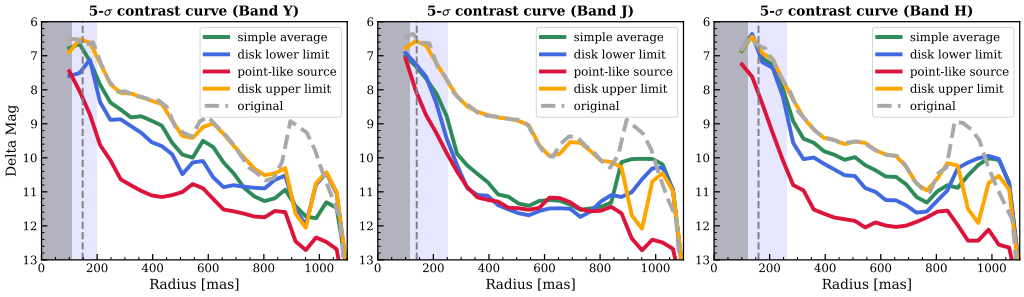

Figure 10.5: Contrast curves (5σ) of HD 100453 taken on the 2015-04-10 for band Y (left), J (center), H (right) respectively.

called "upper limit disc method" because the final image is typically under-subtracted. The map of speckles used, indeed, has always a speckle values lower than the ones of the constant background subtracted image. An example of the results obtained with these two additional sub-methods is shown in the second and third row of Fig. 10.4.

10.5 Method characterization

10.5.1 Contrast curves

To characterize our sample, we created 5-sigma contrast curves for each source. We note also that this is preliminary, because the throughput was not included yet. We measured first of all the stellar flux photometry using the flux images as done in Chapter 7, secondly, using the measured FWHM of the central star, we measured the standard deviation over all the disc with a step large as $r_{\rm out}$ - $r_{\rm in}$ $\sim$ FWHM. We used an iterative process to reach convergence: the process rejects values below or above the specified threshold of two times the standard deviations from the average.

The value of the standard deviation at each radius was divided by the stellar flux value of the central star and converted in Δmag. We note that everything inside a radius of 75 mas was masked (size of the coronographic mask radius), this is shown in the contrast curves as a gray box from where the curves start. Moreover, we haven't applied any correction to account for self-subtraction (i.e. throughput) and thus our curves have to be considered as a lower limit. In Fig. 10.6 we show as an example the case of HD 100453. We show the SRDI-SA (green) along with the sub-methods: SRDI-LD (blue), SRDI-UD (orange), SRDI-PS (red) . The original image is plotted with a dashed gray line and, as expected, has a small value of Δmag. The peak at radii between 800 mas and 1100 mas is the speckle contribution. The SRDI-UD sub-method shows a contrast curve very similar to the original image, with the difference of a significant reduction of the ring-like emission mainly related to speckles (800 mas<R<1100 mas). This sub-method is, indeed, able to remove all the point-like artifacts, but not the diffuse emission coming from the star. Finally, the SRDI-LD sub-method presents better contrast curves than the SRDI-UD sub-method, still preserving the contribution from the disc. Moreover, the peak at radii $\sim$1200 mas is due to the corner of the image. The corner is noisy mainly when the PUPIL tracking mode was used, considering that the image have to be rotated with different angles and part of the image is falling in just one over few exposures. The signal-to-noise is, then, lower. For all the type of tracking mode, instead, part of the sky inside the image is already out from the field of view and those pixels are considered as

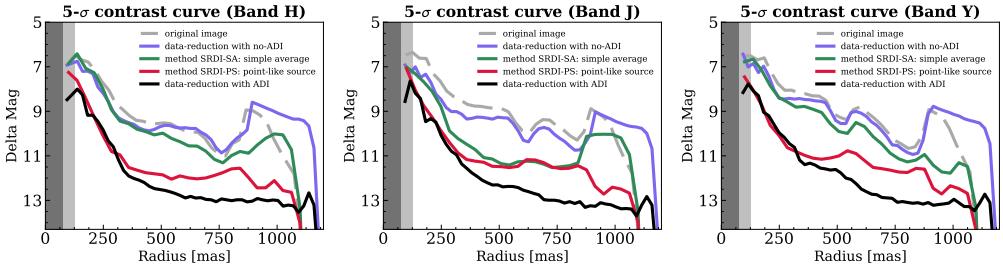

Figure 10.6: Contrast curves (5σ) of HD 100453 taken on the 2015-04-10 for band Y (left), J (center), H (right) respectively. In the plots are shown the curves with the ADI (black) and no-ADI (purple) technique applied and the curves for our new technique developed: simple average method (green line) and point-like source method (red line) along with the contrast curve before the method applied (gray).

zero and masked in order to measure the standard deviation.

The SRDI-PS sub-method is subtracting the overall continuum emission and, for this reason, it is not the most suitable sub-method to address the question regarding the presence of discs. Its contrast curve is, in general, lower than the one obtained with SRDI-LD, considering that the overall continuum emission is subtracted at the beginning and it reaches contrast for which most likely point-like sources can be found. The simple average curves (green lines) have a worse contrast curves than the sub-methods SRDI-PS and SRDI-LD. The contrast of SRDI-LD is similar to SRDI-PS just in the case of the J band, where the speckles are better subtracted. The cleanest subtraction is, in general, reached in band J for the SRDI-LD sub-method (e.g. HD 100453, Fig. 10.6). This is because the speckle map are centered in the J band.

We derived the contrast curves for all the targets, in the following we describe the overall results, but we do not show all of them in this elaborate giving the fact this is preliminary. Considering the SRDI-LD sub-method, we achieved the best contrast in the J band ($\leq$12 mag) of the targets: HD 100546 (days: 2015-05-04 and 2015-05-29) and HD 100453 (days: 2015-04-10 and 2016-01-16) and HD141569. Also targets such as HD 104237, HD150193, HD 179218, HD 190073 (day: 2015-06-19), HD 169142 (day: 2015-06-28, 2015-07-05 and 2015-06-07) reach a quite high contrast (Δmag $\leq$11 mag). We found the worst contrast in the targets observed without the coronagraph: HD 142527 and HD 97048. In particular, we reach just Δmag $\sim$6 mag in HD 142527 for all the Bands H, J and Y and Δmag $\sim$8 mag in the case of HD 97048. We note that the KK Oph target has bad contrast curves. In this case all our sub-methods do not work properly because the center star image does not have a clear observation. Without this we were not able to estimate the speckles slope value with accuracy and this generates a worst contrast curve. For the SRDI-PS sub-method, the best contrast ratios are achieved in the targets HD 100453 and HD 100546, reaching a contrast of $\sim$ 12 magnitudes in band H, J and Y. Also targets such as HD 169142, HD 145718, HD 104237, HD 150193, MWC 297, HD 190073 reach a quite high contrast. Instead, the worst contrast is achieved for HD 142527 (which was only observed without a coronagraph), reaching a 5σ-contrast in band Y of only $\sim$ 3 mag, band J of $\sim$ 2 mag and in band H of $\sim$ 3.5 mag, vividly illustrating the improvements in contrast achievable by using the coronagraph.

10.5.2 Comparison with other techniques: ADI

In order to compare our results obtained with SRDI-PS with already known methods, we create (5 - σ) contrast curves on HD 100453 (day: 2015-04-10) with images where the ADI and no-ADI techniques were applied. We used the data as provided by the SPHERE data center[1] (Delorme et al. 2017a; Galicher et al. 2018). For classical ADI image (cADI) the image "cube_reduced_image_corrthput.fits" was used, which is the reduced image corrected from throughput, before being stacked. For no-ADI we used the image "cube_reduced_image.fits", which is the reduced image without the correction from throuput, not available for no-ADI products. For both images (cube of different frames) we created band Y, J and H images, considering that for this detection the IRDIFS-EXT mode was used. An inner working angle (IWA) of $\sim$ 0.15" (gray box in the plots) was considered.

The contrast curves from the ADI technique (black line) and the one without applying ADI (purple line) are shown in the top panel of Fig. 10.6 together with our methods: simple average method (green line) and point-like source method (red line). With a gray dashed line is shown the contrast curve before applying any post-processing. For this target, ADI reaches a better contrast curve going up to 13 magnitudes in contrast, whereas our best case (in red) reaches 12.5 magnitude. In the inner part of the disc ($\lesssim$ 400 mas) the contrast curves of our SRDI-PS sub-method are better or comparable to ADI for all the three different bands, whereas in some parts of the outer part of the disc ADI can reach up to one magnitude of contrast more than our method. However, we stress that ADI can only be applied to targets where a sufficient field rotation can be achieved (requiring long continuous observations), whereas SRDI-PS and the known SDI (similar to SRDI-SA here shown) have no restrictions and may be considerably cheaper in terms of observing time.

10.5.3 Reference star images

We used the same reference stars (RS) described in Chap. 7. We measured the peak flux of the contrast curve in each band where an evident maximum is present and no companion was visible. We report that the average radius for which a drop in the flux was found: 108 mas for H Band, 104 mas for J band and 100 mas for Y Band. The maximum radius corresponds to 126 mas (gray box in the contrast curves), obtaining similar results to the ones quoted in Chap. 7. Moreover, the contrast curves of the RS still show a bump at $\sim$ 550 mas for Y Band, $\sim$ 700 mas for J band and $\sim$ 850 mas for H Band, probably related to the presence of speckles. In the case of the SRDI-UD sub-method this contribution is still high, whereas it is smaller in the case of the SRDI-LD sub-method. Furthermore, we inspect by eye some of the RS: HIP 81903, HD 101800, HIP 99742, HIP 94651, HIP 86098, HIP 87794, HIP 77785. In band H and J, we measured an emission next to the coronagraph similar to a bright ring as it is possible to see in the case of the SRDI-LD sub-method. The average radius of this emission is $\sim$ 148 mas (with values between 130 and 160 mas) for H band and $\sim$ 133 mas ($125 < R < 145$ mas) for J Band. Our sub-methods use a radial stretch of the image and create a ring in H band larger than the one observed, which corresponds to the radial extension in J Band. In the case of Y Band, instead, the flux values are negative and the structure elongated typically in one direction, suggesting an over-subtraction with a major axis large in average $\sim$ 136 mas and the minor axis $\sim$ 116 mas. The bright PSF residual is still evident in band H and J. Our sub-methods are able to decrease this stellar light, but not to completely

[1] https://sphere.osug.fr/spip.php?rubrique16

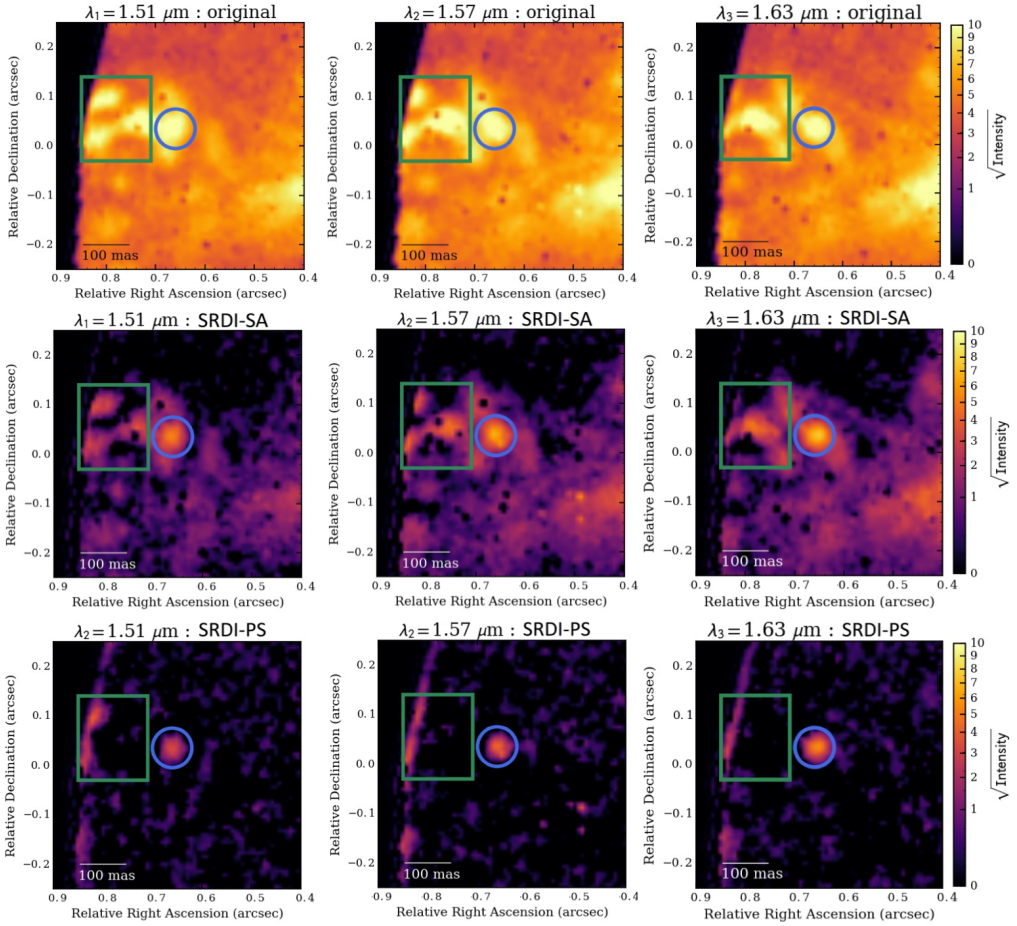

Figure 10.7: MWC 297 (day: 2015-04-29). Three frames (λ=1.51, 1.57, 1.63 μm respectively left, center, right) of the original image (top row), the SRDI-SA sub-method (center row) and the SRDI-PS sub-method (bottom row). The images shows with a blue circle the companion candidate found in the MWC 297 system as described in Chap. 8 and with a green rectangle the speckles.

delete it. In some of science images the spikes are still present, but less dominant than in the RS thanks to the longer exposures times. Moreover, the effect of having Y band over-subtracted and H band under-subtracted is still present in our science images.

10.6 Comparison of the results

As we underlined previously this study was done as a test, it will need a further implemetation to directly compare it with the results of Chap. 7. However, thanks to the technique here described, we detected a disc structure in HD 169142, HD 100546, HD 100453, MWC 297, AK Sco. HD 179218 is controversial so we do not present its results. The only disc detection not present using known techniques is MWC 297 in H band, which resembles the shape of a spiral arm with an azimuthally variable intensity and a bright

clump in the opposite side. A zoom-in view of the original and post-processed images for this companion is presented in Fig. 10.7 for three different frames of band H. We show on the top row the images before post-processing, on the center and bottom row respectively the SRDI-SA and SRDI-PS sub-methods. With a blue circle we underline the position of the companion candidate and with a green square the speckles removal. In Fig. 10.8 and 10.9 we show for comparison the results obtained for SRDI-PS and SRDI-LD for several targets. We underline that the results on the detection of point-like sources, such as MWC 297 and R Cra, HD 100453, for images taken in FIELD tracking mode are cleaner than using PCA-SDI. In particular, the corners are better cleaned, as show the image taken for HD 100453, where a second point-like source was here detected in the corner of SRDI-PS. This point-like source is not visible in the PCA-SDI nor in the PCA-ADI image presented in Chap. 9. The PSF residual is present in all our sources and it is difficult to remove it just with this technique. Regarding the disc detection the implementation of SRDI-LD and SRDI-UD gave a lower and upper limit disc emission. However, the use of PCA is clearly improving the contrast and it allowed us to detect features here not possible to be detected. The technique used in SRDI-LD cleans the image more than the use of the SRDI-PA alone (similar to SDI). In particular, we show in Fig. 10.4 the comparison of all the methods implemented for Y, J, H bands alone or all of them combined. If we compare the images for Y, J, H combined, it is possible to see that the images look similar when using SRDI-PA or SRDI-LD, but just SRDI-LD is able to reach the 15σ for all the extension of the spiral arms (see contour curves). Moreover, in both H and J band images it is possible to see better the presence of emission in the outer disc (on the west side). Finally, the Y band image is less over subtracted when using SRDI-LD than with SRDI-PA. The SRDI-PS method is noisy in the inner part of the disc when such a bright disc is present, while it provides clean results in the outer disc (e.g., MWC 297, Fig. 10.9). We believe that the implementation of this routine where the spectral profile of speckles is taken into account, together with PCA-SDI, would improve the disc signal compared to PCA-SDI alone. However, this methods may be further improved and developed.

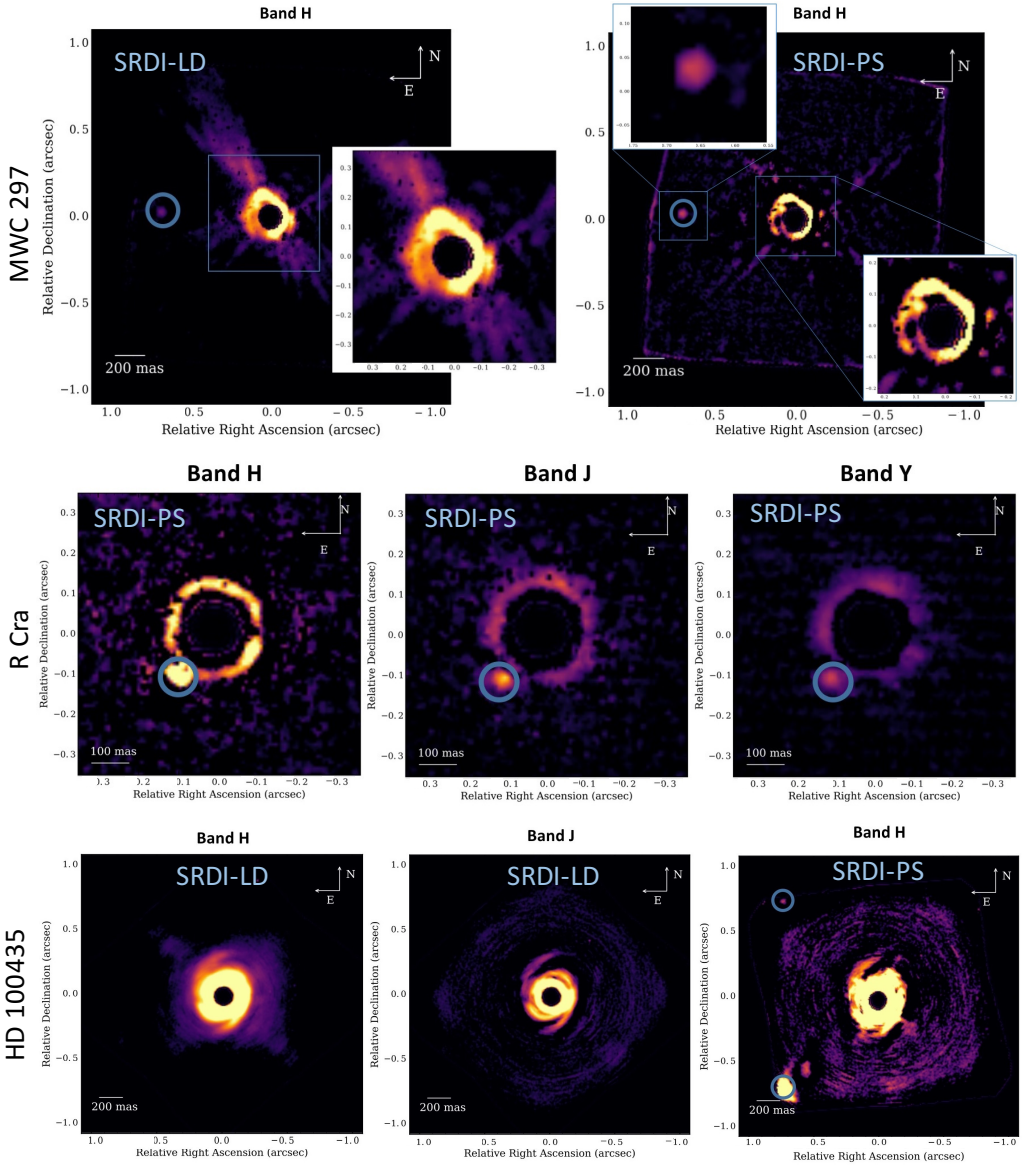

Figure 10.8: MWC 297 (top panel): on the left we show the image after post-process with SRDI-LD and on the right SRDI-PS. R Cra (middle panel) using SRDI-PS in H (left), J (center) and Y (right) bands. HD 100453 (bottom panel): band H (left) and J (center) after using SRDI-LD (on the 2015-04-10) and band H after using SRDI-PS (on the 2016-01-16).

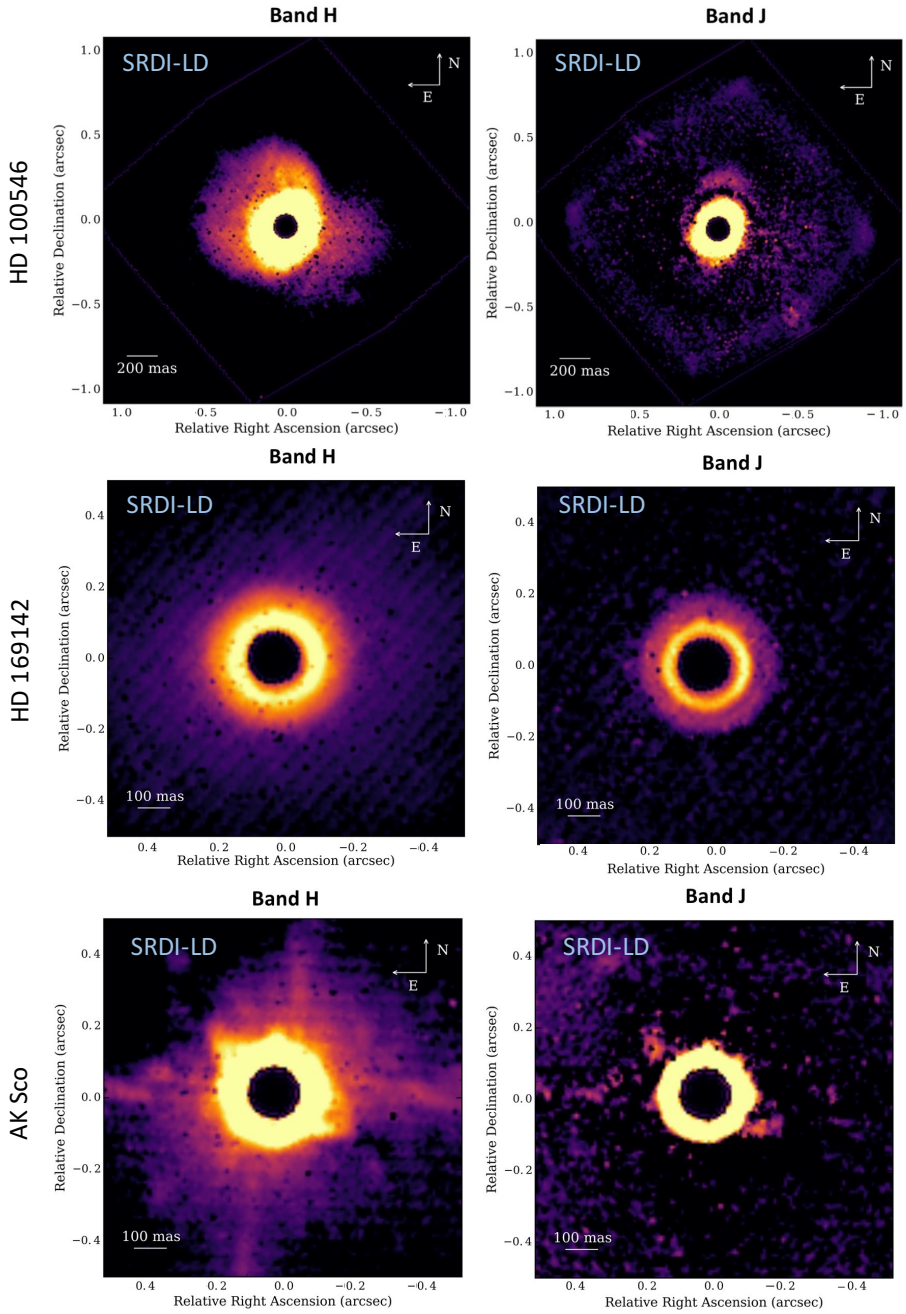

Figure 10.9: HD 100546 (top panel), HD 169142 (middle panel) and AK Sco (bottom panel). On the right we show the Band H and on the left we show Band J. All the images made use of the post-process with SRDI-LD technique.

Conclusions and future prospectives

Astronomer (J. Vermeet, 1668, Louvre Museum of Paris)

Somewhere, something incredible is waiting to be known.
(C. Sagan)

Chapter 11

Conclusions and future prospectives

In this Chapter, I will summarize the main results described in this thesis (Section 11.1), the main additional projects that I did but are not included in this manuscript (Section 11.2) and, finally, the future prospective in this field with a focus on my research (Section 11.3). As shown during all of the Chapters, the synergy between different techniques and between theory and observations is fundamental to better constrain the star and planet formation process.

11.1 Main conclusions

During this PhD thesis, I focused on a problem still open to date in the star and planet formation research field: the direct or indirect detection of low mass companions in young stars and their relation with disc sub-structures. The main idea is to observe planets while they form to constrain their formation mechanism and their interaction with the disc. Transition discs are considered to be some of the best candidates to study planet formation, due to their large cavity possibly formed by planets. The large amount of high quality observations coming online needs to be compared with theoretical models or simulations in order to get insights on the complex phenomena occurring inside them.

In this thesis, first of all, I provided a broad overview of recent observational discoveries regarding disc and planets properties. I described the dynamical evolution and thermal structure of a gaseous and dusty disc. Moreover, I underlined fundamental concepts and described the theory behind (sub-)stellar/planetary companions formation (**Part I**). I then described two complementary type of observations of discs around young Herbig stars through ALMA (**Part II**) and SPHERE (**Part III**), probing respectively the distribution of large and small grains in discs. SPHERE observations allowed us also to unveil the presence of young low-mass companions and spectrally characterize one of them (**Part III**). I used the state-of-the-art methods to post-process the images and to model the observational results obtained. I summarize below the main results presented during this thesis:

- **Part II**: A great variety of structures is present in discs, such as large cavities, gaps, horseshoes, spiral arms and shadows. Sometimes these features can be present at the same time in one disc either at the same or different wavelength. I note that to date the most accredited scenario to explain discs with large cavities in both gas and dust or with warps is the dynamical clearing by a companion.

  In Chap.5 I described my analysis on a specific system published in "A dust and gas cavity in the disc around CQ Tau revealed by ALMA" (Ubeira Gabellini et al. 2019). We analyzed spatially resolved ALMA observations of the continuum emission (λ=

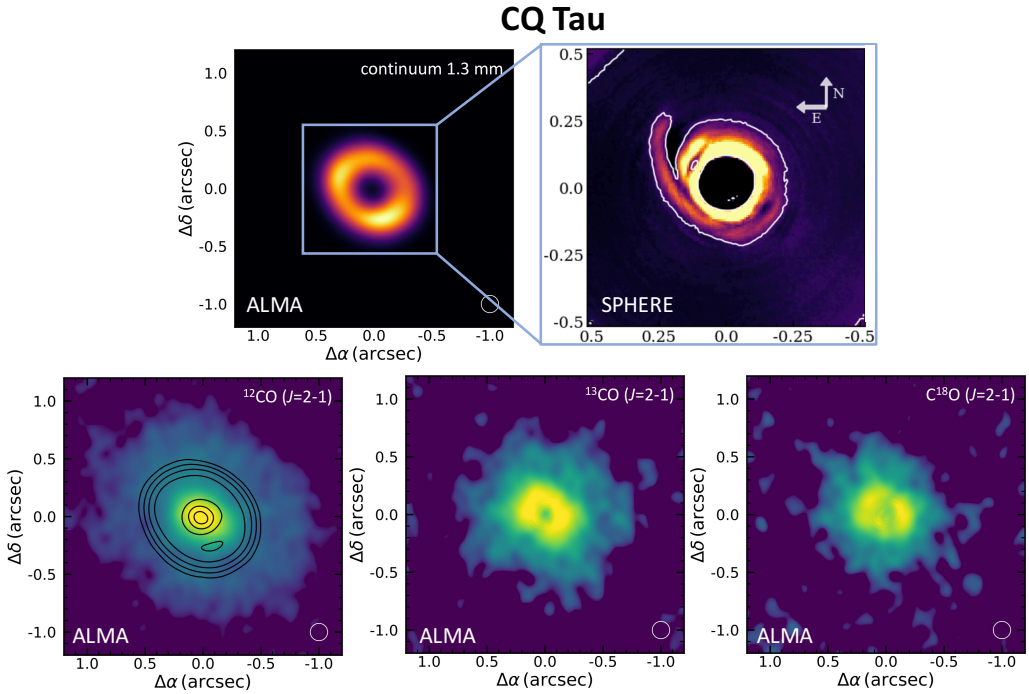

Figure 11.1: Summary of CQ Tau ALMA and SPHERE observations. We show the continuum emission (top left) and the three CO isotopologues (bottom) described in Chap. 5 along with the scattered light result obtained with SPHERE and shown in Chap. 7. In the continuum a ring-like structure is present, while the scattered light emission show multiple spiral arms.

1.3 mm) and CO isotopologues (^{12}CO, ^{13}CO, C^{18}O J = 2-1) integrated intensity from the disc around the nearby (d = 162 pc), intermediate mass ($M_\star = 1.67\ M_\odot$) pre-main-sequence star CQ Tau. The results are shown in Fig. 11.1. We employed a thermo-chemical model DALI to model the inner disc in continuum, and in both ^{13}CO and C^{18}O emission together with the disc SED. The models show that the radial profile of the cavity in the dust continuum is described by a Gaussian ring centered at $R_{dust} = 53$ au and with a width of $\sigma = 13$ au. For the gas, a distinct inner cavity with size between ~ 15 and 25 au and a density lower of a factor between $\sim 10^1$ and $\sim 10^3$ is needed to reproduce the data. We note that the cavity radius and level of density lowering are degenerate, but they can be constrained with reasonable uncertainties. In the CQ Tau disc the gas radial extent is a factor of two broader than that of the large dust grains. The computed dust-to-gas ratio is not radially constant throughout the disc. Moreover, the global dust-to-gas ratio is found to be ~ 0.09, higher than the typical values assumed (~ 0.01), most likely because of carbon depletion. Finally, we performed a set of SPH simulations (post-processed with a radiative trasfer tool) to investigate whether the presence of a massive planet might be responsible for the radial structure of the disc around CQ Tau. We found that a massive planet with a mass of $M_p = 6 - 9\,M_J$ located at $R_p = 20$ au from the central star can reproduce qualitatively the gas and dust profiles of the CQ Tau disc.

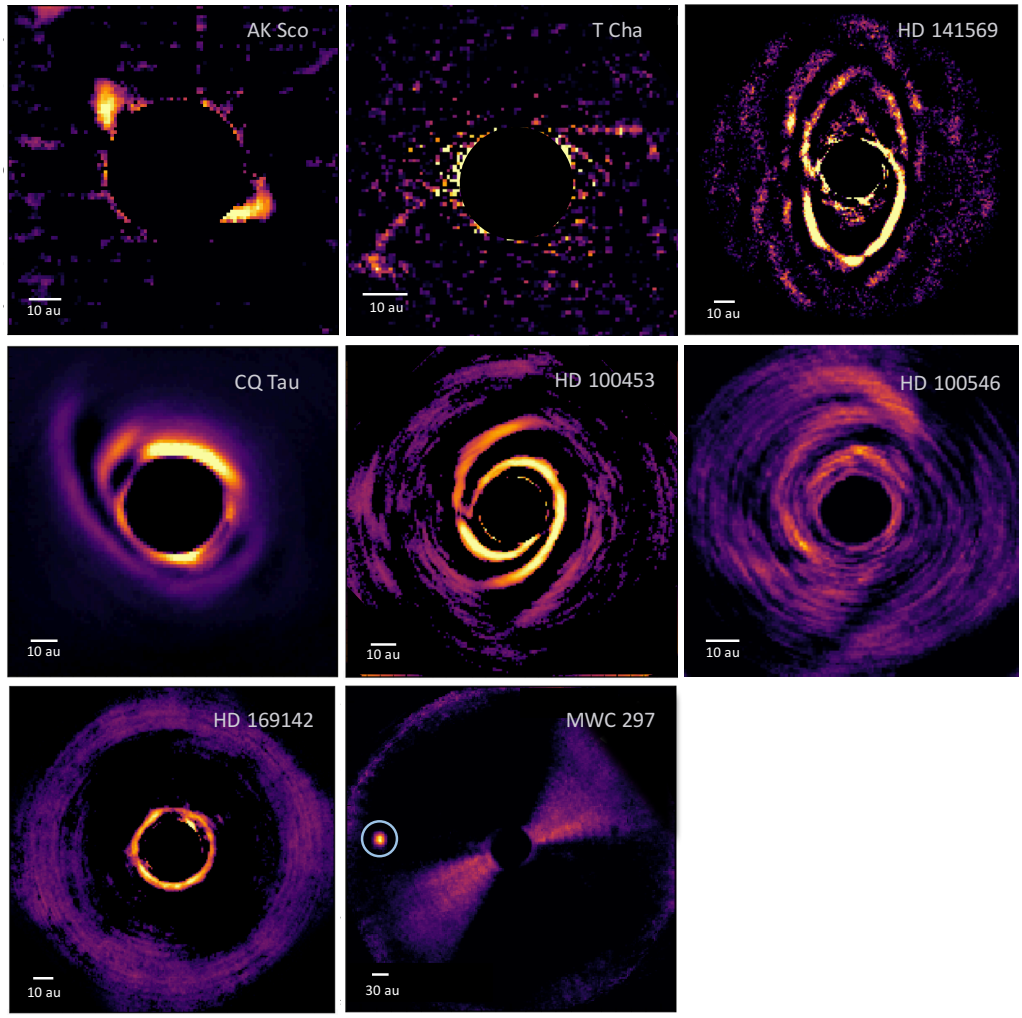

Figure 11.2: Summary of SPHERE data of the resolved disc (Chap. 9) and of the companion around MWC 297 (Chap. 8). In the first row, we show the thin ring disc detection; in the second row, we show the spiral-like discs and in the third row we show the ring-like disc of HD 169142 and the companion around MWC 297 (blue circle).

- **Part III** focuses on SPHERE observations. In Chap. 6, I provided an overview on the high contrast imaging (focusing on the SPHERE instrument) and on the post-processing techniques used during this thesis (Angular and Spectral Differential Imaging). In Chap. 7, I presented the analysis done on the VLT/SPHERE data of an heterogeneous sample of 22 nearby Herbig stars. The main focus of this study was to test the model prediction of Maaskant et al. (2013, 2014). These authors suggested that large near-infrared excess observed in the SEDs of Group I Herbig Ae/Be stars can be explained by the presence of a large gap in their discs. On the contrary, the SEDs of Group II sources are supposed to be continuous and should not present such large gaps. A paper is in preparation regarding this work:

"An heterogeneous SPHERE-IFS Survey of 22 Nearby Herbig Ae/Be Stars: Are All Group I Discs Transitional?". We post-processed high-contrast images using the Vortex Imaging Pipeline (VIP, Gomez Gonzalez et al. 2017a) and adapted this in order to post-process SPHERE-IFS data. The post-processing was done using PCA-SDI that uses just the spectral information (Pueyo et al. 2012) and it was performed in full frame. We detected seven disc structures out of 22 sources, five for the Group I targets (HD 100453, HD 100546, HD 169142, CQ Tau and T Cha) and two for the Group II (AK Sco and HD 141569), according to the classification of Meeus et al. (2001). We note that, on one side, HD 141569 is in a transition phase between Class II and debris disc with a large cavity and for this reason it is still under debate if it should or not considered in this classification. On the other side, also if AK Sco owns a low far-IR excess, typical of a Group II source, it shows also a high m_{30} - m_{13}, typical of a Group I. In both classifications, the fraction with detected discs is different between Group I and II discs, suggesting that the scenario proposed by Maaskant et al. (2013, 2014) is plausible and there can be a relation between the Group I sources and the detection in scattered light of the outer edge of the dust gap.

In the following Chapters 8 and 9, I presented data post-processed with PCA-SDI, as the ones previously described, but also 1) PCA-ADI that uses just the angular information (performed either in full frame - Absil et al. 2013 - or in concentric 2-FWHM wide annuli) and 2) a combination of PCA-SDI and PCA-ADI performed in a single step called PCA-ASDI. In Chap. 8, I show the results obtained for the MWC 297 source, where we detect and confirm the presence of a novel companion gravitationally bound to the host star (see Fig. 11.2) with data spanning a $\sim$ 3 yr period. The results of this work are published in the ApJ Letter "Discovery of a low-mass companion embedded in the disc of the young massive star MWC 297". Astrometry favours a gravitationally bound object. Spectral characterization suggests a young (<1 Myr) low-mass companion with M$\sim$0.1 - 0.5 $M_{\odot}$ and with high extinction. Its large separation ($\sim$245 au) supports formation via gravitational instability. The mass ratio ($\sim$ 0.01) is similar to the one of PDS 70, the first confirmed planet within a disc cavity, but in the stellar mass regime. The target is extremely interesting given the young stellar host age. Finally, we propose that the companion could be responsible for the dust gap inferred by Alonso-Albi et al. (2009).

In Chap. 9, we performed the same analysis done in Chapter 8 through VIP with the sources of the sample in Chap. 7 with a disc detection. Moreover, we compared the results with the thermal and line emission of ALMA observations and with polarized scattered light data. This allowed us to unveil new details regarding the coupling between gas and small grains at larger separations and to better constrain the planet formation scenario of some sources. We found that HD 100453, HD 100546, CQ Tau have a disc structure which resembles a spiral; HD 169142 and HD 141569 have a ring-like disc; finally, AK Sco and T Cha presents a highly inclined disc. Group I substructures are compatible with transitional discs and with various shapes (e.g., spirals). The salient features of individual sources can be summarized as follows:

- We detect in HD 100453 that the spiral arms in scattered light follow the profile detected in the ALMA gas emission described in Rosotti et al. (2019a), going further out than in PDI observations.

– We were able to detect not just the inner ring of HD 169142, but also the outer ring.
– CQ Tau presents interesting features in scattered light compared to the continuum emission, with a spiral arm with a high pitch angle and multiple spirals inside it at the edge of the cavity in millimeter emission.

The intriguing results obtained in particular for HD 100453, HD 100546, HD 169142 and CQ Tau will give us the possibility to study more in detail the connection between total intensity and polarized light. The result of seven targets is shown in Fig. 11.2. We can confirm the trend found by van Boekel et al. (2003) that Group I discs in our survey are in general well separated from Group II sources in the diagram IRAS $m_{12} - m_{60}$ versus $L_{\rm NIR}/L_{\rm IR}$. Moreover, all the sources that show a thin ring are above the threshold line and with $m_{12} - m_{60} > 0$. This parameter space may be considered a gray area where sources are typically classified as Group II by Meeus et al. (2001) and van Boekel et al. (2003) and are considered as Group I according to a different criterion (e.g., AK Sco, Garufi et al. 2017). All the other disc shape (e.g., spirals, multiple rings) are below the curve. We also compared our detections with radiative transfer models (presented in Appendix C). We found that Group I discs are typically thicker (higher flaring angle or scale height) with respect to Group II, in particular for what regards the spiral-like discs. To confirm this trend we will need to enlarge our disc sample and to model each of these discs in detail. This will also help us to better constrain the process of discs clearing around pre-main sequence stars.

Finally, in Chap. 10, we described the routine developed by us to post-process SPHERE-IFS data in order to search for both point-like sources and disc emission in the near-IR. This pipeline is similar to SDI, but it combines the known radial variation with wavelength of stellar artifacts with the information of the spectral slope of the star. This slope is, indeed, expected to be different from the one of planets and sometimes of discs and it would help to exploit an additional factor to post-process the image. As SDI, this method is applicable to sources with extended disc emission, it is not sensitive to variations of the PSF over time and it can be used with both FIELD and PUPIL tracking mode.

11.2 Further work not included inside this thesis

During this thesis, I have actively collaborated also to three additional projects not described in the main text. Considering the relevance of the contribution, we report here a summary of them.

- I have collaborated actively with Dr. M. Robberto (STScI, Baltimore) to perfom a study of the IMF of the Orion Nebula Cluster with an HST survey. This was recently published: "HST survey of the Orion Nebula Cluster in the H_2O 1.4 μm absorption band: I. A census of substellar and planetary mass objects" (Robberto et al. 2020). With our survey, we detected 4510 sources down to masses of 2 - 3 $M_{\rm Jup}$ (the minimum mass for opacity-limited fragmentation of pre-stellar cores) for a 1 Myr isochrone at distance of 400 pc. We had the possibility to disentangle young sub-stellar sources from the background galactic population and extragalactic sources. After deriving the mass of each target, we reconstructed the Initial Mass Function in particular focusing on the low-mass tail. We showed that IMF do not present a second very-low mass peak, reveled to be background stars, but show

an extension to lower masses. This is consistent with a single formation scenario regulated by a common set of physical processes. This last part is fully described in an accompanying paper.

- During three months spent at the Monash University (Melbourne), I started to collaborate with K. Hirsh, D. Price and C. Pinte on the work "Observational appearance of circumbinary discs" (MNRAS, in prep.). This is a follow-up project a the recently submitted paper (Hirsh et al. 2020). We performed hydrodynamical simulations with PHANTOM and post-processed them through radiative transfer calculations (through MCFOST). The presence of binaries and embedded planets, indeed, is able to distort the disc structure and produce asymmetric features, e.g. line profiles can be significantly distorted (Regály et al. 2014). The project includes a systematic study on how the disc surface density is altered by different eccentricity, scale height and mass ratio, obtaining observational signatures such as the symmetry of the line profiles, the variation of the gas kinematic data with respect to a simple keplerian rotation. We obtained observative signatures of this process, such as moment zero, one, two maps (on ^{12}CO, ^{13}CO and C^{18}O) and line profiles. Interestingly, these maps can be significantly distorted by the presence of a companion inside a cavity both in the case of polar and co-planar orbit and depending on their mass ratio. We modeled also the channel maps, obtaining intriguing results such as the presence of high velocity not asymmetric emission coming possibly from a stream of material going toward the binary. Comparing the evidences of cavity size and kinematic distortion of models with the ones of observations can be used to discriminate between different scenarios and constrain the parameters degeneration. Examples of systems which can benefit of this study will be: HD 142527, CQ Tau and HD 100546.

- I have worked with V. Christiaens in the post-processing of SPHERE-IFS data on novel data on which he is the PI. The results on this will end up in a publication.

11.3 Future directions

Combining planet detections around pre-main-sequence stars with different techniques is one of the most discussed topic in planet formation to date. Three are the diagnostics mainly used to detect new-born planets (see Section 1.5.5): direct imaging, kinematic signatures and different disc geometries (e.g. gap, cavities or spirals). Kinematic signatures, in particular, may complement the weaknesses of High Contrast Imaging (HCI). At young age native discs are indeed optically thick in the infrared and direct imaging may be not able to discriminate between embedded protoplanets and their disc. A scientific goal in this regards would be to image a planetary companion through different techniques to probe the fidelity of each of them. So far the only example of direct detection of a planet is PDS 70 b (Keppler et al. 2018): a $\sim$ 5-10 M_{Jup} planet embedded in its natal disc and inside a cavity. Moreover, in HD 163296, Pinte et al. (2018b) and Teague et al. (2018) were able to unveil for the first time the presence of giant planets at large separation though kinematics. In HD 97048, Pinte et al. (2019) detected a local deviation from keplerianity which suggests the presence of a planet inside a gap. A planet was instead never observed at the same location through kinematic and direct imaging together. Combining kinematics detection with high-contrast imaging of protoplanets embedded in their native discs may be particularly synergetic. They can provide, indeed an independent measure of luminosity and mass of the planet: a good estimate to allow to discriminate between

different formation models. Futhermore, it is needed to probe which conditions kinematic distortions are related to planets and which to disc structures. This may be tested with 3D hydrodynamical models.

A code to discriminate embedded planet from disc emission with SPHERE-IFS.

During my PhD, I have developed a novel technique to remove the stellar artifact from the scattered light images called Spectral-Radial Differential Imaging (SRDI, see Chapter 10), which is able to detect point-like sources or preserve the disc contribution. This technique exploits a study on the spectral slope. First of all, it is important to compute analytically a relation to use the information of the spectral slope, here it was taken empirically as a sinusoidal form (Eq. 10.5). The code will have to be included in VIP and it will be tested through the routines developed there. It will be implemented together with PCA in order to better exploit its potentiality. To test this, forward modeling will have to be performed by injecting fake companions and recovering them. An extra step regarding this work will be to co-add the information of Angular Differential Imaging (ADI) and SRDI and test if the novel combination is more efficient than the current ASDI. Finally, an analysis on the disc structure needs to be done. This is more complicated due to the fact that the spectral slope of the disc emission can be similar to the one of the star. Anyway combining SDI with a spectral slope study should give us a way to better constrain the disc emission mainly in the innermost part of the disc, more affected by stellar emission. A test on the reliability of this method will be the injection of fake disc structures such as rings and spirals (e.g., Christiaens et al. 2019b). Moreover, in principle this could also be extended to all IFU data, with the caveat of checking before the different physics behind.

The case of MWC 297

A follow-up project on the formation of the discovered companion around the massive B-type star (17 solar masses) MWC 297 (Chap. 8) needs to be done. In this regards, we need to test if the companion detected in the near-IR around MWC 297 is able to produce a gap in the millimeter. This may be done through simulations of high-resolution ALMA observations. It is well-understood, indeed, that massive planets open gaps (e.g. Dipierro et al. 2016), so it is likely that such a massive companion is responsible for the gap in dust thermal emission as proposed by Alonso-Albi et al. (2009). Moreover, this system is particularly interesting given its young age. In this project, I would like to test the scenario of the seed of the companion discovered been generated via gravitational instability. If this is verified, it will, indeed, provide evidence for a correlation between formation of high mass companions and planets in the case of similar mass ratio.

HD 169142, HD 100453 and CQ Tau

Three out of 22 sources analyzed by us would need further analysis to exploit all the information inside them: HD 169142, HD 100453 and CQ Tau. First of all, HD 169142 is the perfect candidate to provide a comparison between total intensity emission and polarized light (Sec. 9.2.3). Polarized images are more suited to detect disc emission since they are less affected by stellar light. At the same time, it will be important to give more observative constrains on the polarization fraction and on the grain properties. This study may be extended also to different geometries and not face-on disc, to test whether polarized emission is always the best solution to observe discs or not.

Secondly, as described in Sec. 9.2.1, different wavelengths trace the emission coming from different vertical layers and radial locations. In particular, the continuum comes

from the midplane, while the gas, dynamically coupled with the small grains, comes from upper layers. As shown in Chap. 9 in HD 100453 we see two spiral arms extending more than what previously seen in PDI observations. Moreover, they seem to be spatially related to the ^{12}CO emission. However, while the Northern spiral arm (S4) seems to be coincident with the gas emission, the Southern spiral arm (S3) present a small shift. If these features are related they may trace different vertical layers. It is indeed known that the CO emitting layer is not expected to be emitted exactly at the same layer as the one of the H_2, most abundant gas tracer. For this reason a follow-up project will be to test this scenario by injecting a spiral with two different z/R and derive the projected spiral arms correspondent. This may allow us also to test the post-processing technique used to see if some of the features observed may be due to it.

Finally, I would like to further test the disc around CQ Tau described in Sec. 9.2.4, in particular for what regards the connection between ALMA and SPHERE results. In Wölfer et al. (2020, in prep.), we analyze the disc kinematics on CQ Tau. It would be nice to further compare the results presented in this manuscript with the ones obtained in kinematics. It would be important to test whether a single inner planet inclined and eccentric will be able to carve a deeper cavity in the gas through hydrodinamical simulations. Moreover, I would like to verify if the spirals visible at the edge of the two symmetric clumps present in the continuum are related to them or not. Finally, it would be nice to test if the large pitch angle observed may be related to the presence of an outer companion as it is for HD 100453 or it can be produced by some other phenomenon and to projections effects.

Appendices

Appendix A

Details of the instrument and techniques used

A.1 Imaging in the near-IR with SPHERE

SPHERE is an instrument installed at one of the UT3 Nasmyth foci of the VLT. It is able to perform imaging, low-resolution spectroscopic, and polarimetric characterization of exoplanets, reaching the highest image quality and contrast performance in a narrow field around bright targets observed in the visible or near infrared. SPHERE is composed by:

- SAXO: Sphere AO for eXoplanet Observation. It is the adaptive optics module of SPHERE. It is designed in order to correct for the turbulence perturbation at high frequency.
- CPI: The common infrastructure which receives direct light from the telescope and it is built to provide highly stabilized, AO-corrected, and coronagraphic beams to the three sub-instruments.

The sub-instruments are:

- IFS: The integral field spectrograph producing a cube composed by 39 monochromatic images taken simultaneously over time (4D cube), with a spectral resolution of R$\sim$50 if the IRDIFS mode is used (0.95 - 1.35μm, just Y-J) or R$\sim$30 if the IRDIFS-EXT mode is used (0.95 - 1.65μm, Y-J-H)
- IRDIS: The Infrared Dual-band Imager and Spectrograph able to provide classical imaging (CI), dual-band imaging (DBI), dual-polarization imaging (DPI) and long slit spectroscopy (LSS). The wavelength observed can be between 0.95 - 2.32μm (with R$\sim$50) or between 0.95 - 1.65 (with R$\sim$350).
- ZIMPOL: The Zurich Imaging Polarimeter provides near diffraction limited classical imaging and dual-polarization imaging (DPI), which in the visible goes below 30 mas resolution.

The observations with IRDIS in dual-band imaging mode and IFS (IRDIFS and IRDIFS EXT modes) can be taken simultaneously. In particular, in the IRDIFS mode IRDIS is operated in the filter pair H2 (1.5888μm) and H3 (1.6671μm) and IFS in the bands Y J (0.95-1.35 μm, R $\sim$ 54). In the IRDIFS EXT mode, instead, IRDIS is operated in the filter pair K1 (2.1025μm) and K2 (2.2550μm) and IFS in the bands Y JH (0.95-1.65 μm, R $\sim$ 33).

In particular in this manuscript, we present observations made with SPHERE-IFS. The IFS is a lenslet-based integral field unit (called BIGRE, Antichi et al. 2009), providing a

1.″73 x 1.″73 FOV that is Nyquist sampled at 0.95 μm. The raw data comes as 21000 spectra. Each spectrum from a spaxel is projected on a rectangular area of 5.1 x 41 pixels on the detector. During data reduction, the image is converted into a (x,y,λ) data cube and it is resampled by the pipeline over a square regular grid at $(7.4 \text{ mas})^2$ / spaxel. The coronagraphs are presented as a Lyot mask in the focal plane, a Lyot stop in the downstream pupil and an apodizer in the upstream pupil.

A.2 Radio-interferometry with ALMA

In order observe at long wavelengths and to reach a high angular resolution, the diameter of the telescope should be large. It is, indeed, valid the relation: $\theta = 1.22\lambda/D$, where λ is the wavelength and D is the diameter of the telescope. The largest single dish telescope able to image at radio wavelength (e.g. at 7 mm) has a diameter of 100 meters and it is able to reach a resolution of $\sim 17''$. Astronomical interferometry has the goal to achieve high angular resolution using smaller telescopes. The Atacama Large Millimeter/Submillimeter Array (ALMA) is an example of this in the radio wavelength, whereas the Very Large Telescope Interferometer (VLTI) uses interferometry in the infrared.

For what regards detailed information on ALMA and on the interferometric technique we refer to the ALMA Manual. ALMA is an aperture synthesis telescope consisting of 66 high-precision antennas that can be positioned in a number of different configurations. Aperture synthesis means that images have the same angular resolution of a single telescope whose aperture size is comparable to the largest baseline used. It can operate at different observing wavelengths in the range from submillimeter and millimeter. The array is located on the Chajnantor plain of the Chilean Andes, where the weather is typically dry and the sky condition clear. This is a really important condition to observe at this type of wavelength. Millimeter and submillimeter light is indeed easily absorbed by water vapor in the atmosphere. In the 12-m Array, there are fifty antennas of 12 meter, which are used for sensitive, high-resolution imaging. These antennas are complemented by the Atacama Compact Array (ACA), which is composed of twelve closely spaced 7 m antennas and four 12 m antennas for single-dish observations, respectively called the 7-m Array and the TP Array. These antennas are used mainly to enhance wide-field imaging of extended structures.

An interferometer samples the power spectrum of the sky brightness distribution, contrary to direct imaging which uses a CCD camera on an optical telescope. Interferometry is based on the measure of the Fourier transform of the sky. Each pair of antennas (called baseline), in a single integration, samples a single point in this power spectrum at a position in Fourier space, which is directly related to the distance between the pair of antennas and the position angle of the baseline vector. Short baselines are the antennas which are close together and sample large-scale angular structure, whereas long baselines sample very small-scale angular structure. The earth rotate, thus, the baseline projection on the celestial sphere also rotates. This is also a factor to take into account through the so called technique Earth Rotation Synthesis.

In order to reconstruct the images, it is important to consider the antenna performance. This can be done through the radiation/antenna pattern, a mathematical function that represents the radiation properties of the antenna as function of the space coordinates. Together with the antenna pattern, it is important to define the beamwidth, which is the angular separation between two opposite point sides of the pattern maximum also used to describe the resolution capability of the antenna. A common resolution criterion states that this resolution is equal to the FWHM, which is the angle between two directions in which the radiation intensity is half of the pattern maximum value. The

response of an interferometer is the convolution between the intensity distribution of the source and the radiation pattern of the antenna. The visibility function represents the Fourier transform of the source intensity distribution multiplied by the beam pattern. The coordinates (u,v) represent the couple of spatial frequencies for a given time that the interferometer can observe. Combining visibilities over a large number of baselines (the uv-coverage), the interferometer sample the Fourier plane. In order to reconstruct an image, this plane have to be inverted through a Fourier transform. The quality of the reconstructed image is sensitive to the uv-coverage. Antennas are periodically reconfigured to provide different array configurations. The combination of different configurations may improve the uv-coverage. It is important also to consider the presence of the thermal noise which can corrupt the visibility measurements, particularly for high PWV levels.

In the aperture synthesis, sky measurements consist in values of the real and imaginary part of the visibility function at discrete location in the Fourier plane. Incomplete coverage in the u-v plane gives rise to a loss of information on the source. This means that the unmeasured parts can be filled with an infinite number of different images consistent with the data. The Fourier transform cannot be applied on the raw data, there is the need of introducing a transfer function. This creates a regular gridding in the u-v plane. The visibility function is thus multiplied by a weighting function to reach an uniform coverage of data in the u-v plane. We note that there is the known "zero spacing" problem, which consists in the fact that, to avoid collisions, it is not possible to set antennas closer than their diameter. This leads to a hole in the distribution of baselines at short and zero baseline separations, correspondent to large angular structure. This can be a problem mainly for extended or large-scale structures because there can be problems in resolving the emission for which the emitted power is dominated by their large-scale structures. The short spacing gap in the uv-coverage can be filled in by adding ACA observations, but this is not needed in the disc observations.

The image deconvolution is usually performed through the CLEAN algorithm. This allows synthesis imaging of complex objects even with a poor Fourier plane coverage. The Hogbom, the Clark and Cotton-Schwab are examples of CLEAN algorithms. A critical factor in the cleaning is the weighting. Three are the methods commonly used to evaluate the weighting associated to each cells: natural, uniform or robust weighting. The natural weighting favors the signal-to-noise ratio using weighting to data inversely as their variances. The sampling function is more concentrated in the center of the u-v plane, thus the weight of the inner regions will be higher than the one of the outer regions. The uniform weighting applies instead equal weights to each cell in the grid, obtaining an increase of the resolution of the images but with a lower signal-to-noise. This is due to the fact that equal weights are applied to cells with different number of measurements. The robust weighting is a combination between the two weighting previously described. In particular, this allows to sweep across these methods to find the best combination of weighting, given the sample in the u-v plane.

Appendix B

More details on the sources with a disc detection

In this Appendix, we present a comparison of observations taken in different days and methods and a study of the significance of the results presented in Chap. 9 through contrast curves, signal-to-noise maps and STIM maps. Finally, we collect in Table B.1 the photometry used to derive the diagram in Fig. 9.19.

B.1 Comparison with observations of different days and methods

In this subsection, we show some of the observations described in Chapter 9 comparing different observing days. In particular, the four epochs of observation analyzed for HD 100453 are described in Chapter 9. For HD 100546 we post-processed images of four epochs, but just two of them are presented in this Section because they are the one with the highest quality coronagraphic observations. At the same way, also for HD 169142 we show just two epochs (2015-06-07 and 2015-06-28): the ones with higher exposure time. For T Cha, we showed in Chapter 9 the post-processed images for the day 2015-05-30, considering that the one obtained in the 2015-05-31 were too noisy, and thus the final images are not shown here neither. Finally, for CQ Tau, AK Sco and HD 141569 we analyzed just a single epoch, already described in Chapter 9. In this Section, we show for both HD 100546 and HD 169142 the post-processed images obtained through the use of four techniques PCA-ASDI, PCA-SDI, PCA-ADI, PCA-ANNULI for both epochs. Finally, for CQ Tau and HD 169142 we compared different techniques to show more details on the point-like sources detected.

In Fig. B.1 we show the post-processed images of the observations of HD 100546 for two epochs: 2015-05-04 and 2016-05-31. The first one was already described in Section 9.2.2, and the second is shown here for comparison. On top of each image is shown the $3-\sigma$ contour curve of the image PCA-SDI of the different techniques. Most of the emission is recovered thanks to the PCA-SDI method during both the observing days shown. All the spirals detected by Follette et al. (2017), with the exception of S6 and A are recovered. In both the epochs it is possible to see the S7 spiral at a separation of $0''.1$. The other techniques, show the same spirals, but they do not recover the most symmetric ones (S2, S3) and they highlight more the asymmetries (e.g. S5, S6).

In Fig. B.2 we show the observations of two epochs (2015-06-07 and 2015-06-28). Just the first ring at $\sim 0''.2$ and not the one at $\sim 0''.6$ is confirmed by the second epoch observations. In PCA-ANNULI the disc is visibly distorted revealing a pattern of fake spirals and point-like sources. We note the presence of the point-like source in the PCA-ADI image. Moreover, we show a zoom-in view of the final images obtained using the PCA-ADI technique and different number of principal components and wavelengths (Fig. B.3). It is possible to see in the image of the observing day 2015-06-07 two point-

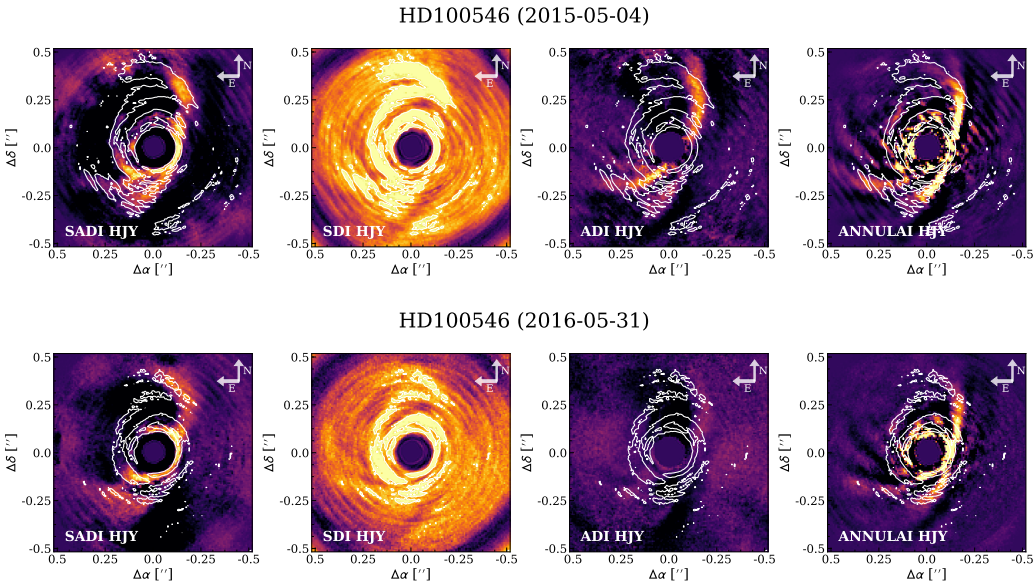

Figure B.1: On the top row, we show the observing day: 2015-05-04, while on the bottom the 2016-05-31 for the final images with YJH combined for PCA-ASDI (left), PCA-SDI (center left), PCA-ADI (center right) and PCA-ANNULI (right). The contour curve on top of each image is the 3−σ contour curve of the image PCA-SDI for comparison.

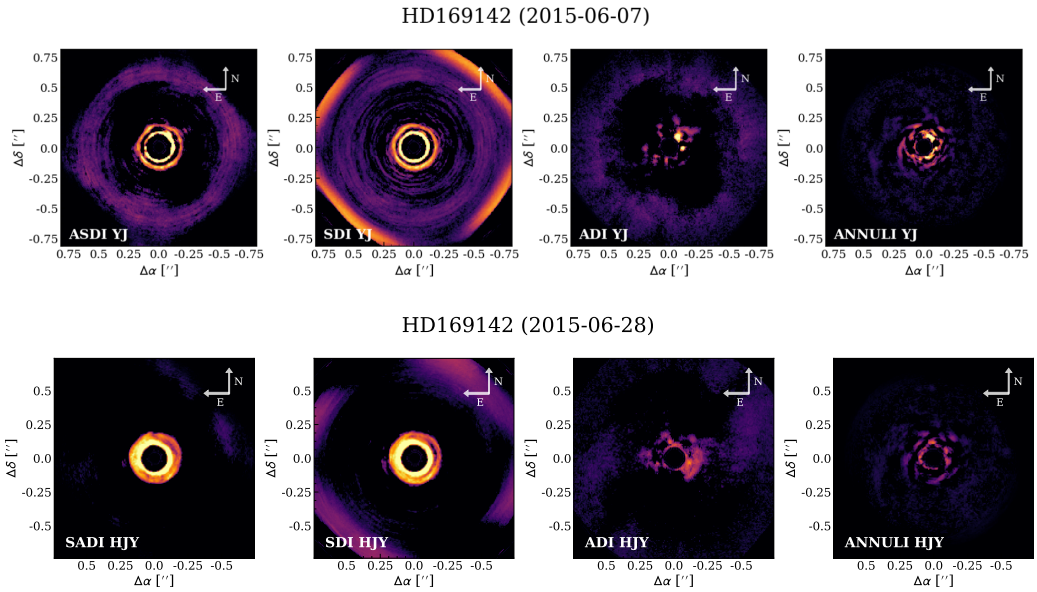

Figure B.2: Post-processed images of HD 169142 using PCA-ASDI (left), PCA-SDI (center left), PCA-ADI (center right) and PCA-ANNULI (right) for the observing day 2015-06-07 (top) and 2015-06-28 (bottom). The one on the top cover YJ wavelength, whereas the one on the bottom has YJH combined. These images are produced not by multiplying by R^2, but taking the colorbar as a square root of the typical map.

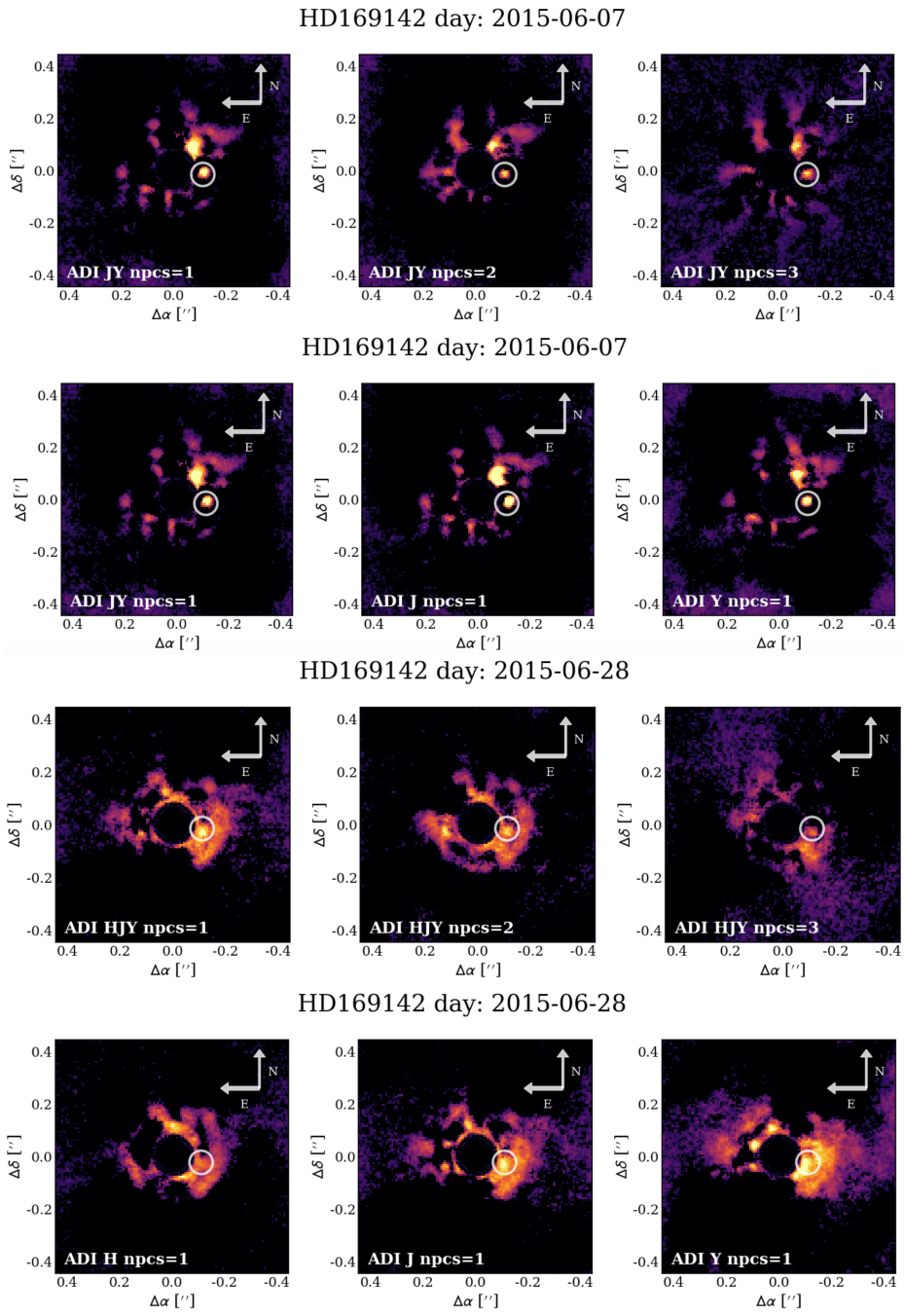

Figure B.3: Observations taken on the 2015-06-07 (top) and on the 2015-06-28 (bottom). The first and the third rows show the image combined with all the frames and with three number of principal components. The second and the fourth rows show the results for each Bands. With a white circle the presence of a point-like source to be confirmed.

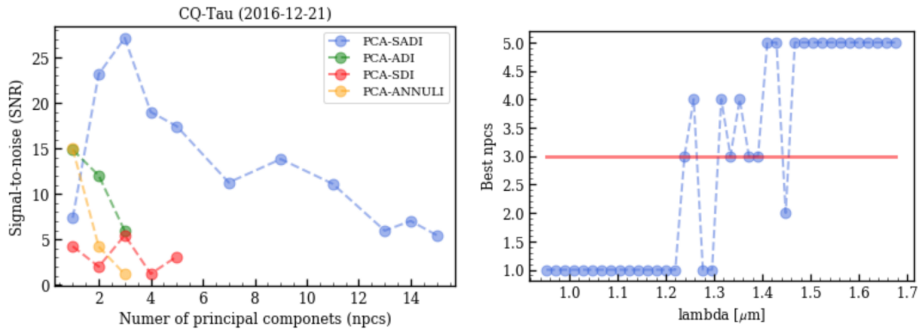

Figure B.4: (Left: signal-to-noise onto the companion candidate versus number of principal component for the different techniques used. Right: best npcs found among the signal-to-noise derived for each frame.

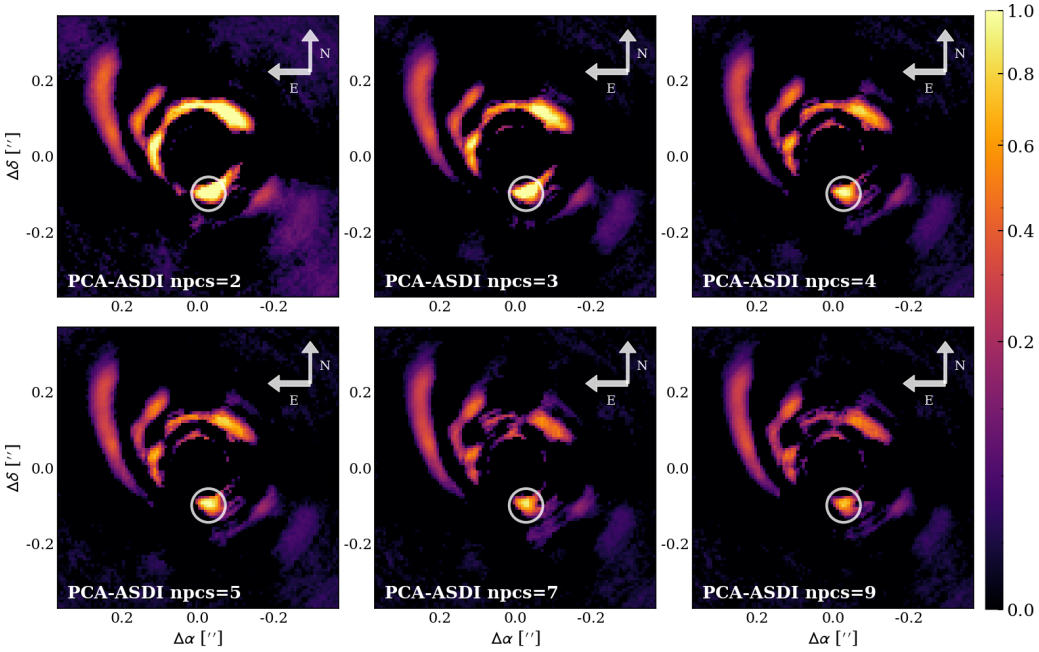

Figure B.5: PCA-ASDI images varying the number of principal components: two (top left), three (top center), four (top right), five (bottom left), seven (bottom center), nine (bottom right). In all the images the companion candidate is visible. The spiral arms called S1, S2, S3 and S5 are visible. S6 is barely visible.

like sources. The one on the top is visible just in this observation, whereas the one on the bottom is present also in the observations taken on the 2015-06-28. In particular the source is visible using number of principal components equal to both one, two and three in both the observing days. The source is present in the combined YJH image of 2015-06-28 and in the combined YJ image of 2015-06-07. During the 2015-06-07 the source is observed in Y, J, and H bands with number of principal components equal to one. During 2015-06-28, the source is visible clearly just in J band. The fact that this source was detected multiple times may suggest that it may be a real companion. A more detailed analysis will anyway have to be performed.

Regarding the CQ Tau point-like source detection (left Fig. B.4) we show the signal-to-noise of the companion candidate for each method used, varying the number of principal components. The signal was computed through aperture photometry in an aperture radius equal to the mean full width half maximum (fwhm) measured for the star. The noise was estimated using an aperture annulus large from 3 fwhm to 4 fwhm. This was done to avoid the bright signal coming from the disc at the same separation of the putative companion. Using this method, the best image to study the point-like source is the one post-processed through PCA-ASDI, where npcs is equal to 3. We note that for npcs equal to one the signal-to-noise of the putative companion is higher when using PCA-ADI and PCA-ANNULI, like suggested by the contrast curves of Fig. B.7. In right Fig. B.4, we estimated the signal-to-noise of an annulus large as 2 fwhm at the same separation of the point-like source for each frame. In such a way, we got the signal-to-noise of the companion for each frame and npcs from one to twenty and we took as best npcs the one where the SNR was maximized at each frame. With a red line we show the median of the values derived: it corresponds to three, as found in the image on the left. In Fig. B.5 we show the PCA-ASDI images obtained varying the number of principal components. In all the images the point-like source is clearly visible and in the same position. From npcs equal to four, the source reveals itself as a point-like source profile, whereas the S5 feature reveals itself as a spiral feature. We note that the signal-to-noise detected is pretty high in several detections and through different techniques. For PCA-ADI and PCA-ANNULI the npcs where the companion reaches the best contrast is one, but it is visible also using values as two or three. For PCA-ASDI, if npcs is equal to one or two, the source is embedded in some disc emission, whereas for npcs from three to nine the signal is strong and with a point-like feature. The flux decreases afterwards.

B.2 Comparison between the contrast curves

We have already described the contrast curves obtained for HD 100453 and HD 100546 in section 9.3, comparing several techniques used to post-process data. In the following, we will show the contrast curves obtained for HD 169142, CQ Tau, T Cha, AK Sco, HD 141559 exploiting the techniques used in Chapter 9: PCA-SDI, PCA-ASDI, PCA-ADI, PCA-ANNULI. For HD 169142, CQ Tau, AK Sco, HD 141569 we consider the number of principal component equal to one. For T Cha, instead, we compared npcs equal to one and two. Moreover, we note that AK Sco is the only target observed in FIELD tracking mode, whereas all the others were observed in PUPIL tracking mode. We note that the contrast curves where a disc is present are not smooth. This is due to the fact that the disc emission has not been modeled and subtracted yet. This will be an extra step worth to be done.

For HD 169142, we compared the contrast curves obtained in two different epochs (Fig. B.6): respectively on the left for 2015-06-07 and on the right for 2015-06-28. We reach

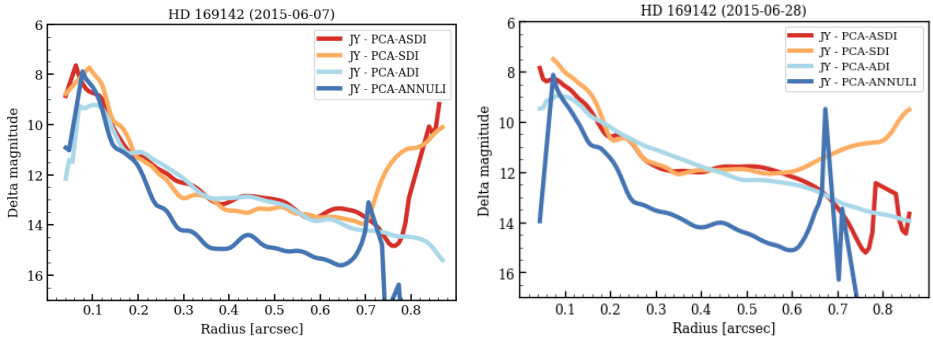

Figure B.6: Contrast curves for HD 169142 for the observing day 2015-06-07 (left) and 2015-06-28 (right), showing the results obtained with PCA-ASDI (red), PCA-SDI (orange), PCA-ADI (light blue) and PCA-ANNULI (dark blue).

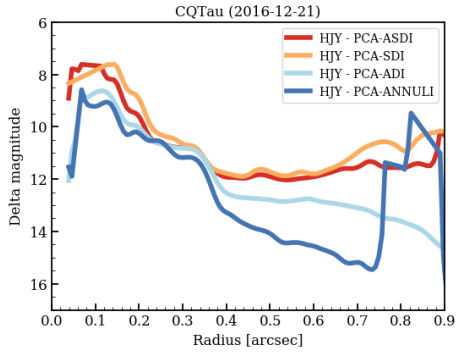

Figure B.7: Contrast curves for PCA-ASDI (red), PCA-SDI (orange), PCA-ADI (light blue) and PCA-ANNULI (dark blue). The contrast curves reaching the best contrast is the one of PCA-ANNULI (up to ∼16 mag). PCA-ADI has similar contrast to PCA-ANNULI up to ∼0″.4.

a better signal-to-noise in 2015-06-07 for PCA-SDI, PCA-ASDI and PCA-ADI, whereas PCA-ANNULI give comparable results for both epochs. This is consistent with the fact that we detected the outer ring just during 2015-06-07. The signal, indeed is also there quite low.

In Figure B.7, we show the contrast curves obtained for CQ Tau with the same methods used in Fig. B.13. PCA-ADI (light blue) and PCA-ANNULI (dark blue) have a better contrast than PCA-ASDI (red) and PCA-SDI (orange) in both the inner and outer disc. This can explain why the point-like source is not visible in the PCA-ASDI and PCA-SDI images, where the disc emission is still present. We note that the contrast curves are not smooth and all of them present a higher contrast up to 0″.4. This is plausibly due to the high asymmetric disc emission of CQ Tau visible in the images.

Moreover, we compared the contrast curves obtained for T Cha (Fig. B.8) varying the npcs from one (left) to two (right). The contrast obtained through PCA-ANNULI is always the best both using npcs equal to one or two. The image obtained through PCA-SDI shows a bad contrast using npcs equal to one, whereas using npcs equal to two, the contrast behaves similarly to PCA-ADI and PCA-ASDI. Moreover, PCA-ANNULI achieves better contrast using npcs=2 for separation < 0.8 arcsec. While PCA-ADI and

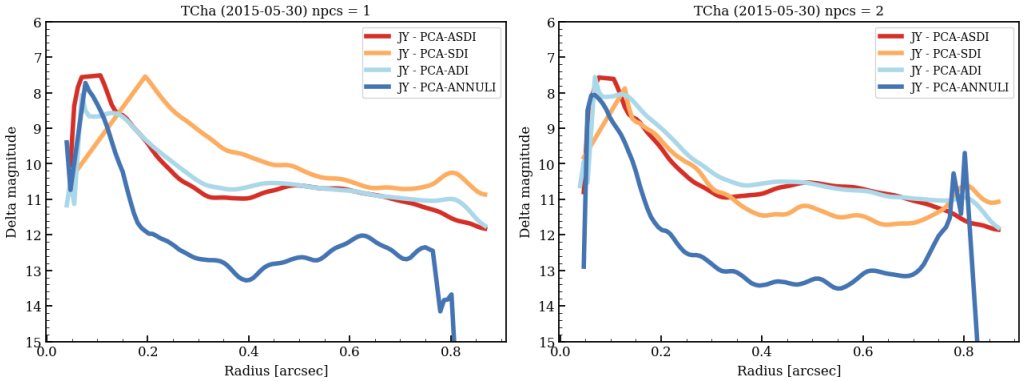

Figure B.8: Contrast curves obtained for T Cha on the 2015-05-30. On the left, we show the results obtained with npcs equal to one and on the right with npcs equal to two. With the different colors, we show the four methods used.

PCA-ASDI behave similarly both using npcs equal to one and to two.

Finally, in Fig. B.9, we present the contrast curves obtained for AK Sco and HD 141569 with the different methods. For AK Sco, PCA-ADI and PCA-ANNULI have a bad contrast because the observations were taken in FIELD tracking mode. The contrast curves of PCA-SDI and PCA-ASDI are really similar, as expected. The presence of a bump in the emission at $0''.2$ is due to the presence of the disc emission. For HD 141569, the contrast curve of the PCA-ANNULI image is clearly the one reaching the best signal-to-noise going up to 16 magnitude. The contrast curves of the other methods reach also a good signal-to-noise $\sim$ 15 mag. This contrast is, however, just enough to detect the brighter part of the ring, but not enough to detect the fainter ring on the North side and the outer ring.

B.3 Comparison with SNR and STIM maps

In this Section, we show the STIM maps and/or the signal-to-noise maps obtained for the images shown in Chpater 9. In particular, we show the STIM and SNR map of HD 100453, HD 100546, CQ Tau; just the STIM map of HD 169142 and just the SNR of HD141569.

In Fig. B.10, we present the signal-to-noise map and the STIM map of the disc around HD 100453 in the case of Y J H combined to give more strength to the spiral detection. The number of principal component used is one. In all of them the spirals are visible and in the PCA-ASDI method also the shadows.

In Fig. B.11, we show the PCA-ASDI images of HD 100546 together with the signal-to-noise and STIM map (for PCA-SDI we refer to Chapter 7). The SNR map highlight the presence of the S3 feature, not visible in the PCA-ASDI post-processed image (left panel). Moreover, also the S5, S6 and S1 spirals are visible. Thanks to the STIM map, it is possible to see that the S1 spiral continue as seen in the PCA-SDI method (Chpater 9) and a faint emission coming from the S2 spiral appears as well.

For HD 169142, the signal-to-noise maps do not show any disc feature, while the STIM maps (Fig. B.12, obs. day 2015-06-07) show clearly the presence of three rings in PCA-ASDI and PCA-SDI (even if the outer ring is less visible). In PCA-ASDI the outer ring have two shadows, which however, are not visible in the PCA-SDI, suggesting

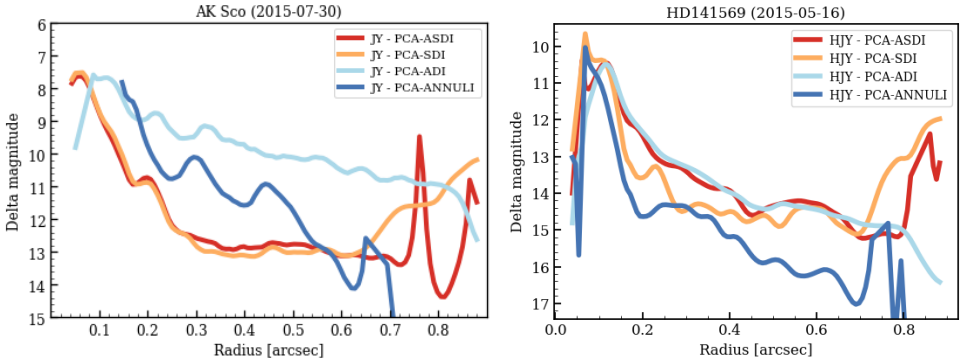

Figure B.9: Contrast curves obtained for AK Sco on the observing day 2015-07-30 (left) and on the HD 141569 observed on the 2015-05-16. We show in dark blue PCA-ANNULI, in light blue PCA-ADI, in orange PCA-SDI and in red the PCA-ASDI method. In particular, for AK Sco the PCA-SDI and PCA-ASDI are really similar considering the action of the angular information was almost not used. For HD 141569, PCA-ANNULI is the method where the signal-to-noise is the best.

they are not real, possible an artefact created by the technique used. With PCA-ADI and PCA-ANNULI no disc feature is visible. The PCA-ANNULI image shows many point-like sources in the same position of the PSF residuals, which seems to be artifacts produced by this technique.

In Fig. B.13, we show the post-processed images of CQ Tau after using PCA-ASDI, PCA-SDI, PCA-ADI, PCA-ANNULI and number of principal components equal to one. We present also the signal-to-noise map (middle panel) and STIM map (bottom panel) of the four methods respectively. In both the maps relative to PCA-ADI the signal coming from the point-like source is clearly visible. The signal in also visible for PCA-ASDI (in the STIM map) and PCA-ANNULI (in the SNR map) although with less contrast. The presence of the bright S1 and S2 are also well visible and with an high signal-to-noise. In the SNR map S5 is observed also if with a lower emission, but with a clear spiral shape. Finally, in the STIM maps (PCA-SDI and PCA-ANNULI) the S3 spirally is visible also if not connected with S1. S6 is visible in the STIM map of the PCA-ANNULI image.

Finally, for HD 141569 we show in Fig. B.14 the signal-to-noise maps for the four different techniques used as done for CQ Tau. This gives strength to the arguments quoted in Chapter 9: the bright ring has a difference in the brightness emission. Multiple rings are seen in the PCA-ANNULI image together with two shadows and a bright stream of material going toward the center.

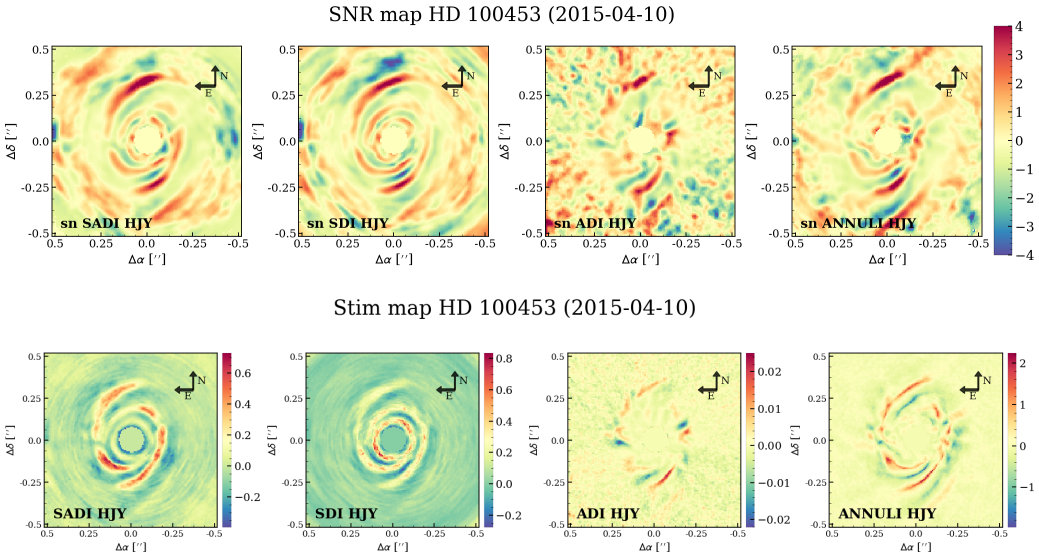

Figure B.10: Post-processed images of HD 100453 on the 4th of May 2015. We show the HJY image after using PCA-ASDI (left), PCA-SDI (center left), PCA-ADI done in full frame (center right) or using the annular version (right). In all of them a two arms disc structure is visible.

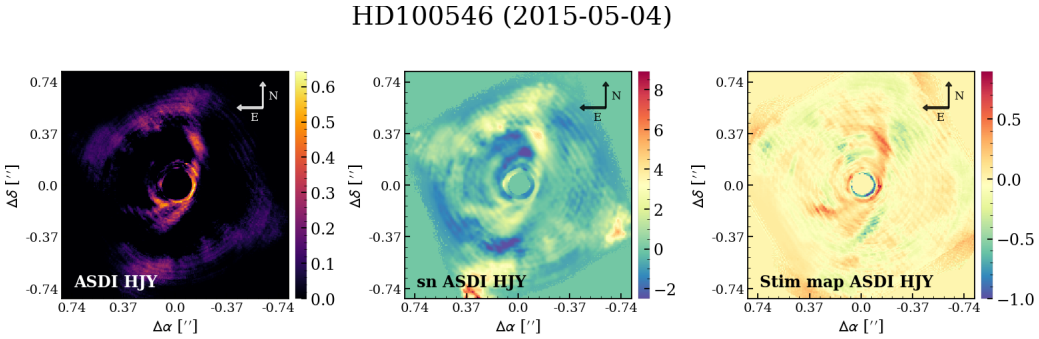

Figure B.11: We show the results on HD 100546 done with PCA-ASDI: post-processed image (left), the signal-to-noise map (center) and the STIM map (right).

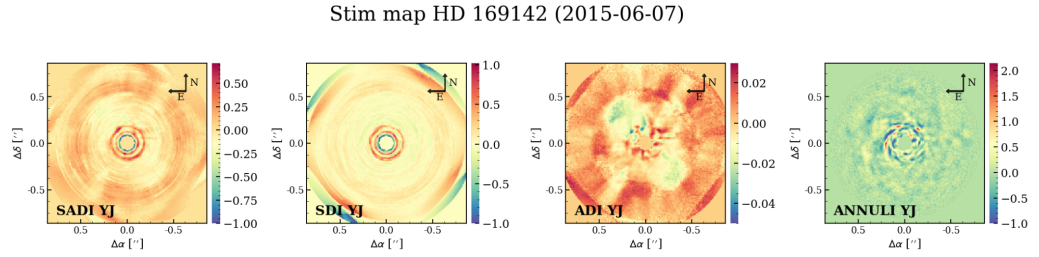

Figure B.12: We show the STIM maps obtained for HD 169142 during the 2015-06-07. The images used the following post-processing methods: PCA-ASDI (left), PCA-SDI (center left), PCA-ADI (center right) and PCA-ANNULI (right).

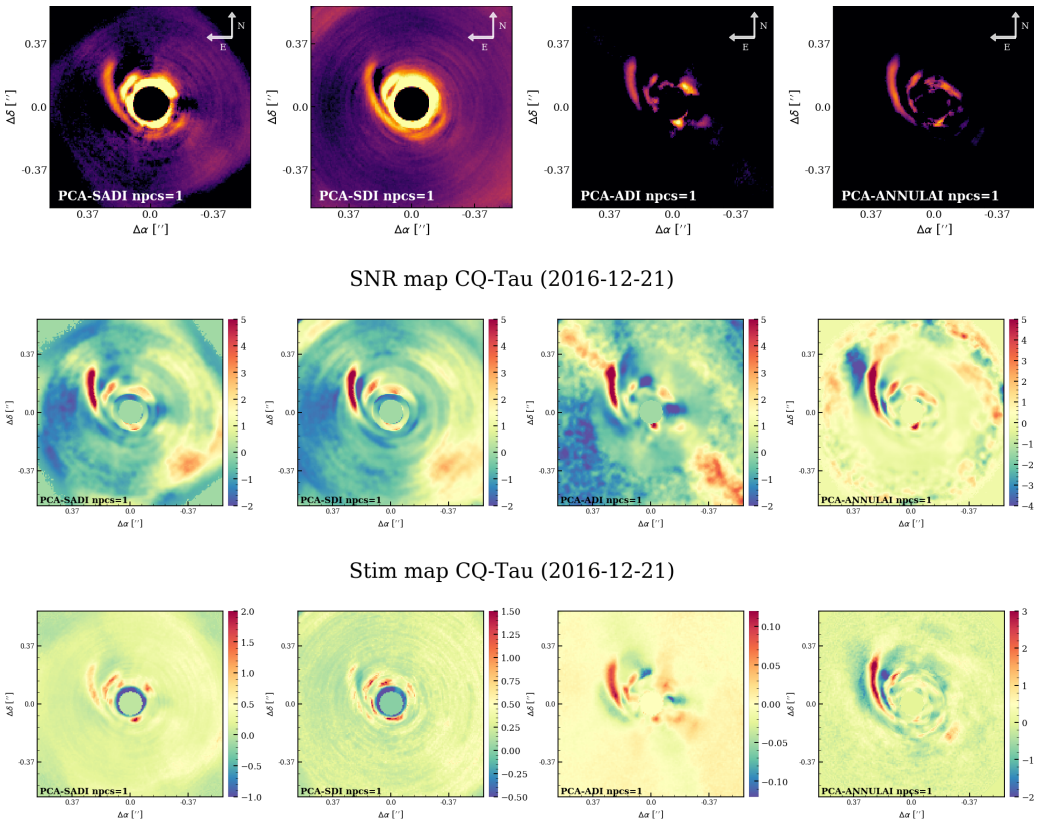

Figure B.13: PCA-ASDI (left), PCA-SDI (center left), PCA-ADI (center right), PCA-ANNULI (right) images. We show on the top row the post-processed images, in the middle panel the signal-to-noise map and on the bottom row the STIM map. A point-like source and multiple spiral arms are clearly visible.

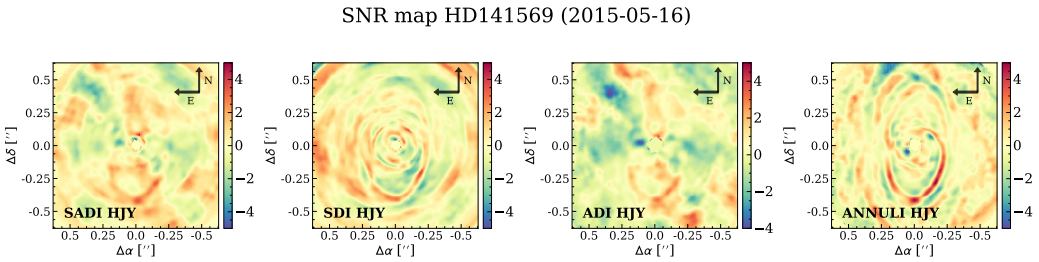

Figure B.14: We present here the signal-to-noise maps obtained for HD 141569 on the 2015-05-16. The images are obtained through PCA-ASDI (left), PCA-SDI (center left), PCA-ADI (center right) and PCA-ANNULI (right). All the images show the presence of an extended disc structure and a large cavity.

Table B.1: Infrared (JHKLM in magnitudes), IRAS (12, 25, 60, 100 micron fluxes in Jy) and (sub-)mm (450, 850, 1100, 1300 micron fluxes in Jy) photometry of sources from literature. Provided thanks to the courtesy of Dr. M. van den Ancker. We note that in this list there is not the CQ Tau for which a list of fluxes is reported in Table 5.3. These values were used to derive the NIR and IR luminosity reported in Fig. 9.19.

Target	Jmag	σ_J	Hmag	σ_H	Kmag	σ_K	Lmag	Mmag	$F_{\nu,12}$	σ_{12}	$F_{\nu,25}$	σ_{25}	$F_{\nu,60}$	σ_{60}	$F_{\nu,100}$	σ_{100}	F_{450}	F_{850}	F_{1100}	F_{1300}
	mag	mag	mag	mag	mag	mag	mag	mag	Jy	Jy	Jy	Jy	Jy	Jy	Jy	Jy	Jy	Jy	Jy	Jy
HD104237	5.813	0.023	5.246	0.059	4.585	0.018	3.67	3.21	2.36e+01	5	2.30e+01	4	1.47e+01	9	9.58e+00	10	0.0	0.0	0.0	0.0
HD132947	8.735	0.021	8.664	0.036	8.623	0.017	5.75	5.75	6.05e-01	7	3.22e-01	11	3.70e+00	0	3.24e+01	0	0.0	0.0	0.0	0.0
HD139614	7.669	0.026	7.333	0.040	6.748	0.026	5.72	5.89	4.11e+00	6	1.81e+01	13	1.93e+01	13	1.39e+01	12	0.0	0.608	0.272	0.242
HD142666	7.351	0.026	6.739	0.027	6.077	0.017	4.97	4.69	8.57e+00	4	1.12e+01	6	7.23e+00	8	5.46e+00	7	1.090	0.298	0.180	0.127
HR5999	5.907	0.018	5.220	0.027	4.386	0.036	3.04	2.47	1.80e+01	4	1.45e+01	6	1.44e+01	12	6.32e+01	0	0.0	0.082	-0.12	-0.04
HD145718	7.690	0.024	7.263	0.029	6.693	0.021	0.00	0.00	5.68e+00	4	5.89e+00	6	5.01e+00	12	3.14e+00	14	0.0	0.0	0.0	0.0
HD150193	6.947	0.020	6.214	0.020	5.476	0.017	4.19	3.76	1.76e+01	3	1.81e+01	5	8.13e+00	9	1.62e+01	0	0.455	0.123	0.0	0.045
AKSco	7.676	0.026	7.059	0.033	6.503	0.020	5.61	5.28	2.60e+00	5	5.06e+00	7	6.11e+00	9	1.38e+01	0	0.242	0.083	0.036	0.0
KKOph	9.072	0.027	7.233	0.040	5.795	0.026	4.02	3.43	9.87e+00	11	9.56e+00	10	6.14e+00	10	1.78e+01	0	-1.90	0.097	0.036	0.052
MWC297	6.127	0.019	4.387	0.214	3.041	0.236	1.24	0.53	1.59e+02	4	2.24e+02	4	9.14e+02	7	1.80e+03	10	2.460	0.681	0.452	0.237
RCrA	6.935	0.018	4.951	0.020	2.858	0.262	1.69	1.04	1.14e+02	5	2.54e+02	6	6.06e+02	5	4.34e+03	0	-0.45	-0.11	0.0	0.0
SCrA	8.194	0.021	7.051	0.024	6.107	0.021	5.13	3.91	0.0000	0	0.0000	0	0.0000	0	0.0000	0	-0.45	-0.11	0.0	0.0
HD179218	6.994	0.020	6.645	0.026	5.995	0.018	4.68	4.18	2.34e+01	5	4.36e+01	4	2.99e+01	9	1.74e+01	8	0.0	0.0	0.0	0.071
HD190073	7.194	0.019	6.647	0.017	5.855	0.027	4.58	4.17	7.16e+00	6	5.53e+00	7	1.92e+00	9	1.00e+00	0	0.0	0.0	0.0	0.0
HD97048	7.267	0.023	6.665	0.049	5.941	0.029	4.61	4.56	1.45e+01	6	4.03e+01	5	6.99e+01	9	2.50e+02	0	0.0	2.580	0.0	0.452
HD100453	6.945	0.026	6.390	0.038	5.600	0.021	4.36	4.01	7.23e+00	4	3.36e+01	5	3.94e+01	11	2.39e+01	13	0.0	0.0	0.0	0.265
HD100546	6.425	0.020	5.962	0.031	5.418	0.023	4.02	3.75	6.58e+01	3	2.43e+02	4	1.65e+02	9	9.86e+01	21	0.0	0.0	0.0	0.465
TCha	8.27	0.0	7.28	0.0	6.61	0.0	5.65	5.39	5.60e-01	6	1.69e+00	6	6.30e+00	6	1.06e+01	0	0.0	0.198	0.0	0.064
HD141569	6.872	0.027	6.861	0.040	6.821	0.026	6.64	6.66	5.49e-01	7	1.87e+00	7	5.53e+00	9	3.47e+00	10	0.066	0.014	-0.036	0.009
HD142527	6.503	0.029	5.715	0.031	4.980	0.020	3.89	3.50	1.04e+01	4	2.12e+01	5	1.05e+02	12	8.47e+01	16	0.0	3.537	0.0	1.190
HD169142	7.323	0.033	6.916	0.048	6.412	0.046	5.73	5.39	2.95e+00	4	1.84e+01	5	2.96e+01	9	2.34e+01	11	0.0	0.471	0.287	0.197

Appendix C

RADMC3D: flared vs flat discs

C.1 A disc model with RADMC3D

We performed radiative transfer calculations of the 21 sources described in Chapter 7. The target CQ Tau was not included in this analysis because it was extensively studied in Chapter 5. We used the RADMC3D code (Dullemond et al. 2012) to perform these computations. The aim of this work was to produce a simple model for each source: a flat or flared disc (if possible) able to fit the Spectral Energy Distribution profile. With the best models, we were then able to produce contrast curves for the Y, J, H combined image to compare with the SPHERE results obtained in Chapter 7 and 9. When the model has a contrast smaller than the one observed, the disc should be visible through our observation (if the model is correct); on the contrary, if the contrast of the model is higher, the disc emission (even if present) could be obscured by the noise present in our images.

C.1.1 Observational SED

We combined data from previous works in order to have the SED for all our targets (black dots in Fig. C.2). We used the photometry, distance (d[pc], Table 8.1) and Spectral Type (Sp.T., Table 8.1) given in literature in order to derive the effective temperature of each target and to create the SED blackbody profile. The SEDs plots in Fig. C.2 were corrected for the extinction using the law from Cardelli et al. (1989) with $R_{\rm v}$=3.1, as for regular ISM values, with the exception of R CrA and S CrA where we used $R_{\rm v}$=4.5 as suggested by Neuhäuser & Forbrich (2008). Both R CrA and S CrA are located in the Corona Australis star forming region and we assume that their extinction is mostly due to the wide spread forming cloud. The value of $A_{\rm v}$ was derived using an average of the color excess in a range of wavelengths between 0.1 and 0.9 μm. This value was used as described in Cardelli et al. (1989) in order to correct the photometry. Having the SEDs and the value of the distance for each source we derived the values of stellar luminosity and of the stellar radius. We were then able to place them into the HR diagram and derive from that the stellar mass and the age using the tracks of Chabrier et al. 2000 and Baraffe et al. 1998.

C.1.2 Model parametrization

In order to model our discs, we used the code RADMC3D. We created a grid of models following the analytical prescription of a generic protoplanetary disc, described by its

pressure scale height and surface density profiles. The scale height profile $H(r)$ is given by:

$$H(r) = H_0 \left(\frac{r}{r_{\rm pivot}} \right)^{\psi}, \tag{C.1}$$

where H_0 is the value of $H(r)$ at the location $r_{\rm pivot}$ and ψ is the flaring index. We varied both H_0 and ψ to find the best agreement. The surface density profile $\Sigma(r)$ is given by:

$$\Sigma(r) = \Sigma_0 \left(\frac{r}{r_{\rm sig}} \right)^{p}, \tag{C.2}$$

where Σ_0 is the surface density normalization at $r_{\rm sig}$ and p is the power exponent of the surface density distribution as a function of radius, kept fixed as $p = -2$ (e.g. Acke et al. 2005) for radii smaller than the disc radius. For $r > r_{\rm disc}$, we set a cut-off in the surface density profile fixing $p = -12$. Moreover, both the radius at which the surface density ($r_{\rm sig}$) and the scale height normalization ($r_{\rm pivot}$) are fixed to 100 au. Σ_0 is derived from the value of disc mass, a parameter that we varied. Given $H(r)$ and $\Sigma(r)$, we can thus write the density as:

$$\rho(r,z) = \frac{\Sigma(r)}{H(r)\sqrt{2\pi}} \ \exp\left(-\frac{1}{2} \left(\frac{z}{H(r)} \right)^2 \right) \tag{C.3}$$

We used the stellar parameters (M_*, R_*, $A_{\rm v}$, $T_{\rm eff}$, d) as described in Table C.1. $R_{\rm in}$ is assumed to be equal to the sublimation radius: $R_{\rm sub} = 0.07(L_*/L_\odot)^{1/2}$ au (assuming a dust sublimation temperature of 1500 K; Dullemond & Dominik 2005). The outer radius was taken as 250 au for all of the targets. The dust-to-gas mass ratio is fixed at the typical value of 0.01 and the background density is fixed at 10^{-30} g/cm^3. The number of photons for the thermal and scattering Monte Carlo calculation is taken respectively as $2 \cdot 10^6$ and $\cdot\, 10^6$. We assumed the dust temperature to be identical to the gas temperature. We note that in order to maximize the resolution power in the inner part of the disc, where more resolution is needed, we divided the disc into two blocks. The first one with 191 points of resolution extends up to R1, while the second one with 100 points ends at R2. In particular, R2 was fixed at the dimension of our observed SPHERE images. Typically R1 is fixed to 100 au, even if when R2 is smaller than 120 au, R1 is taken as 50 au. The values R1 and R2 used for each source are written in Table C.1. We used spherical coordinates to generate the grid and then we converted the spherical coordinates into cylindrical in order to define the disc properties. Finally, the isotropic scattering was switched on.

In order to perform such calculations the opacity have to be defined. We create an opacity file using the DIANA tool[1] (Woitke et al. 2016). We consider grains with no carbonaceous material, but just silicates. We adopted as minimum and maximum grain size respectively $a_{\rm min} = 0.1$ μm and $a_{\rm max} = 1$ mm. Moreover, to compute the opacity we chose a set of 400 wavelengths ranging from 0.1 μm to 10 mm. Everything else was kept as default. Each model assumes $n(a) \propto a^{-3.5}$. In Fig. C.1, we show the opacity and albedo used to derive our RADMC3D models.

We used these parameters to create spatial and spectral grids. Finally, using the quantities previously described, we calculated the disc density, the volume of each grid cell and the mass in dust and gas of the disc thanks to the dust-to-gas ratio.

[1] http://dianaproject.wp.st-andrews.ac.uk/data-results-downloads/fortran-package/

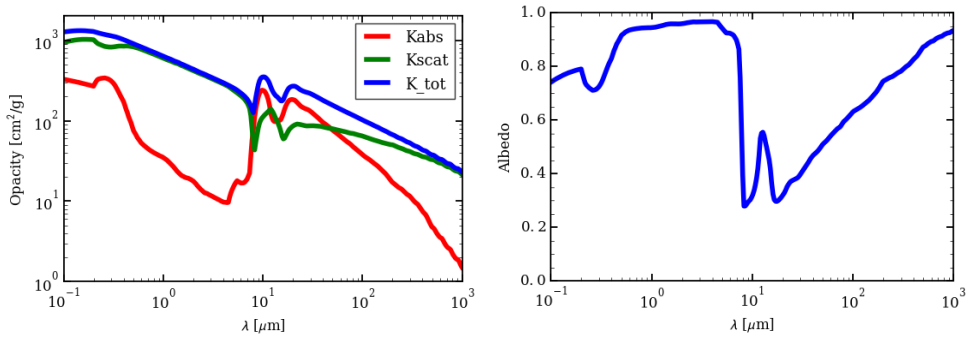

Figure C.1: Left: Opacity used for our RADMC3D models as described in Section C.1.2. The red line is the contribution of the absorption scattering, while the green line is the one from the scattering. The blue line is the combination of both. The contribution from scattering is maximum at the wavelengths we are interested to. Right: Albedo used in our RADMC3D models. It was produced using the opacity as described in Section C.1.2 (left panel).

C.1.3 A model to fit the Spectral Energy Distribution

We ran thermal Monte Carlo radiative transfer calculations and generated a model to represent the SED observed for each source. Fig. C.2 shows the observations in black dots (taken from previous works, see C.1.1) and the stellar blackbody as derived from our fit with a black line. We fitted our discs SED with models with less free parameters possible to be able to compare the results of all the sources. We kept as free parameters the flaring angle (ψ), the scale height (h/r) and the disc mass ($M_{\rm disc}$). The inclination was fixed (Tab. C.1) with the exception of HD 132947 and HD 145718 where no previous disc inclination estimate was done. Finally, for T Cha and HD 141569 we also test a further model with the presence of a cavity/gap in the disc.

Simple model

We found the best agreement with the data, by changing the free parameters by eye. We varied the disc mass ranging from 0.0002 to 0.12 $M_\odot$; for ψ we tested the following parameters: 0, 0.5/7, 1/7, 1.5/7, 2/7, 3/7 and, finally, for h/R at R_{pivot} we varied the values from 0.02 to 0.15. For HD 132947 and HD 145718, once we had the best SED fitting, we varied the disc inclination within the following values: 0°, 10°, 30°, 45°, 60°, 90°. For the purpose of this thesis, the main focus of our SED modeling is on the near/far-infrared. The millimeter regime ($\lambda > 50$ μm) thus was fitted just if possible without adding extra free parameters.

For some sources, we modeled the disc as very massive (e.g. HD 97048 and HD 142527), or less massive in the case of HD 141569. The disc mass is consistent with the values reported in Dominik et al. (2003) for the following discs: HD 150193, HD 104237. HD 132947 does not have data at mm wavelengths and derivation of the inclination. Our fit cannot be based on previous results for the inclination, with the result that the disc mass is greatly uncertain. For HD 142527, there are observations at the mm-wavelength, but it was not possible to fit the data at millimeter and near-infrared range simultaneously. Increasing, indeed, the value of disc mass, no variation in the the SED model at millimeter is visible. On one hand, an explanation is that this disc has a different distribution of grains

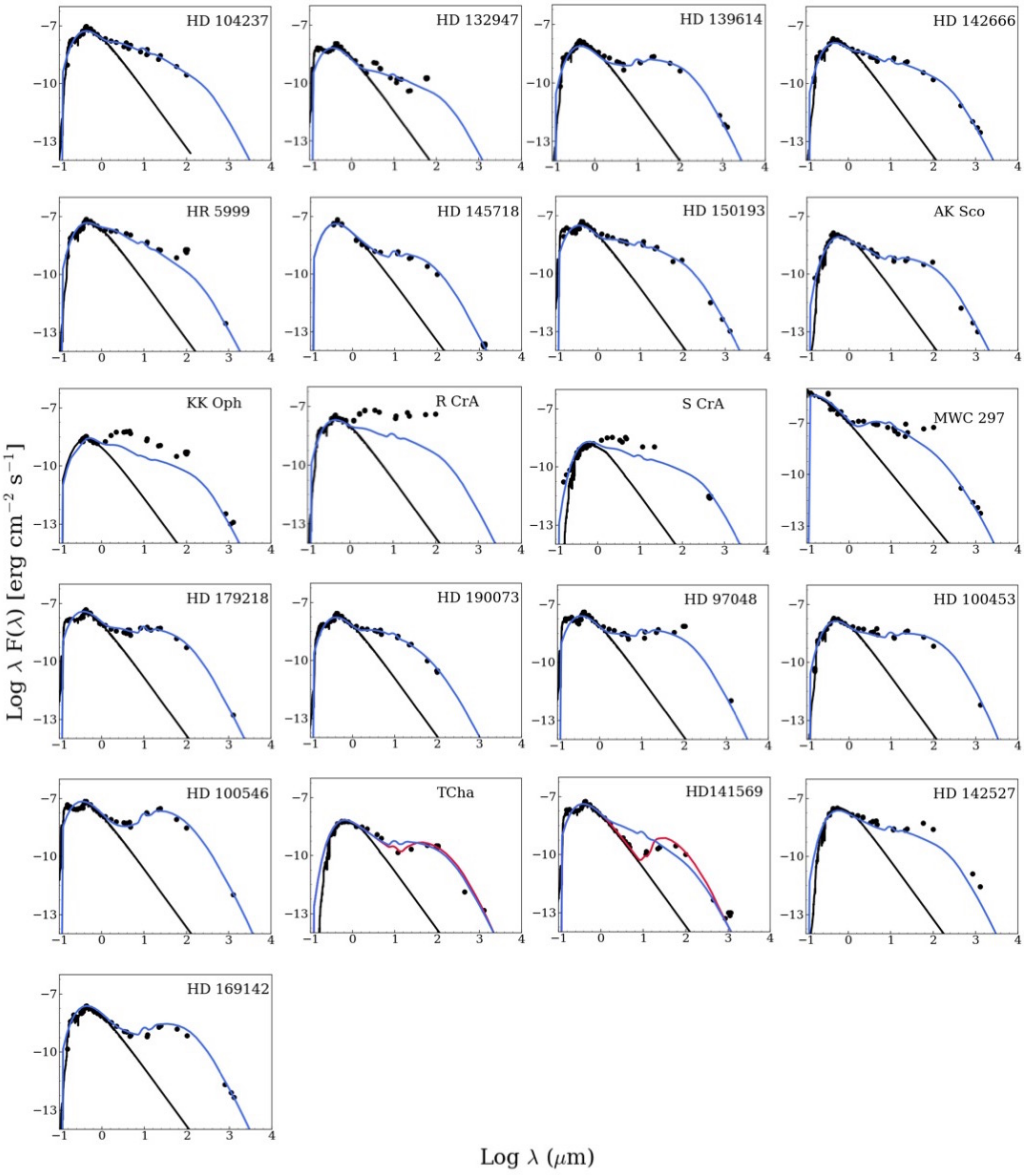

Figure C.2: Observed Spectral Energy Distribution of all the stars in our sample. The black lines show the stellar stellar photosphere model used to fit the data, the black points are the observations and the blue lines are the SED modelling by RADMC3D models. The red curves in T Cha and HD 141569, are models where we included the presence of a gap or cavity respectively.

Table C.1: RADMC3D parameters used to model the SED. The parameters are the name of the target, the inclination, the inner disc radius, the luminosity, the flaring angle, the disc mass, the scale height, the two radius chosen for the resolution, the stellar magnitude and full width half maximum. The FWHM is reported here as the average between the one measured for sources, epochs and x/y coordinates. This was used to generate the models. For KK Oph we used the value measured for H band also for J and Y. In the case of HD 141569 and T Cha we report here the simple model. The values of the parameters chosen for the cavity model are described in Section C.1.3 and Table C.2.

ID	Star Name	i [deg]	Ref.	$R_{\rm in}$ au	L_* $L_\odot$	ψ	$M_{\rm disc}$ $M_\odot$	$h/r[hrpivot]$	$R1$ au	$R2$ au	mag H mag	mag J mag	mag Y mag	FWHM H arcsec	FWHM J arcsec	FWHM Y arcsec
1	HD 104237	31	Hales et al. (2014)	0.32	21.3	0.5/7	0.06	0.08	50	116	5.310	5.751	6.056	0.045	0.039	0.036
2	HD 132947	30	Zorec et al. (2016)	0.45	40.7	0.5/7	0.005	0.03	100	411	8.003	8.445	8.7496	0.045	0.038	0.035
3	HD 139614	20	Matter et al. (2014)	0.17	5.9	2/7	0.04	0.15	100	145	7.594	7.467	7.404	0.048	0.049	0.056
4	HD 142666	60	Rubinstein et al. (2018)	0.21	8.7	1/7	0.05	0.12	100	160	6.537	6.979	7.284	0.045	0.040	0.038
5	HR 5999	58	Preibisch et al. (2006)	0.51	52.5	0.5/7	0.005	0.11	100	159	5.978	6.080	6.186	0.046	0.041	0.039
6	HD 145718	62	Lazareff et al. (2017)	0.2	8.5	2/7	0.001	0.05	100	163	6.508	6.638	6.673	0.048	0.046	0.048
7	HD 150193	38	Fukagawa et al. (2003)	0.34	23.4	1/7	0.01	0.1	100	163	6.312	6.754	7.058	0.045	0.038	0.035
8	AK Sco	70	Czekala et al. (2015)	0.14	4.2	2/8	0.01	0.15	100	152	7.029	7.278	7.487	0.045	0.040	0.037
9	KK Oph	70	Kreplin et al. (2013)	0.16	5.12	2/7	0.02	0.13	100	237	9.422	9.566	9.620	0.085	0.085	0.085
10	MWC 297	5	Alonso-Albi et al. (2009)	13.8	38904.5	1/7	0.07	0.025	100	404	4.601	4.590	4.567	0.048	0.048	0.059
11	R CrA	45	Correia et al. (2005)	0.22	9.77	1/7	0.02	0.15	100	165	6.886	6.9719	7.064	0.047	0.047	0.046
12	S CrA	60	Gahm et al. (2018)	0.11	2.4	1/7	0.04	0.15	100	140	8.831	9.183	9.444	0.051	0.050	0.054
13	HD 179218	57	Fedele et al. (2008)	0.74	112.2	2/7	0.03	0.12	100	286	6.444	6.885	7.190	0.047	0.041	0.039
14	HD 190073	12	Eisner et al. (2004)	1.66	562.3	0.5/7	0.003	0.1	100	958	6.742	7.183	7.488	0.044	0.039	0.036
15	HD 97048	41	van der Plas et al. (2017b)	0.41	34.7	2/7	0.12	0.12	100	199	7.211	7.246	7.274	0.044	0.039	0.037
16	HD 100453	34	Wagner et al. (2015)	0.17	6.17	1/5	0.06	0.17	50	112	6.554	6.995	7.300	0.047	0.043	0.042
17	HD 100546	44	Mendigutía et al. (2017b)	0.34	23.4	3/7	0.06	0.15	50	118	6.648	6.681	6.703	0.048	0.041	0.038
18	T Cha	69	Pohl et al. (2017b)	0.10	2.2	2/7	0.01	0.1	50	118	–	7.204	7.587	7.865	0.037	0.036
19	HD 141569	53	Mawet et al. (2017b)	0.28	16.59	0.5/7	0.0002	0.03	50	119	6.783	6.823	6.860	–	0.038	0.034
20	HD 142527	27	Boehler et al. (2017)	0.21	9.12	1/7	0.1	0.1	100	169	5.730	6.002	6.223	0.044	0.041	0.036
21	HD 169142	13	Panić et al. (2008)	0.31	20.41	3/7	0.03	0.08	100	123	7.193	7.280	7.372	0.048	0.043	0.043

(with possibly more larger grains) with respect to the one fixed for all our models. On the other hand, observations in polarized scattered light of this target show the presence of a large cavity (r∼0.″8, Avenhaus et al. 2014b) not considered in this model. For the HD 132947 and HD 142527 targets thus, we decided not to take into account $\lambda > 50$ μm for the SED fitting. The model of the disc around KK Oph well describe the observation both in the millimeter and optical regimes, but underestimates the near and far-infrared regime. As known, this target is a binary, but in our models we considered just the brightest star and not the T Tauri companion. This may explain the higher emission coming from the infrared wavelengths. Furthermore, we found two populations of discs: flared and flat. A high flaring angle ψ ($> 2/7$) is found for HD 169142, T Cha, HD 100546, HD 179218, R CrA and HD 139614; whereas HD 104237, HD 132947, HR 5999, HD 190073 and HD 141569 appear to have extremely flat discs with $\psi \leq 0.5/7$. HD 139614, AK Sco, KK Oph, HD 142527, T Cha, HD 142666, HR 5999 and HD 97048 have a thick discs (h/R > 0.1), whereas HD 132947 and HD 145718, have a thinner discs (h/R ≤ 0.02). The blue line in Fig. C.2 shows the best SED fiiting as computed by RADMC3D using the model just described. Using this simple model, we were able to fit most of the discs SED with a good agreement. The model described is not the only possible model to fit the SED of the targets presented. Several parameters are indeed degenerate. However, the model presented in this Appendix was chosen as a representative model able to describe the SED and to give us some prediction on the contrast needed to image all the discs.

Degeneracies

Different choices of the parameters used can still give a good fit of the SED. We performed a test on how our results were affected by errors in the inclination and we found that the near-IR and far-IR regime are just slightly affected. The SED fitting is not able to distinguish between different inclinations and thus we decided to keep this parameter fixed as found in previous works (see Table C.1), which are more reliable considering that they derive the inclination not just through the SED fitting. An other degenerancy of these models is the possibility that the discs have gaps, cavities or more complicated structures. However, for the sources were including a cavity or gap was not needed, we do not add this information.

Different model approach

For HD 141569 and T Cha, it was not possible to find a good agreement between model and the observations using the simple model approach. We fitted these discs also with a quite large cavity or a gap respectively. The SED fitting improved with this hypothesis and it is possible to see the best model in Fig. C.1.1 with a red line. Before reaching the best model shown, however, we tried to use different models.

We chose an inner radius much larger than the sublimation radius. All the other parameters were tentatively kept the same. For HD 141569 it is well known that the disc is at an intermediate stage between a transitional disc and a debris disc. This suggests that also the grains should have been grown up to larger sizes. In the model in red, we varied the inner radius finding as best parameter $R_{\rm in}$ 20 au and a completely empty cavity. The other parameters are: h/r= 0.005, ψ=1/7 and $M_{\rm disc}$=0.0002 $M_\odot$). For T Cha, instead, we create a model with a gap. The target has, indeed, still some infrared excess and it was not possible to fit it with a completely cleared-out cavity. The model shown with a red line was fitted through a model with $R_{\rm in}$ = 0.1 au, a gap from $R_{\rm in,\,gap}$=0.3 au to $R_{\rm out,\,gap}$=10 au and a gap depletion of 0.01 (h/r= 0.15, ψ=1.5/7 and $M_{\rm disc}$=0.005 $M_\odot$).

Table C.2: RADMC3D parameters used to model the SED with a gap or cavity. The parameters are the name of the target, the inner radius of the disc ($R_{\rm in}$), the inner ($R_{\rm gap1}$) and outer ($R_{\rm gap2}$) radius of the gap, the depletion inside the gap ($\delta_{\rm in}$), the flaring angle, the disc mass and the scale height. We keep the other parameters as described in Table C.1. We note that T Cha has a gap, while HD 141569 has a cavity.

ID	Star Name	$R_{\rm in}$ au	$R_{\rm gap1}$ au	$R_{\rm gap2}$ au	$\delta_{\rm in}$	ψ	$M_{\rm disc}$ $M_\odot$	$h/r[hrpivot]$
18	T Cha	0.10	0.30	10	0.01	1.5/7	0.005	0.15
19	HD 141569	0.28	0.28	20	–	1/7	0.0002	0.005

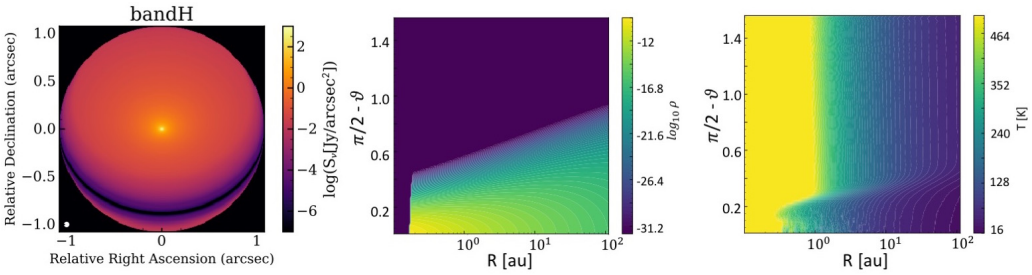

Figure C.3: RADMC3D model of HD 100543 (parameters in Table C.1). Left: the model convoluted with a gaussian beam (white circle on the bottom left, $\sim$0.047″). We show the band H image of the best representative model, J and Y bands images looks very similar. Center: density profile. Right: temperature profile.

The presence of an inner not depleted disc from 0.1 to 0.3 au was kept in order to have a good fit of the near infrared excess. With these small changes in the model, the SED models are in agreement with the data (Fig. C.2).

For the sources: R CrA, S CrA and KK Oph, instead, the simple models previously described always underestimate the observations both in the near and far infrared. We tried to change parameters like the inclination or the inner radius to have a better agreement. The inclination is almost not affecting the SED fitting and adding a larger cavity generates in the near-IR a lower instead of a higher emission. A possible explanation is the presence of a close binary in the case of KK Oph and a wide binary for S CrA. For R CrA the presence of additional circumstellar material, such as an envelope, can increase the flux at longer wavelengths. Moreover, the higher flux in near-IR can be due to scattered light in the circumstellar material. An extra hypothesis may be the presence of the additional brown dwarf companion detected by (Mesa et al. 2019). However, including additional companions or an envelope in our modeling would be beyond the scope of this Appendix. Finally, for R CrA and S CrA we consider a model where the sublimation radius is considered at a $T_{\rm in}$=2500 K instead of $T_{\rm in}$=1500 K, used in all the other modeling. These stars, indeed, have a higher extinction and the dust sublimation radius is dependent by the grain size. If the grains are larger, the inner radius should be, indeed, smaller. All the described attempt do not provide great improvements, so we kept the simple model SED fitting as best model.

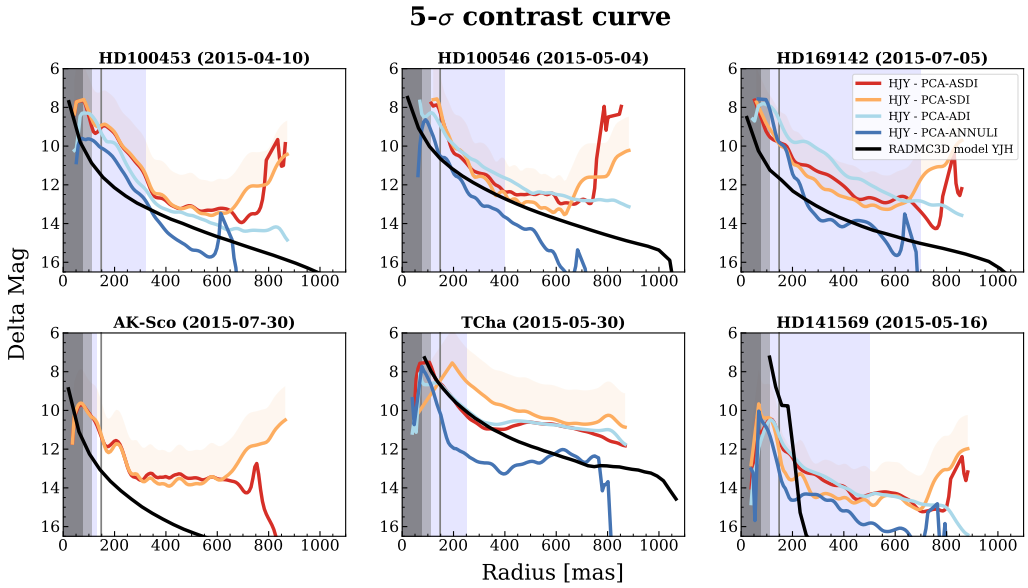

Figure C.4: Contrast curves of the disc emission of the RADMC3D models where we resolve the disc. They are shown together with PCA-SDI (orange), PCA-ASDI (red) observations and, if PUPIL tracking mode was used, PCA-ANNULI (blue), PCA-ADI (light blue). We show the disc size for our resolved discs (light blue box), the coronagraph size (dark gray box) and the separation until when the coronagraph may have still an effect (the light gray box together with the gray vertical line). The orange box is the 5-σ contrast curve of PCA-SDI.

C.1.4 Generation of the contrast curves derived from the model

Once the SED fitting was considered adequate, we used RADMC3D to create one image for each of the three Bands (H, J, Y). For clarity, the synthetic images were computed with disc emission alone, i.e. without the stellar contribution. In particular, we generated an image at 1.55 μm for the H band, one at 1.245 μm for the J Band and one at 1.05 μm for the Y Band. Those values are the averaged values each band in the observations 1.45 - 1.66 μm (band H), 1.19 - 1.3 μm (band J) and 0.99 - 1.11 μm (band Y). As for our SPHERE observations, we applied a mask of diameter of 0.15 arcsec (coronagraph size). We used the FWHM measured from the flux images (listed in Table C.1) as an average between all the sources and epochs, to convolve the images of the model with a gaussian beam of $\sigma = \mathrm{FWHM[arcs]}/(2\sqrt{2\ \log 2})$. For all the three different images created (at 1.55, 1.245 and 1.05 μm), we used a value of FWHM averaged between the three bands. The values are indeed not greatly varying. Moreover, we corrected the flux for the distance of each source and convert the flux units in Jy/arcsec^2. An example of the image produced for HD 100453 in H band is shown in teh left panel of Fig. C.3, while in the central and right panels the density and temperature profiles are respectively shown.

The last step was to create the contrast curves for the models. To do so, we needed to divide the flux coming from the disc by the stellar flux at each band separately. We used the model of the stellar blackbody derived previously (see Section C.1.3) and converted the values to Jy/arcsec^2. Having the same units for both disc and stellar flux, we could derive its contrast in Δmag for each points of the grid. On each image we computed the radial profile. We computed the mean, median and standard deviation over the entire

disc in annulii of size equal to a FWHM. Finally, in order to compare the models with the observational results of Chapter 7 and 9, we averaged the contrast curves obtained for band Y, J, and H, obtaining a single contrast curve. Our contrast curves are shown in Fig. C.4 and C.5 with the models (black line) along with the 5σ-contrast curves of observations (orange: PCA-SDI; red: PCA-ASDI; blue: PCA-ANNULI; light blue: PCA-ADI). We note that the contrast curves of the models are the emission of disc over the stellar flux, while the contrast curves of the observations are the contrast of the noise (σ). Comparing them would help to understand that if the flux of the model is higher than the σ, some disc emission should be visible in scattered light observations in the case the model used is the one representing the real disc structure. In Fig. C.4 and C.5, we show with a light blue box the disc size for our resolved discs. The dark gray box shows instead the coronagraph size and the light gray box together with the gray vertical line show the separation until when the coronagraph may have still an effect. The orange box is the 5-σ contrast curve of PCA-SDI.

The contrast obtained for the modes is higher or comparable to the one of observations (at least for one of the techniques used) in the case of HD 100453, HD 100546, HD 169142, T Cha, HD 141569. We note that the models shown for both T Cha and HD 141569 are the ones where a gap or cavity was included (red line in Fig. C.2). The case of AK Sco is peculiar. The observed contrast curve obtained reaches $\sim$14 mag, similar to the contrast obtained in the five other discs reported above, but the contrast curve of the model is below. This would be in agreement with no detecting the disc. However, we are able to resolve an almost edge on disc and thus possibly the model we used to fit the SED should be flatter than what we considered. Moreover, we note that in HD 139614, HD 179218 and HD 97048, the model is close to the observational contrast, even if it is below. This means that, with the same exposure time and observation strategy used for the resolved discs, we would possibly be able to detect a disc structure also in these three discs. Finally, for HD 104237, HD 132947, MWC 297, HD 150193, HD 142666, S Cra, HD 190073, HD 142527, HD 145718, HR 5999, R Cra and KK Oph, the contrast curve of the model is always way below the observed curves. This means that if we assume that the disc model is correct, the disc may be present, but not visible. We note that the model of HD 142527 shows a high value of scale height. Typically, the other discs with a high flaring angle or scale height have a contrast higher than what we found. However, this target is peculiar: in polarized light it shows a large cavity, not modeled here and that is almost large as our field of view. Although we would model it carefully thus, we do not expect to see a disc emission inside our image. We note that we show the contrast for Y, J, H band combined (where possible), but the observed contrast is the best for band J. Bands H and Y are indeed respectively over or under-subtracted and the noise is higher. Moreover, in none of the sources where no disc is resolved the contrast curve of the model is found to be above the observational contrast. We cannot thus conclude that some of the target observed have no disc, but all of them are compatible with the model we presented considering they are below the contrast threshold.

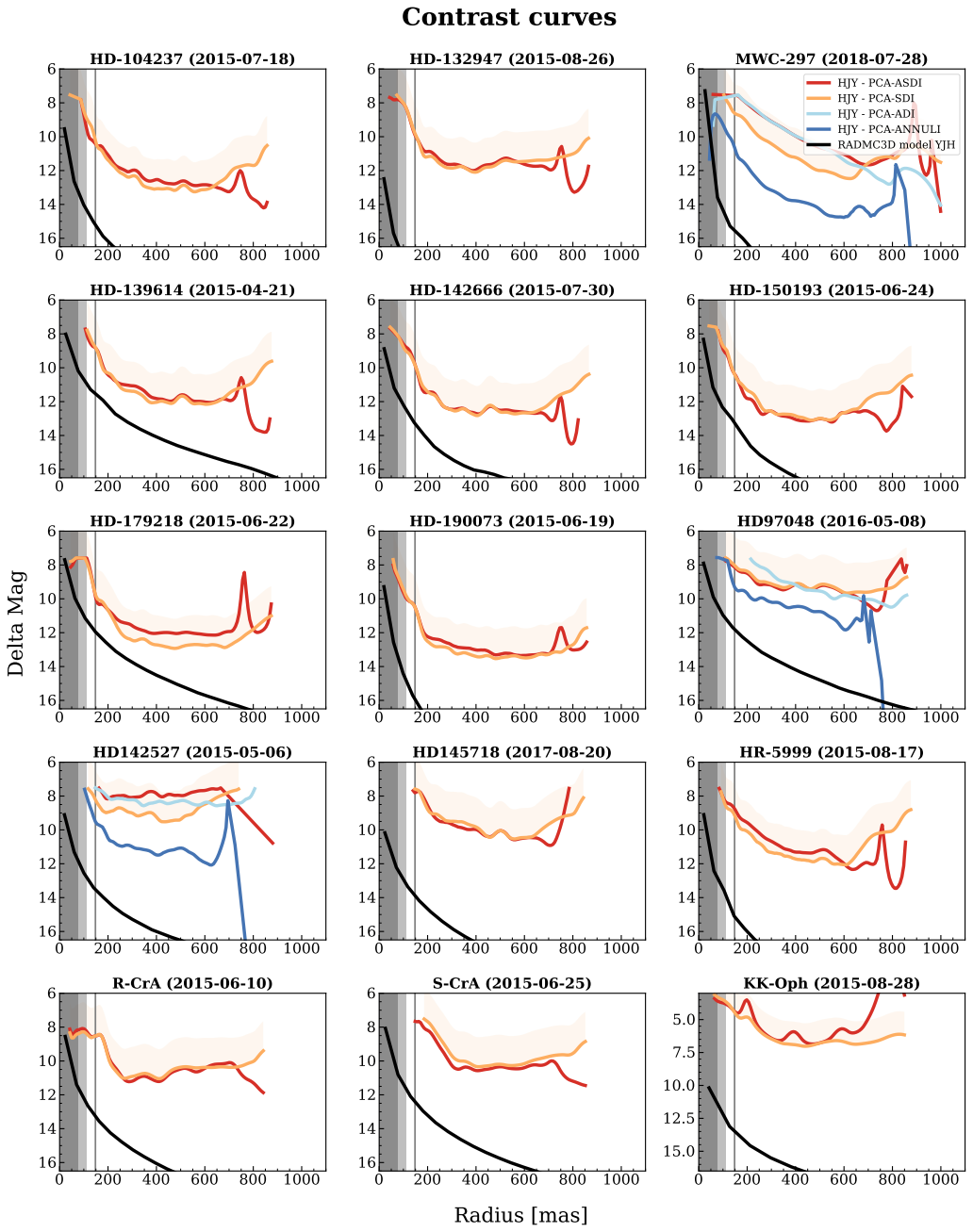

Figure C.5: Contrast curves of the disc emission of the RADMC3D models of the discs with no detection. They are shown together with PCA-SDI (orange), PCA-ASDI (red) observations and, if PUPIL tracking mode was used, PCA-ANNULI (blue), PCA-ADI (light blue). We show the coronagraph size (dark gray box) and the separation until when the coronagraph may have still an effect (the light gray box together with the gray vertical line). The orange box is the 5-σ contrast curve of PCA-SDI.

Appendix D

Discussion on the literature results of individual targets

We describe in the Appendix the previous works related to the sample described for what concerns the detection of disc structure.

D.1 Group I targets

All the targets here presented were classified as Class II, Group I sources from the analysis of their spectral energy distribution (SED). For MWC 297 we refer to the description in the Chapter 8; for HD 100546, HD 100543, HD 169142 and T Cha, we refer to the Chapter 9. For CQ Tau we refer to Chapter 5. For what concern the target properties, we refer to table 7.1 and 8.1.

HD 179218. HD 179218 is an Herbig star of Spectral type of A0IVe. It is located at a distance of $\sim$ 266 pc (Gaia Collaboration et al. 2018), it has a mass of $\sim$ 2.98 $M_{\odot}$ and it was classified as group Ia source according to the Meeus et al. (2001), which suggests a flared disc structure. Fedele et al. (2008) presented observations taken with VLTI/MIDI. This dusty disc is flared and shows a double ring-like in 10 μm emission. The first ring has a peak at 1 au and the second at $\sim$ 20 au. The oxygen emission is compact and flared and has a peak between 3 - 6 au, suggesting or a lack of gas in the outer disc or chemical effects which lower the oxygen emission. Mendigutía et al. (2017b) measured an excess in the H_{α} emission and discovered a spatially unresolved emission, which means that the size of the emitting region is smaller than 0.21 au. The inclination is found between 30° and 50° and the accretion rate is $\sim 10^{-8}$ $M_{\odot}$ yr^{-1}. Taha et al. (2018) modelled the SED with the presence of a gap from $\sim$ 3 to $\sim$ 10 au and where most of the dust mass is located in the first 30 au of the outer disc. The authors were able to resolve for the first time the circumstellar emission in the PAH bands at 8.6 and 11.3 μm of size $\sim$ 100 mas, finding agreement with an extension of PAH disc larger than the dust disc. Wheelwright et al. (2010) claims a detection of a companion around HD 179218 at a separation of $\sim$ 2.5 arcsec and with a variation of magnitude in band K of 6.6.

HD 139614. HD 139614 is an Herbig star of Spectral type of A7Ve. It is located at a distance of $\sim$ 135 pc (Gaia Collaboration et al. 2018), it has a mass of $\sim$ 1.48 $M_{\odot}$ (Vioque et al. 2018a) and it was classified as group I object according to the Meeus et al. (2001). Matter et al. (2014) defined this disc as pre-transitional disc: his SED has a near-infrared excess, a deficit in the flux around 6 μm and it rises again at mid-infrared and far-infrared wavelengths, suggesting a gap in the disc distribution. The infrared spectrum suggests a flared disc. The authors performed a SED modelling (assuming inclination $\sim$ 20° and PA $\sim$ 112°), where they found more agreement with a two-component than a one-component disc. They suggested the presence of an inner disc from 0.22 to 2.3 AU, an outer disc from

5.6 AU and a gap in between. This scenario is supported by the steep temperature profile, which reaches values higher than 300 K at its inner edge. This suggests the existence of a warm disc component meaning that the inner edge of the outer disc would be directly illuminated by the central star. A planet can be the reason behind the formation of the gap as explained by Matter et al. (2016). In particular, a 3 M_{Jup} planet at a separation of ∼4.5 au could be responsible for such disc structure in the dust, but not in the gas. Carmona et al. (2017) observed the CO spectra at 4.7 μm with ESO/VLT CRIRES. The authors found the presence of gas from 1 au up to 15 au in ^{12}CO. In the less abundant isotopologues, instead, there is a drop in the profiles for $R <$ 5-6 au. Observations made by Laws et al. (2019) (with GPI/PDI) claimed a spiral-like disc structure with a break in the innermost arm emission (probably a shadow) produced by a misaligned inner disc. At the same time, Muro-Arena et al. (2019) resolved the disc structure using data taken with SPHERE/PDI, showing a very broad shadow region toward the East side and a ring-like disc structure. This shadow cannot be produced by a single inclined ring given its amplitude. The inner ring shows an opposite behavior with respect to the outer ring.

HD 142527. HD 142527 is a target with a mass of ~ 1.61 $M_{\odot}$ and with a spectral type of F7IIIe. It is known to be a binary system with an M-dwarf companion (Lacour et al. 2016). It is located in the Sco OB2-3 association and it has a distance of 157 pc (Gaia Collaboration et al. 2018). Fukagawa et al. (2006) discovered a peculiar morphology in H and K Band. The disc is face-on and have two bright arcs, asymmetric in size and brightness (extending from $\sim$ 100 to 490 au), and one spiral arm. This suggested the presence of an unseen (for that time) eccentric binary. Casassus et al. (2015b) observed the target with ALMA from 34 to 700 GHz in order to test the trapping predictions. Millimeter size grains are really abundant in the crescent. The conclusion was that dust trapping is efficient for grains observable at centimeter wavelengths and that the largest dust grains are concentrated in the 34 GHz clump. Perez et al. (2015a) detected emission in the three CO (J = 2-1) isotopologues ^{12}CO, ^{13}CO and C^{18}O. A cavity is present in both gas and dust, with the dust cavity larger than the gas cavity ($\sim$ 90 au). The disc inclination was determined to be $\sim 28°$. Avenhaus et al. (2017) observed the target using ZIMPOL on SPHERE in polarimetric differential imaging. The scattered light images allowed them to detect the outer disc with higher resolution, finding spirals going into the cavity. Moreover, a large gap is present going from $\sim$ 30 to $\sim$ 140 au and where two clear shadows are detected. Dust scattering was detected with a high signal-to-noise ratio suggesting the presence of an inner disc inclined combined with a dust halo. The measured inclination of the disc is not compatible with the prediction made by Perez et al. (2015a) and with such inclination cannot be responsible for such shadows. Boehler et al. (2017) presented new ALMA data at 0.88 mm, ^{13}CO and C^{18}O (J = 3-2). The cavity is of $\sim$ 120 au and shows asymmetries in dust and gas. The authors found an extreme gas-to-dust ratio of 1.7. Observations reveals also an inner disc of $\sim$ 50 au in size. The presence of the observed binary companion is demonstrated by Price et al. (2018a) to be a possible explanation for the presence of such disc structure.

HD 97048. HD 97048 has a spectral type of B9.5Ve+sh with a stellar mass of ~ 2.25 $M_{\odot}$. It is located in the Ced 111 region at a distance of 185 pc (Gaia Collaboration et al. 2018). Doucet et al. (2007) used VISIR in order to observe the target in the 8.6 and 11.3 μm aromatic features. The authors revealed a large (320 au in the PAH, 135 au in the continuum) disc inclined to the line of sight. Ginski et al. (2016), using SPHERE/IRDIS with DPI and ADI, found gaps and rings. The gap is at ∼39 au and the ring is at ∼46

au. Their modelling suggests that the disc is flared. van der Plas et al. (2017b) observed the disc in band 7, band 3 and in the ATCA configuration detecting both dust and gas components. The authors adopted an inclination of $\sim 41°$. The continuum extends up to 355 au, the dust cavity is visible up to 43 au at 853 μm (but not at 9 mm) and an emitting ring is centered at ~ 150 au. The gas, instead, extends up to a factor of 2.4 beyond the dust emission, its radial structure can be fitted by three different power-laws and it do not show a cavity.

D.2 Group II targets

All the targets here presented were classified as Class II, Group II sources from the analysis of their spectral energy distribution (SED) based on the SEDs shown in Fig. C.2. For AK Sco and HD 141569, we refer to the Chapter 9.

HD 145718. HD 145718 is an Herbig star of Spectral type of A5, with a mass of 1.8 $M_\odot$. It is located in the Sco OB2-2 region at a distance of ~ 152 pc (Gaia Collaboration et al. 2018) and it was classified as a Class II, Group II source. Few studies were done on this target. Carmona et al. (2010) confirmed HD 145718 to be a nearby young Herbig Ae/Be star and suggested follow-up observations at high-angular resolution for this target, together with other three. In Guimarães et al. (2006) HD 145718 is described to be a photometrically variable. It was found evidence of circumstellar activity, due to the presence of redshifted absorption features in the Balmer lines.

R CrA. R CrA is an Herbig star of Spectral type of A1e-F7evar, with a mass of 1.89 $M_\odot$ and it was considered a Group II source by the work of Acke & van den Ancker (2004). It is located in the NGC 6729 region at a distance of ~ 153 pc (Mesa et al. 2019). Mannings (1994) estimated a disc mass of 0.02 $M_\odot$ using sub-millimeter observations. Groppi et al. (2007) derived an upper mass limit of 0.012 $M_\odot$. Compared with other Herbig stars, this target is in a particularly early evolutionary phase (Malfait et al. 1998) and it is embedded in its natal massive envelope, which still dominates his SED at long wavelengths. Correia et al. (2005) observed R CrA with MIDI at the VLTI. The mid-IR emission shows a resolved asymmetric structure of ~ 6 au radius, suggesting a inclined disc geometry. Their fit of the inclination is of $\sim 45°$ and a position angle of $\sim 62°$. The inclination is consistent with the work done by Clark et al. (2000) in near-infrared imaging polarimetry (near-infrared wavebands J, H and Kn) where they found $\sim 50°$. Kraus et al. (2009) detected with VLTI/AMBER signatures of an extended and compact component. The brightness is highly asymmetric and the authors proposed different scenarios to explained it. The one that seems to agree most with the data is a model with a puffed up inner rim. The SED suggests the presence of relatively large amount of silicate dust grains. Finally, it was recently discovered the presence of a Brown Dwarf companion by Mesa et al. 2019, as previuosly suggested by several authors (e.g. Takami et al. 2003; Forbrich et al. 2006; Choi et al. 2008). Rigliaco et al. 2019 show the presence of an asymmetric emission with a prominent arm pointing toward the North-East already suggested by Mesa et al. 2019.

HD 150193. HD 150193 is a source of spectral type B9.5Ve and of mass 1.89 $M_\odot$ (Vioque et al. 2018a). It is situated in the ρ Ophiuchus region at a distanze of 151 pc (Gaia Collaboration et al. 2018). The presence of a T Tauri companion at a distance of $1\farcs1$ of F9Ve spectral type was reported by Carmona et al. (2007) and Fukagawa et al. (2003) and it is visible also in the corner of our data. A circumstellar disc of a size of

1.″3 was detected by Fukagawa et al. (2003) with the Subaru 8.2m telescope. The authors measured a disc inclination of $\sim 38°$. Moreover, Fukagawa et al. (2010) found presence of asymmetries.

S CrA. S CrA is a star of Spectral type G5Ve. It is located at a distance of ~ 130 pc (Gaia Collaboration et al. 2018) and it has a mass of ~ 1.45 $M_\odot$. This target is know to be a tight visual binary composed by two T Tauri stars extremely similar in all the parameters (Gahm et al. 2018). The only difference can be found in the degree of veiling and the emission line profiles (Gahm et al. 2018). It was observed by Vural et al. (2012) with VLTI/AMBER, where the authors measured ring-fit radii of ~ 0.73 mas and ~ 0.85 mas respectively for H and K Bands, possibly a circumstellar disc. They suggested the presence of a hot inner rim.

HR 5999. HR 5999 is part of the Lupus star forming region at a distance of 161 pc (Gaia Collaboration et al. 2018). It is a young source (3 Myr) of spectral type A5-7III/IVe+sh with a mass of 2.43 $M_\odot$ (Vioque et al. 2018a). Several works found agreement with a boundary layer highly inclined disc (e.g. Perez et al. 1993) due to his photometric and spectroscopic variability. The near and mid-infrared (MIR) excesses are strong (Hillenbrand et al. 1992) and the millimetric wavelengths is weak (Henning et al. 1994) suggesting a circumstellar disc of low mass ($M_{disc} \sim 0.006$ $M_\odot$, Siebenmorgen et al. 2000). Spatially resolved measurements in MIR (Preibisch et al. 2006) suggest a smaller extent of the emission for this target and this is consistent with an inclination of i$\sim$58, a PA$\sim$ 115° and a small outer radius, probably due to the close binary clearing. The first observational study of the target with AMBER/VLTI (Bands H, K) at the sub-au scale was done by Benisty et al. (2011), who found a resolved ring with an inner diameter of ~ 6 mas and a more compact emission from H Band.

HD 190073. HD 190073 is a target of spectral type A2IVpe and with a large mass of 5.60 $M_\odot$. The recent release of Gaia-DR2 has shown that the target is more distant (890 pc, Gaia Collaboration et al. 2018) than what previous papers suggested (e.g. to be located within 300 pc van den Ancker et al. 1998). As described by Pogodin et al. (2005), the variability of its emission lines demonstrates the presence of stellar wind and a dense equatorial circumstellar disc. Several studies were done in order to study the presence of a magnetic field in HD 190073. In particular, Catala et al. (2007) discovered a structured and variable magnetic field, indication that the circumstellar environment can have an impact on the observed polarization features (Järvinen et al. 2015). There is still uncertainty on the inclination of this disc, but it is consistent with an almost face-on inclination ranging from 12° to 50° (Eisner et al. 2004).

HD 104237. HD 104237 target of spectral type of A4IVe+sh has a mass of 1.85 $M_\odot$ (Vioque et al. 2018a). It was cataloged by Gaia to have a distance of 108 pc (Gaia Collaboration et al. 2018). Its SED suggests the presence of a self-shadowed dust disc and that the target is a Group II source (Meeus et al. 2001). Böhm et al. (2004) discovered HD 104237 to be part of a binary system. The authors found evidences of circumstellar gas detected in Brγ line coming from a gaseous inner (<1 au) disc (Kraus et al. 2008). A strong oxygen emission (at 63.2 μm) was detected using PACS (through the Herschel Space Telescope), which indicates a significant amount of gas around this system (Meeus et al. 2012). Hales et al. (2014) revealed the presence of CO-rich circumstellar disc and fitted its profile suggesting a flat disc geometry.

HD 142666. HD 142666 has a spectral type of A8Ve and it is located in the Sco OB2-2 association at a distance of 149 pc (Gaia Collaboration et al. 2018). It is a quite massive source $\sim$1.49 $M_{\odot}$ (Vioque et al. 2018a). The target has been observed with VLT/NACO in polarimetric differential imaging at the near-IR wavelengths by Garufi et al. (2017), who found a compact disc ($\sim$ 60 au) and evidences for a cavity not larger than 10 au. Obervations at sub-mm wavelengths of ^{12}CO (J = 2 - 1) show an unresolved emission (Panić & Hogerheijde 2009). Moreover, the combined emission in the near-IR and CO rotovibrational lines show evidence for no or a small cavity (Banzatti et al. 2018) . Finally, Rubinstein et al. (2018) predicted a high degree of dust settling in the disc and inferred that ALMA data present a cavity ($\sim$ 10 au) in large grains.

HD 132947. HD 132947 is a 2.22 $M_{\odot}$ (Vioque et al. 2018a) target and has a spectral type of B9V. It has a distance of 382 pc (Gaia Collaboration et al. 2018).

KK Oph. KK Oph is an Herbig star of spectral type of A6Ve and of mass of 1.51 $M_{\odot}$ (Vioque et al. 2018a). It is located in the Sco OB2-2 association at a distance of 221 pc (Gaia Collaboration et al. 2018). The disc around KK Oph was classified by Meeus et al. (2001) as Group II disc. This is a known binary system (Leinert et al. 1997) with a separation of 1.61$''$ (Herbig 2005; Carmona et al. 2007). The primary and the secondary are respectively hot and cool T-Tauri. Kreplin et al. (2013) used near-infrared VLTI/AMBER interferometry in order to study this target. The disc inclination is large ($\sim$ 70°, almost edge-on) and the companion orbits in a co-planar plane.

Acronyms

ADI Angular Differential Imaging.

ALMA Acatama Large Millimeter Array.

CARMA Combined Array for Research in Millimeter-wave Astronomy.

ELT Extremely Large Telescope.

GI gravitational instability.

GPI Gemini Planet Imager.

HCI High Contrast Imaging.

HST Hubble Space Telescope.

IFS Integral Field Spectrograph.

JWST James Webb Space Telescope.

MRI magneto-rotational instability.

NaCo Nasmyth Adaptive Optics System, NAos, Coudé Near Infrared Camera, COnica.

NEGFC negative fake companion technique.

NG-VLT Next Generation VLT.

NIR Near-Infrared.

NOEMA NOrthern Extended Millimeter Array.

PCA Principal Component Analysis.

PdBI Plateau de Bure Interferometer.

PDI Polarimetric Differential Imaging.

PMS Pre-Main Sequence.

PSF Point Spread Function.

SDI Spectral Differential Imaging.

SKA Square Kilometre Array.

SMA Submillimeter Array.

SNR Signal to Noise Ratio.

SPHERE Spectro-Polarimetric High-contrast Exoplanet REsearch instrument.

STIM Standardized Trajectory Intensity Mean.

TESS the Transiting Exoplanet Survey Satellite.

VLA Very Large Array.

VLT Very Large Telescope.

List of Figures

List of Tables

Bibliography

Absil, O., Milli, J., Mawet, D., et al. 2013, *Astron. Astrophys.*, 559, L12

Acke, B. & van den Ancker, M. E. 2004, *Astron. Astrophys.*, 426, 151

Acke, B. & van den Ancker, M. E. 2006, *Astron. Astrophys.*, 457, 171

Acke, B., van den Ancker, M. E., & Dullemond, C. P. 2005, *Astron. Astrophys.*, 436, 209

Acke, B., Verhoelst, T., van den Ancker, M. E., et al. 2008, *Astron. Astrophys.*, 485, 209

Aikawa, Y., Miyama, S. M., Nakano, T., & Umebayashi, T. 1996, *Astrophys. J.*, 467, 684

Alcalá, J. M., Natta, A., Manara, C. F., et al. 2014, *Astron. Astrophys.*, 561, A2

Alencar, S. H. P., Melo, C. H. F., Dullemond, C. P., et al. 2003, *Astron. Astrophys.*, 409, 1037

Alexander, R., Pascucci, I., Andrews, S., Armitage, P., & Cieza, L. 2014, in Protostars and Planets VI, ed. H. Beuther, R. S. Klessen, C. P. Dullemond, & T. Henning, 475

Alexander, R. D. & Armitage, P. J. 2007, *Mon. Not. R. Astron. Soc.*, 375, 500

Alexander, R. D., Clarke, C. J., & Pringle, J. E. 2006, *Mon. Not. R. Astron. Soc.*, 369, 229

Allard, F., Guillot, T., Ludwig, H.-G., et al. 2003, in IAU Symposium, Vol. 211, Brown Dwarfs, ed. E. Martín, 325

Allard, F., Homeier, D., & Freytag, B. 2012, Philosophical Transactions of the Royal Society of London Series A, 370, 2765

ALMA Partnership, Brogan, C. L., Pérez, L. M., et al. 2015, *Astrophys. J. Lett.*, 808, L3

Alonso-Albi, T., Fuente, A., Bachiller, R., et al. 2009, *Astron. Astrophys.*, 497, 117

Aly, H., Dehnen, W., Nixon, C., & King, A. 2015, *Mon. Not. R. Astron. Soc.*, 449, 65

Aly, H., Lodato, G., & Cazzoletti, P. 2018, Monthly Notices of the Royal Astronomical Society

Amara, A. & Quanz, S. P. 2012, *Mon. Not. R. Astron. Soc.*, 427, 948

Andersen, J., Lindgren, H., Hazen, M. L., & Mayor, M. 1989, *Astron. Astrophys.*, 219, 142

André, P. 2002, in EAS Publications Series, Vol. 3, EAS Publications Series, ed. J. Bouvier & J.-P. Zahn, 1–38

André, P., Ward-Thompson, D., & Greaves, J. 2012, Science, 337, 69

Andrews, S. M. 2020, Observations of Protoplanetary Disk Structures

Andrews, S. M., Huang, J., Pérez, L. M., et al. 2018a, *Astrophys. J.*, 869, L41

Andrews, S. M., Huang, J., Pérez, L. M., et al. 2018b, *Astrophys. J. Lett.*, 869, L41

Andrews, S. M., Rosenfeld, K. A., Kraus, A. L., & Wilner, D. J. 2013, *Astrophys. J.*, 771, 129

Andrews, S. M., Wilner, D. J., Espaillat, C., et al. 2011, *Astrophys. J.*, 732, 42
Andrews, S. M., Wilner, D. J., Hughes, A. M., Qi, C., & Dullemond, C. P. 2009, *Astrophys. J.*, 700, 1502
Andrews, S. M., Wilner, D. J., Hughes, A. M., Qi, C., & Dullemond, C. P. 2010, *Astrophys. J.*, 723, 1241
Andrews, S. M., Wilner, D. J., Hughes, A. M., et al. 2012, *Astrophys. J.*, 744, 162
Andrews, S. M., Wilner, D. J., Zhu, Z., et al. 2016, *Astrophys. J. Lett.*, 820, L40
Ansdell, M., Williams, J. P., Manara, C. F., et al. 2017, *Astron. J.*, 153, 240
Ansdell, M., Williams, J. P., Trapman, L., et al. 2018, *Astrophys. J.*, 859, 21
Ansdell, M., Williams, J. P., van der Marel, N., et al. 2016, *Astrophys. J.*, 828, 46
Anthonioz, F., Ménard, F., Pinte, C., et al. 2015, *Astron. Astrophys.*, 574, A41
Antichi, J., Dohlen, K., Gratton, R. G., et al. 2009, *Astrophys. J.*, 695, 1042
Armitage, P. J. 2007, Lecture notes on the formation and early evolution of planetary systems
Armitage, P. J. 2010, Astrophysics of Planet Formation
Armitage, P. J., Livio, M., & Pringle, J. E. 2001, *Mon. Not. R. Astron. Soc.*, 324, 705
Armitage, P. J. & Rice, W. K. M. 2005, arXiv e-prints, astro
Artymowicz, P. 1993, *Astrophys. J.*, 419, 155
Artymowicz, P. & Lubow, S. H. 1994, *Astrophys. J.*, 421, 651
Arzamasskiy, L., Zhu, Z., & Stone, J. M. 2018, *Mon. Not. R. Astron. Soc.*, 475, 3201
Ataiee, S., Pinilla, P., Zsom, A., et al. 2013, *Astron. Astrophys.*, 553, L3
Avenhaus, H., Quanz, S. P., Garufi, A., et al. 2018, The Astrophysical Journal, 863, 44
Avenhaus, H., Quanz, S. P., Meyer, M. R., et al. 2014a, *Astrophys. J.*, 790, 56
Avenhaus, H., Quanz, S. P., Schmid, H. M., et al. 2017, *Astron. J.*, 154, 33
Avenhaus, H., Quanz, S. P., Schmid, H. M., et al. 2014b, *Astrophys. J.*, 781, 87
Bacciotti, F., Girart, J. M., Padovani, M., et al. 2018, *Astrophys. J. Lett.*, 865, L12
Bae, J., Pinilla, P., & Birnstiel, T. 2018, *Astrophys. J. Lett.*, 864, L26
Bae, J. & Zhu, Z. 2018, *Astrophys. J.*, 859, 118
Bailer-Jones, C. A. L., Rybizki, J., Fouesneau, M., Mantelet, G., & Andrae, R. 2018, *Astron. J.*, 156, 58
Ballabio, G., Dipierro, G., Veronesi, B., et al. 2018, *Mon. Not. R. Astron. Soc.*, 477, 2766
Banzatti, A., Garufi, A., Kama, M., et al. 2018, *Astron. Astrophys.*, 609, L2
Banzatti, A., Testi, L., Isella, A., et al. 2011, *Astron. Astrophys.*, 525, A12
Baraffe, I., Chabrier, G., Allard, F., & Hauschildt, P. H. 1998, *Astron. Astrophys.*, 337, 403
Baraffe, I., Chabrier, G., Barman, T. S., Allard, F., & Hauschildt, P. H. 2003, *Astron. Astrophys.*, 402, 701
Baraffe, I., Homeier, D., Allard, F., & Chabrier, G. 2015, *Astron. Astrophys.*, 577, A42
Barenfeld, S. A., Carpenter, J. M., Ricci, L., & Isella, A. 2016, The Astrophysical Journal, 827, 142
Baruteau, C., Crida, A., Paardekooper, S. J., et al. 2014, in Protostars and Planets VI, ed. H. Beuther, R. S. Klessen, C. P. Dullemond, & T. Henning, 667
Basri, G. & Bertout, C. 1989, *Astrophys. J.*, 341, 340
Bate, M. R., Bonnell, I. A., & Price, N. M. 1995, *Mon. Not. R. Astron. Soc.*, 277, 362
Beckwith, S. V. W. & Sargent, A. I. 1991, *Astrophys. J.*, 381, 250
Beckwith, S. V. W., Sargent, A. I., Chini, R. S., & Guesten, R. 1990, *Astron. J.*, 99, 924

Bell, K. R. & Lin, D. N. C. 1994, *Astrophys. J.*, 427, 987
Benisty, M., Juhasz, A., Boccaletti, A., et al. 2015, *Astron. Astrophys.*, 578, L6
Benisty, M., Juhász, A., Facchini, S., et al. 2018, *Astron. Astrophys.*, 619, A171
Benisty, M., Renard, S., Natta, A., et al. 2011, *Astron. Astrophys.*, 531, A84
Benisty, M., Stolker, T., Pohl, A., et al. 2017, *Astron. Astrophys.*, 597, A42
Bergin, E. A., Cleeves, L. I., Crockett, N., & Blake, G. A. 2014, Faraday Discussions, 168
Bergin, E. A., Cleeves, L. I., Gorti, U., et al. 2013, *Nature*, 493, 644
Bergin, E. A., Du, F., Cleeves, L. I., et al. 2016, *Astrophys. J.*, 831, 101
Bergin, E. A. & Williams, J. P. 2018, The determination of protoplanetary disk masses
Bertin, G. & Lodato, G. 1999, *Astron. Astrophys.*, 350, 694
Bertout, C. 1989, , 27, 351
Bertrang, G. H. M., Avenhaus, H., Casassus, S., et al. 2018, *Mon. Not. R. Astron. Soc.*, 474, 5105
Beuzit, J.-L., Feldt, M., Dohlen, K., et al. 2008, Society of Photo-Optical Instrumentation Engineers (SPIE) Conference Series, Vol. 7014, SPHERE: a 'Planet Finder' instrument for the VLT, 701418
Beuzit, J. L., Vigan, A., Mouillet, D., et al. 2019, *Astron. Astrophys.*, 631, A155
Biller, B. A., Males, J., Rodigas, T., et al. 2014, *Astrophys. J. Lett.*, 792, L22
Binney, J. & Tremaine, S. 1987, Galactic dynamics
Birnstiel, T. & Andrews, S. M. 2014a, *Astrophys. J.*, 780, 153
Birnstiel, T. & Andrews, S. M. 2014b, *Astrophys. J.*, 780, 153
Birnstiel, T., Andrews, S. M., & Ercolano, B. 2012a, *Astron. Astrophys.*, 544, A79
Birnstiel, T., Fang, M., & Johansen, A. 2016, , 205, 41
Birnstiel, T., Klahr, H., & Ercolano, B. 2012b, *Astron. Astrophys.*, 539, A148
Bitsch, B., Crida, A., Libert, A. S., & Lega, E. 2013, *Astron. Astrophys.*, 555, A124
Bitsch, B. & Johansen, A. 2016, *Astron. Astrophys.*, 590, A101
Boccaletti, A., Di Folco, E., Pantin, E., et al. 2020, Astronomy Astrophysics, 637, L5
Boccaletti, A., Thalmann, C., Lagrange, A.-M., et al. 2015, *Nature*, 526, 230
Bodenheimer, P. & Pollack, J. B. 1986, , 67, 391
Boehler, Y., Weaver, E., Isella, A., et al. 2017, *Astrophys. J.*, 840, 60
Bohlin, R. C., Savage, B. D., & Drake, J. F. 1978, *Astrophys. J.*, 224, 132
Böhm, T., Catala, C., Balona, L., & Carter, B. 2004, *Astron. Astrophys.*, 427, 907
Boley, A. C. 2009, The Astrophysical Journal, 695, L53–L57
Bonnefoy, M., Boccaletti, A., Lagrange, A. M., et al. 2013, *Astron. Astrophys.*, 555, A107
Bonnefoy, M., Chauvin, G., Lagrange, A. M., et al. 2014, *Astron. Astrophys.*, 562, A127
Bonnell, I., Martel, H., Bastien, P., Arcoragi, J.-P., & Benz, W. 1991, *Astrophys. J.*, 377, 553
Bonnell, I. A. 1994, *Mon. Not. R. Astron. Soc.*, 269, 837
Booth, A. S., Walsh, C., Kama, M., et al. 2018, *Astron. Astrophys.*, 611, A16
Borucki, W., Koch, D., Boss, A., et al. 2004, in ESA Special Publication, Vol. 538, Stellar Structure and Habitable Planet Finding, ed. F. Favata, S. Aigrain, & A. Wilson, 177–182
Boss, A. P. 1997, Science, 276, 1836
Bowler, B. P. 2016, *Publ. Astron. Soc. Pac.*, 128, 102001
Bowler, B. P., Liu, M. C., Kraus, A. L., & Mann, A. W. 2014, *Astrophys. J.*, 784, 65
Brauer, F., Dullemond, C. P., & Henning, T. 2008, *Astron. Astrophys.*, 480, 859

Brauer, R., Pantin, E., Di Folco, E., et al. 2019, Astronomy Astrophysics, 628, A88
Bressan, A., Marigo, P., Girardi, L., et al. 2012, *Mon. Not. R. Astron. Soc.*, 427, 127
Brittain, S. D., Carr, J. S., Najita, J. R., Quanz, S. P., & Meyer, M. R. 2014, *Astrophys. J.*, 791, 136
Brown, J. M., Blake, G. A., Qi, C., Dullemond, C. P., & Wilner, D. J. 2008, *Astrophys. J. Lett.*, 675, L109
Brown, J. M., Blake, G. A., Qi, C., et al. 2009, *Astrophys. J.*, 704, 496
Bruderer, S. 2013, *Astron. Astrophys.*, 559, A46
Bruderer, S., van der Marel, N., van Dishoeck, E. F., & van Kempen, T. A. 2014, *Astron. Astrophys.*, 562, A26
Bruderer, S., van Dishoeck, E. F., Doty, S. D., & Herczeg, G. J. 2012, *Astron. Astrophys.*, 541, A91
Bryden, G., Chen, X., Lin, D. N. C., Nelson, R. P., & Papaloizou, J. C. B. 1999, *Astrophys. J.*, 514, 344
Burgasser, A. J. 2014, in Astronomical Society of India Conference Series, Vol. 11, Astronomical Society of India Conference Series, 7–16
Burrows, C. J., Stapelfeldt, K. R., Watson, A. M., et al. 1996, *Astrophys. J.*, 473, 437
Calvet, N., D'Alessio, P., Watson, D. M., et al. 2005, *Astrophys. J. Lett.*, 630, L185
Cameron, A. G. W. 1973, , 18, 407
Canovas, H., Caceres, C., Schreiber, M. R., et al. 2016, *Mon. Not. R. Astron. Soc.*, 458, L29
Canovas, H., Hardy, A., Zurlo, A., et al. 2017, *Astron. Astrophys.*, 598, A43
Canovas, H., Schreiber, M. R., Cáceres, C., et al. 2015, *Astrophys. J.*, 805, 21
Cardelli, J. A., Clayton, G. C., & Mathis, J. S. 1989, *Astrophys. J.*, 345, 245
Carmona, A., Thi, W. F., Kamp, I., et al. 2017, *Astron. Astrophys.*, 598, A118
Carmona, A., van den Ancker, M. E., Audard, M., et al. 2010, *Astron. Astrophys.*, 517, A67
Carmona, A., van den Ancker, M. E., & Henning, T. 2007, *Astron. Astrophys.*, 464, 687
Carr, J. S., Tokunaga, A. T., & Najita, J. 2004, *Astrophys. J.*, 603, 213
Carson, J., Thalmann, C., Janson, M., et al. 2013, *Astrophys. J. Lett.*, 763, L32
Casassus, S. 2016, Publications of the Astronomical Society of Australia, 33, e013
Casassus, S., Avenhaus, H., Pérez, S., et al. 2018, *Mon. Not. R. Astron. Soc.*, 477, 5104
Casassus, S., Hales, A., de Gregorio, I., et al. 2013a, *Astron. Astrophys.*, 553, A64
Casassus, S., Marino, S., Pérez, S., et al. 2015a, *Astrophys. J.*, 811, 92
Casassus, S., van der Plas, G., M, S. P., et al. 2013b, *Nature*, 493, 191
Casassus, S., Wright, C. M., Marino, S., et al. 2015b, *Astrophys. J.*, 812, 126
Castelli, F., Hubrig, S., Järvinen, S. P., & Schöller, M. 2020, *Mon. Not. R. Astron. Soc.*, 491, 2010
Catala, C., Alecian, E., Donati, J.-F., et al. 2007, *Astron. Astrophys.*, 462, 293
Cazzoletti, P., Ricci, L., Birnstiel, T., & Lodato, G. 2017, Astronomy Astrophysics, 599, A102
Cazzoletti, P., van Dishoeck, E. F., Pinilla, P., et al. 2018, *Astron. Astrophys.*, 619, A161
Cesaroni, R., Galli, D., Lodato, G., Walmsley, C. M., & Zhang, Q. 2007, in Protostars and Planets V, ed. B. Reipurth, D. Jewitt, & K. Keil, 197
Cesaroni, R., Galli, D., Lodato, G., Walmsley, M., & Zhang, Q. 2006, *Nature*, 444, 703
Chabrier, G., Baraffe, I., Allard, F., & Hauschildt, P. 2000, *Astrophys. J.*, 542, 464
Chabrier, G., Johansen, A., Janson, M., & Rafikov, R. 2014, Protostars and Planets VI,

619
Chapillon, E., Guilloteau, S., Dutrey, A., & Piétu, V. 2008, *Astron. Astrophys.*, 488, 565
Chauvin, G., Lagrange, A.-M., Dumas, C., et al. 2005, *Astron. Astrophys.*, 438, L25
Chen, X. P., Henning, T., van Boekel, R., & Grady, C. A. 2006, *Astron. Astrophys.*, 445, 331
Chiang, E. I. & Goldreich, P. 1997, *Astrophys. J.*, 490, 368
Choi, M., Hamaguchi, K., Lee, J.-E., & Tatematsu, K. 2008, *Astrophys. J.*, 687, 406
Christiaens, V., Casassus, S., Absil, O., et al. 2019a, *Mon. Not. R. Astron. Soc.*, 486, 5819
Christiaens, V., Casassus, S., Absil, O., et al. 2019b, *Mon. Not. R. Astron. Soc.*, 486, 5819
Christiaens, V., Casassus, S., Absil, O., et al. 2018, *Astron. Astrophys.*, 617, A37
Christiaens, V., Casassus, S., Perez, S., van der Plas, G., & Ménard, F. 2014, *Astrophys. J. Lett.*, 785, L12
Ciesla, F. J. 2007, *Astrophys. J. Lett.*, 654, L159
Cieza, L. A., Casassus, S., Pérez, S., et al. 2017, *Astrophys. J. Lett.*, 851, L23
Clark, S., McCall, A., Chrysostomou, A., et al. 2000, *Mon. Not. R. Astron. Soc.*, 319, 337
Clarke, C. & Carswell, B. 2014, Principles of Astrophysical Fluid Dynamics
Clarke, C. J. 2009, *Mon. Not. R. Astron. Soc.*, 396, 1066
Clarke, C. J. 2009, Monthly Notices of the Royal Astronomical Society, 396, 1066
Clarke, C. J., Gendrin, A., & Sotomayor, M. 2001, *Mon. Not. R. Astron. Soc.*, 328, 485
Clarke, C. J., Tazzari, M., Juhasz, A., et al. 2018, *Astrophys. J. Lett.*, 866, L6
Claudi, R., Maire, A.-L., Mesa, D., et al. 2019, Astronomy Astrophysics, 622, A96
Cleeves, L. I., Öberg, K. I., Wilner, D. J., et al. 2016, *Astrophys. J.*, 832, 110
Cleeves, L. I., Öberg, K. I., Wilner, D. J., et al. 2018, *Astrophys. J.*, 865, 155
Cockell, C. S., Léger, A., Fridlund, M., et al. 2009, Astrobiology, 9, 1
Collins, K. A., Grady, C. A., Hamaguchi, K., et al. 2009, *Astrophys. J.*, 697, 557
Correia, S., Koehler, R., Meeus, G., & Zinnecker, H. 2005, ArXiv Astrophysics e-prints
Cossins, P., Lodato, G., & Testi, L. 2010, *Mon. Not. R. Astron. Soc.*, 407, 181
Creech-Eakman, M. J., Chiang, E. I., Joung, R. M. K., Blake, G. A., & van Dishoeck, E. F. 2002, *Astron. Astrophys.*, 385, 546
Crida, A., Morbidelli, A., & Masset, F. 2006, , 181, 587
Cruz, K. L., Kirkpatrick, J. D., & Burgasser, A. J. 2009, *Astron. J.*, 137, 3345
Cugno, G., Quanz, S. P., Hunziker, S., et al. 2019, Astronomy Astrophysics, 622, A156
Currie, T., Cloutier, R., Brittain, S., et al. 2015, *Astrophys. J. Lett.*, 814, L27
Cutri, R. M., Skrutskie, M. F., van Dyk, S., et al. 2003, VizieR Online Data Catalog, 2246
Czekala, I., Andrews, S. M., Jensen, E. L. N., et al. 2015, *Astrophys. J.*, 806, 154
D'Alessio, P., Calvet, N., & Hartmann, L. 2001, *Astrophys. J.*, 553, 321
D'Angelo, G. & Lubow, S. H. 2008, *Astrophys. J.*, 685, 560
D'Angelo, G., Lubow, S. H., & Bate, M. R. 2006, *Astrophys. J.*, 652, 1698
Dartois, E., Dutrey, A., & Guilloteau, S. 2003, *Astron. Astrophys.*, 399, 773
de Boer, J., Salter, G., Benisty, M., et al. 2016, *Astron. Astrophys.*, 595, A114
de Gregorio-Monsalvo, I., Ménard, F., Dent, W., et al. 2013, *Astron. Astrophys.*, 557, A133

Debes, J. H., Weinberger, A. J., & Song, I. 2008, The Astrophysical Journal, 684, L41–L44
Delorme, P., Meunier, N., Albert, D., et al. 2017a, in SF2A-2017: Proceedings of the Annual meeting of the French Society of Astronomy and Astrophysics, ed. C. Reylé, P. Di Matteo, F. Herpin, E. Lagadec, A. Lançon, Z. Meliani, & F. Royer, 347–361
Delorme, P., Schmidt, T., Bonnefoy, M., et al. 2017b, *Astron. Astrophys.*, 608, A79
Dent, W. R. F., Greaves, J. S., & Coulson, I. M. 2005, *Mon. Not. R. Astron. Soc.*, 359, 663
Dent, W. R. F., Pinte, C., Cortes, P. C., et al. 2019, *Mon. Not. R. Astron. Soc.*, 482, L29
Dipierro, G. & Laibe, G. 2017, *Mon. Not. R. Astron. Soc.*, 469, 1932
Dipierro, G., Laibe, G., Alexander, R., & Hutchison, M. 2018a, *Mon. Not. R. Astron. Soc.*, 479, 4187
Dipierro, G., Laibe, G., Price, D. J., & Lodato, G. 2016, *Mon. Not. R. Astron. Soc.*, 459, L1
Dipierro, G., Pinilla, P., Lodato, G., & Testi, L. 2015a, *Mon. Not. R. Astron. Soc.*, 451, 974
Dipierro, G., Price, D., Laibe, G., et al. 2015b, *Mon. Not. R. Astron. Soc.*, 453, L73
Dipierro, G., Ricci, L., Pérez, L., et al. 2018b, *Mon. Not. R. Astron. Soc.*, 475, 5296
Dominik, C., Dullemond, C. P., Waters, L. B. F. M., & Walch, S. 2003, *Astron. Astrophys.*, 398, 607
Donehew, B. & Brittain, S. 2011, *Astron. J.*, 141, 46
Dong, R. & Fung, J. 2017a, *Astrophys. J.*, 835, 38
Dong, R. & Fung, J. 2017b, *Astrophys. J.*, 835, 146
Dong, R., Fung, J., & Chiang, E. 2016, The Astrophysical Journal, 826, 75
Dong, R., Hall, C., Rice, K., & Chiang, E. 2015a, *Astrophys. J. Lett.*, 812, L32
Dong, R., Li, S., Chiang, E., & Li, H. 2018a, *Astrophys. J.*, 866, 110
Dong, R., Liu, S.-y., Eisner, J., et al. 2018b, *Astrophys. J.*, 860, 124
Dong, R., Zhu, Z., Fung, J., et al. 2016, *Astrophys. J. Lett.*, 816, L12
Dong, R., Zhu, Z., Rafikov, R. R., & Stone, J. M. 2015b, *Astrophys. J. Lett.*, 809, L5
D'Orazio, D. J., Haiman, Z., Duffell, P., MacFadyen, A., & Farris, B. 2016, *Mon. Not. R. Astron. Soc.*, 459, 2379
Doucet, C., Habart, E., Pantin, E., et al. 2007, *Astron. Astrophys.*, 470, 625
Draine, B. T. 2003, *Astrophys. J.*, 598, 1017
Draine, B. T. 2006, *Astrophys. J.*, 636, 1114
Draine, B. T. & Lee, H. M. 1984, *Astrophys. J.*, 285, 89
Drew, J. E., Busfield, G., Hoare, M. G., et al. 1997, *Mon. Not. R. Astron. Soc.*, 286, 538
Du, F., Bergin, E. A., & Hogerheijde, M. R. 2015, *Astrophys. J. Lett.*, 807, L32
Duchêne, G. & Kraus, A. 2013, , 51, 269
Duchêne, G., McCabe, C., Pinte, C., et al. 2010, *Astrophys. J.*, 712, 112
Duffell, P. C. & Chiang, E. 2015, *Astrophys. J.*, 812, 94
Duffell, P. C. & Dong, R. 2015, *Astrophys. J.*, 802, 42
Dullemond, C. P. & Dominik, C. 2004, *Astron. Astrophys.*, 421, 1075
Dullemond, C. P. & Dominik, C. 2005, *Astron. Astrophys.*, 434, 971
Dullemond, C. P., Dominik, C., & Natta, A. 2001, *Astrophys. J.*, 560, 957
Dullemond, C. P., Hollenbach, D., Kamp, I., & D'Alessio, P. 2006, Models of the Structure and Evolution of Protoplanetary Disks
Dullemond, C. P., Hollenbach, D., Kamp, I., & D'Alessio, P. 2007, in Protostars and Planets V, ed. B. Reipurth, D. Jewitt, & K. Keil, 555

Dullemond, C. P., Juhasz, A., Pohl, A., et al. 2012, RADMC-3D: A multi-purpose radiative transfer tool, Astrophysics Source Code Library

Dunhill, A. C., Alexander, R. D., & Armitage, P. J. 2013, *Mon. Not. R. Astron. Soc.*, 428, 3072

Dunkin, S. K., Barlow, M. J., & Ryan, S. G. 1997, *Mon. Not. R. Astron. Soc.*, 286, 604

Durisen, R. H., Boss, A. P., Mayer, L., et al. 2007, in Protostars and Planets V, ed. B. Reipurth, D. Jewitt, & K. Keil, 607

Dutrey, A., Guilloteau, S., Duvert, G., et al. 1996, *Astron. Astrophys.*, 309, 493

Dutrey, A., Guilloteau, S., Prato, L., et al. 1998, *Astron. Astrophys.*, 338, L63

Dzib, S. A., Loinard, L., Ortiz-León, G. N., Rodríguez, L. F., & Galli, P. A. B. 2018, *Astrophys. J.*, 867, 151

Eisenhauer, F., Abuter, R., Bickert, K., et al. 2003, Society of Photo-Optical Instrumentation Engineers (SPIE) Conference Series, Vol. 4841, SINFONI - Integral field spectroscopy at 50 milli-arcsecond resolution with the ESO VLT, ed. M. Iye & A. F. M. Moorwood, 1548–1561

Eisner, J. A., Lane, B. F., Hillenbrand, L. A., Akeson, R. L., & Sargent, A. I. 2004, *Astrophys. J.*, 613, 1049

Eistrup, C., Walsh, C., & van Dishoeck, E. F. 2016, *Astron. Astrophys.*, 595, A83

Elbakyan, V. G., Vorobyov, E. I., Rab, C., et al. 2018, Monthly Notices of the Royal Astronomical Society, 484, 146

Epstein, P. S. 1924, Phys. Rev., 23, 710

Espaillat, C., Calvet, N., D'Alessio, P., et al. 2007, *Astrophys. J. Lett.*, 670, L135

Espaillat, C., D'Alessio, P., Hernández, J., et al. 2010, The Astrophysical Journal, 717, 441–457

Espaillat, C., Muzerolle, J., Najita, J., et al. 2014, Protostars and Planets VI, 497

Facchini, S., Birnstiel, T., Bruderer, S., & van Dishoeck, E. F. 2017, *Astron. Astrophys.*, 605, A16

Facchini, S., Juhász, A., & Lodato, G. 2018a, *Mon. Not. R. Astron. Soc.*, 473, 4459

Facchini, S., Juhász, A., & Lodato, G. 2017, Monthly Notices of the Royal Astronomical Society, 473, 4459–4475

Facchini, S., Lodato, G., & Price, D. J. 2013, *Mon. Not. R. Astron. Soc.*, 433, 2142

Facchini, S., Pinilla, P., van Dishoeck, E. F., & de Juan Ovelar, M. 2018b, *Astron. Astrophys.*, 612, A104

Farris, B. D., Duffell, P., MacFadyen, A. I., & Haiman, Z. 2014, *Astrophys. J.*, 783, 134

Favre, C., Cleeves, L. I., Bergin, E. A., Qi, C., & Blake, G. A. 2013, *Astrophys. J. Lett.*, 776, L38

Fedele, D., Carney, M., Hogerheijde, M. R., et al. 2017, *Astron. Astrophys.*, 600, A72

Fedele, D., Tazzari, M., Booth, R., et al. 2018, *Astron. Astrophys.*, 610, A24

Fedele, D., van den Ancker, M. E., Acke, B., et al. 2008, *Astron. Astrophys.*, 491, 809

Feldt, M., Olofsson, J., Boccaletti, A., et al. 2017, *Astron. Astrophys.*, 601, A7

Flaherty, K. M., Hughes, A. M., Rosenfeld, K. A., et al. 2015, *Astrophys. J.*, 813, 99

Flaherty, K. M., Hughes, A. M., Teague, R., et al. 2018, The Astrophysical Journal, 856, 117

Flock, M., Henning, T., & Klahr, H. 2012, *Astrophys. J.*, 761, 95

Flock, M., Ruge, J. P., Dzyurkevich, N., et al. 2015, *Astron. Astrophys.*, 574, A68

Follette, K. B., Rameau, J., Dong, R., et al. 2017, *Astron. J.*, 153, 264

Follette, K. B., Tamura, M., Hashimoto, J., et al. 2013, *Astrophys. J.*, 767, 10

Forbrich, J., Preibisch, T., & Menten, K. M. 2006, *Astron. Astrophys.*, 446, 155
Francis, L. & van der Marel, N. 2020, Dust depleted inner disks in a large sample of transition disks through long-baseline ALMA observations
Frank, J., King, A. R., & Raine, D. J. 1985, Accretion power in astrophysics
Fukagawa, M., Tamura, M., Itoh, Y., Hayashi, S. S., & Oasa, Y. 2003, *Astrophys. J. Lett.*, 590, L49
Fukagawa, M., Tamura, M., Itoh, Y., et al. 2006, *Astrophys. J. Lett.*, 636, L153
Fukagawa, M., Tamura, M., Itoh, Y., et al. 2010, *Publ. Astron. Soc. Jpn.*, 62, 347
Fung, J. & Chiang, E. 2016, The Astrophysical Journal, 832, 105
Fung, J. & Dong, R. 2015, *Astrophys. J. Lett.*, 815, L21
Fung, J., Shi, J.-M., & Chiang, E. 2014, *Astrophys. J.*, 782, 88
Gahm, G. F., Petrov, P. P., Tambovsteva, L. V., et al. 2018, *Astron. Astrophys.*, 614, A117
Gaia Collaboration, Brown, A. G. A., Vallenari, A., et al. 2018, ArXiv e-prints
Gaia Collaboration, Brown, A. G. A., Vallenari, A., et al. 2016, *Astron. Astrophys.*, 595, A2
Galicher, R., Boccaletti, A., Mesa, D., et al. 2018, *Astron. Astrophys.*, 615, A92
Garcia Lopez, R., Natta, A., Testi, L., & Habart, E. 2006, *Astron. Astrophys.*, 459, 837
Garufi, A., Avenhaus, H., Pérez, S., et al. 2020, Astronomy Astrophysics, 633, A82
Garufi, A., Benisty, M., Pinilla, P., et al. 2018, ArXiv e-prints, arXiv:1810.04564
Garufi, A., Meeus, G., Benisty, M., et al. 2017, *Astron. Astrophys.*, 603, A21
Garufi, A., Quanz, S. P., Avenhaus, H., et al. 2013, *Astron. Astrophys.*, 560, A105
Garufi, A., Quanz, S. P., Schmid, H. M., et al. 2016, *Astron. Astrophys.*, 588, A8
Gibbons, P. G., Mamatsashvili, G. R., & Rice, W. K. M. 2014, *Mon. Not. R. Astron. Soc.*, 442, 361
Ginski, C., Stolker, T., Pinilla, P., et al. 2016, *Astron. Astrophys.*, 595, A112
Girardi, L., Groenewegen, M. A. T., Hatziminaoglou, E., & da Costa, L. 2005, *Astron. Astrophys.*, 436, 895
Goldreich, P. & Tremaine, S. 1979, *Astrophys. J.*, 233, 857
Goldreich, P. & Tremaine, S. 1980, *Astrophys. J.*, 241, 425
Goldreich, P. & Ward, W. R. 1973, *Astrophys. J.*, 183, 1051
Goldsmith, P. F., Bergin, E. A., & Lis, D. C. 1997, in American Astronomical Society Meeting Abstracts, Vol. 191, American Astronomical Society Meeting Abstracts, 32.02
Gómez de Castro, A. I. 2009, *Astrophys. J. Lett.*, 698, L108
Gómez de Castro, A. I., Loyd, R. O. P., France, K., Sytov, A., & Bisikalo, D. 2016, *Astrophys. J. Lett.*, 818, L17
Gomez Gonzalez, C. A., Absil, O., & Van Droogenbroeck, M. 2018, *Astron. Astrophys.*, 613, A71
Gomez Gonzalez, C. A., Wertz, O., Absil, O., et al. 2017a, *Astron. J.*, 154, 7
Gomez Gonzalez, C. A., Wertz, O., Absil, O., et al. 2017b, *Astron. J.*, 154, 7
Grady, C. A., Polomski, E. F., Henning, T., et al. 2001, *Astron. J.*, 122, 3396
Grady, C. A., Woodgate, B., Bruhweiler, F. C., et al. 1999, *Astrophys. J. Lett.*, 523, L151
Gratton, R., Ligi, R., Sissa, E., et al. 2019, Astronomy Astrophysics, 623, A140
Greaves, J. S. & Rice, W. K. M. 2010, *Mon. Not. R. Astron. Soc.*, 407, 1981
Greco, J. P. & Brandt, T. D. 2016, *Astrophys. J.*, 833, 134
Groppi, C. E., Hunter, T. R., Blundell, R., & Sandell, G. 2007, *Astrophys. J.*, 670, 489
Guerri, G., Robbe-Dubois, S., Daban, J.-B., et al. 2009, Apodized Lyot Coronagraph for

VLT-SPHERE: Laboratory tests and performances of a first prototype in the visible
Guidi, G., Tazzari, M., Testi, L., et al. 2016, *Astron. Astrophys.*, 588, A112
Guillot, T., Lin, D. N. C., Morel, P., Havel, M., & Parmentier, V. 2014, in EAS Publications Series, Vol. 65, EAS Publications Series, 327–336
Guilloteau, S. & Dutrey, A. 1998, *Astron. Astrophys.*, 339, 467
Guilloteau, S., Dutrey, A., Piétu, V., & Boehler, Y. 2011, *Astron. Astrophys.*, 529, A105
Guilloteau, S., Dutrey, A., & Simon, M. 1999, *Astron. Astrophys.*, 348, 570
Guilloteau, S., Dutrey, A., Wakelam, V., et al. 2012, *Astron. Astrophys.*, 548, A70
Guimarães, M. M., Alencar, S. H. P., Corradi, W. J. B., & Vieira, S. L. A. 2006, *Astron. Astrophys.*, 457, 581
Hales, A. S., De Gregorio-Monsalvo, I., Montesinos, B., et al. 2014, *Astron. J.*, 148, 47
Halko, N., Martinsson, P.-G., & Tropp, J. A. 2009, Finding structure with randomness: Probabilistic algorithms for constructing approximate matrix decompositions
Hartmann, L. 2009, Accretion Processes in Star Formation: Second Edition
Hartmann, L., Calvet, N., Gullbring, E., & D'Alessio, P. 1998, *Astrophys. J.*, 495, 385
Hartmann, L. & Kenyon, S. J. 1996, , 34, 207
Hartmann, L., Kenyon, S. J., & Hartigan, P. 1993, Protostars and Planets III, ed. E. H. Levy & J. Lunine (Tucson: Univ. Arizona Press), 497
Hashimoto, J., Dong, R., Kudo, T., et al. 2012, *Astrophys. J. Lett.*, 758, L19
Hendler, N. P., Pinilla, P., Pascucci, I., et al. 2018, *Mon. Not. R. Astron. Soc.*, 475, L62
Henning, T., Launhardt, R., Steinacker, J., & Thamm, E. 1994, *Astron. Astrophys.*, 291, 546
Herbig, G. H. 1960, *Astrophys. J.*, 131, 632
Herbig, G. H. 2005, *Astron. J.*, 130, 815
Hernández, J., Calvet, N., Hartmann, L., et al. 2005, *Astron. J.*, 129, 856
Hillenbrand, L. A., Strom, S. E., Vrba, F. J., & Keene, J. 1992, *Astrophys. J.*, 397, 613
Hinkley, S., Bowler, B. P., Vigan, A., et al. 2015, *Astrophys. J. Lett.*, 805, L10
Hinkley, S., Oppenheimer, B. R., Soummer, R., et al. 2007, *Astrophys. J.*, 654, 633
Hirsh, K., Price, D. J., Gonzalez, J.-F., Giulia Ubeira-Gabellini, M., & Ragusa, E. 2020, arXiv e-prints, arXiv:2008.08008
Hopkins, P. F. 2013, *Mon. Not. R. Astron. Soc.*, 430, 1653
Hoyle, F. 1960, , 1, 28
Huang, J., Andrews, S. M., Dullemond, C. P., et al. 2018, The Astrophysical Journal, 869, L42
Huang, J., Andrews, S. M., Öberg, K. I., et al. 2020, *Astrophys. J.*, 898, 140
Huang, J., Andrews, S. M., Pérez, L. M., et al. 2018, *Astrophys. J. Lett.*, 869, L43
Huélamo, N., de Gregorio-Monsalvo, I., Macias, E., et al. 2015, *Astron. Astrophys.*, 575, L5
Huélamo, N., Lacour, S., Tuthill, P., et al. 2011, *Astron. Astrophys.*, 528, L7
Hughes, A. M., Duchêne, G., & Matthews, B. C. 2018, , 56, 541
Hughes, A. M., Wilner, D. J., Andrews, S. M., Qi, C., & Hogerheijde, M. R. 2011, *Astrophys. J.*, 727, 85
Hughes, A. M., Wilner, D. J., Qi, C., & Hogerheijde, M. R. 2008, *Astrophys. J.*, 678, 1119
Hutchison, M., Price, D. J., & Laibe, G. 2018, *Mon. Not. R. Astron. Soc.*, 476, 2186
Huygens, C. 1698, The celestial worlds discover'd:
Ikoma, M., Nakazawa, K., & Emori, H. 2000, *Astrophys. J.*, 537, 1013
Ireland, M. J. 2013, *Mon. Not. R. Astron. Soc.*, 433, 1718

Ireland, M. J. & Kraus, A. L. 2008, *Astrophys. J. Lett.*, 678, L59
Isella, A. 2006, Universitá degli studi di Milano
Isella, A., Benisty, M., Teague, R., et al. 2019, *Astrophys. J. Lett.*, 879, L25
Isella, A., Carpenter, J. M., & Sargent, A. I. 2009, *Astrophys. J.*, 701, 260
Isella, A., Guidi, G., Testi, L., et al. 2016, Phys. Rev. Lett., 117, 251101
Isella, A., Pérez, L. M., Carpenter, J. M., et al. 2013, *Astrophys. J.*, 775, 30
Itoh, Y., Oasa, Y., Kudo, T., et al. 2014, Research in Astronomy and Astrophysics, 14, 1438
Ivanov, P. B., Papaloizou, J. C. B., & Polnarev, A. G. 1999, *Mon. Not. R. Astron. Soc.*, 307, 79
Janson, M., Thalmann, C., Boccaletti, A., et al. 2016, *Astrophys. J. Lett.*, 816, L1
Järvinen, S. P., Carroll, T. A., Hubrig, S., et al. 2018, *Astrophys. J. Lett.*, 858, L18
Järvinen, S. P., Carroll, T. A., Hubrig, S., et al. 2015, *Astron. Astrophys.*, 584, A15
Jeans, J. H. 1902, Philosophical Transactions of the Royal Society of London Series A, 199, 1
Jennings, J., Ercolano, B., & Rosotti, G. P. 2018, Monthly Notices of the Royal Astronomical Society, 477, 4131–4141
Jin, S., Li, S., Isella, A., Li, H., & Ji, J. 2016, *Astrophys. J.*, 818, 76
Johansen, A., Oishi, J. S., Mac Low, M.-M., et al. 2007, *Nature*, 448, 1022
Juhász, A., Benisty, M., Pohl, A., et al. 2015, *Mon. Not. R. Astron. Soc.*, 451, 1147
Juhász, A. & Rosotti, G. P. 2018, *Mon. Not. R. Astron. Soc.*, 474, L32
Juhász, A. & Facchini, S. 2017, Monthly Notices of the Royal Astronomical Society, stw3389
Kama, M., Bruderer, S., van Dishoeck, E. F., et al. 2016, VizieR Online Data Catalog, 359
Kanagawa, K. D., Tanaka, H., Muto, T., Tanigawa, T., & Takeuchi, T. 2015, *Mon. Not. R. Astron. Soc.*, 448, 994
Kanagawa, K. D., Tanaka, H., & Szuszkiewicz, E. 2018, *Astrophys. J.*, 861, 140
Kataoka, A., Tsukagoshi, T., Momose, M., et al. 2016, *Astrophys. J. Lett.*, 831, L12
Kennedy, G. M., Matrà, L., Facchini, S., et al. 2019, Nature Astronomy, 3, 230–235
Kenyon, S. J. & Hartmann, L. 1987, *Astrophys. J.*, 323, 714
Keppler, M., Benisty, M., Müller, A., et al. 2018, ArXiv e-prints
Keppler, M., Penzlin, A., Benisty, M., et al. 2020, Astronomy Astrophysics, 639, A62
Keppler, M., Teague, R., Bae, J., et al. 2019, *Astron. Astrophys.*, 625, A118
Köhler, R. 2011, *Astron. Astrophys.*, 530, A126
Kokubo, E. & Ida, S. 1998, , 131, 171
Kozai, Y. 1962, *Astron. J.*, 67, 591
Kratter, K. & Lodato, G. 2016, , 54, 271
Kratter, K. M., Matzner, C. D., & Krumholz, M. R. 2008, *Astrophys. J.*, 681, 375
Kratter, K. M. & Murray-Clay, R. A. 2011, *Astrophys. J.*, 740, 1
Kraus, A. L. & Ireland, M. J. 2012, *Astrophys. J.*, 745, 5
Kraus, S., Hofmann, K.-H., Benisty, M., et al. 2008, *Astron. Astrophys.*, 489, 1157
Kraus, S., Hofmann, K.-H., Malbet, F., et al. 2009, *Astron. Astrophys.*, 508, 787
Kraus, S., Kreplin, A., Young, A. K., et al. 2020, arXiv e-prints, arXiv:2004.01204
Krauss, O., Wurm, G., Mousis, O., et al. 2007, *Astron. Astrophys.*, 462, 977
Kreplin, A., Weigelt, G., Kraus, S., et al. 2013, *Astron. Astrophys.*, 551, A21

Krumholz, M. R. 2011, *Astrophys. J.*, 743, 110
Kudo, T., Tamura, M., Kitamura, Y., et al. 2008, *Astrophys. J. Lett.*, 673, L67
Kuhn, J. R., Potter, D., & Parise, B. 2001, *Astrophys. J. Lett.*, 553, L189
Kurucz, R. 1991, Davis Philip A.G., Upgren A.R. and Janes K.A., (eds.). L. Davis Press, Schenectady, 27
Lacour, S., Biller, B., Cheetham, A., et al. 2016, *Astron. Astrophys.*, 590, A90
Lada, C. J. 1987, Symposium - International Astronomical Union, 115, 1–18
Lada, C. J. & Wilking, B. A. 1984, *Astrophys. J.*, 287, 610
Lafrenière, D., Doyon, R., Marois, C., et al. 2007a, *Astrophys. J.*, 670, 1367
Lafrenière, D., Marois, C., Doyon, R., Nadeau, D., & Artigau, É. 2007b, *Astrophys. J.*, 660, 770
Lagrange, A. M., Bonnefoy, M., Chauvin, G., et al. 2010, Science, 329, 57
Laibe, G. 2014, *Mon. Not. R. Astron. Soc.*, 437, 3037
Laibe, G., Gonzalez, J. F., & Maddison, S. T. 2012, *Astron. Astrophys.*, 537, A61
Laibe, G. & Price, D. J. 2012, *Mon. Not. R. Astron. Soc.*, 420, 2345
Laibe, G. & Price, D. J. 2014, *Mon. Not. R. Astron. Soc.*, 440, 2136
Lambrechts, M. & Johansen, A. 2012, *Astron. Astrophys.*, 544, A32
Lau, Y. Y. & Bertin, G. 1978, *Astrophys. J.*, 226, 508
Laws, A. S. E., Harries, T. J., Setterholm, B. R., et al. 2019, The Astrophysical Journal, 888, 7
Lazareff, B., Berger, J.-P., Kluska, J., et al. 2017, *Astron. Astrophys.*, 599, A85
Lee, M. H. 2000, , 143, 74
Leinert, C., Richichi, A., & Haas, M. 1997, *Astron. Astrophys.*, 318, 472
Lenzen, R., Hartung, M., Brandner, W., et al. 2003, in , Vol. 4841, Instrument Design and Performance for Optical/Infrared Ground-based Telescopes, ed. M. Iye & A. F. M. Moorwood, 944–952
Levenhagen, R. S. & Leister, N. V. 2006, *Mon. Not. R. Astron. Soc.*, 371, 252
Li, H., Colgate, S. A., Wendroff, B., & Liska, R. 2001, *Astrophys. J.*, 551, 874
Li, H., Finn, J. M., Lovelace, R. V. E., & Colgate, S. A. 2000, *Astrophys. J.*, 533, 1023
Lidov, M. L. 1962, , 9, 719
Ligi, R., Vigan, A., Gratton, R., et al. 2018, *Mon. Not. R. Astron. Soc.*, 473, 1774
Lin, C. C. & Shu, F. H. 1964, *Astrophys. J.*, 140, 646
Lin, D. N. C. & Papaloizou, J. 1979, *Mon. Not. R. Astron. Soc.*, 186, 799
Lin, D. N. C. & Papaloizou, J. 1986, *Astrophys. J.*, 309, 846
Lin, D. N. C. & Papaloizou, J. C. B. 1993, in Protostars and Planets III, ed. E. H. Levy & J. I. Lunine, 749
Lin, D. N. C. & Pringle, J. E. 1987, *Mon. Not. R. Astron. Soc.*, 225, 607
Lin, D. N. C. & Pringle, J. E. 1990, *Astrophys. J.*, 358, 515
Lin, M.-K. 2012, *Astrophys. J.*, 754, 21
Lissauer, J. J. 1987, , 69, 249
Liu, H. B. 2019, *Astrophys. J. Lett.*, 877, L22
Liu, S.-F., Jin, S., Li, S., Isella, A., & Li, H. 2018a, *Astrophys. J.*, 857, 87
Liu, Y., Dipierro, G., Ragusa, E., et al. 2019, Astronomy Astrophysics, 622, A75
Liu, Y., Dipierro, G., Ragusa, E., et al. 2018b, ArXiv e-prints
Liu, Y., Henning, T., Carrasco-González, C., et al. 2017, *Astron. Astrophys.*, 607, A74
Lodato, G. 2007, Nuovo Cimento Rivista Serie, 30, 293

Lodato, G. 2008, , 52, 21
Lodato, G., Delgado-Donate, E., & Clarke, C. J. 2005, *Mon. Not. R. Astron. Soc.*, 364, L91
Lodato, G., Dipierro, G., Ragusa, E., et al. 2019, *Mon. Not. R. Astron. Soc.*, 886
Lodato, G. & Facchini, S. 2013, Monthly Notices of the Royal Astronomical Society, 433, 2157–2164
Lodato, G. & Price, D. J. 2010, *Mon. Not. R. Astron. Soc.*, 405, 1212
Lodato, G., Scardoni, C. E., Manara, C. F., & Testi, L. 2017, ArXiv e-prints
Long, F., Herczeg, G. J., Pascucci, I., et al. 2017, *Astrophys. J.*, 844, 99
Long, F., Pinilla, P., Herczeg, G. J., et al. 2018a, The Astrophysical Journal, 869, 17
Long, Z. C., Akiyama, E., Sitko, M., et al. 2018b, The Astrophysical Journal, 858, 112
Looper, D. L., Bochanski, J. J., Burgasser, A. J., et al. 2010, The Astronomical Journal, 140, 1486
Lovelace, R. V. E., Li, H., Colgate, S. A., & Nelson, A. F. 1999, *Astrophys. J.*, 513, 805
Lubow, S. H. & D'Angelo, G. 2006, *Astrophys. J.*, 641, 526
Lubow, S. H., Seibert, M., & Artymowicz, P. 1999, *Astrophys. J.*, 526, 1001
Luhman, K. L. 2012, , 50, 65
Luhman, K. L., Esplin, T. L., & Loutrel, N. P. 2016, *Astrophys. J.*, 827, 52
Luhman, K. L., Stauffer, J. R., Muench, A. A., et al. 2003, *Astrophys. J.*, 593, 1093
Lynden-Bell, D. & Pringle, J. E. 1974a, *Mon. Not. R. Astron. Soc.*, 168, 603
Lynden-Bell, D. & Pringle, J. E. 1974b, *Mon. Not. R. Astron. Soc.*, 168, 603
Lyra, W., Johansen, A., Klahr, H., & Piskunov, N. 2009, *Astron. Astrophys.*, 493, 1125
Maaskant, K. M., Honda, M., Waters, L. B. F. M., et al. 2013, *Astron. Astrophys.*, 555, A64
Maaskant, K. M., Min, M., Waters, L. B. F. M., & Tielens, A. G. G. M. 2014, *Astron. Astrophys.*, 563, A78
Macías, E., Espaillat, C. C., Osorio, M., et al. 2019, The Astrophysical Journal, 881, 159
Macintosh, B., Graham, J. R., Barman, T., et al. 2015, Science, 350, 64
Macintosh, B., Graham, J. R., Ingraham, P., et al. 2014, Proceedings of the National Academy of Science, 111, 12661
Maire, A.-L., Langlois, M., Dohlen, K., et al. 2016, in , Vol. 9908, Ground-based and Airborne Instrumentation for Astronomy VI, 990834
Malbet, F., Benisty, M., de Wit, W.-J., et al. 2007, *Astron. Astrophys.*, 464, 43
Malfait, K., Bogaert, E., & Waelkens, C. 1998, *Astron. Astrophys.*, 331, 211
Mamajek, E. E. 2005, *Astrophys. J.*, 634, 1385
Manara, C. F., Morbidelli, A., & Guillot, T. 2018, *Astron. Astrophys.*, 618, L3
Manara, C. F., Mordasini, C., Testi, L., et al. 2019, *Astron. Astrophys.*, 631, L2
Manara, C. F., Rosotti, G., Testi, L., et al. 2016, *Astron. Astrophys.*, 591, L3
Manara, C. F., Tazzari, M., Long, F., et al. 2019, Astronomy Astrophysics, 628, A95
Manara, C. F., Testi, L., Herczeg, G. J., et al. 2017, *Astron. Astrophys.*, 604, A127
Manara, C. F., Testi, L., Natta, A., & Alcalá, J. M. 2015, *Astron. Astrophys.*, 579, A66
Manara, C. F., Testi, L., Natta, A., et al. 2014, *Astron. Astrophys.*, 568, A18
Manara, C. F., Testi, L., Rigliaco, E., et al. 2013, *Astron. Astrophys.*, 551, A107
Mannings, V. 1994, *Mon. Not. R. Astron. Soc.*, 271, 587
Mannings, V. & Sargent, A. I. 1997, *Astrophys. J.*, 490, 792
Manoj, P., Ho, P. T. P., Ohashi, N., et al. 2007, *Astrophys. J. Lett.*, 667, L187

Marechal, Y., Coulomb, J. L., Meunier, G., & Touzot, G. 1994, IEEE Transactions on Magnetics, 30, 3558
Marel, N. v. d., Cazzoletti, P., Pinilla, P., & Garufi, A. 2016, The Astrophysical Journal, 832, 178
Marigo, P., Girardi, L., Bressan, A., et al. 2017, *Astrophys. J.*, 835, 77
Marino, S., Casassus, S., Perez, S., et al. 2015, *Astrophys. J.*, 813, 76
Marleau, G. D. & Cumming, A. 2014, *Mon. Not. R. Astron. Soc.*, 437, 1378
Marocco, F., Day-Jones, A. C., Lucas, P. W., et al. 2014, *Mon. Not. R. Astron. Soc.*, 439, 372
Marois, C., Correia, C., Véran, J.-P., & Currie, T. 2014, in IAU Symposium, Vol. 299, Exploring the Formation and Evolution of Planetary Systems, ed. M. Booth, B. C. Matthews, & J. R. Graham, 48–49
Marois, C., Doyon, R., Nadeau, D., et al. 2005, *Publ. Astron. Soc. Pac.*, 117, 745
Marois, C., Lafreniere, D., Doyon, R., Macintosh, B., & Nadeau, D. 2006, The Astrophysical Journal, 641, 556
Marois, C., Macintosh, B., Barman, T., et al. 2008, Science, 322, 1348
Marois, C., Macintosh, B., & Véran, J.-P. 2010a, Society of Photo-Optical Instrumentation Engineers (SPIE) Conference Series, Vol. 7736, Exoplanet imaging with LOCI processing: photometry and astrometry with the new SOSIE pipeline, 77361J
Marois, C., Zuckerman, B., Konopacky, Q. M., Macintosh, B., & Barman, T. 2010b, *Nature*, 468, 1080
Marsh, K. A. & Mahoney, M. J. 1992, *Astrophys. J. Lett.*, 395, L115
Martin, R. G. & Lubow, S. H. 2017, *Astrophys. J. Lett.*, 835, L28
Masset, F. & Snellgrove, M. 2001, *Mon. Not. R. Astron. Soc.*, 320, L55
Mathis, J. S., Rumpl, W., & Nordsieck, K. H. 1977, *Astrophys. J.*, 217, 425
Matter, A., Labadie, L., Augereau, J. C., et al. 2016, *Astron. Astrophys.*, 586, A11
Matter, A., Labadie, L., Kreplin, A., et al. 2014, *Astron. Astrophys.*, 561, A26
Matzner, C. D. & Levin, Y. 2005, *Astrophys. J.*, 628, 817
Mauron, N. & Dole, H. 1998, *Astron. Astrophys.*, 337, 808
Mawet, D., Choquet, É., Absil, O., et al. 2017a, *Astron. J.*, 153, 44
Mawet, D., Choquet, É., Absil, O., et al. 2017b, *Astron. J.*, 153, 44
Mawet, D., Milli, J., Wahhaj, Z., et al. 2014, *Astrophys. J.*, 792, 97
Mawet, D., Pueyo, L., Lawson, P., et al. 2012, Society of Photo-Optical Instrumentation Engineers (SPIE) Conference Series, Vol. 8442, Review of small-angle coronagraphic techniques in the wake of ground-based second-generation adaptive optics systems, 844204
Mayama, S., Hashimoto, J., Muto, T., et al. 2012, *Astrophys. J. Lett.*, 760, L26
Mayor, M., Marmier, M., Lovis, C., et al. 2011, ArXiv e-prints
Mayor, M. & Queloz, D. 1995, *Nature*, 378, 355
McClure, M. K., Bergin, E. A., Cleeves, L. I., et al. 2016, *Astrophys. J.*, 831, 167
Meeus, G., Montesinos, B., Mendigutía, I., et al. 2012, *Astron. Astrophys.*, 544, A78
Meeus, G., Waters, L. B. F. M., Bouwman, J., et al. 2001, *Astron. Astrophys.*, 365, 476
Mendigutía, I., Mora, A., Montesinos, B., et al. 2012, *Astron. Astrophys.*, 543, A59
Mendigutía, I., Oudmaijer, R. D., Garufi, A., et al. 2017a, *Astron. Astrophys.*, 608, A104
Mendigutía, I., Oudmaijer, R. D., Mourard, D., & Muzerolle, J. 2017b, *Mon. Not. R. Astron. Soc.*, 464, 1984
Mendigutía, I. 2013, Astronomische Nachrichten, 334, 129–132

Menu, J., van Boekel, R., Henning, T., et al. 2014, *Astron. Astrophys.*, 564, A93
Mesa, D., Bonnefoy, M., Gratton, R., et al. 2019, A&A, subm.
Miley, J., Panic, O., Wyatt, M., & Kennedy, G. 2018, ArXiv e-prints
Milli, J., Mouillet, D., Lagrange, A. M., et al. 2012, *Astron. Astrophys.*, 545, A111
Min, M. 2009, in Astronomical Society of the Pacific Conference Series, Vol. 414, Cosmic Dust - Near and Far, ed. T. Henning, E. Grün, & J. Steinacker, 356
Min, M. 2015, in European Physical Journal Web of Conferences, Vol. 102, European Physical Journal Web of Conferences, 00016
Min, M., Dullemond, C. P., Kama, M., & Dominik, C. 2011, , 212, 416
Min, M., Rab, C., Woitke, P., Dominik, C., & Ménard, F. 2016, *Astron. Astrophys.*, 585, A13
Min, M., Stolker, T., Dominik, C., & Benisty, M. 2017, *Astron. Astrophys.*, 604, L10
Miotello, A., Bruderer, S., & van Dishoeck, E. F. 2014, *Astron. Astrophys.*, 572, A96
Miotello, A., van Dishoeck, E. F., Kama, M., & Bruderer, S. 2016, VizieR Online Data Catalog, 359
Miotello, A., van Dishoeck, E. F., Williams, J. P., et al. 2017, *Astron. Astrophys.*, 599, A113
Miyake, K. & Nakagawa, Y. 1993, , 106, 20
Mizuno, H. 1980, Progress of Theoretical Physics, 64, 544
Molyarova, T., Akimkin, V., Semenov, D., et al. 2017, *Astrophys. J.*, 849, 130
Monnier, J. D., Berger, J.-P., Millan-Gabet, R., et al. 2006, The Astrophysical Journal, 647, 444
Montesinos, M., Perez, S., Casassus, S., et al. 2016, *Astrophys. J. Lett.*, 823, L8
Mora, A., Merín, B., Solano, E., et al. 2001, *Astron. Astrophys.*, 378, 116
Morbidelli, A., Bottke, W. F., Nesvorný, D., & Levison, H. F. 2009, , 204, 558
Morbidelli, A. & Crida, A. 2007, , 191, 158
Mordasini, C., Alibert, Y., Klahr, H., & Henning, T. 2012, Astronomy Astrophysics, 547, A111
Mouillet, D., Larwood, J. D., Papaloizou, J. C. B., & Lagrange, A. M. 1997, *Mon. Not. R. Astron. Soc.*, 292, 896
Mulders, G. D., Min, M., Dominik, C., Debes, J. H., & Schneider, G. 2013, *Astron. Astrophys.*, 549, A112
Mulders, G. D., Pascucci, I., Manara, C. F., et al. 2017, *Astrophys. J.*, 847, 31
Muro-Arena, G. A., Benisty, M., Ginski, C., et al. 2019, arXiv e-prints, arXiv:1911.09612
Muro-Arena, G. A., Dominik, C., Waters, L. B. F. M., et al. 2018, Astronomy Astrophysics, 614, A24
Muto, T., Grady, C. A., Hashimoto, J., et al. 2012, *Astrophys. J. Lett.*, 748, L22
Muto, T., Tsukagoshi, T., Momose, M., et al. 2015, *Publ. Astron. Soc. Jpn.*, 67, 122
Muzerolle, J., Allen, L. E., Megeath, S. T., Hernández, J., & Gutermuth, R. A. 2010, *Astrophys. J.*, 708, 1107
Muzerolle, J., Allen, L. E., Megeath, S. T., Hernández, J., & Gutermuth, R. A. 2009, The Astrophysical Journal, 708, 1107–1118
Najita, J. R. & Kenyon, S. J. 2014a, *Mon. Not. R. Astron. Soc.*, 445, 3315
Najita, J. R. & Kenyon, S. J. 2014b, *Mon. Not. R. Astron. Soc.*, 445, 3315
Nakagawa, Y., Sekiya, M., & Hayashi, C. 1986, , 67, 375
Natta, A., Grinin, V., & Mannings, V. 2000, Protostars and Planets IV, 559
Natta, A., Prusti, T., Neri, R., et al. 2001, *Astron. Astrophys.*, 371, 186

Natta, A., Testi, L., & Randich, S. 2006, *Astron. Astrophys.*, 452, 245
Nealon, R., Dipierro, G., Alexander, R., Martin, R. G., & Nixon, C. 2018, Monthly Notices of the Royal Astronomical Society, 481, 20–35
Nelder, J. A. & Mead, R. 1965, The Computer Journal, 7, 308
Neuhäuser, R. & Forbrich, J. 2008, The Corona Australis Star Forming Region, ed. B. Reipurth, 735
Ogilvie, G. I. & Lubow, S. H. 2002, *Mon. Not. R. Astron. Soc.*, 330, 950
Oja, T. 1987, *Astron. Astrophys. Supp. Ser.*, 68, 211
Okuzumi, S., Momose, M., Sirono, S.-i., Kobayashi, H., & Tanaka, H. 2016, *Astrophys. J.*, 821, 82
Okuzumi, S. & Ormel, C. W. 2013, *Astrophys. J.*, 771, 43
Olofsson, J., Benisty, M., Le Bouquin, J.-B., et al. 2013, *Astron. Astrophys.*, 552, A4
Ormel, C. W., Ida, S., & Tanaka, H. 2012, *Astrophys. J.*, 758, 80
Ormel, C. W. & Klahr, H. H. 2010, *Astron. Astrophys.*, 520, A43
Osorio, M., Anglada, G., Carrasco-González, C., et al. 2014, *Astrophys. J. Lett.*, 791, L36
Owen, J. 2015, in AAS/Division for Extreme Solar Systems Abstracts, Vol. 47, AAS/Division for Extreme Solar Systems Abstracts, 119.18
Owen, J. E. 2014, *Astrophys. J.*, 789, 59
Owen, J. E. 2016, , 33, e005
Owen, J. E., Ercolano, B., & Clarke, C. J. 2011, *Mon. Not. R. Astron. Soc.*, 411, 1104
Owen, J. E. & Lai, D. 2017, *Mon. Not. R. Astron. Soc.*, 469, 2834
Paardekooper, S. J., Baruteau, C., & Kley, W. 2011, *Mon. Not. R. Astron. Soc.*, 410, 293
Paardekooper, S. J. & Mellema, G. 2006, *Astron. Astrophys.*, 459, L17
Paardekooper, S. J. & Papaloizou, J. C. B. 2009, *Mon. Not. R. Astron. Soc.*, 394, 2283
Pairet, B., Cantalloube, F., Gomez Gonzalez, C. A., Absil, O., & Jacques, L. 2019, Monthly Notices of the Royal Astronomical Society, 487, 2262–2277
Panić, O. & Hogerheijde, M. R. 2009, *Astron. Astrophys.*, 508, 707
Panić, O., Hogerheijde, M. R., Wilner, D., & Qi, C. 2008, *Astron. Astrophys.*, 491, 219
Panić, O., Hogerheijde, M. R., Wilner, D., & Qi, C. 2009, *Astron. Astrophys.*, 501, 269
Papaloizou, J. & Lin, D. N. C. 1984, *Astrophys. J.*, 285, 818
Papaloizou, J. C. B., Nelson, R. P., Kley, W., Masset, F. S., & Artymowicz, P. 2007, Protostars and Planets V, 655
Pascucci, I., Testi, L., Herczeg, G. J., et al. 2016, *Astrophys. J.*, 831, 125
Pérez, L. M., Carpenter, J. M., Andrews, S. M., et al. 2016, Science, 353, 1519
Pérez, L. M., Carpenter, J. M., Chand ler, C. J., et al. 2012, *Astrophys. J. Lett.*, 760, L17
Pérez, L. M., Chandler, C. J., Isella, A., et al. 2015, *Astrophys. J.*, 813, 41
Pérez, L. M., Isella, A., Carpenter, J. M., & Chandler, C. J. 2014, *Astrophys. J. Lett.*, 783, L13
Perez, M. R., Grady, C. A., & The, P. S. 1993, *Astron. Astrophys.*, 274, 381
Pérez, S., Casassus, S., Hales, A., et al. 2020, *Astrophys. J. Lett.*, 889, L24
Perez, S., Casassus, S., Ménard, F., et al. 2015a, *Astrophys. J.*, 798, 85
Perez, S., Dunhill, A., Casassus, S., et al. 2015b, *Astrophys. J. Lett.*, 811, L5
Perrot, C., Boccaletti, A., Pantin, E., et al. 2016, *Astron. Astrophys.*, 590, L7
Perryman, M., Hartman, J., Bakos, G. Á., & Lindegren, L. 2014, *Astrophys. J.*, 797, 14
Pineda, J. E., Szulágyi, J., Quanz, S. P., et al. 2019, *Astrophys. J.*, 871, 48
Pinilla, P., Benisty, M., & Birnstiel, T. 2012a, *Astron. Astrophys.*, 545, A81

Pinilla, P., Birnstiel, T., Ricci, L., et al. 2012b, *Astron. Astrophys.*, 538, A114
Pinilla, P., Flock, M., Ovelar, M. d. J., & Birnstiel, T. 2016, *Astron. Astrophys.*, 596, A81
Pinilla, P., Tazzari, M., Pascucci, I., et al. 2018, *Astrophys. J.*, 859, 32
Pinilla, P., van der Marel, N., Pérez, L. M., et al. 2015, *Astron. Astrophys.*, 584, A16
Pinte, C., Fouchet, L., Ménard, F., Gonzalez, J. F., & Duchêne, G. 2007, *Astron. Astrophys.*, 469, 963
Pinte, C., Harries, T. J., Min, M., et al. 2009, *Astron. Astrophys.*, 498, 967
Pinte, C., Ménard, F., Duchêne, G., & Bastien, P. 2006, *Astron. Astrophys.*, 459, 797
Pinte, C., Ménard, F., Duchêne, G., et al. 2018a, *Astron. Astrophys.*, 609, A47
Pinte, C., Padgett, D. L., Ménard, F., et al. 2008, *Astron. Astrophys.*, 489, 633
Pinte, C., Price, D. J., Menard, F., et al. 2020, arXiv e-prints, arXiv:2001.07720
Pinte, C., Price, D. J., Ménard, F., et al. 2018b, *Astrophys. J. Lett.*, 860, L13
Pinte, C., van der Plas, G., Ménard, F., et al. 2019, Nature Astronomy, 3, 1109
Piétu, V., Dutrey, A., & Guilloteau, S. 2007, Astronomy Astrophysics, 467, 163–178
Pogodin, M. A., Franco, G. A. P., & Lopes, D. F. 2005, *Astron. Astrophys.*, 438, 239
Pohl, A., Benisty, M., Pinilla, P., et al. 2017a, *Astrophys. J.*, 850, 52
Pohl, A., Pinilla, P., Benisty, M., et al. 2015, *Mon. Not. R. Astron. Soc.*, 453, 1768
Pohl, A., Sissa, E., Langlois, M., et al. 2017b, *Astron. Astrophys.*, 605, A34
Pollack, J. B., Hubickyj, O., Bodenheimer, P., et al. 1996, , 124, 62
Pontoppidan, K. M., Blake, G. A., van Dishoeck, E. F., et al. 2008, *Astrophys. J.*, 684, 1323
Posselt, W., Holota, W., Kulinyak, E., et al. 2004, Society of Photo-Optical Instrumentation Engineers (SPIE) Conference Series, Vol. 5487, NIRSpec: near-infrared spectrograph for the JWST, ed. J. C. Mather, 688–697
Powell, D., Murray-Clay, R., Pérez, L. M., Schlichting, H. E., & Rosenthal, M. 2019, The Astrophysical Journal, 878, 116
Preibisch, T., Kraus, S., Driebe, T., van Boekel, R., & Weigelt, G. 2006, *Astron. Astrophys.*, 458, 235
Price, D. J., Cuello, N., Pinte, C., et al. 2018a, *Mon. Not. R. Astron. Soc.*, 477, 1270
Price, D. J. & Laibe, G. 2015, *Mon. Not. R. Astron. Soc.*, 451, 813
Price, D. J., Wurster, J., Tricco, T. S., et al. 2018b, , 35, e031
Pringle, J. E. 1981, , 19, 137
Pringle, J. E. & King, A. 2007, Astrophysical Flows
Pudritz, R. E. & Ray, T. P. 2019, Frontiers in Astronomy and Space Sciences, 6, 54
Pueyo, L., Crepp, J. R., Vasisht, G., et al. 2012, *Astrophys. J. Suppl.*, 199, 6
Pérez, L. M., Benisty, M., Andrews, S. M., et al. 2018, The Astrophysical Journal, 869, L50
Pérez, S., Casassus, S., Baruteau, C., et al. 2019, The Astronomical Journal, 158, 15
Qi, C., Öberg, K. I., Andrews, S. M., et al. 2015, *Astrophys. J.*, 813, 128
Qi, C., Öberg, K. I., Wilner, D. J., et al. 2013, Science, 341, 630
Quanz, S. P., Amara, A., Meyer, M. R., et al. 2015, *Astrophys. J.*, 807, 64
Quanz, S. P., Amara, A., Meyer, M. R., et al. 2013a, *Astrophys. J. Lett.*, 766, L1
Quanz, S. P., Avenhaus, H., Buenzli, E., et al. 2013b, *Astrophys. J. Lett.*, 766, L2
Quanz, S. P., Schmid, H. M., Geissler, K., et al. 2011, *Astrophys. J.*, 738, 23
Racine, R., Walker, G. A. H., Nadeau, D., Doyon, R., & Marois, C. 1999, *Publ. Astron. Soc. Pac.*, 111, 587

Rafikov, R. R. 2002, *Astrophys. J.*, 569, 997
Rafikov, R. R. 2005, *Astrophys. J. Lett.*, 621, L69
Ragusa, E., Dipierro, G., Lodato, G., Laibe, G., & Price, D. J. 2017, *Mon. Not. R. Astron. Soc.*, 464, 1449
Ragusa, E., Lodato, G., & Price, D. J. 2016, *Mon. Not. R. Astron. Soc.*, 460, 1243
Ragusa, E., Rosotti, G., Teyssandier, J., et al. 2018, *Mon. Not. R. Astron. Soc.*, 474, 4460
Rameau, J., Chauvin, G., Lagrange, A. M., et al. 2013, *Astrophys. J. Lett.*, 772, L15
Rameau, J., Follette, K. B., Pueyo, L., et al. 2017, *Astron. J.*, 153, 244
Regály, Z., Juhász, A., Sándor, Z., & Dullemond, C. P. 2012, *Mon. Not. R. Astron. Soc.*, 419, 1701
Reggiani, M., Christiaens, V., Absil, O., et al. 2017, ArXiv e-prints
Reggiani, M., Christiaens, V., Absil, O., et al. 2018, *Astron. Astrophys.*, 611, A74
Reggiani, M., Quanz, S. P., Meyer, M. R., et al. 2014, *Astrophys. J. Lett.*, 792, L23
Regály, Z., Király, S., & Kiss, L. L. 2014, The Astrophysical Journal, 785, L31
Reipurth, B. 1990, in IAU Symposium, Vol. 137, Flare Stars in Star Clusters, Associations and the Solar Vicinity, ed. L. V. Mirzoian, B. R. Pettersen, & M. K. Tsvetkov, 229
Rice, W. K. M., Armitage, P. J., Bonnell, I. A., et al. 2003, *Mon. Not. R. Astron. Soc.*, 346, L36
Rice, W. K. M., Armitage, P. J., Wood, K., & Lodato, G. 2006a, *Mon. Not. R. Astron. Soc.*, 373, 1619
Rice, W. K. M., Lodato, G., Pringle, J. E., Armitage, P. J., & Bonnell, I. A. 2004, *Mon. Not. R. Astron. Soc.*, 355, 543
Rice, W. K. M., Lodato, G., Pringle, J. E., Armitage, P. J., & Bonnell, I. A. 2006b, *Mon. Not. R. Astron. Soc.*, 372, L9
Rigliaco, E., Gratton, R., Mesa, D., et al. 2019, Astronomy Astrophysics, 632, A18
Rigliaco, E., Natta, A., Testi, L., et al. 2012, *Astron. Astrophys.*, 548, A56
Robberto, M., Gennaro, M., Gabellini, M. G. U., et al. 2020, HST survey of the Orion Nebula Cluster in the H_2O 1.4 m absorption band: I. A census of substellar and planetary mass objects
Rodigas, T. J., Stark, C. C., Weinberger, A., et al. 2015a, *Astrophys. J.*, 798, 96
Rodigas, T. J., Weinberger, A., Mamajek, E. E., et al. 2015b, *Astrophys. J.*, 811, 157
Rodmann, J., Henning, T., Chandler, C. J., Mundy, L. G., & Wilner, D. J. 2006, *Astron. Astrophys.*, 446, 211
Ros, K. & Johansen, A. 2013, *Astron. Astrophys.*, 552, A137
Rosenfeld, K. A., Andrews, S. M., Hughes, A. M., Wilner, D. J., & Qi, C. 2013a, *Astrophys. J.*, 774, 16
Rosenfeld, K. A., Andrews, S. M., Hughes, A. M., Wilner, D. J., & Qi, C. 2013b, *Astrophys. J.*, 774, 16
Rosenfeld, K. A., Andrews, S. M., Wilner, D. J., Kastner, J. H., & McClure, M. K. 2013c, *Astrophys. J.*, 775, 136
Rosenthal, E. D., Gurwell, M. A., & Ho, P. T. P. 1996, *Nature*, 384, 243
Rosotti, G. P., Benisty, M., Juhász, A., et al. 2019a, *Mon. Not. R. Astron. Soc.*, 2689
Rosotti, G. P., Ercolano, B., & Owen, J. E. 2015, *Mon. Not. R. Astron. Soc.*, 454, 2173
Rosotti, G. P., Ercolano, B., Owen, J. E., & Armitage, P. J. 2013, *Mon. Not. R. Astron. Soc.*, 430, 1392
Rosotti, G. P., Juhasz, A., Booth, R. A., & Clarke, C. J. 2016, *Mon. Not. R. Astron. Soc.*, 459, 2790

Rosotti, G. P., Tazzari, M., Booth, R. A., et al. 2019b, *Mon. Not. R. Astron. Soc.*, 486, 4829

Rubinstein, A. E., Macías, E., Espaillat, C. C., et al. 2018, *Astrophys. J.*, 860, 7

Ruge, J. P., Flock, M., Wolf, S., et al. 2016, *Astron. Astrophys.*, 590, A17

Ruíz-Rodríguez, D., Ireland, M., Cieza, L., & Kraus, A. 2016, *Mon. Not. R. Astron. Soc.*, 463, 3829

Rybicki, G. B. & Lightman, A. P. 1979, Radiative processes in astrophysics

Safronov, V. S. 1969, Evoliutsiia doplanetnogo oblaka.

Safronov, V. S. 1972, Evolution of the protoplanetary cloud and formation of the earth and planets.

Sallum, S., Follette, K. B., Eisner, J. A., et al. 2015, *Nature*, 527, 342

Sanchis, E., Testi, L., Natta, A., et al. 2020, Astronomy & Astrophysics, 633, A114

Sargent, A. I. & Beckwith, S. 1987, *Astrophys. J.*, 323, 294

Scardoni, C. E., Rosotti, G. P., Lodato, G., & Clarke, C. J. 2020, *Mon. Not. R. Astron. Soc.*, 492, 1318

Schisano, E., Covino, E., Alcalá, J. M., et al. 2009, *Astron. Astrophys.*, 501, 1013

Setterholm, B. R., Monnier, J. D., Davies, C. L., et al. 2018, *Astrophys. J.*, 869, 164

Shakura, N. I. & Sunyaev, R. A. 1973, A&A, 24, 337

Shakura, N. I. & Sunyaev, R. A. 1973, *Astron. Astrophys.*, 500, 33

Shu, F. H. 1977, *Astrophys. J.*, 214, 488

Shu, F. H., Adams, F. C., & Lizano, S. 1987, , 25, 23

Siebenmorgen, R., Prusti, T., Natta, A., & Müller, T. G. 2000, *Astron. Astrophys.*, 361, 258

Sierra, A. & Lizano, S. 2020, The Astrophysical Journal, 892, 136

Siess, L., Dufour, E., & Forestini, M. 2000, *Astron. Astrophys.*, 358, 593

Simbulan, C., Tamayo, D., Petrovich, C., Rein, H., & Murray, N. 2017, *Mon. Not. R. Astron. Soc.*, 469, 3337

Simon, J. B. & Armitage, P. J. 2014, *Astrophys. J.*, 784, 15

Simon, J. B., Armitage, P. J., Li, R., & Youdin, A. N. 2016, *Astrophys. J.*, 822, 55

Simon, J. B., Hughes, A. M., Flaherty, K. M., Bai, X.-N., & Armitage, P. J. 2015, *Astrophys. J.*, 808, 180

Sissa, E., Gratton, R., Garufi, A., et al. 2018, *Astron. Astrophys.*, 619, A160

Skemer, A. J., Hinz, P., Montoya, M., et al. 2015, Society of Photo-Optical Instrumentation Engineers (SPIE) Conference Series, Vol. 9605, First light with ALES: A 2-5 micron adaptive optics Integral Field Spectrograph for the LBT, 96051D

Smallwood, J. L., Lubow, S. H., Franchini, A., & Martin, R. G. 2019, Monthly Notices of the Royal Astronomical Society, 486, 2919–2932

Smith, B. A. & Terrile, R. J. 1984, Science, 226, 1421

Smith, N., Bally, J., Licht, D., & Walawender, J. 2005, Astronomical Journal, 129, 382

Smith, W. H. 1987, *Publ. Astron. Soc. Pac.*, 99, 1344

Soderblom, D. R. 2015, in Asteroseismology of Stellar Populations in the Milky Way, Vol. 39, 3

Soummer, R., Ferrari, A., Aime, C., & Jolissaint, L. 2007, *Astrophys. J.*, 669, 642

Soummer, R., Pueyo, L., & Larkin, J. 2012, *Astrophys. J. Lett.*, 755, L28

Sparks, W. B. & Ford, H. C. 2002, *Astrophys. J.*, 578, 543

Stamatellos, D. & Whitworth, A. P. 2009, *Mon. Not. R. Astron. Soc.*, 392, 413

Stammler, S. M., Birnstiel, T., Panić, O., Dullemond, C. P., & Dominik, C. 2017, *Astron.*

Astrophys., 600, A140
Stephens, I. W., Yang, H., Li, Z.-Y., et al. 2017, *Astrophys. J.*, 851, 55
Stepinski, T. F. & Valageas, P. 1996, *Astron. Astrophys.*, 309, 301
Stevenson, D. J. 1991, , 29, 163
Stolker, T., Dominik, C., Avenhaus, H., et al. 2016, *Astron. Astrophys.*, 595, A113
Stolker, T., Dominik, C., Min, M., et al. 2016, Astronomy Astrophysics, 596, A70
Stolker, T., Sitko, M., Lazareff, B., et al. 2017, *Astrophys. J.*, 849, 143
Strom, K. M., Strom, S. E., Edwards, S., Cabrit, S., & Skrutskie, M. F. 1989a, *Astron. J.*, 97, 1451
Strom, K. M., Strom, S. E., Edwards, S., Cabrit, S., & Skrutskie, M. F. 1989b, *Astron. J.*, 97, 1451
Su, K. Y. L., MacGregor, M. A., Booth, M., et al. 2017, *Astron. J.*, 154, 225
Syer, D. & Clarke, C. J. 1995, *Mon. Not. R. Astron. Soc.*, 277, 758
Szulágyi, J., Dullemond, C. P., Pohl, A., & Quanz, S. P. 2019, *Mon. Not. R. Astron. Soc.*, 487, 1248
Szulágyi, J., Plas, G. v. d., Meyer, M. R., et al. 2018, *Mon. Not. R. Astron. Soc.*, 473, 3573
Szulágyi, J. & Mordasini, C. 2016, Monthly Notices of the Royal Astronomical Society: Letters, 465, L64–L68
Taha, A. S., Labadie, L., Pantin, E., et al. 2018, *Astron. Astrophys.*, 612, A15
Takami, M., Bailey, J., & Chrysostomou, A. 2003, *Astron. Astrophys.*, 397, 675
Takeuchi, T., Miyama, S. M., & Lin, D. N. C. 1996, *Astrophys. J.*, 460, 832
Tan, J. C., Beltrán, M. T., Caselli, P., et al. 2014, in Protostars and Planets VI, ed. H. Beuther, R. S. Klessen, C. P. Dullemond, & T. Henning, 149
Tang, Y.-W., Guilloteau, S., Dutrey, A., et al. 2017, *Astrophys. J.*, 840, 32
Tazzari, M., Testi, L., Ercolano, B., et al. 2016, *Astron. Astrophys.*, 588, A53
Teague, R., Bae, J., Bergin, E. A., Birnstiel, T., & Foreman-Mackey, D. 2018, The Astrophysical Journal, 860, L12
Teague, R., Guilloteau, S., Semenov, D., et al. 2016, *Astron. Astrophys.*, 592, A49
Terebey, S., Shu, F. H., & Cassen, P. 1984, *Astrophys. J.*, 286, 529
Testi, L., Birnstiel, T., Ricci, L., et al. 2014, Protostars and Planets VI, 339
Testi, L., Natta, A., Shepherd, D. S., & Wilner, D. J. 2001, *Astrophys. J.*, 554, 1087
Testi, L., Natta, A., Shepherd, D. S., & Wilner, D. J. 2003, *Astron. Astrophys.*, 403, 323
Thalmann, C., Janson, M., Garufi, A., et al. 2016, *Astrophys. J. Lett.*, 828, L17
Thalmann, C., Mulders, G. D., Hodapp, K., et al. 2014, *Astron. Astrophys.*, 566, A51
Thatte, N., Abuter, R., Tecza, M., et al. 2007, Monthly Notices of the Royal Astronomical Society, 378, 1229–1236
Thé, P. S., de Winter, D., & Perez, M. R. 1994, *Astron. Astrophys. Supp. Ser.*, 104, 315
Thi, W. F., van Dishoeck, E. F., Blake, G. A., et al. 2001, *Astrophys. J.*, 561, 1074
Thommes, E. W., Duncan, M. J., & Levison, H. F. 2003, , 161, 431
Tielens, A. G. G. M., Tokunaga, A. T., Geballe, T. R., & Baas, F. 1991, *Astrophys. J.*, 381, 181
Tinbergen, J. 2005, Astronomical Polarimetry, by Jaap Tinbergen, Cambridge, UK: Cambridge University Press, 2005
Tjin A Djie, H. R. E., The, P. S., Andersen, J., et al. 1989, *Astron. Astrophys. Supp. Ser.*, 78, 1
Tobin, J. J., Hartmann, L., Chiang, H.-F., et al. 2011, *Astrophys. J.*, 740, 45

Tobin, J. J., Kratter, K. M., Persson, M. V., et al. 2016, *Nature*, 538, 483
Toci, C., Lodato, G., Fedele, D., Testi, L., & Pinte, C. 2020, *Astrophys. J. Lett.*, 888, L4
Tohline, J. E. 2002, , 40, 349
Tomida, K., Machida, M. N., Hosokawa, T., Sakurai, Y., & Lin, C. H. 2017, *Astrophys. J. Lett.*, 835, L11
Toomre, A. 1964, *Astrophys. J.*, 139, 1217
Trapman, L., Ansdell, M., Hogerheijde, M. R., et al. 2020, *Astron. Astrophys.*, 638, A38
Trapman, L., Miotello, A., Kama, M., van Dishoeck, E. F., & Bruderer, S. 2017, *Astron. Astrophys.*, 605, A69
Tripathi, A., Andrews, S. M., Birnstiel, T., & Wilner, D. J. 2017, *Astrophys. J.*, 845, 44
Trotta, F., Testi, L., Natta, A., Isella, A., & Ricci, L. 2013, *Astron. Astrophys.*, 558, A64
Troup, N. W., Nidever, D. L., De Lee, N., et al. 2016, *Astron. J.*, 151, 85
Turner, N. J., Fromang, S., Gammie, C., et al. 2014, in Protostars and Planets VI, ed. H. Beuther, R. S. Klessen, C. P. Dullemond, & T. Henning, 411
Ubeira-Gabellini, M. G., Christiaens, V., Lodato, G., et al. 2020, The Astrophysical Journal, 890, L8
Ubeira Gabellini, M. G., Miotello, A., Facchini, S., et al. 2019, Monthly Notices of the Royal Astronomical Society, 486, 4638–4654
Uyama, T., Muto, T., Mawet, D., et al. 2020, The Astronomical Journal, 159, 118
van Boekel, R., Henning, T., Menu, J., et al. 2017, *Astrophys. J.*, 837, 132
van Boekel, R., Waters, L. B. F. M., Dominik, C., et al. 2003, *Astron. Astrophys.*, 400, L21
van den Ancker, M. E., de Winter, D., & Tjin A Djie, H. R. E. 1998, *Astron. Astrophys.*, 330, 145
van der Marel, N., Pinilla, P., Tobin, J., et al. 2015, *Astrophys. J. Lett.*, 810, L7
van der Marel, N., van Dishoeck, E. F., Bruderer, S., et al. 2016, *Astron. Astrophys.*, 585, A58
van der Marel, N., van Dishoeck, E. F., Bruderer, S., et al. 2013, Science, 340, 1199
van der Marel, N., Verhaar, B. W., van Terwisga, S., et al. 2016, Astronomy & Astrophysics, 592, A126
van der Marel, N., Williams, J. P., Ansdell, M., et al. 2018, *Astrophys. J.*, 854, 177
van der Plas, G., Ménard, F., Canovas, H., et al. 2017a, *Astron. Astrophys.*, 607, A55
van der Plas, G., Ménard, F., Gonzalez, J. F., et al. 2019, *Astron. Astrophys.*, 624, A33
van der Plas, G., van den Ancker, M. E., Waters, L. B. F. M., & Dominik, C. 2015, *Astron. Astrophys.*, 574, A75
van der Plas, G., Wright, C. M., Ménard, F., et al. 2017b, *Astron. Astrophys.*, 597, A32
van Dishoeck, E. F. 2014, Faraday Discuss., 168, 9
van Dishoeck, E. F. & Black, J. H. 1988, *Astrophys. J.*, 334, 771
van Terwisga, S. E., van Dishoeck, E. F., Ansdell, M., et al. 2018, *Astron. Astrophys.*, 616, A88
van Zadelhoff, G.-J., van Dishoeck, E. F., Thi, W.-F., & Blake, G. A. 2001, *Astron. Astrophys.*, 377, 566
Veronesi, B., Lodato, G., Dipierro, G., et al. 2019, *Mon. Not. R. Astron. Soc.*, 489, 3758
Veronesi, B., Ragusa, E., Lodato, G., et al. 2020, Monthly Notices of the Royal Astronomical Society, 495, 1913–1926
Vieira, S. L. A., Corradi, W. J. B., Alencar, S. H. P., et al. 2003, *Astron. J.*, 126, 2971
Vigan, A., Langlois, M., Moutou, C., & Dohlen, K. 2008, Society of Photo-Optical In-

strumentation Engineers (SPIE) Conference Series, Vol. 7014, Long slit spectroscopy for exoplanet characterization in SPHERE, 70144M
Vink, J. S., O'Neill, P. M., Els, S. G., & Drew, J. E. 2005, *Astron. Astrophys.*, 438, L21
Vioque, M., Oudmaijer, R. D., Baines, D., Mendigutía, I., & Pérez-Martínez, R. 2018a, *Astron. Astrophys.*, 620, A128
Vioque, M., Oudmaijer, R. D., Baines, D., Mendigutía, I., & Pérez-Martínez, R. 2018b, *Astron. Astrophys.*, 620, A128
Visser, R., van Dishoeck, E. F., & Black, J. H. 2009, *Astron. Astrophys.*, 503, 323
Vural, J., Kreplin, A., Kraus, S., et al. 2012, *Astron. Astrophys.*, 543, A162
Wagner, K., Apai, D., Kasper, M., et al. 2016, Science, 353, 673
Wagner, K., Apai, D., Kasper, M., & Robberto, M. 2015, *Astrophys. J. Lett.*, 813, L2
Wagner, K., Dong, R., Sheehan, P., et al. 2018, *Astrophys. J.*, 854, 130
Walker, M. F. 1956, *Astrophys. J. Suppl.*, 2, 365
Walmswell, J., Clarke, C., & Cossins, P. 2013, *Mon. Not. R. Astron. Soc.*, 431, 1903
Walsh, C., Daley, C., Facchini, S., & Juhász, A. 2017, *Astron. Astrophys.*, 607, A114
Walsh, C., Juhász, A., Pinilla, P., et al. 2014, *Astrophys. J. Lett.*, 791, L6
Walsh, K. J., Morbidelli, A., Raymond, S. N., O'Brien, D. P., & Mandell, A. M. 2011, *Nature*, 475, 206
Ward, W. R. 1991, in Lunar and Planetary Science Conference, Vol. 22, Lunar and Planetary Science Conference, 1463
Waters, L. B. F. M. & Waelkens, C. 1998, , 36, 233
Weidenschilling, S. J. 1977, *Astrophys. Space Sci.*, 51, 153
Weigelt, G., Grinin, V. P., Groh, J. H., et al. 2011, *Astron. Astrophys.*, 527, A103
Weingartner, J. C. & Draine, B. T. 2001, *Astrophys. J.*, 548, 296
Wertz, O., Absil, O., Gómez González, C. A., et al. 2017, *Astron. Astrophys.*, 598, A83
Westmoquette, M. S., Exter, K. M., Christensen, L., et al. 2009, arXiv e-prints, arXiv:0905.3054
Wheelwright, H. E., Oudmaijer, R. D., & Goodwin, S. P. 2010, *Mon. Not. R. Astron. Soc.*, 401, 1199
Whipple, F. L. 1972, in From Plasma to Planet, ed. A. Elvius, 211
White, J. A. & Boley, A. C. 2018, *Astrophys. J.*, 859, 103
White, J. A., Boley, A. C., Hughes, A. M., et al. 2016, *Astrophys. J.*, 829, 6
Whitney, B. A., Robitaille, T. P., Bjorkman, J. E., et al. 2013, *Astrophys. J. Suppl.*, 207, 30
Whittet, D. C. B., Kirrane, T. M., Kilkenny, D., et al. 1987, *Mon. Not. R. Astron. Soc.*, 224, 497
Williams, J. P. 2012, Meteoritics and Planetary Science, 47, 1915
Williams, J. P. & Best, W. M. J. 2014, *Astrophys. J.*, 788, 59
Williams, J. P. & Cieza, L. A. 2011, , 49, 67
Windmark, F., Birnstiel, T., Güttler, C., et al. 2012a, *Astron. Astrophys.*, 540, A73
Windmark, F., Birnstiel, T., Ormel, C. W., & Dullemond, C. P. 2012b, *Astron. Astrophys.*, 544, L16
Winn, J. N. & Fabrycky, D. C. 2015, , 53, 409
Woitke, P., Min, M., Pinte, C., et al. 2016, *Astron. Astrophys.*, 586, A103
Wolf, S. & Voshchinnikov, N. V. 2004, Computer Physics Communications, 162, 113
Wolk, S. J. & Walter, F. M. 1996, *Astron. J.*, 111, 2066
Wolszczan, A. 1994, Science, 264, 538

Wolszczan, A. & Frail, D. A. 1992, *Nature*, 355, 145
Wu, Y.-L., Close, L. M., Eisner, J. A., & Sheehan, P. D. 2017, The Astronomical Journal, 154, 234
Wyatt, M. C. 2018, Debris Disks: Probing Planet Formation, 146
Yen, H.-W., Koch, P. M., Manara, C. F., Miotello, A., & Testi, L. 2018, ArXiv e-prints
Youdin, A. & Johansen, A. 2007, *Astrophys. J.*, 662, 613
Youdin, A. N. & Goodman, J. 2005, *Astrophys. J.*, 620, 459
Young, M. D. & Clarke, C. J. 2015, *Mon. Not. R. Astron. Soc.*, 452, 3085
Yu, M., Evans, Neal J., I., Dodson-Robinson, S. E., Willacy, K., & Turner, N. J. 2017, *Astrophys. J.*, 841, 39
Yu, M., Willacy, K., Dodson-Robinson, S. E., Turner, N. J., & II, N. J. E. 2016, The Astrophysical Journal, 822, 53
Zhang, K., Bergin, E. A., Blake, G. A., Cleeves, L. I., & Schwarz, K. R. 2017, Nature Astronomy, 1, 0130
Zhang, K., Isella, A., Carpenter, J. M., & Blake, G. A. 2014, *Astrophys. J.*, 791, 42
Zhang, S., Zhu, Z., Huang, J., et al. 2018, *Astrophys. J. Lett.*, 869, L47
Zhu, Z. 2015, *Astrophys. J.*, 799, 16
Zhu, Z., Hartmann, L., Nelson, R. P., & Gammie, C. F. 2012a, *Astrophys. J.*, 746, 110
Zhu, Z., Nelson, R. P., Dong, R., Espaillat, C., & Hartmann, L. 2012b, *Astrophys. J.*, 755, 6
Zhu, Z., Nelson, R. P., Hartmann, L., Espaillat, C., & Calvet, N. 2011, *Astrophys. J.*, 729, 47
Zhu, Z., Zhang, S., Jiang, Y.-F., et al. 2019, *Astrophys. J. Lett.*, 877, L18
Zorec, J., Frémat, Y., Domiciano de Souza, A., et al. 2016, *Astron. Astrophys.*, 595, A132
Zurlo, A., Vigan, A., Galicher, R., et al. 2016, *Astron. Astrophys.*, 587, A57

List of Publications

Refereed publications

1) M. Robberto, Gennaro, **M. G. Ubeira Gabellini**, et al.: "HST survey of the Orion Nebula Cluster in the H_2O 1.4 μm absorption band: I. A census of substellar and planetary mass objects", AAS paper, accepted, 2020.

2) **M. G. Ubeira Gabellini**, V. Christiaens, G. Lodato, D. Fedele, M. van den Ancker, C.F. Manara, D. Price: "Discovery of a low-mass companion embedded in the disk of the young massive star MWC 297", ApJL, Feb. 2020, 890, 1, L8.

3) **M. G. Ubeira Gabellini**, A. Miotello, S. Facchini, E. Ragusa, G. Lodato , L. Testi, et al.: "A dust and gas cavity in the disc around CQ Tau revealed by ALMA" MNRAS paper, publ., 2019, 486, 4638-4654.

4) K. Hirsh, D. J. Price, J-F Gonzalez, **M. G. Ubeira-Gabellini**, E. Ragusa: "On the cavity size in circumbinary discs", MNRAS paper, in pres., Aug. 2020.

5) E. Rigliaco, R. Gratton, D. Mesa, V. D'Orazi, M. Bonnefoy, J.M. Alcalá, S. Antoniucci, F. Bacciotti, M. Dima, B. Nisini, L. Podio, M. Barbieri, R. Claudi, S. Desidera, A. Garufi, E. Hugot, M. Janson, M. Langlois, E.L. Rickman, E. Sissa, **M. Ubeira Gabellini**, et al.: "Investigating the nature of the extended structure around the Herbig star RCrA using integral field and high-resolution spectroscopy", A&A paper, 2019.

6) D. Mesa, M. Bonnefoy, R. Gratton, Van Der Plas, V. D'Orazi, E. Sissa, A. Zurlo, E. Rigliaco, T. Schmidt, M. Langlois, A. Vigan, **M.G. Ubeira Gabellini** et al.: "Exploring the RCrA environment with SPHERE: Discovery of a new stellar companion", A&A paper, publ., 2019, 624, A4.

7) K.L. Luhman, M. Robberto, J.C. Tan, M. Andersen, **M.G. Ubeira Gabellini**, et al.: "New evidence for the dynamical decay of a multiple system in the Orion Kleinmann-Low Nebula", ApJ paper, publ., 2017, 838, L3.

Publications in preparation

1) **M. G. Ubeira Gabellini**, M. van den Ancker, D. Fedele, G. Lodato, V. Christiaens, C.F. Manara: "An heterogeneous SPHERE-IFS Survey of Nearby Herbig Ae/Be Stars: Are All Group I Discs Transitional?", MNRAS paper, in prep., 2020.

2) K. Hirsh, **M. G. Ubeira-Gabellini**, D. J. Price,C. Pinte, J-F Gonzalez, G.Lodato: "Observational appearance of circumbinary discs", MNRAS paper, in prep., 2020.

3) L. Wölfer, S. Facchini, N.T. Kurtovic, R. Teague, E.F. van Dishoeck, M. Benisty, B. Ercolano, G. Lodato, A. Miotello, L.M. Perez, G. Rosotti, L.Testi, **M. G. Ubeira Gabellini** "A highly non-Keplerian protoplanetary disc. Spiral structure in the gas disc of CQ Tau", A&A paper, in prep., 2020.

Publications in conference proceedings or in not-referred journals

1) **M. G. Ubeira Gabellini**, M. van den Ancker, D. Fedele, G. Lodato, C.F. Manara: "A new Companion Candidate around the Herbig Star V921 Sco", RNAAS, 2019, 3,4.

2) **M. G. Ubeira Gabellini**, M. E. van den Ancker, D. Fedele, G. Lodato and C.F. Manara: "An Unbiased SPHERE-IFS Survey of Nearby Herbig Ae/Be Stars: Are All Group I Disks Transitional?" Proceedings IAU Symposium No. 345, 2019.

3) Lodato, G., Veronesi, B., **Ubeira Gabellini, M.**, Ragusa, E., Franchini, A., Dipierro, G.: "Planet formation in the ALMA era", Toward a Science Campus in Milan: A Snapshot of Current Research at the Physics Department Aldo Pontremoli, Springer International Publishing, 2018.

Acknowledgments

For completeness, I report below the formal acknowledgements sections of the individual Chapter of my thesis which are published or in preparation. After that I report the general acknowledgements.

Chapter 5: The first published paper makes use of the following ALMA data: ADS/JAO.ALMA#2013.1.00498.S, ADS/JAO.ALMA#2016.A.000026.S, and ADS/JAO.ALMA#2017.1.01404.S. ALMA is a partnership of ESO (representing its member states), NSF (USA) and NINS (Japan), together with NRC (Canada) and NSC and ASIAA (Taiwan) and KASI (Republic of Korea), in cooperation with the Republic of Chile. The Joint ALMA Observatory is operated by ESO, auI/NRAO and NAOJ. This work was partly supported by the Italian Ministero dell´ Istruzione, Università e Ricerca through the grant Progetti Premiali 2012 – iALMA (CUP C52I13000140001), by the Deutsche Forschungs-gemeinschaft (DFG, German Research Foundation) - Ref no. FOR 2634/1 TE 1024/1-1, and by the DFG cluster of excellence Origin and Structure of the Universe (www.universe-cluster.de). We are thankful to Antonella Natta, Antonio Garufi, Mario van den Ancker, Carlo F. Manara, Philippe Delorme, Sabine Moehler, Maddalena Reggiani and Elena Sissa for useful discussions.

Chapter 7: The paper in preparation made use of the SPHERE Data Centre, jointly operated by OSUG/IPAG (Grenoble), PYTHEAS/LAM/CeSAM (Marseille), OCA/Lagrange (Nice) and Observatoire de Paris/LESIA (Paris) and supported by a grant from Labex OSUG@2020 (Investissements d'avenir – ANR10 LABX56). We thank Laszlo Szucs and Cornelis P. Dullemond for usefull discussions about the RADMC3D code and to Christophe Pinte, regarding the results obtained and presented in the Appendix C.1.

Chapter 8: The second published paper has made use of the SPHERE Data Centre, jointly operated by OSUG/IPAG (Grenoble), PYTHEAS/LAM/CeSAM (Marseille), OCA/Lagrange (Nice) and Observatoire de Paris/LESIA (Paris) and supported by a grant from Labex OSUG@2020 (Investissements d'avenir – ANR10 LABX56). In particulary we thank Philippe Delorme, Sabine Moehler and Elena Sissa for usefull discussions.

Chapter 9: For what regards the preliminary results presented in this Chap., we thank Maddalena Reggiani and Valentin Christiaens for useful discussion about the VIP code and developments of novel routines.

I had received funding from the European Union's Horizon 2020 research and innovation programme under the Marie Skłodowska-Curie grant agreement No 823823 (RISE DUSTBUSTERS project) and from an ESO studenship. Moreover, I acknowledge Prof. G. Lodato, Dr. D. Fedele who supervised me for the entire period of the PhD, Dr. L. Testi and Dr. M. van den Ancker for the time spent during a one year ESO studentship and finally Prof. D. Price, Dr. C. Pinte and Dr. V. Christiaens for the three months spent in Melbourne thanks to the DUSTBUSTERS collaboration. Each of these times were extremely useful to build part of this PhD. Finally, I am grateful for all the discussions born within the DUSTERBUSTERS collaboration and during the ESO Star and Planet formation meetings, forge of new ideas and productivity. An open eye on different projects was essential to keep always high the passion for science.

More personally, I want to acknowledge a number of people that were fundamental throughout these years for the scientific and personal growth. First of all I want to acknowledge Prof. G. Lodato and Dr. D. Fedele. Their presence was indeed essential both during exciting and difficult periods: with their guidance, they give me the strength to move forward also when the path seemed to be not smooth. A special thanks is for Dr. V. Christiaens: his collaboration was essential for the success of the work. Together with a nice collaborator, I found also a real friend. I want to thank the colleagues and friends Claudia, Benni, Marti, Enri, Gianni, Noemi, Chiara, Giulia, Alessia and Hossam that were always present to help both from a technical point of view or with a word or a smile. I want also to thank all my family, my mum Anna and my father José Luis, my aunt Laura, my cousins Chiara, Michele, Chiara, Giorgio, Ale, Sofi, Franci, Simo, Carlo, Fede and family friends Emma, Sandro and Angela who supported me throughout all the personal career. A special thanks is also for Don Giorgio and Don Michele who help me to understand that everything that happen is for something good. Thanks to them, I had the support needed to sail even in rough waters. I want also to thank all the friends - the list of everyone is too long - in particular Giulia, Andrea, Peppe, Cate, Silvia, Shaggy, Agne, Davide, Miriam for their concrete presence during these years. I thank Silvia and Chiara for the useful suggestions regarding an artistic perspective. Finally, I want to thank Max who shared with me the weight of not easy choices and because he was always present to find ways to enjoy the work. Last but not least, I want to thank the referee Prof. Laura Perez and Dr. Antonio Garufi for carefully reading this manuscript. Their comments helped greatly indeed to improve the thesis.